IAEA-TECDOC-1163 (electronic version)

Heat Transport and Afterheat Removal for Gas Cooled Reactors Under Accident Conditions

IAEA

The originating Section of this publication in the IAEA was:
Nuclear Power Technology Development Section
International Atomic Energy Agency
Wagramerstrasse 5
P.O. Box 100
A-1400 Vienna, Austria

Heat Transport and Afterheat Removal for Gas Cooled Reactors Under Accident Conditions
IAEA, VIENNA, 2000
IAEA-TECDOC-1163

FOREWORD

The Co-ordinate Research Project (CRP) on Heat Transport and Afterheat Removal for Gas-Cooled Reactors Under Accident Conditions was organised within the frame of the International Working Group on Gas Cooled Reactors (IWGGCR). This International Working Group serves as a forum for exchange of information on national programmes, provides advice to the IAEA on international co-operative activities in advanced technologies of gas cooled reactors (GCRs), and supports the conduct of these activities.

Advanced GCR designs currently being developed are predicted to achieve a high degree of safety through reliance on inherent safety features. Such design features should permit the technical demonstration of exceptional public protection with significantly reduced emergency planning requirements. For advanced GCRs, this predicted high degree of safety largely derives from the ability of the ceramic coated fuel particles to retain the fission products under normal and accident conditions, the safe neutron physics behaviour of the core, the chemical stability of the core and the ability of the design to dissipate decay heat by natural heat transport mechanisms without reaching excessive temperatures. Prior to licensing and commercial deployment of advanced GCRs, these features must first be demonstrated under experimental conditions representing realistic reactor conditions, and the methods used to predict the performance of the fuel and reactor must be validated against these experimental data. Within this CRP, the participants addressed the inherent mechanisms for removal of decay heat from GCRs under accident conditions.

The objective of this CRP was to establish sufficient experimental data at realistic conditions and validated analytical tools to confirm the predicted safe thermal response of advance gas cooled reactors during accidents. The scope includes experimental and analytical investigations of heat transport by natural convection conduction and thermal radiation within the core and reactor vessel, and afterheat removal from the reactor. Code-to-code and code-to-experiment benchmarks were performed for verification and validation of the analytical methods.

The following Member State national institutions participated in the performance of this CRP:

Institute of Nuclear Energy Technology (INET)	China
Commissariat a l'Energie Atomique (CEA)	France
Forschungszentrum Julich (FZJ)	Germany
Japan Atomic Energy Research Institute (JAERI)	Japan
Netherlands Energy Research Foundation (ECN)	The Netherlands
OKBM	Russian Federation
Oak Ridge National Laboratory (ORNL)	USA

This report has been edited by H. Niessen (FZJ) and S. Ball (ORNL), and documents the CRP activities with respect to the technical areas of code-to-code and code-to-experiment validation of code predictions for normal operation and loss of cooling accidents with and without simultaneous depressurisation. The tests and calculations addressed GCR heat transfer phenomena inside the reactor vessel as well as in the reactor cavity external to the reactor vessel.

EDITORIAL NOTE

In preparing this publication for press, staff of the IAEA have made up the pages from the original manuscript(s). The views expressed do not necessarily reflect those of the IAEA, the governments of the nominating Member States or the nominating organizations.

Throughout the text names of Member States are retained as they were when the text was compiled.

The use of particular designations of countries or territories does not imply any judgment by the publisher, the IAEA, as to the legal status of such countries or territories, of their authorities and institutions or of the delimitation of their boundaries.

The mention of names of specific companies or products {whether or not indicated as registered) does not imply any intention to infringe proprietary rights, nor should it be construed as an endorsement or recommendation on the part of the IAEA.

CONTENTS

CHAPTER 1

INTRODUCTION

The background for the general problem of GCR heat removal, along with the rationale for the Coordinated Research Project Charter, is described in Chapter 2. In the modular GCRs, much emphasis is put on passive heat removal systems for the reactor vessel cavity. These systems can function as the primary means of heat removal in the ultimate accident - a postulated failure of all active cooling (including loss of coolant pressurization) and shutdown systems. The fact that the modern GCRs can safely survive this type of hypothetical accident places a greater emphasis on the design of vessel cavity cooling systems and validation of the vessel cavity cooling phenomena, as represented by the codes.

Chapter 3 deals with code to code benchmark problems, describing the calculational models and comparing results for the following cases:

– **VGM RCCS Mockup** - Code-to code benchmark exercises were performed using the Russian VGM RCCS mockup as described in section 3.1. The description of the benchmark problem was provided by OKBM (Russia). The participants of the Benchmark are INET (China), OKBM (Russia), ORNL (USA). Solution of the benchmark was useful from the viewpoint of results comparison obtained by using different codes, and of making clear some problems connected with heat transfer from the reactor vessel to the cooling panel.

– **HTTR Analysis of Heat Up Accidents** - The loss of core flow accident simulation in the depressurized condition of HTTR Heat up accident was selected as another benchmark problem (section 3.2). In the simulation, all circulators of the primary PWC stop without the reactor scram. Results of short term and long term calculations obtained by GRSAC (USA), IGM and GTAS (Russia) and THYDE-HTGR (Japan) codes were compared.

– **HTR-10 Analysis of Heat Up Accidents** – Four benchmark problems of MTERR-10 are defined in section 3.3 to verify the heat transport ability of the RCCS of HTR-10 and validate the computer codes. The HTR-10 reactor is a high temperature gas-cooled test reactor being built in INET, China. This project aims to research the application of HTR including steam generation, steam-cycle, process heat generation and methane reforming and to verify the inherent safety of HTR and also to develop technology in China. The HTR-10 reactor has two independent passive reactor cavity cooling systems (RCCS) to remove afterheat from reactor during accidents.

– **GT-MHR Plutonium Burner** - The benchmark problem for the GT-MHR Plutonium Burner plant design (section 3.4) was provided by the US, with analysis contributions from China, Netherlands, Russian Federation, and US. The problem consists of calculating RCCS performance and core conditions for normal operation, plus the response to long-term LOFC accidents with scram both with and without a postulated depressing action.

Chapter 4 deals with code to experimental benchmark problems, describing the experimental data and calculational models, and comparing results for the following cases:

– **HTTR RCCS Mockup** – This problem described in section 4.1, provided a comparison between code calculations and a comprehensive test of a cavity cooling system (HTTR-RCCS). The HTTR-RCCS test has been developed by JAERI to demonstrate the capability of the RCCS to remove reactor decay heat during accidents. Both general flow codes and engineer codes are

used for this comparison; and the relative effect of different modes of heat transfer (radiation and natural convection) is discussed in the section.

– **The SANA-1 Experiments** - Experiments for the self-acting removal of the after heat from a pebble bed are discussed in section 4.2. The modeling and interpretation of these data are presented as a code-to-experiment benchmark problem. In detail we included tests with fully and partly heated pebble beds to enforce or depress natural convection effects. The results of the benchmark calculation of the participating parties China, France and Germany were in good agreement with the experimental data and could accurately represent the complex effects of heat transfer in a pebble bed.

The Appendix, is divided into two parts. The first part (A.1.) give detailed experimental data sets for the SANA-1 benchmarks. The second part (A.2.) of the appendix describes the computer codes that have been used by the participants.

CHAPTER 2

AFTERHEAT REMOVAL IN MODULAR GAS-COOLED REACTORS

The primary emphasis of the Coordinated Research Project was on afterheat removal under accident conditions. However, it is also important to consider other aspects of incorporation of the passive heat removal systems into the design. Both considerations are discussed below.

2.1. AFTERHEAT REMOVAL UNDER ACCIDENT CONDITIONS

The reactor cavity cooling systems (RCCS) for GCRs are typically safety grade systems, either with passive or with highly-reliable, redundant forced-convection cooling systems, designed to remove all of the core afterheat in the unlikely case of failure or unavailability of the main and all other shutdown cooling systems. The objective of most RCCS designs is to serve as an ultimate heat sink, ensuring the thermal integrity of the fuel, core, vessel, and critical equipment within the reactor cavity for the entire spectrum of postulated accident sequences. The requirements for RCCS performance and reliability may vary considerably depending on the particular reactor design features, power level, materials, containment type, and investment protection or licensing considerations. In some cases, these requirements could be extremely stringent if afterheat removal is the critical factor in determining maximum design power level and the need (or not) for a sealed containment structure.

A common solution to the problem of ensuring adequate heat removal is to over design (the capacity of) the system. This would not normally be acceptable for the RCCS, however, because during normal operation, and in some cases for normal shutdowns, excessive parasitic heat losses are undesirable. On the other hand, since the RCCS is necessarily a large, distributed structure in the reactor cavity not easily amenable to inspection and cleaning, allowances would usually be necessary for the inevitable fouling and degradation occurring over the reactor lifetime.

Another challenging aspect of RCCS design is the fact that the heat load distribution during long-term loss of forced convection (LOFC) accidents can vary considerably with the accident characteristics. For example, in a pressurized LOFC, natural circulation within the vessel causes the peak vessel temperatures to occur near the top, while for depressurized LOFC accidents, the peak temperatures appear near the vessel belt-line. Furthermore, for rapid-depressurization accidents, the RCCS may be required to withstand a simultaneous hot jet of coolant gas impinging on the structure and an over pressurization of the cavity. For steam cycle HTRs, pressurization of the cavity from steam line leaks may also be a design consideration.

Because of the wide variety of requirements for RCCS performance and reliability, analysis methods and (validated) codes for predicting detailed RCCS and vessel temperature profiles must be used in conjunction with whole-system accident simulators to determine the adequacy of the design. This means that, in fact, two types of analytical tools are needed for confirmation of a safe shutdown: one, a very detailed finite-element or finite-difference model (typically with >10,000 nodes) for steady-state thermal analysis, and the another a simpler dynamic model (>100 nodes) that can be used in the overall accident analysis.

This emphasis on performance and reliability of passive cooling systems for the reactor vessel is unique to the MHR concept because of its potential for surviving the remotely possible accidents that could result in both loss of coolant and total loss of all active cooling systems. Current reactor designs (LWRs) have achieved satisfactory levels of safety by using combinations of diverse (and expensive) safety-grade active systems. The intent of the RCCS is to provide an ultimate heat sink for the

"thermally stable" GCR, which can withstand a loss of both coolant and forced cooling without fuel failure or fission product release.

Because of the complexities and subtleties of the GCR afterheat removal problem, it is especially useful and helpful for researchers with a wide variety of backgrounds and experience, such as the Chief Scientific Investigators of this Coordinated Research Project, to work together on its resolution.

2.2. OTHER ASPECTS OF AFTERHEAT REMOVAL

While much of the focus of RCCS design is on performance during accident conditions, it must be kept in mind that these extreme conditions are not likely to exist during the life of a modular GCR plant. Thus the effect of the RCCS on normal operation of the plant, both at power and during shutdowns must be addressed along with other considerations as discussed below.

2.2.1 Afterheat Removal Systems Performance During Normal Operation and Shutdown

Since the heat removed from the reactor vessel during normal operation is a parasitic heat loss, it would be desirable for this to be minimized. However, in passive systems, engineered means for reducing heat removal except during accident conditions are normally not advisable, since the probability of failure of the control mechanism might make the overall RCCS predicted failure rate excessive.

Another concern with some RCCS designs is the potential for severely overcooling the vessel and cavity if the reactor is shutdown (e.g., for refuelling or extended maintenance) during very cold weather shutdowns. There is also a concern regarding freezing of the coolant fluid in liquid-cooled RCCS designs.

2.2.2 System Failure and Recovery

The main focus of the Coordinated Research Project is on performance of afterheat removal systems that function "as designed" during postulated accident sequences. However, the designers, operators, and regulators need to be cognizant of the variations in heat removal capabilities of the systems over the full range of accident conditions due to possible modes of RCCS degradation and failure. Such considerations should include:

- Failure modes for various RCCS design options - passive systems: air-cooled, water-cooled, CO_2 critical-temperature-cooled (TIPACS); or active systems. Redundancy requirements. Effects of selected RCCS design option on containment design (none, filtered, or sealed),
- Failure modes and effects analysis (FMEA) of internal (e.g., vessel depressurization, fouling, leakages, ...) and external (e.g., earthquakes, floods, very hard freezes, ...) events,
- Stresses and deformations in the RCCS (and the vessel) due to localized/uneven heating (or cooling). Analyses may need to consider both steady state and transient cases; and
- Performance monitoring (on-line diagnostics), in-service inspection (ISI), remote maintenance, and ad hoc repair methods during accident scenarios. In allowing credit for ad hoc repair of damaged afterheat removal systems during an accident, GCRs will typically have an advantage over most other concepts due to the very long time responses in accident progression sequences.

The use of passive afterheat removal systems in GCRs also presents unique challenges in quantifying reliability, which means that the regulators, who may have limited experience in licensing

passive heat removal systems, may tend to be overly conservative about allowing extremely small unavailability or failure rates. On the other hand, validation of claims of extremely small failure probability rates (e.g., 10^{-6}/yr) is very difficult.

In some cases, the design may even need to account for extremely low probability "complete" failures of the RCCS, and in the case of below-ground silo reactor designs, account for conduction to the surrounding earth. For this it is desirable to have minimal insulation within the RCCS cooling panels.

2.2.3. System Design and Licensing

Some of the aspects of design and licensing an RCCS would be conventional; thus many of the standard structural design codes (ASME Codes, for example) could be applied to construction and inspection requirements, and some of the licensing requirements for emergency core cooling systems for conventional LWRs would also apply directly. On the other hand, certain unique characteristics of the GCR with a (passive) RCCS make direct application of LWR licensing standards inappropriate.

The adequacy of the RCCS design for plant licensing will depend on the RCCS' capability in maintaining acceptable vessel and core component temperatures during postulated accident sequences. This in turn will depend on thermal and nuclear responses of the reactor that may be beyond the common interests of the Coordinated Research Project participants. The RCCS heat removal capabilities under accident conditions, however, involve parameters of universal concern, and some were noted in the benchmark problem solutions as being crucial, and therefore of licensing concern:

- Reactor vessel and panel emissivities: Since thermal radiation accounts for a major fraction of the heat transfer from the vessel to the RCCS, emissivities would play a major role in the licensability of the RCCS. The design and periodic monitoring of the surfaces is crucial,
- Water vapor in the cavity (or other materials that could affect the radiant heat transport) may need to be accounted for,
- Redundancies in coolant flow paths to offset effects of blockages or breaks may be needed,
- Means of monitoring performance under normal conditions to detect potential problems with heat removal capacity under accident conditions,
- Assessments of repair and recovery capabilities, including ad hoc measures that could be taken during accident sequences, could affect licensability.

Some relief for the advanced concepts from perhaps overly conservative licensing restrictions in these matters was signaled recently by a change in German Atomic Law (1994) which now requires that ".... also events, whose occurrence is practically excluded....would not require incisive counter measures...."

CHAPTER 3

MODEL VALIDATION
CODE TO CODE BENCHMARK EXERCISES

3.1. VGM RCCS MOCKUP

3.1.1. Description of the benchmark

3.1.1.1. Introduction

One of the remarkable features of high temperature gas cooled reactors (HTGR) is a possibility to remove the residual heat through the reactor vessel surface to the ultimate sink due to natural heat transfer processes (radiation, convection, conduction).

Study of heat transport from the core to the ultimate sink is very important for substantiation of safety and for licensing of HTGRs. Apparently, the study may be performed both calculational and experimental methods.

The heat transport from the core to the ultimate heat sink may be divided on three characteristic parts:

– core - reactor vessel,

– reactor vessel - reactor cavity cooling system (RCCS),

RCCS - ultimate heat sink.

One of the benchmark problems was formulated on the base of the VGM reactor project for heat transfer from the reactor vessel to the reactor cavity cooling system. The work was done as a part of the IAEA Co-ordinated Research Project on "Heat Transport and Afterheat Removal for Gas-Cooled Reactors under Accident Conditions".

3.1.1.2. VGM reactor

VGM is a modular type-high temperature helium cooled reactor. The reactor of 200 MW thermal power was developed to validate main technical options for production of high temperature process heat.

The reactor vessel is located in a tight concrete pit filled with air of atmospheric pressure (Fig. 3-1). The reactor vessel includes a cylinder, an elliptical lower head welded to the cylinder and a demountable upper head. The upper head is joined with the cylinder by a flange. The lower head has a tube to discharge fuel elements.

The reactor vessel is built into the cavity on supports welded to the vessel. At the lower supports level there are two stub tubes for welding of cross duct vessels connecting the reactor vessel with two vessels for arrangement of the intermediate heat exchanger, the steam generator and the heat exchanger of the shutdown cooling system. The reactor vessel has also stub tubes for refueling system, absorber ball system and stand pipes. The upper head of 150mm width has penetrations for other systems and a manhole. The lower part of the reactor vessel is covered with insulation of 100mm thickness.

3.1.1.3. Reactor cavity cooling system (RCCS)

The RCCS is designed to transfer heat from the reactor cavity to circulating water. The RCCS includes cooling tubes, inlet and outlet manifolds and a reflective screen. The cooling

tubes form three independent units (Fig. 3-2).

The cooling tubes are uniformly arranged around the perimeter on the reflective screen except areas with cross duct vessels. Every unit has own inlet and outlet manifolds.

The heat removed from the reactor cavity depends on temperatures of the cooling tubes and the vessel wall. In the upper part of the reactor there is a plate (Fig. 3-3) which determines the upper head temperature state.

Distribution of temperatures along the reactor vessel and on the plate is shown in Figs. 3-4 and 3-5 respectively. Data on emissivities and parameters of cooling water is given in Table 3-1. Conductivity of materials for reactor vessel, cooling tubes and insulation is presented in Table 3-2.

3.1.1.4. Benchmark problem

Benchmark problem for VGM reactor is set proceeding from simple conditions: to calculate total power transferred from the reactor vessel to the RCCS by radiation and convection at the given temperature distribution. The calculation is executed for two cases:

– helium pressure inside the reactor vessel is equal to nominal value (pressurized conditions);

– helium pressure inside the reactor vessel is equal to atmospheric one (depressurized conditions.).

Table 3-1 Data for calculation

Parameter	Value
Accident conditions (pressurized)	
Temperature of water at inlet of the RCCS, °C	43
Flowrate of water through three units, kg/s	29.46
Helium pressure in the plenum between the plate and the upper head, MPa	4.9
Emissivity of the pressure vessel	0.8
Emissivity of the surface cooler	0.8
Accident conditions (depressurized)	
Temperature of water at inlet of the RCCS, °C	42
Flowrate of water through three units, kg/s	30.9
Helium pressure in the plenum between the plate and the upper head, MPa	0.1
Emissivity of the pressure vessel	0.8
Emissivity of the surface cooler	0.8

Table 3-2 Conductivity of materials

Temperature, °C	St20, cooling tubes W/mK	St 15X12HMCDA, reactor vessel W/mK	Insulation W/mK
30-100	56.5	41	-
200	-	39	0.079
300	-	37.5	0.098
400	-	36	0.117

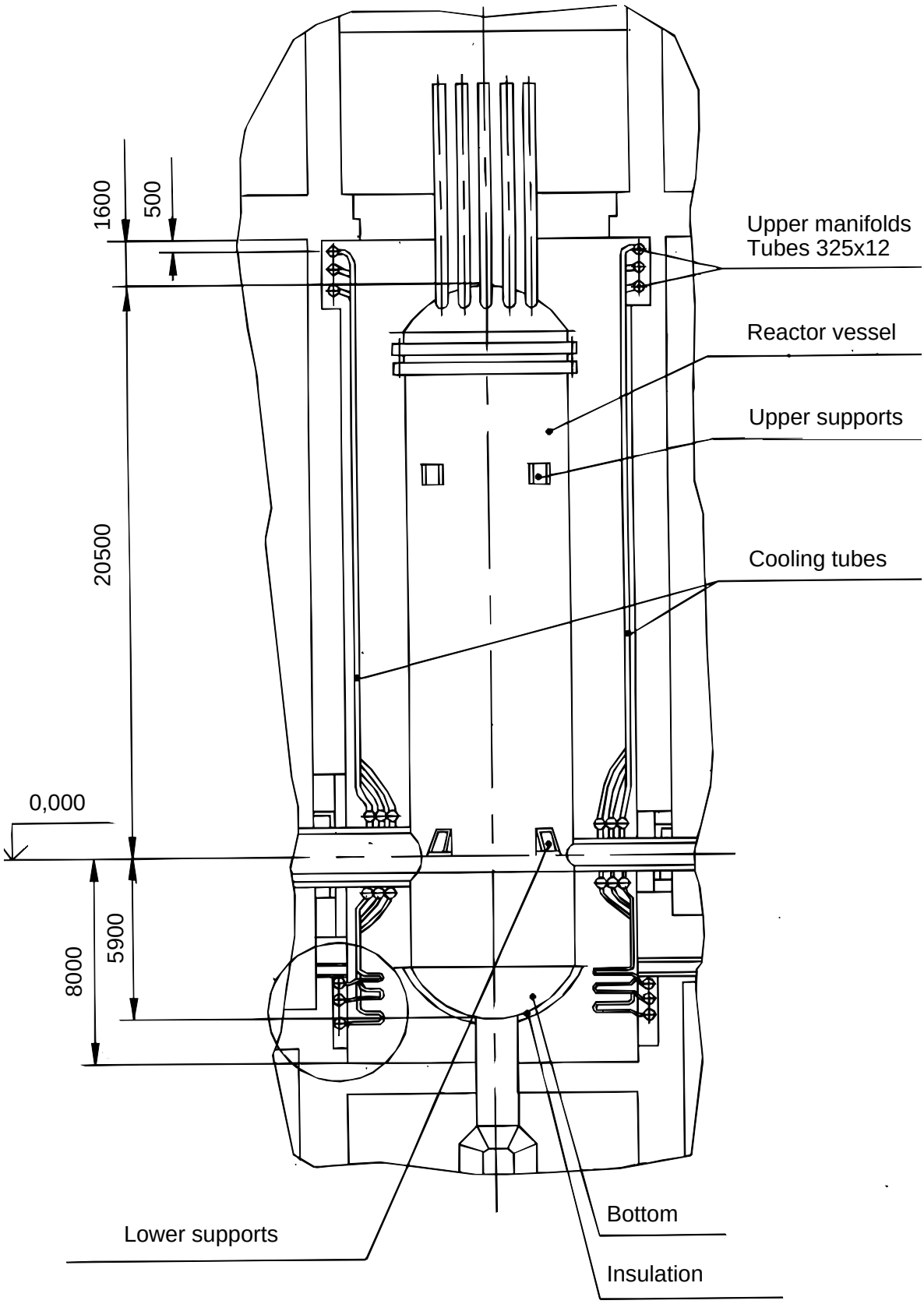

Fig. 3-1 Arrangement of the reactor cavity cooling system

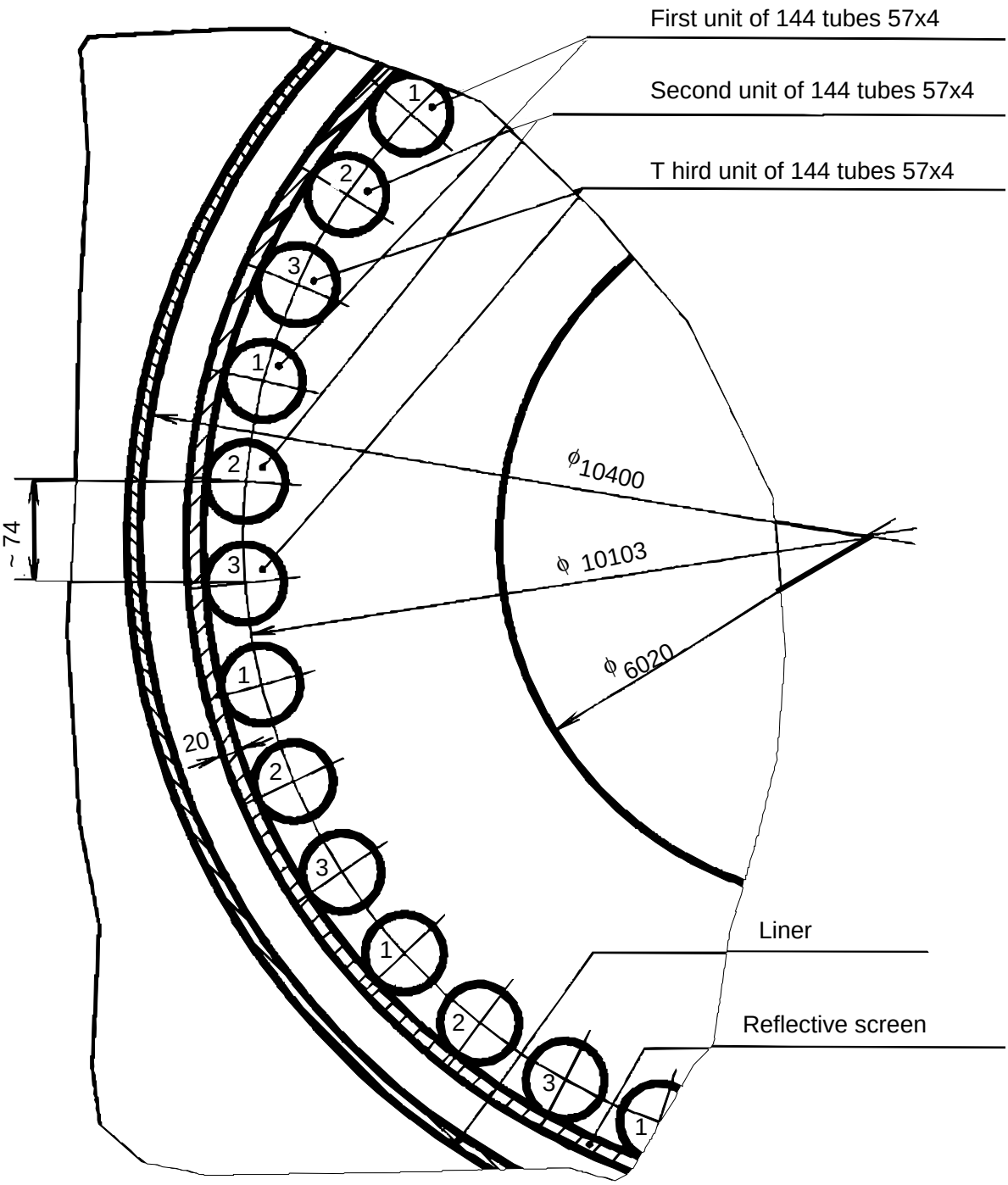

Fig. 3-2 Reactor cavity cooling system

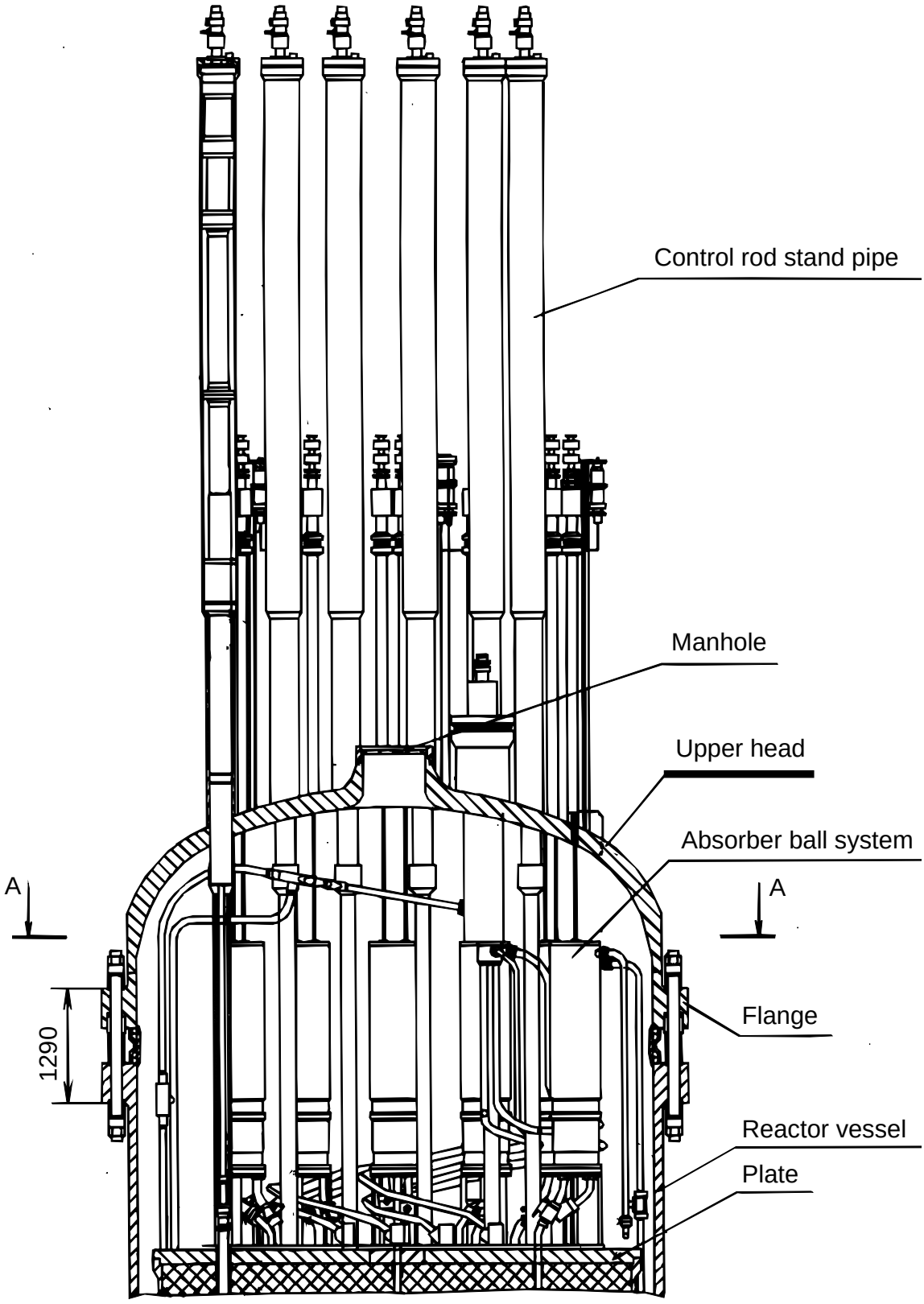

Fig. 3-3 Upper part of the reactor vessel

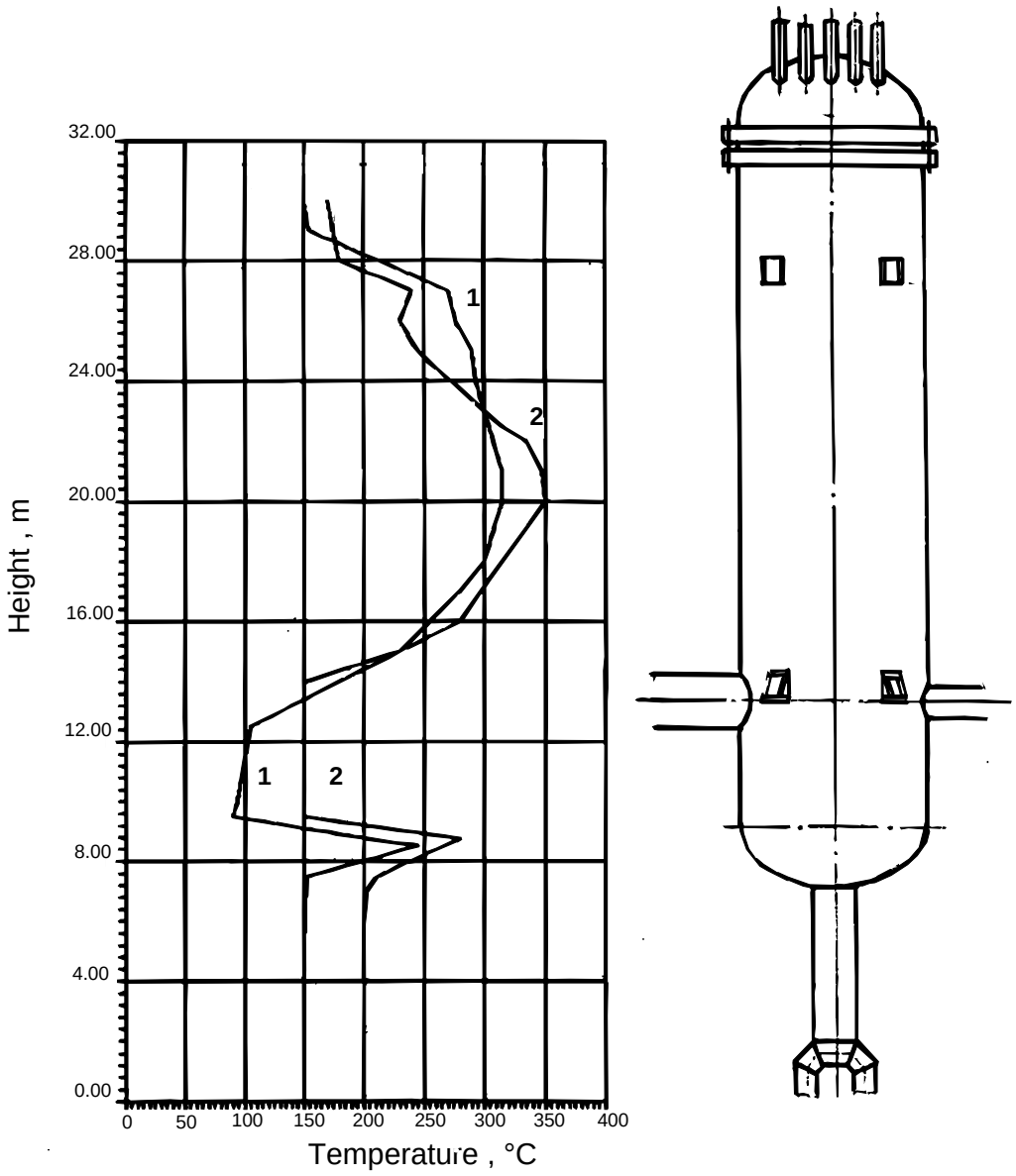

Fig. 3-4 Temperature distribution on the height of the reactor vessel
1 –pressurized conditions
2 –depressurized conditions

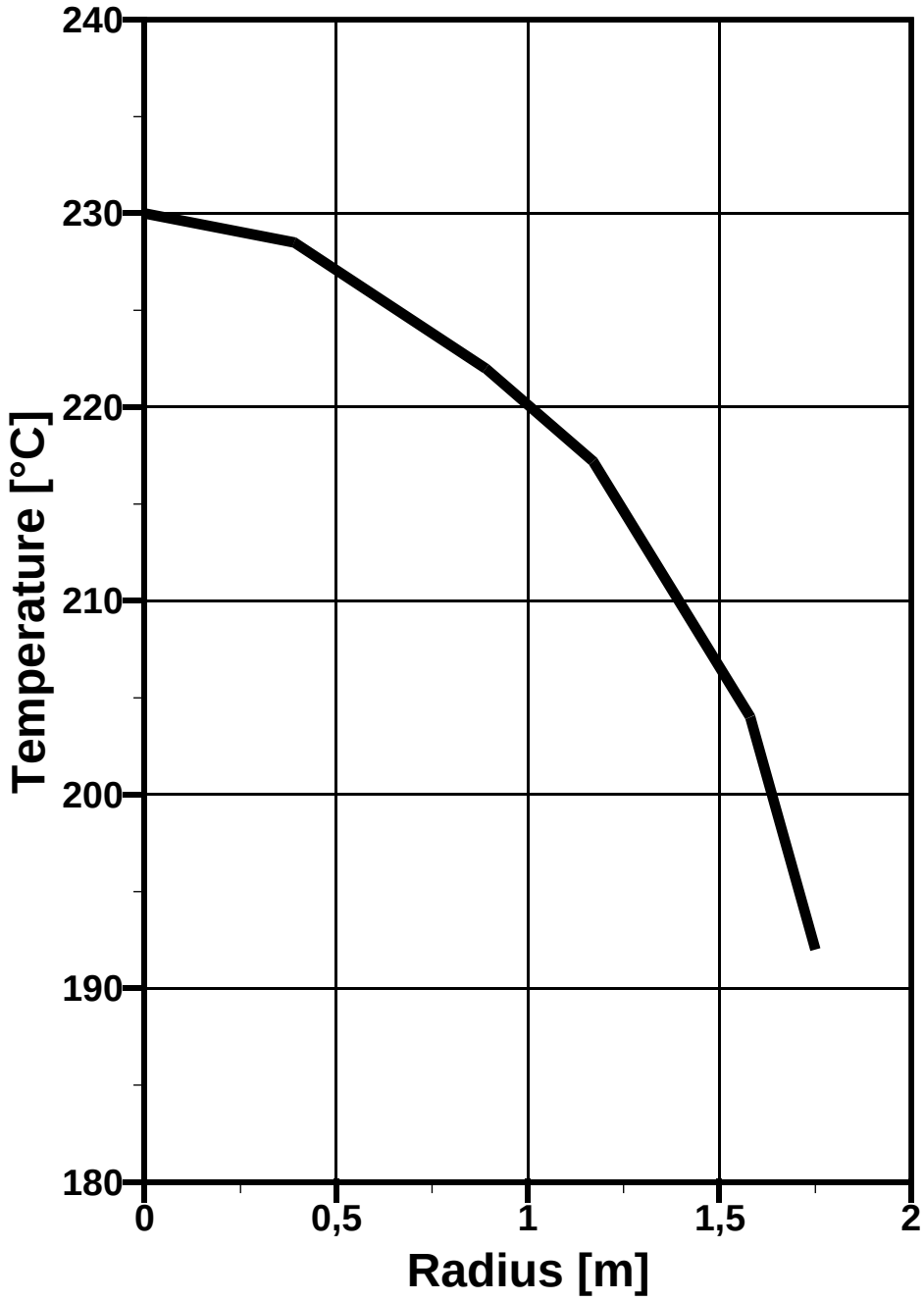

Fig. 3-5 Temperature distribution on the plate versus radius for pressurized and depressurized conditions.

3.1.2. Analysis of benchmark problem defined on VGM reactor results

This benchmark problem was analysed by using THERMIX, a computer programme used for 2-dimensional thermal hydraulic analysis of a pebble bed HTGR.

In estimating heat transferred in natural convection, heat exchange coefficient h is calculated from Nussel number Nu, where Nu can be calculated by the following formulas:

Formula 1:	$Nu = 0.096(Gr\,\mathrm{Pr})^{0.306}$		(1)
Formula 2:	$Nu = 0.180(Gr\,\mathrm{Pr})^{0.250}$	$\mathrm{GrPr} > 10^3$	(2)
Formula 3:	$Nu = 0.138(Gr\,\mathrm{Pr})^{0.258}$		(3)
Formula 4:	$Nu = 0.1947(Gr\,\mathrm{Pr})^{0.250}$	$10^9 > \mathrm{GrPr} > 6.0 \times 10^6$	(4)

Pressurized Accident

Table 3-3 shows the analysis results by using with Nu calculated from formula 1-4. Figures 3-6 and 3-7 respectively are the temperature curves of the WCP and water via height of water cooling tubes with insulator thickness d=100.mm. The fraction of heat transfer in mechanism of natural convection of air are given in Table 3-4.

Depressurized Accident

The analysis result of the thermal response and the fraction of heat transfer in mechanism of natural convection of air in cavity are shown in Tables 3-5 and 3-6. The analysis results show that the heat transfer rate, outlet temperature and the maximum temperature of WCP estimated with Nu given in Formula 2,3 and 4 are almost the same. However, these values estimated with Nu given in Formula 1 are much higher than those estimated with Nu given in Formula 2,3 and 4 above.

Sensitivity Analysis

In order to analyze the influence of emissivity coefficient ε between the RPV and WCP on heat removed from RPV, its sensitivity was analysed. Table 3-7 shows the analysis results.

It can be seen that the afterheat of VGM reactor can be removed from the core mainly by radiation. Under the two accident conditions, the heat transfer rates of the RCCS respectively are 1.10 --1.22 MW and 1.18 -- 1.30 MW responding to different natural convection calculation formulas. The variable net emissivity coefficient ε between the RPV and the WCP has strong influence on the heat transfer rate of the RCCS.

Table 3-3 Thermal response of VGM under pressurized accident with insulator thickness d=100. Mm

condition	parameter	Q_{con} MW	G kg/s	T_{in} °C	T_{out} °C	T_{wcp}^{max} °C
no natural convection exists in reactor	of air cavity	1.01	29.46	43.0	51.2	60.1
natural convection of air exists in reactor cavity with P_{air}=1 bar	formula 1	1.22	29.46	43.0	52.9	62.9
	formula 2	1.11	29.46	43.0	52.0	61.5
	formula 3	1.10	29.46	43.0	51.9	61.4
	formula 4	1.12	29.46	43.0	52.1	61.6

Table 3-4 Fraction of heat transfer of natural convection of air in reactor cavity under pressurized accident

insulator thickness (mm) used formula	100.	50.
1	17.2%	17.2%
2	9.0%	9.0%
3	8.2%	9.0%
4	9.8%	9.8%

Table 3-5 Thermal response of VGM under depressurized accident condition with insulator thickness d=100mm

condition / parameter		Q_{con} MW	G kg/s	T_{in} °C	T_{out} °C	T_{wcp}^{max} °C
no natural convection exists in reactor	of air cavity	1.08	30.9	42.	50.4	62.0
natural convection of air exists in reactor cavity	formula 1	1.30	30.9	42.	52.1	64.8
	formula 2	1.19	30.9	42.	51.2	63.3
	formula 3	1.18	30.9	42.	51.5	63.2
	formula 4	1.20	30.9	42.	51.3	63.5

Table 3-6 Fraction of heat transfer of natural convection of air in reactor cavity under depressurized accident

insulator thickness (mm) used formula	100.
1	16.9%
2	9.2%
3	8.5%
4	10.0%

Table 3-7 Sensitivity analysis of emissivity coefficient ε between the RPV and WCP under pressurized accident condition with insulator thickness d=100mm

formula	ε	Q_{con} MW	T_{out} °C	T_{wcp}^{max} °C
	0.40	0.559	47.5	53.1
	0.50	0.707	48.7	55.5
formula 3	0.60	0.876	50.1	58.1
	0.70	1.07	51.7	60.9
	0.80	1.29	53.5	64.1

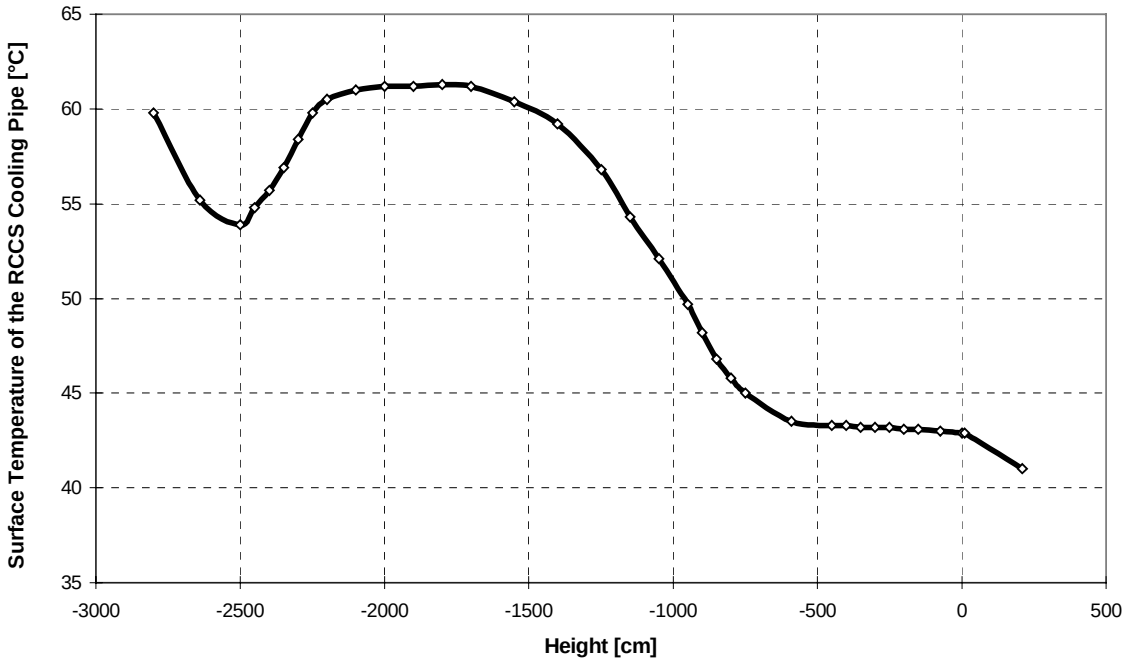

Fig. 3-6 Temperature distribution of the RCCS water cooling pipe along the pipe height

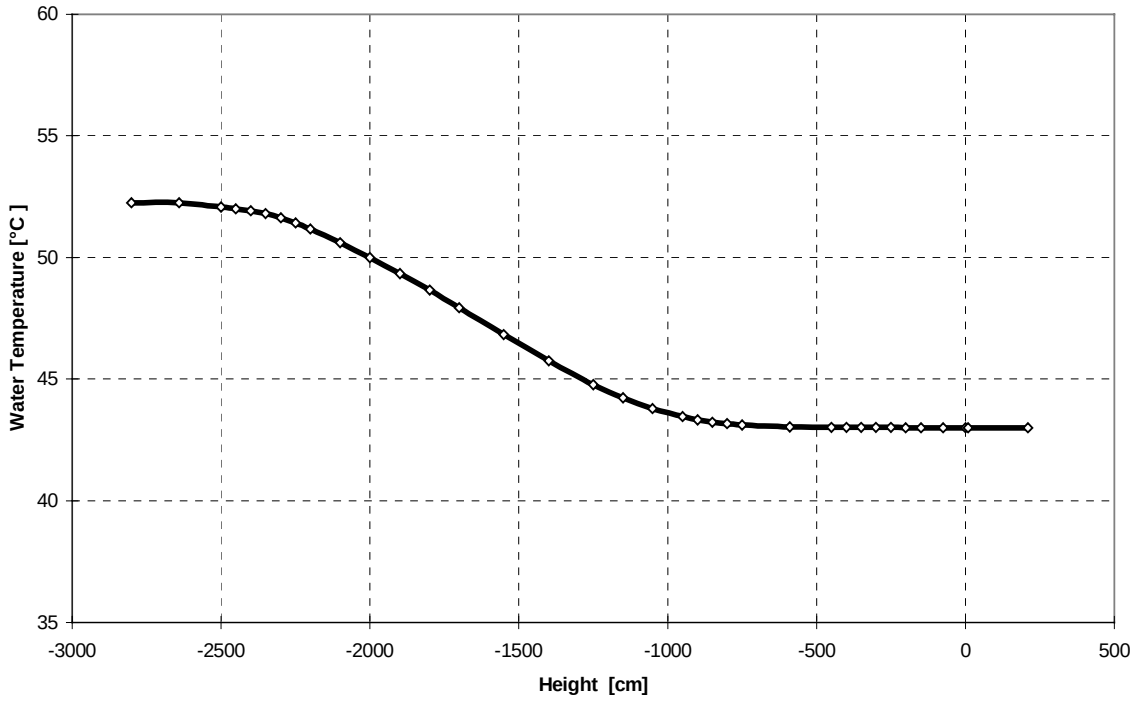

Fig. 3-7 Temperature distribution of the RCCS cooling water along the height of the RCCS pipe

3.1.3. Analysis Of VGM Reactor Cavity Cooling System Benchmark Problem with the Moreca Code

3.1.3.1. Introduction

The benchmark problem [1] provided by Dr. N. Kuzavkov of the Experimental Machine Building Design Bureau, OKBM, Nizhny Novgorod, Russia, was analyzed at ORNL as a part of the IAEA Coordinated Research Program (CRP) on "Heat Transport and Afterheat Removal for Gas-Cooled Reactors (GCRs) under Accident Conditions." ORNL has developed a 3-D accident simulator for the MHTGR, the MORECA code,[2] which incorporates an approximate (fast-running) model of the RCCS. [3] As contrasted to the more detailed (many-thousand-node) finite difference or finite element modeling (using the FIDAP code, for example) to determine the detailed temperature distributions for various operational assumptions, this analysis of the VGM RCCS uses the same types of models used in MORECA, and is primarily concerned with estimating overall heat removal and maximum core and structural component temperatures in accidents.

3.1.3.2. Problem Description and ORNL Analysis Approach

The reactor and RCCS arrangement is shown in Fig. 3-8 from the OKBM reference. Circulation of cooling water in the RCCS tubes is provided by natural convection. The annulus between the reactor vessel and the RCCS is at a partial (100 Pa) vacuum. Calculated vessel temperature profiles were supplied by OKBM for two accident conditions corresponding to a pressurized and a depressurized heatup accident shown in Fig. 3-9 (Fig. 13 from [1]). The problem suggested by OKBM is to calculate the total power removed by the RCCS for the two given vessel temperature profiles, and to show the distribution of air flows and temperatures in the cavity and water temperatures in the cooling tubes. The model used in MORECA for vessel-to-RCCS heat transport includes "textbook" approximations for radiation heat transfer view (or shape) factors and net heat transport, with Rayleigh and Grashof Number-based correlations for estimating overall convection heat transfer in the annulus between the vessel and the cooling panels. Modeling techniques used in this analysis is described in detail in the ORNL benchmark problem report for the JAERI HTTR (see section 4.2.2) experiment. In this case, the vessel and RCCS models consisted of 26 axial regions each (with no azimuthal sector breakdown). Temperature data for the 26 node temperatures were scaled from the figure and used as input. The bottom 6 nodes included the 50mm layer of Kaowool insulation specified. The primary heat transport mechanism is T4 radiation. The Eckert-Carlson Grashof Number-based correlation [4] is used to calculate convective heat transfer in the annulus.

3.1.3.3. Results

The ORNL results are presented for the two problem conditions-pressurized and depressurized (primary system) vessel loss-of-forced-circulation accidents. Outputs showing the radiative and convective heat transfer for each of the 26 sections (along with the cooling water temperature profile) are given in Figs. 3-10 and 3-11 for Cases 1 (pressurized) and 2 (depressurized). The "best estimated" predictions of total RCCS power are 1.23 MW (pressurized) and 1.33 MW (depressurized), with about 15% of the total heat transfer being due to convection in both cases. The coolant outlet temperatures were 53 and 52°C, respectively. The ORNL calculations are shown in comparison to those of China [5], [6] and Russia [7].

Case 1

Pressurized Accident:	Total Q (MW)	Q-Radiative (MW)	Q-Convective (MW)
China	1.22	1.01	0.21
ORNL	1.23	1.04	0.19
Russia	0.83	0.76	0.07

Case 2

Depressurized Accident:	Total Q (MW)	Q-Radiative (MW)	Q-Convective (MW)
China	1.30	1.08	0.22
ORNL	1.33	1.13	0.20
Russia	0.93	0.86	0.07

3.1.3.4. Sensitivity Studies

Since most of the heat transfer is by radiation, variations in total power vs. emissivity values were studied. The percentage changes (pressurized vs. depressurized) were essentially the same for each variation studied. The reference value for all surfaces was 0.8. Reduction of all emissivities to 0.6 cut the power to 68% of the reference case value, and for emissivities of 0.7, the power was reduced to 83%. If it is assumed that the Kaowool insulation surface emissivity is halved (0.4), the total power removed is reduced by less than 0.5%. Assuming that the RCCS cooling coil temperatures were uniform and fixed at the inlet temperature (instead of varying with heat load) resulted in only a 1% increase in power removed.

3.1.3.5. Conclusions

We have found this to be a very interesting verification exercise, and are grateful to Dr. Kuzavkov and his colleagues at OKBM for their generosity in supplying the problem and their analyses to the CRP,

Variations in emissivity values for the vessel-to-cooling panel radiant heat exchange process were shown to have a nearly direct proportional effect on heat loss (at given vessel temperatures), as noted in the previous analysis of the HTTR experiment,

Because the vessel is surrounded by cooling panels at a nearly constant uniform temperature and the emissivities are high, the calculated radiant heat transfer to the RCCS should not be sensitive to view factor or net radiation exchange modeling distinctions.

REFERENCES TO SECTION 3.1.3.

[1] Bespalow, V. Golovko, N. Kuzavkov, V. Lunin, and O. Myagkov,"Benchmark Problem Definitions for VGM Heatup Accidents (GRP-1)," OKBM, Nizhny Novgorod, Russia, Mar. 1994, (IAEA Reference 622-I3-RC-503)

[2] S. J. Ball and D. J. Nypaver, MORECA-2: Interactive Simulator for Modular High-Temperature Gas-Cooled Reactor Core Transients and Heatup Accidents with ATWS Options, NUREG/CR-5945 (ORNL/TM-12233), Oak Ridge National Laboratory, October 1992

[3] J. C. Conklin, Modeling and Performance of the MHTGR Reactor Cavity Cooling System, NUREG/CR-5514 (ORNL/TM-11451), Oak Ridge National Laboratory, April 1990

[4] E. R. G. Eckert and W. O. Carlson, "Natural Convection in Air Layer Enclosed Between Two Vertical Plates with Different Temperatures," Intl. J. Heat and Mass Trans., Vol. 2, p. 106, 1961

[5] B. Lee, Z. Gao, Z. Jiang, and B. Yang, "Analysis of Benchmark Problem Defined on VGM Reactor," INET, Tsinghua University, October 1994

[6] Z. Jiang and Z. Gao, "Comparison Analysis of Calculation Results of Benchmark Problems on VGM RCCS," INET, Tsinghua University, January 1995

[7] V. Golovko, N. Kuzavkov, and O. Myagkov, "Analysis of VGM Reactor Cavity Cooling System Benchmark Problem," OKBM, June 30, 1995

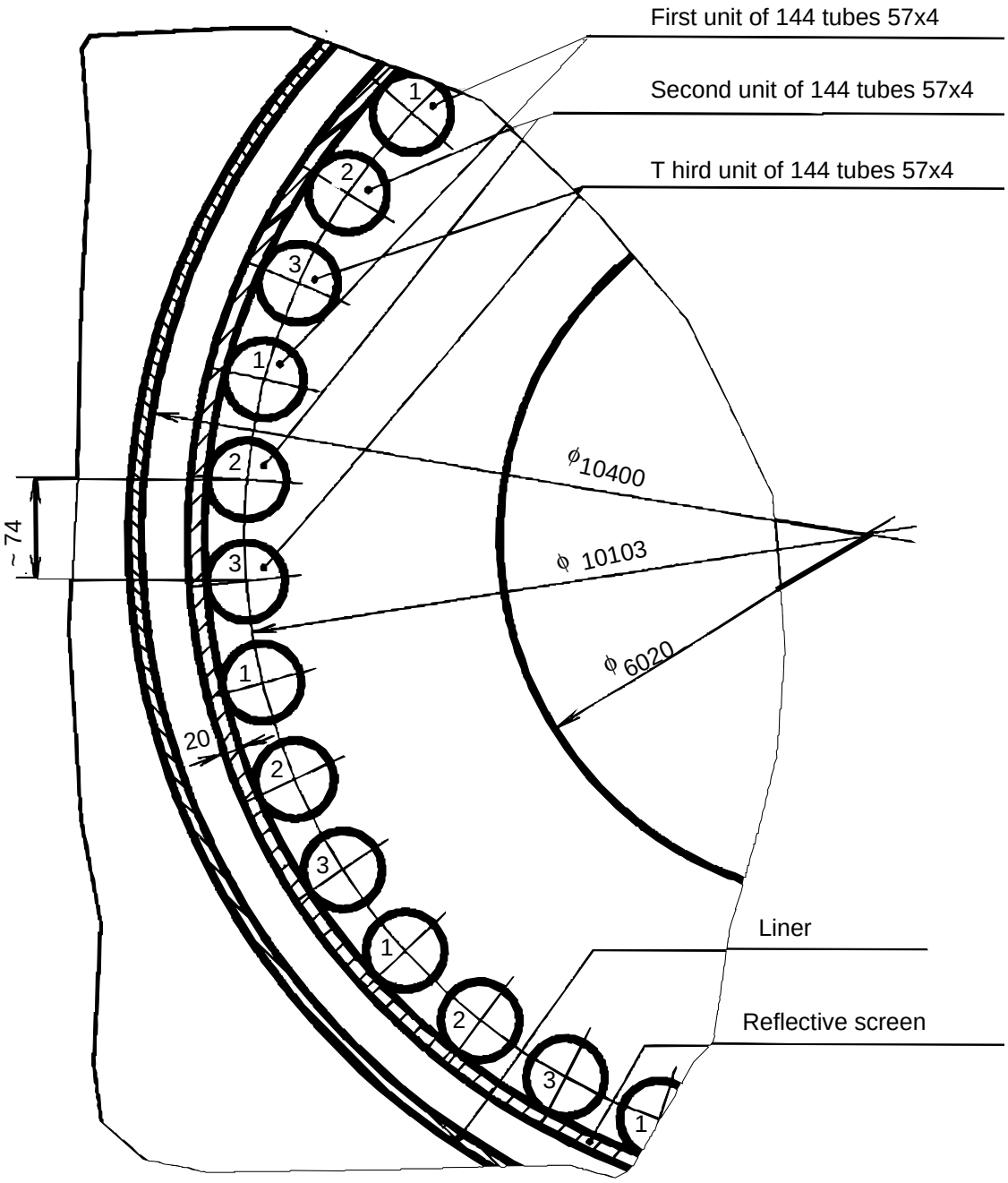

Fig. 3-8 VGM surface cooler arrangement (dimensions mm)
(from [1] see also section 3.1.)

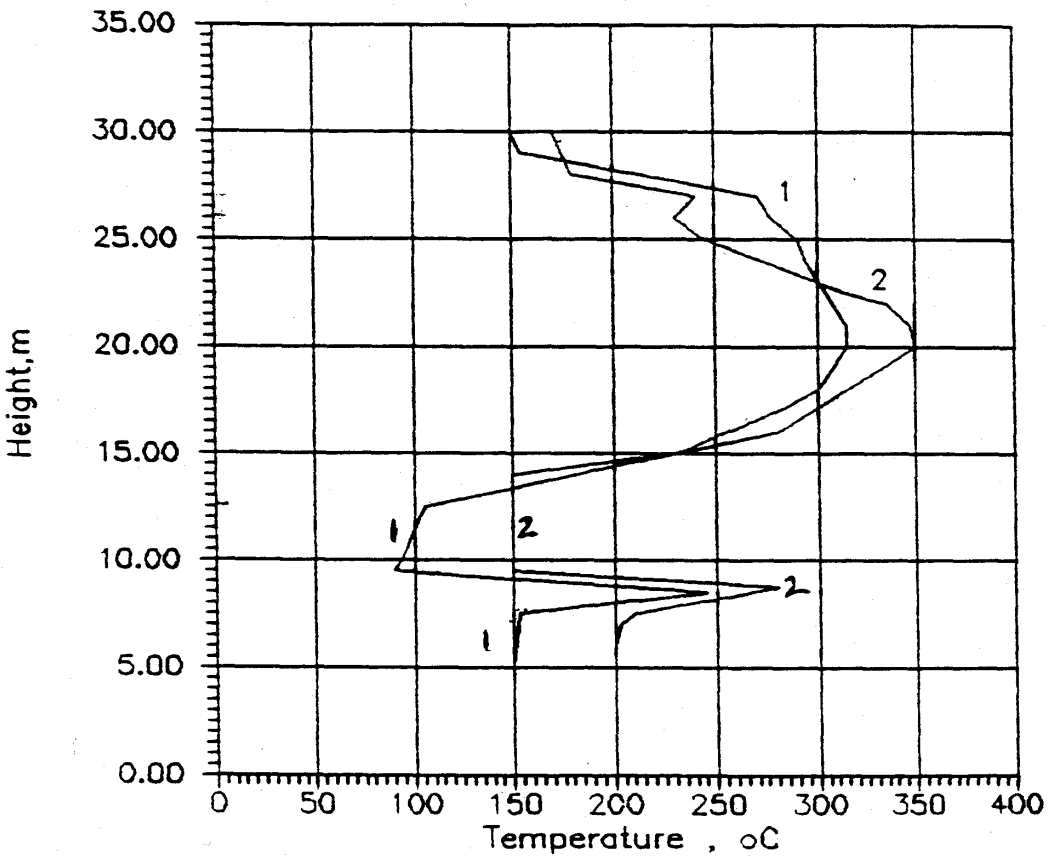

Fig. 3-9 Temperature distribution with height of the reactor vessel
(from [1] see section 3.1.)

*Curve 1: pressurized
Curve 2: depresurized
* Note: labels on lower part of curves are inferred

VGM case #1 data - Vessel temps (°C) - Pressurized

Vessel node temperatures (from Fig. 3-9), from bottom to top (°C) =

150.0 150.0 151.0 152.0 232.0 90.0 94.0 100.0 106.0 150.0 218.0 244.0 267.0
300.0 302.0 315.0 318.0 316.0 312.0 300.0 290.0 280.0 277.0 255.0 180.0 152.0

T-Cool-in (°C) = 43.0 Water flow (kg/s) = 29.46 Annulus Press (Pa) = 101325.

Annulus h (W/cm^2-sec) = 2.325
Shape factor: Top & bottom of vessel to RCCS tubes = 0.257

Heat losses & cooling water outlet temperatures for each node
(note: bottom nodes 1-6 are insulated)

Node	Connective loss (W)	Radiative loss (W)	Coolant temp (°C)
1	1940.	1128.	43.
2	719.	1707.	43.
3	725.	1723.	43.
4	731.	1740.	43.
5	1229.	3080.	43.
6	322.	734.	43.
7	1650.	6354.	43.
8	1896.	7295.	43.
9	2149.	8282.	43.
10	4189.	17143.	44.
11	7784.	37468.	44.
12	9254.	47814.	44.
13	10591.	58355.	45.
14	12577.	76042.	46.
15	12670.	77149.	46.
16	13453.	85044.	47.
17	13608.	86878.	48.
18	13446.	85514.	49.
19	13160.	82909.	50.
20	12376.	75567.	50.
21	11726.	69779.	51.
22	11085.	64294.	52.
23	10876.	62660.	52.
24	9532.	51854.	53.
25	5311.	24052.	53.
26	6558.	5667.	53.

Fig. 3-10 Reference case output: VGM RCCS benchmark problem - pressurized

Total heat loss to RCCS (MW) = 1.230
Heat loss via radiation, convection (MW) = 1.040 0.190
Ratio: convective loss / total = 0.1541

VGM case #2 data - Vessel temps (°C) - depressurized

Vessel node temperatures (from Fig. 2), from bottom to top (°C) =

200.0 200.0 201.0 207.0 265.0 152.0 150.0 150.0 150.0 150.0 214.0 252.0 290.0
315.0 325.0 342.0 350.0 348.0 340.0 297.0 255.0 238.0 235.0 225.0 180.0 172.0

T-Cool-in (°C) = 42.0 Water flow (kg/s) = 30.90 Annulus Press (Pa) = 101225.

Annulus h (W/cm^2-sec) = 2.361
Shape factor: Top & bottom of vessel to RCCS tubes = 0.257
Heat losses & cooling water outlet temperatures for each node
(Note: bottom nodes 1-6 are insulated)

Node #	Convective loss (W)	Radiative loss (W)	Coolant temp(°C)
	3115.	1912.	42.
	1179.	2862.	42.
1	1186.	2882.	42.
2	1229.	3000.	42.
3	1605.	4074.	42.
4	830.	1946.	42.
5	4193.	17256.	42.
6	4186.	17240.	43.
7	4178.	17224.	43.
8	4171.	17208.	43.
9	7506.	36075.	43.
10	9644.	51409.	44.
11	11881.	70454.	44.
12	13389.	85250.	45.
13	13980.	91674.	46.
14	15021.	103416.	47.
15	15493.	109237.	48.
16	15323.	107638.	49.
17	14769.	101682.	50.
18	12040.	73814.	50.
19	9497.	52051.	51.
20	8495.	44570.	51.
21	8305.	43289.	52.
22	7723.	39280.	52.
23	5276.	24127.	52.
24	8054.	7442.	52.

Fig. 3-11 Reference case output: VGM RCCS benchmark problem – depressurized
Total heat loss to RCCS (MW) = 1.329
Heat loss via radiation, convection (MW) = 1.127, 0.202
Ratio: convective loss / total = 0.1522

3.1.4. Results of Calculations of The VGM RCCS Benchmark

3.1.4.1. Introduction

Analysis of the benchmark problem was performed in the frame of the IAEA Coordinated Research Program on "Heat Transport and Afterheat Removal for Gas-Cooled Reactors under Accident Conditions".

The benchmark problem on heat transport from the reactor vessel to the cooling panels was presented by OKBM on the base of VGM reactor [1].

3.1.4.2. Model features and limitations

The DUPT code was used for the calculations (brief description see Appendix A.2.2). The region to be calculated is divided into rectangular meshes as shown in Fig. 3-12. Special study to optimize a number of nodes was taken on the experience of similar calculations.

The cooling panels are assumed to cover all the cavity wall. This leads to some decreasing heat losses from the reactor vessel at given temperature distribution on the outer vessel surface. Emissivity of the heat transfer surfaces is the same and equal to 0.8.

To short iteration process of heat transfer and to reduce expenditure of computer time, heat capacity of the reactor vessel was taken more lower than the real value.

The calculations is also carried out using SM1 code (description in Appendix A.2.2).

3.1.4.3. Results

The calculation with using DUPT code showed the following results. Heat losses from the reactor vessel for pressurized and depressurized conditions are 1170 kW and 1320 kW respectively. Fractions of the heat transferred by air convection are 14.5 and 20% respectively.

Figure 3-13 shows velocity profile between the upper plate and the upper head and in the reactor cavity.

There are clear rising and falling airflows along vertical surfaces. In the middle area of the annulus between the reactor vessel and the cooling panels horizontal flows arise, at the boundaries of cylindrical part of the reactor vessel and in the rest of the reactor cavity - recirculation zones are formed. This intensifies heat transport from lower area to the upper part of the reactor cavity and from the upper plate to the upper head. The air temperatures in the reactor cavity vary from 129°C (upper part) to 52°C (lower part) for pressurized conditions and from 133°C to 59°C for depressurized conditions.

In accordance with the calculations on SM1 code, the heat transferred to the reactor cavity cooling system is 1280 and 1360 kW with and without pressure in the primary circuit respectively. Fractions of the heat transferred by air convection are 19.5 and 26% respectively.

3.1.4.4. Sensitivity Study

To estimate influence of emissivity on the heat losses, calculations on DUPT code were performed for emissivity values of 0.6 and 0.7. If the power for emissivity of 0.8 is the reference case, then for emissivities of 0.6 and 0.8 the power was reduced to 68% and 83% of the reference case value respectively.

3.1.4.5. Conclusions

- The calculations show insufficient role of convection in heat transfer from the reactor vessel to the cooling panels (<26%). This is due to high emissivity of the surfaces, high temperature on cylindrical part of the reactor vessel and reduced level of temperatures on the lower and upper heads of the vessel that is unfavourable for the convection development,
- Since a major part of the heat is transferred by radiation, the total power is well sensitive to emissivity values.

REFERENCE TO SECTION 3.1.4.

V.Bespalov, V.Golovko, N.Kuzavkov, V.Lunin and O.Myagkov "Benchmark Problem Definitions for VGM Heatup Accidents (GRP-1)", OKBM, Nizhny Novgorod, Russia, Mar.1994, (IAEA Reference 622-13-RC-503).

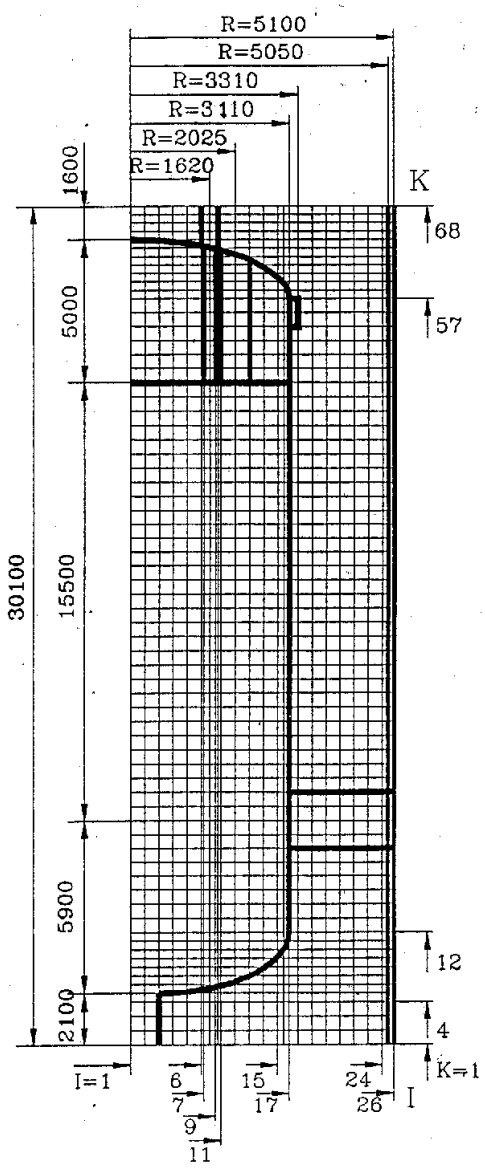

Fig. 3-12 DUPT code computation grid

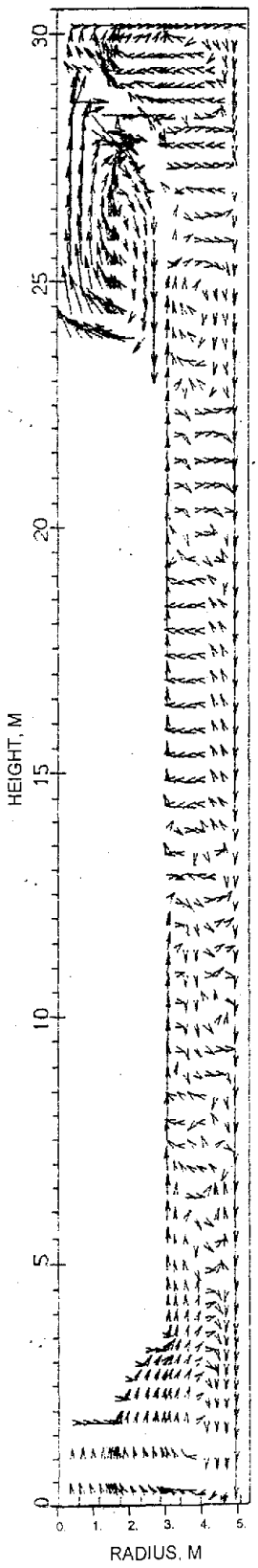

Fig. 3-13 Velocity vectors

3.1.5. Comparison and Conclusions on VGM Reactor Cavity Cooling System Benchmark Problem

3.1.5.1. Introduction

The VGM benchmark problem was analyzed by INET (China), OKBM (Russia) and ORNL (USA). The benchmark problem was provided by OKBM [1]. The benchmark exercises were made by using codes THERMIX (China), DUPT and SM1 (Russia), and MORECA (USA) [2, 3 and 4].

For the benchmark problem, models in THERMIX, SM1 and MORECA are based on "textbook" approximations for calculation of view factors and net heat transport by radiation and Grashof Number-based correlation for convective heat transfer in the annulus.

DUPT 2D-code includes heat and mass transfer equations on the basis of Business approximation. Radiative heat transfer is calculated by division the whole surface into elementary surfaces and finding for them view factors.

3.1.5.2. Benchmark Problem Analysis

The calculated results of total, radiative and convective heat transfer for pressurized and depressurized conditions are presented in Table 3-8.

Comparison of the results shows:

For all cases radiative heat losses are ≥ 74% of total power,

Radiative heat losses for pressurized conditions are close to each other. The same is for the depressurized case. To some extent this is due to the fact that quantity of heat transferred by radiation depends basically on the surface of simple cylindrical shape. The rest surface of complex shape has low temperature (cooling panel) or its fraction in heat transfer by radiation is not large (upper and lower heads),

Difference in convective heat losses is more substantial. The reason is complexity of convective heat transfer calculation and use of different models and approximations.

Table 3-8 Heat losses from the reactor vessel to RCCS

	Total power, kW	Radiative power, kW	Convective power, kW	Fraction of total power transferred by convection, %
Pressurized accident				
INET	1220	1010	210	17.2
(China)	1110		100	9.0
	1100		90	8.2
	1120		110	9.8
OKBM				
(Russia)	1170	1000	170	14.5
	1280	1030	250	19.5
ORNL				
(USA)	1230	1040	190	15.4
Depressurized accident				
INET	1300	1080	220	16.9
(China)	1190		110	9.2
	1180		100	8.5
	1200		120	10.0
OKBM	1320	1120	200	20.0
(Russia)	1360	1100	260	26.0
ORNL	1330	1130	200	20.0
(USA)				

Table 3-9 contains statistical processing of the calculated results taking into account that the data obtained by the benchmark participants are independent.

The processing is carried out for two cases:

– All the data are included into consideration (column 1),

– Data calculated by correlations 2, 3, 4 and [2] are excluded as giving underestimated values (column 2).

The results presented in Table 2 shows that the range of possible values of the total power is not more than ±12% with confidence level of 0.95. Exclusion of the results obtained on correlations 2, 3, 4 and [2] makes the range not more than ±7.3% with the same confidence level.

Table 3-9 Statistical processing of the calculated results

	Total power kW Calculated	Mean		2σ		Range of probable values	
		1	2	1	2	1	2
Pressurized	1220						
INET	1110						
(China)	1100						
	1120						
		1176	1225	139	90	1176±11,8%	1225±7,3%
OKBM	1170						
(Russia)	1280						
ORNL	1230						
(USA)							
Depressurize	1300						
d INET	1190						
(China)	1180						
	1200						
		1268	1328	152	50	1268±12%	1328±3,9%
OKBM	1320						
(Russia)	1360						
ORNL	1330						
(USA)							

3.1.5.3. Sensitivity Studies

The benchmark participants studied sensitivity of total power variation vs. emissivity values. It is important because most of heat transfer is by radiation (> 80%). Results of the calculations are given in Table 3-10.

Table 3-10 Comparison of the results on sensitivity studies

	Total power, %		
	ε = 0,6	ε = 0,7	ε = 0,8
INET (China)	68	83	100
OKBM (Russia)	68	83	100
ORNL (USA)	68	83	100

Table -310 shows that the results are the same at given value of the emissivity and heat losses are well depend on emissivity. At given vessel temperature distribution heat losses are changed almost direct proportionally vs. emissivity.

3.1.5.3. Conclusions

Calculations on VGM benchmark problem give good agreement in total and radiative heat transfer,

As the statistical processing of the results showed, the total and radiative vessel-to-cooling panel heat transfer is calculated with the relative error not more than ± 12% and ± 4%, respectively at confidence level of 0.95,

Fraction of radiative heat transfer is more 74% of the total vessel-to-cooling panel heat exchange. Therefore, as sensitivity studies indicate, the total heat are well depend on emissivity,

Solution of VGM benchmark problem with participation of specialists from China, Russia and USA was useful as allowed to compare results computed by different codes and to reveal difficulties connected with heat transfer from the reactor vessel to the cooling panel.

REFERENCES TO SECTION 3.1.5.

V. Bespalov, V. Golovko, N. Kuzavkov, V. Lunin and O. Myagkov, “Benchmark Problem Definitions for VGM Heatup Accidents (GRP-1)”, OKBM, Nizhny Novgorod, Russia, Mar. 1994, (IAEA Reference 622-13-RC-503).

B. Lee, Z. Gao, Z. Jiang, and B. Yang, “Analysis of Benchmark Problem Defined on VGM Reactor”, INET, Tsinghua University, October 1994.

V. Golovko, N. Kuzavkov, O. Myagkov, S. Shepelyov, S. Tonny, “Analysis of VGM Reactor Cavity Cooling System Benchmark Problem,” OKBM, 1997 (see section 3.1.4.).

S. J. Ball, “Analysis of VGM Reactor Cavity Cooling System Benchmark Problem with the MORECA Code”, Oak Ridge National Laboratory, 1995

3.2. HTTR ANALYSIS OF HEAT UP ACCIDENTS

3.2.1. Description of HTTR Analysis of Heat Up Accidents

3.2.1.1. Introduction

The HTTR [1] is now under construction at Oarai Research Establishment of Japan Atomic Energy Research Institute foreseeing the first criticality in FY 1998. After a start up test, several tests planned for the HTTR will be carried out to demonstrate the excellent safety features of high temperature gas-cooled reactors (HTGRs) such as its high fuel performance, negative temperature coefficient of reactivity, large amount of core heat capacity and so on. Results of the tests will be used for designing the next generation HTGRs, especially, simplifying active safety systems and for developing detailed reactor transient simulation codes. To demonstrate superior inherent safety characteristics of HTGRs, safety demonstration test, including a loss of core flow accident simulation and control rod (C/R) withdrawal accident simulation, will be carried out using the HTTR. The loss of core flow rate accident simulation is analysed as the benchmark problem of the HTTR analysis of heat up accidents.

3.2.1.2. Analysis of HTTR heat-up accidents with the GRSAC code

3.2.1.2.1. Outline

The HTTR has been so designed as to be an engineering test reactor which aims at establishing and upgrading the technological basis necessary for HTGR developments and conducting various irradiation tests for innovative basic researches. The main reactor facilities of the HTTR such as the reactor pressure vessel (RPV), primary cooling system (PCS), containment vessel, fuel handling machine, etc, are housed in the reactor building, as shown in Fig.3-14. The RPV made of 2-1/4Cr-1Mo steel is 13.2m in height and 5.5m in diameter, and contains the core consisting of fuel and C/R guide blocks, replaceable and permanent reflector blocks, metallic and graphite core support structure, etc., as shown in Figs. 3-15 and 3-16. The main cooling system (MCS) is composed of the PCS, the secondary helium cooling system and the pressurized water cooling system. The major specification, and major nuclear and thermo-hydraulic characteristics are shown in Tables 3-11 and 3-12, respectively. Additional nuclear and thermo-hydraulic data are shown in Table 3-13.

3.2.1.2.2. Core and reactor internals

The core consists of 30 fuel block columns and 7 C/R guide blocks, where each column is composed of 5 blocks stack and its height and diameter are 2.9m and 2.3m, respectively. The core is surrounded in all sides by replaceable reflector blocks that form upper, under and side reflectors. Each block is a prismatic graphite block of 0.36m across flats and 0.58m in height. A fuel block, as shown in Fig.3-17, consists of graphite block with vertical holes of 0.041m in diameter, graphite sleeves of 0.034m in diameter, fuel compacts and so on. Fuel compacts are contained in a graphite sleeves to form a fuel rod. Fuel rods are contained inside vertical holes of graphite blocks. Coolant of helium gas flows through annular channels outside a graphite sleeve.

The core with replaceable reflector blocks is located inside the RPV and supported by the reactor internals which consists of the metallic and graphite core support structure as shown in Figs.3-15 and 3-16. The vertical structure of the reactor internals involves 8 layers of permanent reflector blocks (PRBs), and its total height is approximately 8m. The PRBs form a near cylindrical cavity of approximately 4.2m in equivalent diameter. Located inside this cavity are the core, hot plenum blocks(HPBs), support posts and core bottom insulation layer. The core restraint mechanism is placed along the periphery of every layer of the PRBs to hold the PRBs tightly together at all operation condition like hoops for a barrel. The HPBs array contains

passages which collect the coolant flow from each column and distribute it into the plenum under the HPB array. The support posts structurally support the core and HPB array while providing the hot plenum to receive the coolant flow exiting the core. The bottom insulation layer is made up of fore axial layers of two graphite blocks and two carbon blocks. The coolant enters the RPV through the annular passage of the concentric hot gas duct, then, flows upward to the upper plenum via two side flow passages: one is an inner passage between the PRBs and side shielding blocks and the other an outer passage between side shielding blocks and RPV. Finally, the coolant entering the upper plenum flows downward to the hot plenum through the core via coolant channels in fuel blocks and C/R guide blocks. Besides the bulk of the coolant the core, small amounts of the coolant flows through the gaps between adjacent blocks.

3.2.1.2.3. Cooling System

The cooling system is composed of the MCS, auxiliary cooling system (ACS) and two vessel-cooling systems (VCSs). The cooling system is schematically shown in Fig.5. The MCS is composed of the PCS, secondary helium cooling system and pressurized water cooling system. The PCS has two heat exchangers, an intermediate heat exchanger (IHX) and a primary pressurized water cooler (PPWC), in parallel. The ACS is in the standby condition during the normal operation and is operated to remove the residual heat from the core when the reactor is scrammed. The VCSs are operated at 100% flow rate during normal operation to cool biological shielding concrete around the RPV and to cool the RPV and fuel indirectly when the core is no longer cooled effectively by neither the MCS nor the ACS.

The HTTR has two operation modes, one is parallel-loaded operation and the other single loaded operation. The IHX and PPWC are operated simultaneously during the former mode. In this mode, heat capacity of the IHX and PPWC is 10 MW and 20 MW, respectively. During the latter mode, only the PPWC is operated to remove all generated heat of 30 MW at core.

3.2.1.3. Benchmark Problem of HTTR Analysis of Heat Up Accidents

The loss of core flow accident simulation is analyzed as the benchmark problem of the HTTR analysis of heat up accidents. The loss of core flow accident simulation simulates conduction cooling behavior during the depressurization accident. In this simulation, all circulators of the PPWC stop during the single loaded operation without the reactor scram. The coolant flow through the core is lost. Reactor power decreased. Fuel temperature once decreased and increases gradually. Temperature and flow rate of the pressurized water at the PPWC inlet are kept constant through the test.

When all circulators of the PCS stop during the rated power operation, maximum fuel temperature, reactor outlet coolant temperature and reactor power should be analyzed based on mass flow rate of primary coolant, heat mass balance, and so on.

3.2.1.4. Data for Analysis

1. Initial condition and heat mass balance for analysis

(a) Initial condition
- Single loaded operation
- All circulators stop
- 102.5% of rated power operation (30.75MW)
- Without scram
- Constant flow rate and temperature of the pressurized water at the PPWC inlet

(b) Heat mass balance(Single loaded operation)

- Reactor inlet coolant temperature 397 °C
- Reactor outlet coolant temperature 869 °C
- Maximum fuel temperature 1381 °C
- Primary pressure 4.177 MPa
- Core flow rate 44.06 ton/hr
- Effective core flow 88%
- Pressurized water inlet temperature (150 °C)
- Pressurized water outlet temperature (190 °C)
- Pressurized water flow rate (640 ton/hr)

2. Dynamic characteristics parameter

(a) Prompt neutron lifetime

$$l = 6.66\times10^{-4} \text{ (sec)}$$

(b) Decay constant of delayed neutron precursor(1/sec)

$\lambda_1 = 4.656$

$\lambda_2 = 1.68$

$\lambda_3 = 0.3732$

$\lambda_4 = 0.1392$

$\lambda_5 = 0.03804$

$\lambda_6 = 0.01524$

(c) Delayed neutron fraction

$\beta_1 = 1.224 \times10^{-4}$

$\beta_2 = 5.445 \times10^{-4}$

$\beta_3 = 1.7217 \times10^{-3}$

$\beta_4 = 8.37 \times10^{-4}$

$\beta_5 = 9.675 \times10^{-4}$

$\beta_6 = 1.656 \times10^{-4}$

$\beta = 4.35869\times10^{-3}$

Amount of reactivity insertion

Tempe-rature	Reactivity insertion by moderator (%Δk/k)		Temperature	Reactivity insertion by fuel (%Δk/k)	
(°C)	Decrease of heat removal events	Increase of heat removal events	(°C)	Decrease of heat removal events	Increase of heat removal events
27	1.098	7.04	27	1.79	4.09
127	0.38	6.00	187	1.40	3.21
327	0.0198	3.76	387	0.99	2.26
527	0.0952	1.86	587	0.623	1.44
727	0.0	0.0	787	0.3	0.688
927	-0.53	-2.03	987	0.0	0.0
1127	-1.784	-4.49	1187	-0.281	-0.638
1227	-2.87	-6.11	1387	-0.536	-1.225
			1587	-0.777	-1.79

3. Sequence

All circulators of PPWC stop during the single loaded operation without the reactor scram. The coolant flow through the core is lost within 10 seconds. Reactor power decreases. Fuel temperature once decreases and increases gradually. Temperature and flow rate of the pressurized water at the PPWC inlet are kept constant through the test.

4. Properties of structural materials

Attachment 1 [2]

IG-110 : Fuel, C/R and replaceable reflector blocks, and support posts

PGX : Permanent reflector, hot plenum, lower plenum and bottom blocks

ASR-0RB : Carbon blocks 2•1/4Cr-1Mo steel : RPV

5. Heat transfer correlation

Attachment 2 [2]

6. Core data

Active core equivalent diameter	2.3 m
Active core height	2.9 m
Fuel compact inner diameter	10×10^{-3} m
Fuel compact outer diameter	26×10^{-3} m
Sleeve inner diameter	26.25×10^{-3} m
Sleeve outer diameter	34×10^{-3} m
Coolant channel outer diameter	41×10^{-3} m
Number of hot channels	1
Number of average channels	953
Peaking factor	1.167

Power density

Block number	height(m)	Hot channel (kcal/s)	Average channel (kcal/s)
1 (Reflector)	1.46	0.0	0.0
2 (Fuel)	1.16	7.94324064×10^{3}	6.806575893×10^{3}
3 (Fuel)	0.58	9.128296713×10^{3}	7.822019463×10^{3}
4 (Fuel)	0.58	5.619801718×10^{3}	4.815597016×10^{3}
5 (Fuel)	0.58	3.622339965×10^{3}	3.103975977×10^{3}
6 (Reflector)	0.58	0.0	0.0

REFERENCES TO SECTION 3.2.1.

S.Saito, et al., “Design of High Temperature Engineering Test Reactor (HTTR)”, JAERI-1332 (1994).

M.Hirano and K.Hada, “Development of THYDE-HTGR computer code for transient thermal hydraulics of High Temperature Gas Cooled Reactor”, JAERI- M 90-07(1990).

Table 1 (3.2.1.) Major specification of HTTR

Thermal power	30MW
Outlet coolant temperature	850°C/950°C
Inlet coolant temperature	395°C
Fuel	Low enriched UO_2
Fuel element type	Prismatic block
Direction of coolant flow	Downward-flow
Pressure vessel	21/4Cr-1Mo Steel
Number of main cooling loop	1
Heat removal	IHX and PWC (parallel loaded)
Primary coolant Pressure	4 MPa
Containment type	Steel containment
Plant lifetime	20 years

Table 2 (3.2.1.) Thermal-hydraulic characteristics

Thermal power	30MW
Core diameter	2.3m
Core height	2.9m
Average power density	2.5MW/m^3
Fuel loading	off-load, 1 batch
Excess reactivity	15%Δk
Uranium enrichment	3~10wt%
average	about 6wt%
Fuel burn up(average)	22GWd/t
Reactivity coefficient	
fuel temperature coefficient	-(1.5~4.6) 10-5Δk/k/°C
moderator temperature coefficient	(-17.1~0.99) 10-5 Δk/k/°C
power coefficient	-(2.4~4.0) 10-3Δk/k/MW
Prompt neutron lifetime	0.67~0.70ms
Effective delayed neutron fraction	0.0047~0.0065
Total coolant flow	10.2kg/s(950°C)
Inlet coolant temperature	395°C
Outlet coolant temperature	950°C
Power peaking factor	
radial	1.1
axial	1.7
Effective core coolant flow rate	88%
Maximum fuel temperature	1492°C

Table 3 (3.2.1.) Additional data for the benchmark calculation

Axial peaking factors	
Inlet to outlet , with the active core axial length divided into 10 equal sections	0.5373, 0.6545, 0.8043, 0.9313, 1.2410, 1.286, 1.472, 1.293, 1.136, 0.6446
Radial peaking factors: centreline to outer effective diameter of the active core; 5 radial rings of approximately equal radius spacing	Ring / Percent to total volume 1 / 1.64 2 / 9.84 3 / 19.67 4 / 29.51 5 / 39.34
Temperature coefficient of reactivity feedback term	$\Delta k/k/^{\circ}C$ T(°C)
Fuel coefficient	$-3.09\times10^{-5}+13.3\times10^{-9}\times T$
Moderator coefficient	$-6.23\times10^{-5}-8.33\times10^{-9}\times T$
Time dependent of afterheat function	t; sec
P(0): initial power	$P/P(0)=0.125t^{-0.261}$
RCCS cooling water temperature	28°C
RCCS panel radiation shields	
Top and bottom cooling panels	1 shield
Side panels	3 shields
Emissivity for metal surface	0.8
Time for depressurization	5 minutes(ramp)
Xenon reactivity effects	Zero

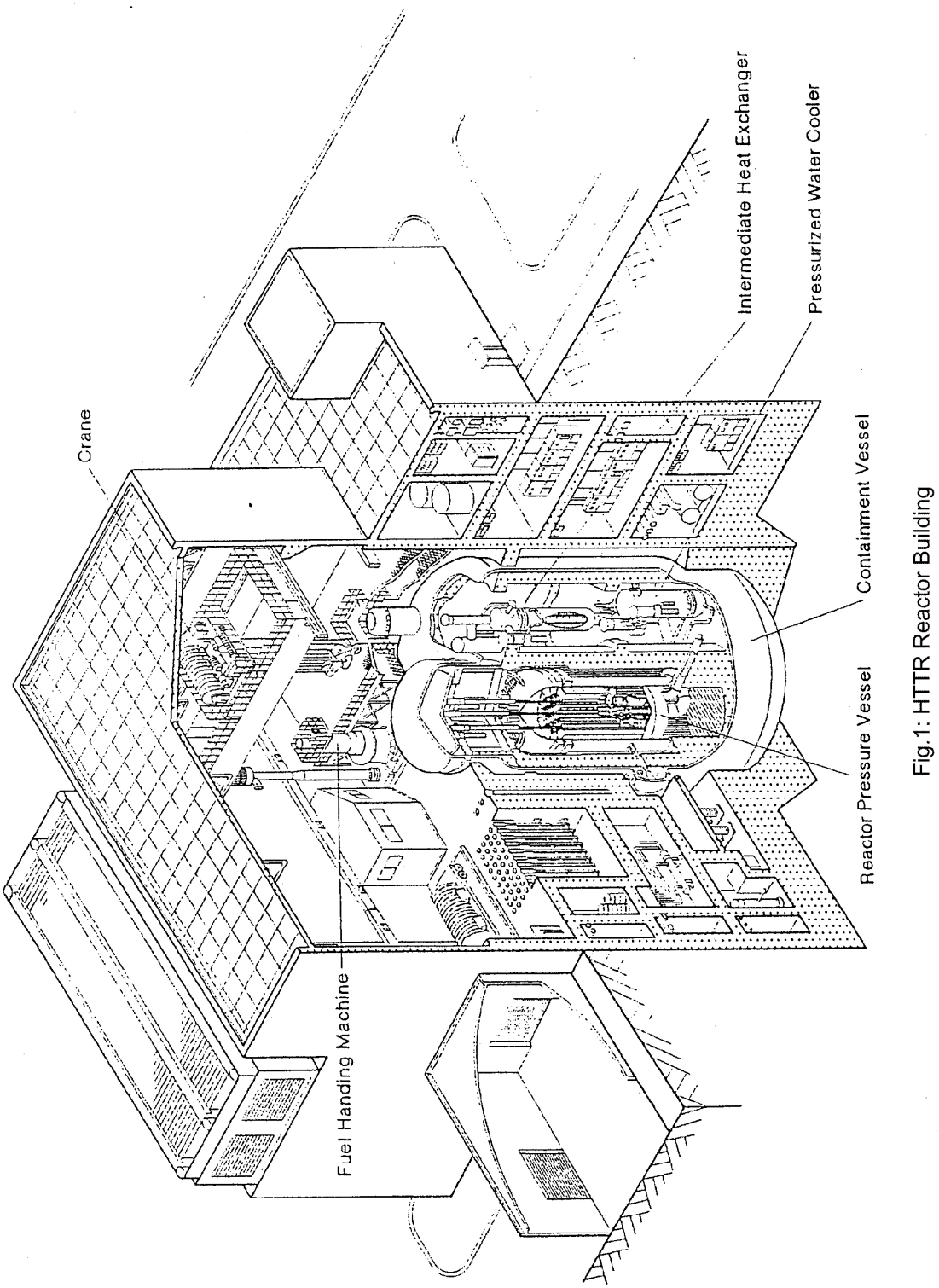

Fig. 3-14 HTTR Reactor building

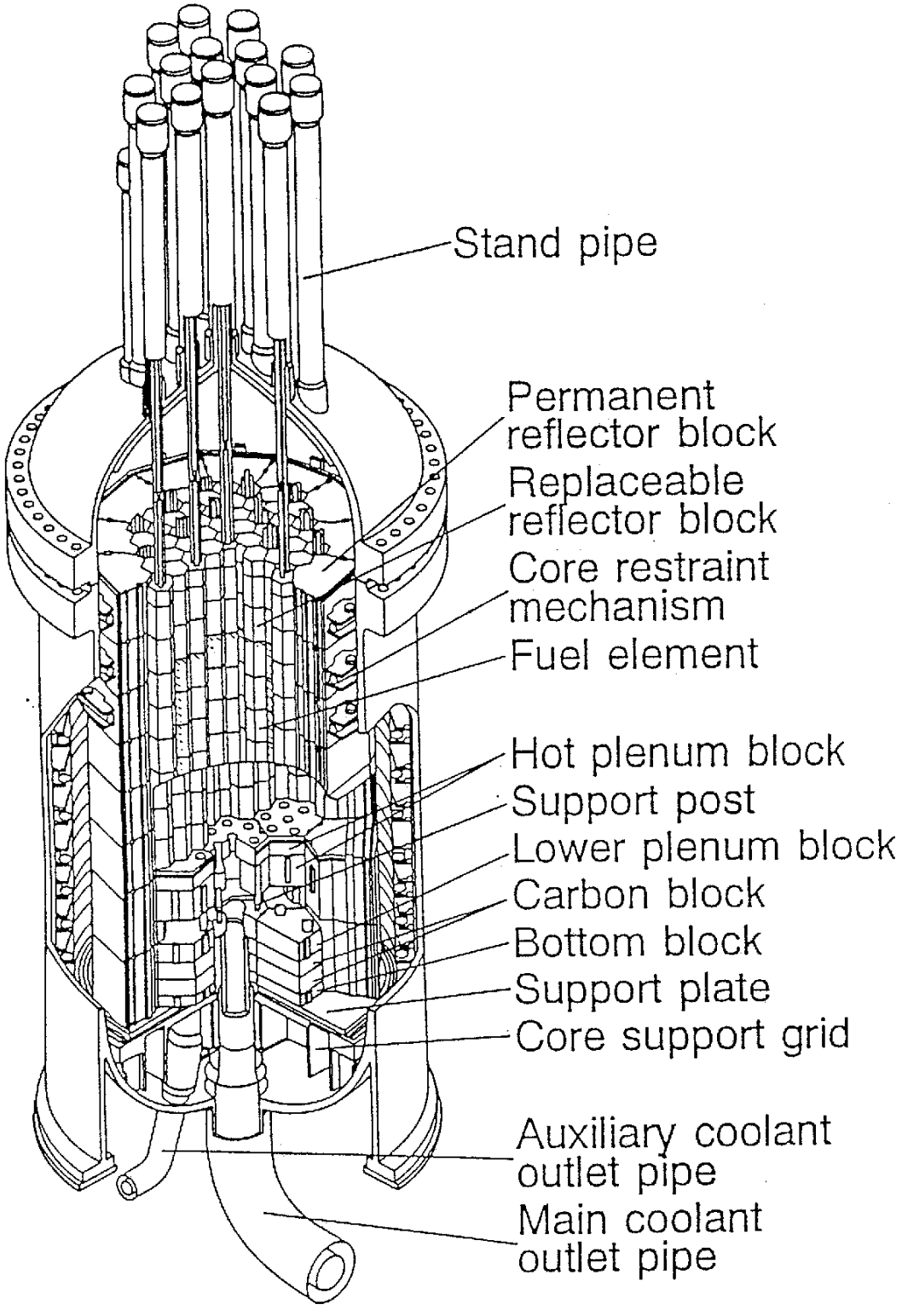

Fig. 3-15 Bird's Eye View of Reactor Vessel and Core

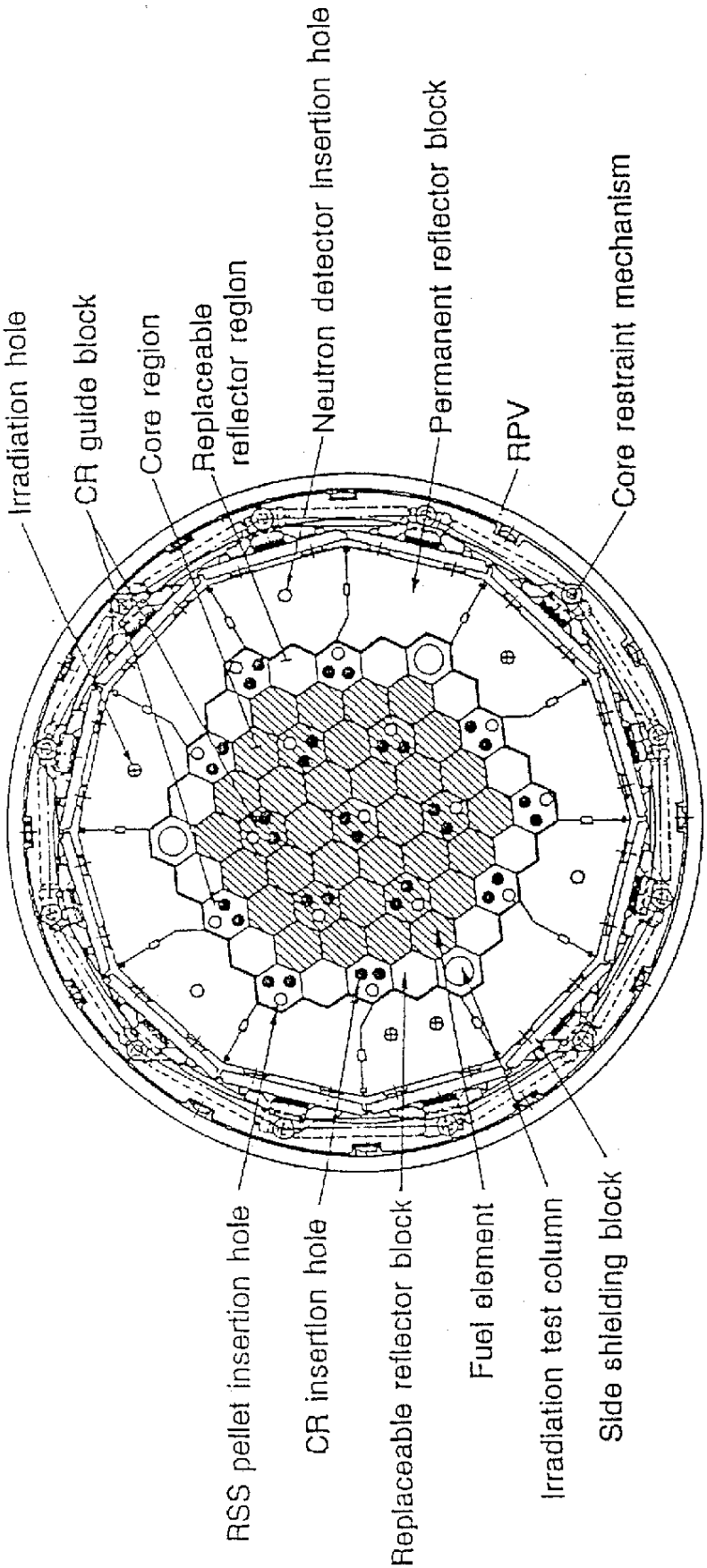

Fig. 3: Horizontal Cross Section of HTTR

Fig. 3-16 Horizontal Cross Section of HTTR

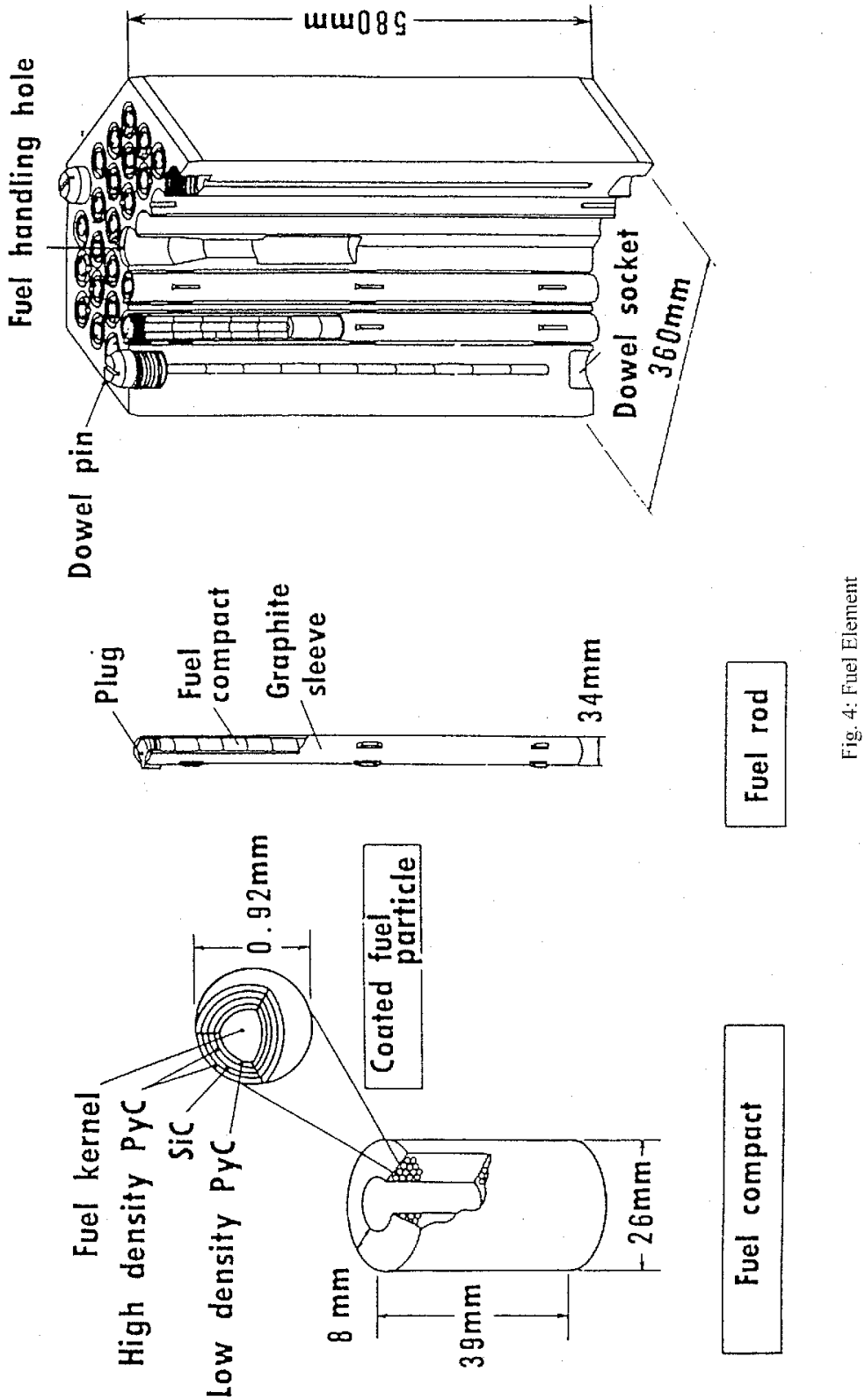

Fig. 4: Fuel Element

Fig. 3-17 Fuel Element

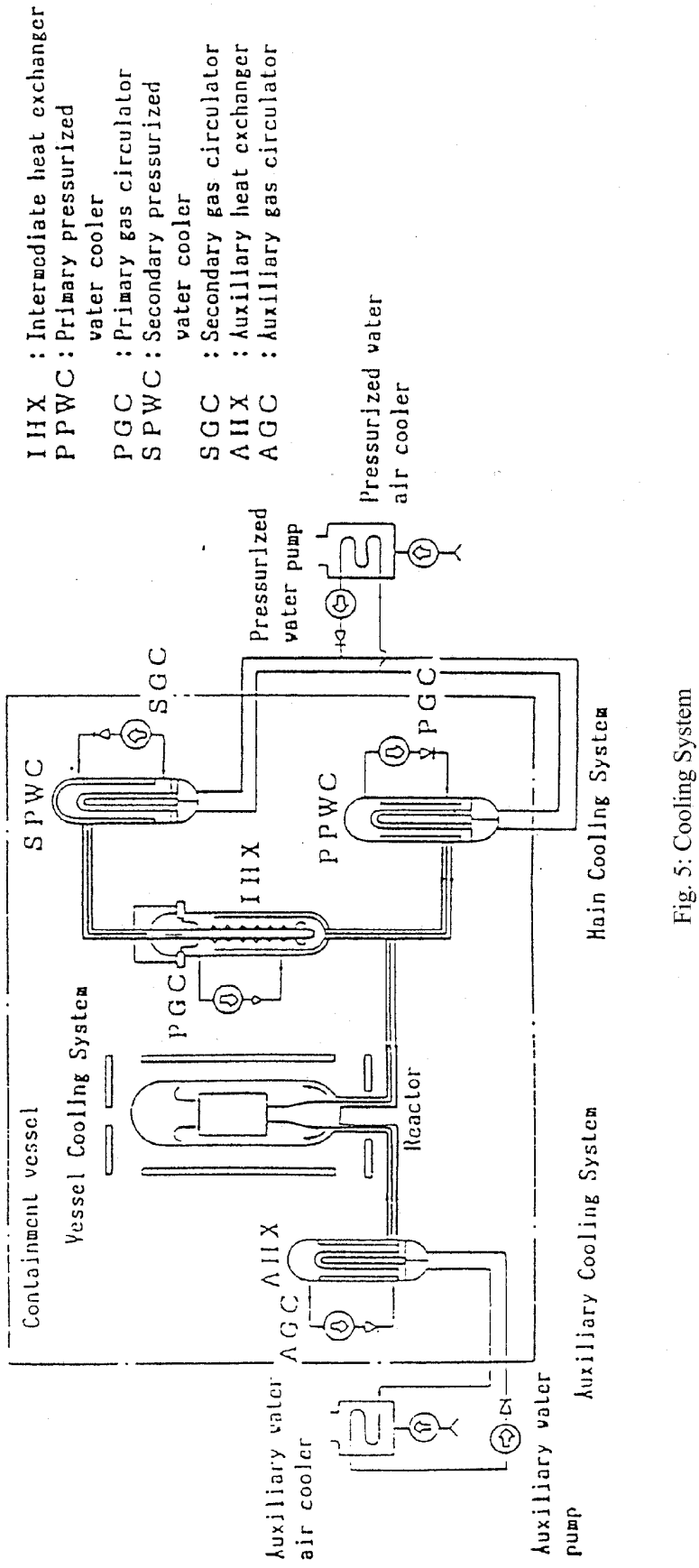

Fig. 5: Cooling System

Fig. 3-18 Cooling System

3.2.2. Analysis of HTTR Heat Up Accidents with the GRSAC Code

3.2.2.1. Introduction

The ORNL analysis of HTTR heat-up transients and accidents was done using GRSAC (Graphite Reactor Severe Accident Code). GRSAC, and its predecessor MORECA code[1], have been developed at ORNL over the past 20 years, and have been used at several different institutions to simulate accident scenarios for a wide variety of gas-cooled reactor designs, thus enhancing their credibility via numerous V&V exercises. A more detailed description of GRSAC is in the Appendix (A.2.3).

3.2.2.2. Special Features for HTTR Simulation

Several special features were needed in GRSAC to model the HTTR. Instead of using the nominal 163 radial nodes for the active core, 61 were used, with a total of 144 radial nodes used for the relatively large HTTR side reflector (Fig. 3-19). Axial and radial power peaking factors for the core were derived from the JAERI data (Section 3.2.1), where the radial peaking factors in GRSAC had to be renormalized to account for the large side reflector, and adjusted to account for the non-fissioning areas in the control rod drive (CRD) regions. Special core heat transfer and friction factor correlations were also used as provided by JAERI[2]. Fuel and moderator temperature coefficients of reactivity are modeled as functions of temperature. The flow coastdown input function for loss of forced convection (LOFC) accident scenarios assumed a circulator coastdown to a nominal (~0.1%) core flow in about 1min. The benchmark specification did not include an estimate of xenon poisoning, so it was assumed to be zero. Generally, beginning-of-cycle (BOC) parameters were used.

Based on V&V benchmark problems using the HTTR reactor cavity cooling system (RCCS) mockup, it was demonstrated that good approximations of the total heat removed from the vessel were possible using the simplified (~100 node) model for the vessel and RCCS. In place of the GRSAC air-cooled RCCS model, one based on the ORNL model developed for the HTTR RCCS experiment mockup was used.

The core helium inlet coolant in the HTTR flows upward along the outside of the core barrel (as in the U.S. design GT-MHR, and MORECA), thus cooling the vessel during normal operation, as opposed to the reference GRSAC case, where the coolant goes directly from the circulator to the inlet plenum. A special model feature was added to GRSAC to include the vessel cooling flow path for the HTTR case.

3.2.2.3. Solution of the benchmark problem

The benchmark HTTR heatup accident problem is an LOFC accident (without depressurization) and with no scram for the duration of the accident. Fig. 3-20 is a post-run plot showing GRSAC code results of the accident for the short term (10min.). The maximum fuel temperature peaks at 1065°C or 24°C above the initial value, about 1min after the start of the accident. Plots of the reactor power, flow, and pressure transients are also shown. In the longer term (Fig. 3-21), the fuel temperature peak at t=12.2 h is 1082°C. After the recriticality the maximum fuel temperature climbs gradually, nearly leveling off at about 1060°C after 120 h (5 days). In the plot (lower right) showing a blowup of the power trace at recriticality note the characteristic oscillatory behavior that occurs when the power first increases. The vessel maximum temperature transient (upper right) is very mild, peaking at only 7°C higher than its normal value of 335°C after 16hrs.

Numerous variations on the reference case were run to determine sensitivities of the results to changes in input parameter assumptions. Other runs showed that whenever a scram

occurs, the maximum core temperatures decrease slowly but surely, at a rate of about 125°C per day. It can be concluded that the HTTR can readily withstand the design basis accident used as the benchmark problem.

REFERENCES TO SECTION 3.2.2.

Ball, S. J., and D. J. Nypaver, "Interactive Simulations of Gas-Turbine Modular HTGR Transients and Heatup Accidents," Advanced Reactor Safety 1994 International Topical Meeting, Pittsburgh, Penn., 17-21 April, 1994.

Saito, S., T. Tanaka, et. al., "Design of High Temperature Engineering Test Reactor (HTTR)," JAERI-1332, Japan Atomic Energy Research Institute, Oarai Research Establishment, September 1994.

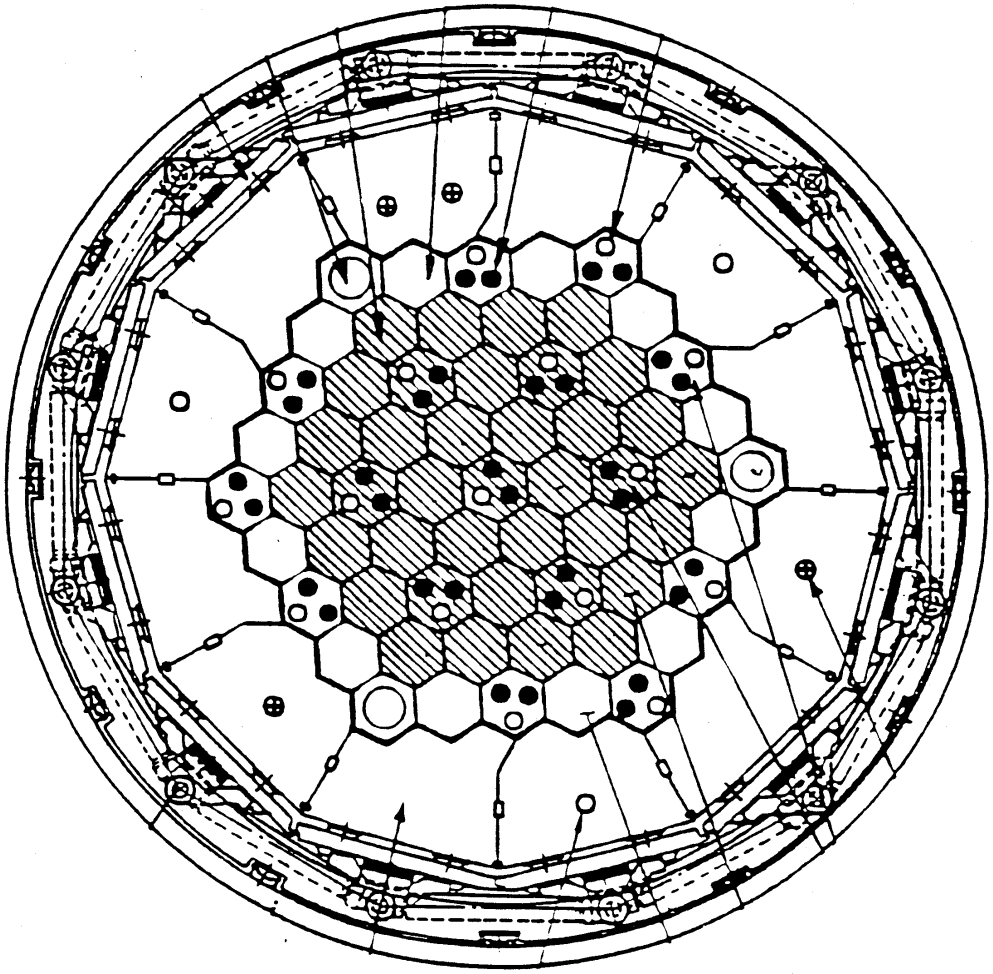

Fig. 3-19 HTTR Core, with active core (shaded region) modelled by 61 radial nodes, and the side reflector by 144 radial nodes

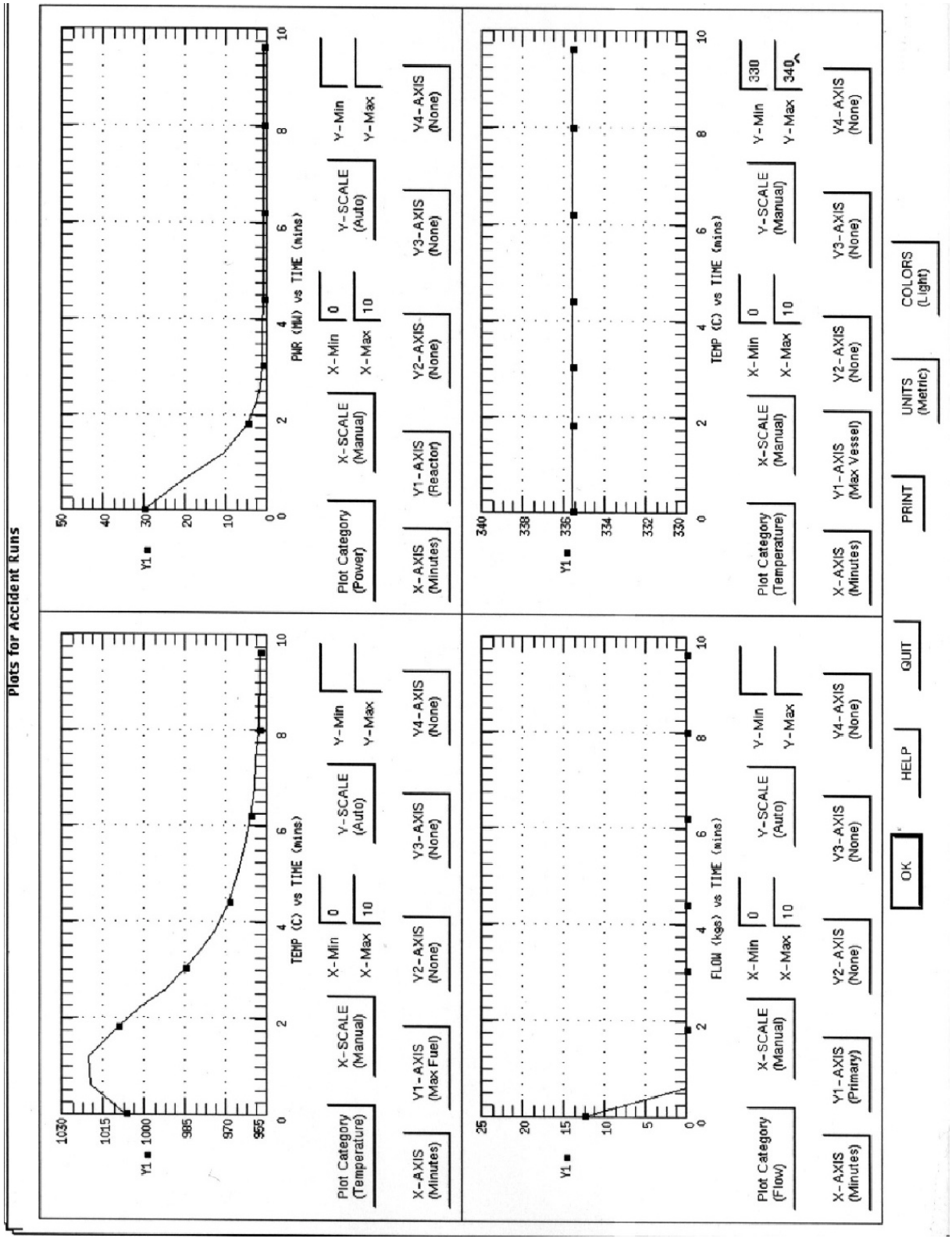

Fig. 3-20 GRSAC post-run plot of short-term results of HTTR benchmark accident case: Pressurized LOFC with ATWS showing maximum fuel, reactor power, flow coastdown, and maximum vessel temperature vs. time

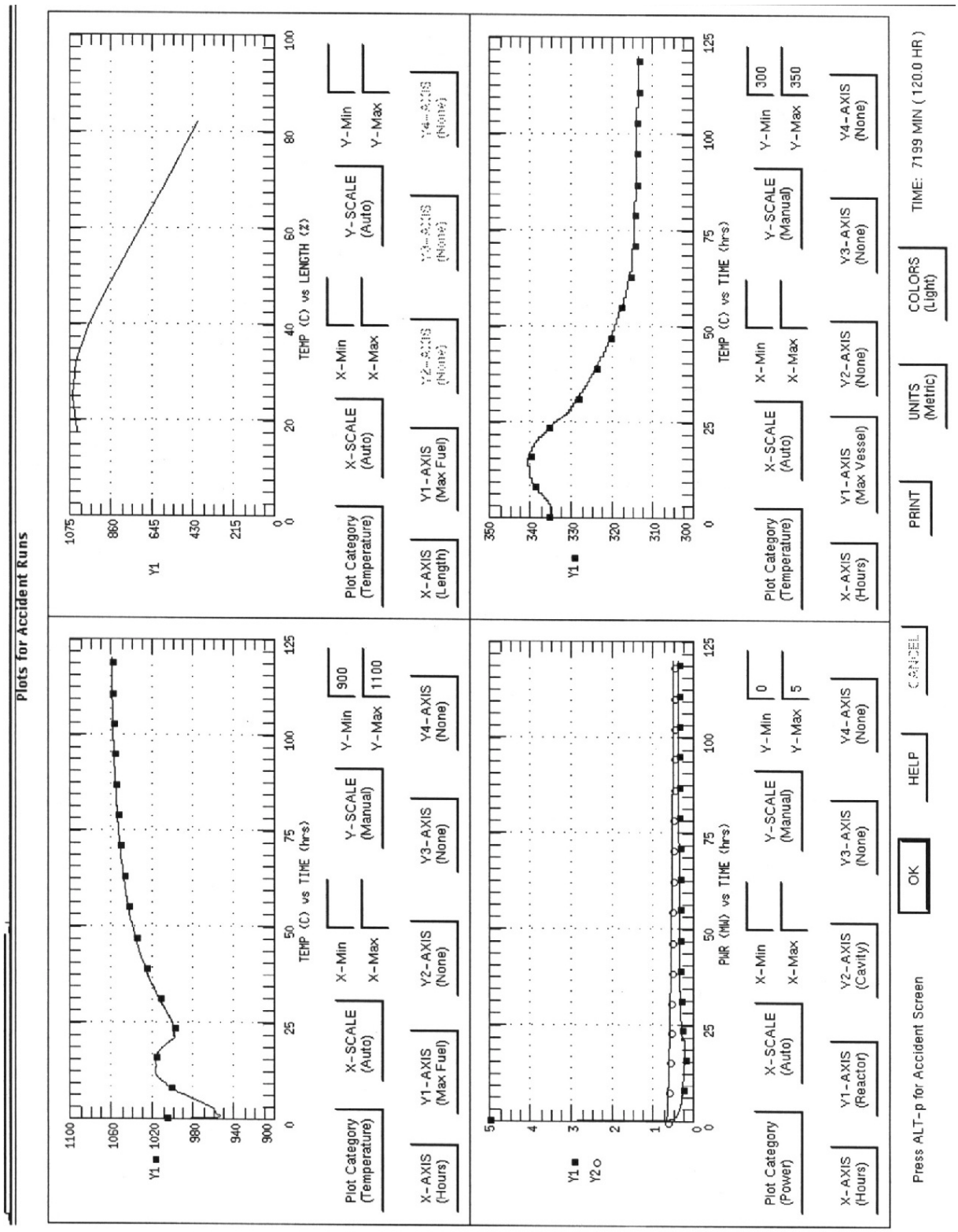

Fig. 3-21 GRSAC on-line plot of long-term results of HTTR benchmark accident case: Pressurized LOFC with ATWS showing time responses and an axial profile of maximum fuel temperature at time = 120 h

3.2.3. Results of Calculations of HTTR Heat-up Accidents

3.2.3.1. Introduction

The OKBM analysis of HTTR heat up accidents was done as a part of the IAEA Coordinated Research Program on "Heat Transport and Afterheat Removal for Gas-Cooled Reactors under Accident Conditions". VGM and GTAS codes were used for the analysis. The codes were developed to analyze safety problems of VG-400, VGM and other HTGRs.

VGM - code allows to analyze transients with account of reactivity feedback, change of flowrates and temperatures in circuits, fuel and moderator temperatures. The fuel and moderator temperatures are computed without affects of convective and radiative heat transfer. Therefore, the calculations with VGM - code were performed only for the initial phase of the accident when convection and radiation affect insignificantly on fuel and moderator temperatures.

Temperature distributions in the core and reactor vessel temperature for long-term period were calculated by using GTAS - code. Description of the codes is given in item A.2.2.

3.2.3.2. Model Features and Limitations

The calculation of reactor power transient was performed by using of VGM - code for 1000 s of the accident process. Values of reactivity coefficients for fuel and moderator vs. temperature, axial and radial peaking factors are taken from [1].

It was taken that the forced flowrate through the core is linearly changed, during 10s from nominal value to zero. Temperatures and flowrate in the second circuit are not changed during 1000s.

Calculations of core and reactor vessel temperatures during 100 hours are based on GTAS - Code. HTTR calculation grid is shown in Fig. 3-23.

Temperature of RCCS cooling coils was adopted 20°C emissivity of graphite and metallic structures is 0.8.

Core heat transfer coefficients for Re≥2000 are calculated using a correlation from [2]:

$$Nu = 0.018\ Re^{0.8}$$

For laminar flow Nu = 3.66. A correlation for friction factor in turbulent region is derived from [3]:

$$\lambda = 0.316/Re^{0.25}$$

For laminar flow $\lambda = 64/Re$. GTAS - code is not intended for calculations of reactivity effects. Therefore, time of recriticality due to decrease of fuel and moderator temperatures was not determined

Decay power vs. time was calculated using the function given in [1].

3.2.3.3. Results

The analysis of the HTTR benchmark problem with loss of forced flowrate and with no scram gives the following results.

Figure 3-23 shows transient behaviour of the reactor power from rated value up to residual power. The reactor power is rapidly dropped due to negative reactivity feedback connected with change of fuel and moderator temperatures.

Figures 3-24 and 3-25 show fuel and reactor vessel temperatures during long-time period with and without pressure in the primary circuit. The temperatures are calculated without taking into account uncertainties of the input data.

The curve of maximum fuel temperatures is derived on basis of extraction of maximum temperature value over the whole volume of the core for the given moments of time. As can be seen, maximum fuel temperature is quickly dropped in beginning of the accident due to heat transfer to more "cold" moderator, then insignificantly increases, and after that continue decreasing. Average fuel temperature decreases at the beginning, and gradually drops after insignificant rise. The rise lasts ~10 hours, after that the temperature slowly decreases. For the depressurized accident fuel temperatures in the core central region are more than for the pressurized one by reason of less active heat removal from the core at the expense of helium natural convection.

It is also given fuel temperatures in the core central region in which there are conditions for its more rapid increase as heat generation is close to maximum value, but axial and radial heat removal is more difficult as compared to the rest core volume.

Reactor vessel temperature decreases almost from the very beginning of the accident. Maximum temperatures are not more than 400 °C for both pressurized and depressurized conditions

3.2.3.4. Sensitivity Study

The sensitivity study is performed for maximum fuel temperatures at variation of emissivity and decay power. The calculations are provided only for the depressurized accident as for maximum fuel temperature case.

Figure 3-26 gives fuel temperatures at decay power 20% more than the reference values. Maximum fuel and vessel temperatures are inconsiderably changed, but the temperatures fall more slowly as compared to the reference case (Fig. 3-24). By 60h the fuel and vessel temperatures reach maximum differences from the reference values (85°C and 25°C respectively).

Variation of emissivity of graphite and metallic surfaces from 0.8 to 0.6 leads to the same effects with some differences in values. Thus, by 60 h the fuel and vessel temperatures are higher than for reference case on 40°C and 45°C respectively.

Therefore, the variation of the input data in significant range does not result in significant rise of temperatures.

3.2.3.5. Conclusions

- The HTTR benchmark problem study using VGM and GTAS codes without taking into account recriticallity give the following results,
- Maximum fuel temperatures decrease during the whole process as for pressurized and depressurized accidents,
- In core region with maximum power density the fuel temperatures rise after early drop, then decrease slowly. The same is for averaged fuel temperatures and reactor vessel temperatures,
- Maximum fuel temperature in the accident formulated as the benchmark problem is well lower as compared to limit value of 1600°C,
- Maximum reactor vessel temperature does not exceed 400°C,
- Values of maximum fuel temperature and course of the curves inconsiderably depend on uncertainties of input parameters.

REFRENCES TO SECTION 3.2.3.

S. J.Ball, E-mailed letter,January 8,1998, Oak Riage National Laboratory.

V.I. Subbotin et al., “Gidrodinamika i teploobmen v yadernich energeticheskich ustanovkach”, M., Atomizdat, 1995.

I.E. Idel’chik, “Spravochnik po gidravlicheskim soprotivleniyam”, M., “Mashinostroenie”, 1975.

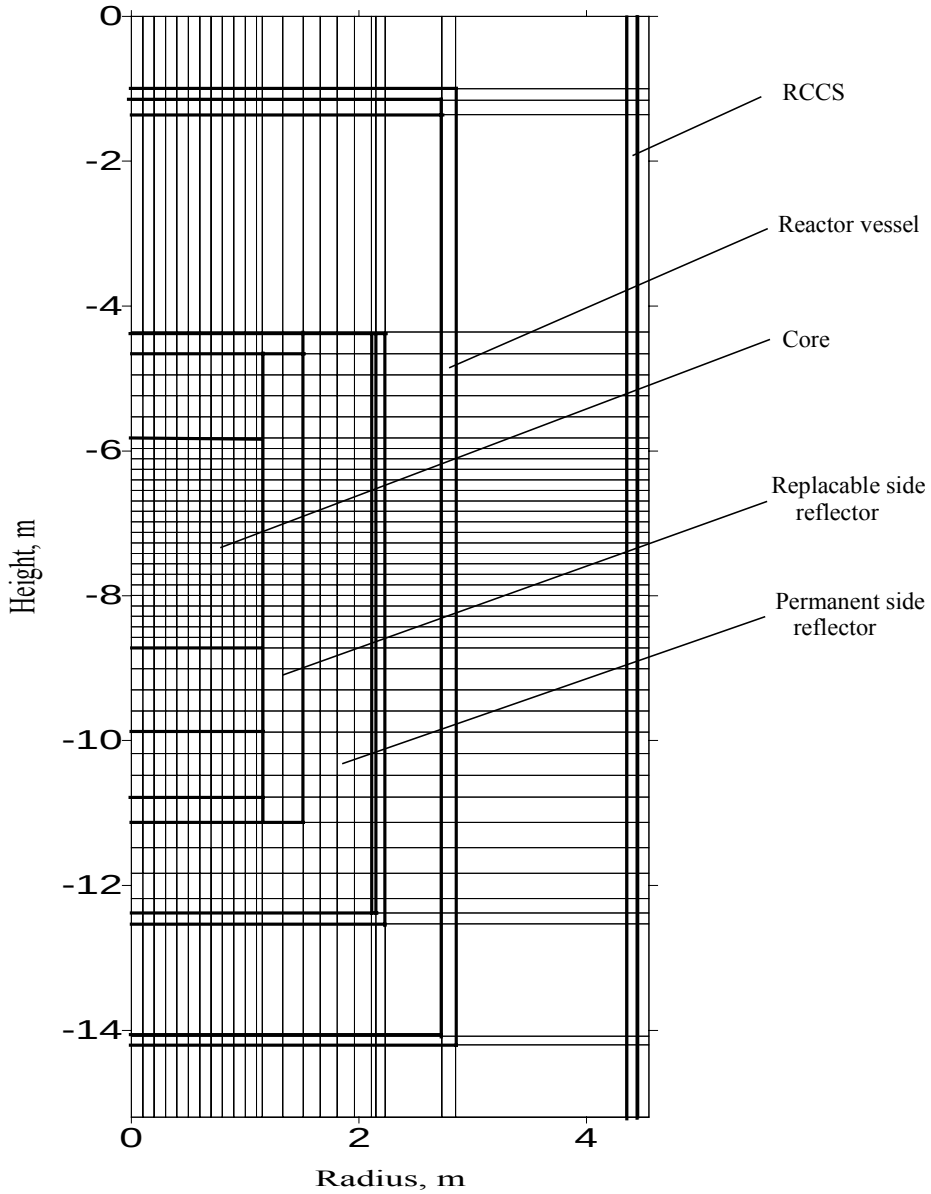

Fig. 3-22 GTAS - code Computational Grid

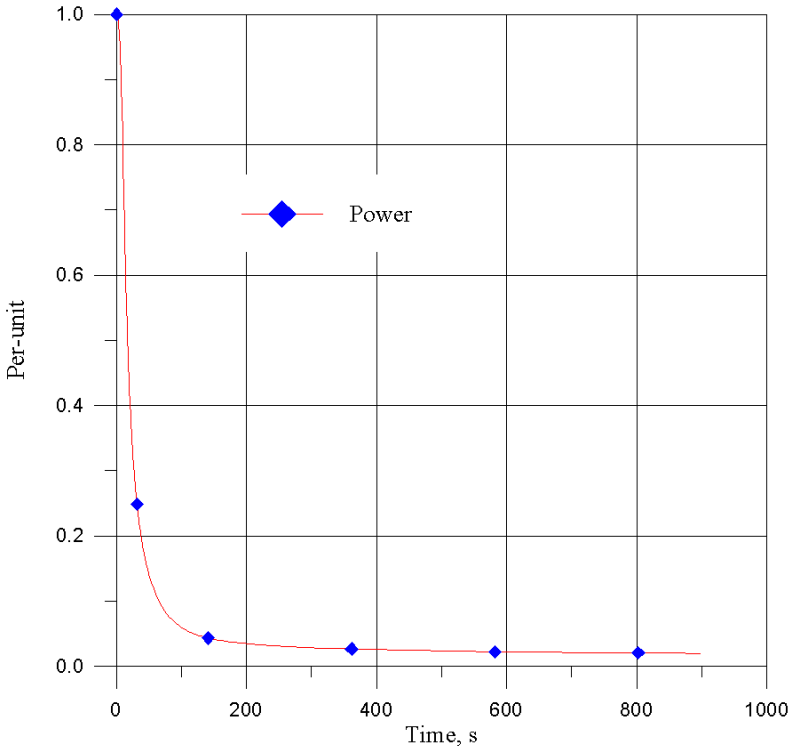

Fig. 3-23 Reactor Power Transient

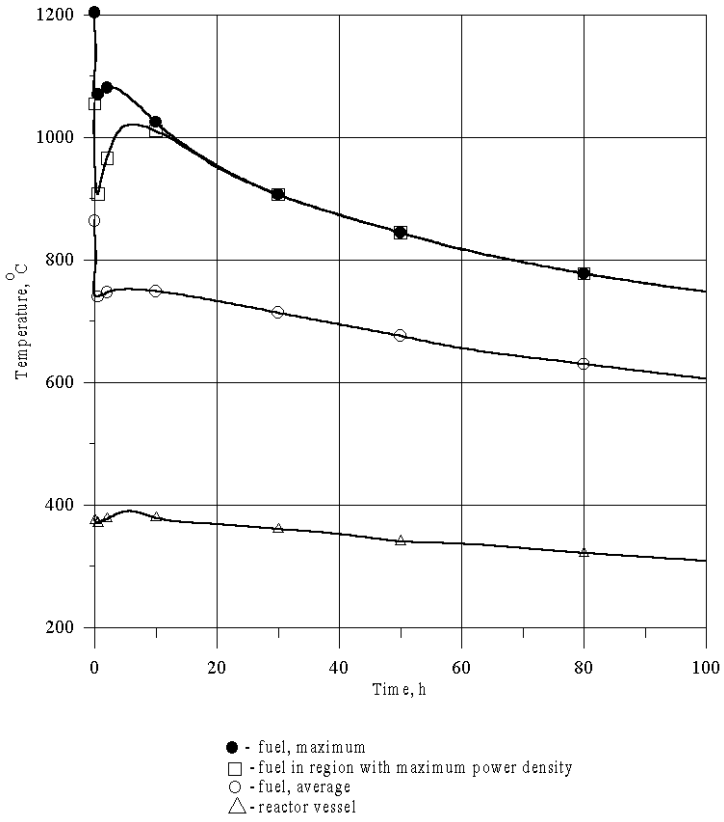

Fig. 3-24 Fuel and Reactor Vessel Temperatures. Depressurized Conditions

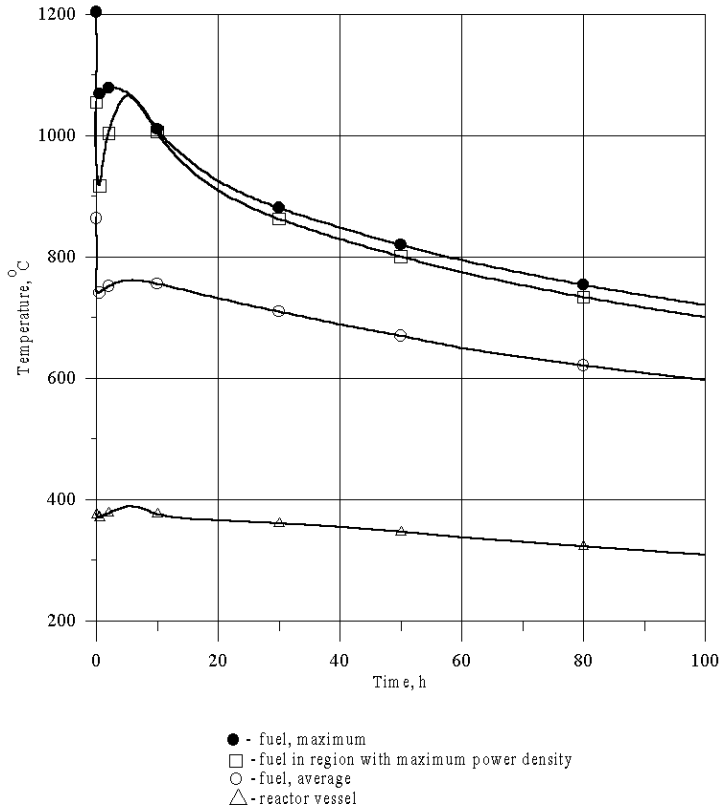

Fig. 3-25 Fuel and Reactor Vessel Temperatures. Pressurized Conditions

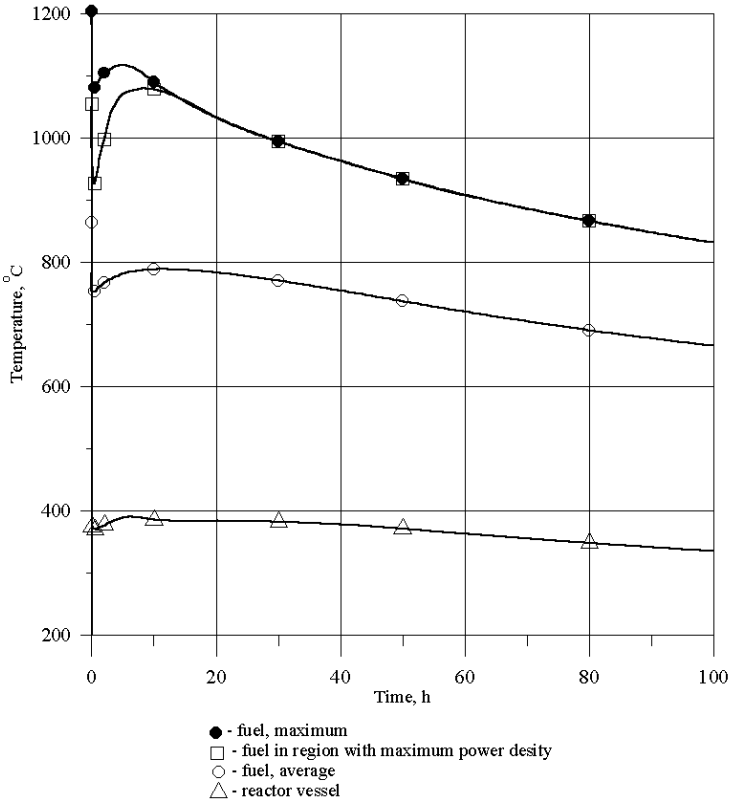

Fig. 3-26 Fuel Temperatures. 20% Increase of Decay Heat. Depressurized Conditions

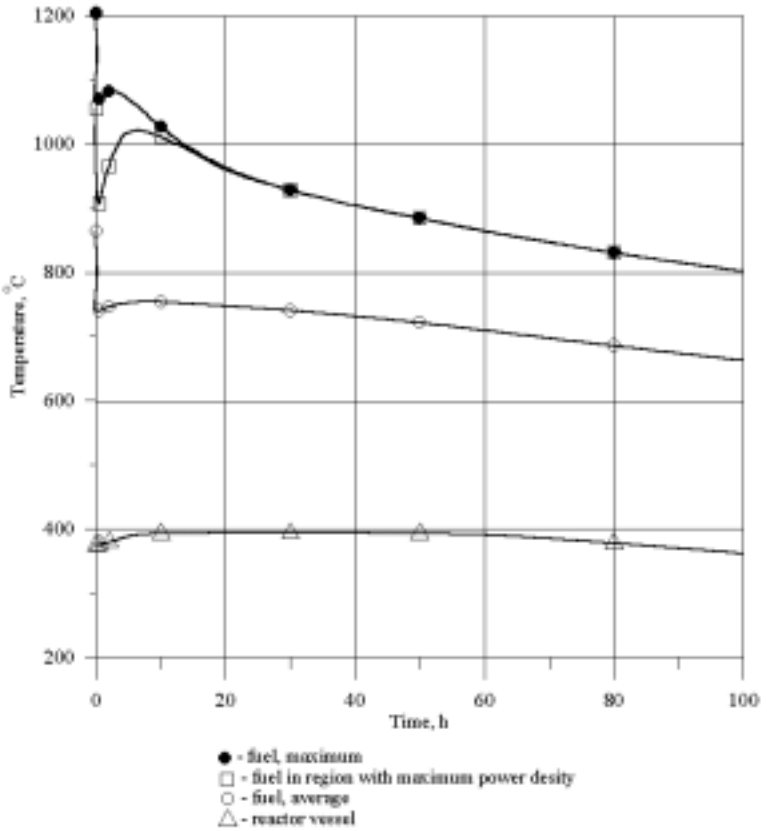

Fig. 3-27 Fuel Temperatures at Emissivity of 0.6. Depressurized Conditions

3.2.4. Analysis of HTTR Heat Up Accidents with the THYDE-HTGR Code

3.2.4.1. Analytical Code

The transient behavior is analyzed using the THYDE-HTGR code[1]. The THYDE-HTGR code is used to analyze the transient thermal-hydraulic characteristics of the PCS, secondary helium cooling system, PWCS and ACS. In the THYDE-HTGR code, the coolant flow paths, including the reactor core, are simulated by a flow network model with nodes of finite volume and junctions which are in contact with the nodes. Thermal-hydraulic transients are calculated by solving conservation equations of mass, momentum and energy in helium gas and water. Temperature distributions in the structure such as fuel rods, moderator graphite, heat transfer tubes in the IHX and pipes are obtained by solving the one-dimensional transient heat conduction equation. An analytical model of the HTTR system is shown in Fig. 3-27.

3.2.4.2. Analytical Results

In this calculation, all gas circulators of the main cooling system stop. Figs. 3-28 – 3-29 show results of the loss of coolant accident simulation from 0 second to 8000 seconds after all gas circulators stop. Coolant mass flow rate decreases rapidly after circulators stop as shown in Fig. 3-28. Maximum fuel temperature increases from 1381°C to 1387°C at 23 seconds, then decreases to about 1190°C at 400 seconds as shown in Fig. 3-29. The temperature increases gradually after 400 seconds, but does not exceed 1387°C. Reactor power decreases to about 5% within 400 seconds rapidly as shown in Fig. 3-30. Reactor outlet coolant temperature also decreases from 869°C to about 750°C within 400 seconds as shown in Fig. 3-30.

REFERENCE TO SECTION 3.2.4.

[1] M.Hirano and K.Hada,Development Of Thyde-HTGR:Computer Code For Transient Thermal-Hydraulics of High-Temperature Gas-Cooled Reactor JAERI-M90-07(1990)

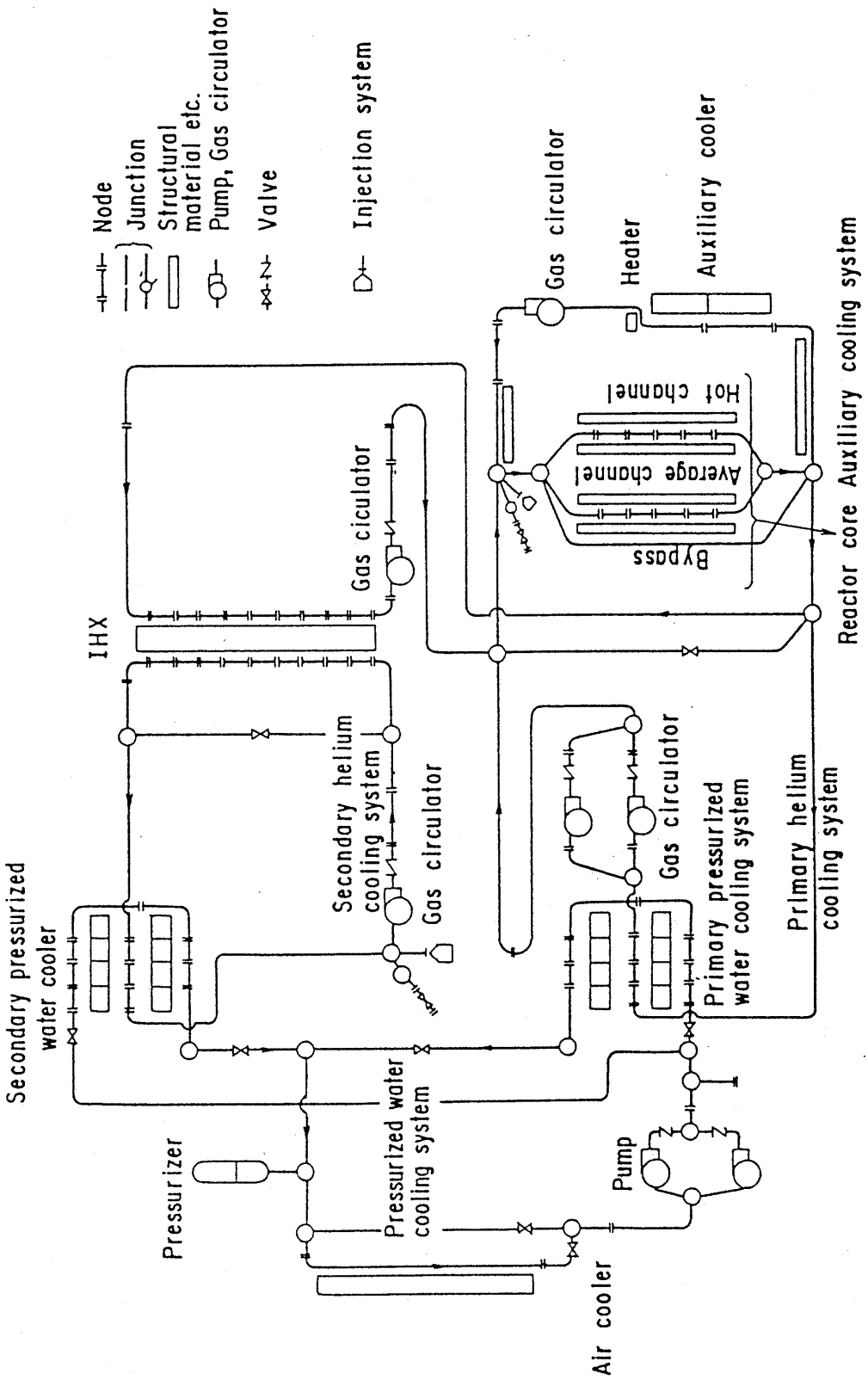

Fig.1: Analytical Model of THYDE-HTGR Code

Fig.3-28 Analytical Model of THYDE-HTGR Code

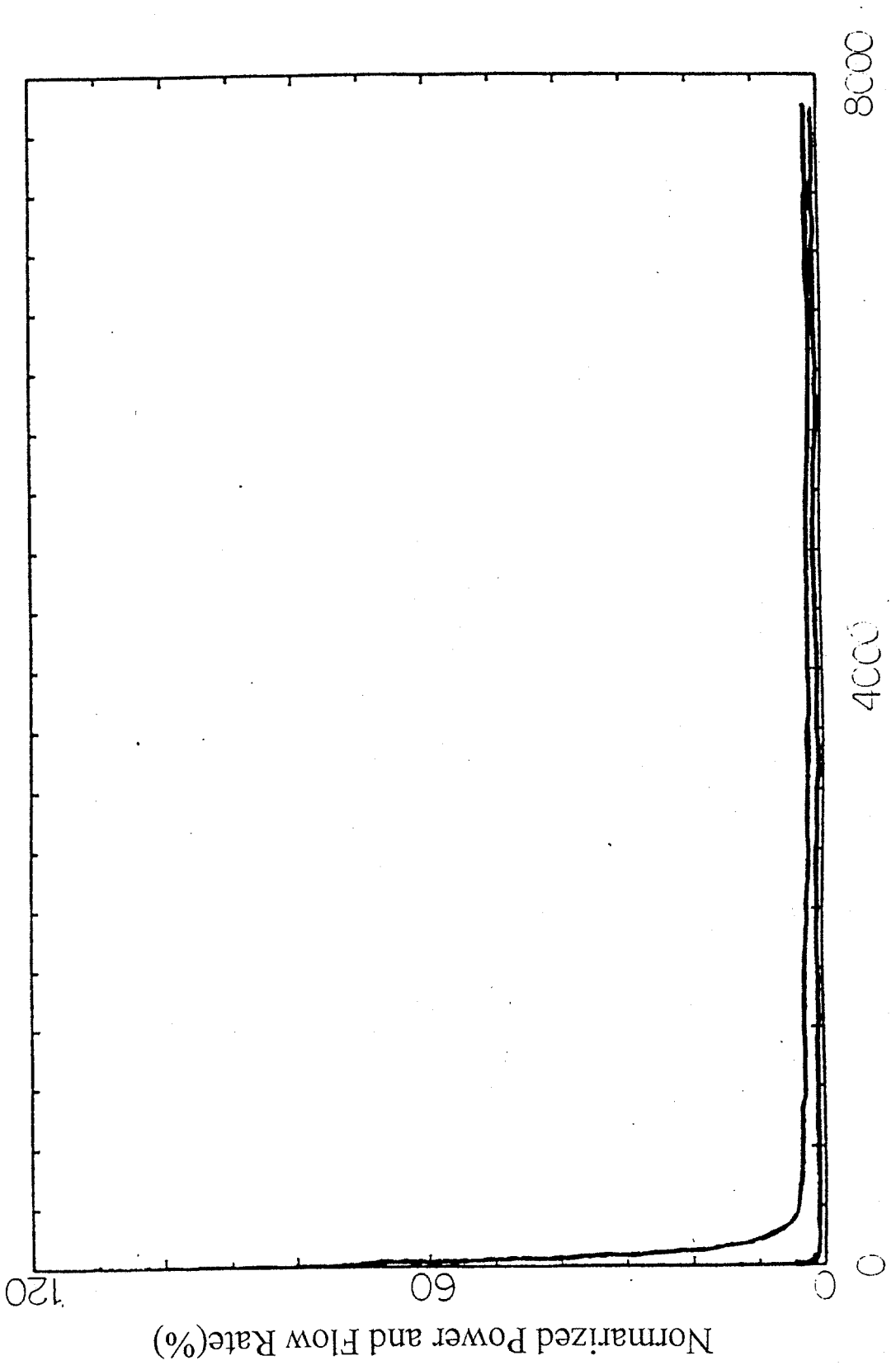

Fig. 2: Transient of Mass Flow Rate and Reactor Power

Fig. 3-29 Transient of Mass Flow Rate and Reactor Power

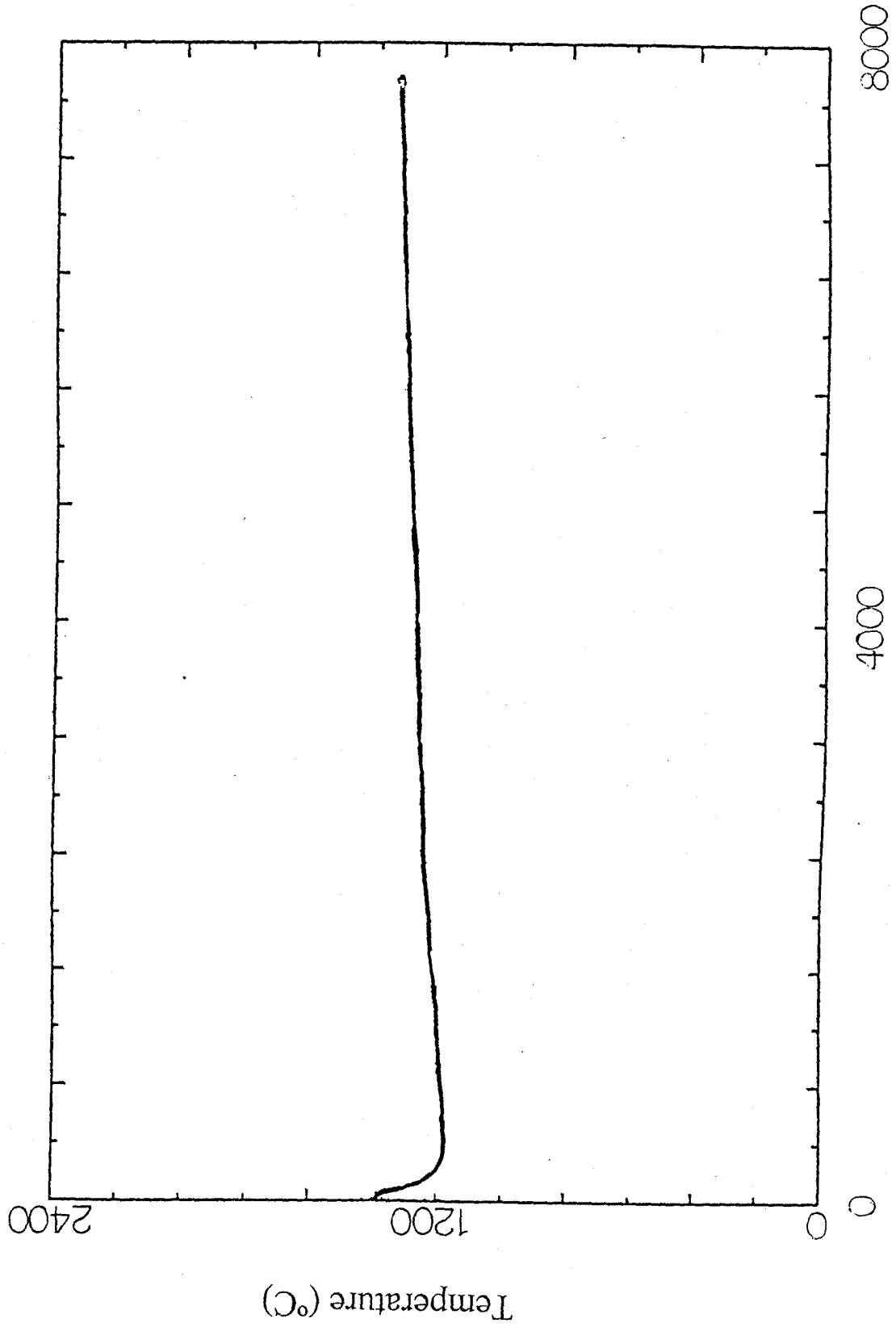

Fig. 3: Maximum Fuel Temperature Transient

Fig. 3-29 Maximum Fuel Temperature Transient

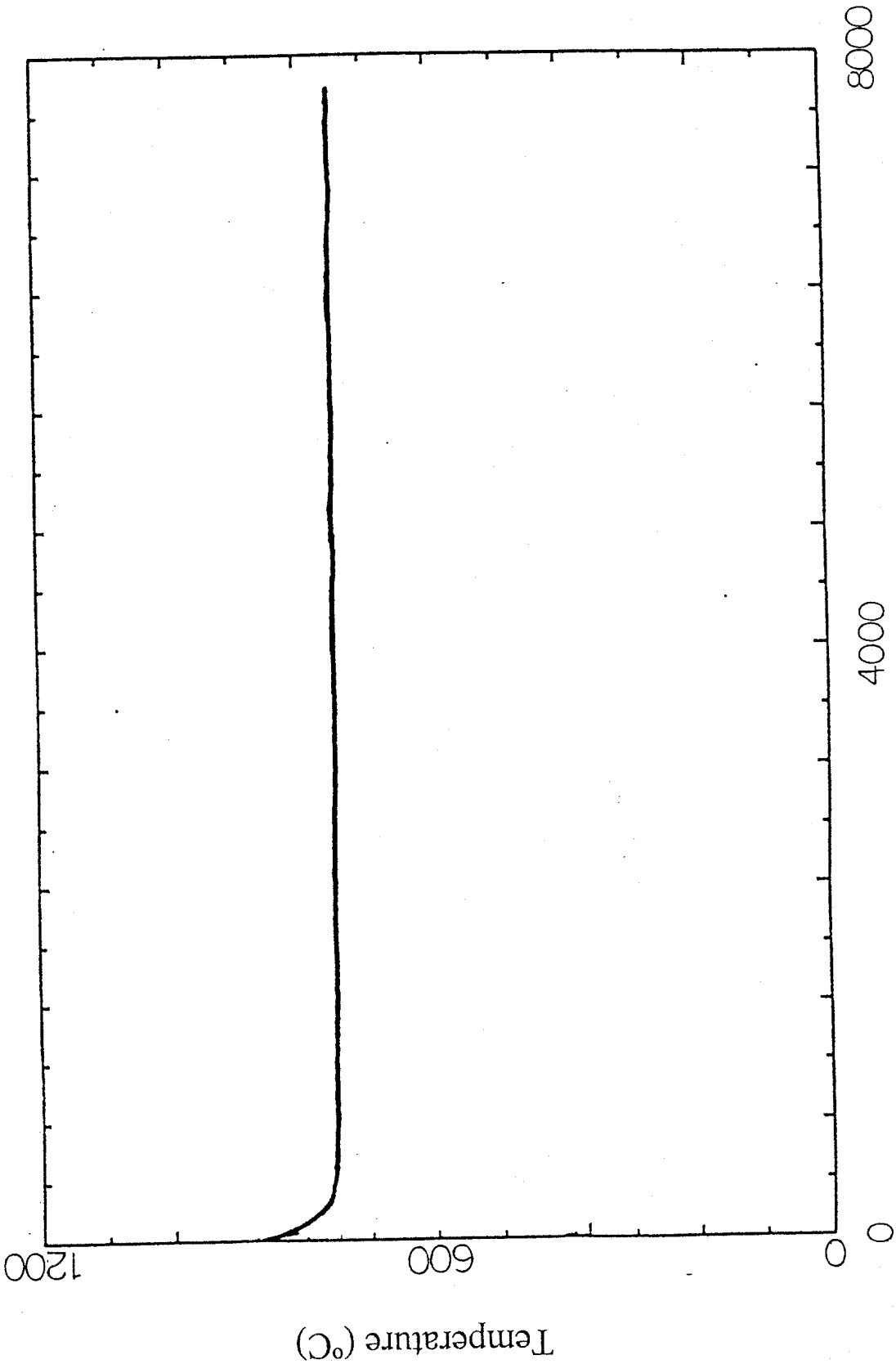

Fig. 4: Reactor Outlet Temperature Transient

Fig. 3-30 Reactor Outlet Temperature Transient

3.2.5. Comparison and Conclusions

3.2.5.1. Results Comparison and Discussion

The loss of core flow accident simulation in the depressurized condition is selected as the benchmark problem of the HTTR analysis of heat up accidents. In the simulation, all circulators of the Pressurized Water Cooler (PWC) in a primary circuit stop without the reactor scram.

The benchmark problem was analyzed by USA (GRSAC code), Russia (VGM and GTAS codes) and Japan (THYDE-HTGR code).

Reactor Power

Table 3-14 shows the comparison of time that reactor power becomes nearly equal to zero during the heat up accident. These values were read from figures, therefore, the correctness of the values depend on the time scale of the figures. Anyhow, reactor power decreases in two to five minutes after all circulators stop

Table 3-14 Comparison of the time that reactor power becomes nearly equal to zero

	USA	Russia	Japan
Time(second)	200	120	300

Maximum fuel temperature

Table 3-15 shows the comparison of the maximum fuel temperature and elapsed time after the start of the accident. The results of Russia and Japan show rapid decrease in maximum fuel temperature at early times of the accident, it increases gradually after the decrease in the results of Japan, whereas, monotonically decreases in Russian results. The results of USA show two peaks in fuel temperature in shorter and longer terms. After recriticallity the maximum fuel temperature increases gradually.

The maximum fuel temperature of Japan is considerably higher than those of USA and Russia. The causes of the difference will be mainly the use of conservative initial fuel temperature, about 1380°C and lack of VCS model in the analysis of THYDE-HTGR code. When nominal value of initial fuel temperature is used, the maximum fuel temperature will be reduced at about 1200°C.

The differences in the behaviour of fuel temperature will be due to the difference in physical properties of fuel, heat transfer characteristics between fuel and coolant and so on used in the calculations. Further information exchange will be necessary to correct comparison of each analytical code.

Table 3-15 Comparison of the maximum fuel temperature and elapsed time

		USA	Russia	Japan
Maximum fuel Temperature (°C)	Short term	1065(24)	1250(100)	1387(6)
(difference from initial temperature)	Long term	1082(41)		>1350
Elapsed time	Short term (second)	60	0	0
	Long term (hour)	12.2		>2.2

Vessel temperature

Table 3-16 shows the comparison of the maximum vessel temperature and elapsed time obtained in each calculation. The results of both USA and Russia show qualitatively same behavior. Vessel temperature increases in early stage and decreases gradually to surrounding temperature. Duration time of the maximum vessel temperature is much longer in Russia than in USA. This would be due to same reason as described before.

Table 3-16 Comparison of the maximum vessel temperature and elapsed time

	USA	Russia	Japan
Maximum vessel temperature (°C) (difference from initial temperature)	335 (7)	400 (60)	
Elapsed time (hour)	16	2—10	

3.2.5.2. Conclusions

- Qualitatively, agreement was good in the behaviour of reactor power and vessel temperature transients. The reactor power decreases almost zero in 2 to 5 minutes. Vessel temperature shows the maximum value at 2 to 20 hours after the onset of the accident,
- There were much difference in the behaviour and the values of the maximum fuel temperature. The reason will be due to the differences of initial fuel temperature, fuel properties, heat transfer characteristics and the models used in the benchmark analysis,
- Further information exchange will be necessary to make accurate comparison of each code.

3.3. HTR–10 ANALYSIS OF HEAT UP ACCIDENTS

3.3.1. Benchmark Problem Definition on HTR-10

3.3.1.1. Introduction

HTR-10 reactor is a high temperature gas-cooled test reactor to be built in INET, China. It has the inherent safety features of advanced HTGRs, such as automatically being shut down because of negative temperature reactivity coefficient, passive afterheat removal capability by which the residual heat is transported from the reactor in mechanisms of conduction, natural convection and radiation, etc. The project of HTR-10 not only aims at verify important technologies of GCRs, but also has the following research objectives:

- application range research, include research of electricity, steam and district heat generation, GT-cycle, process heat generation and methane reforming, etc.,
- testing of relevant components, e.g., graphite core structure, steam generator, helium blower and fuel handling facility,
- verification of inherent safety of HTR-10,
- mass-test of fuel elements.

The primary system of HTR-10[1] consists of the reactor vessel, the hot gas duct vessel and the steam generator vessel, shown in Fig.3-31. The main data of HTR-10 is given in Table 3-17.

Table 3-17 HTR-10 main data

parameter	value
thermal power (Mw)	10
primary helium pressure (MPa)	3.0
inlet helium temperature (°C)	250
outlet helium temperature (°C)	700
primary coolant flow rate (kg/s)	4.3
outlet steam pressure at the S.G. (MPa)	4.0
outlet steam temperature at the S.G. (°C)	440
secondary steam flow rate (kg/s)	3.47
core volume (m^3)	5.0
core diameter (m)	1.80
core height (avg.) (m)	1.97
H/D Ratio	1.09
diameter of fuel element (cm)	6
number of fuel elements	27,500
burn-up (avg.) (MWd/t)	80,000

The passive decay heat removal system of HTR-10 consists of two independent reactor cavity cooling system (RCCS).

As part of the Coordinated Research Program on "Heat Transport and Afterheat Removal for Gas Cooled Reactors under Accident Conditions", three benchmark problems are defined on HTR-10. The aims of this activity are:

– to verify heat transport ability of RCCS of HTR-10 under heatup experiment condition and accident condition,
– to confirm inherent safety features RCCS of HTR-10,
– to validate tools of predicting response of GCRs in code-to-code comparison methods,
– to study heat transport processes of HTR-10 under steady and transient conditions.

These benchmark problems respective are defined under heating experiment condition and LOCA depressurization accident.

3.3.1.2. Component Structure[1]

HTR-10 is a pebble bed high temperature gas-cooled test reactor. The components in the RPV consist of the graphite reflector, carbon thermal shield, metal components, reactor shutdown system, fuel element recycling system, and etc., seen in Fig.3-31.

Component in Reactor Vessel

– Fuel Element and pebble bed

A fuel element in HTR-10 is a sphere whose diameter is 6.0 cm. It consists of the fuel zone and the non-fuel zone. The coated fuel particles are scattered in the graphite base to compose the fuel zone of thickness 5.0cm. The non-fuel zone consists of the pure graphite. A coated fuel particle has a TRISO structure. Its fuel kernel is coated with the sparse PyC layer, inside dense PyC layer, SiC layer and outside dense PyC layer. The specification is given in Table 3-18.

Table 3-18 Specification of fuel element

parameter	**value**
fuel element diameter (cm)	6
thickness of non-fuel zone (mm)	5
fuel kernel diameter (μ m)	500
thickness of sparse PyC layer (μ m)	90
thickness of inside dense PyC layer (μ m)	40
thickness of sparse Pyro SiC layer (μ m)	35
thickness of outside dense PyC layer (μ m)	40
maximum fuel temperature (^{o}C)	1600

The pebble bed consists of a cylinder body and a cone bottom whose cone angle is 30 degree. Its specification is seen in Table 3-19.

Table 3-19 Specification of pebble bed

parameter	**value**
effective height(m)	1.97
effective diameter(m)	1.80
cone angle of pebble bed bottom(degree)	30.
average volume(m^3)	5.0
fuel element charging mode	multi-circulation

Graphite reflector

The graphite reflector consists of the side, top and bottom reflectors.

The side reflector is composed of layers of graphite bricks. There are 20 bricks in one layer. Every brick has a hole at the part near the RPV to form a cold gas channel. At the same layer, 10 control rod guiding holes, 7 absorbing ball holes and 3 irradiation holes are located on the inner part. The specification is given in Table 3-20a, 3-20b.

Table 3-20a Specification of side graphite reflector

Parameter	value
number of brick layers	10
number of bricks on one layer	20
brick radial length (m)	0.775
effective outside diameter of brick(m)	3.35
total height(m)	3.6

Table 3-20b Specification of channels in side graphite reflector

channel	parameter	value
cold gas channel	hole number	20
	hole diameter(m)	0.08
	hole center diameter(m)	2.92
control rod channel, irradiation hole and absorbing ball channel	total hole number	20
	hole diameter(m)	0.13
	hole center diameter(m)	2.05

The bottom graphite reflector consists of layers of bricks. The top layer, forming the bottom of the pebble bed cavity, has a 30 degree slope. A slope graphite brick has two zones. The inner one has many small holes. The outer one has no holes. There exist a small horizontal plenums between the 1st and 2nd layers to gather the gas passing through the top graphite brick layer. Bigger gas holes are uniformly drilled on the 2nd and 3rd to let the gas smoothly flow down. The hot gas mixing plenum is located between 3rd and 4th brick layers. In order to let the fuel element pebbles smoothly pass through the bottom graphite and carbon components, a graphite jacket protection tube is installed as the discharging tube. Table 3-21a, 3-21b are the specification of the bottom graphite reflector. The total height of the bottom graphite reflector is 1.60m.

Table 3-21a Specification of side graphite reflector

layer	component	parameter	value
1	slope part	number of bricks on one layer	10
		inside effective diameter(m)	0.5
		outside effective diameter of bricks with gas holes(m)	1.115
		outside effective diameter of bricks without gas holes(m)	1.8
	inner part with holes	number of bricks	10
2,3		brick outside diameter(m)	1.8
4	outer part	number of bricks	20
		brick outside diameter	3.35

Table 3-21b Specification of channels in bottom graphite reflector

channel		parameter	value
gas hole in top layer	hole	number	640
	hole	diameter(m)	0.02
	height	(m)	0.075
small horizontal plenum	inside	diameter(m)	0.762
	outside	diameter(m)	1.234
	hole I	number of holes	10
		hole diameter(m)	0.025
	hole II	number of holes	10
bigger holes on 2nd,		hole diameter(m)	0.03
3rd layers	hole III	number of holes	10
		hole diameter(m)	0.035
	hole IV	number of holes	10
		hole diameter(m)	0.04
hot gas mixing plenum	height	(m)	0.35
	outside	diameter(m)	1.8

The top reflector consists of brick layers. There are 20 bricks on every layer. Besides the cold gas channel, control rod channels, irradiation channels, absorbing ball channels, fuel element charging channels, a cold gas plenum is located on the top of the pebble bed. Table 6 is the specification of the top graphite reflector.

Table 3-22 Specification of top graphite reflector

parameter	value
number of bricks of one layer	20
thickness(m)	0.8
brick outside diameter(m)	3.35

Carbon brick

The carbon brick thermal insulator consists of top, bottom and side reflectors. The top carbon thermal insulator is one layer of 20 carbon bricks. The side carbon thermal insulator is one radial layer of bricks. The bottom thermal insulator consists of 2 layer carbon bricks. The fuel element charging tube, absorbing ball tubes, control rod guide channels, radiation channels and measurement channels pass through the top carbon layer. The cold gas channel and the absorbing ball channels also pass through the bottom carbon brick layers. Table 3-23 is the specification.

Table 3-23 Specification of carbon brick layers

component	parameter	value
	number of layer	1
side carbon	total height(m)	4.800
brick layer	outside diameter(m)	3.800
	radial thickness(m)	0.225
top carbon brick	number of layer	1
layer	outside diameter(m)	3.800
	thickness(m)	0.400
	number of layers	2
bottom carbon	outside diameter(m)	3.800
	total height(m)	1.20

Metal component

The metal components in the RPV consist of the core vessel (CV), the upper and the lower supporters and the metal discharging tube. Specification of CV is given in Table 3-24.

Table 3-24 Specification of core vessel

component	parameter	value
core vessel	material	SA387-11
	inside diameter (m)	3.82
	shell thickness (m)	0.03
	height (m)	7.37
top thermal shield	material (m)	nodular cast iron
	outside diameter (m)	3.96
	inner diameter (m)	3.82
	thickness (m)	0.3

Reactor vessel

The reactor vessel of HTR-10 consists of the shell body, the upper and the lower closure. Its total height is 10.25m . It is made of SA516-70. Its specification is shown in Table 3-25.

Table 3-25 Specification of reactor vessel

component	parameter	value
head closure	maximum outside diameter (m)	4.68
	maximum inner diameter (m)	4.10
	head closure thickness (m)	0.10
	flange height (m)	0.60
	head closure height (m)	1.59
shell body	material	SA516-70
	flange height (m)	0.60
	inner diameter (m)	4.10
	shell thickness (m)	0.0 7
	height of normal part (m)	2.882
	height of strengthened part (m)	3.80
bottom closure	maximum outside diameter (m)	4.34
	maximum inner diameter (m)	4.10
	bottom closure thickness (m)	0.10

RCCS[3][4]

Two independent and parallel RCCS of 125KW are designed. One RCCS consists of a cavity cooler inside the reactor cavity, an air cooler in the chimney channel and associated Tubes. A cavity cooler is made of 50 tubes connected by steel fins that arranged in parallel to the inner surface of the reactor cavity. The top and bottom of the tubes are connected by two circular plenums. Two tubes connect the plenums to the air cooler. The hot uprising tube connects the upper plenum, across the reactor cavity, with the inlet of the air cooler. The cold downcoming tube connects the outlet of the cooler, across the regulating water tank and reactor cavity, with the lower plenum of the cavity cooler. A finned air cooler is installed at the channel of a chimney in height of 14.0m.

Water cooler

Two water coolers, described in section 1, are located at the inner surface of the reactor cavity. The 100 tubes of the two coolers are parallelly welded on an annular steel wall forming a water cooling wall. The main data of the water coolers are given in Table 3-26.

Table 3-26 Specification of water cooler

parameter	value
cooler number	2
capacity/cooler	125 KW/cooler
cooling tube number/cooler	50
cooling tube length (m)	11.2
cooling tube outside diameter (m)	0.042
cooling tube inner diameter (m)	0.032
annular tube outside diameter (m)	0.152
annular tube inner diameter (m)	0.142
water cooling wall outside diameter (m)	6.09
water cooling wall inner diameter (m)	6.006

Air cooler[2]

Two air coolers are located in the two chimneys at the side of the reactor hall. An air cooler consists of 60 heat exchange tubes. The tubes are arranged into two rows. The flow path number is 2. Its length and width are 3.0m and 2.0m respectively. There are ring fins on the heat exchange tubes to enlarge the heat exchange area. The data of an air cooler are given in Table 3-27.

Table 3-27 Data of an air cooler

parameter	value
heat exchange tube outside diameter (mm)	25
heat exchange tube inner diameter (mm)	20
heat exchange tube number	60
flow path number	2
heat exchange area(outside area of base tubes) A_o (m^2)	13.279
fin pitch b (mm)	2.3
fin thickness (mm)	0.4
fin diameter (mm)	57
flow area S_a (m^2)	5.3
ratio of rib area to heat exchange tube	23.4

The pressure resistance drop of the air side can be calculated by

$$\Delta p = 0.521 V_f^{1.504} N \quad \text{mm-H}_2\text{O}$$

$$V_f = \frac{G}{\rho S_a} \quad \text{m/sec}$$

where Vf is the standard confront wind velocity, G the air flow rate, ρ the air density, Sa the flow area outside the heat exchange tube and N the tube row number.

The heat transfer coefficient of the air side α_a is

$$\alpha_a = 390 V_f^{0.718} \qquad \text{kcal/m}^2 \cdot \text{hr} \cdot {}^{o}\text{C}$$

The heat transfer coefficient α_w of the water side can be calculated by the Nusselt number,

$$Nu = 0.023 \,\text{Re}^{0.8}\, \text{Pr}^{0.4}$$

The heat transferred by the air cooler Q can be calculated by

$$Q = \frac{A_0}{R}(T_w - T_a)\ \text{kcal/hr}$$

$$R = \frac{1}{\alpha_w}\frac{A_o}{A_i} + r_i\frac{A_o}{A_i} + \frac{b}{\lambda_w}\frac{A_o}{A_m} + r_f + r_o + \frac{1}{\alpha_a} \quad m^2 \cdot hr \cdot {}^oC / kcal$$

where A_0 is the total outside area of base Tubes, A_i the inside area of the heat exchange tubes, A_m the average of A_o and A_i , T_w the water temperature, T_a the air temperature, r_f the fin heat resistance, r_i the filth heat resistance inside the Tubes with the inner surface area of heat exchange tubes as basis, r_o the filth heat resistance outside the tubes with the outside surface area of base tubes as basis (r_o=0.0002~0.0004m^2hr^oC/kcal), λ_w the thermal conductivity of Tubes, b the thickness of Tubes. (r_f+R_w= $r_f + \frac{b}{\lambda_w}\frac{A_o}{A_m} = 0.00021 m^2 hr^oC$/kcal).

Chimney

Two chimneys are built on a side of the reactor hall. Its cross section is a rectangle. The height of the uprising stage, length and width of the cross section at the top and the bottom of a chimney are 12.0m, 3.0m and 1.50m. Two air doors are located at the upper and the lower parts of a chimney. The main data of a chimney is given in Table 3-28. The atmosphere environment temperature is 30 °C.

Table 3-28 Data of a chimney

parameter	value
total height (m)	26.0
uprising stage length (m)	12.0
cross section length (m)	3.0
cross section width at top and bottom (m)	1.5
cross section width at middle (m)	2.0

Regulation tank

A water tank is designed in the RCCS. The exhaust Tube, water processing tube and water compensation Tube are leaded from the water tank. Its specification is given in Table 3-29.

Table 3-29 Specification of regulation tank

parameter	value
operation pressure (MPa)	0.1
outside diameter (m)	1.2
inside diameter (m)	1.19
height (m)	2.7
volume (m^3)	~3.0
water volume (m^3)	~2.0
nitrogen volume (m^3)	~1.0

Water loop system

The water loop system is shown in Fig.1. The coordinate heights of the inlet and outlet of the cavity cooler, the inlet and the outlet of the air cooler are -5.724m, 5.476m, 14.0m, 14.0m. The specification of the associate tubes are given in Table 3-30.

Table 3-30 Specification of associate tubes of water loop

parameter	value
tube outside diameter (m)	0.152
tube inside diameter (m)	0.142
cooling tube length (m)	11.2
uprising tube length (m)	20.0
comingdown tube length (m)	25.0
uprising tube height (m)	9.05
comingdown height (m)	19.95

Thermal Shielding Panel

In order to prevent too much heat from being removed by the RCCS under normal operation condition, a thermal shielding panel is hung on the RPV, seen in Fig.3-31. It consists of two thin steel plates. Table 3-31 is the specification.

Table 3-31 Specification of thermal shielding panel

parameter	value
number of plates	2
plate thickness(mm)	1
inside diameter of inner plate(m)	5.04
inside diameter of inner plate(m)	5.07
total height(m)	10.91
material	SA38711

Reactor Cavity

The reactor vessel and the water coolers are installed in the reactor cavity. The thermal shields are located at the inner surface of the concrete cavity. The reactor cavity consists of two parts, i.e., the upper part and the lower part. Its total height is 21.5m.

The thermal shields are the top, bottom and side ones. The main data of the thermal shields are shown in Table 3-32 and the specification of the cavity is given in Table 3-33.

Table 3-32 Specification of thermal shields in reactor cavity

component	parameter	value
top shield	diameter (m)	9.0
	thickness (m)	0.30
side shield	outside diameter (m)	6.4
	thickness (m)	0.10
	height (m)	11.936
lower shield	diameter (m)	6.4
	thickness (m)	0.10

Table 3-33 Specification of reactor cavity

component	parameter	value
upper cavity	inner diameter (m)	9.0
	side thickness (m)	1.0
	top thickness (m)	1.5
	height (m)	6.464
lower cavity	inner diameter (m)	6.40
	side thickness (m)	2.30
	bottom thickness (m)	1.50
	height (m)	12.036

3.3.1.3. Thermal Property Parameter

The given thermal property data of the materials in HTR-10 include density, thermal conductivity, specific heat capacity, viscosity, and emissivity and etc. In the thermal-hydraulic analysis, they can be determined by the following relations and Tables.

Fuel Pebble Element

– Thermal conductivity

$$\lambda = 1.2768\left(\frac{0.06829 - 0.3906\times10^{-4}T}{dosis + 1.931\times10^{-4}T} + 1.228\times10^{-4}T + 0.042\right), \quad T < 1200^{\circ}C$$

where λ [W/cm/K], T[°C], fast neutron irradiation dose [10^{21}]

– Specific heat at constant volume

$$c_v = 1.75(0.645 + 3.14\times10^{-3}T - 2.809\times10^{-6}T^2 + 0.959\times10^{-9}T^3), \quad T < 1200^{\circ}C$$

where c_v[W/cm^3/K], T[°C]

Uniformed Pebble Bed

– Thermal conductivity

$$\lambda = 1.1538\times10^{-6}(T+100)^{1.6622}, \quad T>250^{\circ}C$$

where λ [W/cm/K], T[°C]

– Specific heat at constant volume

$$c_v = 1.75(0.645 + 3.14\times10^{-3}T - 2.809\times10^{-6}T^2 + 0.959\times10^{-9}T^3), \quad T < 1200^{\circ}C$$

where c_v [W/cm^3/K], T[°C]

Graphite Reflector

– Thermal conductivity

conductivity with effect of fast neutron irradiation

$$\lambda = 1.15F[1.5648 - 0.3162\log(T+100)], \quad T < 2000^{\circ}C$$

$$F = \frac{F_1}{Y - F_2} + F_3$$

$$F_1 = -0.0054705 + 0.00038214\left(\frac{T}{1000}\right) + 0.13487\left(\frac{T}{1000}\right)^2$$

$$F_2 = -0.013951 + 0.12064\left(\frac{T}{1000}\right) - 0.32955\left(\frac{T}{1000}\right)^2$$

$$F_3 = -0.07264 + 0.41459\left(\frac{T}{1000}\right) + 0.23149\left(\frac{T}{1000}\right)^2$$

$$Y = \frac{dosis}{10}, \quad dose<2.5$$

where λ [W/cm/K], T[°C], fast neutron irradiation dose [10^{21}]

conductivity without effect of neutron irradiation

$$\lambda = 1.15\left[1 - 1.084\left(\frac{T}{1000}\right) + 0.743\left(\frac{T}{1000}\right)^2 - 0.213\left(\frac{T}{1000}\right)^3\right], \quad T < 1700^{\circ}C$$

where λ [W/cm^3/ K], T[°C]

– Specific heat at constant volume

$$c_v = 1.75(0.645 + 3.14\times10^{-3}T - 2.809\times10^{-6}T^2 + 0.959\times10^{-9}T^3), \quad T < 1200^{\circ}C$$

where [w/cm^3/K], T[°C]

Carbon Brick

– Thermal conductivity

$\lambda = 0.05 + 3.0 \times 10^{-5} T$, T<1000°C

where λ[W/cm/K], T[°C]

– Specific heat at constant volume

$c_v = 1.75(0.645 + 3.14 \times 10^{-3} T - 2.809 \times 10^{-6} T^2 + 0.959 \times 10^{-9} T^3)$, T < 1200°C

where c_v[W/cm^3/K], T[°C]

Helium

– Density

$$\rho = 48.12 \frac{P}{T}[1.0 + 0.4446(\frac{P}{T^{1.2}})]^{-1}$$

293K <T < 1573K, 1bar <P<100bar

standard deviation:

$\sigma = 0.03\sqrt{P}\%$

where ρ[kg/m^3], P[bar], T[K]

– Specific heat

specific heat at constant volume

$c_v = 5195$ w/ cm^3 /K

specific heat at constant pressure

c_p=3117 w/kg/K

standard deviation

$\sigma = 0.05P^{(0.6-0.1\frac{T}{T_0})}$ %

where P[bar], T[K], To=273.15K

– Dynamic viscosity

$\eta = 3.674 \times 10^{-7} T^{0.7}$

where η[kg/m/s], T[K]

standard deviation:

$\sigma = 0.0015T\%$

where T[K]

– Heat conductivity

$\lambda = 2.682 \times 10^{-3}(1.0 + 1.23 \times 10^{-3} P)T^{0.71(1.0-2.0\times10^{-3}P)}$

where λ [W/cm/K], P[bar], T[K]

Air

– Density

$\rho = 336.95(\frac{P}{T})$,

where ρ [kg/m^3], P[bar], T[K]

– Specific heat at constant pressure

$c_p = 1009$ J/kg/K

– Dynamic viscosity

$\eta = 3.87 \times 10^{-7} T^{0.68}$

where η[kg/m/s], T[K]

– Heat conductivity

$\lambda = 4.373 \times 10^{-4} T^{0.715}$ where λ [W/cm/K], T[$^{\circ}$C]

Water

– Density

$\rho = 998.2 - 0.212(T - 20) - 0.0051(T - 20)^2 + 2.25 \times 10^{-5}(T - 20)^3$,

where ρ[kg/m^3], T[K]

– Specific heat at constant pressure

$c_p = 4179$ J/kg/K

Dynamic viscosity

$\eta = 10^{-4}[10.0 - 0.228905(T - 20) + 3.0745 \times 10^{-3}(T - 20)^2 - 1.77125 \times 10^{-5}(T - 20)^3]$

where η[kg/m/s], T[K]

– Heat conductivity

$\lambda = 0.5988 + 0.0017(T - 20) - 5.0 \times 10^{-6}(T - 20)^2 - 2.0875 \times 10^{-8}(T - 20)^3$

where λ[W/cm/K], T[°C]

The conductivity, specific heat capacity and emissivity of other components respectively are given in Tables 3-34 to 3-36.

Table 3-34 Conductivity of materials

material	**component**	**λ (W/cm/K)**
SA387-11	water cooler	0.37
	air cooler	0.37
SA516-70	reactor vessel	0.37
concrete	reactor cavity	0.07803
thermal shield	thermal shield panel	0.002

Table 3-35 Specific heat capacity of materials

material	**component**	**Cp(J/cm^3/K)**
SA387-11	water cooler	3.68
	air cooler	
SA516-70	reactor vessel	3.68
concrete	reactor cavity	1.76
thermal shield	thermal shield panel	0.0001

Table 3-36 Emmissivity of materials

component	ε
core vessel	0.80
reactor vessel	0.80
surface cooler	0.80

The heat transferred by thermal radiation from one of the components in Table 3-36 to its adjacent component, such as core vessel to reactor vessel, can be approximately expressed by:

$$Q = A_1 \varepsilon \sigma (T_1^4 - T_2^4)$$

$$\varepsilon = \frac{1}{\frac{1}{\varepsilon_1} + \frac{A_1}{A_2}(\frac{1}{\varepsilon_2} - 1)}$$

where A_1, ε_1 and T1 are the surface area, emissivity and temperature of the inner component, A_2 , ε_2 and T_2 are surface area, emissivity and temperature of the outside component, σ the Stefen-Boltzman constant.

3.3.1.4. Neutron Dynamics Parameters

Prompt neutron lifetime

$L=7.656\times10^{-4}$(sec)

Delayed neutron fraction

$\beta_1=2.976\times10^{-4}$; $\beta_2=1.592\times10^{-3}$

$\beta_3=1.4035\times10^{-3}$; $\beta_4=2.57\times10^{-3}$

$\beta_5=6.87\times10^{-4}$; $\beta_6=2.693\times10^{-4}$

Decay constant of delayed neutron pressure (1/sec)

$\lambda_1=1.249\times10^{-2,}$ $\lambda_2=3.13\times10^{-2}$

$\lambda_3=1.17\times10^{-1}$; $\lambda_4=3.046\times10^{-1}$

$\lambda_5=1.13$; $\lambda_6=2.898$

Reactivity coefficient:

doppler coefficient=-2.5×10^{-5} (1/K)

temperature coefficient of moderator=-6.0×10^{-5} (1/K)

temperature coefficient of reflector=$+3.4\times10^{-5}$ (1/K)

3.3.1.5. Reactor Relative Power Distribution

The reactor power distribution of HTR-10 under normal steady state condition is given in Table 3-37.

Table 3-37 Reactor relevant power distribution

RZ	2	6	10	14	18	22	26	30	34	36	42	46	50	58	62	65	74	78	82	86	94	96	102	105	110
6.7	5.4	5.3	5.3	5.4	5.5	5.4	6.6	5.8	5.9	6.1	6.3	6.4	6.5	6.9	6.7	6.9	7.1	7.2	7.2	7.3	7.4	7.4	7.3	7.3	7.4
11.6	5.4	5.3	5.3	5.4	5.5	5.4	5.6	5.7	5.9	6.1	6.2	6.4	6.8	6.9	6.7	6.8	7.1	7.2	7.2	7.3	7.4	7.4	7.3	7.3	7.3
14.9	5.4	5.3	5.3	5.4	5.5	5.4	5.6	5.7	5.9	6.8	6.2	6.4	6.5	6.9	6.7	6.8	7	7.1	7.2	7.2	7.3	7.4	7.3	7.3	7.3
17.7	5.4	5.3	5.3	5.4	5.5	5.4	5.5	5.7	5.9	6	6.2	6.4	6.5	6.8	6.7	6.8	7.1	7.1	7.1	7.2	7.3	7.3	7.2	7.3	7.3
20	5.3	5.3	5.3	5.4	5.5	5.4	5.5	5.7	5.9	6	6.2	6.3	6.5	6.8	6.6	6.8	7	7.1	7.1	7.2	7.3	7.3	7.2	7.2	7.2
22.2	5.3	5.3	5.3	5.4	5.5	5.4	5.5	5.7	5.8	5	5.1	6.3	6.5	6.8	6.6	6.7	7	7	7.1	7.1	7.2	7.3	7.2	7.2	7.2
24.1	5.3	5.3	5.3	5.3	5.4	5.3	5.5	5.6	5.8	5	6.1	6.3	6.5	6.8	6.6	6.7	6.9	7	7.1	7.1	7.2	7.2	7.2	7.2	7.2
27.8	5.3	5.2	5.2	5.3	5.4	5.4	5.5	5.7	6.8	6	6.1	6.5	6.4	6.7	6.5	6.6	6.9	6.9	7	7	7.2	7.2	7.1	7.1	7.1
32.6	5.3	5.2	5.2	5.3	5.4	5.3	5.6	5.6	5.8	5.9	5	6.2	6.3	6.6	6.4	6.6	6.8	6.9	6.9	6.9	7.1	7.1	7	7	7
36.8	5.3	5.2	5.2	5.3	5.3	5.3	5.4	5.5	5.7	5.9	5.9	6.1	6.3	6.5	6.4	6.5	6.7	6.8	6.8	6.9	7	7	6.9	6.9	6.9
40.6	5.3	5.2	5.2	5.2	5.3	5.2	6.4	5.5	5.7	5.8	5.9	6	6.2	6.5	6.3	6.4	6.6	6.7	6.7	6.8	6.9	6.9	6.8	6.8	6.8
44	5.3	5.2	5.1	5.2	5.3	5.2	5.3	5.5	5.6	5.8	5.8	6	6.1	6.4	6.2	6.4	6.5	6.6	6.8	6.7	6.9	6.8	6.7	6.8	6.8
47.6	5.3	5.2	5.1	5.2	5.2	5.2	5.4	6.5	5.7	5.8	5.8	5.9	6.1	6.3	6.3	6.4	6.8	6.7	6.7	6.7	6.8	6.8	6.8	6.8	6.8
51.4	5.2	5.1	5.1	5.1	5.2	5.2	6.3	5.5	5.8	6.7	5.9	5	6.3	6.2	6.2	6.4	6.6	6.6	6.6	6.6	6.8	6.7	6.7	6.7	6.7
54.8	5.2	5.1	5.1	5.1	5.2	5.2	6.3	5.4	5.6	5.7	5.7	5.8	6	6.2	6.2	6.3	6.5	6.6	6.5	6.6	6.7	6.7	6.6	6.6	6.6
58.1	5.2	5.1	5.1	5.1	5.1	5.1	6.3	5.4	5.5	5.7	5.6	5.6	5.9	6.2	6.1	6.2	6.4	6.5	6.5	6.5	6.7	6.6	6.5	6.6	6.6
61.7	5.2	5.1	5.1	5.1	5.1	5.2	6.3	5.4	5.5	5.7	5.6	5.8	5.9	6.2	6.2	6.3	6.5	6.5	6.5	6.6	6.6	6.7	6.6	6.5	6.5
66.5	5.2	5.1	5.1	5.1	5.1	5.2	6.3	5.4	5.5	5.7	5.6	5.7	5.9	6.1	6.1	6.2	6.4	6.5	6.5	6.5	6.7	6.7	6.4	6.4	6.4
69.2	5.2	5.1	5.1	5.1	5.1	5.2	5.3	5.4	5.5	5.7	5.6	5.7	5.9	6.1	6.1	6.2	6.4	6.5	6.5	6.5	6.6	6.6	6.4	6.4	6.4
72.5	5.2	5.1	5.1	5.1	5.2	5.2	5.3	5.4	5.6	5.7	5.6	5.8	5.9	6.2	6.2	6.3	6.4	6.5	6.5	6.6	6.6	6.7	6.4	6.4	6.4
76.5	5.2	5.1	5.1	5.1	5.2	5.2	6.3	5.5	5.6	5.7	5.7	5.8	5.9	6.2	6.1	6.2	6.4	6.5	6.3	6.4	6.6	6.5	6.4	6.4	6.4
80.6	5.3	5.2	5.2	5.2	5.3	5.3	5.4	5.6	5.8	5.8	5.8	5.9	6	6.3	6.2	6.3	6.5	6.5	6.6	6.6	6.5	6.7	6.6	6.6	6.6
84.5	5.3	5.3	5.3	5.3	5.4	5.5	5.6	5.7	5.8	6	5.9	6.1	6.2	6.4	6.4	6.5	6.7	6.7	6.4	6.5	6.6	6.6	6.4	6.5	6.5
88.2	5.4	5.4	5.4	5.5	5.6	5.6	5.8	5.9	6	6.2	6.1	6.3	6.4	6.7	6.6	6.7	6.9	7	6.8	6.8	6.9	6.9	6.8	6.8	6.8

Table 3-37 Reactor relevant power distribution (continued)

RZ	114	118	122	126	34	138	142	145	154	168	162	168	172	175	181	185	188	193	195	98	205	209	214	221
6.7	7.3	7.3	7.2	7.2	7.1	7	6.9	6.9	6.7	6.7	6.6	6.4	6.3	6.3	6.2	6.1	6	5.9	5.9	5.9	5.7	5.6	5.5	6.3
11.6	7.3	7.3	7.2	7.2	7.1	7	6.9	6.8	6.7	6.6	6.5	6.4	6.3	6.3	6.1	6.1	6	6	5.9	5.9	5.8	5.7	5.6	6.4
14.9	7.3	7.3	7.2	7.1	7	7	6.9	6.8	6.7	6.6	6.5	6.4	6.3	6.2	6.1	6.1	6	6	5.9	5.9	5.9	5.8	5.7	6.6
17.7	7.3	7.2	7.1	7.1	7	7	6.9	6.8	6.7	6.6	6.5	6.4	6.3	6.2	6.1	6.1	6	6	6	5.9	5.9	5.8	5.8	6.7
20	7.2	7.2	7.1	7.1	7	6.9	6.8	6.8	6.6	6.6	6.5	6.3	6.3	6.2	6.1	6.1	6	6	6	6	6	5.9	5.9	6.8
22.2	7.2	7.2	7.1	7	7	6.9	6.8	6.7	6.6	6.5	6.4	6.3	6.2	6.2	6.1	6.1	6	6	6	6	6	6	6	7
24.1	7.2	7.2	6.9	7	6.9	6.9	6.8	6.7	6.6	6.5	6.4	6.3	6.2	6.2	6.1	6.1	6	6	6	6	6.1	6.1	6.1	7.2
27.8	7.1	7.1	6.8	6.9	6.8	6.8	6.7	6.6	6.6	6.4	6.3	6.2	6.1	6.1	5.9	5.9	5.9	5.8	5.9	5.7	5.8	6.1	6.1	
32.6	7	7	6.8	6.8	6.7	6.7	6.6	6.5	6.5	6.3	6.3	6.2	6.1	6	5.9	5.9	5.9	5.9	5.9	5.7	5.9	6.1	6.1	
36.8	6.9	6.9	6.7	6.7	6.6	6.6	6.5	6.5	6.4	6.3	6.2	6.1	6	6	5.9	5.9	6.9	5.9	6	5.8	6	6.1	6.1	
40.8	6.8	6.8	6.5	6.7	6.5	6.5	6.4	6.4	6.3	6.2	6.1	6.1	6	6	5.9	5.9	6.9	5.9	6	5.8	6.1	6.1	6.1	
44	6.7	6.7	6.7	6.6	6.5	6.5	6.4	6.3	6.3	6.2	6.1	6	5.9	5.9	5.9	5.9	6.9	6	6	6.9	6.1	6.1	6.1	
47.6	6.8	6.7	6.6	6.6	6.5	6.5	6.3	6.2	6.2	6.1	5.9	5.9	5.8	5.8	5.7	5.7	5.8	5.7	5.7	5.9	6.1			
61.4	6.7	6.7	6.5	6.5	6.4	6.4	6.2	6.2	6.1	6	5.9	5.8	5.8	5.7	5.7	5.7	5.8	5.7	5.8	6.9	6.1			
64.8	6.6	6.6	6.5	6.5	6.4	6.3	6.1	6.1	6	6	5.8	5.8	5.7	5.7	5.7	5.6	5.8	5.7	5.8	5.9	6.1			
58.1	6.6	6.5	6.4	6.4	6.3	6.3	6.1	6	6	5.8	5.6	5.6	5.6	5.5	5.5	5.4	5.8	5.8	5.9	5.9	6.1			
61.7	6.5	6.5	6.4	6.3	6.2	6.2	6	5.9	5.9	5.8	5.8	5.6	5.4	6.5	5.4	5.5	5.6	5.8	5.9	6.9	6.1			
65.5	6.4	6.4	6.3	6.3	6.2	6.2	6	5.9	5.8	5.8	5.6	5.6	5.4	6.5	6.5	5.5	5.6	5.8	5.9	6.9				
68.2	6.4	6.4	6.3	6.3	6.2	6.2	5.9	5.9	5.8	5.8	5.6	5.6	5.4	6.5	5.4	5.5	5.6	5.8	5.9					
72.6	6.4	6.4	6.3	6.3	6.2	6.2	6	5.9	5.8	5.8	5.6	6.6	5.4	5.4	5.4	5.5	5.6	5.8	5.9					
76.6	6.4	6.3	6.2	6.2	6.1	6	5.9	5.8	5.7	5.7	5.5	5.5	5.4	5.4	5.4	5.5	5.6							
80.6	6.5	6.69	6.4	6.4	6.3	6.2	6.1	6	5.9	5.7	5.5	5.5	5.4	5.5	6.4	5.5	5.6							
84.6	6.4	6.4	6.3	6.3	6.2	6.1	5.9	5.9	5.8	5.8	5.6	5.6	5.5	5.5	5.4	5.5	5.6							
88.2	6.8	6.7	6.6	6.6	6.5	6.4	6.2	6.1	6	5.9	5.7	5.8	5.5	5.5	5.4	5.5	5.6							

Table 3-37 Reactor relevant power distribution (continued)

RZ	229	244	252	260	275	283	290	288	305	314	321	328	337	345	354	352	368	375	391
6.7	5.9	5.1	4.7	3.9	3.1	2.8	2.4	2	1.7	1.5	1.2	1	0.7	0.5	0.4	0.3	0.2	0.1	0.1
11.5	6.1	5.2	4.8	4	3.2	2.8	2.5	2	1.8	1.5	1.3	1	0.7	0.5	0.4	0.3	0.2	0.1	0.1
14.9	6.2	5.4	4.9	4.1	3.2	2.9	2.5	2.1	1.8	1.5	1.3	1	0.7	0.5	0.4	0.3	0.2	0.1	0.1
17.7	6.4	5.5	5	4.1	3.3	2.9	2.6	2.1	1.8	1.6	1.3	1.1	0.8	0.6	0.4	0.3	0.2	0.1	0.1
20	6.5	5.6	5.1	4.2	3.4	3	2.6	2.2	1.9	1.6	1.3	1.1	0.8	0.6	0.4	0.2	0.2	0.1	0.1
22.2	6.7	5.5	5.3	4.3	3.5	3.1	2.7	2.2	1.9	1.6	1.4	1.1	0.8	0.6	0.4	0.2	0.1	0.1	0.1
24.1	6.9	5.9	5.4	4.4	3.5	3.1	2.8	2.2	1.9	1.6	1.4	1.1	0.8	0.6	0.4	0.2	0.1	0.1	0.1
27.8																			
32.6																			
36.8																			
40.6																			
44																			
47.6																			
51.4																			
54.8																			
68.1																			
61.7																			
65.5																			
69.2																			

3.3.1.6. Benchmark Problem

In order to confirm the safety features of designed RCCS, i.e., the RCCS can safely carry away the heat generated in the core under heatup experiment and accident conditions, benchmark problem 1 and 2 are defined in the first stage of the CRP. In this stage, it is focused on studying heat transport from reactor vessel to water panel and verify heat removal ability of RCCS under heatup experiment condition and LOHS depressurization accident. The analysis results of these two benchmark problems show that it is indeed that the RCCS can safely remove the heat generated in the core under the two conditions and the heat transport ability of RCCS is even too strong. Therefore, a thermal shield plate is added between the reactor vessel and the water panel. With this new design structure, benchmark problems 3 and 4 are defined to study heat transport from reactor core to water panel under heating experiment and LOHS depressurization accident conditions. They are defined in the followings.

Prob.1 Heatup experiment I [5]

This benchmark problem is designed to verify heat transport ability of RCCS under steady condition of heatup experiment. In the heating experiment condition, It is assumed that the two water coolers are all in operation, but the helium blower is turned off, the operation pressure of the primary system is 1.0 bar and the reactor power is about 200kW. the surface temperature of the core vessel is given Table A1. Under this condition, it is required to analyze heat transfer rate of the RCCS of HTR 10. The temperature field of the reactor vessel, the water cooler, the air cooler, the thermal shield, reactor cavity, the mass flow rate of the water coolers and the air coolers also should be calculated.

Prob.2 LOHS depressurization accident I [5]

In order to study heat transport processes of transient of HTR-10, which are outside the RPV, this benchmark problem is defined under the condition of the depressurization accident of HTR-10. The varying surface temperature of the core vessel is shown Table A2, which is the function of time. The temperature distribution at the normal steady state with 10MW operating power is used as initial temperature distribution of reactor. Under this condition, the temperature field of the reactor vessel, the water coolers, the air coolers, the thermal shield, reactor cavity, the mass flow rate of the water coolers and the air coolers should be analyzed.

Prob.3 Heatup experiment II[6]

The heatup experiment will be carried out on the HTR-10, in which the primary blower is closed and the system pressures in the RPV and the concrete cavity cabinet are 1.0bar. When the steady state is reached, the reactor thermal power is 200kW; the operation parameters of the RCCS are, inlet water temperature T_{win}= 64.5°C, water mass flow rate G= 5.0 kg/s. It is required that **a.** 2D temperature fields of the pebble bed, graphite reflector and carbon thermal insulator; **b.** surface temperature of the CV, RPV and WCP; **c.** temperature field of water in RCCS be analyzed.

Prob.4 LOCA depressurization accident II

In order to verify passive safety feature of HTR-10's RCCS under superheat case, this benchmark problem is defined under the LOCA depressurization accident of HTR-10 for heatup experiment. This accident can be divided into two stages, i.e., Stage 1, helium spurt from primary loop and reactor automatically shutdown and Stage 2, decay heat is passively removed from the core. It is assumed that HTR-10 initially operates at the following initial condition.

– reactor thermal power 10.5MW
– primary pressure 30. bar
– average helium inlet/outlet temperature 250./700. °C
– total mass flow rate of helium 4.3 kg/s
– mass flow rate for core cooling 3.87 kg/s

In Stage 1, the pressure of the primary loop will drop quickly until it balances with that in the reactor cavity, when a rupture of a pipe with big diameter occurs. The reactor protection system (RPS) detects the accident occurrences by detecting signals of decreasing rate of the primary pressure and the mass flow ratio between the primary and secondary system. If it is detected out this signal, then the RPS will scram the reactor, turn off the primary blower and close its valve and isolate the whole primary and secondary system. It is assumed in the benchmark problem that the protecting actions of the active reactor shutdown and the blower closing fail, thus natural circulation will happen in the primary loop and the pebble-bed core will be heated up obviously. At the end of this stage, the primary natural circulation will disappear due to gradual temperature homogenization of the primary loop and the reactor shutdown will be automatically realized by means of the fuel element doppler effect. According transient features of the accident, the following assumptions for the first stage are made

– primary loop pressure is assumed to promptly decrease from 30bar to 1 bar,
– helium mass flow rate also decreases quickly from 4.3kg/s to 0.143kg/s ,and then keeps constant,
– during the first stage, the helium inlet temperature keeps constant 250°C,
– point neutron dynamics model of 6 delayed neutron groups is used to analyze the core physics transient without active reactor scram,
– the first stage duration is assumed to be about 360 (sec). After the first stage, the primary natural circulation will disappear and the reactor shutdown will be realized automatically.

In Stage 2, the reactor afterheat will be gradually removed from the core in the mechanisms of heat conduction and radiation to the RCCS and it is assumed that:

– the primary pressure keeps constant 1bar and effect of natural convection in the pebble-bed core can be neglected,
– calculation result of the reactor temperature field at the first stage end is used as the initial condition,
– transient process data of the decay heat are given in Table 3-38,
– the RCCS on the reactor cavity wall keeps the constant heat transfer coefficient 0.4 (W/cm2/K) and surface temperature 70°C.

It is required to predict transient behaviour of HTR-10 under this condition, i.e., to analysis temperature feedback reactivity, reactor power, maximum and average temperature of fuel elements.

Table 3-38 Reactor power of HTR-10 under heating accident

time (sec.)	reactor power (MWt)	time (sec.)	reactor power (MWt)
0.0	0.224	9.96	556.
0.364	0.165	14.0	537.
0.626	0.140	18.0	520.
1.29	0.109	22.0	506.
2.46	0.0875	29.0	484.
3.29	0.0794	39.0	457.
4.29	0.0729	49.0	435.
5.29	0.0681	59.0	416.

Table 3-38 Reactor power of HTR-10 under heating accident **(continued)**

6.29	575.	69.0	400.
6.79	573.	79.0	385.
7.29	570.	89.0	371.
7.79	567.	100.0	358.
8.29	564.		

REFERENCES TO SECTION 3.3.1.

[1] Institute of Nuclear Energy Technology, Tsinghua University, Primary Safety Analysis Report of 10MW High Temperature Test Reactor, Jan.27, 1994.

[2] Yiwei Ma, Jifu Lui and Huiguang Qian, "Air Cooler", Haerbin University, Chemical Industry Press, RPC, 1994.

[3] Hua shaozeng, Yang Xuening, etc., translator, Practical Fluid Resistance Handbook, National Defence Industry Press, China.

[4] Thermal-hydraulic Department of Institute of Nuclear Energy Technology, Tsinghua University, “Design Report of Afterheat Removal System of HTR-10”, July, 1994.

[5] Zuying Gao, Baoyan Lee, Zhiqiang Jiang, Benchmark Problem Definition of HTR-10, Thermal-hydraulic Department of Institute of Nuclear Energy Technology, Tsinghua University, Beijing,China, Mar., 1994.

[6] Zuying Gao, Baoyan Lee, Definition and Solution of Benchmark Problem of 200kW Heatup Experiment of HTR-10, 3rd Research Cooperation Meeting on Heat Transport and Afterheat Removal for Gas-cooled Reactors under Accident Conditions, Nov., 1995.

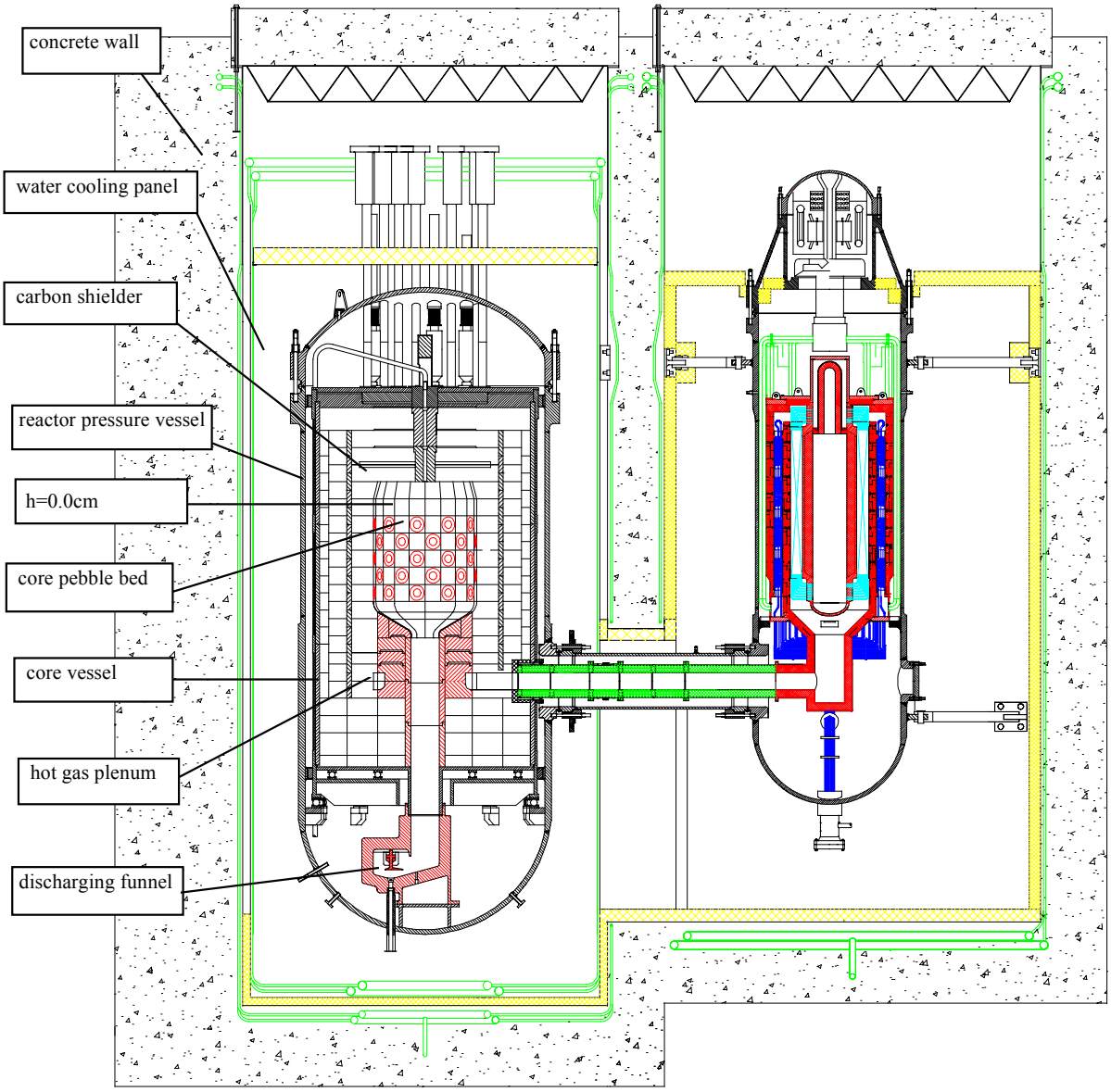

Fig.3-31 General Design Chart of HTR-10

Table A1 Surface temperature distribution of CV at heatup experiment

Node	R(M)	Z(M)	Value (C)	Node	R(M)	Z(M)	Value (C)
1	0	-1.9	297.5	37	1.94	2.025	343.5
2	0.065	-1.9	297.4	38	1.94	2.1	340.9
3	0.13	-1.9	297.1	39	1.94	2.175	338.2
4	0.19	-1.9	296.8	40	1.94	2.25	335.5
5	0.25	-1.9	296.3	41	1.94	2.325	332.8
6	0.315	-1.9	295.6	42	1.94	2.4	330
7	0.445	-1.9	293.6	43	1.94	2.725	317.3
8	0.575	-1.9	291.1	44	1.94	3.025	305.4
9	0.705	-1.9	287.9	45	1.94	3.375	289.6
10	0.835	-1.9	284	46	1.94	3.6	276.6
11	0.9	-1.9	281.8	47	1.94	4	240.2
12	0.96	-1.9	279.7	48	1.94	4.4	211.4
13	1.09	-1.9	274.5	49	1.94	4.8	193.7
14	1.42	-1.9	257.4	50	1.94	4.87	192.1
15	1.5	-1.9	252.6	51	1.94	4.97	190
16	1.675	-1.9	240.9	52	1.94	5.37	180.8
17	1.788	-1.9	232.6	53	1.94	5.77	172.4
18	1.9	-1.9	223.9	54	0	5.77	213.5
19	1.91	-1.9	223.1	55	0.065	5.77	213.5
20	1.94	-1.9	220.7	56	0.13	5.77	213.3
21	1.94	-1.6	230.3	57	0.19	5.77	213.2
22	1.94	-1.2	289.6	58	0.25	5.77	213
23	1.94	-0.4	328.4	59	0.315	5.77	212.3
24	1.94	0	345.1	60	0.445	5.77	206.5
25	1.94	0.18	351.3	61	0.575	5.77	205.9
26	1.94	0.36	356.5	62	0.705	5.77	205.1
27	1.94	0.54	360.7	63	0.835	5.77	204.1
28	1.94	0.72	363.5	64	0.9	5.77	203.5
29	1.94	0.9	364.9	65	0.96	5.77	203
30	1.94	1.08	364.9	66	1.09	5.77	201.7
31	1.94	1.26	363.3	67	1.42	5.77	197.4
32	1.94	1.44	360.4	68	1.5	5.77	196.2
33	1.94	1.62	356.2	69	1.675	5.77	193.2
34	1.94	1.8	350.9	70	1.788	5.77	191.2
35	1.94	1.875	348.6	71	1.9	5.77	188.4
36	1.94	1.95	346.1	72	1.91	5.77	173.3

Table A2 Surface temperature data of CV under LOHS accident

t (hr)	0	0.3	1	4.9	8	12	8	24	33	43	53	63	73	83	93	103	113	120
1	191	191	191	192	192	193	195	196	198	198	197	194	191	186	182	177	172	169
2	191	191	191	192	192	193	195	196	198	198	197	194	191	186	182	177	172	169
3	191	191	191	192	192	193	195	196	198	198	197	194	191	186	182	177	172	169
4	191	191	191	191	192	193	195	196	198	198	197	194	190	186	182	177	172	169
5	191	191	191	191	192	193	194	196	197	198	196	194	190	186	181	177	172	168
6	191	191	191	191	192	193	194	196	197	197	196	193	190	186	181	176	171	168
7	190	190	190	190	191	192	193	195	196	197	195	193	189	185	180	176	171	167
8	189	189	189	189	190	191	192	194	195	195	194	192	188	184	179	175	170	167
9	187	187	187	188	189	189	191	192	194	194	193	190	187	182	178	173	169	165
10	186	186	186	186	187	188	189	191	192	192	191	188	185	181	176	172	167	164
11	185	185	185	186	186	187	188	190	191	191	190	187	184	180	176	171	166	163
12	184	184	184	185	185	186	187	189	190	190	189	187	183	179	175	170	166	162
13	182	182	182	183	183	184	185	186	188	188	187	184	181	177	173	168	164	161
14	174	174	175	176	176	177	178	179	180	180	179	177	173	170	166	161	157	154
15	172	172	173	174	174	174	175	177	178	178	177	174	171	168	164	160	155	153
16	167	167	169	169	169	169	170	171	172	172	171	169	166	162	159	155	151	148
17	163	164	166	165	165	165	166	167	168	168	167	165	162	159	155	151	147	145
18	158	162	162	160	160	160	161	162	163	163	162	160	157	154	150	147	143	141
19	158	162	162	160	159	160	160	161	162	162	161	159	157	153	150	146	143	140
20	156	161	161	158	158	158	159	160	161	161	160	158	155	152	149	145	141	139
21	167	168	169	169	169	170	171	172	173	173	171	169	166	162	158	154	150	147
22	184	185	186	187	187	188	190	192	192	190	186	182	178	173	168	163	159	155
23	201	202	203	204	206	209	212	212	211	206	201	195	189	183	177	172	167	163
24	212	212	213	218	221	224	226	226	222	216	209	202	196	189	183	177	171	168
25	216	216	217	223	227	230	232	231	226	219	212	205	198	191	185	179	173	169
26	219	220	220	228	232	236	237	235	230	222	215	207	200	193	186	180	174	170
27	223	223	223	232	237	241	241	239	233	225	217	209	201	194	188	181	175	171
28	225	226	226	237	242	245	245	242	236	227	219	210	203	195	188	182	176	172
29	228	228	229	241	246	249	249	245	238	229	220	211	204	196	189	183	177	173
30	230	230	231	244	250	253	252	247	239	230	221	212	204	196	189	183	177	173
31	232	232	233	248	254	256	254	249	240	231	221	212	204	197	190	183	177	173
32	234	234	234	250	257	259	256	250	241	231	221	212	204	196	189	183	176	172
33	234	235	235	253	260	261	257	251	241	231	221	212	204	196	189	182	176	172
34	234	235	236	255	262	262	258	251	241	231	221	212	203	195	188	182	175	171
35	235	235	236	255	262	263	258	251	241	230	220	211	203	195	188	181	175	171
36	235	235	236	256	263	263	258	251	241	230	220	211	203	195	188	181	175	171
37	235	235	236	256	263	263	258	251	240	230	220	211	202	194	187	181	174	170
38	235	235	236	256	263	263	258	251	240	229	219	210	202	194	187	180	174	170
39	235	235	236	256	263	263	257	250	240	229	219	210	201	194	186	180	174	170

Table A2 Surface temperature data of CV under LOHS accident **(continued)**

40	235	235	236	256	263	263	257	250	239	228	218	209	201	193	186	179	173	169
41	235	235	235	256	263	263	257	249	239	228	218	209	200	193	185	179	173	169
42	235	234	235	256	263	262	256	249	238	227	217	208	200	192	185	178	172	168
43	232	232	232	252	259	259	253	246	235	224	214	205	197	190	183	176	170	166
44	228	227	227	246	253	254	249	241	231	221	211	202	194	187	180	173	167	164
45	219	218	218	235	243	245	241	234	225	215	205	197	189	182	175	169	163	160
46	212	211	211	226	233	236	233	227	218	209	200	192	185	178	171	165	160	156
47	196	195	195	200	205	209	209	206	199	192	184	177	171	165	159	154	149	146
48	188	188	188	187	188	190	190	188	183	177	171	165	160	154	149	145	140	137
49	190	189	188	184	183	182	180	178	174	169	164	158	153	149	144	140	135	132
50	190	189	188	184	182	181	179	177	173	168	163	158	153	148	143	139	135	132
51	190	189	188	184	182	180	178	176	172	167	162	157	152	147	143	138	134	131
52	184	183	182	178	176	173	171	169	165	161	156	151	147	142	138	134	130	127
53	177	174	171	167	166	164	162	159	156	152	148	144	140	136	132	128	124	122
54	249	248	244	231	225	220	213	209	203	197	191	185	179	173	167	162	156	153
55	249	248	244	231	225	220	213	209	203	197	191	185	179	173	167	162	156	153
56	249	247	244	231	225	219	213	209	203	197	191	185	179	173	167	162	156	153
57	249	247	243	231	225	219	213	208	203	197	191	185	179	173	167	162	156	153
58	249	247	243	231	225	219	213	208	203	197	191	185	179	173	167	161	156	153
59	249	246	242	230	224	218	212	208	202	196	190	184	178	172	167	161	156	152
60	247	241	236	224	219	213	207	203	197	192	186	180	174	168	162	157	152	148
61	237	236	232	222	217	211	205	201	196	190	184	178	172	167	161	156	151	147
62	231	230	229	220	215	210	204	200	194	189	183	177	171	166	160	155	150	146
63	225	225	225	218	213	208	203	198	193	188	182	176	170	165	159	154	149	146
64	223	223	223	217	212	207	202	198	192	187	181	175	170	164	159	154	148	145
65	221	221	221	216	211	206	201	197	192	186	181	175	169	164	158	153	148	145
66	217	217	217	213	208	204	199	195	190	185	179	173	168	162	157	152	147	144
67	208	208	208	204	200	196	192	189	184	179	174	169	163	158	153	148	143	140
68	206	206	206	201	198	194	190	187	183	178	172	167	162	157	152	147	142	139
69	201	201	200	194	191	188	185	182	178	173	168	163	158	153	148	144	139	136
70	199	196	193	187	184	181	178	175	172	167	162	157	153	148	143	139	135	132
71	195	193	190	184	182	179	176	173	170	165	160	156	151	147	142	138	134	131
72	178	175	172	168	167	165	162	160	157	153	149	145	140	136	132	128	125	122

Analysis of the HTR–10 Heat Up Accidents with the TAC–NC Code

3.3.2.1. Analytical Code

Temperature transients during the heatup experiment condition were analyzed with a thermal-hydraulics code TAC-NC [1] developed for the HTTR licensing. The TAC-NC based on the TAC-2D[2] can calculate the heat transfer by natural circulation as well as by conduction and radiation during the accidents.

Natural circulation is calculated by a one-dimensional flow network model. The basic flow network equations to be solved are the steady-state, one-dimensional momentum equation for each flow path and the continuity equation, equation of state and energy equation for each plenum which connects each path.

The momentum equation for each flow path has the following forms:

$$\frac{Du_i}{Dt} = -\frac{1}{\rho_i}\left(\frac{\partial P}{\partial z}\right)_i - g - \left(\frac{\lambda_i}{d_i} + c_i\right)\frac{1}{2}|u_i|u_i$$

where:

c: inlet resistance coefficient in the flow path

d: hydraulic diameter of the flow path

g: gravity

i: flow path number

P: fluid pressure temperature transient was analyzed by the thermal hydraulics code TAC-NC.

r : fluid density

$$\frac{D}{Dt} = \frac{\partial}{\partial t} + u\frac{\partial}{\partial z}$$

The verification of the TAC-NC was carried out by comparison of the experimental results obtained in a test facility [3].

3.3.2.2. Analytical Model

$$10^7 \le Ra \le 10^{11}$$

$$\mathbf{Nu = 0.05[Ra \times f(Pr)]^{1/3}}$$

$$\mathbf{f(Pr) = [1 + (0.5 / Pr)^{9/16}]^{16/9}}$$

The analytical model is shown in Fig. 3-32. The RPV, cooling walls and thermal shield consist of 12 axial regions each. The cooling water path is simulated by one-dimensional flow net work. The Rayleigh Number-based correlations [4] defined by the following equations are used to calculate convective heat transfer in the annulus.

where:

Nu: Nusselt Number

Pr: Prandtl Number

Ra: Rayleigh Number

The effective thermal conductivity is calculated from the Nusselt Number and used as input data for the analysis.

The radiation heat transfer is calculated by the following equation according to the Stefan-Boltzmann law.

$$Q = \sigma(T_{RPV}^4 T_{CW}^4) A_{RPV} \frac{1}{\frac{1}{\varepsilon_{RPV}} + \frac{A_{RPV}}{A_{CW}}(\frac{1}{\varepsilon_{CW}} 1)}$$

where:

A : Heat Transfer Area

Q : Radiation Heat Transfer

T : Temperature

s : Stefan-Boltzmann constant

e : emissivity

subscript

RPV: Reactor Pressure Vessel

CW: Cooling Wall

The air cooler is simulated by the large heat sink in this analysis (see Fig. 1).

3.3.2.3. Analytical Results

Heat-up test experiment

Table 3-39 shows the temperature of the RPV, cooling water, cooling wall, the total heat removal by the RCCS and the flow rate of cooling water in the heatup test experiment. The total heat removal by the RCCS is 208 kW and the flow rate of the cooling water is 7.8 kg/s when the outlet temperature of the air cooler is 50□C.

This results show that nearly 80 % of the heat transfer is by radiation and less than 20 % is by natural convection. The radiation heat transfer is dominant among overall heat transfer in the annulus.

Depressurization accident

Figure 3-33 shows the transient behaviour of the outlet water temperature of the cooling wall, flow rate of cooling water and heat removal by the RCCS. The peak heat removal by the RCCS is 113kW at about 18hrs after the initiation of the accident. It decreases gradually after that. The flow rate of cooling water increases from 6.1kg/s to 6.4kg/s during the first 18 hours and decreases gradually. The outlet temperature of cooling water does not change apparently.

Figure 3-34 shows the temperature distribution of the RPV cooling wall of the RCCS and Core Vessel. It is confirmed that the maximum RPV temperature is at most 180 °C.

3.3.2.4. Sensitivity Study of Natural Convection in Annulus and Outlet Temperature of Air Cooler

The effective thermal conductivity calculated by the Rayleigh Number-based correlation was used to analyze the natural convection heat transfer in the annulus between the RPV and cooling walls in this analysis. In the sensitivity study, the several analyses were carried out with

parameters of the effective thermal conductivity in the annulus. Fig. 3-35 shows the relationship between the heat removal by the RCCS and effective thermal conductivity of the annulus. The heat removal by the RCCS increases by only 5% as the effective thermal conductivity increases by 50%. Even if another experimental correlation is used to calculate the effective thermal conductivity, overall heat transfer does not change drastically.

In the next sensitivity study, the effects of the outlet temperature of the air cooler were investigated because our analytical model does not simulate the air cooler in detail. The effect of the inlet temperature is shown in also Fig. 3-35. The heat removal by the RCCS decreases by approximately 2% as the outlet temperature increase by 10°C. This result would be useful to compare the results using more sophisticated model by Chinese experts.

3.3.2.5. Discussions

In our analyses the air cooler is not modelled accurately because we recognized that major purpose of this study is to evaluate the heat transfer in the annulus. In order to design the RCCS accurately, the heat transfer in the cooling tower should be analyzed accurately. However, it is confirmed that the water cooling RCCS functions well during the accident and also the heat transfer by natural convection is not dominant in case that the water cooling RCCS is installed.

The water cooling RCCS is reliable to cool the RPV and easy to design comparing with the air cooling RCCS because the air flow around the RPV is deviated due to the effects of nozzle locations. The HTTR uses the active water cooling RCCS for the concrete and RPV cooling. However, we found that several problems are to be solved for the next generation HTGR.

– If the water pipe is ruptured, the splashed water has the possibility to cause brittle fracture of the RPV. In the HTTR, all water tubes are covered with plates or boxes,

The water cooling RCCS in the HTTR removes too much heat from the RPV during the normal operations since the temperature of the cooling wall is kept lower than 90□C. If the heat removal in the normal operations is over the limit, the outlet temperature of 950□C and outlet power of 30 MW do not achieved simultaneously. Therefore, the HTTR uses thermal reflecting plates between the RPV and cooling wall. This complicated structure is not acceptable economically and technically,

– The water cooling RCCS it needs affiliated systems such as a water purification system.

The water cooling RCCS is reliable but needs the complicated structures and affiliated systems. Hence, if the natural convection heat transfer in the annulus is investigated both experimentally and theoretically, the air cooling RCCS is suitable for the next generation HTGR.

3.3.2.6. Conclusions

The radiation heat transfer is approximately 80% of overall heat transfer in the annulus between the RPV and water-cooling wall.

The effect of the natural convection in the annulus is limited in case that the water cooling RCCS is installed.

The water cooling RCCS functions well during both the heatup experiment and depressurization accident.

The water cooling RCCS needs the complicated structures and affiliated systems. If the natural convection in the annulus is evaluated accurately, the air cooling RCCS is better than the water cooling RCCS for the next generation HTGR .

REFERENCES TO SECTION 3.3.2.

K. Kunitomi et al., "Depressurization Accident Analysis for the HTTR by the TAC-NC", Energy.
Vol. 16, No. 1/2, P471-480, (1991).

S. S. Clerk and J. F. Perterson, "TAC-2D A General Purpose Two-dimensional Heat Transfer Code", GA-9292, September (1969).

Hishida et al., "Studies on the Primary Pipe Rupture Accident of a High Temperature Gas Cooled Reactor", NURETH-4, Oct. (1989).

W. Churchill, Heat Exchanger Design Handbook, 2.5.8 (1983).

Table 3-39 Analytical Results of Problem 1

Heat removal by RCCS	208 kW
RPV temperature	Max. 257 °C
Cooling wall temperature	Max. 58 °C
Cooling water temperature:	
Inlet	50.0 °C
Outlet	56.4 °C
Mass flow rate	7.8 kg/s

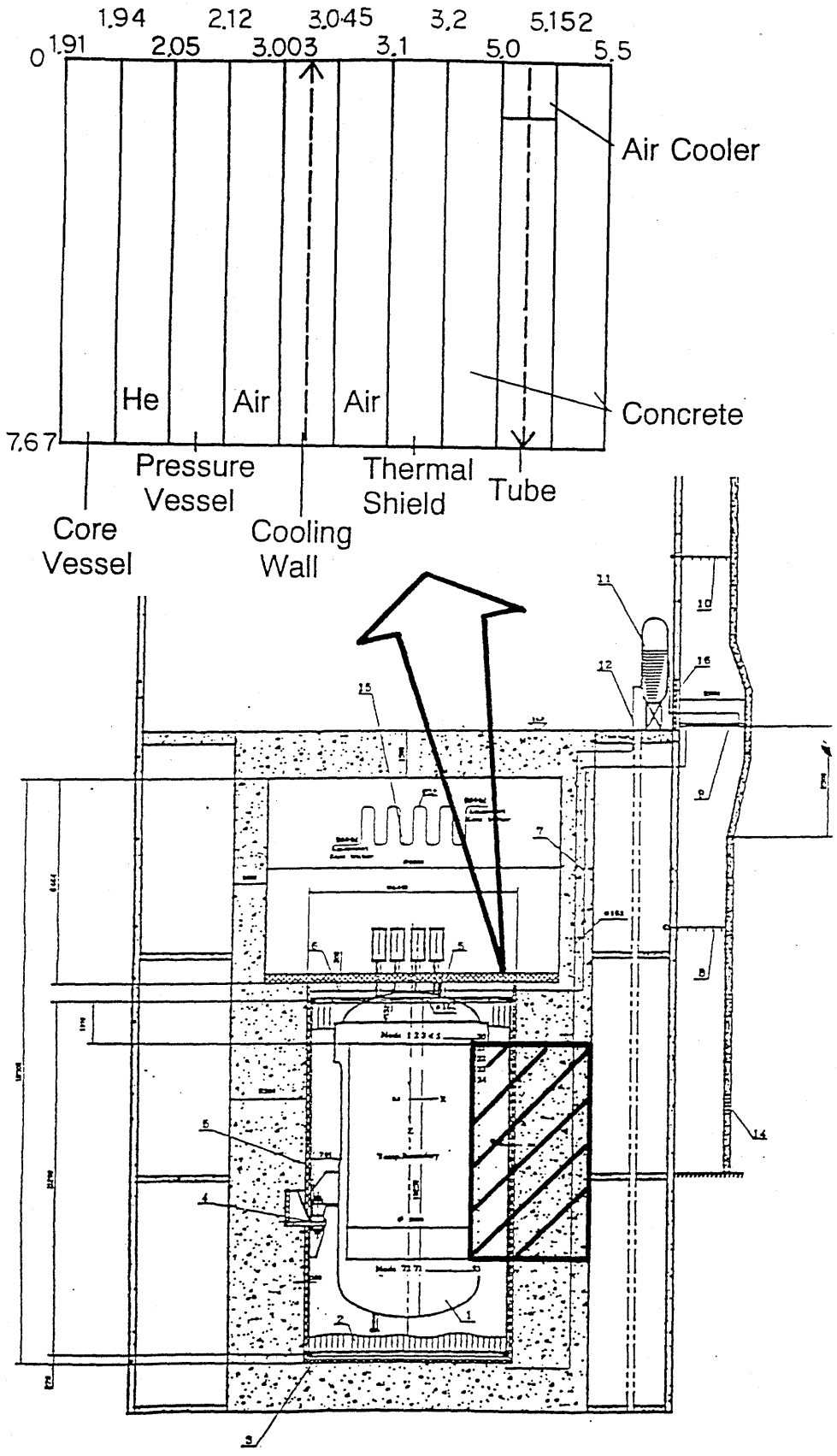

Fig. 3-32 Analytical Model

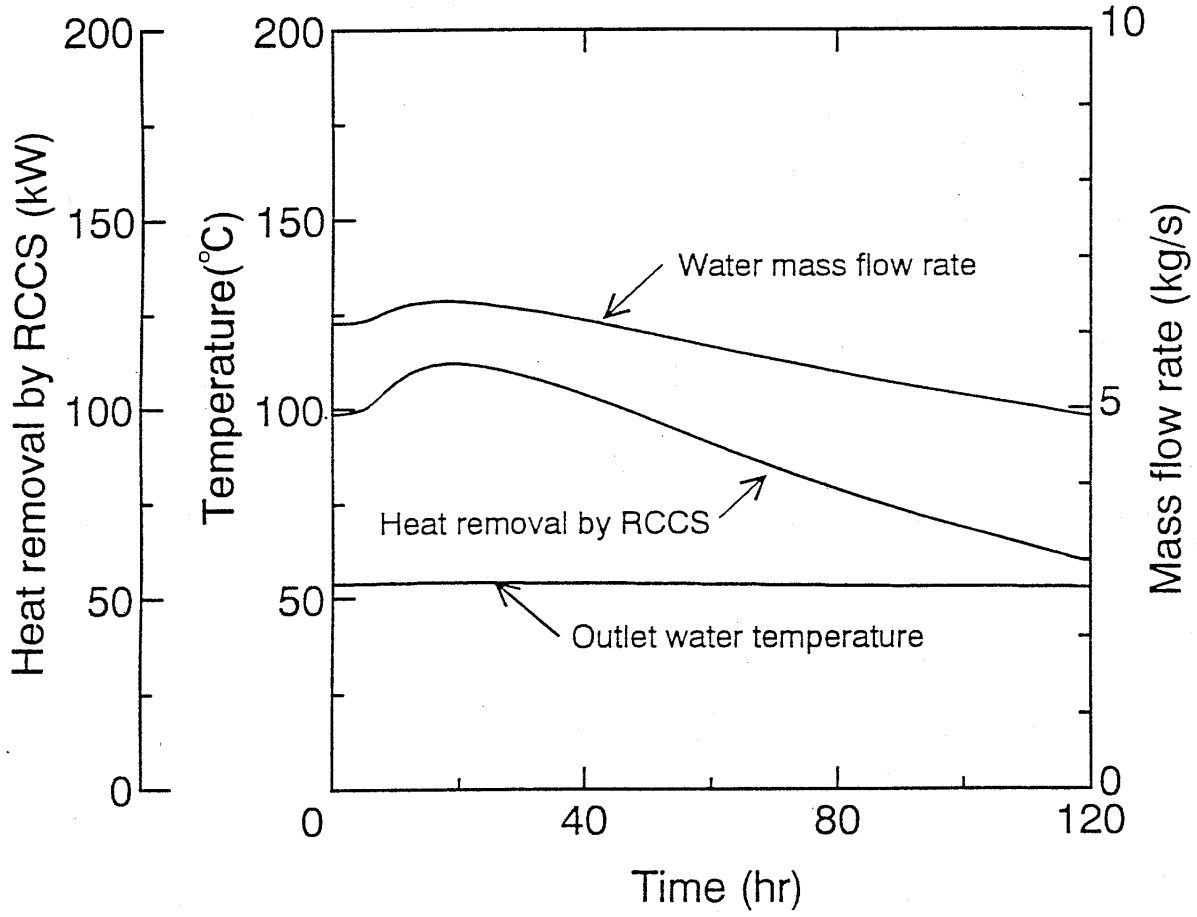

Fig. 3-33 Thermal Transient during Depressurization Accident

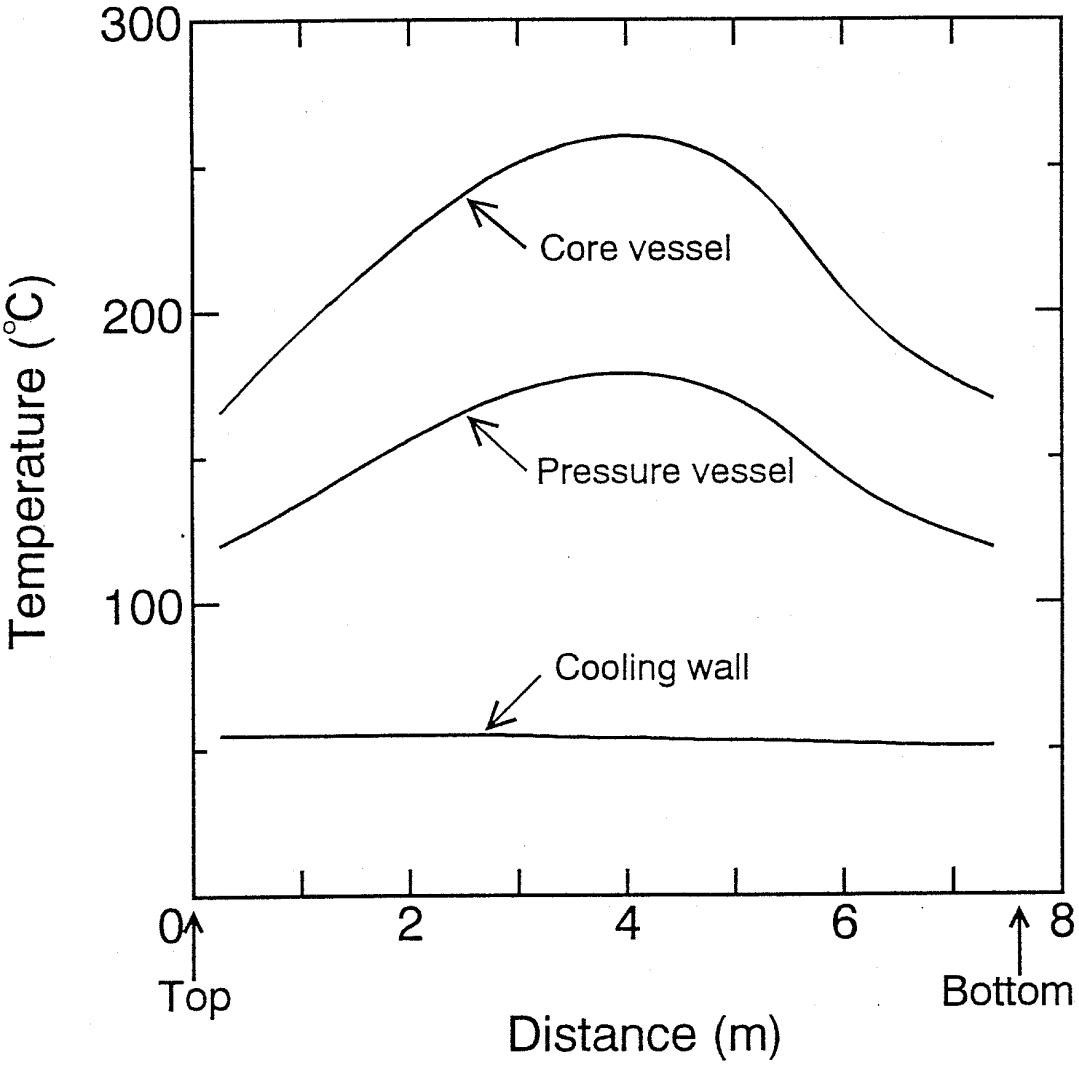

Fig. 3-34 Temperature Distribution at 18hr

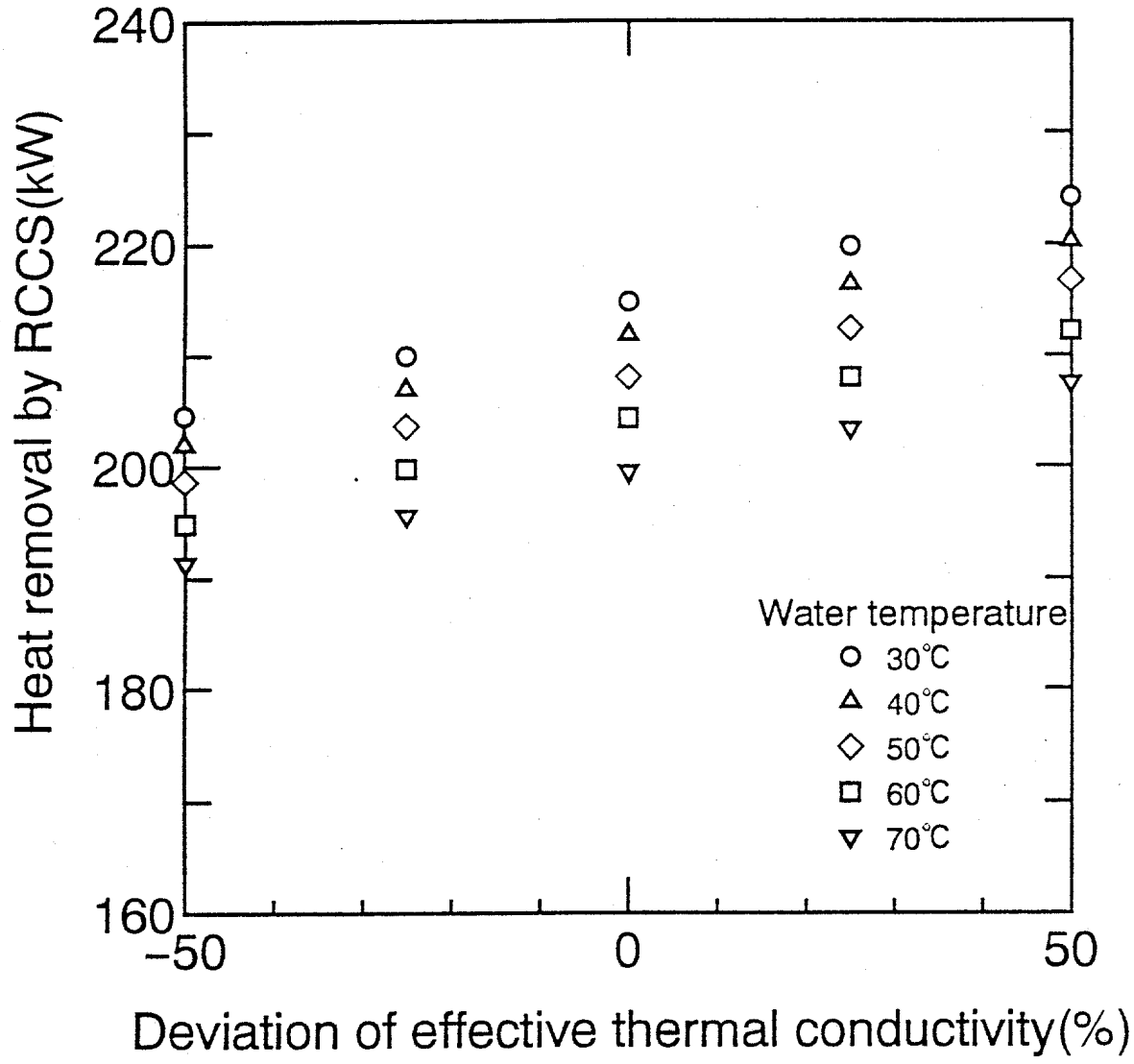

Fig. 3-35 Effect of Natural Convection

3.3.3. Analysis of Benchmark Problems Defined on HTR-10

3.3.3.1. Introduction

These benchmark problems was analyzed [1][2][3] by using THERMIX, a computer program used for 2-dimensional thermal hydraulic analysis of a pebble bed HTGR.

3.3.3.2. Heatup Experiment I

The axial temperature fields of the surfaces of the core vessel (CV), RPV and the water-cooling panel (WCP) are given in Fig.3-36. The influence of natural convection and net emissivity coefficient ε between RPV and WCP are shown in Table 3-40.

Table 3-40 Natural Convection Analysis and Net Emissivity Coefficient Sensitivity Analysis

Case	**Q_{con} KW**	**G_w kg/s**	**$T_{w,in}$ ºC**	**$T_{w,out}$ ºC**	T_{rpv}^{max} ºC	T_{wcp}^{max} ºC
without N.C. ε=0.68	194.0	5.04	65.3	74.6	271.2	80.8
with N.C. ε=0.68	215.0	5.22	64.5	74.4	270.2	80.9
with N.C. ε=1.0	280.0	5.73	64.7	76.5	364.9	83.0
with N.C. ε=0.50	176.0	4.86	64.4	73.1	290.0	79.4

Considering natural convection, the heat transfer rate of the RCCS is 215.0 KW which is about 9.8% higher than that without considering natural convection, i.e. 21.0 KW higher. If ε increases from 0.68 to 1.0, the heat transfer rate of the RCCS will increase 30.2%, i.e. increase 65.0KW; and if ε decreases form 0.68 to 0.50, i.e., decrease 39.0KW.

3.3.3.3. Depressurization Accident I

The axial temperature fields of the reactor vessel, RPV and WCP at the initial state of LOHS depressurization accident condition with given reactor power is shown in Fig.3-37. The heat transfer rate, flow rate, inlet and outlet temperatures of the water cooler, which are time dependent, shown in Fig. 3-37 and 3-38. Their maximum values are given in Table 3-41.

Table 3-40 Maximum Values of Main Thermal-hydraulic Parameters of Water Cooler and Air Cooler under LOHS Accident

Parameter	**Maximum value**
Heat transfer rate Q Kw	101.06
Inlet temperature T_{in} ºC	51.2
Outlet temperature T_{out} ºC	57.4
Flow rate G kg/sec	3.90

The maximum temperature of the core vessel, RPV and WCP at time t=0.0, 24.0, 103.0 hour respectively are 236.2ºC, 176.2ºC, 64.0ºC; 252.5ºC, 190.0ºC, 64.2ºC, and 183.4ºC, 139.1ºC, 57.4ºC.

3.3.3.4. Heatup Experiment II

Under the 200kW heating experiment condition, the heat transfer rates of the HTR-10

water cooler is 200.0 kW. The central axial temperature, axial surface temperatures of the side graphite reflector and side carbon thermal insulator are shown in Fig.3-40. The axial surface temperatures of the CV, RPV and WCP can be seen in Fig.3-41. The maximum temperatures of main components of HTR-10 are shown in Table 3-42.

Table 3-42 Maximum Temperatures of Main Components of HTR-10 under Heating Experiment Condition

Components	**Maximum temperature (°C)**
Fuel element	1264.0
Side graphite reflector surface	706.0
Graphite carbon surface	569.4
Core vessel surface	399.0
Reactor pressure vessel surface	330.1
Water cooling panel surface	73.9

It can be seen that the heat generated in the core is completely removed by the RCCS. The maximum fuel element temperature is 1264.0ºC, lower than its safety limit 1600ºC.

3.3.3.5. Depressurization Accident II

In the first stage of accident that the natural circulation is established without reactor scram. The transient behaviors of the reactor power and the reactivities and the fuel element temperatures are respectively shown in Figs.3-42 and 3-43.

In the second stage of accident, the transient behaviours of the reactor power and maximum and average temperature of fuel elements are given in Figs 3-44, 3-45 and 3-46. The peak value of maximum temperature of fuel element is 898ºC.

3.3.3.6. Conclusions

– The RCCS of HTR-10 can safely remove heat generated in reactor core from core bed to the ultimate sink, i.e. atmosphere under both heatup experiment and accidents,
– The heat transport ability of RCCS of HTR-10 is big enough, and it carries away too much heat from RPV under steady state. Therefore, a steel plate is added between RPV and water cooling panel to prevent too much heat is removed RPV,
– The fraction of heat transported from RPV to RCCS in mechanism of natural convection is relatively rather less, about 10%, i.e., heat is mainly transported in mechanism of radiation from RPV to RCCS.

The net emissivity coefficient ε between RPV and WCP has strong effect on heat transport rate of RCCS.

In general, the analysis results of heat transport ability of the RCCS of HTR-10 show that HTR-10 can automatically shutdown under superheating condition and the decay heat can be safely removed from the reactor core in passive mode by its RCCS.

REFERENCES TO SECTION 3.3.3.

Zuying Gao, Baoyan Lee, Zhiqiang Jiang, Analysis of Benchmark Problems of HTR-10, 2nd Research Cooperation Meeting on Heat Transport and Afterheat Removal for Gas-cooled Reactors under Accident Conditions, JAERI, Japan, Nov., 1994.

Zuying Gao, Baoyan Lee, Definition and Solution of Benchmark Problem of 200kW Heatup Experiment of HTR-10, 3rd Research Cooperation Meeting on Heat Transport and Afterheat Removal for Gas-cooled Reactors under Accident Conditions, Nov., 1995.

Zuying Gao, Baoyan Lee, Zhiqiang Jiang, Benchmark Problem on Heat up Accident of HTR-10.

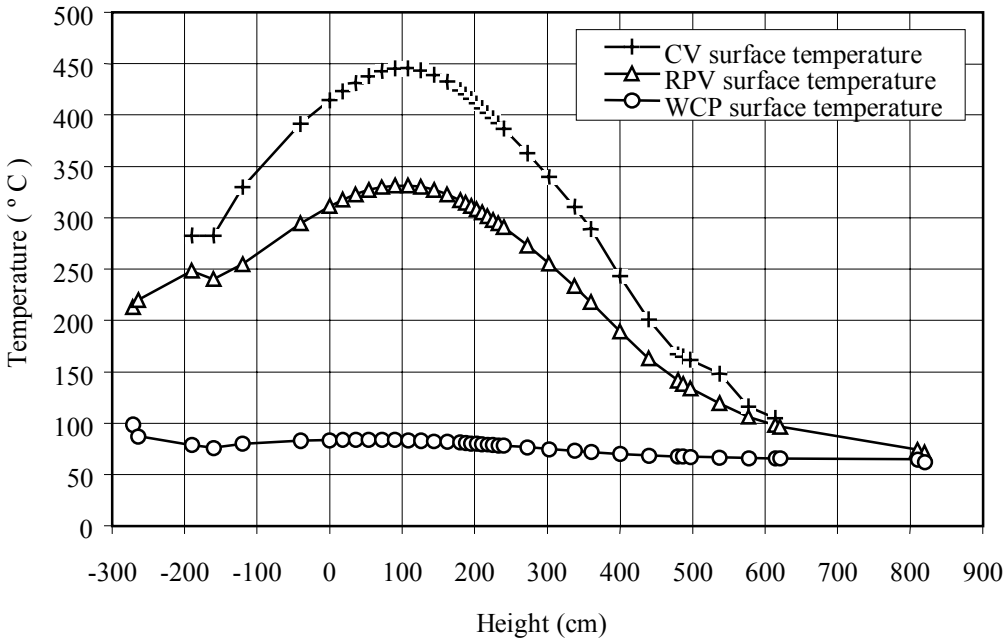

Fig.3-36 Surface Temperature of CV, RPV and WCP

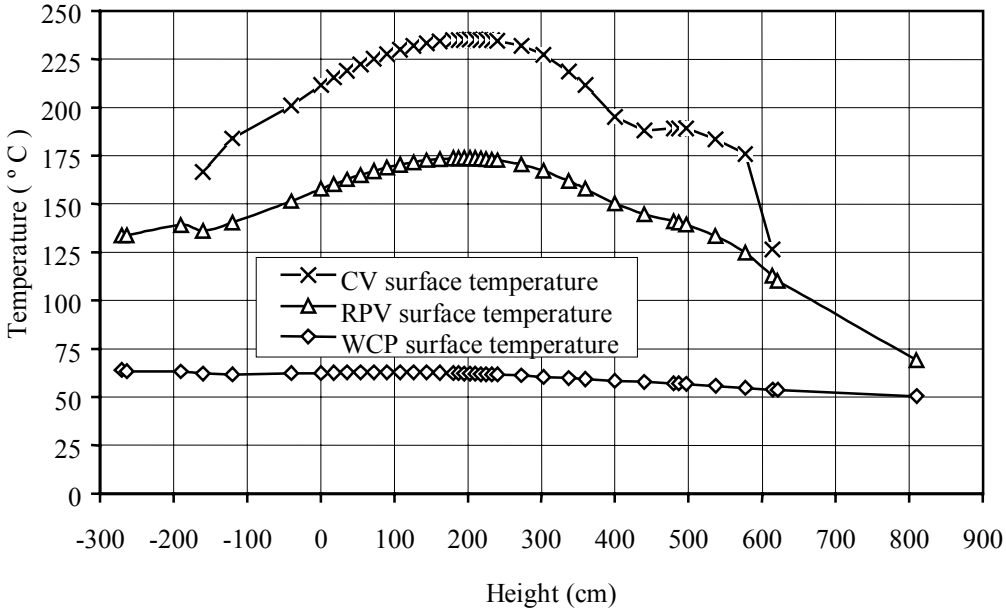

Fig..3-37 Surface Temperature of CV, RPV and WCP
at Initial Status

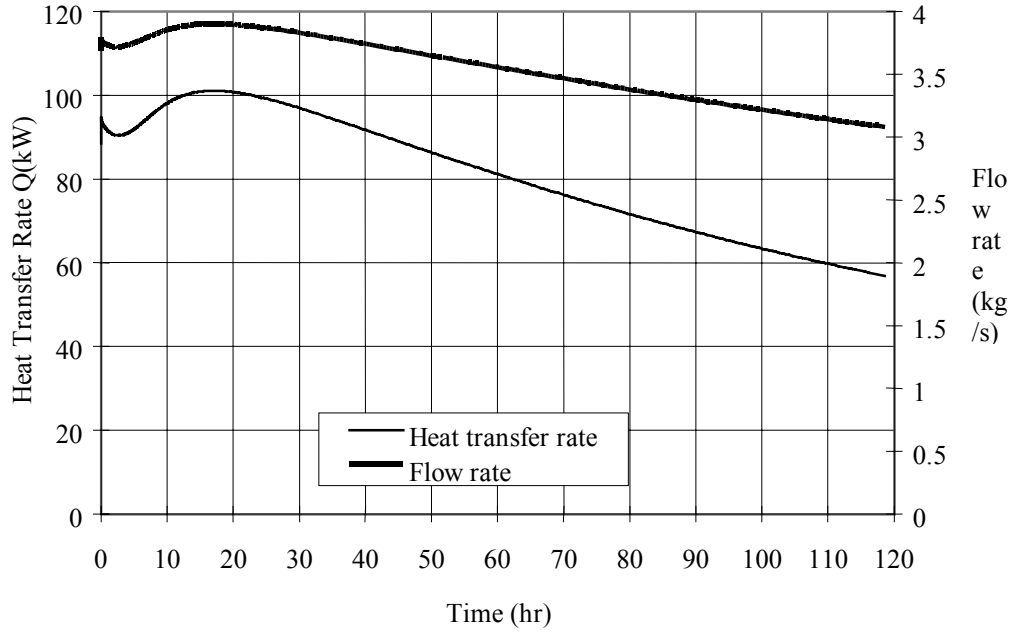

Fig.3-38 Heat Transfer Rate and Flow Rate of RCCS of Depressurization Accident

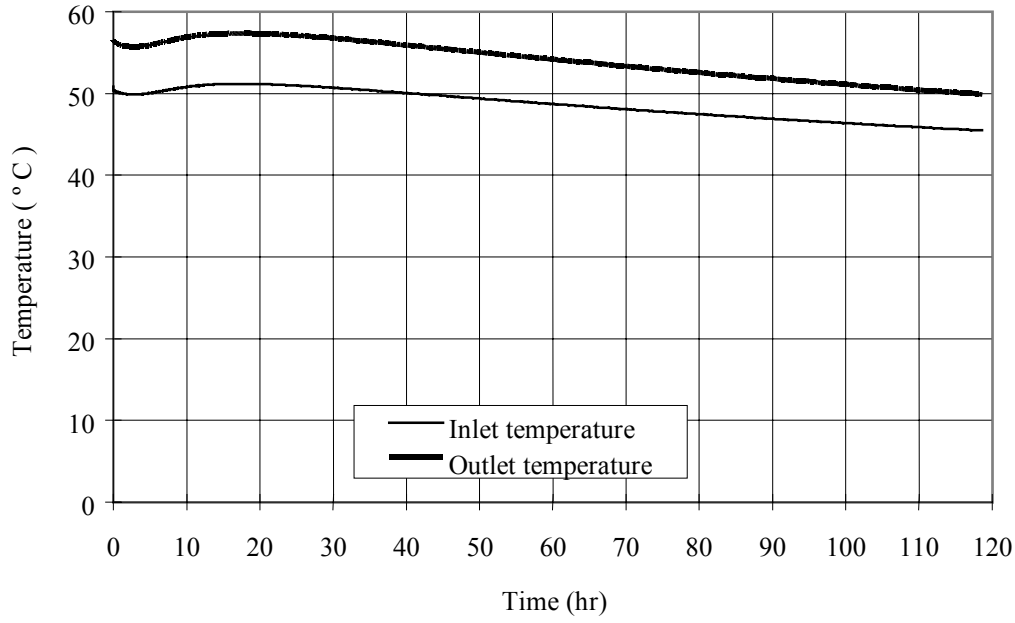

Fig.3-39 Inlet and Outlet Temperature Curves of RCCS Under Depressurization Accident I

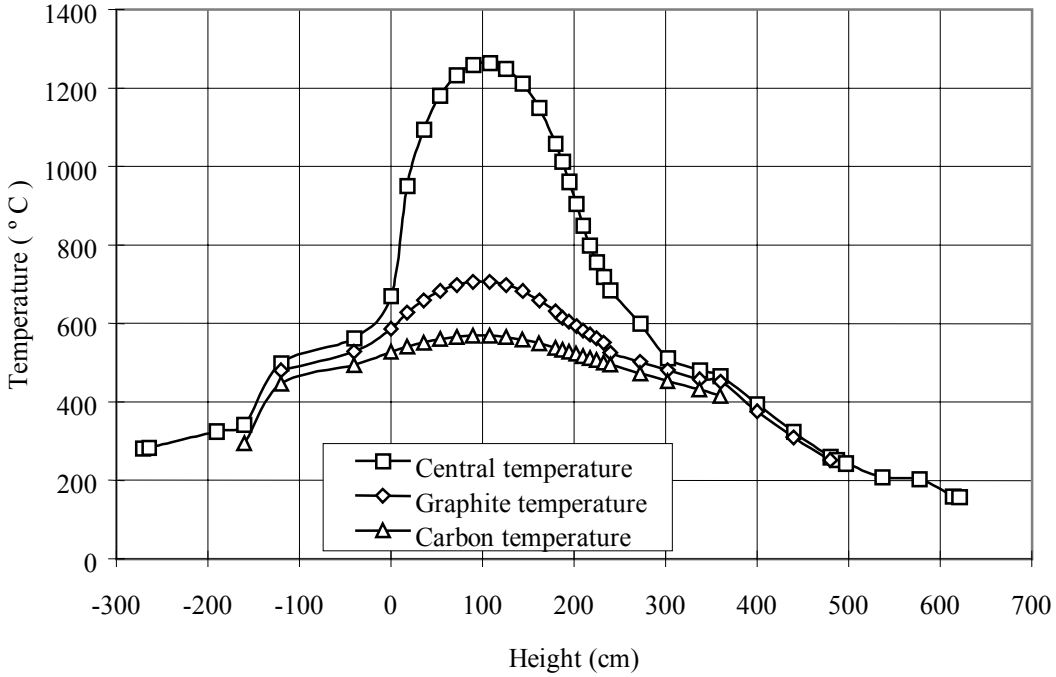

Fig.3-40 Temperature Curves of Axial Centre, Inside Side Surface Graphite Reflector and Carbon

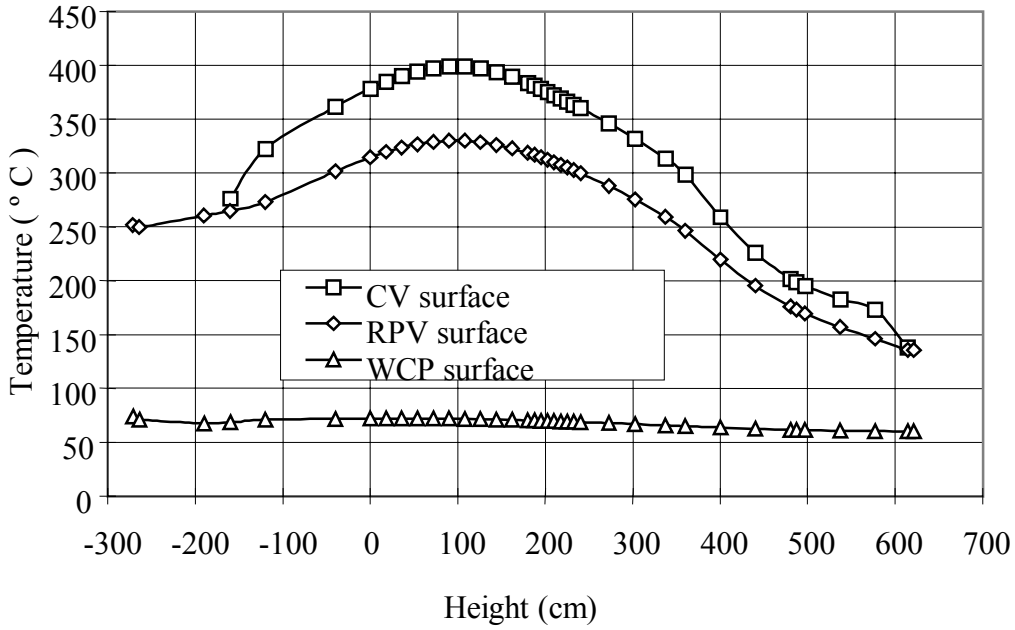

Fig 3-41 Side Surface Temperature Curves of CV, RPV and WCP of Heatup Experiment II

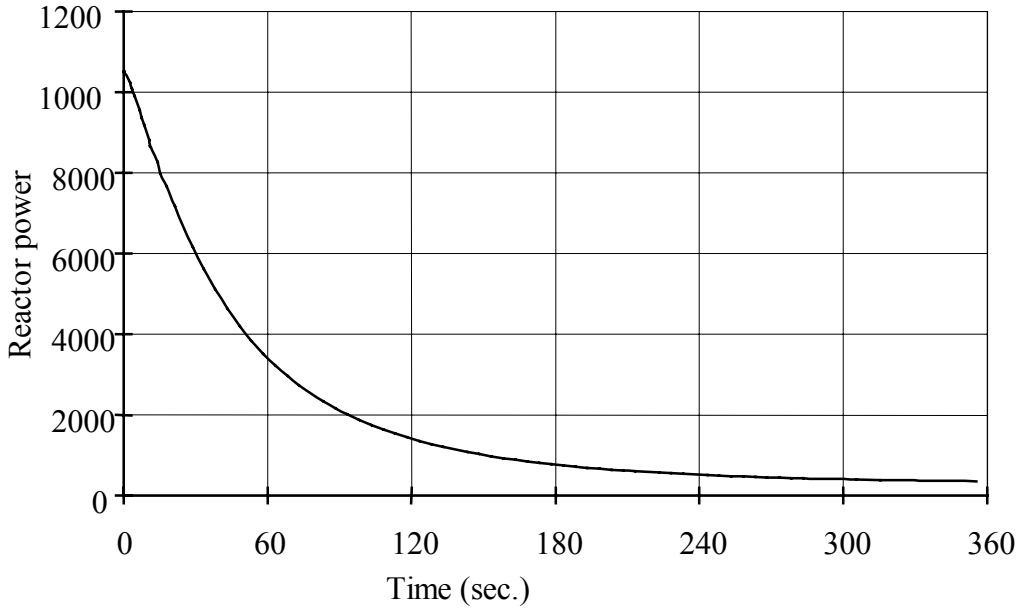

Fig.3-42 Transient Curve of the Reactor Power in the Accident First Stage under Accident II

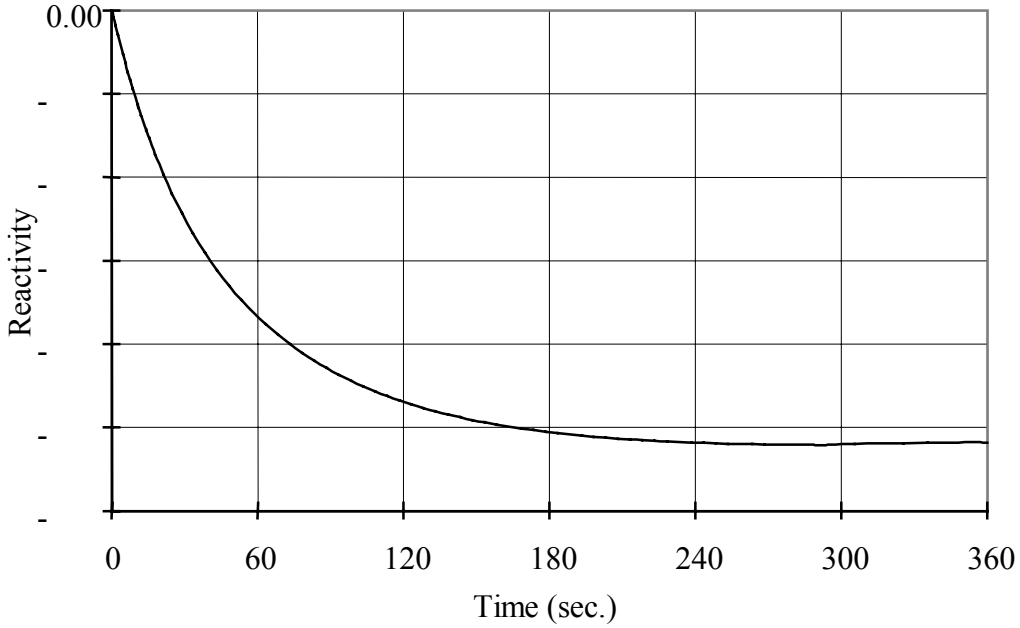

Fig. 3-43 Transient Curve of HTR-10 Temperature Feedback Reactivity in the Accident First Stage under Accident II

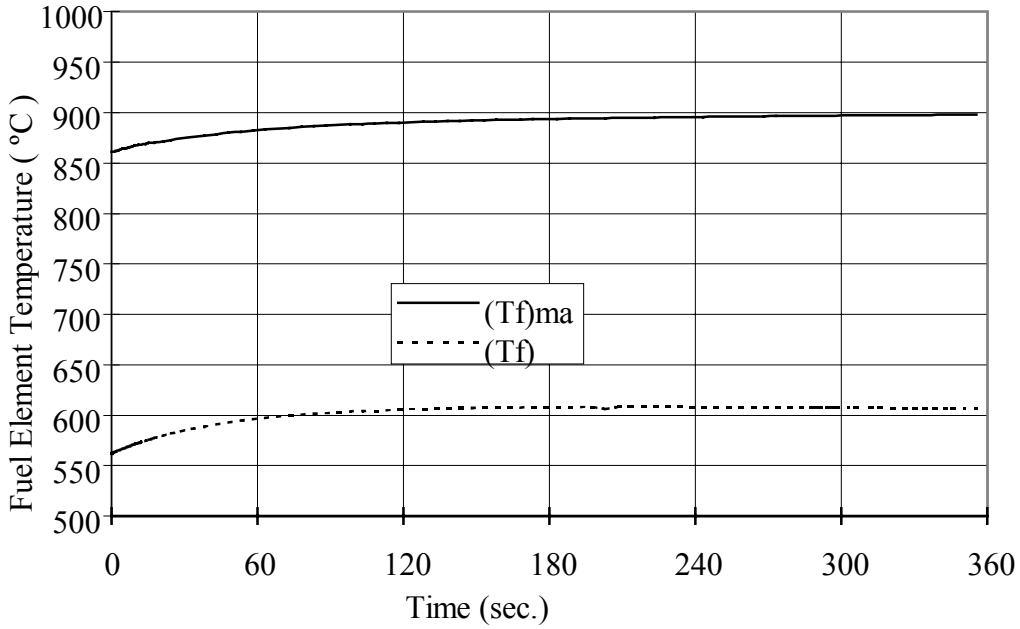

Fig. 3-44 Transient Curve of Fuel Element in the Accident First Stage under Accident II

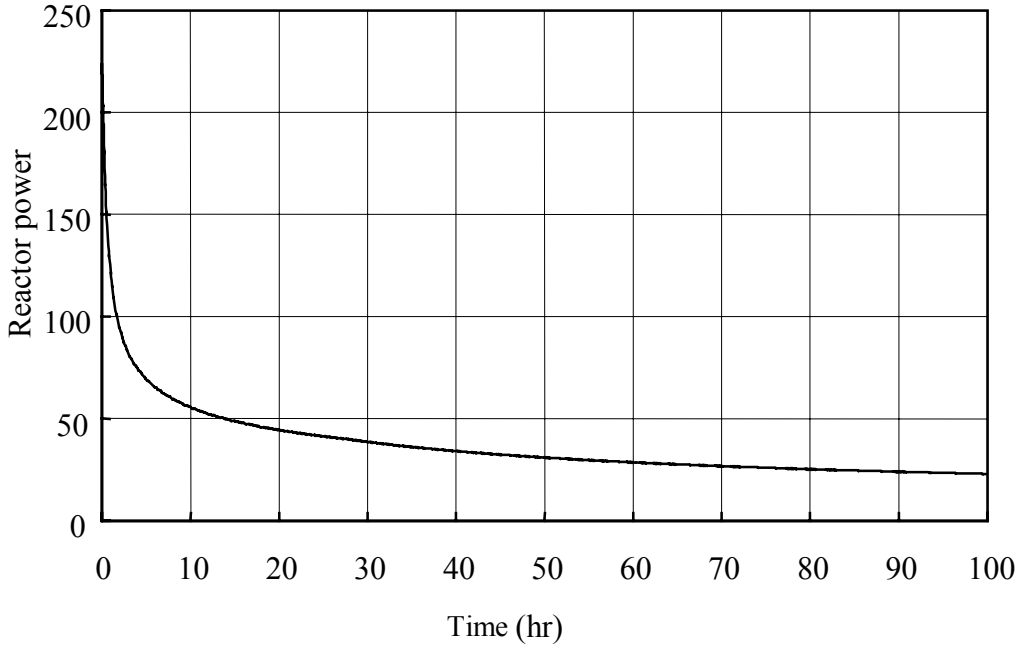

Fig. 3-45 Transient Curve of the Reactor Power in the Accident Second Stage under Accident II

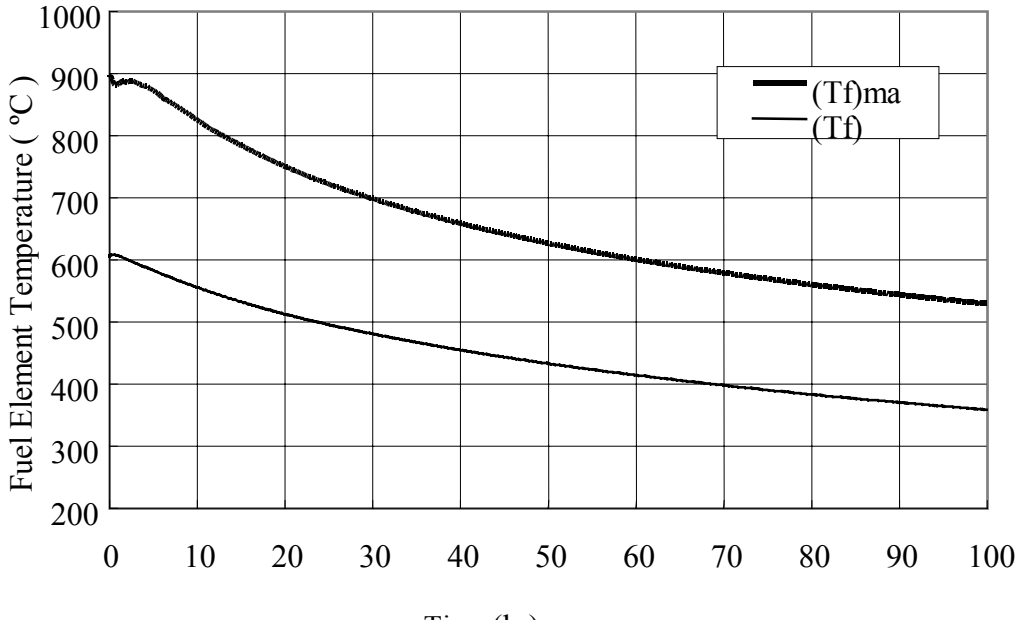

Fig. 3-46 Transient Max. and Avg. Temperature of the Fuel Element in the Accident Second Stage under Accident II

Note: The height of the top of core bed is z=0 cm

3.3.4. Comparison and Conclusion of HTR-10 Benchmark Problems

3.3.4.1. Results Comparison and Analysis

The benchmark problems defined on HTR-10 reactor, which were provided by Gao Zuying, et al. at INET of China, were analyzed by INET of China and Atomic Energy Research Institute of Japan respectively with their code THERMIX and TAC-NC.

Heat Transfer Rate

Table 3-43 shows the comparison results of heat transfer rate of RCCS in heat-up experiment and depressurization accident. It can be seen that the total heat transfer rates given by China and Japan are close, but the fraction of heat transferred by natural convection given by China is lower than that given by Japan.

Table 3-43 Comparison between results of RCCS heat transfer rate

Operating Condition	**Nation**	Q_T**(kW)**	Q_R**(kW)**	Q_C**(kW)**	R_C**(%)**
Heat-up Experiment	China	215	194	21	9.8
	Japan	208	-	-	20
Depressurization Accident	China*	101.06	-	-	-
	Japan*	113	-	-	-

Note: Q_T is total heat transfer rate by RCCS.
Q_R is heat transfer rate by radiation.
Q_C is heat transfer rate by natural convection.
R_C is Q_C/Q_T .
* values are that at time = 18 hour after the initiation of the accident.

Flow Rate and Maximum Temperatures

Table 3-44 shows the comparison results of flow rate of RCCS, the maximum temperatures of RPV and water cooling panel (WCP), as well as inlet and outlet cooling water temperatures. It can be seen that the flow rate given by Japan is greater than that given by China. The temperature of cooling water given by Japan is lower than that given by China. It may be caused by that the friction coefficient and boundary condition of the natural convection used by Japan are different from those by China. The maximum temperatures of RPV given by Japan and China are close both for heat-up experiment and depressurization accident.

Table 3-44 Comparison between results of flow rate and maximum temperature

Operating Condition	Nation	G_W kg/s	T_{RPV}^{max} □C	T_{WCP}^{max} □C	$T_{W,in}$ □C	$T_{W,out}$ □C
Heat-up Experiment	China	5.22	270.2	80.9	64.5	74.4
	Japan	7.8	257	58	50	56.4
Depressurization Accident	China*	3.9	190.0	64.2	51.2	57.4
	Japan*	6.4	180	58	-	-

Note: * values are that at time = 18 hour after the initiation of the accident.

Sensitivity Analysis

The sensitivity analysis of emissivity between RPV and WCP was carried out by China. Table 3-45 gives the comparison of heat transfer rates using different emissivities. It shows that the net emissivity between RPV and WCP has strong effect on the heat transfer rate of RCCS.

Table 3-45 Sensitivity analysis result of emissivity by China

	0.5	0.68	1.0
Q (kW)	176.0	215.0	280.0
Q_i / $Q_{0.68}$	82.2%	100%	130.2%

The sensitivity study of effective thermal conductivity was carried out by Japan to analyze the natural convection heat transfer in the annulus between RPV and WCP. The result is that the heat removal by RCCS increases by only 5% as the effective thermal conductivity increases by 50%. No sensitivity analysis on emissivity was given by Japan.

3.3.4.2. Conclusions

– The total heat transfer rate given by China is close to that given by Japan,
– The heat is mainly transported in the mechanism of radiation from RPV to RCCS. The heat transfer by natural convection is about 10% given by China and 20% given by Japan,
– The heat removal rate of RCCS is evidently influenced by the emissivity between RPV and WCP. The effect of natural convection on the total heat transfer rate is limited.

REFERENCES TO SECTION 3.3.4.

[1] Gao Zuying, Li Baoyan and Jiang Zhiqiang, "Benchmark Problem Definition of HTR-10", INET, Tsinghua University, Beijing, China.

[2] Gao Zuying, Li Baoyan and Jiang Zhiqiang, "Analysis of Benchmark Problems Defined on HTR-10", INET, Tsinghua University, Beijing, China.

[3] K. Kunitomi, A. Saikusa and M. Hishida, "Analysis of Benchmark Problem for Chinese HTR-10 Test Module", Japan Atomic Energy Research Institute.

3.4. GT-MHR PLUTONIUM BURNER

3.4.1. CRP-3 Benchmark Problem Description for GT-MHR PU Burner Accidents

3.4.1.1. Introduction

The Gas Turbine Modular Helium Reactor (GT-MHR), when fueled with surplus weapon grade plutonium, has the unique capability to obtain burn-up of 90% of the initially charged plutonium-239 in a once through reactor cycle while generating electricity at plant efficiencies of nearly 50%. The plutonium content and quality in the spent fuel is so low that there is little or no military or commercial incentive for reprocessing and recycle. The spent fuel is well suited for disposal as whole elements in a geologic repository. The unique inherent passive safety characteristics of the GT-MHR result in a design that is meltdown proof and insensitive to operator errors. The high efficiency of the GT-MHR results in minimal environmental impact and substantial advantages in plant economics.

The Russian Federation Ministry for Atomic Energy (MINATOM), General Atomics (GA) in the United States, and more recently Framatome in France and Fuji Electric in Japan are participating in a cooperative program to develop the GT-MHR for disposition of surplus weapon grade plutonium in Russia. The near term objective of this program is to construct a GT-MHR plant at Seversk (Tomsk-7) that would burn weapon grade plutonium and would replace the power provided by the plutonium production reactors at that site. Fuel development and plant design activities are underway at several Russian institutes and were completed and fully documented in October 1997.

3.4.1.2. Plutonium-Fueled GT-MHR Description

The GT-MHR is a passively safe, helium cooled, graphite moderated, advanced reactor system that is based on existing technology. Thermal energy is converted to electric power by use of a direct Brayton cycle helium gas turbine power conversion system.

The GT-MHR reference plant consists of four 600MWt (286MWe) modules capable of providing a total net electrical generation capacity of 1144 MWe. As shown in Fig. 3-47, which shows the arrangement of one module, the reactor core is contained in an uninsulated steel reactor pressure vessel that is connected by a cross vessel to a vessel that contains the power conversion system. The reactor and power conversion vessels are, respectively, 8.4m and 8.5m in diameter. The modules are located below grade in a 39 m deep, high pressure, low leakage containment with characteristics typical of those of commercial light water reactors.

Refractory coated particle fuel is used in the plutonium-fueled GT-MHR. The fuel is in the form of tiny (200mm diameter) plutonium oxide fuel kernels coated first with a porous graphite buffer layer followed by layers of silicon carbide and pyrolytic carbon. This system of particle coatings is referred to as a TRISO coating. The coated fuel particle total diameter is about 635mm. The particles are mixed with graphitic material and formed into cylindrical fuel rod compacts 12.45mm in diameter and 49.3mm long. The fuel rod compacts are inserted into hexagonal prismatic graphite fuel element blocks 0.79m high and 0.35m wide across the flats, and weighing about 115kg. The fuel element configuration is identical to that successfully demonstrated in the Fort St. Vrain reactor in the United States. A standard fuel element contains about 22 million coated fuel particles.

The reactor's annular core (Fig. 3-48) consists of 1020 hexagonal prismatic fuel elements stacked in a ten element high annular array of 102 columns. One third of the fuel elements are replaced annually. Because the plutonium-fueled GT-MHR uses no fertile fuel material, excess reactivity control and negative temperature feedback are provided by erbium oxide poison rods located in selected fuel holes in the graphite fuel elements. The core has a strong negative

temperature coefficient of reactivity.

The direct Brayton cycle power conversion system results in considerable simplification of balance of plant design relative to conventional Rankine steam cycle plant designs. The entire power conversion system is located in the power conversion vessel. The turbomachine consists of a generator, gas turbine, and two compressor sections submerged in helium and vertically mounted on a single shaft supported by magnetic bearings. The power conversion system includes three compact heat exchangers: a highly effective recuperator and water-cooled precooler and intercooler.

The GT-MHR process flow is shown in Fig. 3-49. Helium coolant exits the reactor core at 850°C and 7.01MPa, flows through the center hot duct within the cross vessel, and is expanded through the turbine in the power conversion vessel. The turbine directly drives the electric generator and the high and low pressure compressors. Helium exits the turbine at 510°C and 2.64MPa and flows through the highly effective recuperator to return as much energy as possible to the cycle, and then the precooler to reject heat to the ultimate heat sink. Relatively cold helium at 26°C passes through the recuperator. Helium at 490°C and 7.07MPa flows from the recuperator exit, through the outer annulus within the cross vessel, and back to the core inlet and downward through the core to complete the loop.

The GT-MHR retains virtually all fission products within the fuel particle coatings under all accident conditions. This retention is accomplished through a combination of inherent safety characteristics and selection of passive design features.

3.4.1.3. Water-cooled Reactor Cavity Cooling System (RCCS) Preliminary Design

3.2.1.2.4. RCCS Functional Description

A simplified schematic diagram of the RCCS is shown in Fig. 3-50.

The RCCS consists of:

– Surface cooler (two independent cooler arrays, natural circulation)
– RCCS headers
– Heat exchanger (water-to-water)
– Quench tank (for expansion, filling)
– Connecting piping, measurement system

The RCCS functions include:

Heat removal from reactor cavity during normal operations to maintain the reactor vessel, the cavity, and concrete silo temperatures within required limits. In normal operation, the maximum vessel temperature should not exceed 490□C, and the maximum concrete temperature should not exceed 80□C,

Heat removal from reactor cavity during postulated accident (emergency) conditions to maintain reactor vessel, in-vessel structures, fuel, reactor cavity, and silo concrete temperatures within required limits. In emergency conditions, the maximum vessel temperature should not exceed 540□C, and the maximum concrete temperature should not exceed 100□C,

Transition from normal mode (1.) to emergency mode (2.) is made without any necessary actions by the operator or controlling equipment. Emergency cooling functions should be maintainable without intervention for at least 48 hours,

Heat removal from the heat exchanger during normal operation is by means of a secondary-side cooling water system (forced circulation), with no boiling taking place (primary or secondary) and with both sides at atmospheric pressure,

During accident conditions, if the heat exchanger secondary side forced circulation cooling system is not available, boiling in the surface coolers, compensated by makeup water fed to the quench tank, becomes the heat sink mechanism.

3.4.1.4. Benchmark Problem Description for Postulated Heatup Accidents

An initial condition (system capacity) check and two loss of forced convection (LOFC) accidents are to be analyzed as the benchmark problems for the GT-MHR Pu burner:

Calculate steady state (normal operation) RCCS heat removal, with one or both surface cooler panels operational, and verify that temperature limits are not exceeded,

The first LOFC is accompanied by a rapid depressurization and scram, and is a study of conduction cooling behavior. With an immediate loss of cooling flow to the core, the balance of plant does not need to be part of the simulation; only the core, vessel, and RCCS need to be modeled. The RCCS should be assumed to function as designed, in one case with forced cooling of the heat exchanger, and the other in the boil-off mode (assuming sufficient makeup water is available). The objective is to predict the transient reactor vessel temperatures, RCCS heat removal rates, and core fuel temperatures throughout the course of the accident,

The second accident case is an LOFC accompanied by a scram, but without a depressurization. For the purposes of this analysis, it is to be assumed that the primary system pressure remains at its initial value; otherwise a model (and many operational assumptions) would be required for modeling the effect of the balance of plant transients on the primary system pressure. As in the first LOFC case, the objective is to predict the transient reactor vessel temperatures, RCCS heat removal rates, and core fuel temperatures throughout the course of the accident with both assumed modes of heat exchanger cooling.

A schematic diagram of a suggested model for the benchmark problem is shown in Fig. 3-51.

3.4.1.5. Supplementary information on the benchmark problem

1. Accept the following flowrates for the calculation of core temperatures under nominal reactor power:

– total core flowrate 320 kg/s
– fraction of the total flowrate for cooling of absorber rods 3,2 %
– the rest flowrate of ~311 kg/s goes through the core fuel blocks and gaps between fuel and inside and outside reflector blocks. The average gap between the blocks is 2 mm.
– Fractions of the flowrate for fuel blocks and gaps are to be calculated, on an assumed bypass flow of 10%

2. Boundary conditions for calculations of heat removal from the reactor vessel to the iron-concrete closure and further to the air (upper direction) and to the RCCS (side and lower directions) for nominal power and accidents

2.1. Upper direction

– Average distance between the upper head of the vessel and the iron-concrete closure (no insulation)	2 m
– Thickness of the closure	1.8 m
– Equivalent conductivity of the closure	3W/mK
– Thermal capacity of the closure	0.7kJ/kgK
– Equivalent density of the closure	3000 kg/m
– Emissivity of a metallic liner of the closure	0.
– Air temperature in the room above the closure	30°C
– Heat transfer coefficient from the closure upper surface to the air	12W/m^{2}K

– Effect of stand pipes on heat transfer is not taken into account.

2.2. Radial direction

– The following boundary condition is given for simplified calculations o heat transfer to the RCCS:
  - average temperature of cooling tubes with shield for RCCS mod without boiling 65°(
– The following boundary conditions are given for more detaile calculations of the RCCS:
  - average temperature of riser tubes with shield for RCCS mode withou boiling 65°(
  - Average riser temperature with boiling 140°(
  - average temperature of downcomer tubes for RCCS mode withou boiling 40°(
  - thickness of the concrete wall 1.2r
  - conductivity of the concrete 1.5W/mK
  - thermal capacity of the concrete 0.83kJ/kgK
  - emissivity of a concrete steel liner 0.
  - air temperature in the room after the concrete wall 30°(
  - heat transfer coefficient from the outside surface of the concrete wall to the air 12W/m^{2}K

Lower direction

– Average distance between the lower head of the vessel and the cooling tubes 1r
– A boundary condition is average temperature of the cooling tubes fo 40°(

RCCS

mode without boiling

3. Irradiative graphite conductivity of fuel and reflector blocks vs temperature is taken in accordance with data for graphite H-451 (instead of data for graphite given in Table 4 below as per ORNL Letter 11 Feb 97)

Table 4 of the benchmark description

Temperature °C	500	600	800	1000	1200	1400	1600
Graphite conductivity W/mK	29.3	31.4	35.6	37.7	41.4	42.3	43.0

Adopt the following estimated values of compact conductivity vs temperature:

Temperature °C	500	600	800	1000	1200	1400	1600
Equivalent compact conductivity, W/mK	30	27	24	22	20	19	18

Radial clearance between a compact and graphite block is 0.1mm

Equivalent conductivity of the core and reflectors is to be calculated

4. It is assumed that no flow is between the reactor vessel and the shell.
5. Calculation of heat removal in pressurized and depressurized conditions is carried out for each accident duration of 100h.
6. Compute the following functions which characterize heat removal from the core to the RCCS for pressurized and depressurized events:

- axial temperature distribution of fuel, lower and upper reflectors at radius of 1.72m with maximum power density for nominal power and 20, 50, 100h of the accidents,
- radial temperature distribution of fuel, inside and outside reflectors in a plane of maximum power density (near the core mid-plane) for nominal power and 20, 50, 100h of the accidents,
- reactor vessel temperature distribution (outer surface) along the height fo nominal power and 20, 50, 100 h of the accidents,
- maximum and average fuel temperatures, and maximum reactor vessel temperature vs. time for duration of 100 h,
- the total power transferred from the reactor vessel in upper, side and lower directions vs. time for comparison with variation of decay power,
- fraction of the total power transferred in side and lower directions to the RCCS and to the air in upper direction.

7. Evaluate effect of the following input data variation on transient fuel and reactor vessel temperatures (only for depressurized accident):

   increase of decay power by 10%,

   increase of the average gap between fuel and reflector blocks to 2.5 mm at the same fraction of flowrate for cooling of absorber rods (3.2%),

   decrease of metallic surface emissivity from 0.8 to 0.6 without change of graphite emissivity 0.9,

   decrease of graphite thermal conductivity of core and reflector blocks by 25%,

   increase of average temperature of cooling tubes up to 140°C instead of 65°C and 40°C respectively for side and lower panels.

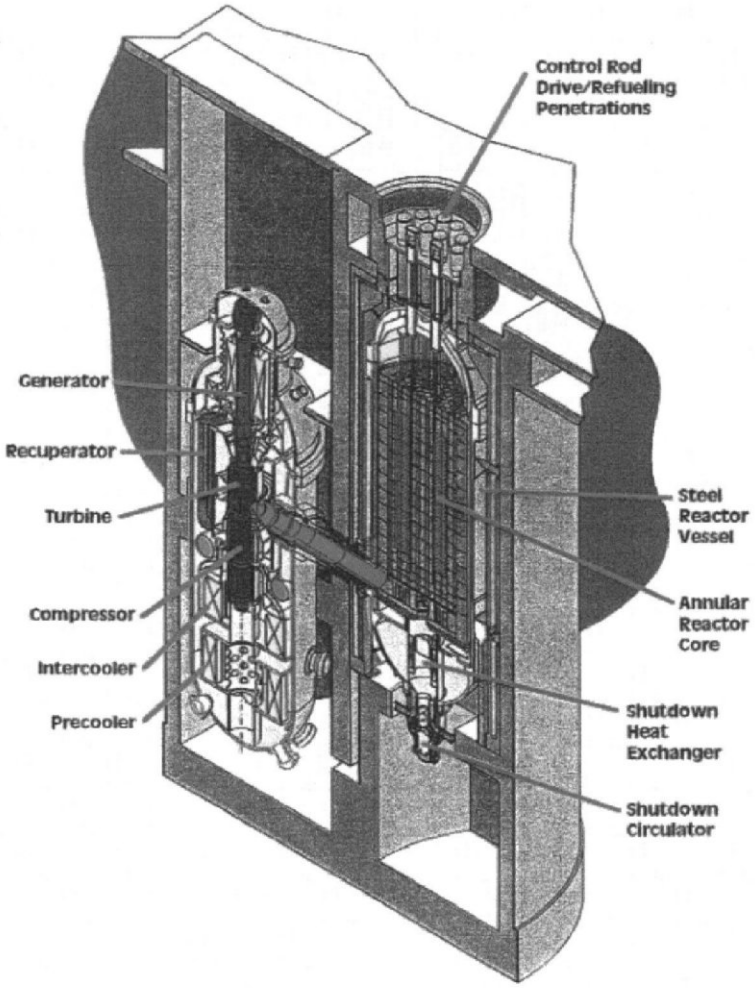

Fig. 3-47 GT-MHR module general arrangement

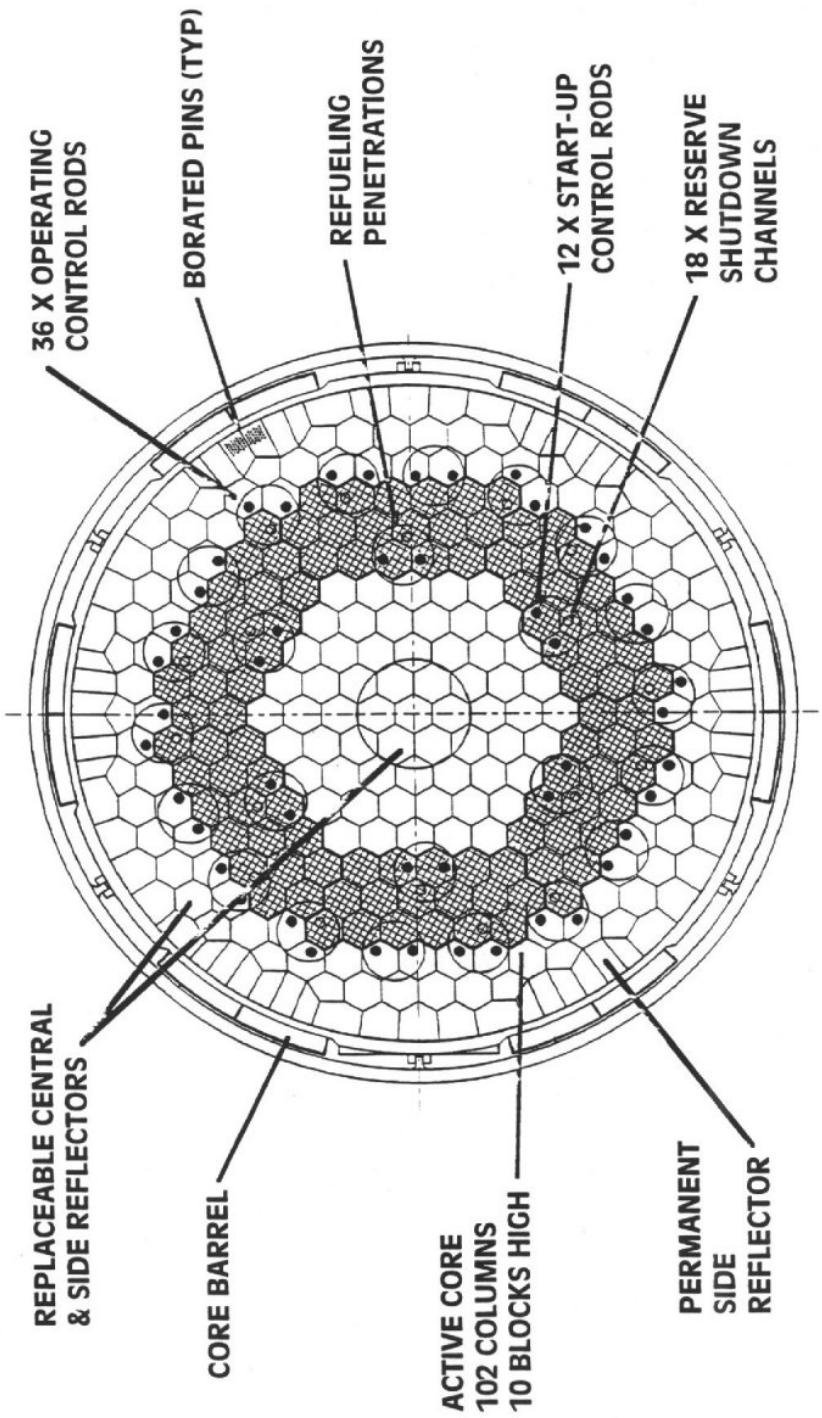

Fig 3-48 GT-MHR core layout

Fig. 3-49 GT-MHR power conversion process flow diagram

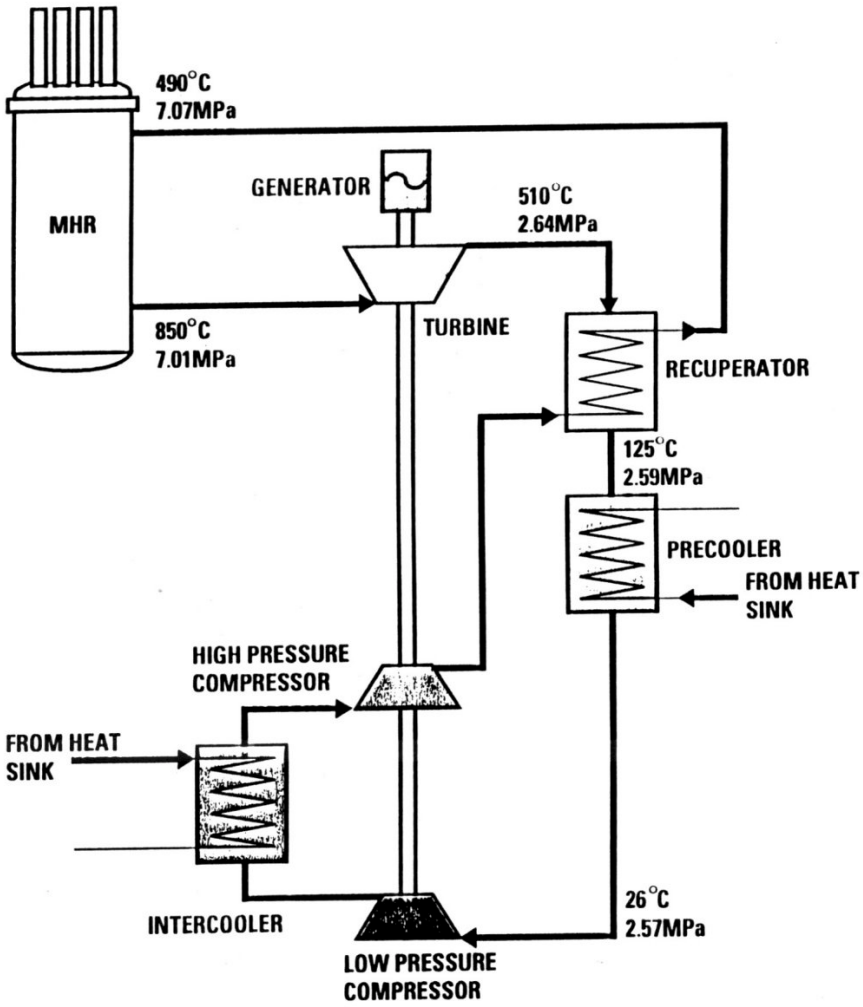

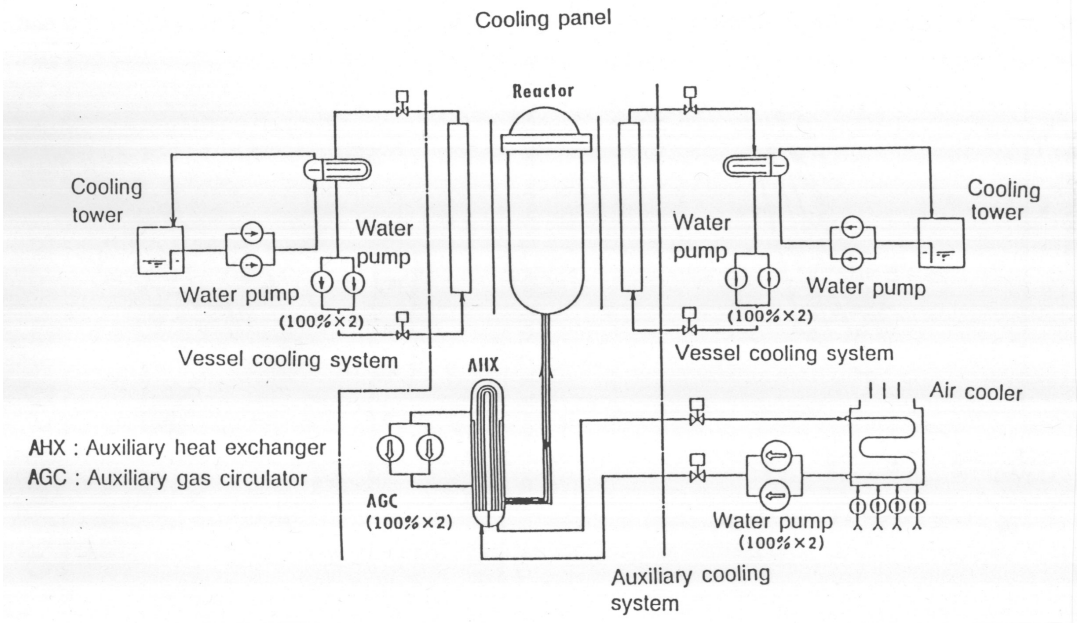

Fig. 3-50 Schematic diagram of GT-MHR Reactor Cavity Cooling System (RCCS)

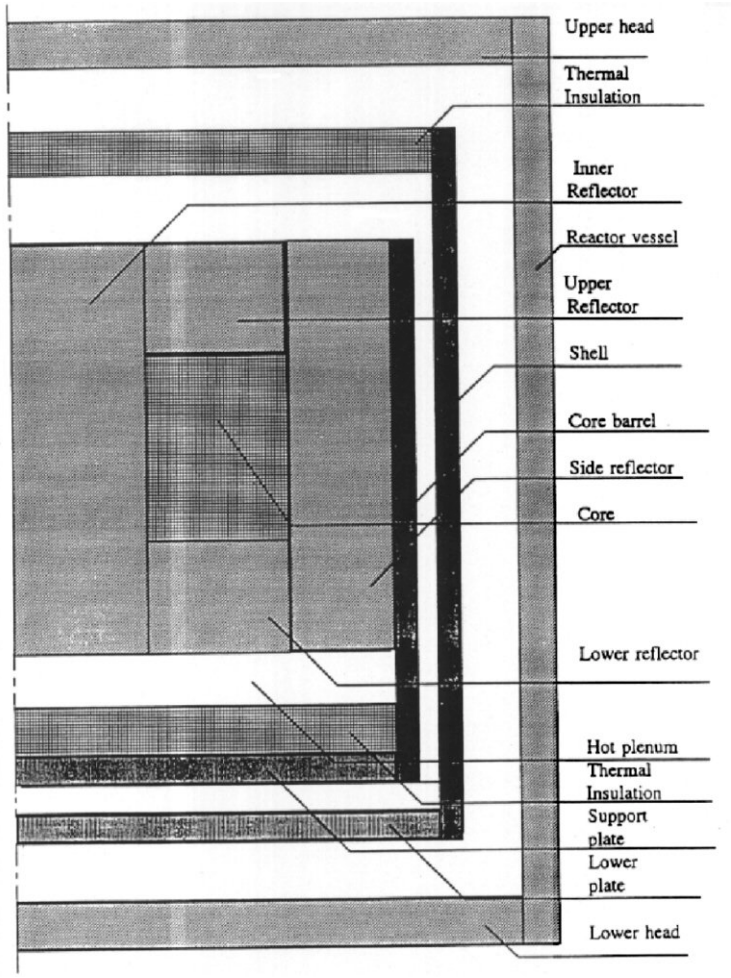

Fig. 3-52 Suggested model schematic diagram for benchmark problem

3.4.2. Analysis of Benchmark Problem for GT-MHR Burner Heat-Up Accidents

3.4.2.1. Introduction

The benchmark problem analysis was done as a part of the IAEA Coordinated Research Program on "Heat Transport and Afterheat Removal for Gas-Cooled Reactors under Accident Conditions".

The benchmark problem on heat transport from the modular helium reactor with gas turbine (GT-MHR) to the reactor cavity cooling system (RCCS) for loss of forced convection accidents, was formulated by Oak Ridge National Laboratory Ref. [1, 2] and OKBM's supplementary information on the basis of the system design data furnished by General Atomics and OKBM.

The objective is to predict:

– Fuel and reactor vessel temperatures for the normal operation with one of both surface cooler panels,

– Fuel and reactor vessel temperatures and RCCS heat removal rates throughout the course of the accident with depressurization of the primary circuit for two modes of the RCCS operation: with forced cooling of the heat exchanger and in the boiloff mode,

– The same as in the previous case, only without loss of pressure in the primary circuit,

– The benchmark analysis is performed using GTAS code (brief description is given in item 4.2.2.).

3.4.2.2. Model features and limitations

Temperature distributions in the core, reflectors and reactor vessel for the reactor operation at rated power and after scram without forced cooling of the core were calculated with the following model features and limitations.

The whole flowrate of 320kg/s comes to the core inlet between the core barrel and a shell which is located before the reactor vessel. There is no flow between the shell and the reactor vessel.

The coolant flows only through channels of the fuel blocks, absorber rods and gaps between the core and reflector columns. It is assumed that there is no mass exchange between the cooling channels and the gaps, i.e. leakages in radial direction through joints of the fuel and reflector blocks are absent.

Core heat transfer coefficients for Re≥2000 are calculated using a correlation from [4]:

$$Nu = 0.018\ Re^{0,8}$$

For laminar flow Nu = 3.66

A correlation for friction in turbulent region is derived from [5]:

$$\lambda = 0.316/Re^{0,25}$$

For laminar flow $\lambda=64/Re$

Emissivity for all graphite and metallic surfaces is assumed to be 0.8 and for fuel rod surface to be 0.9.

The heat transferred to the RCCS is basically determined by the high level of reactor vessel temperatures and insufficiently depends on temperatures of the cooling tubes.

Average temperature of cooling tubes with shield is 65°C for RCCS mode without boiling.

The steam-water temperature in the boiloff mode is 140 °C. This corresponds to 0,25 MPa pressure that is taken to provide a stable of steam-water circulation in the surface cooler panels.

3.4.2.3. Results

Radial distributions of core fuel and reflector graphite temperatures for steady nominal state and throughout the course of the accidents (5, 20, 50 and 100hrs) are shown in Figs. 3-53 and 3-54 for pressurized and depressurized conditions respectively. The calculation is carried out for a section near the core mid-plane with peak values of power density.

The radial temperature distributions for steady nominal state show significant gradients at boundaries between the inner, outer reflectors and the core. As core and reflector temperatures rise in the course of the accident, the gradients at the boundaries decrease, at the same time they increase in the rest of core and reflector blocks.

Axial distributions of core fuel, upper and lower reflector graphite temperatures for steady nominal state and throughput the course of the accidents (5, 20 and 100hrs) are given in Figs 3-55 and 3-56 for pressurized and depressurized conditions respectively. The temperature distributions are computed for radius of 1.72m with peak values of power density.

Temperature distributions along the height of the reactor vessel for steady nominal state and throughout the course of the accidents are presented on Figs. 3-57 and 3-58 for pressurized and depressurized conditions respectively.

Maximum fuel, core barrel and reactor vessel temperatures vs time for pressurized and depressurized conditions are shown in Figs. 3-59 and 3-60.

Maximum rate of fuel temperature rise is in first hours after the reactor shutdown. Then the rate falls as decay heat is reduced and heat removal to the RCCS increases. Maximum temperatures of 1400 and 1490°C are reached to 60 and 70 hours for cases with and without pressure respectively. Maximum reactor vessel temperature drops during ~ 10hrs, then increases up to 400 and 420°C after 70hrs and 80hrs respectively.

Figures 3-61 and 3-62 demonstrate core power and heat removal rates vs. time for pressurized and depressurized conditions. In the beginning of the accidents the heat removal rates fall due to decrease of the reactor vessel temperatures. The core power and heat removal rates become equal at 92h and 100h for pressurized and depressurized accidents respectively.

Heat fractions removed from the reactor vessel are presented in Table 3-46.

Table 3-46 Heat fractions

Time, h	Total heat, kW	Side surface, %	Upper surface, %	Lower surface, %
0	2010	78.4	0.2	21.3
5	1480	79.8	0.2	20.3
20	1325	89.8	0.2	10.0
50	1705	95.2	0.2	4.6
100	1815	96.7	0.2	3.1

The calculations show that temperature distributions in pressurized and depressurized accidents are appreciably differ. The difference is explained by influence of helium natural convection in the core without a depressurization of the primary circuit that leads to heat transfer from lower regions to upper ones. As can be seen from Fig. 3-55 the upper reflector temperature increases from the initial value of 490°C up to 1100°C. At the same time, the upper reflector temperature with a depressurization of the primary circuit (Fig. 3-56) raises only to 900°C. Apparently, that the lower reflector temperatures for depressurized conditions decrease more

slowly than in the accident without a depressurization.

The helium natural convection leads to reduction of heat transferred in radial direction without a depressurization of the primary circuit. Because of this phenomenon, the reactor vessel temperature increase from the initial value of 340°C to lower temperature of 400°C (Fig. 3-59) than the value of 425°C in the accident with a depressurization (Fig. 3-60). Besides, the natural convection causes more non-symmetric temperature distribution along the reactor vessel height for pressurized conditions (Fig. 3-57) than in the accident with a depressurization (Fig. 3-58). Main results of the calculations are presented in Table 3-47.

Table 3-47 Main calculation results

Parameter	With pressure	Without pressure
Fuel temperature at steady nominal state, °C:		
in core mid-plane	835	835
maximum value in lower part of the core	960	960
Maximum reactor vessel temperature at steady nominal state, °C	340	340
Maximum fuel temperature in course of the accidents, °C	1400	1490
Time to attain maximum fuel temperature, h	60	70
Maximum reactor vessel temperature in course of the accidents, °C	400	420
Time to attain maximum reactor vessel temperature, h	70	80
Upper reflector maximum temperature, °C:		
steady nominal state	490	490
in the course of the accidents	1100	900
Time at which decay heat gets equal to one removed from the reactor vessel (~1740kW), hr	92	100

3.4.2.4. Sensitivity study

Sensitivity study of fuel and reactor vessel temperatures is performed for the accident with a depressurization because it is characterized by the higher level of temperatures/ Effect of the following input data on transient fuel and reactor vessel temperatures is evaluated:

– decay power (Fig. 3-63)
– average gap between fuel and reflector blocks (Fig. 3-64)
– metallic surface emissivity (Fig. 3-65)
– graphite thermal conductivity (Fig. 3-66)
– average temperature of cooling tubes (Fig. 3-67)

The reference values of maximum fuel and reactor vessel temperatures are 1490°C and 420°C respectively (Fig. 3-60).

Increase of decay power by 10% results in rise of fuel and vessel temperatures up to 1570°C and 440°C respectively.

Increase of average gap between blocks from 2mm to 2,5mm that leads to reduction of flow rate for fuel cooling, has not almost influence on the fuel and vessel temperatures (not more than 5°C).

Decrease of metallic surface emissivity by 25% results in appreciable rise of the vessel temperature (up to 465°C) and in less extent of the fuel temperature rise (up to 1515°C).

Decrease of graphite conductivity by 25% gives significant rise of the fuel temperature (up to 1600°C). At the same time the vessel temperature drops by 20°C due to reduction of heat removal to the RCCS at the expense of more lower graphite conductivity.

The boil off mode with water temperature of 140°C leads to grow of the vessel temperature by 10°C without change the fuel temperature.

The analysis shows that the maximum fuel and reactor vessel temperatures are most sensitive to variation of graphite conductivity and metallic surface emissivity.

The results point to the necessity for an accurate analysis to determine values of graphite conductivity and emissivity and their uncertainty range.

3.4.2.5. Conclusions

Analysis of the benchmark problem for GT-MHR heatup accidents can be summarized as follows:

– Maximum fuel and reactor vessel temperatures are realized in the accident with a depressurization of the primary circuit, and their values do not exceed for the benchmark conditions 1490°C and 420°C respectively,

– The accident without loss of pressure shows significant increase of upper reflector temperatures because of heat transfer by helium natural convection in the core,

– The sensitivity study shows that the maximum fuel and reactor vessel temperatures significantly depend on graphite conductivity and metallic surface emissivity respectively. It needs accurate determination of their values and uncertainty range.

REFERENCES TO SECTION 3.4.2.

[1] S.J. Ball, “CRP-3 Benchmark Problem Description for GT-MHR Pu Burner Accidents”, ORNL February 10, 1997.

[2] S.J. Ball, “CRP-3 Benchmark Problem Description for GT-MHR Pu Burner Accidents”, Supplementary information on the RCCS Design. ORNL April 21, 1997.

[3] N.G.Kuzavkov, “CRP-3 Benchmark Problem Description for GT-MHR Pu Burner Accidents”. Supplementary information on the benchmark problem. OKBM December, 1997.

[4] V.I. Subbotin et al., “Gidrodinamika i teploobmen v yadernich energeticheskich ustanovkach”, M., Atomizdat, 1995.

[5] I.E. Idel’chik, “Spravochnik po gidravlicheskim soprotivleniyam”, M., “Mashinostroenie”, 1975.

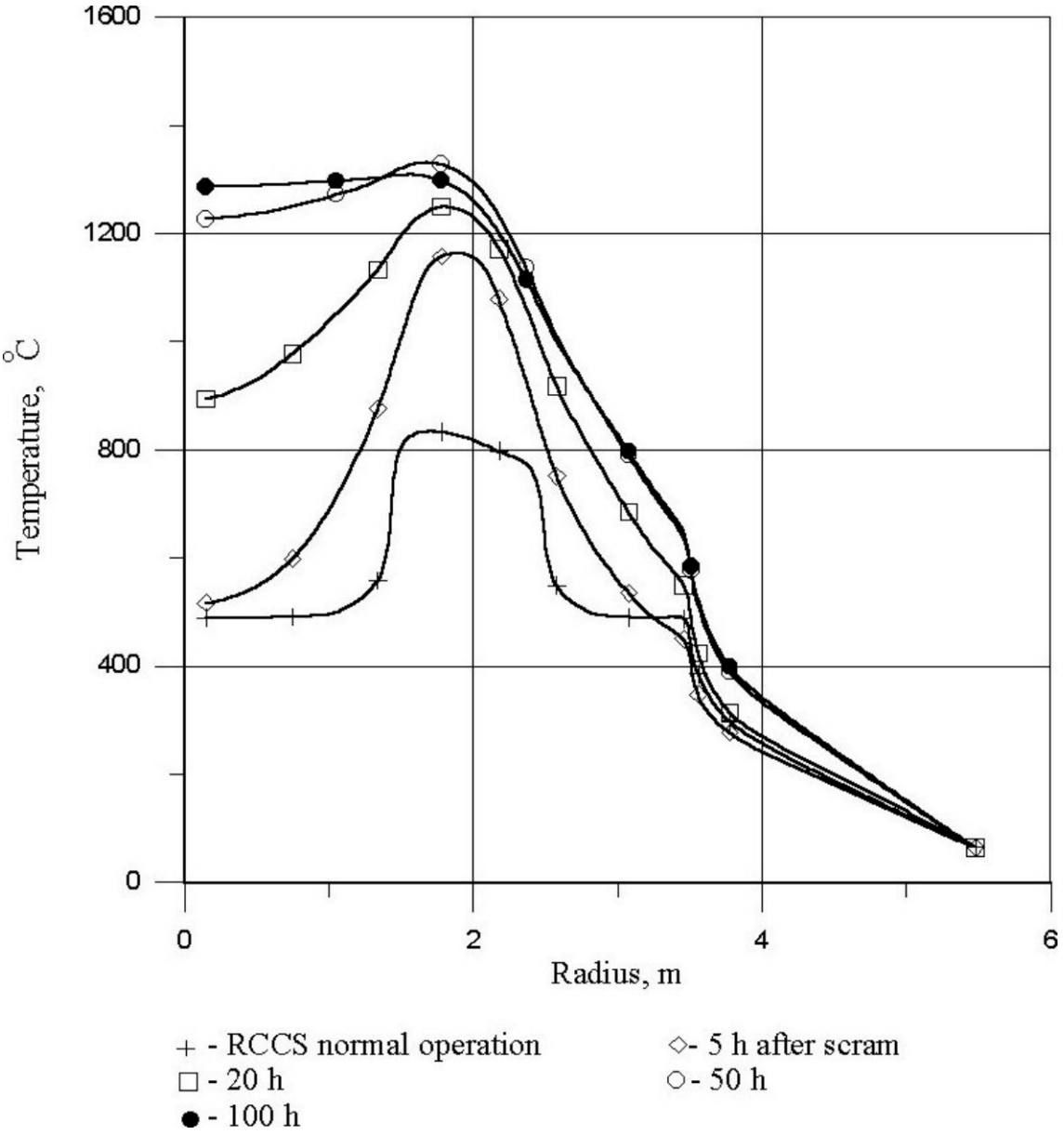

Fig. 3-53 Radial Distribution of Core Fuel and reflector Graphite Temperatures in Core Mid-Plane for Pressurized Conditions

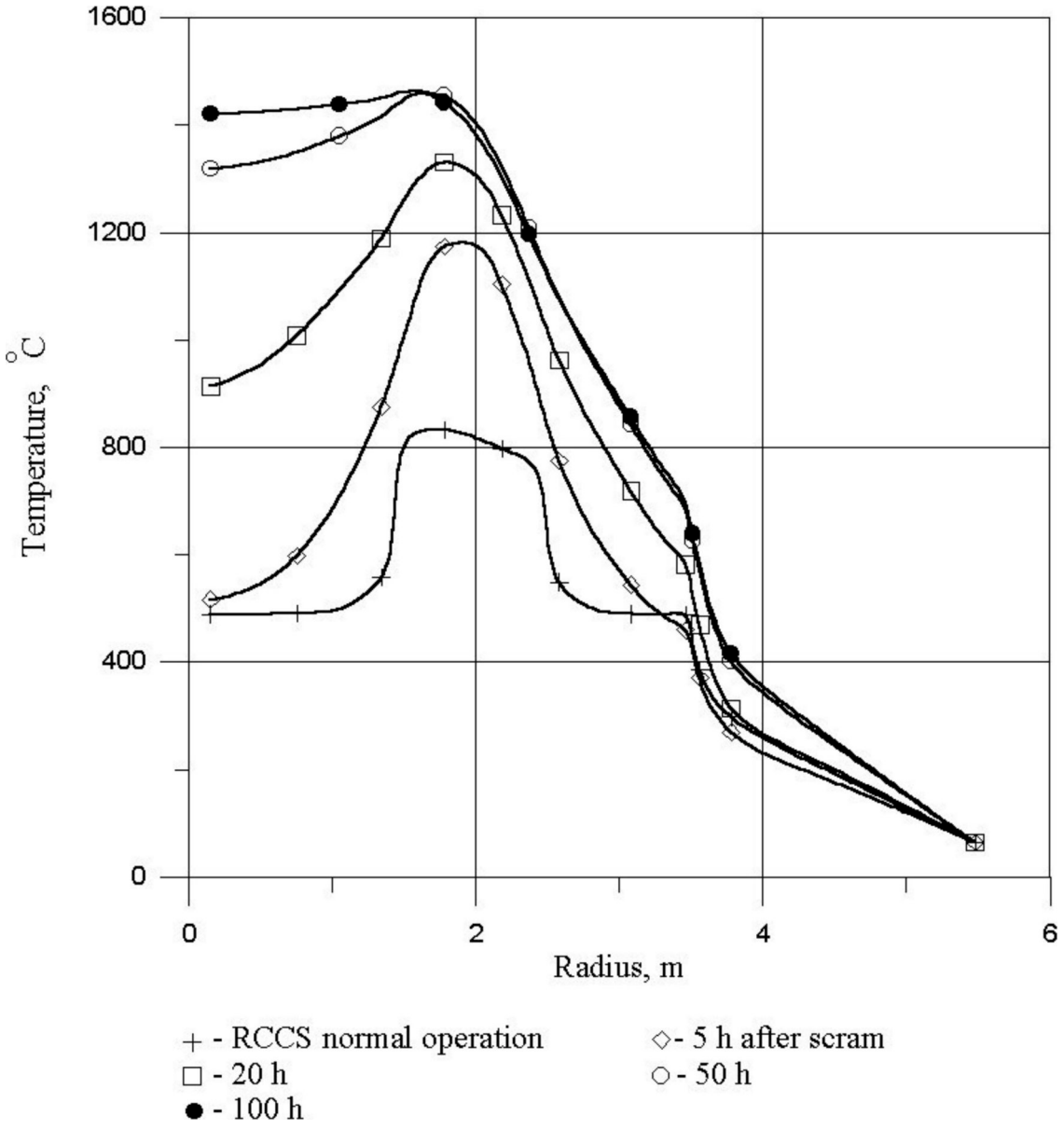

Fig. 3-54 Radial Distributions of Core Fuel and Reflector Graphite Temperatures in Core Mid-Plane for Depressurized Conditions

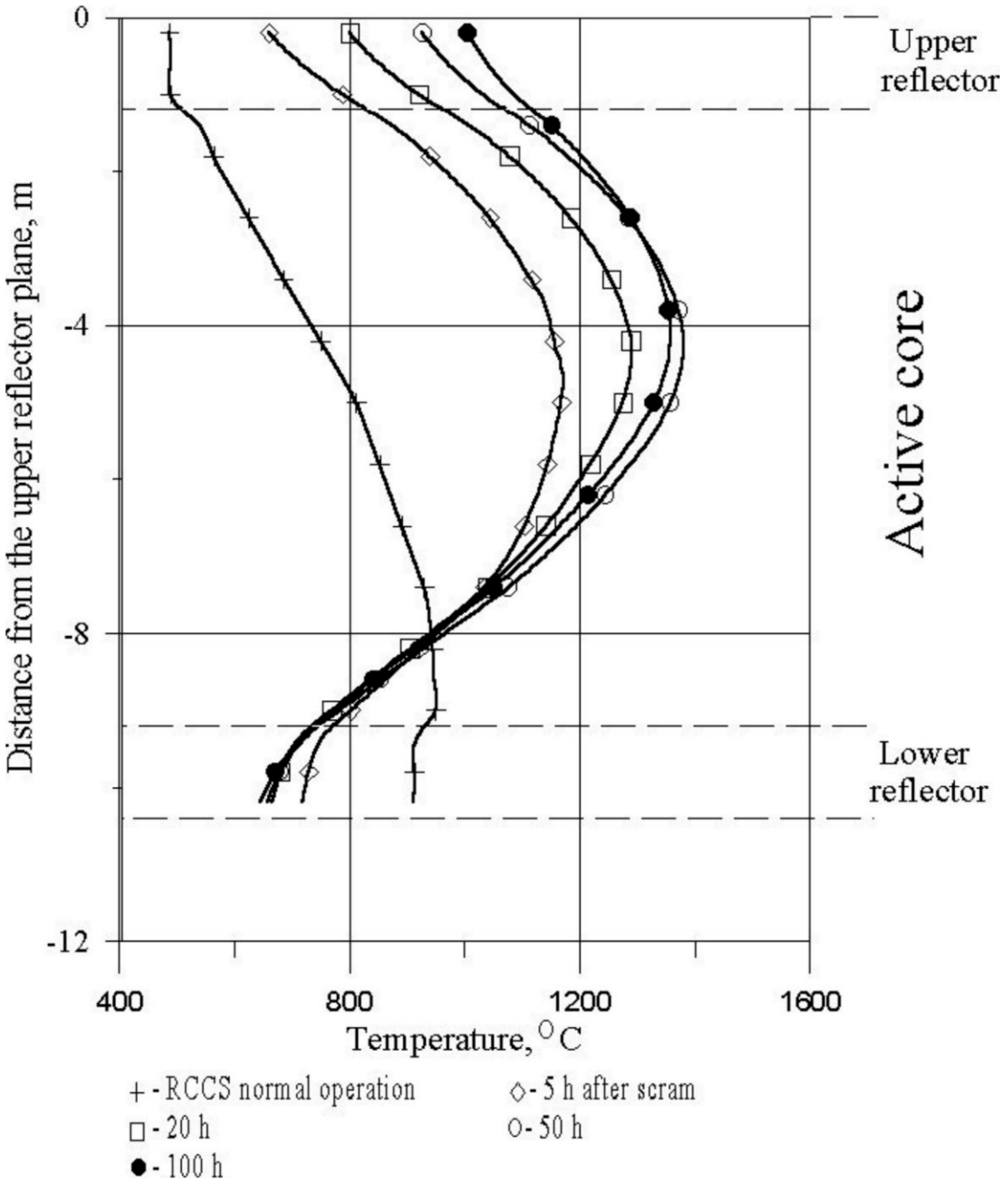

Fig. 3-55 Axial Distribution of Core Fuel and reflector Graphite on Radius of 1.72m for pressurized Conditions

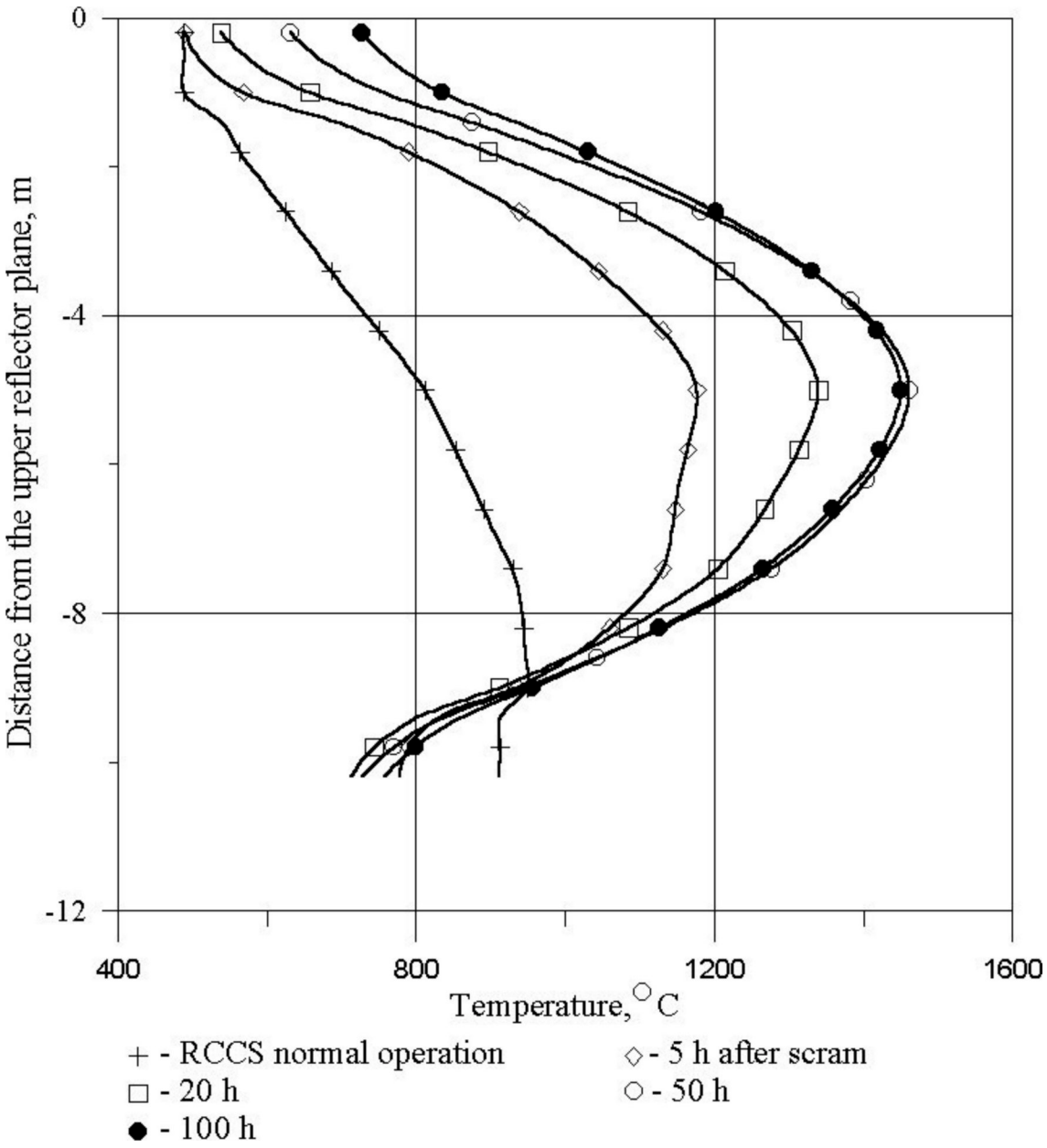

Fig. 3-56 Axial Distributions of Core Fuel and Reflector Graphite on Radius of 1,72m for Depressurized Conditions

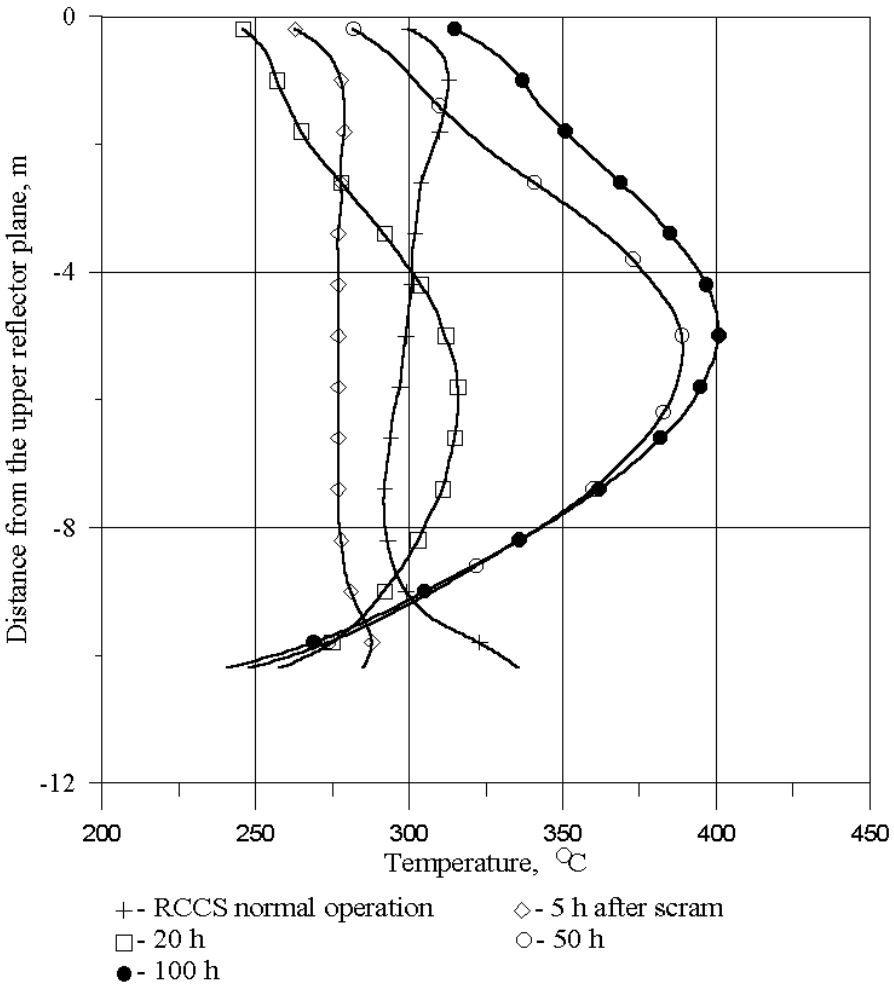

Figure 5. Reactor Vessel Temperature Distributions
along Height for Pressurized Conditions

Fig. 3-57 Reactor Vessel Temperature distributions along Height for Pressurized conditions

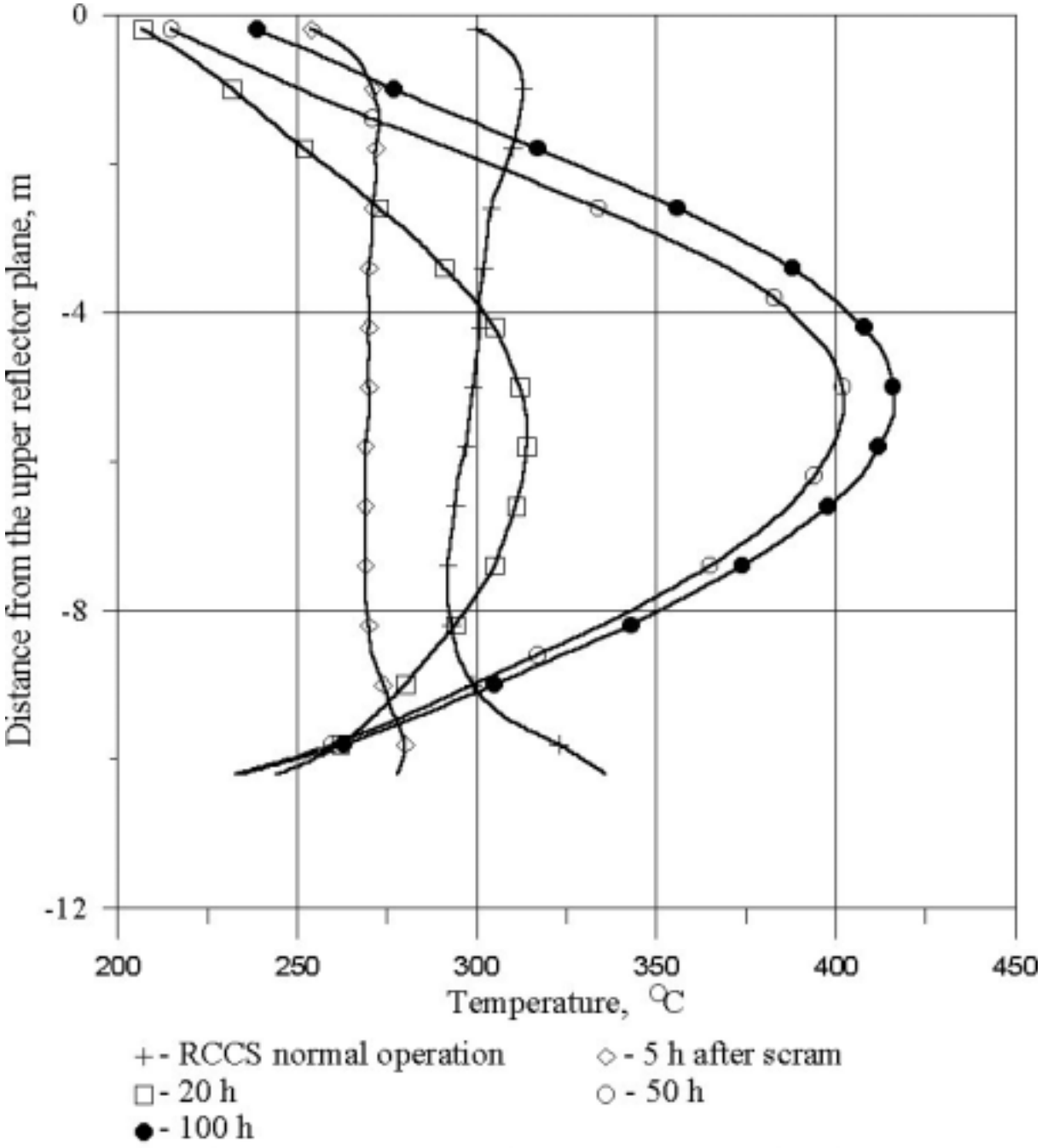

Figure 6. Reactor Vessel Temperature Distributions along Height for Depressurized Conditions

Fig.3-58 Reactor Vessel Temperature Distributions along Height for Depressurized Conditions

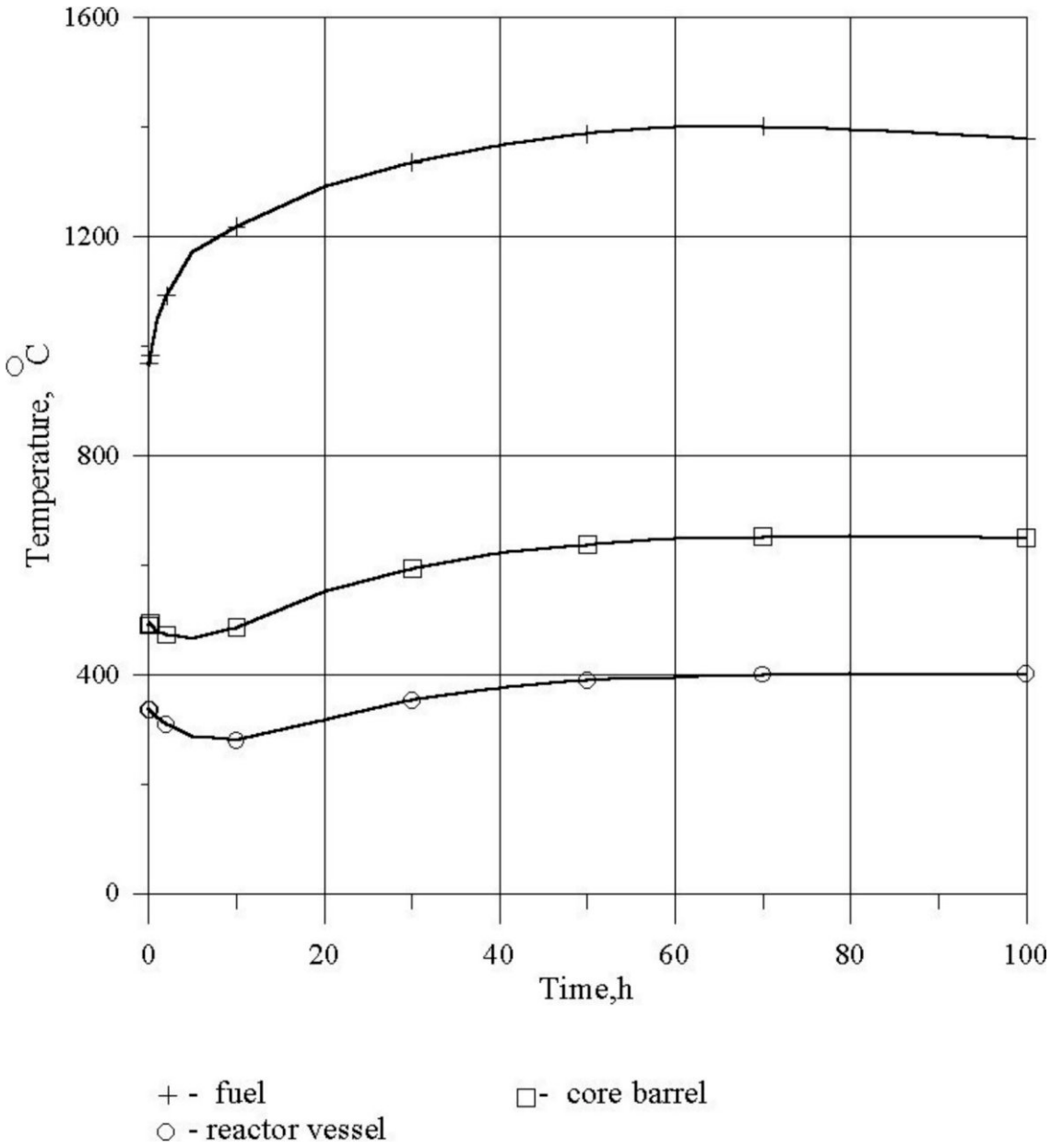

Fig. 3-59 Temperatures vs. Time for Pressurized Conditions

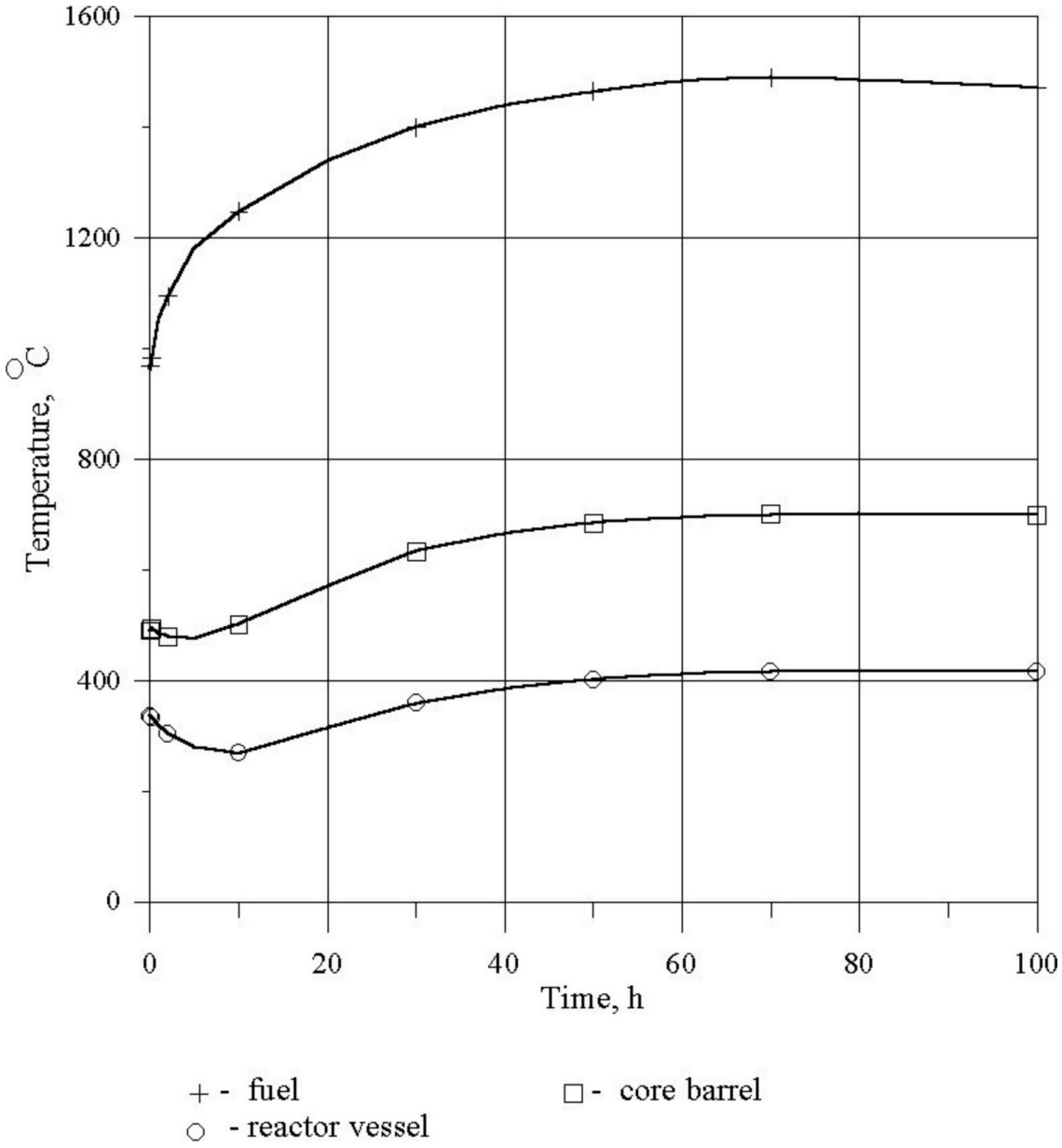

Fig.3-60 Temperatures vs. Time for Depressurized Conditions

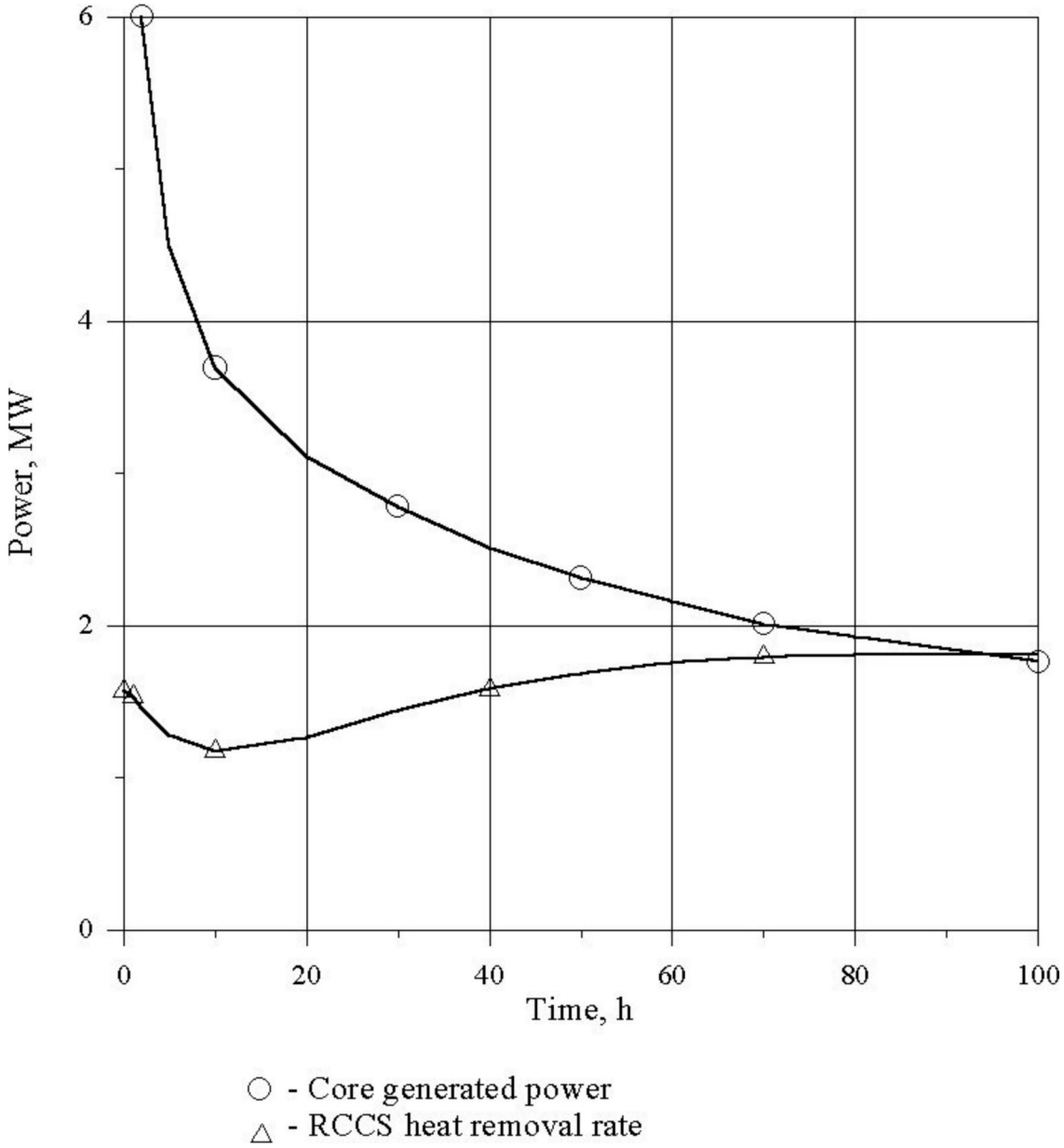

Fig. 3-61 Power vs. Time for Pressurized Conditions

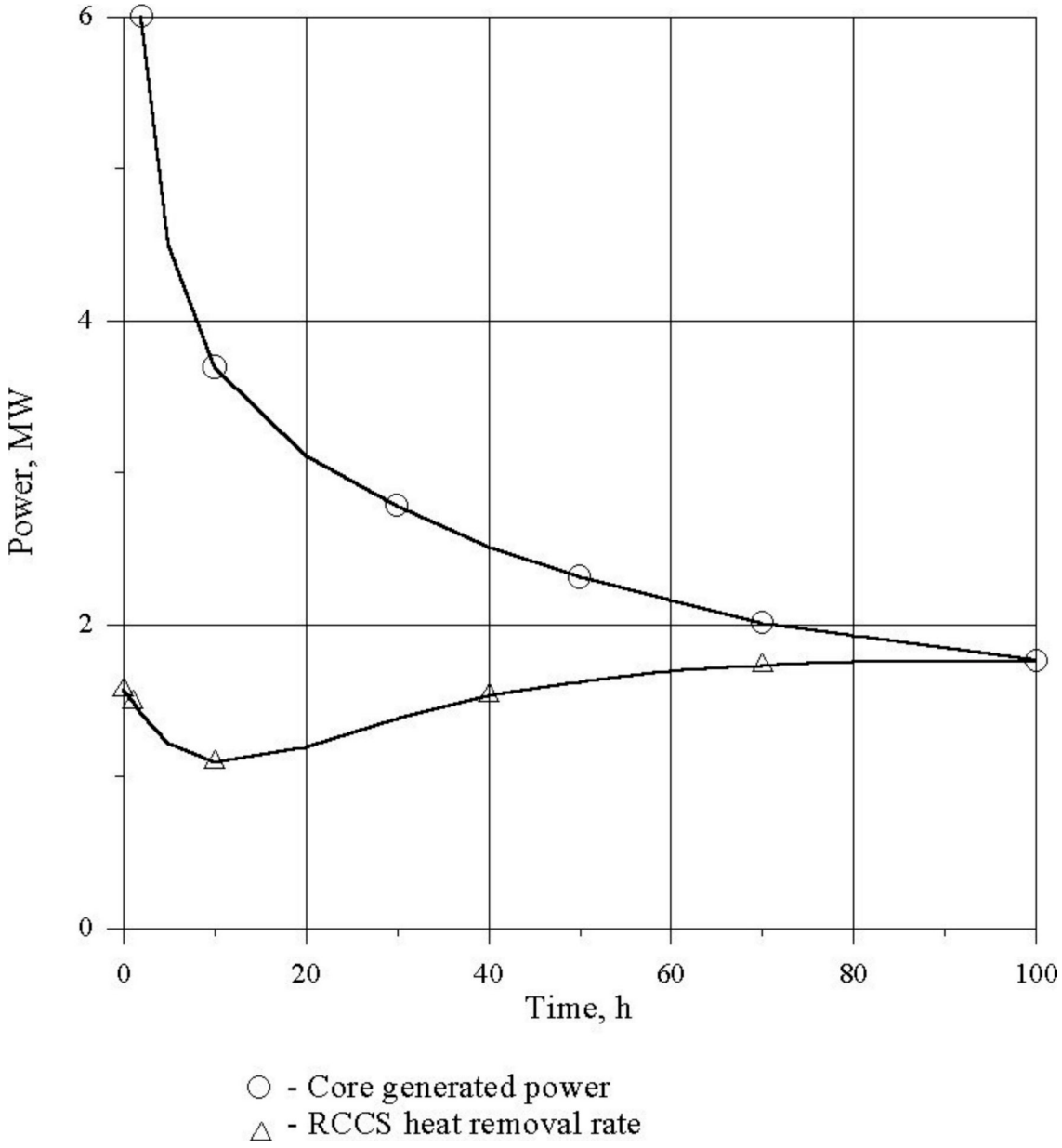

Fig. 3-62 Power vs. Time for Depressurized Conditions

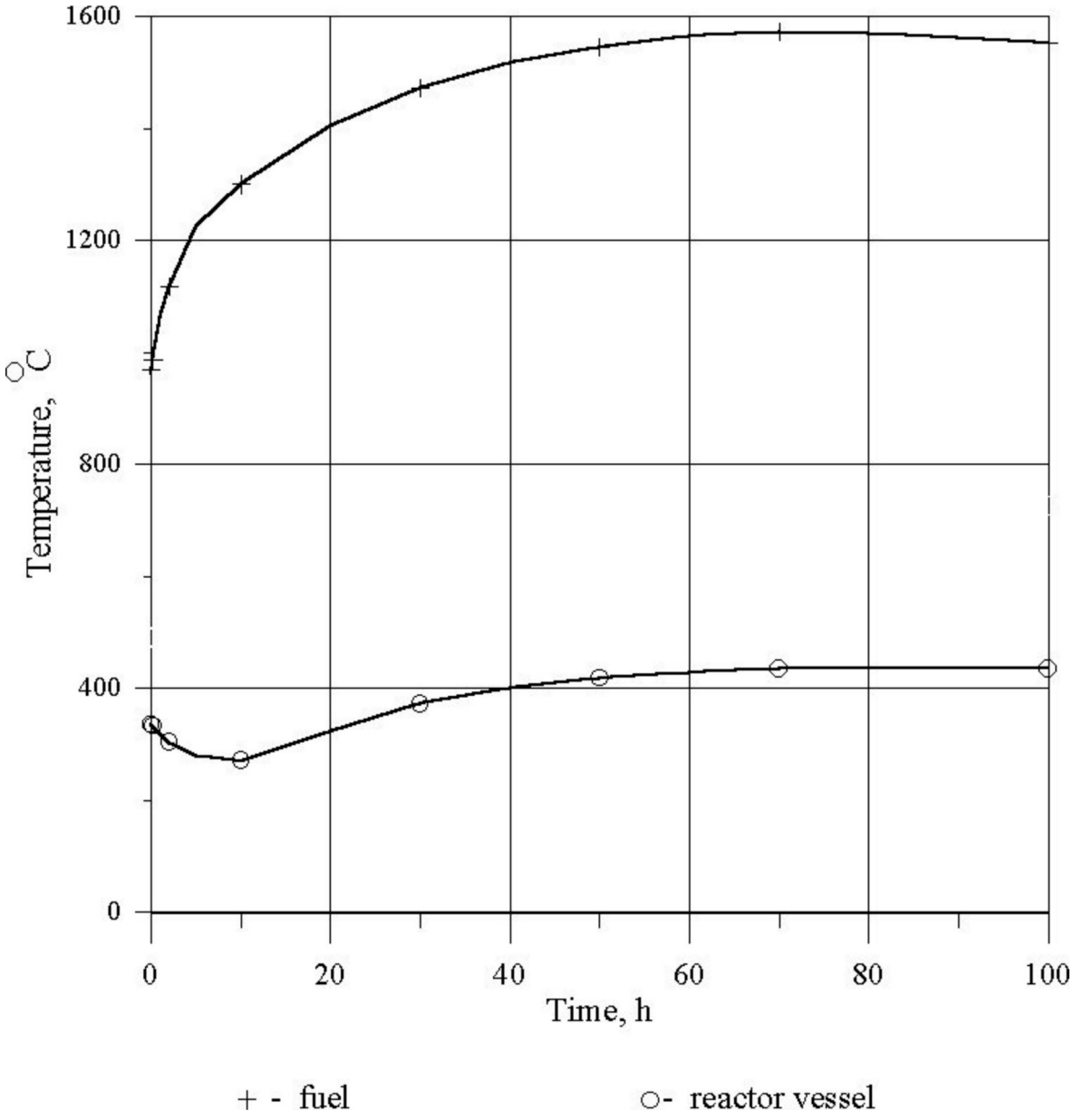

Fig. 3-63 Temperatures vs. Time increase of Decay Power by 10% for Depressurized Conditions

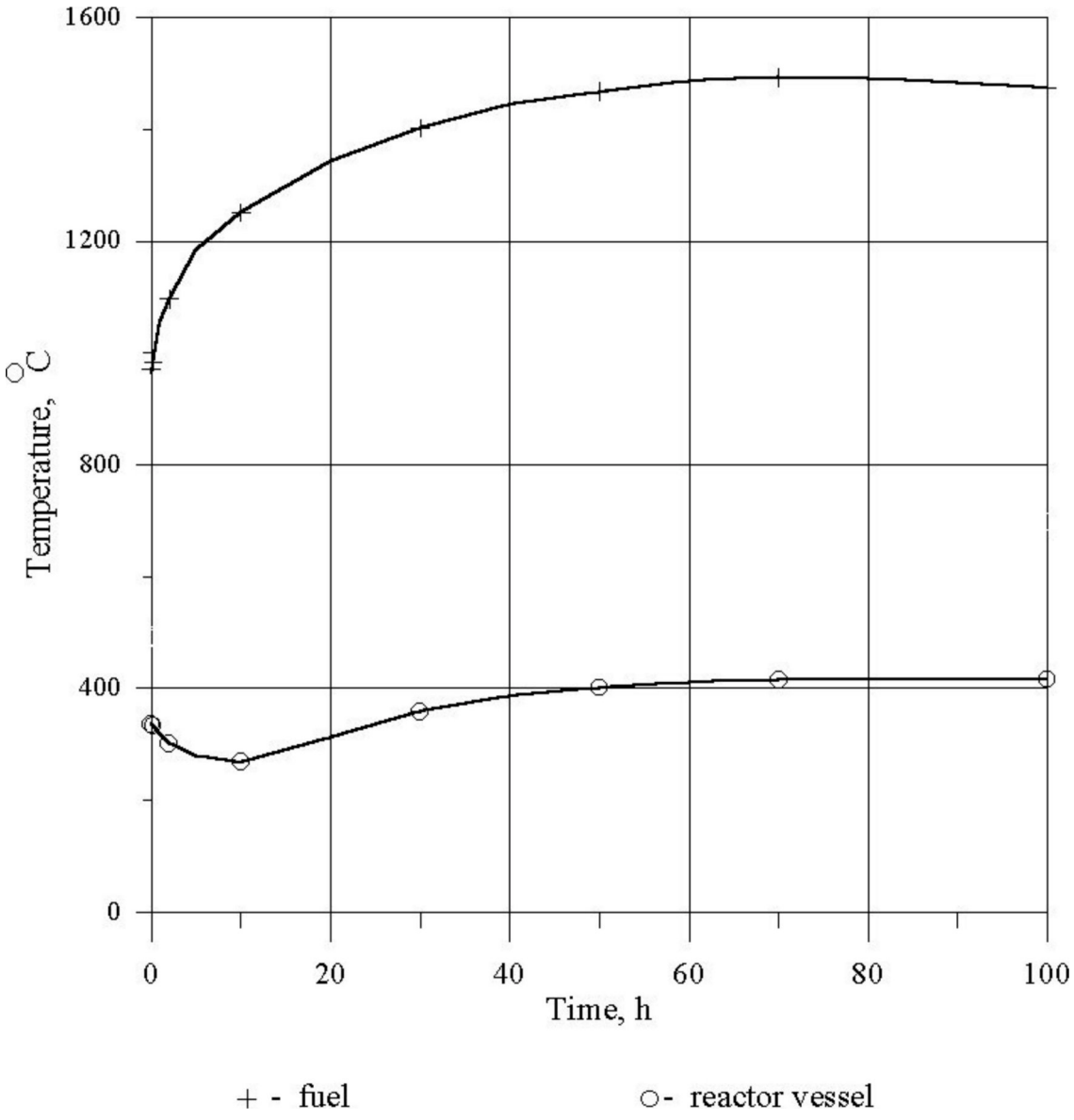

Fig. 3-64 Temperatures vs. Time increase of the average gap to 2.5mm for Depressurized Conditions

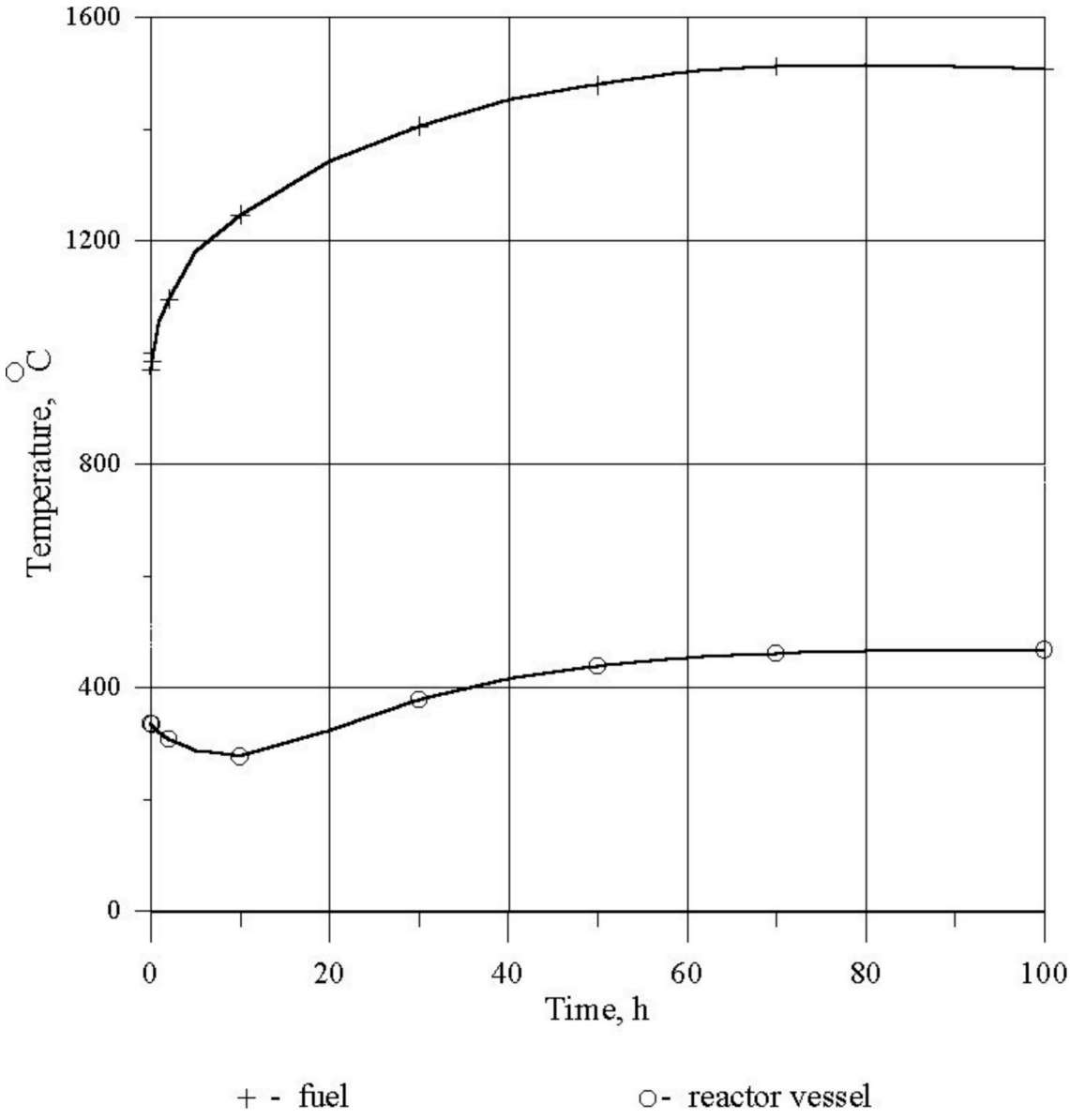

Fig. 3-65 Temperatures vs. Time at 25% of Emissivity for Depressurized Conditions, ε=0.6

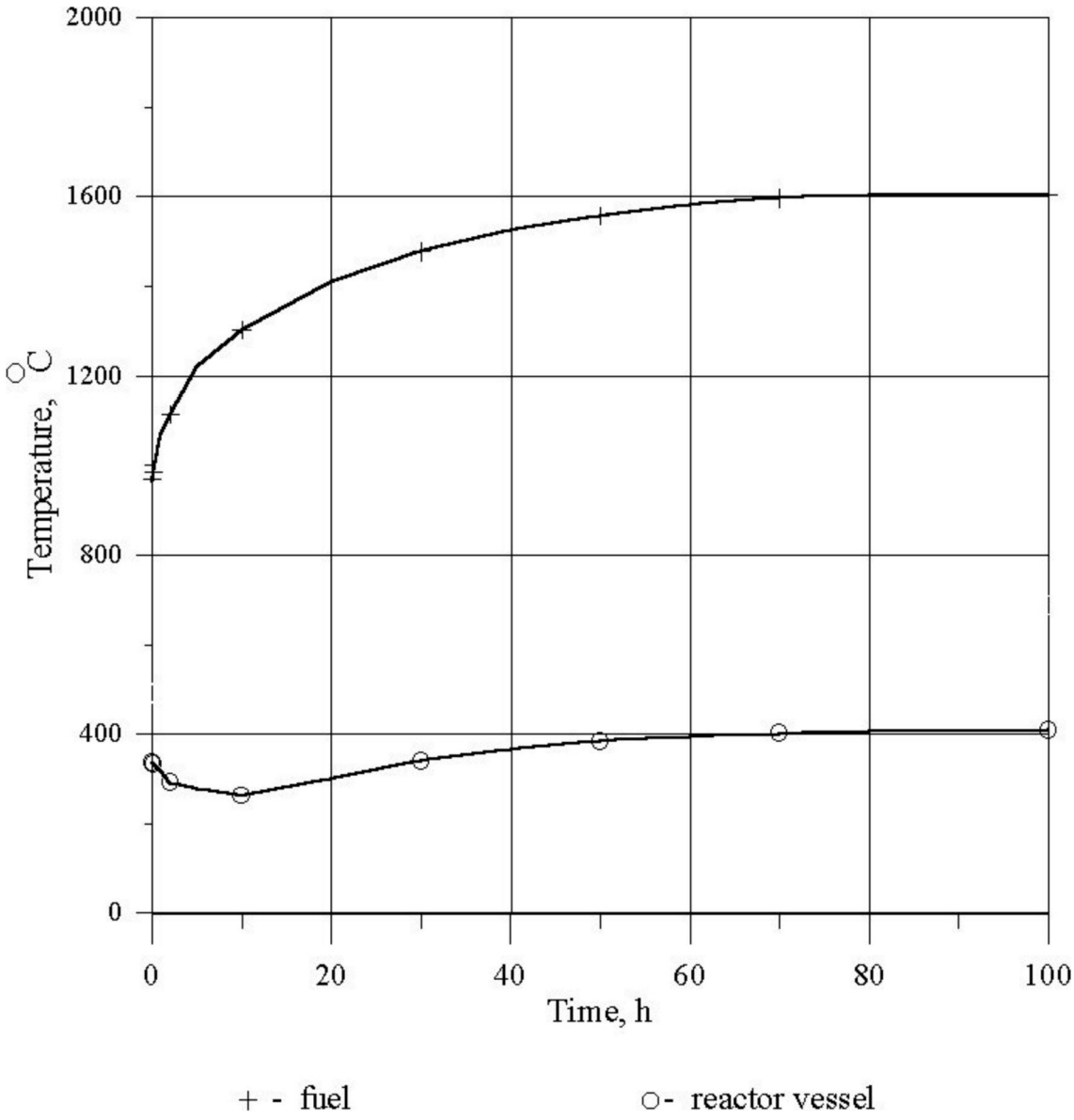

Fig. 3-66 Temperatures vs. Time at 25% Decrease in Graphite Conductivity for Depressurized Conditions

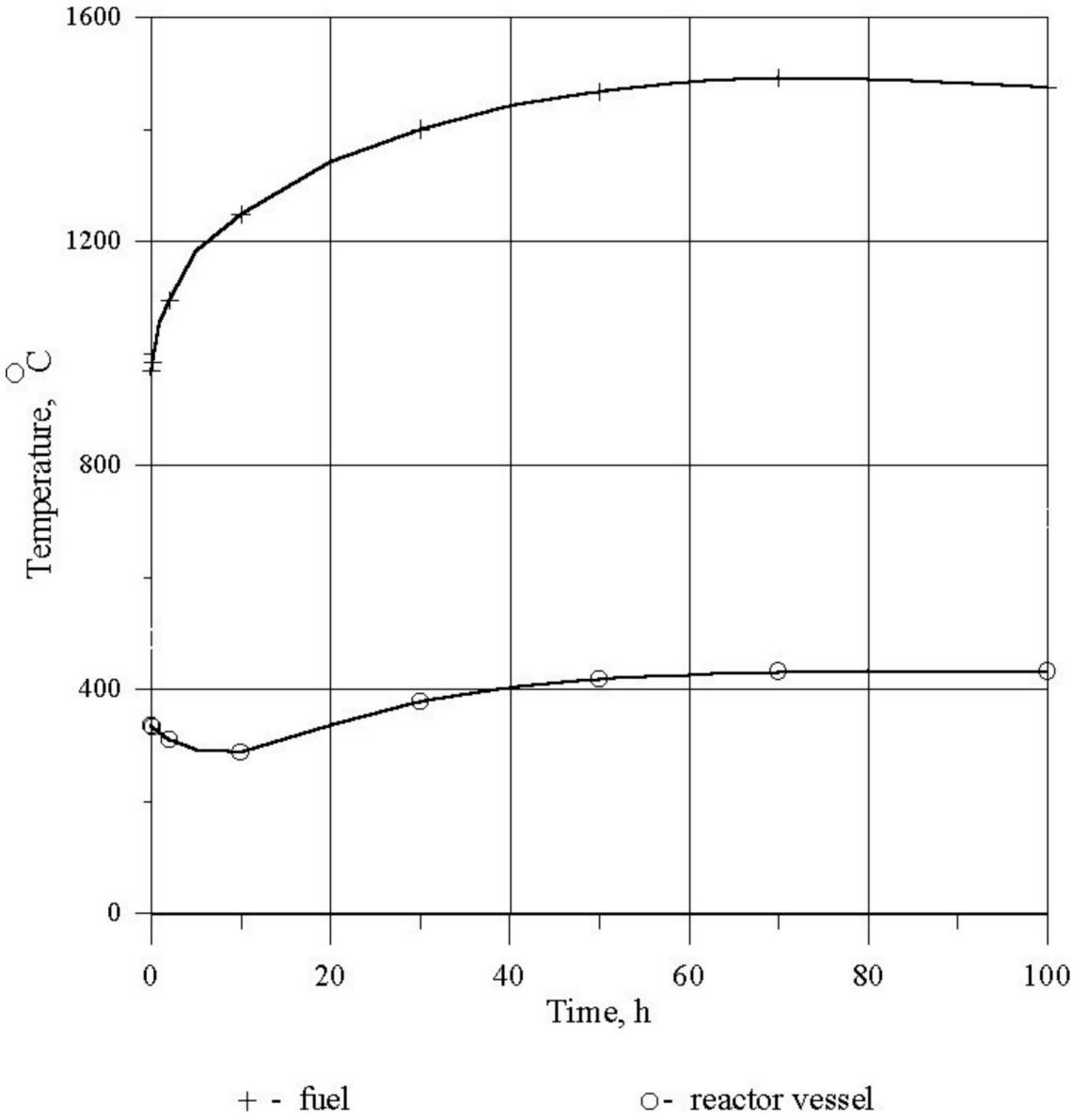

Fig. 3-67 Temperatures vs. Time at Cooling Water Average Temperature of 140°C for Depressurized Conditions

3.4.3. CASTEM model of GT-MHR Plutonium Burner Benchmark

3.4.3.1. Introduction

A model of the 600-MW(t) GT-MHR was developed for the benchmark concerning the loss of forced circulation (LOFC) followed by a scram with depressurization. The code used, CASTEM, allows to develop 3D thermal, structural and fluid mechanical models including 3D radiative heat transfer.

Since both normal operation and transient accidental conditions have to be modelled the 2D axisymetric model includes the following heat transfer features : radiative heat transfer in cavities, conduction in solid structures, thermal-hydraulics of helium in the reactor.

3.4.3.2. Relevant hypothesis and limits of the model

2D in cylindrical coordinates

Heat transfers in the core and the coolant channels are supposed to be approximately 2D axis-symmetric whereas the design of the reactor vessel and the concrete cavity corresponds exactly to this description (Mesh Fig. 3-68).

Helium hydraulics and heat transfer in reactor core and reflectors modelled using a porous media formulation

The semi-heuristic models [1] enable the use of a unique set of equations for solving both the porous medium velocity in the core and the Navier-Stokes solution in channels and cavities of the helium circuit (1). It enables to compute a heat transfer coefficient field in the core, h_{gs}, which couples the local phase volume averaged energy equations [1] of helium (2) and graphite (3).

$$\frac{1}{\varepsilon}\frac{\partial \mathbf{G}}{\partial t}+\frac{1}{\rho\varepsilon}\mathbf{G}.\nabla\mathbf{G}=-\frac{1}{\varepsilon}\nabla p+\upsilon\nabla^2\mathbf{G}-\left[\frac{\upsilon}{K}+\frac{C}{K^{1/2}}\left|\mathbf{V_D}\right|\right]\mathbf{G}+\rho\mathbf{g} \quad (1)^{*}$$

$$\nabla\mathbf{G}=0$$

$$\varepsilon\rho_g C_p^g\frac{\partial T_g}{\partial t}+C_p^g\mathbf{G}.\nabla T=k_g\nabla^2T_g+h_{gs}\frac{A_{gs}}{V}\left(T_s-T_g\right) \quad (2)^{**}$$

$$(1-\varepsilon)\rho_s C_p^s\frac{\partial T_s}{\partial t}=k_s\nabla^2T_s+h_{gs}\frac{A_{gs}}{V}\left(T_g-T_s\right)+\frac{P}{V} \quad (3)^{***}$$

Constant RCCS temperature distribution

The Reactor Cavity Cooling System (RCCS) temperature distribution is considered constant as suggested in the latter description of the benchmark [2]. As a matter of fact, the radiative heat transfer would be dominant between the reactor vessel and the RCCS making the approximation relevant as the temperature influence of the latter is a second rate term.

---

* G is the mass density velocity, ε the porosity, ρ the mass density, p the pore pressure, ν the helium viscosity, K the permeability, C an inertial coefficient and g the gravitational acceleration.

** C^g_p is the helium heat capacity, T_g the helium temperature, k_g the effective helium conductivity, h_{gs} the heat transfer coefficient, A_{gs} the heat exchange surface area between helium and graphite, V the local volume, T_s the local graphite temperature.

*** C^s_p is the graphite heat capacity, k_s the effective graphite conductivity, P the local heat power source.

3.4.3.3. Model main lines

Algorithm

Thermal-hydraulics of the helium and the energy transport equation for the core, the core barrel and lower thermal shield, are treated by an implicit scheme and are simultaneously solved in order to get a stable solution for the fluid-structure heat transfer. The boundary limits are of Neuman type and includes fluid-structures heat exchanges, radiation heat transfer of core-to-upper thermal shield and core barrel-to-lateral thermal shield (i.e. vertical helium channels).

The heat transfer by radiation and conduction in the other solid structures as well as in the air cavity are solved in implicit and coupled to the helium/core system described above by using Fourier type boundary conditions: temperatures are prescribed on the limits of the helium and core fields.

Main correlations used in Equations (1), (2) and (3)

Regular flow friction coefficients and Nusselt number correlations are used for estimating the permeability and the heat transfer coefficient through the reactor core:

- Heat transfer coefficient :

$$Nu_{Dh} = 0.023\,Re_{Dh}^{0.8}\,Pr^{0.33} \quad \text{for Re>10000}$$
$$Nu_{Dh} = 8.24 \quad \text{for laminar flow}$$

- In depressurized conditions the helium mass flow through the core is supposed to be weak enough so that it is in local thermal equilibrium with the graphite.

- Friction coefficients in channels :

$$\lambda_{Dh} = 0.316\,Re_{Dh}^{-0.25} \quad \text{for Re>10000}$$
$$\lambda_{Dh} = 64/Re_{Dh} \quad \text{for laminar flow}$$

Other heat transfer coefficients as well as graphite and other solid materials properties are determined using the listed data from the Coordinated Research Program (CRP-3) letter description [3], later completed by additional informations [2].

3.4.3.4. Results

List of figures:

1. Mesh of the complete reactor and the concrete walls.
2. Vertical temperature distribution at mid radius of the core at nominal operation, after 5 hours, 20 hours and 100 hours (Depressurized conditions).
3. Radial temperature distribution at mid height of the core at nominal operation, after 5 hours, 20 hours and 100 hours (Depressurized conditions).
4. Vertical temperature distribution of the reactor vessel at nominal operation, after 5 hours, 20 hours and 100 hours (Depressurized conditions).
5. Time distributions of the maximum temperatures of the active core, the core barrel and the reactor vessel (Depressurized conditions).

In nominal conditions, the helium flows mainly through the coolant holes in the hexagonal graphite blocs from the upper reflector, through the active core down to the lower reflector before it reaches a collector under the core and the outlet duct conducting the forced flow to the power conversion system. It also flows in parallel through the gaps between all hexagonal blocs as well as between the side and the inner reflectors blocs. The low porosity of the gaps reduces considerably the helium flow, consequently reducing the influence of the convection heat transfer in the inner and lateral reflectors. Hence, in Fig. 3-70 the radial temperature distribution at nominal time clearly shows a step increase across the active core in comparison with the

curves after SCRAM (5, 20 and 100hrs): the leap is due to the heat source but the step indicates that convective heat transfer in the helium dominates at nominal regime compared to the conduction and radiation in the graphite.

While the nominal profile of the vertical distributions in Fig. 3-69 is roughly a linear progression from the top of the active core to its base, the transient profiles tend to be symmetrical in relation to the mid height plan of the core which characterizes our hypothesis of a conductive regime during depressurized LOFC accident.

The local phase volume averaging method used in this porous media approximation [1] or any other method which does not discretize the heat power source in the fuel holes, does not compute the real solid and fluid temperatures which could be significantly different as the heat sources are singularities in the mesh of the graphite. Whereas these methods are relevant for estimating maximum temperature in the non active graphite mesh in between the fuel rods, a post-processing would be required in order to assess a maximum fuel temperature under nominal conditions (in the compact elements of TRISO fuel particles).

3.4.3.5. Comments

Under pressurized LOFC accidents natural convection may change the symmetrical temperature distribution Fig. 3-69. It may also create three dimensional effects in the core: since the core porosity is very low in the inner and side reflectors, the flow can only be substantial if it is vertical through the active core, lower and upper reflectors. Then, a natural convection loop would consist in alternated upon the circumference, ascending and descending flows through the core; its representation being exclusively three-dimensional. Consequently, our model would not be able to catch the features of the convection if it were taking place in the core. Furthermore, a three-dimensional model using a finite element method would be time consuming. A different approach would be adapted:

– 3D system code
– 3D porous media code (enabled in CASTEM with Mixed Hybrids Finite Elements)

REFERENCES TO SECTION 3.4.3.

[1] M.Kaviany, Principles of Heat Transfer in Porous Media, Mechanical Engineers Series, 2nd Ed., Springer, p.397.

[2] Letter from Kuzavkov, 27-11-97, supplementary informations on the benchmark.

[3] Letter from Syd Ball, 11-02-97, description of Pu-burner benchmark.

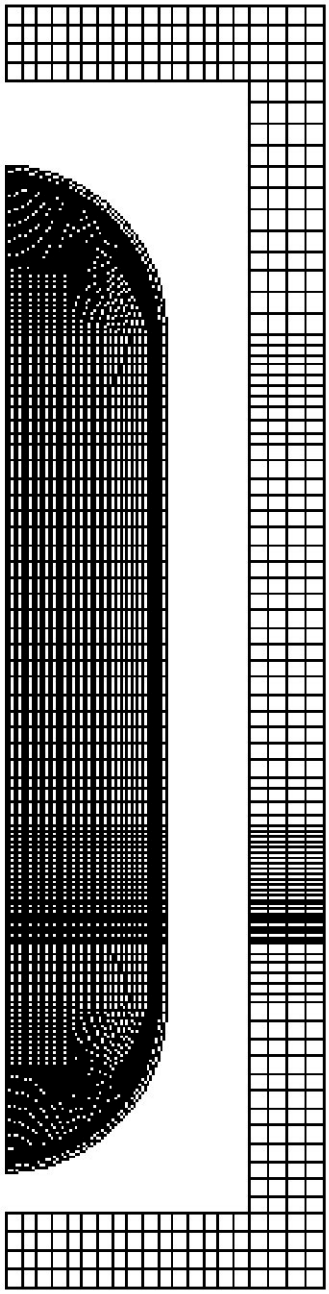

Fig. 3-68 Reactor and concrete mesh

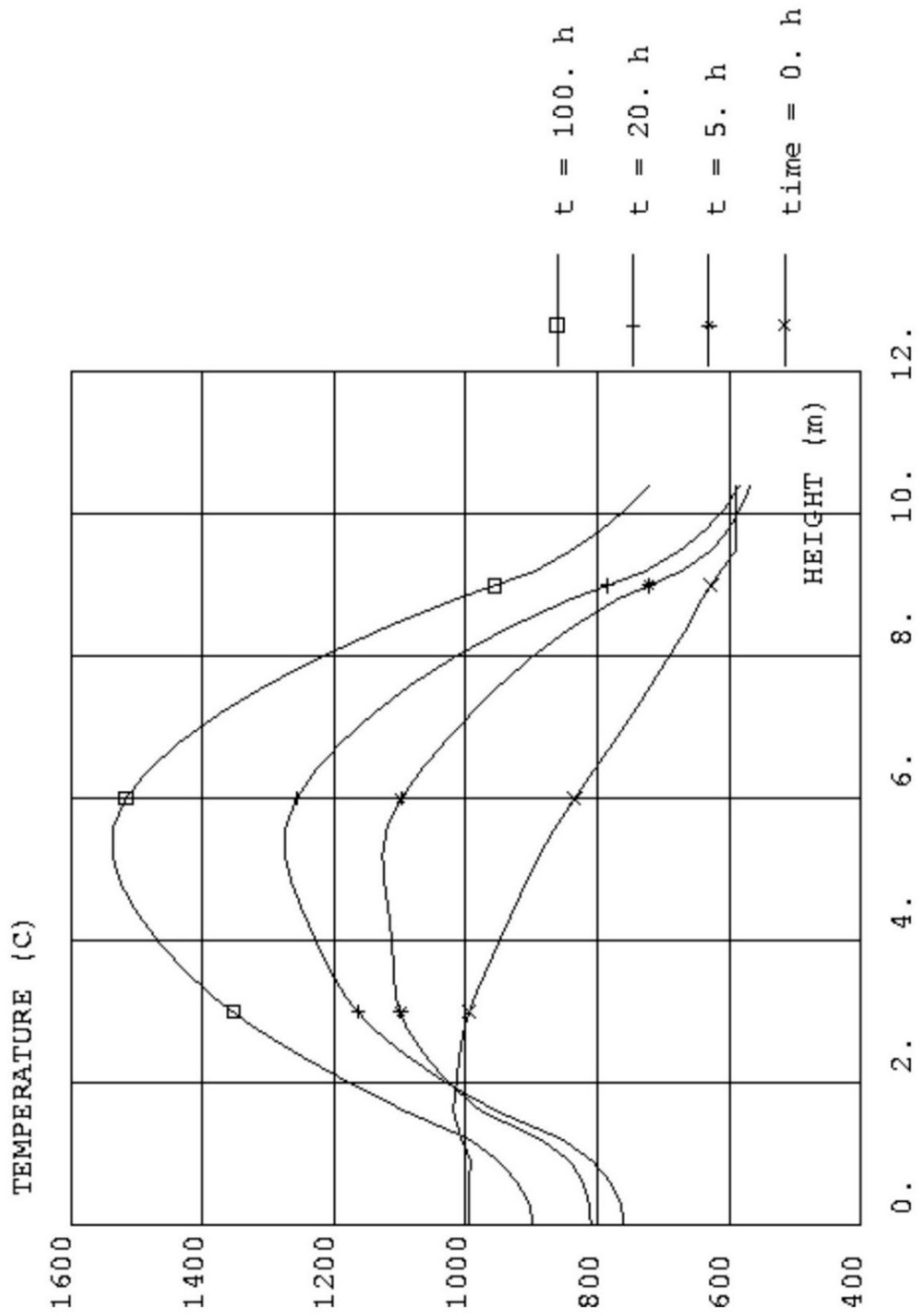

Fig. 3-69 Depressurized conditions – Vertical distributions at mid radius of the core

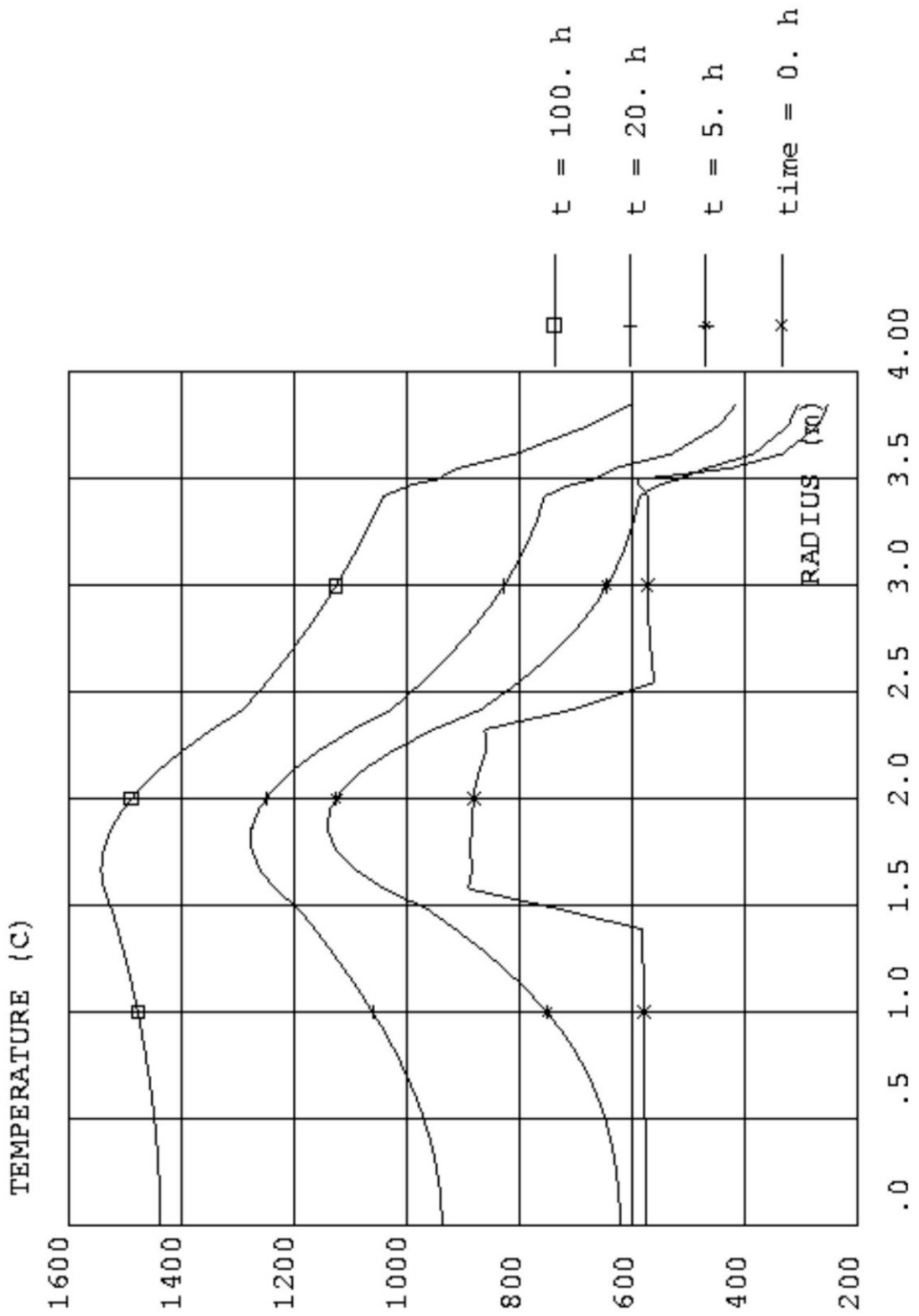

Fig. 3-70 Depressurized conditions – Radial distributions at mid height of the core

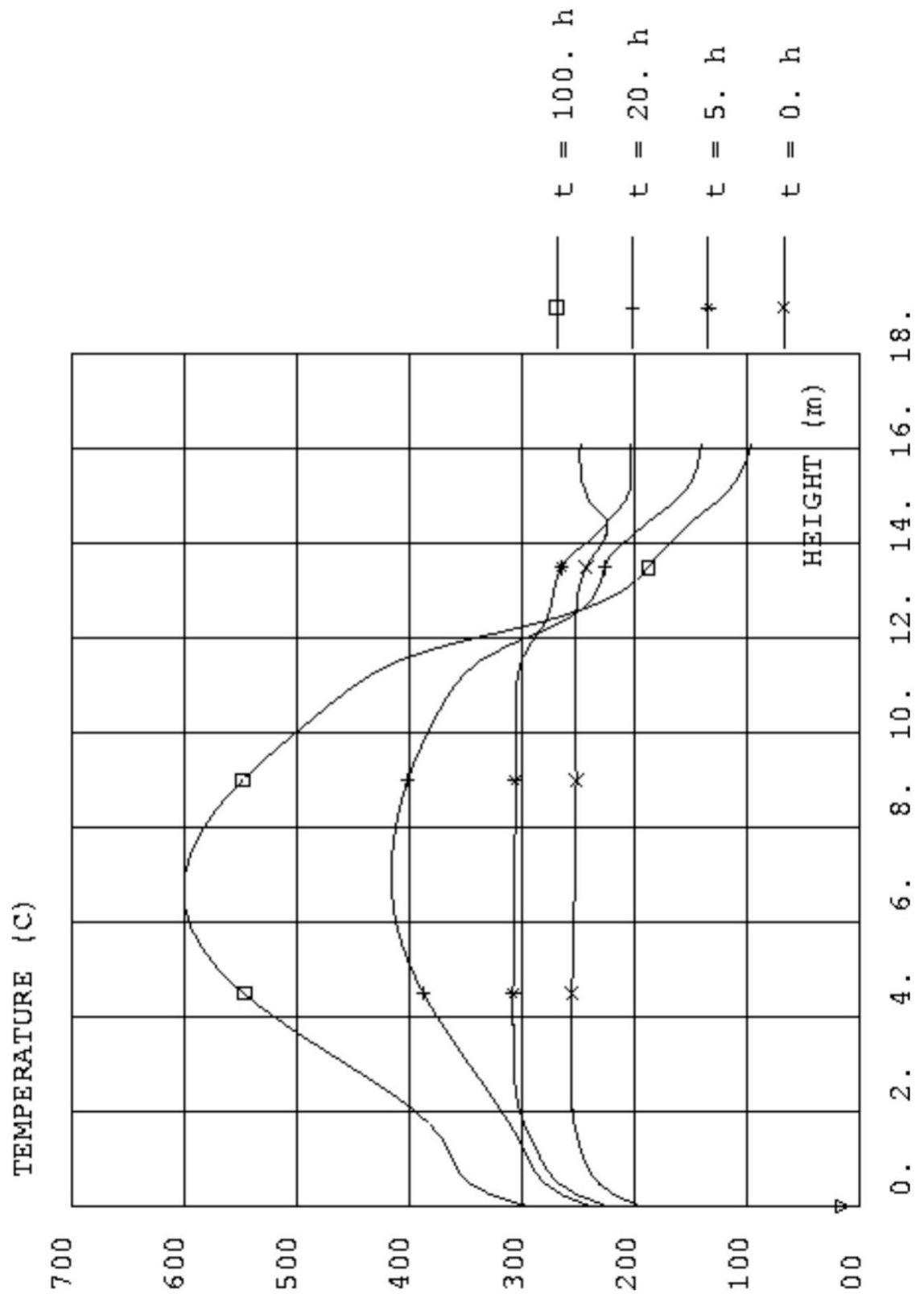

Fig. 3-71 Depressurized conditions – Vertical distributions of the reactor vessel

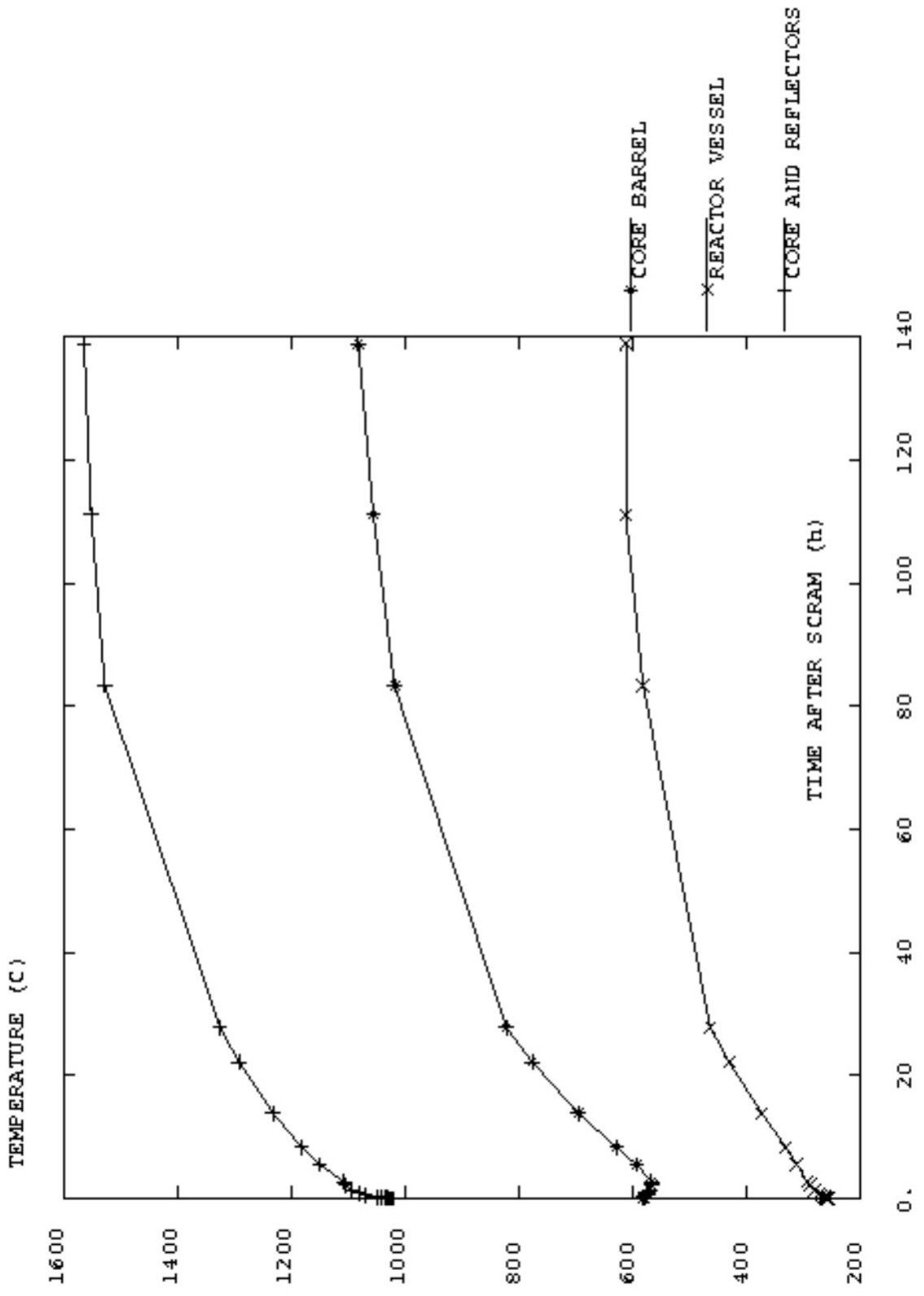

Fig. 3-72 Depressurized conditions – Time distributions of maximum temperatures

3.4.4. Results of the GT-MHR Benchmark with the CFX Code

3.4.4.1. Introduction

The IAEA Co-ordinated Research Programme (CRP) on 'Heat Transport and Afterheat Removal for Gas Cooled Reactors under Accident Conditions' has organised benchmark analyses to support verification and validation of analytical tools used by the participants to predict the thermal behaviour of advanced gas cooled reactors during accidents. One of these benchmark analyses concerns the code-to-code analysis of the Gas Turbine Modular Helium Reactor (GT-MHR) plutonium burner accidents.

This section describes the heat transport inside the reactor core to the Reactor Cavity Cooling System (RCCS). For this purpose, the heat transfer mechanisms as well as the flow patterns inside the core, the reactor pressure vessel, and the cavity have been calculated by the Computational Fluid Dynamics (CFD) code CFX-F3D. The behaviour of the RCCS itself is not described. One calculation considers the full power operation, while two calculations consider Loss of Forced Convection (LOFC) accidents, one at pressurized conditions and the other at depressurized conditions.

CFX-F3D flow modelling software ([1], see also section 4.2.4) performs Computational Fluid Dynamics (CFD) calculations. This code has been developed by AEA Technology and solves (partial differential) conservation equations for mass, momentum (Navier-Stokes equations) and energy together with their boundary conditions. For this purpose, the software uses the finite volume method to discretise these equations. The radiative heat transfer is taken into account. CFX-F3D has been run on a Silicon Graphics Power Challenge workstation.

3.4.4.2. Model Description

The input for CFX-F3D is described in this section. The input for the three calculations (normal operation and the two LOFC calculations) is almost identical. The (small) differences will be specified in this section. The dimensions of the reactor and other data used in the model are given in [2,3,4 and 5]. In the following description, 'benchmark' refers to this data, while 'model' refers to the implementation in the CFX-F3D model. More modelling details can be obtained from [6].

The model is based on a two-dimensional, axi-symmetric (cylindrical) geometry. The grid used for the current problem consists of 29000 cells. In the current problem, the cells contain either gas (air, helium) or solids (graphite, steel). An additional mesh is needed for the radiation calculation. The number of radiation cells used for the current problem is 183 cells.

The following additional models are used:

– The turbulence model selected in this calculation is the well-known k–ε model, because it is widely tested and successfully applied.

– The radiative heat exchange between surfaces is calculated with the Monte Carlo method. This method simulates the physical interactions between photons and their environment. Essentially a photon is selected from a photon source and tracked through the system.

The normal operation (full power) conditions are simulated with a steady state calculation. The LOFC calculations are done as transient calculations. The results of the normal operation was the starting point (initial conditions) for the LOFC calculations.

Core modelling

The benchmark core contains a large amount of cylindrical cooling channels. These cooling channels are not individually modelled. Instead, the helium flows through four large channels through the core and reflectors: one cylindrical channel in the centre of the inner

reflector and three annular channels between the inner reflector and the core, between the core and the outer reflector, and between the side reflector and the core barrel. The total volume of graphite and helium in this model are both identical to the values supplied for the benchmark.

Due to the approximation of the large channels in the model, the heat transfer area between the graphite and the gas phase is much smaller than in the benchmark. The decrease of heat transfer area is compensated by an increase of the heat transfer coefficient in the gas phase. For the normal operation calculation, it is also necessary to modify the thermal conductivity in the graphite.

Since the geometrical differences between the cooling channels in the benchmark and the core are large, the gas phase heat transfer coefficients inside the core cooling channels are calculated using the empirical correlations [7]. The values used in the model compensate for the difference in heat transfer area. In this way, the heat transfer in the model is equal to the heat transfer in the benchmark, for a given temperature difference between graphite and helium.

Normal operation modifications

For the normal operation calculation, additional modifications had to be made. The major heat transport takes place from the graphite to the gas inside the cooling channels. Since the model has only two cooling channels inside the active core, the temperatures in the core would rise to very high values, because of the low area to volume ratio in the model. In order to calculate reasonable temperatures inside the core, the heat production is modelled to be produced in a small region adjacent to the two cooling channels between the active core and the reflectors. This approximation results in the calculation of a flat radial temperature profile inside the core region.

In addition to this modification, the thermal conductivity of graphite is modelled to be anisotropic. In the axial direction the value for graphite is used, while the value in the radial direction compensates the modification mentioned above. In the model, the radial thermal conductivity is set to 710W/mK.

Heat production

For the normal operation calculation, the heat production rate is set at 600MW. For the LOFC calculations, the afterheat production rate given in [2] is used. For the normal operation as well as for the LOFC calculations, it is assumed that the power density does not depend on the radial direction inside the core. The axial power density is a quadratic fit of the density profile given in [2].

Pressure drop inside the core

For the normal operation calculation, flow restrictions inside the cooling channels are included in the model in such a way that the helium distribution over the core and reflector regions equal the values given in [4 and 5].

For the LOFC calculations, restrictions inside the cooling channels are used to model the pressure drop inside the cooling channels and the gaps between the fuel and reflector elements. The pressure drop is based on literature correlations [7].

RCCS modelling

The RCCS tubes, which are in fact three-dimensional, are not modelled in detail. The heat removal by the RCCS tubes at the wall is modelled as a volumetric heat sink. The heat removal rate is based on a total heat transfer coefficient of 4W/m2K and a constant temperature of 313K [4]. The RCCS tubes are divided up proportionally over the volume between the radiation shield and the cavity wall. The interaction between radiation and the RCCS tubes is taken into account as absorption of the radiation in the gas phase. Without modification, the radiative heat transfer from the radiation shield to the cavity wall is too high.

The RCCS on the floor is modelled as a wall. The heat transfer by both radiation and convection from the floor radiation shield to the RCCS tubes is modelled via the heat transfer coefficient, which is estimated to be 10 W/m2K. The temperature of the floor RCCS tubes have a constant temperature of 313K [4].

Cavity structures

The heat transfer through the ceiling and through the wall consists of heat conduction through the concrete structure and heat transfer to the adjacent rooms with a temperature of 303K [4]. The heat transfer coefficients are derived from data in [4]: U = 1.13W/m2K for the ceiling and U = 1.46W/m2K for the wall.

Physical properties

The physical properties of the various solid materials are assumed constant, and are summarised in Table 1. The values are based on the data found in [2and 4]. The emissivity of most materials is assumed to be 0.8 [3]. The emissivity for graphite is set to 0.9 [4]. It is assumed that the gas phase does not interact with radiation.

Table 3-48 Physical properties of solid materials

material	density (kg/m^3)	specific heat (J/kg·K)	thermal conductivity (W/m·K)
steel of reactor vessel	7800	520	33
other steel structures	7800	570	24
insulation	1700	800	2.0
radiation shield	7800	500	16
graphite in core	1700	1840	24 *
graphite in reflector	1700	1840	30

* see also text

3.4.4.3. Results: Normal Operation

The calculated results are shown in Table 3-49 to Table 3-52 as well as in Fig. 3-73 to Fig. 3-85. The results of the normal operation calculation are included in Figures of the LOFC results as the situation at time equal to 0hr, since the normal operation calculation is the initial condition for the LOFC calculations. Note that Fig. 3-77 to Fig. 3-80 only show temperatures in the graphite. Metal structure temperatures are not shown in these Figures. The maximum and average temperatures are determined on several locations for 0, 20, 50 and 100hrs after the start of the accident. The results are summarised in Tables 3-49 and 3-50.

Heat balance

The total power production in the core (600MW) is mainly removed by the helium flow. The helium is heated from 763K (490°C) at the inlet to 1123 K (850°C) at the outlet of the core. A small fraction of the power production (2.64 MW) is lost to the environment (cavity structures and RCCS). Most of this heat loss (94%) is transferred by radiation, and the remaining 6% are transferred by convection. More details can be found in Table 3-51. The heat balance in the cavity is given in Table V. The larger part of the heat is removed by the RCCS. This heat flow is 2.36MW to the RCCS tubes and 0.16MW to the RCCS on the cavity floor, which corresponds to 95% of the heat loss from the reactor vessel. The remaining part (0.12MW, or 5%) is transferred to the cavity wall and ceiling structures.

Core temperatures

The axial and radial temperature profiles in the core are given in Figs 3-77 and 3-79 (thick lines, 0hr). The dips (0, 1.5, 2.4, and 3.4m) in the radial profile are caused by the cooling channels. The temperature field is shown in Fig. 3-83. The highest temperature in the core is 1222 K (949°C), and the average temperature is 1075 K (802°C). The maximum temperature is

located at a position of 2.2m above the bottom of the lower reflector or 1.0m above the bottom of the active core.

Reactor vessel temperatures

The axial temperature profile in the reactor vessel wall is shown in Fig. 3-81 (thick line 0 hr). Due to the helium flow from the inlet through the annulus between the core barrel and the shell, the reactor vessel temperature is constant over a large part of the reactor vessel. High temperatures of about 679K (406C) extends from 4.0 m to 21.5m above the bottom of the reactor vessel, this is at the level of the support plate, the insulation, the lower (hot) plenum, the core, and the upper (cold) plenum.

Cavity temperatures and velocities

The temperature field inside the cavity is shown in Fig. 3-84. The reactor pressure vessel is excluded from this figure. The gas is almost stratified: the temperatures increase from the bottom to the ceiling. Fig. 3-85 shows the velocity field inside the cavity. The maximum gas velocity is 1.3m/s. The gas between the reactor upper head and the cavity ceiling moves with relatively high speeds, caused by the hot reactor upper head. The gas below the reactor vessel is almost stagnant.

Cavity wall temperatures

The average cavity wall concrete temperature is 375K (102°C). The temperature varies between 355K and 380K. The cavity ceiling (without RCCS covering) is quite hot: the highest temperature is 572 K (299°C).

3.4.4.4. Results: Depressurised LOFC accident

The accident considered in this section is a Loss of Forced Convection (LOFC) accompanied by a rapid depressurization and scram. In a depressurized LOFC, the heat transfer capacity of helium by natural convection is very limited. The heat removed by helium is in the order of magnitude of 10 to 100 kW. This is small compared to the decay heat. The heat removal from the core takes place by conduction through the side reflector to the core barrel. The heat is transported to the RCCS and cavity structures through a combination of conduction and radiation.

Core temperature

The maximum and average temperatures of the core can be observed in Fig. 3-73. The highest core temperature of 1644K is reached after 42hr, while the maximum average core temperature is 1421K after 50hr. The radial temperature profiles in the core are shown in Fig. 7 for 0, 20, 50 and 100 hr after the start of the accident.

The axial temperature profiles in the core are shown in Fig. 3-77 for 0, 20, 50 and 100 hr after the start of the accident. During the accident, the temperature profile takes a form similar to the power density profile, since the heat is mainly transferred by conduction. The maximum temperature is located near the mid plane of the active core. The bumps in Fig. 3-77 (also in Fig. 3-78) are caused by the radiation model. The radiation inside the cooling channels is calculated in a relative course grid: the region shown in these figures is subdivided into 10 parts, and therefore, 10 bumps can be seen in these figures. The influence of the bumps on the calculational results is small.

Reactor vessel temperatures

The maximum temperature of the reactor vessel is shown in Fig. 3-74. The temperature profiles in the reactor vessel wall are shown in Fig. 3-81 for 0, 20, 50 and 100hr after the start of the accident. After 4hr, a local maximum temperature of 689K is found between 5 and 6 m above the vessel bottom, which is at the level of the hot plenum (below the graphite). After 9hr, the location with the highest temperature moves to a location near the mid plane of the core. The vessel wall reaches the highest temperature of 736K after 85hr.

Cavity wall temperatures

The temperature of the cavity wall roughly follows the heat release from the reactor vessel. This temperature (Fig. 3-75) decreases about 10K during the first 20 hr, and remains almost constant after that time.

Heat removal

The heat removal of the RCCS located near the cavity wall is shown in Fig. 3-76. For comparison, the afterheat power generation is also included. The heat removed by the bottom RCCS and the cavity ceiling are not included in this Figure. A rough estimate of the heat removal is 0.2MW, which is lower than under normal operation conditions, because the vessel temperatures are lower.

The heat removal decreases to 1.8MW after 26hr, and increases again to 1.9MW after 100hr. Although the maximum temperature of the reactor vessel increases considerably, the heat removal by the RCCS decreases, because the reactor vessel temperatures decrease in general, (see also the temperature profiles in Fig. 3-81).

3.4.4.5. Results: Pressurised LOFC accident

The accident considered in this section is a Loss of Forced Convection (LOFC) accompanied by scram, but without a depressurization. In contrast to a depressurized LOFC, described in the previous section, the heat transfer capacity of helium by natural convection flow is a considerable fraction of the decay heat. The heat removal from the core takes place both by conduction through the side reflector to the core barrel and by convection by helium.

Core temperature

The maximum and average temperatures of the core can be observed in Fig. 3-73. The highest core temperature of 1529K is reached after 8hr, while the maximum average core temperature is 1323K after 10hr. The radial temperature profiles in the core are shown in Fig. 8 for 0, 20, 50 and 100 hr after the start of the accident.

The axial temperature profiles in the core are shown in Fig. 3-78 for 0, 20, 50 and 100 hr after the start of the accident. The maximum temperatures move to the upper part of the active core, which is due to the heat transport by natural convection of helium.

Reactor vessel temperatures

The maximum temperature of the reactor vessel is shown in Fig. 3-74. The temperature fluctuations and the peak in Fig. 3-74 are caused by the large time steps and the relative small number of photons that are used in the Monte Carlo radiation calculation. These fluctuations and peaks average out during the calculation. During the first 10hr of the accident, the reactor vessel wall cools down, because the wall is not heated by the inlet helium flow. Between 50 and 100hr, the highest temperature of the reactor vessel wall is about 680K.

The temperature profiles in the reactor vessel wall are shown in Fig. 3-82 for 0, 20, 50 and 100hr after the start of the accident. The highest temperatures are found near the top of the vessel, due to the high heat transport by the natural convection of helium.

Cavity wall temperatures

The temperature of the cavity wall (Fig. 3-75) decreases about 5K during the first 20 hr, and remains almost constant after that time.

Heat removal

The heat removal of the RCCS located near the cavity wall is shown in Fig. 3-76. The heat removal decreases to 2.1MW after 15hr and remains almost constant after that time.

Table 3-49 Maximum temperatures (K) on selected locations.

Location	normal operation	depressurized LOFC			pressurized LOFC		
	0 hr	20 hr	50 hr	100 hr	20 hr	50 hr	100 hr
Core	1222	1633	1643	1607	1495	1397	1294
core barrel	902	910	945	943	834	837	798
Shell	758	820	853	855	750	785	780
reactor vessel wall	679	699	730	734	671	685	682
reactor vessel upper head	666	541	514	515	616	630	612
reactor vessel lower head	590	514	474	458	564	542	533
wall radiation shield	521	516	531	533	510	516	512
floor radiation shield	481	424	405	406	470	446	438
cavity ceiling	572	502	488	487	566	571	564

Table 3-50 Average temperatures (K) on selected locations.

Location	normal operation	depressurized LOFC			pressurised LOFC		
	0 hr	20 hr	50 hr	100 hr	20 hr	50 hr	100 hr
core	1075	1404	1421	1398	1300	1224	1146
cavity wall	375	366	367	368	371	371	370

Table 3-51 Heat losses from the reactor under normal operation.

	heat transfer (MW)	percentage convection (%)	percentage radiation (%)
reactor vessel wall	2.42	7	93
reactor vessel upper head	0.10	2	98
reactor vessel lower head	0.12	3	97
total	2.64	6	94

Table 3-52 Heat balance over the cavity under normal operation.

	heat loss (MW)	heat removed (MW)	percentage of heat loss (%)
reactor vessel	2.64		
RCCS		2.36	89
RCCS on cavity floor		0.16	6
cavity wall		0.08	3
cavity ceiling		0.04	2

REFERENCES TO SECTION 3.4.5.

[1] CFX-F3D user guide. Computational Fluid Dynamics Services, Oxfordshire, October 1995.

[2] S.J. Ball: CRP-3 TECDOC Submittal for Description of GT-MHR Plutonium Burner Benchmark. Oak Ridge National Laboratories. Letter, 11 February, 1997.

[3] S.J. Ball: CRP-3 TECDOC Additional Information for Description of GT-MHR Plutonium Burner Benchmark. Oak Ridge National Laboratories. Letter, 21 April, 1997.

[4] Kuzavkov: CRP-3 Benchmark Problem Description for GT-MHR Pu Burner Accidents. OKB Mechanical Engineering, E-mail, 27 November, 1997.

[5] Kuzavkov. OKB Mechanical Engineering, E-mail, 18 December, 1997.

[6] N.B. Siccama, H. Koning: *Afterheat Removal from a Helium Reactor Under* Accident Conditions. Petten, Energieonderzoek Centrum Nederland (ECN), ECN-R--97-015, 1998.

[7] Perry's Chemical Engineers' *Handbook*. Sixth Edition. McGraw-Hill Book Company, New York, 1984.

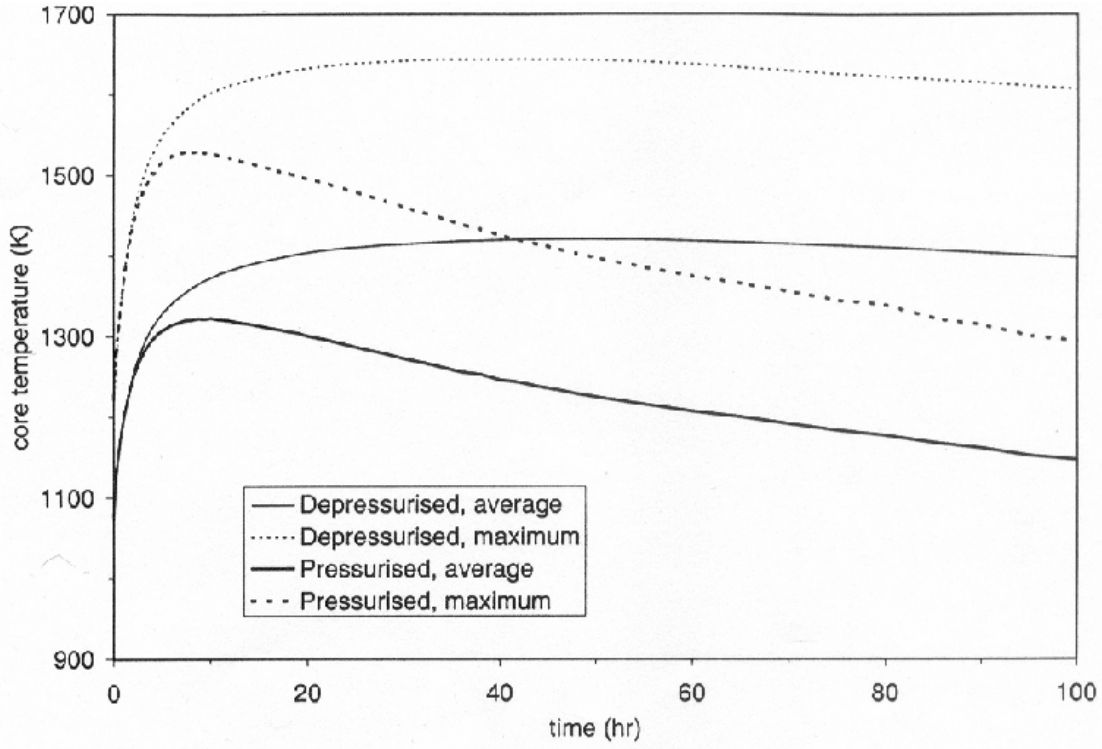

Figure 3-73 Maximum and average core temperatures.

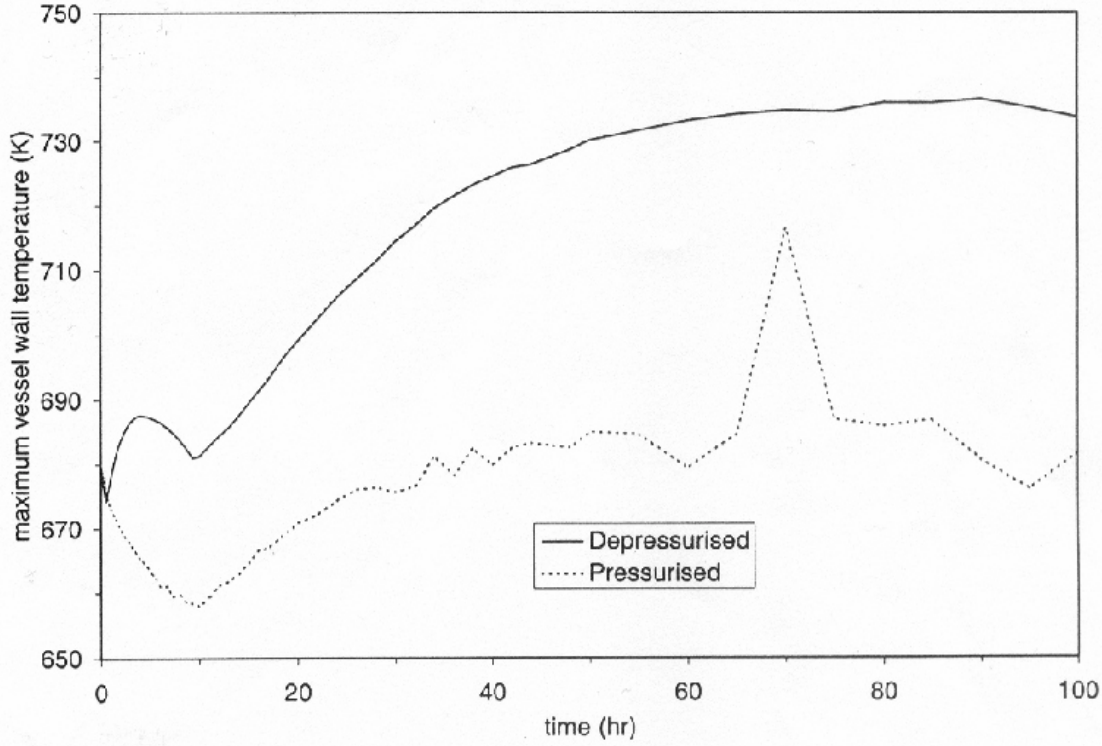

Figure 3-74 Maximum vessel wall temperatures.

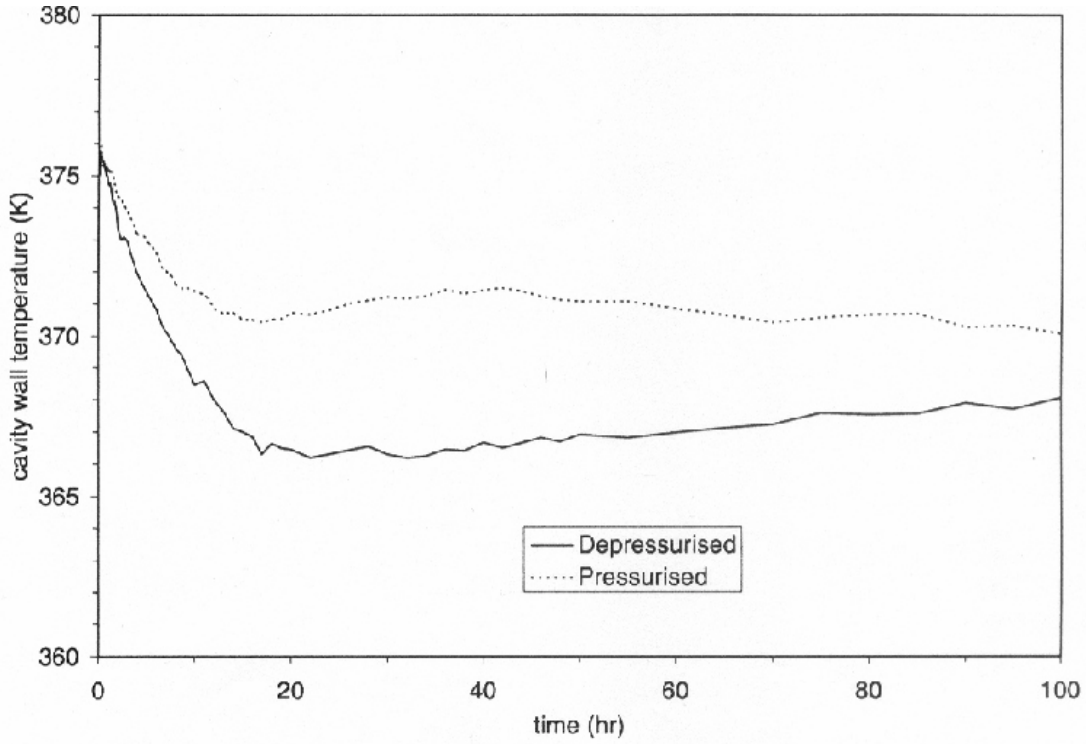

Figure 3-75 Average cavity wall temperatures.

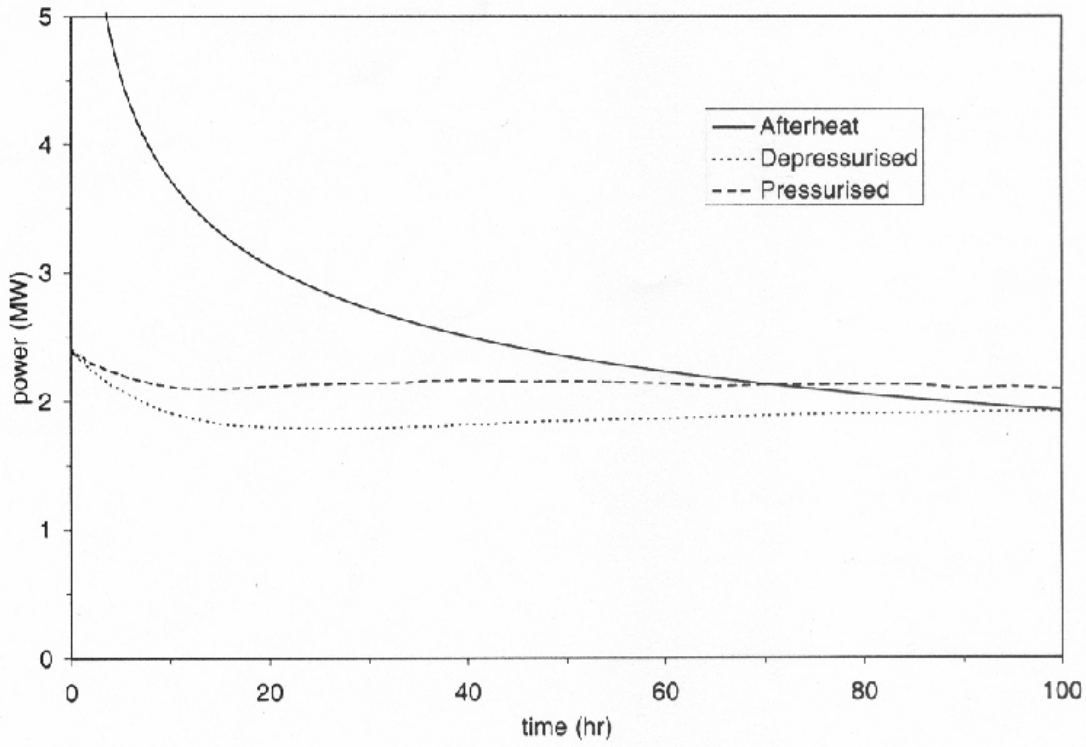

Figure 3-76 Afterheat power generation and power removed by the RCCS.

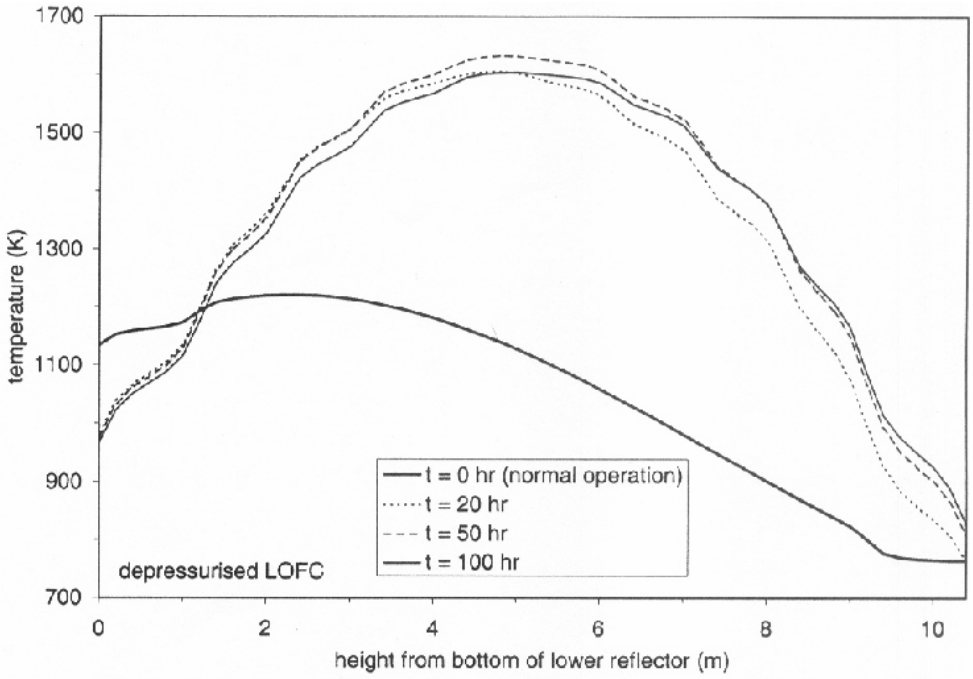

Figure 3-77 Axial temperature profile at a radial distance of 1.72 m for the depressurised LOFC.

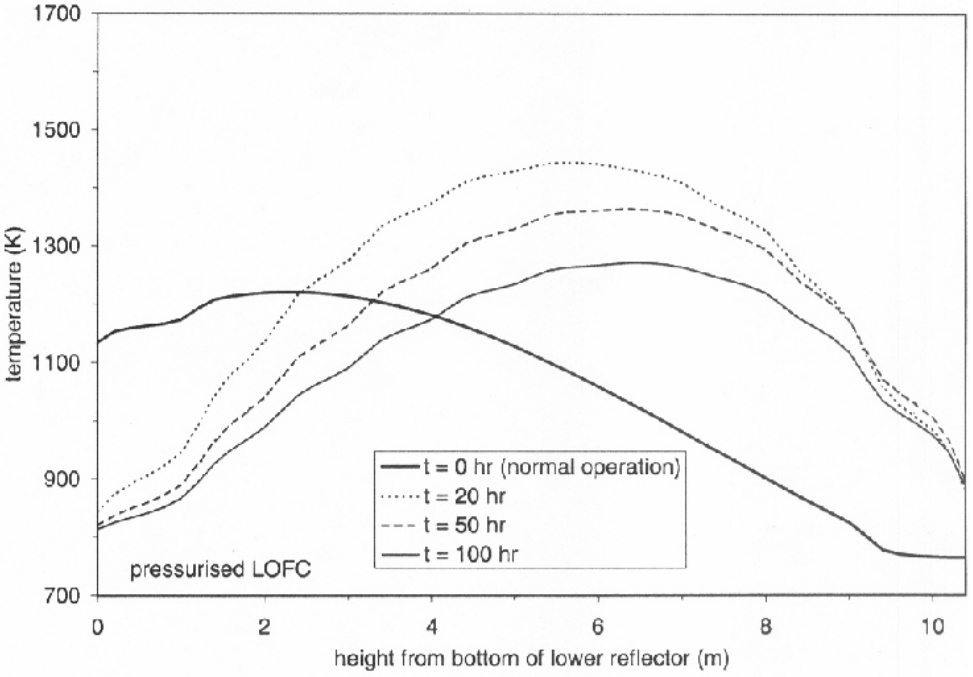

Figure 3-78 Axial temperature profile at a radial distance of 1.72 m for the pressurised LOFC.

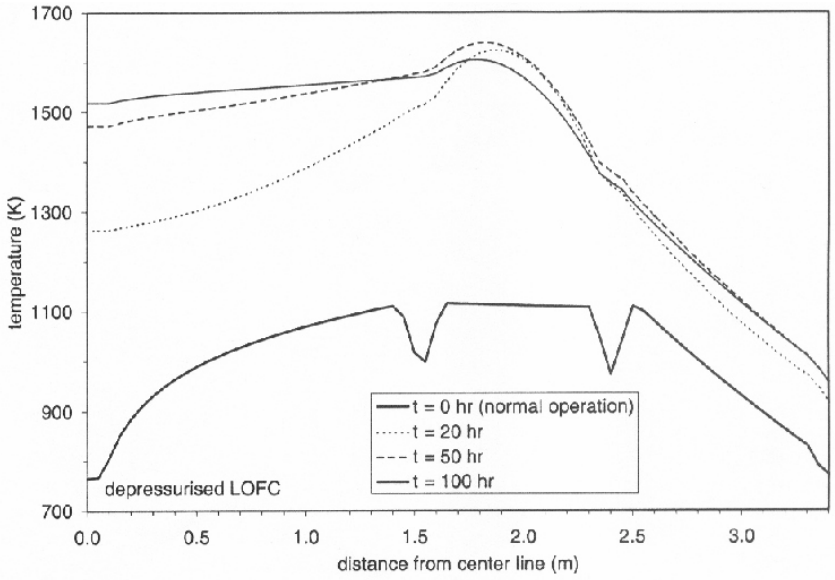

Figure 3-79 Radial temperature profile at reactor mid plane for the depressurised LOFC.

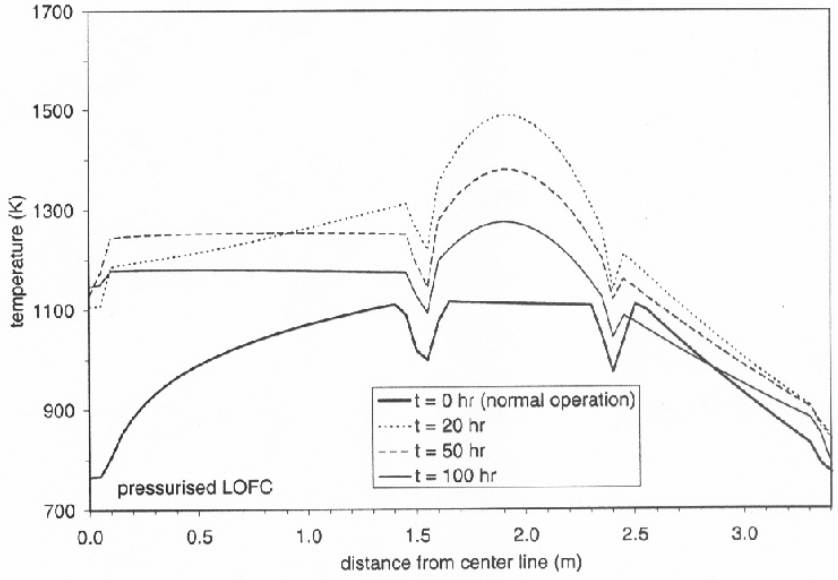

Figure 3-80 Radial temperature profile at reactor mid plane for the pressurised LOFC.

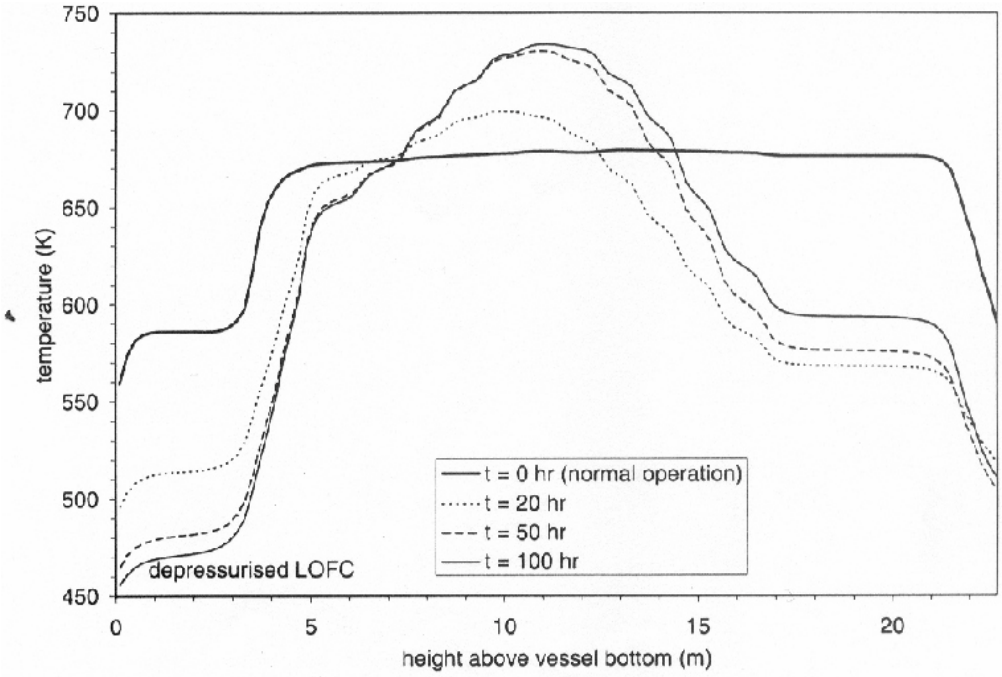

Figure 3-81 Temperature profile in the reactor vessel wall for the depressurised LOFC.

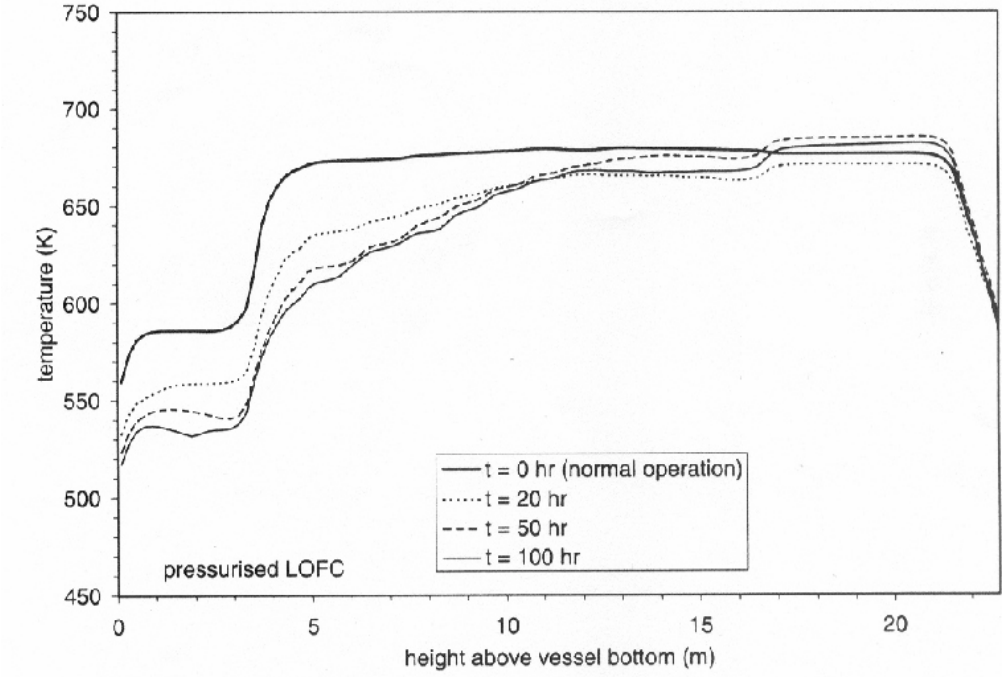

Figure 3-82 Temperature profile in the reactor vessel wall for the pressurised LOFC.

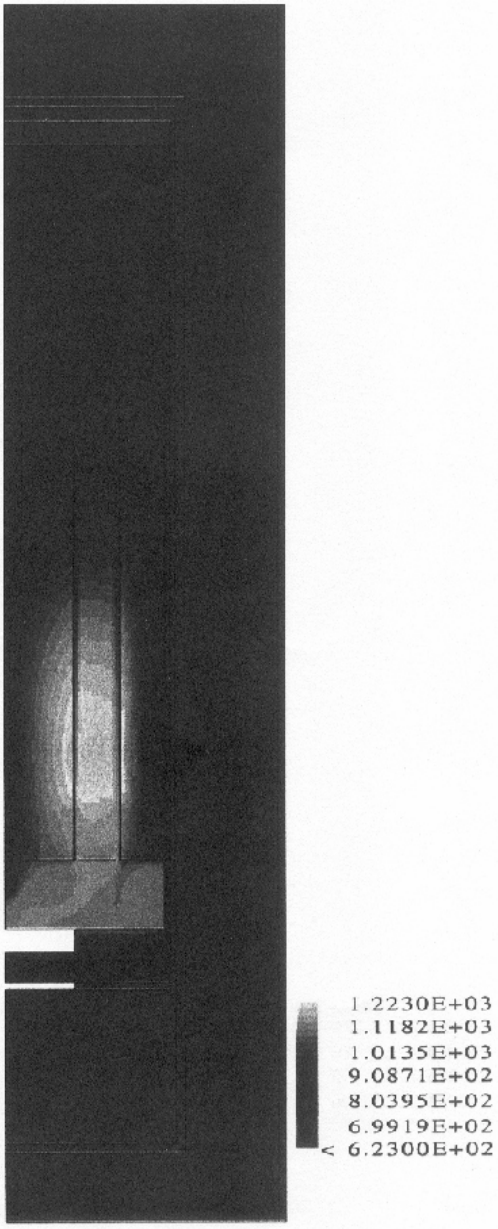

Figure 3-83 Temperature field under normal operation conditions (temperatures in K).

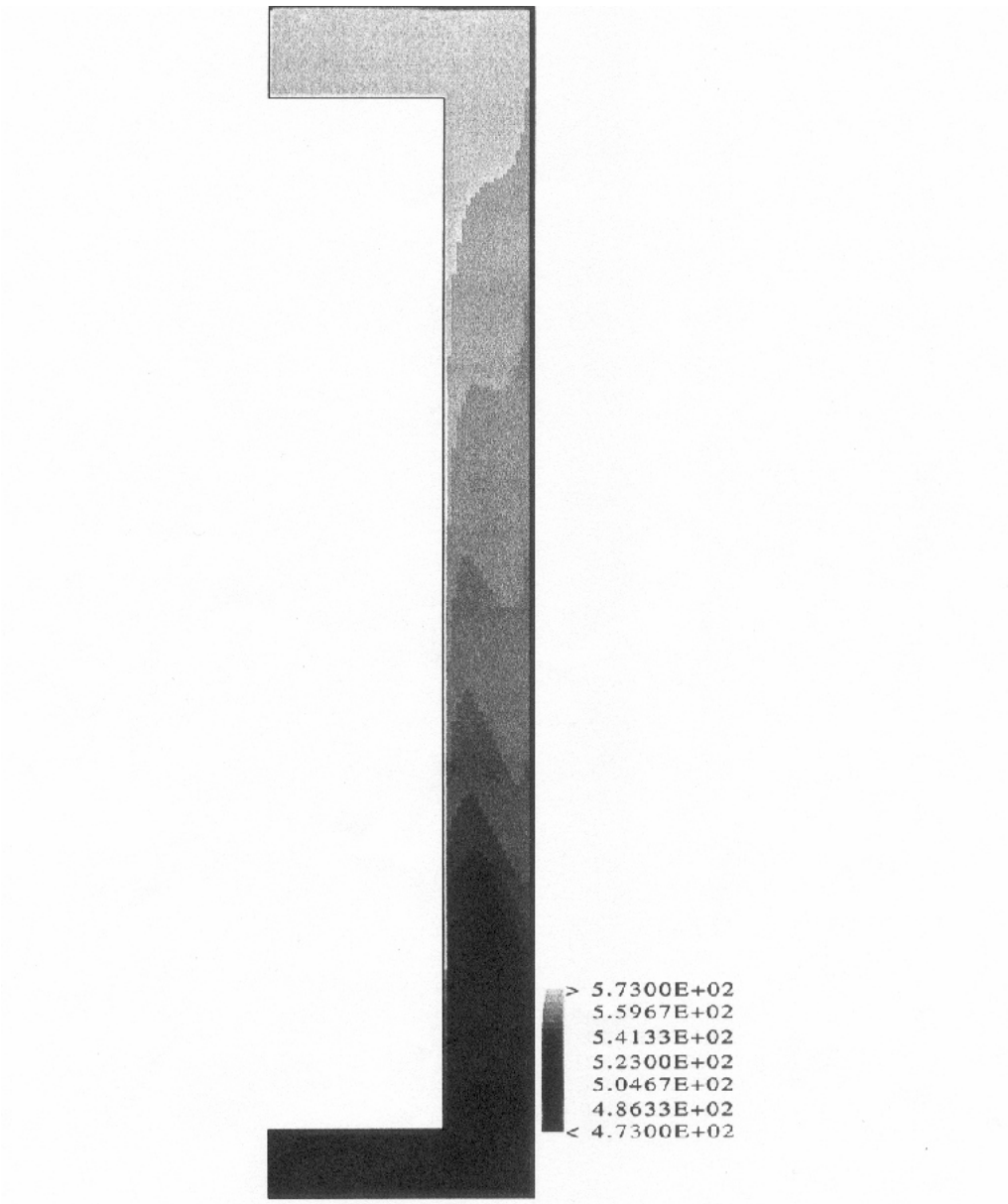

Figure 3–84 Temperature field in the cavity under normal operation conditions (temperatures in K).

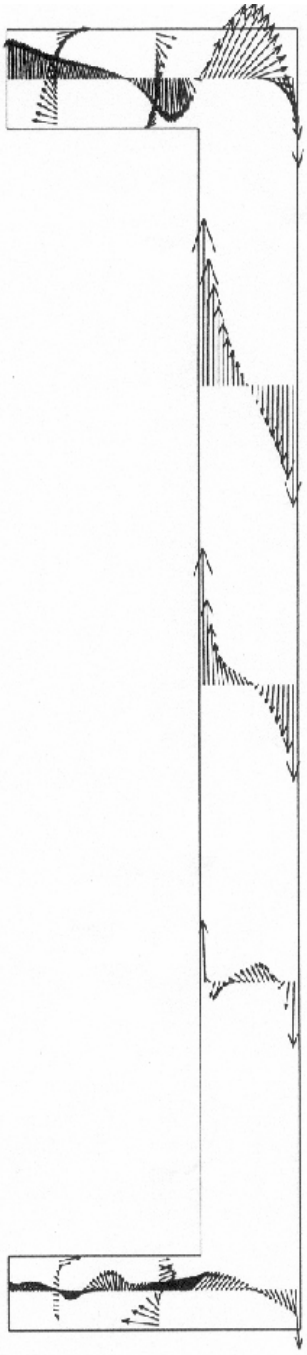

Figure 3-85 Velocity field in the cavity under normal operation conditions

3.4.5. INET Analysis of the GT-MHR Plutonium Burner Benchmark Problem

3.4.5.1. Introduction

The CRP-3 benchmark problem for GT-MHR Plutonium burner accidents, which is furnished by General Atomics and OKMB, is described by Dr. S. J. Ball of the Oak Ridge National Laboratory (ORNL) in the U.S. The Gas Turbine Modular Helium Reactor (GT-MHR), when fueled with surplus weapon grade plutonium, has the unique capability to obtain burnup of 90% of the initially charged plutonium-239 in a once through reactor cycle while generating electricity at plant efficiencies of nearly 50%. The GT-MHR is a passively safe, helium cooled, graphite moderated, advanced reactor system. The GT-MHR reference plant consists of four 600 MWt (286MWe) modules capable of providing a total net electrical generating capacity of 1144 MWe. The reactor core is contained in an uninsulated steel reactor pressure vessel that is connected by a cross vessel to a vessel that contains the power conversion system. The reactor and power conversion vessels are, respectively, 8.4m and 8.5m in diameter. The modules are located below grade in a 39m deep, high pressure, low leakage containment with characteristics typical of those of commercial light water reactors.

The water-cooled Reactor Cavity Cooling System (RCCS) of the GT-MHR removes heat from reactor cavity during normal operations and postulated accident (emergency) conditions to maintain the reactor components within required limits.

An initial condition (system capacity) check and two loss of forced convection (LOFC) accidents are to be analysed as the benchmark problems for the GT-MHR Plutonium burner:

– Calculate steady state (normal operation) RCCS heat removal, with one or both surface cooler panels operational,
– The first LOFC is accompanied by a rapid depressurization and scram, and is a study of conduction cooling behaviour. The RCCS should be assumed to function as designed, in one case with forced cooling of the heat exchanger, and the other in the boiloff mode (assuming sufficient makeup water is available),
– The second accident case is an LOFC accompanied by a scram, but without a depressurization. The RCCS is assumed to function as in the first LOFC case.

3.4.5.2. Analysis Approach and Model

Code

The THERMIX code which is a two-dimensional thermal hydraulic analysis program of a pebble bed in HTGR is used to analysis of the GT-MHR Plutonium Burner Benchmark problem. The INET analysis for the problem includes prediction of reactor performance and RCCS capability during normal operation and accidents.

Models

The simulating models are shown in Figs 3-86 and 3-87. Fig. 3-86 is the THERMIX model to calculate the reactor temperature distribution and Fig.3-87 is the KONVEK model to calculate the forced or natural convection of the Helium coolant. The THERMIX model consists of 29×49 meshes and 30 components to present core, reflector and other constructions. The KONVEK model consists of 24×32 meshes and 8 components to present different constructions.

Conditions

Data providing characteristics for the reactor and RCCS models are provided by OKBM and General Atomics which includes the temperature dependent heat conductivity of blocks structure and other structural materials. The equivalent conductivity of the core and reflectors is

got from the analysis result in reference [3]. The porosity of the core is estimated as 0.181 according to the area proportion of the cooling channels to the core. The porosity of the reflector blocks is estimated as 0.011 for 2mm average gap and 0.014 for 2.5mm average gap. With these values the flow rate fraction can be obtained. The emissivity of 0.80 is used to the surfaces in the cavity.

Because the THERMIX code is a two-dimensional analysis program in (r, z) coordinates, the surface cooler of the RCCS is modelled by an annular fluid boundary outside. The convection heat transfer coefficient in the RCCS tubes is calculated using the following correlation:

$$Nu = 0.023\,Re^{0.8}\,Pr^{0.4} \quad (1)$$

An effective convection heat transfer coefficient (10.4 W/m^2K) is gained by the effective convection heat transfer area. The temperature of water as boundary condition is 65°C in radial direction and 40°C in lower direction in the case with forced cooling of the heat exchanger. The temperature of air in upper boundary is 30°C. With this RCCS model the concrete temperature is below that of the water.

3.4.5.3. Results

Steady state

The steady state (normal operation) vessel temperatures with one and both surface cooler panels operational are shown in Figs 3-88 and 3-89. On the inner vessel surface the maximum temperature is 367°C with both surface cooler panels operational and 445°C with one surface cooler panel operational. In both cases the temperature is below 490°C. The RCCS heat removal rate is 1.5MW with both surface cooler panels operational and 0.74MW with one surface cooler panels operational. The maximum fuel temperature is 1098°C and 1099°C respectively.

LOFC accidents

The first LOFC is accompanied by a rapid depressurization and scram. Fig.3-90a is axial temperature distribution of fuel, lower and upper reflectors at radius of 1.72m with maximum power density for nominal power and 20, 50, 100hr of the accidents. Figure 3-90b is radial temperature distribution of fuel, inside and outside reflectors near the core mid-plane for nominal power and 20, 50, 100hr. Figure 3-90c is reactor vessel temperature distribution (outer surface) along the height for nominal power and 20, 50, 100hr of the accident.

Figure 3-90d is transient maximum fuel temperature. During the accident the maximum fuel temperature reaches the highest value of 1590°C at 87hr. This value is below the safety limit 1600°C. Figure 3-90e is transient maximum reactor vessel temperature. The maximum reactor vessel temperature reaches about 389°C at 97hr, which is also below the required limit 490°C.

Figure 3-90f is transient heat removal rate of RCCS comparing with decay power. The fraction of heat transferred in side and lower directions to the total heat removal is more than 99%, which means less than 1% of heat transfer to the air in upper direction.

The second LOFC is accompanied by a scram without a depressurization. The same parameters of second LOFC are shown in Fig.3-91a-3-91c as that of first LOFC. From the temperature distributions of core and RPV it can be concluded that natural convection carries more heat to the top of the core and transfers heat rapidly outside the core. As a result, the maximum fuel temperature reaches the highest value of 1379°C at 71hr; the maximum reactor vessel temperature reaches about 370°C at 90hr. The transient values are compared with the first LOFC and listed in Table 3-53.

It can be seen that the core temperature distribution is much steeper in the first LOFC

accident (depressurized) as a result of only conduction behavior. Because most of the residual heat in the core is transferred by the natural convection in the second LOFC accident (pressurized), the maximum core temperature is much lower than that in the first LOFC accident.

Table 3-53 Comparison of two LOFC accidents' Transient

		Depressurized LOFC	Pressurized LOFC
Max. Core Temperature	Time(hr)*	87	71
	Temperature(°C)	1590	1379
Max. RPV Temperature	Time(hr)**	97	90
	Temperature(°C)	389	370
RCCS Heat Removal Rate	Time(hr)***	96	82
	Heat(MW)	1.8	1.9

Note: * After this time the maximum fuel temperature goes down,
** At this time the maximum RPV temperature reached its peak value,
*** After this time the RCCS heat removal rate is greater than the residual heat.

Sensitivity analysis

Sensitivity analysis is completed for the first LOFC accident of depressurized case. The effect of following input data on transient fuel and reactor vessel temperature is evaluated.

– Increase of decay power by 10%

Figure 3-92a shows the maximum fuel temperature which peak value is 115°C higher than normal condition. The peak value of maximum reactor vessel temperature is also 14°C higher in Fig.3-92b.

– Increase of the average gap between fuel and reflector blocks to 2.5mm

Figure 3-93a shows the maximum fuel temperature, which peak value is almost the same as the normal condition. The peak value of maximum reactor vessel temperature is also the same as the normal condition in Fig. 3-93b.

– Decrease of metallic surface emissivity from 0.8 to 0.6 without change of graphite emissivity 0.9

The maximum fuel temperature shown in Fig. 3-94a is 46°C higher than normal condition, while the peak value of maximum reactor vessel temperature in Fig. 3-94b is 62°C higher than normal condition.

– Decrease of graphite thermal conductivity of core and reflector blocks by 25%

In Fig. 3-95a the maximum fuel temperature is 202°C higher than the normal condition. The maximum reactor vessel temperature is 10°C lower than the normal condition. So the graphite conductivity influences the process of accident greatly.

– Increase of average temperature of cooling tubes up to 140°C for side and lower panels.

The maximum fuel temperature is 4°C higher than the normal condition as shown in Fig.3-96a. The maximum reactor vessel temperature is about 11°C higher than the normal condition. These results show that boiloff mode of RCCS makes little influence on the fuel temperature but causes some higher RPV temperature.

3.4.5.4. Conclusions

– The steady state (normal operation) maximum vessel temperatures (367°C with both surface cooler panels operational and 445°C with one surface cooler panels operational) do not exceed the required limit of 490°C. The RCCS heat removal rate is 1.5MW with both surface

cooler panels operational and 0.74MW with one surface cooler panels operational.

– In Depressurized LOFC the maximum core fuel temperature (1590°C) is lower than the safety limit of 1600°C, and the vessel temperature (389°C) is below the required limit.

– In Pressurized LOFC the core fuel temperature (1379°C) is much lower than the safety limit 1600°C, and the vessel temperature (370°C) is below the required limit.

– The RCCS can remove the residual heat from the core after the accidents to remain the reactor in safety.

REFERENCES TO SECTION 3.4.5.

[1] S. J. Ball, "CRP-3 Benchmark Problem Description for GT-MHR Plutonium Burner Accidents", ORNL, February 10, 1997

[2] S. J. Ball, "CRP-3 Benchmark Problem Description for GT-MHR Plutonium Burner Accidents: Supplementary Information on the RCCS Design", ORNL, April 21, 1997

[3] H. Bonneville, A. Mejane, "Determination of the Equivalent Conductivity of MHTGR Reactor Fuel Block", 2nd Research Coordination Meeting Issue on Heat Transport and Afterheat Removal for Gas-cooled Reactor under Accident Conditions, JAERI, November 9-11, 1994

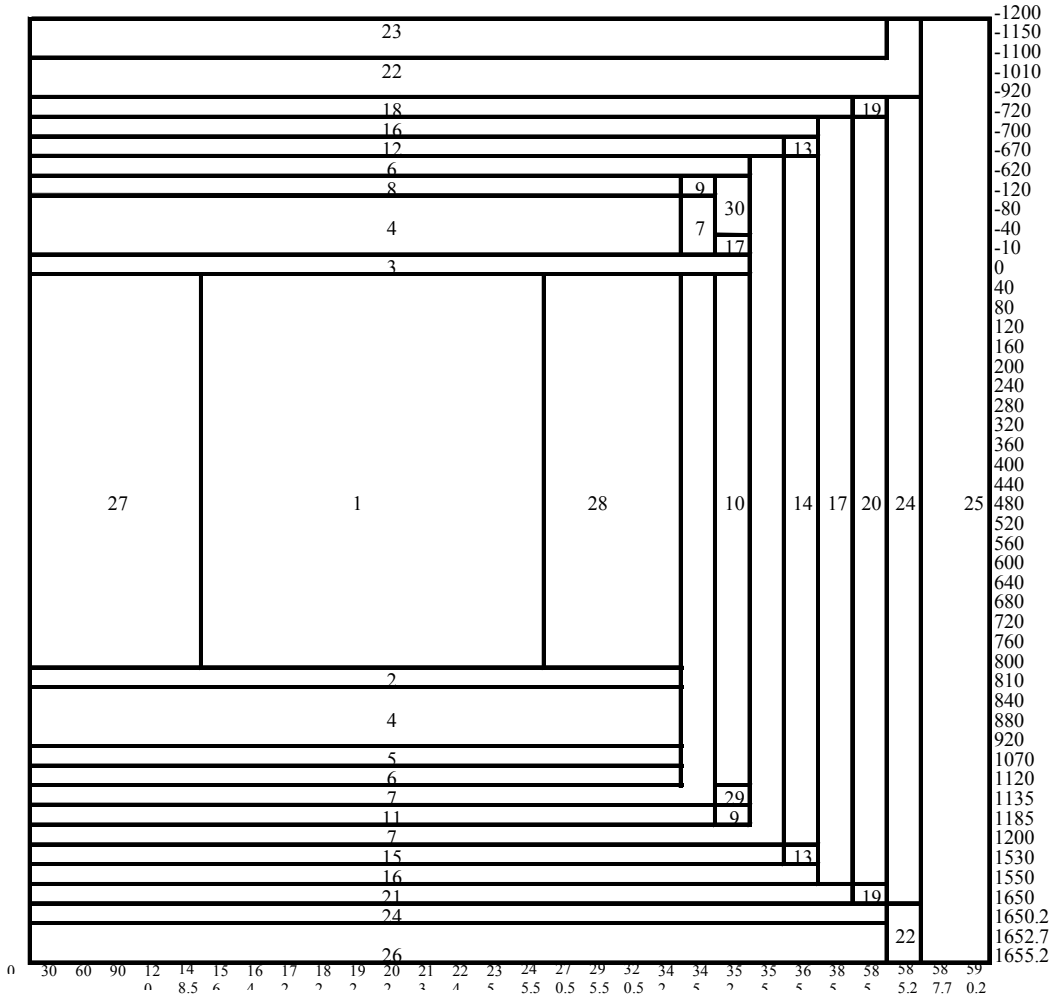

1—Core 2—Hot helium plenum 3—Cold helium plenum 4—Reflector 5—Lower helium cavity 6—Thermal insulation 7—Support plate, core barrel, lower plate and shell 8—Upper helium cavity 9—Solid 10— Helium channel 11—Radial helium gap 12—Upper helium cavity 13—Solid 14—Inside reactor vessel helium cavity 15—Lower helium cavity 16—Upper and lower head 17—Reactor vessel 18—Upper air cavity 19—Solid 20—Outside reactor vessel air cavity 21—Lower air cavity 22—Concrete 23—Air environment 24—Tube wall of RCCS 25—Side RCCS 26—Bottom RCCS 27—Inside reflector 28—Outside reflector 29—Entrance of helium 30—Axial helium gap

*Solid 9, 13 and 19 are added in order to separate the cavities for the demand of THERMIX code.

Fig. 3-86 Simulating Model for GT-MHR Plutonium Burner Benchmark Problem (THERMIX)

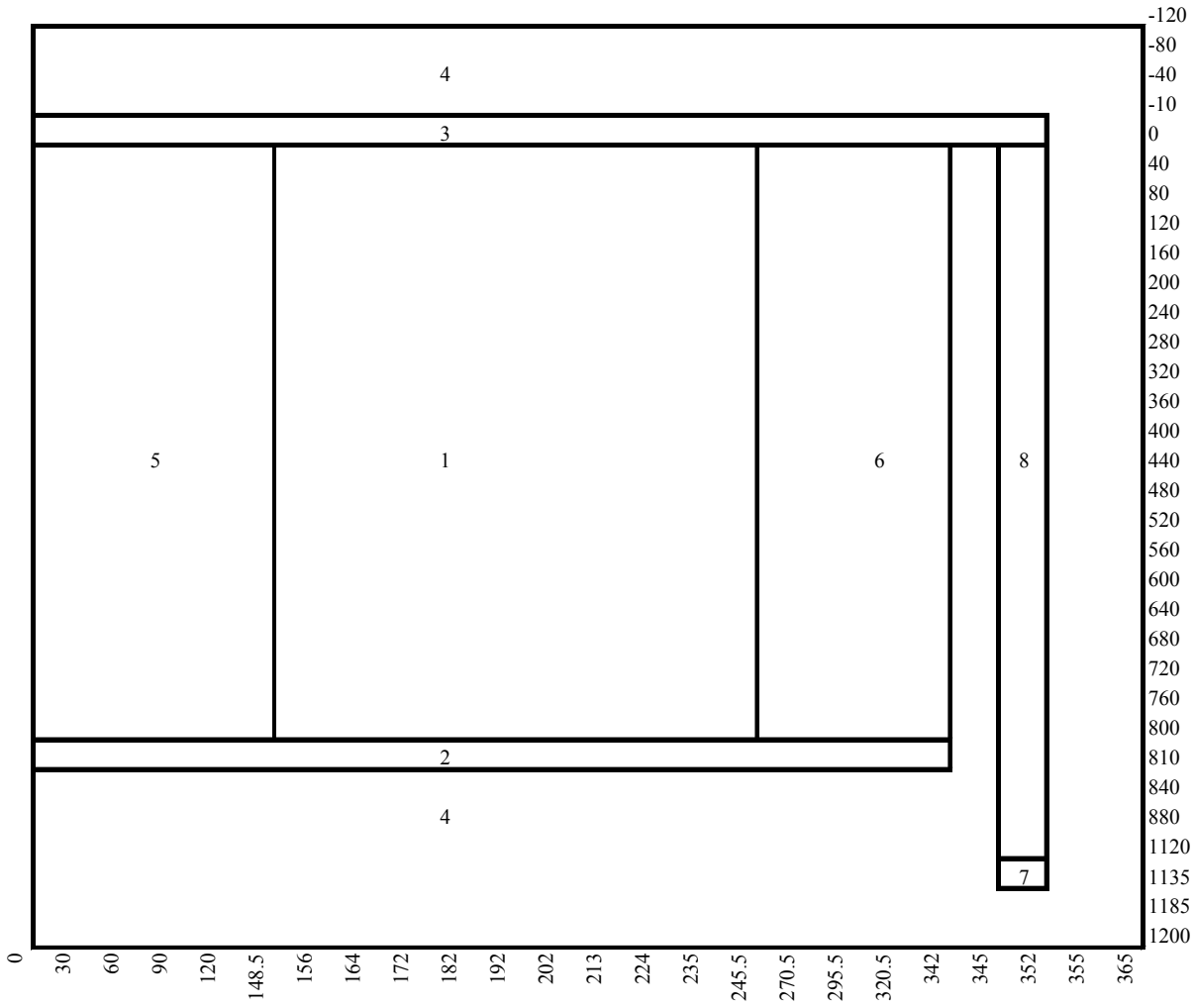

1—Core 2—Hot helium plenum 3—Cold helium plenum 4—Solid Region
5—Inside reflector 6—Outside reflector 7—Entrance of helium 8—Helium channel

Fig. 3-87 Simulating Model for GT-MHR Plutonium Burner Benchmark Problem (KONVEK)

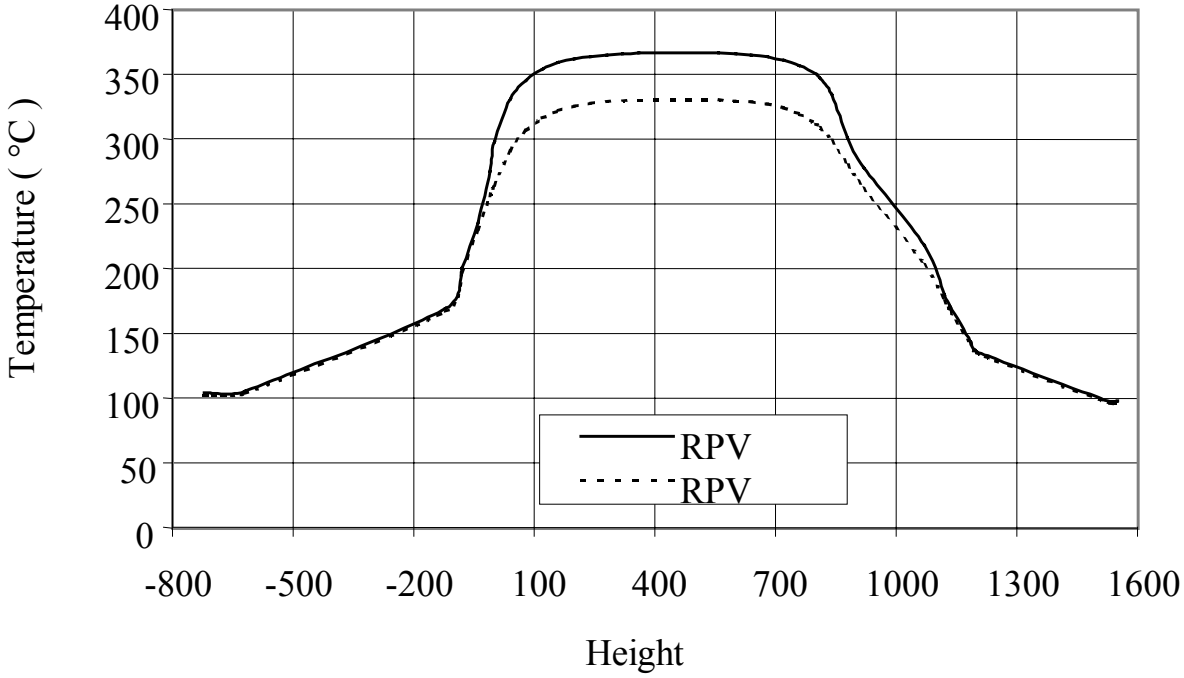

Fig 3-88 Reactor Pressure Vessel Temperature
(With Two Panels)

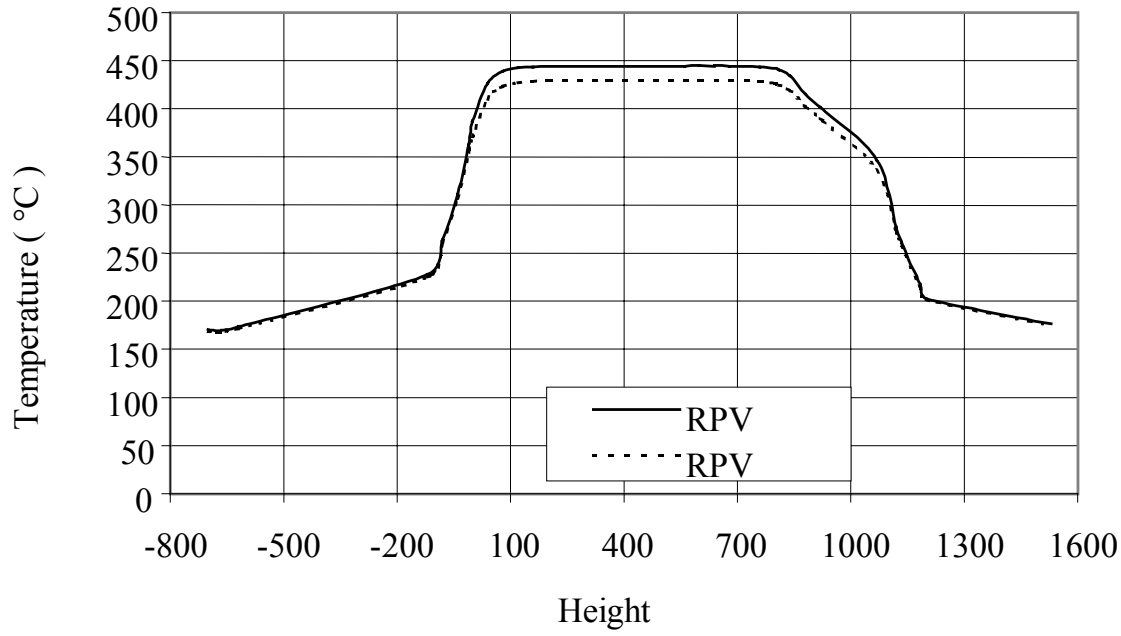

Fig. 3-89 Reactor Pressure Vessel Temperature
(With One Panel)

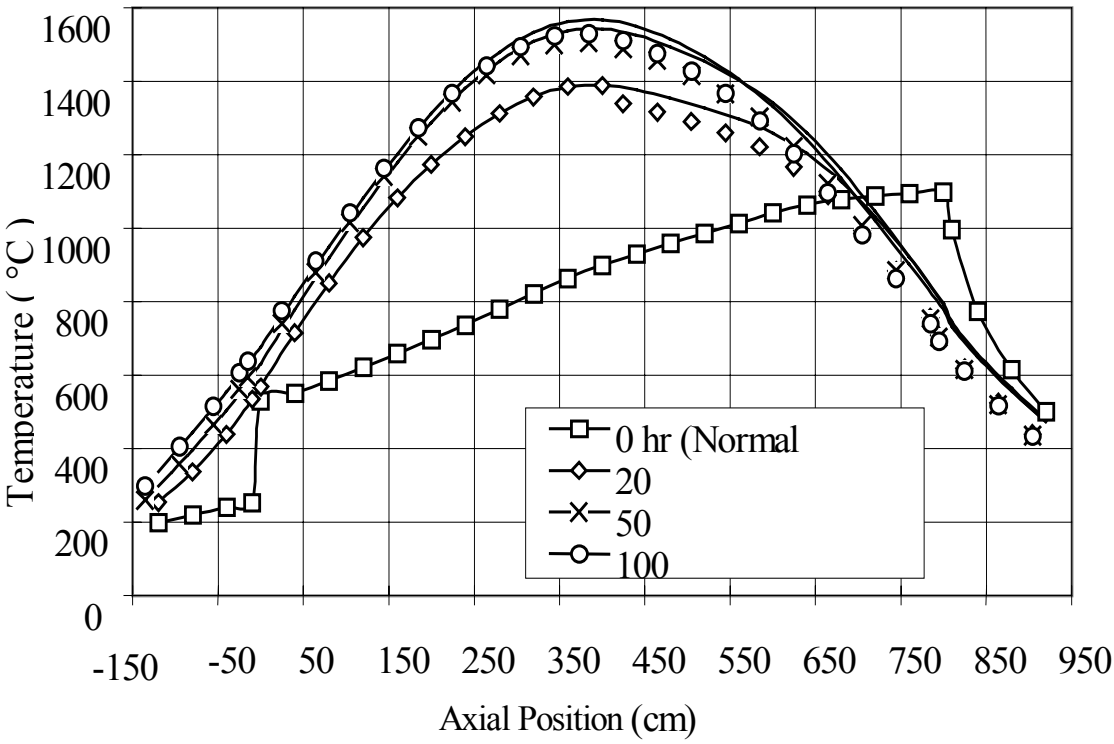

Fig.3-90a Axial Temperature Distribution at Radius of 1.72m of first LOFC (Depressurized)

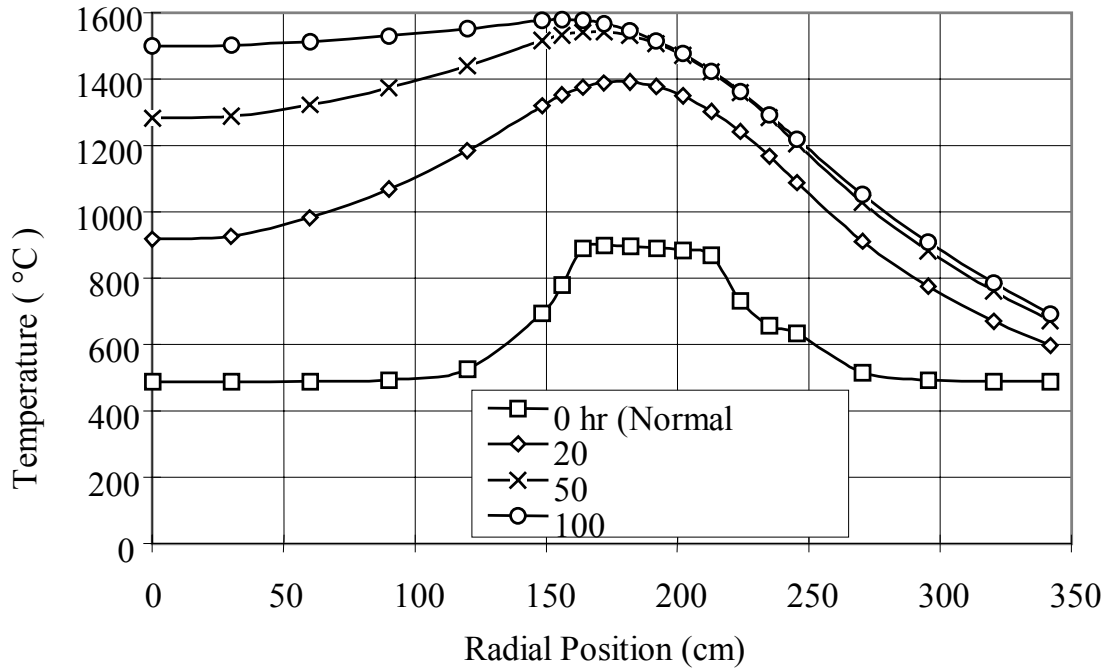

Fig.3-90b Radial Temperature Distribution in the Core Mid-plane of First LOFC (Depressurized)

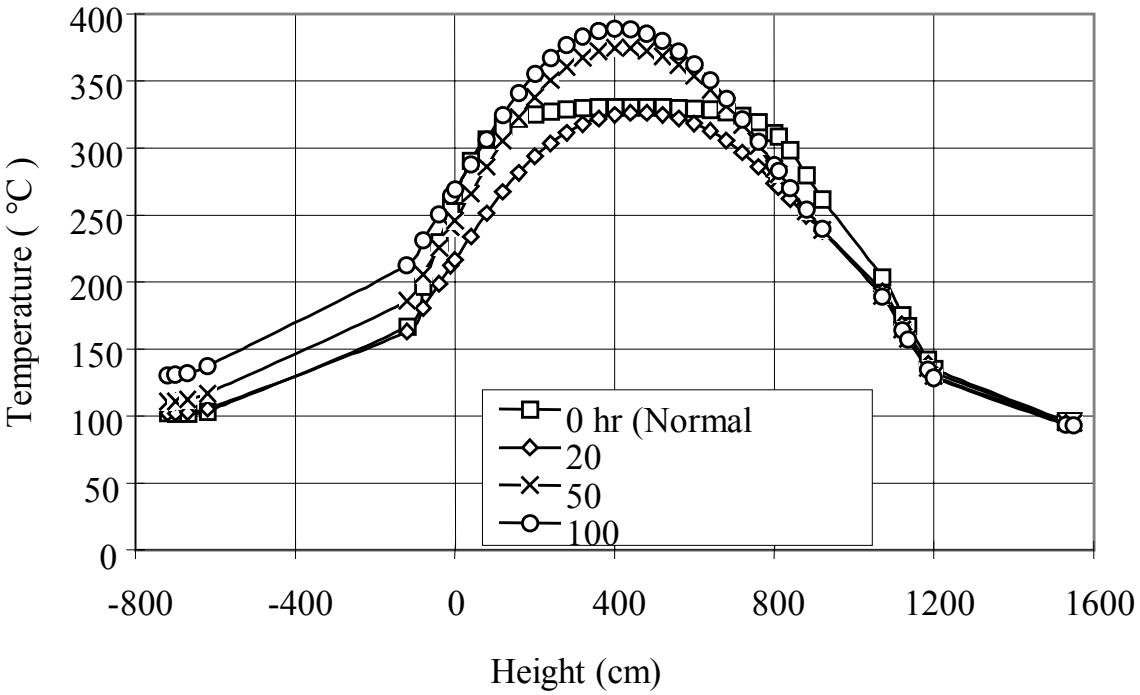

Fig 3-90c RPV Temperature Distribution
of First LOFC (Depressurized)

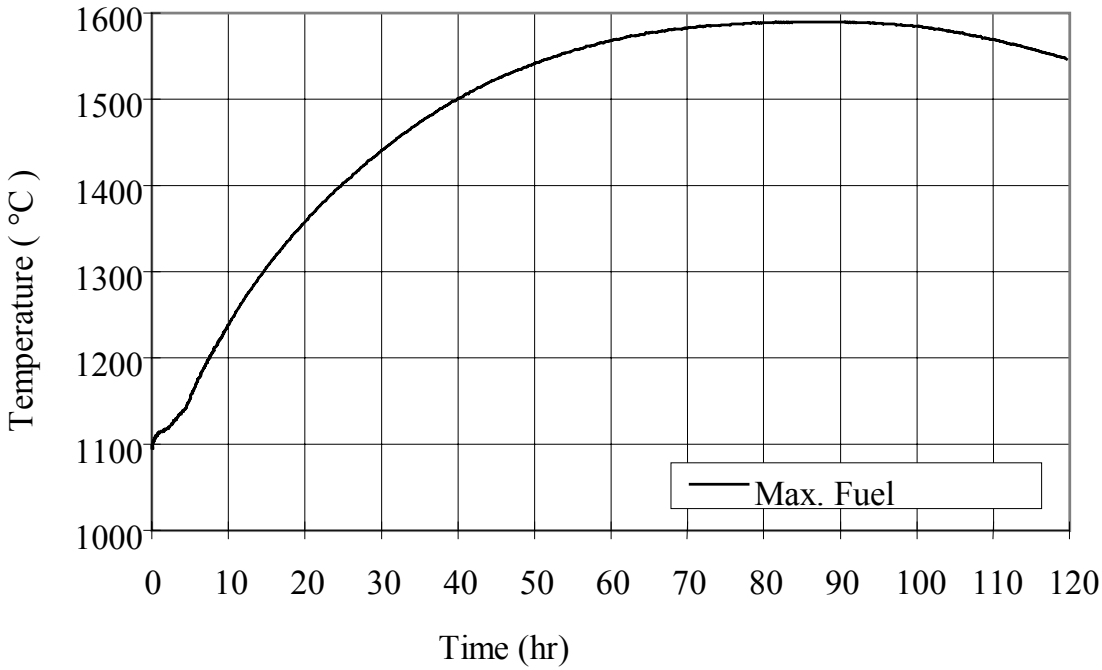

Fig. 3-90d Transient Maximum Fuel Temperature
of First LOFC (Depressurized)

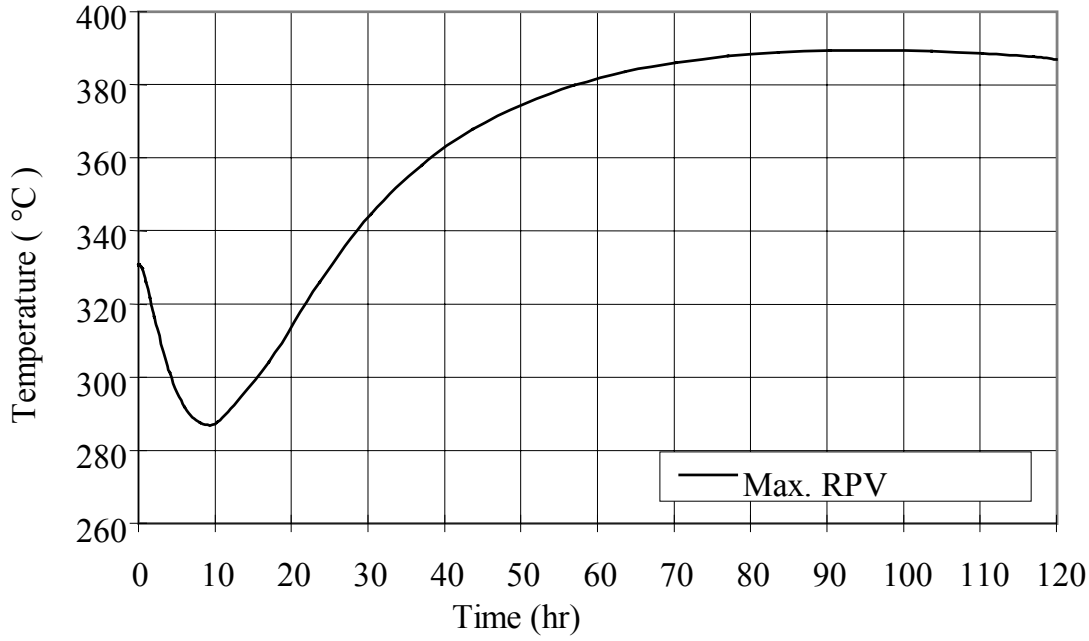

Fig.3-90e Transient Maximum RPV Temperature
of First LOFC (Depressurized)

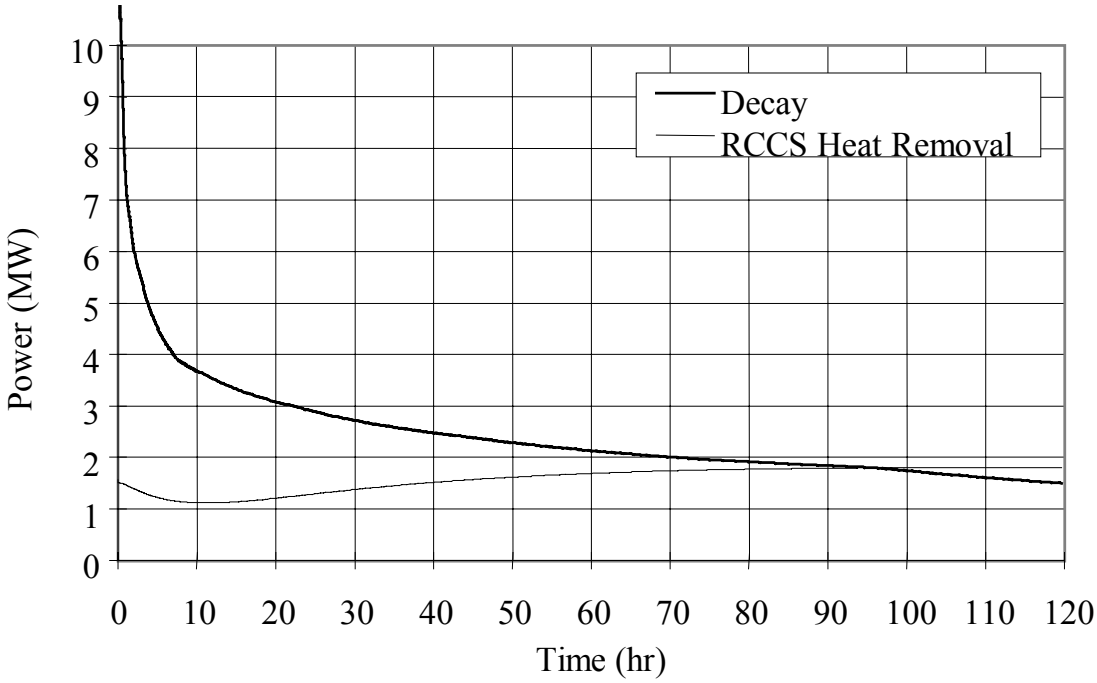

Fig 3-90f Transient Heat Removal Rate
of First LOFC (Depressurized)

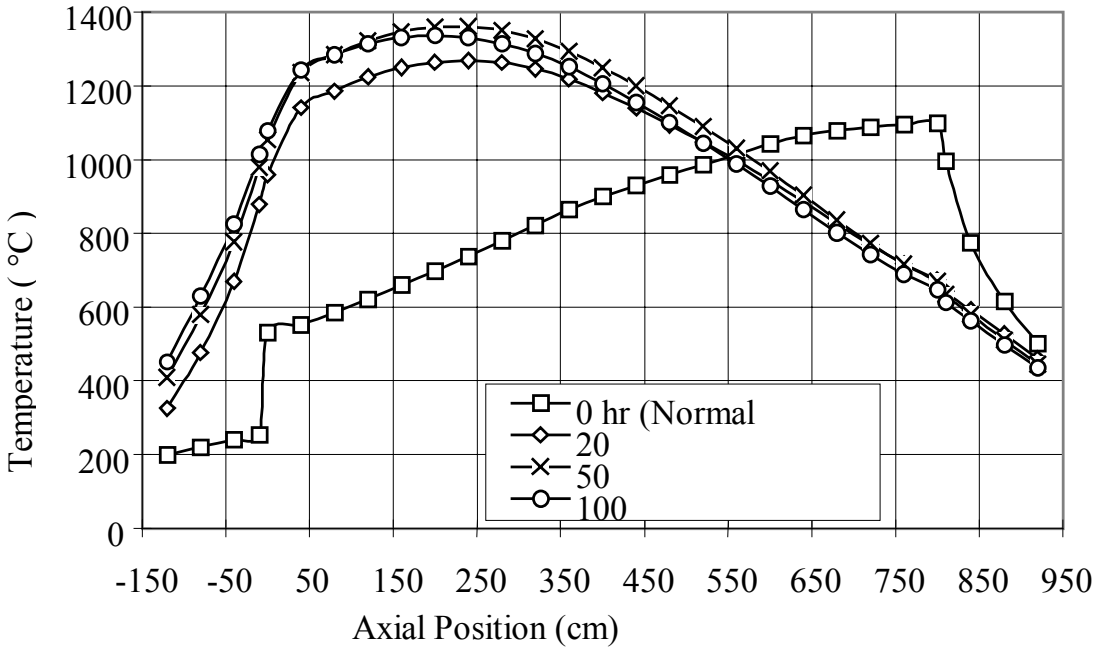

Fig.3-91a Axial Temperature Distribution at Radius of 1.72m
of Second LOFC (Pressurized)

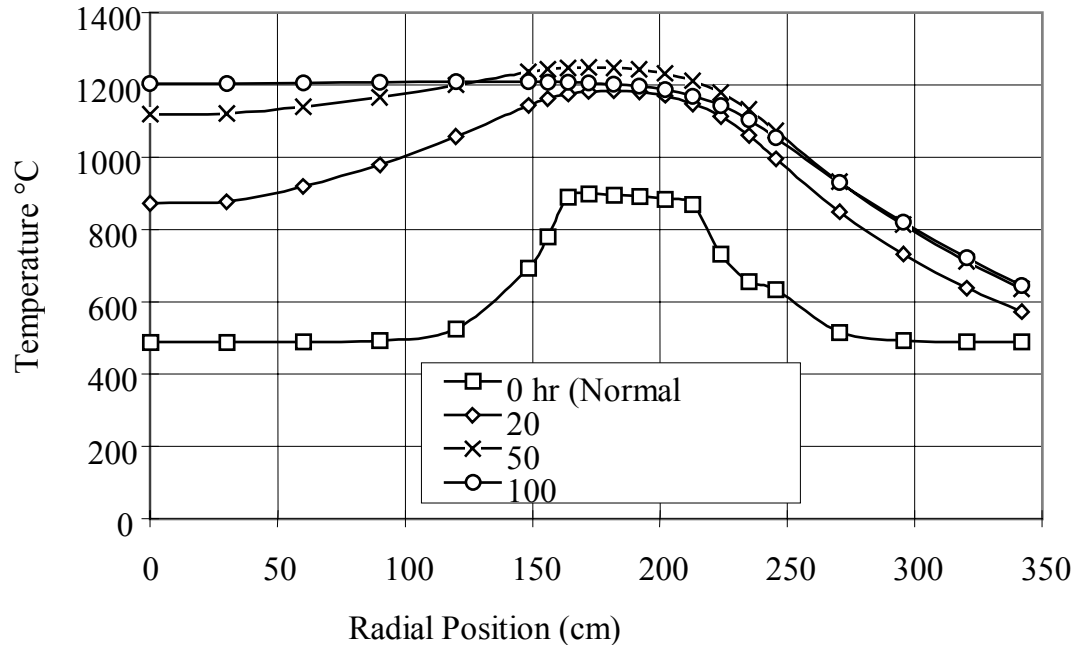

Fig.3-91b Radial Temperature Distribution in the Core Mid-plane
of Second LOFC (Pressurized)

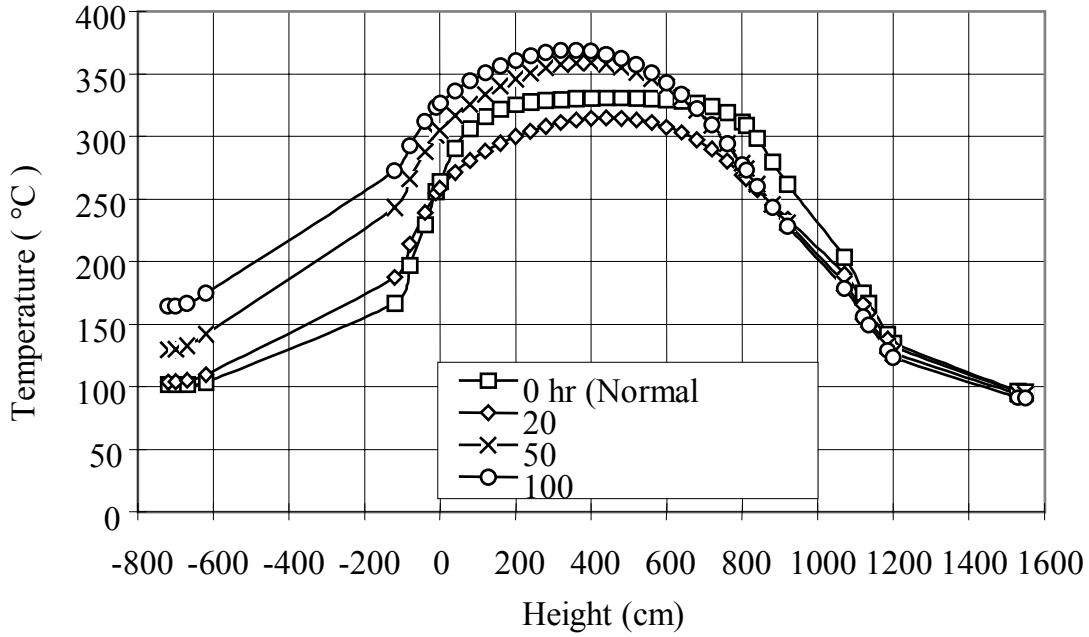

Fig.3-91c RPV Temperature Distribution
of Second LOFC (Pressurized)

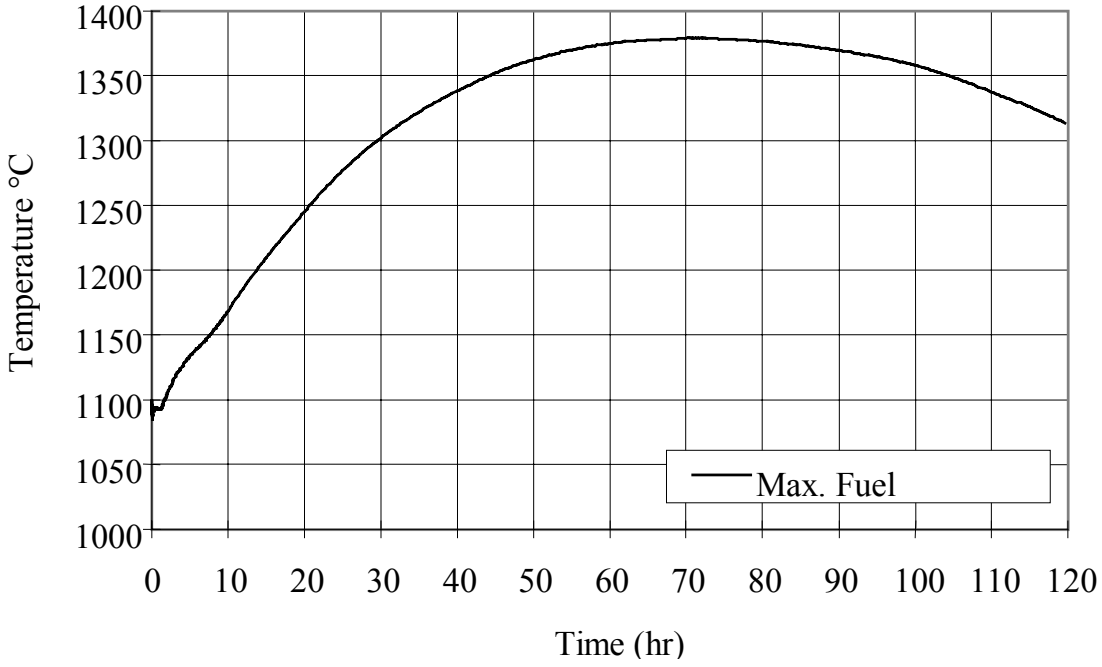

Fig.3-91d Transient Maximum Fuel Temperature
of Second LOFC (Pressurized)

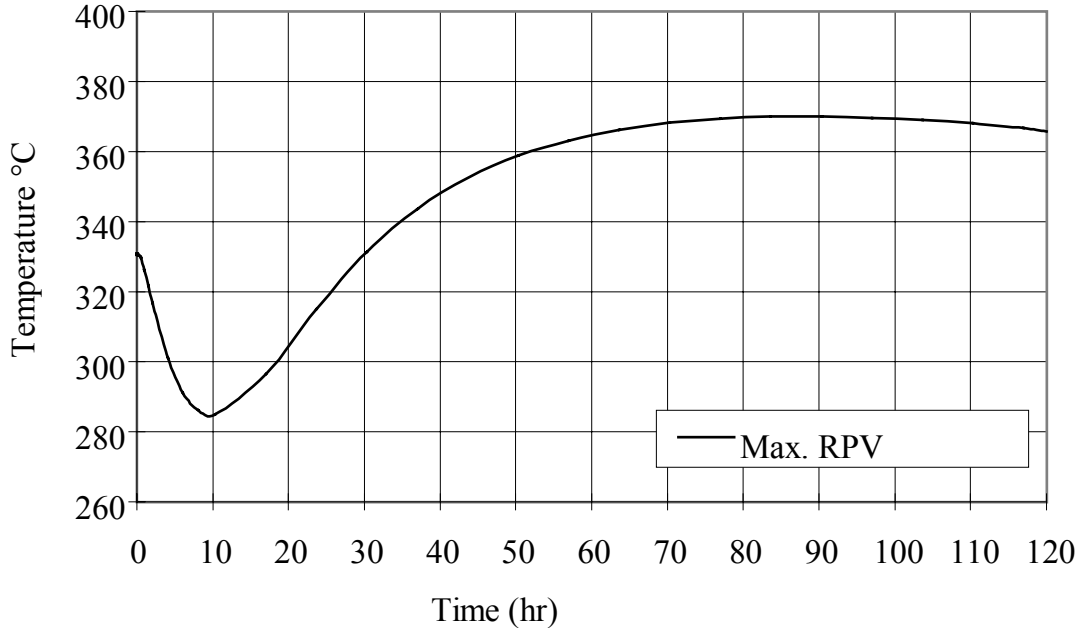

Fig.3-91e Transient Maximum RPV Temperature
of Second LOFC (Pressurized)

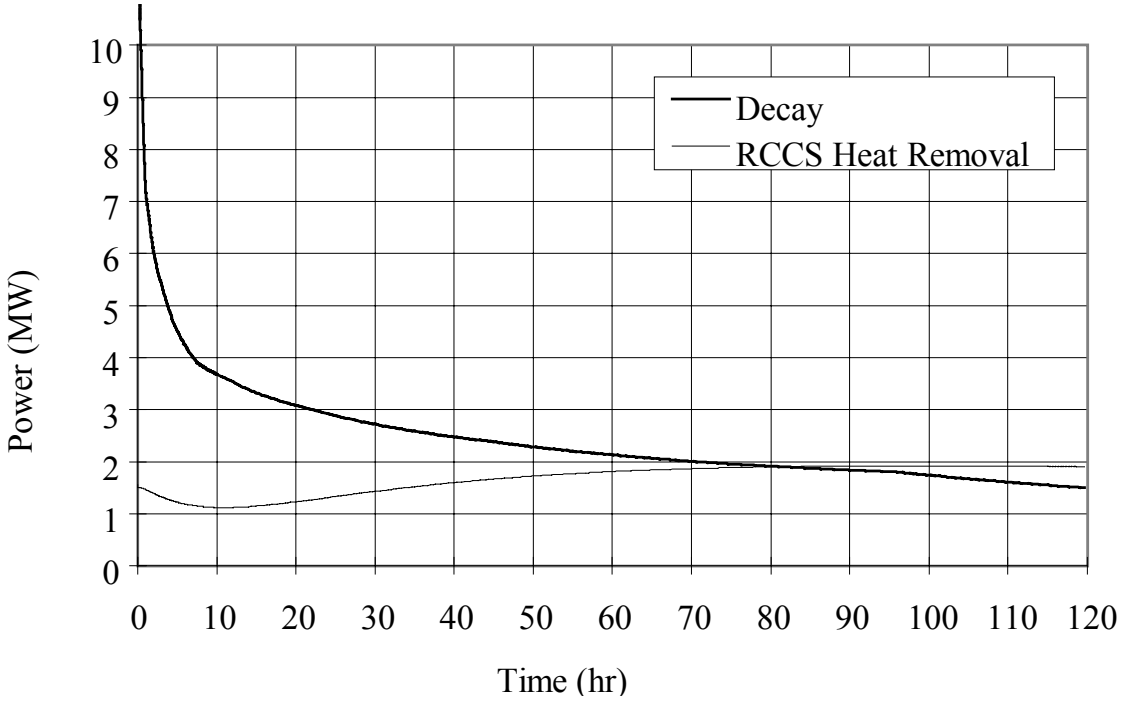

Fig.3-91f Transient Heat Removal Rate
of Second LOFC (Pressurized)

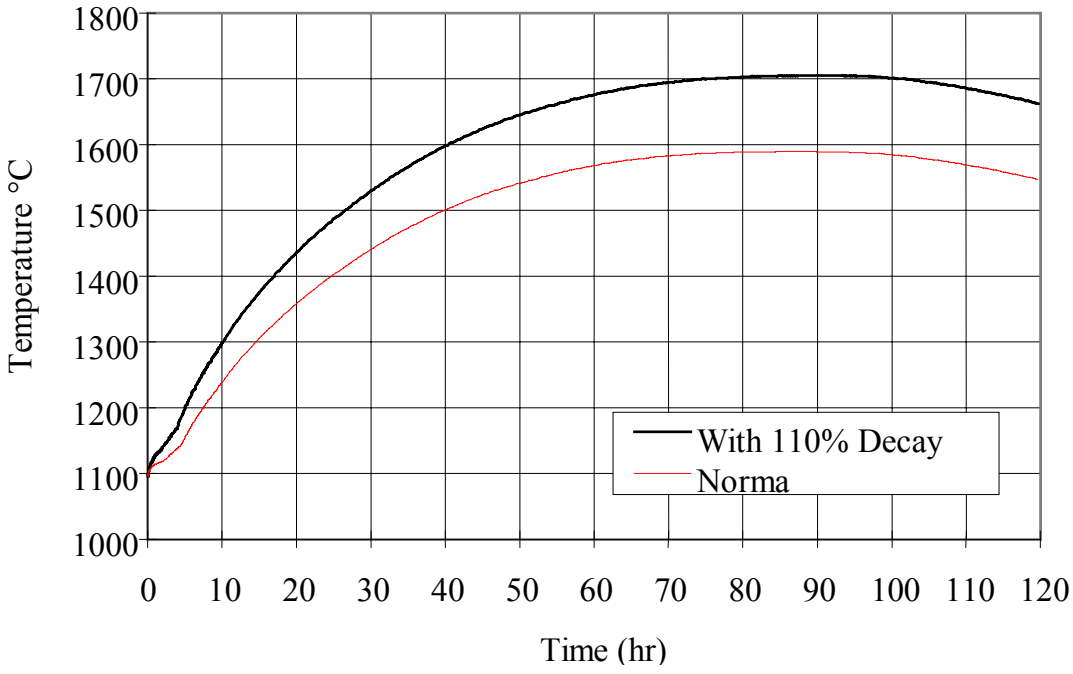

Fig.3-92a Effect of Decay Power on Maximum Fuel Temperature

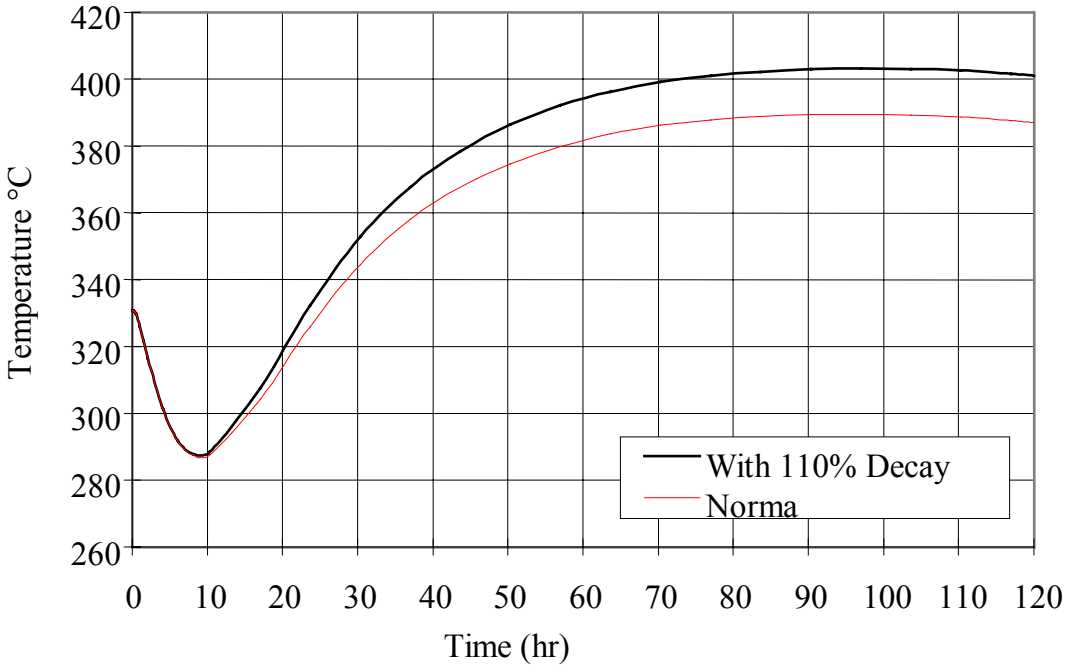

Fig.3-92b Effect of Decay Power on Maximum RPV Temperature

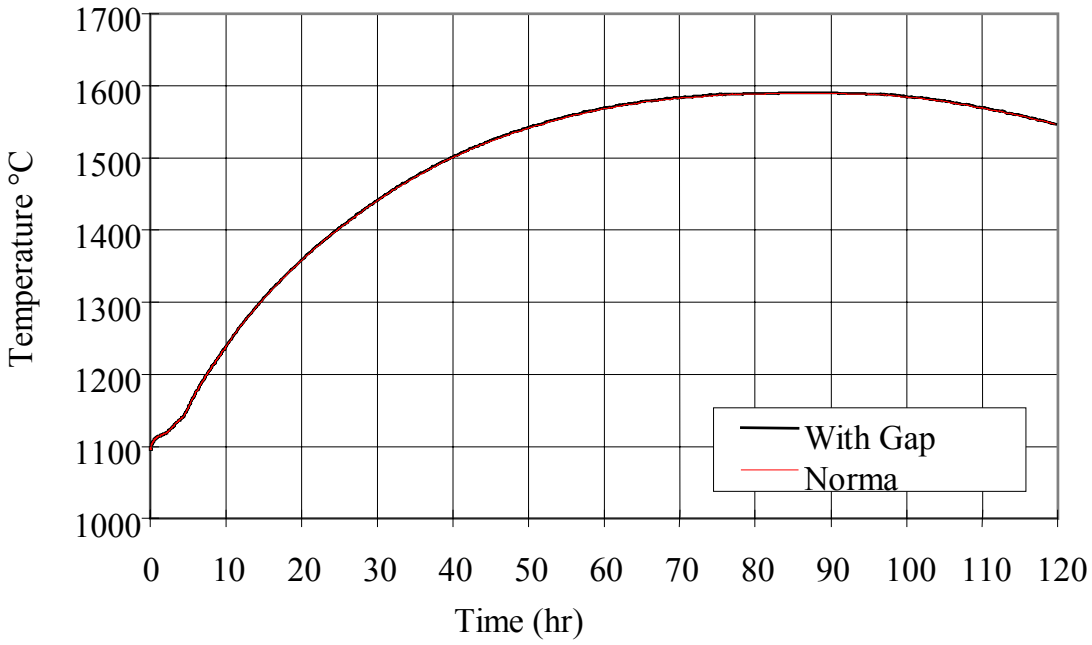

Fig.3-93a Effect of Average Gap between Blocks to 2.5mm on Maximum Fuel Temperature

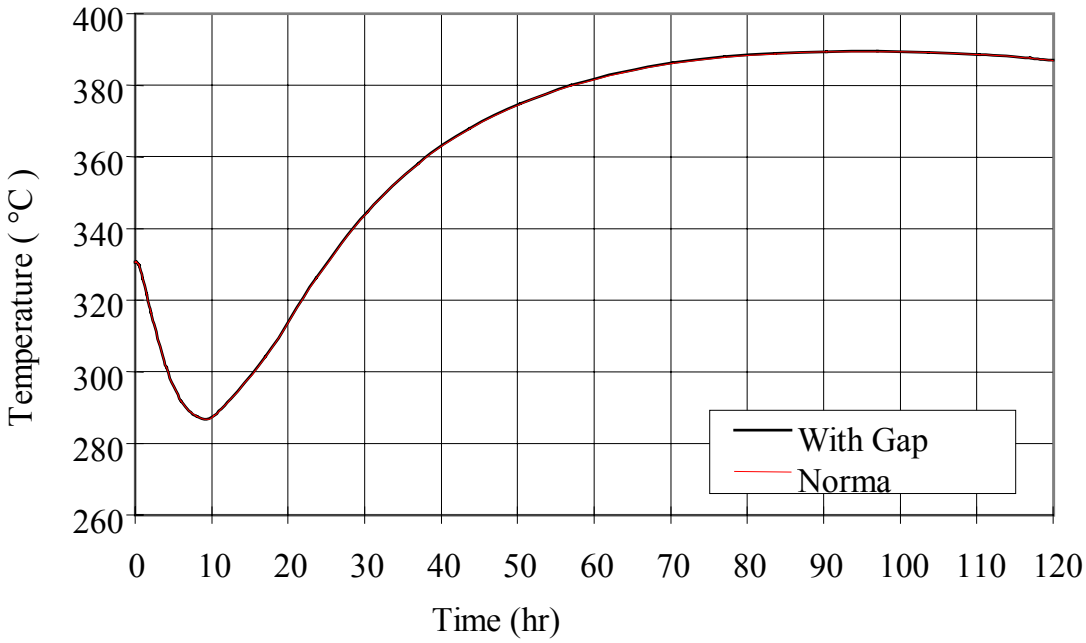

Fig.3-93b Effect of Average Gap between Blocks to 2.5mm on Maximum RPV Temperature

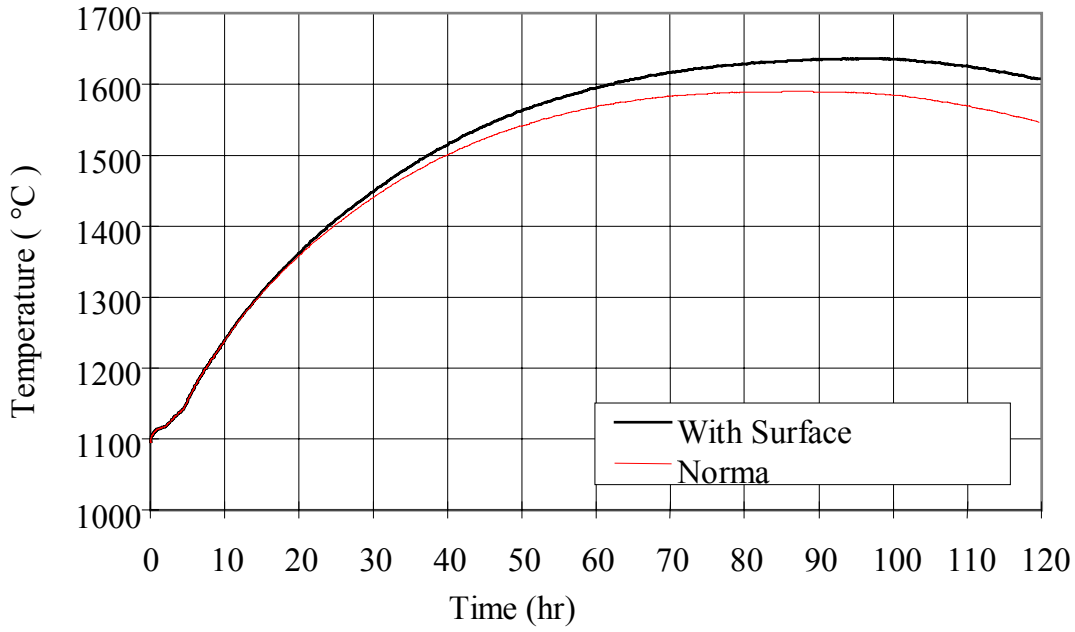

Fig.3-94a Effect of Metallic Surface Emissivity on Maximum Fuel Temperature

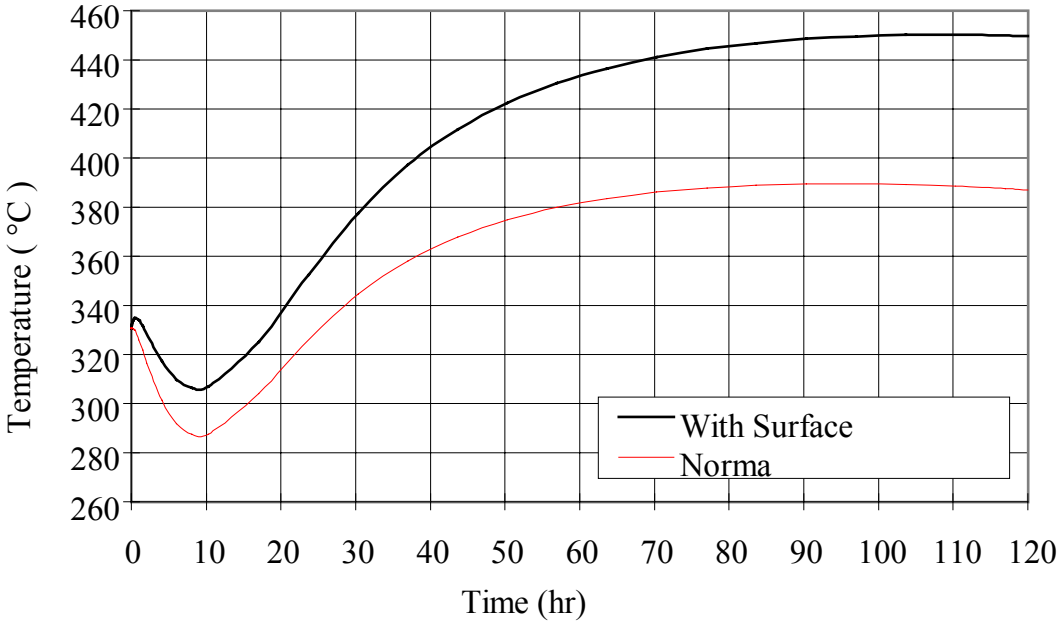

Fig.3-94b Effect of Metallic Surface Emissivity on Maximum RPV Temperature

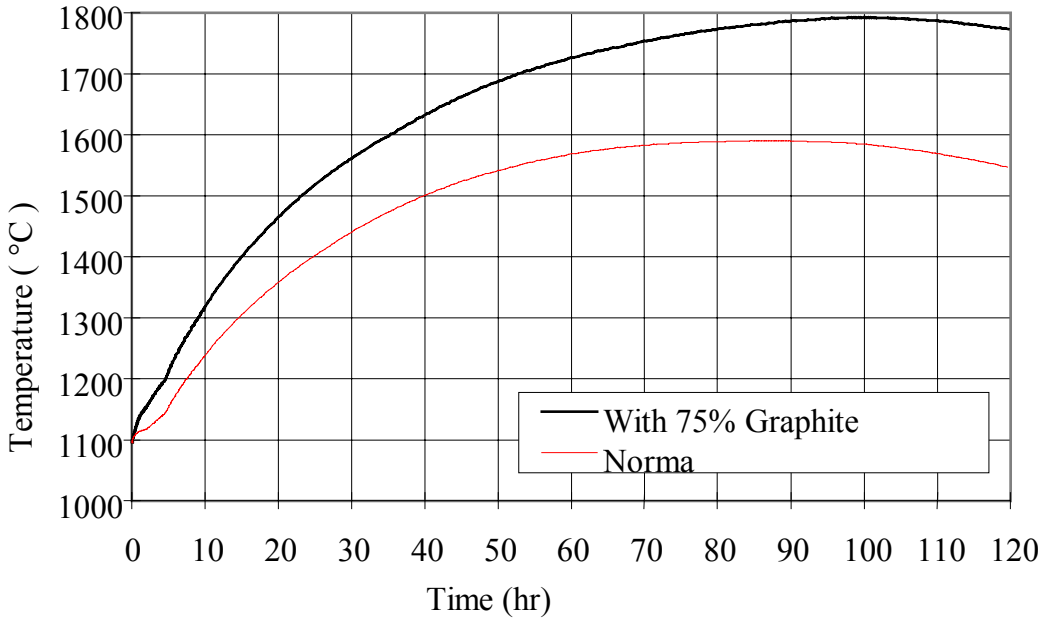

Fig.3-95a Effect of Graphite Thermal Conductivity on Maximum Fuel Temperature

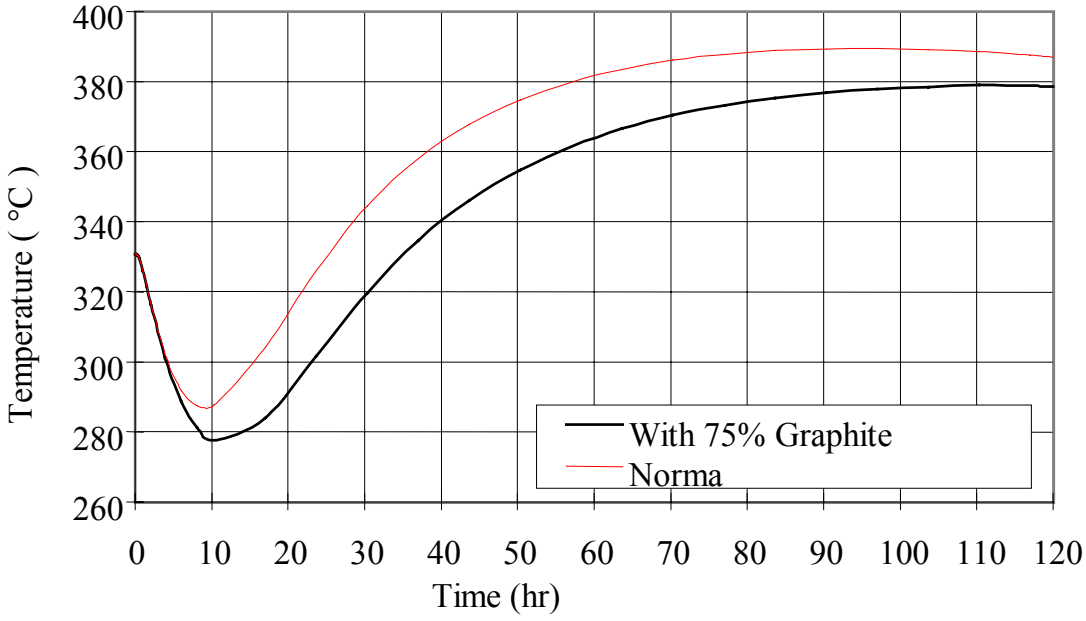

Fig.3-95b Effect of Graphite Thermal Conductivity on Maximum RPV Temperature

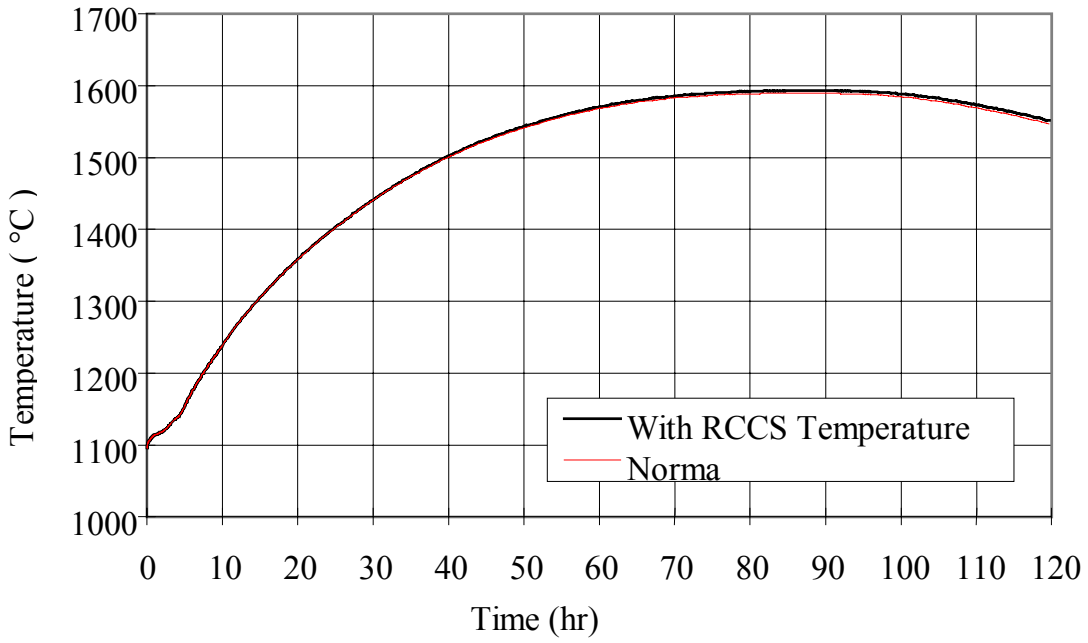

Fig. 3-96a Effect of Cooling Tube Temperature on Maximum Fuel Temperature

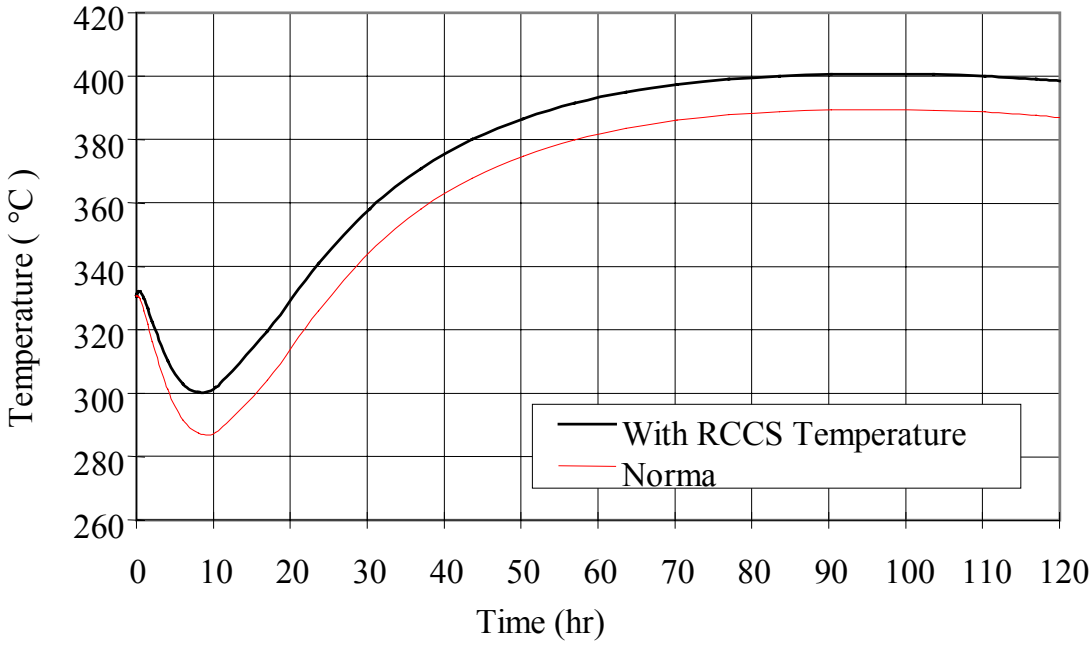

Fig. 3-96b Effect of Cooling Tube Temperature on Maximum RPV Temperature

3.4.6. Results of GT-MHR Plutonium Burner Benchmark Calculations

Syd Ball

Oak Ridge National Laboratory

Oak Ridge, Tennessee 37831,

USA

3.4.6.1. Introduction

Calculations for the GT-MHR Plutonium Burner Benchmark problem were done using the ORNL MORECA code, an interactive workstation-based simulator developed for performing analyses of modular high-temperature gas-cooled reactor (MHTGR) core transients and accidents. MORECA is a forerunner of GRSAC (Graphite Reactor Severe Accident Code), which is described in detail in the Appendix (A.2.3). The GT-MHR version of MORECA had incorporated many specific features of the reactor that are not included in the more general applications code GRSAC, and hence was used for this analysis.

MORECA was originally developed at Oak Ridge National Laboratory for the U.S. Nuclear Regulatory Commission to assess the licensability of the U.S. Department of Energy (DOE) steam cycle design 350MW(t) MHTGR. Subsequently, the code was modified under DOE sponsorship to simulate the 450MW(t) Gas Turbine (GT) design, and later the 600MW(t) version, to aid in development and design studies. Features of the code (MORECA-GT) include detailed modeling of 3D core thermal hydraulics, interactive workstation capabilities that allow user/analyst or "operator" involvement in accident scenarios, and options for studying anticipated transients without scram (ATWS) events.

In addition to the detailed models for the core, MORECA includes models for the vessel, Shutdown Cooling System (SCS), and Reactor Cavity Cooling System (RCCS), and core point kinetics to accommodate ATWS events. A new RCCS model was added to MORECA for this benchmark to accommodate the water-cooled RCCS design for the Plutonium burner (the original GA/DOE design was for an air-cooled RCCS).

3.4.6.2. Reactor Description

Details of the 600MW(t) underground-silo module design are given in the reactor description section (3.1.4.1). In the side-by-side vessel arrangement, the reactor vessel (heat source) is at a higher elevation than the power conversion vessel. Hence for loss of forced circulation (LOFC) accidents, natural circulation flow between vessels is inhibited, thus limiting the potential for damage to the balance-of-plant (BOP) components. The water-cooled RCCS surrounding the reactor vessel provides adequate cooling to prevent fuel and vessel damage if no active primary cooling systems are operable. The RCCS reverts to the boiling mode in a long-term accident if no forced cooling is available.

3.4.6.3. Model Development

Details of the models used in MORECA are given in [1] and [2]. The 3D, hexagonal geometry core model uses one node each for the 84 fuel and 175 reflector elements in each of 14 axial regions for the 600MW(t) core. The annular fuel core representation (259 X 14 = 3626nodes, including the central and side reflectors) thus allows for detailed investigations of azimuthal temperature asymmetries in addition to axial and radial profiles. Variable core

thermal properties are computed functions of temperature and are dependent on orientation and radiation damage. An optional annealing model for graphite accounts for the increase in thermal conductivity that may occur during heatup accidents. Power peaking factors were derived from the data given in the benchmark problem description (Table 4-0) and converted to R-Z geometry. They are used for both at-power and afterheat power distribution.

The model for the water-cooled RCCS was derived directly from that used for the ORNL CRP-3 analysis of the HTTR-RCCS mockup experiment data. No modeling details of the water-side panel are included, only a mean temperature estimate for the panel. Cases for which the panel cooling water supply fails during an accident and the boiling mode is used are also accommodated.

The primary coolant flow models cover the full ranges expected in both normal operation and accidents, including pressurized and depressurized accidents (and in between) for forced and natural circulation, for upflow and downflow, and for turbulent, laminar, and transition flow regimes. The primary loop pressure calculation is suspended in this exercise match to the simplified benchmark problem specification. In the benchmarks, the primary pressure is assumed constant for the duration of the pressurized loss of forced convection (LOFC) accidents, and it is assumed to ramp down to atmospheric pressure for the depressurization LOFC's.

The model for the reactor pressure vessel includes 4 azimuthal quadrants in addition to axial sections to allow for representation of design discontinuities and partial failures in the RCCS cooling function.

3.4.6.4. Benchmark Calculation Results - Steady State

The steady state MORECA predictions for 100% power (600MW) operation are given in the table below. All temperatures are within the design limits as we understand them.

Core Temperatures:
The model for the active annular core divides it into three concentric radial rings X10 axial nodes.

Temperatures (°C) are listed for inlet to outlet for the ten axial nodes:

Inner Ring:									
572	640	703	758	829	870	903	940	956	954
Middle Ring:									
570	636	698	752	821	861	893	929	945	944
Outer Ring:									
561	618	673	721	782	817	846	878	891	889

Vessel Temperatures (°C):	
Top Head:	220
Upper Plenum area:	199
Core area:	234 – 355
Lower Plenum area:	297

RCCS:
Average cooling water temperature: 65°C
Power Removed: 1.88 MW
Convection heating: 11% of total

The power removed by the RCCS was found to be sensitive to the amount of leakage of

the core inlet flow assumed between the vessel and core barrel (shell). In the reference case, the flow was assumed to be nil (0.1%). For the case of a small leakage (1%), the RCCS power increased 37% to 2.58MW, and for a large leakage (10%), it was more than double the reference case (3.93MW).

In the reference case, the fraction of flow bypassing the core fuel element channels was assumed to be 10%. Increasing that to 12.54% had only a minor effect on the predicted maximum fuel temperature (12°C higher)

3.4.6.5. BENCHMARK CALCULATION RESULTS - ACCIDENT CALCULATIONS

3.2.1.2.5. 3.4.6.5.1. LOFC with rapid depressurization and SCRAM

In the first transient, it is assumed that there is a rapid loss of forced convection (LOFC) accompanied by an immediate SCRAM and a ramp down of the primary pressure (in 30 min.). With only atmospheric pressure helium in the system, there is very little convective flow and the problem essentially becomes a core-conduction cooldown calculation. In the reference case run the annealing algorithm in MORECA for core conduction is not activated.

In the reference case calculation, which assumes that RCCS cooling water flow is maintained during the accident, the maximum core temperature peaks at 1552°C after 87h, while the active core average temperature peaks at about 1213°C (see Fig. 3-97). For the case where RCCS boiling occurs, using the OKBM estimate of boiling in the panel region at 140°C; the peak fuel temperature is unaffected. Figure 3-98 shows the afterheat power and the RCCS heat removal, indicating the crossover point occurring 2.5 days into the accident. The maximum vessel temperature for this accident peaks 420°C after 106h (Fig. 3-99). Another peak temperature of interest is that of the control rods located in the side reflector. For the reference case, this value is 1172°C.

Two sensitivity cases were also run. The first case run as a variation on the reference was with an increase in afterheat power of 10%, which is a typical representation of the uncertainty. For this case, the predicted peak fuel temperature was 98°C higher than the reference value, 50°C above the nominal 1600°C limit. In a second case, the increased afterheat was run in combination with the core annealing model, giving a peak fuel temperature of 1527°C, comfortably below the limit, however, the control rod peak temperature increased to 1247°C, perhaps a concern, depending on the material used.

3.2.1.2.6. 3.4.6.5.2. LOFC with SCRAM, at pressure

With the primary pressure maintained at the normal operating level, it is assumed that there is a rapid LOFC and scram. In this case, the convection flows within the core are large, and the resulting recirculation carries heat to the top of the core and vessel. The peak in the maximum core temperature curve is small compared to the depressurized LOFC case, and appears very early in the transient (see Fig. 3-100). For the afterheat vs. RCCS power comparison (Fig. 3-101), note that the crossover occurs much earlier (1 day). The peak vessel temperature is higher in this accident than in the depressurized case, approaching 553°C after about two days (Fig. 3-99).

3.4.6.6. Conclusions

In neither of the benchmark accidents reference cases do any of the peak temperatures exceed the design limits. Additional sensitivity studies would be advisable to revisit these analyses when more details of the design are established.

REFERENCES TO SECTION 3.4.6.

[1] S. J. Ball, MORECA: A Computer Code for Simulating Modular High-Temperature Gas-Cooled Reactor Core Heatup Accidents, NUREG/CR-5712 (ORNL/TM-11823), Oak Ridge National Laboratory, October 1991.

[2] S. J. Ball and D. J. Nypaver, MORECA-2: Interactive Simulator for Modular High-Temperature Gas-Cooled Reactor Core Transients and Heatup Accidents with ATWS Options, NUREG/CR-5945 (ORNL/TM-12233), Oak Ridge National Laboratory, October 1992.

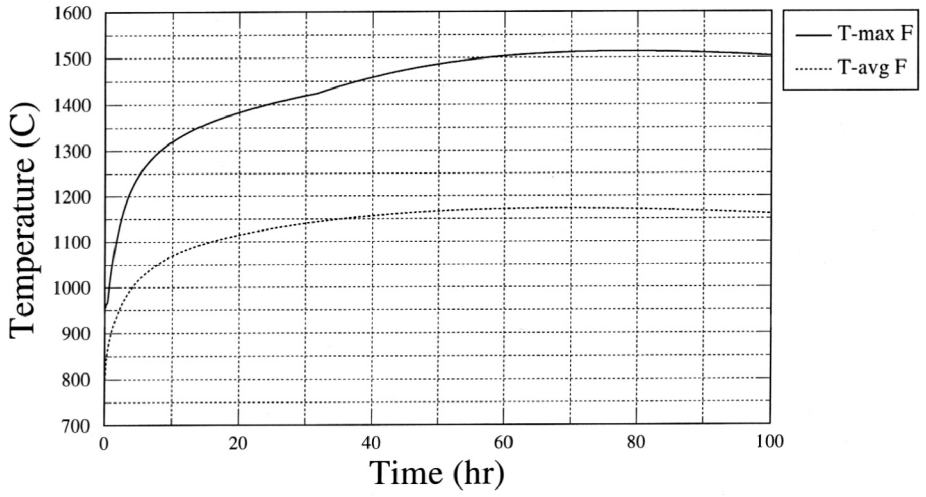

Fig. 3-97 GT-MHR-Pu Benchmark Problem, Depressurized LOFC with SCRAM, normal RCCS cooling: Maximum and average active core temperatures vs. time

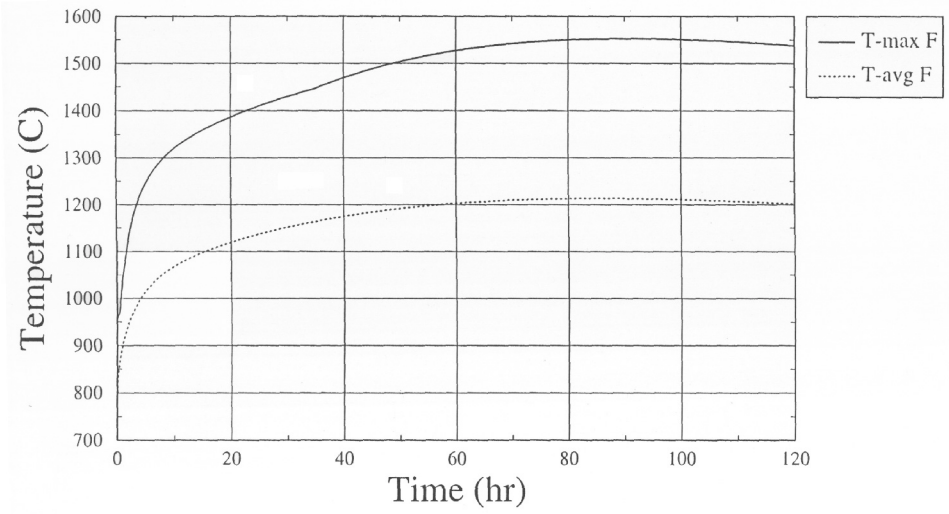

Fig. 3-98 GT-MHR-Pu Benchmark Problem, Depressurized LOFC with SCRAM, normal RCCS cooling: Afterheat and RCCS power vs. time

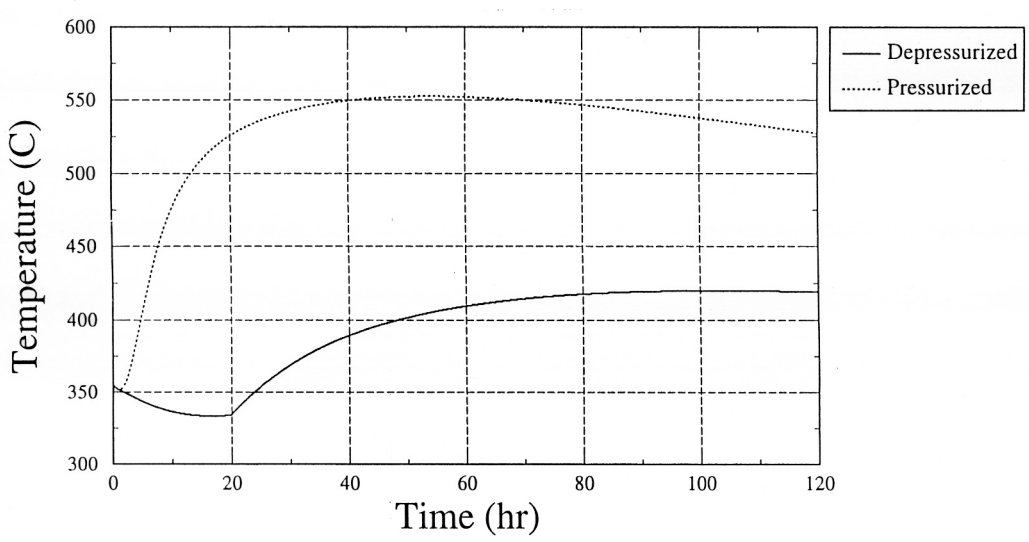

Fig. 3-99 GT-MHR-Pu Benchmark Problem, Depressurized and Pressurized LOFC with SCRAM, normal RCCS cooling: Maximum vessel temperatures vs. time

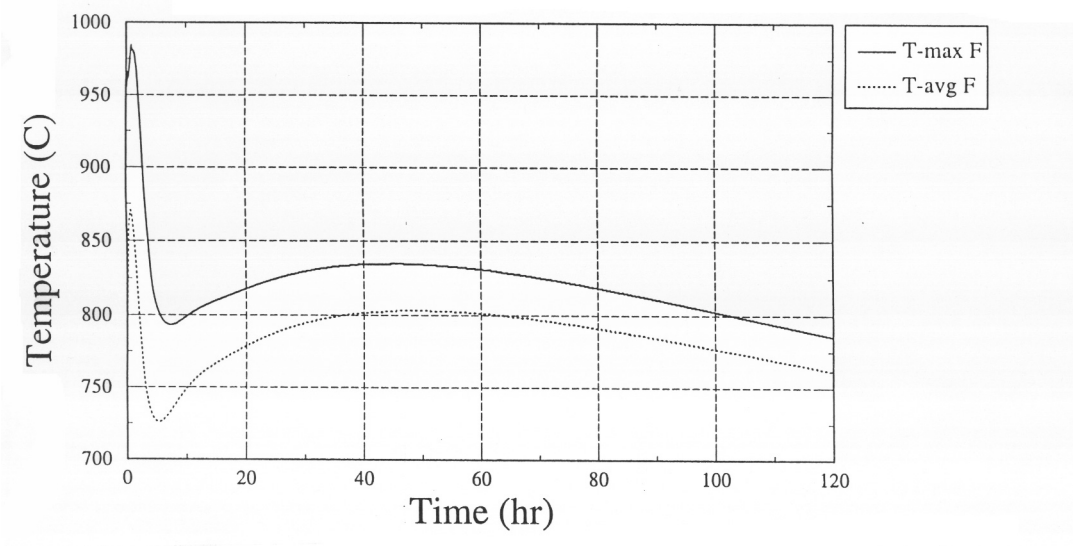

Fig. 3-100 GT-MHR-Pu Benchmark Problem, Pressurized LOFC with SCRAM, normal RCCS cooling: Maximum and average core temperature vs. time

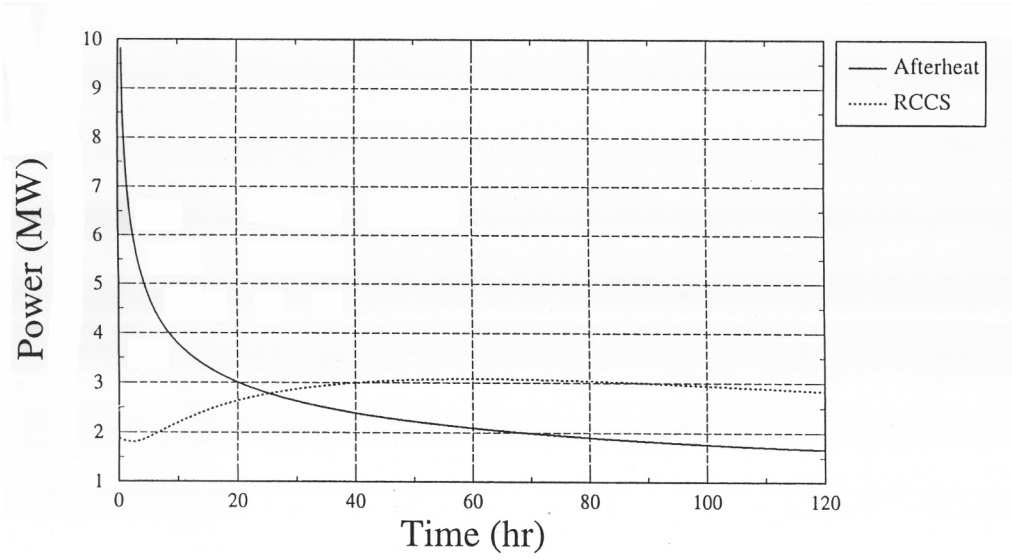

Fig. 3-101 GT-MHR-Pu Benchmark Problem, Pressurized LOFC with SCRAM, normal RCCS cooling: Afterheat and RCCS power vs. time

3.4.7. Comparison and Conclusions

3.4.7.1. Introduction

Two loss of forced circulation (LOFC) postulated accidents were selected as benchmarks for the GT-MHR-Pu, both assuming a scram and fast flow rampdown beginning at time = 0. In the first case, there is also a rapid depressurization (rampdown to atmospheric), while in the second, primary system pressure is assumed to remain constant. These two cases thus cover both the "core conduction cooldown," (when depressurized, the convection heat transfer terms in the core are nil) where the peak temperatures occur near the core beltline as well as the pressurized case, where strong convection flows within the core may tend to equalize core temperatures, and via buoyancy forces, cause higher temperatures near the top of the vessel.

Five countries participated in the benchmark using a wide variety of approaches and codes. France (CEA) used the CASTEM finite element code in a 2D axisymmetric analysis assuming a porous media model and using several tens of thousands of nodes.

Netherlands (ECN) used CFX-F3D, a Computational Fluid Dynamics (CFD) code with 29000 nodes, the k-epsilon model with radiative heat exchange via a Monte Carlo method, and 2D geometry with four equivalent core flow channels. Using just four channels, the modelling required artificial increases in heat transfer coefficients and core conductivities (times 11) to compensate for the smaller-than-actual heat transfer areas in the channels.

Russia (OKBM) used the GTAS code in a 2D porous media model. China (INET) used THERMIX/KONVEK in a 2D, 2000-node approximation. US (ORNL) analysis used MORECA, a 3D special purpose code for hexagonal geometry cores, 205 each 1D core flow channels, and about 4000 nodes.

3.4.7.2. Steady-State Results

Some variations in steady-state results gave different assumptions for accident starting points, and also indicated differences in calculated RCCS capacities. A summary of these results is given in Table 3-54.

Vessel temperatures are very dependent on the insulation between the core and the vessel, and it is likely that the differences shown are mainly due to variations in "insulation modelling." In the US study, it was noted that the RCCS power was very sensitive to the amount of leakage of the core inlet flow assumed between the vessel and core barrel. For example, an increase from the reference value (0.1%) to 1% caused a 37% increase in RCCS power (to 2.58MW).

Table 3-54 Comparison of steady-state results

Country	RCCS Power (MW)	T-Fuel Max (□C)	T-Vessel Max (□C)
China	1.5	1098	367
France	-	1027	260
Netherlands	2.36	949	406
Russia	1.43	948	310
US	1.88	956	355

3.4.7.3. LOFC with scram and depressurization

The results of the participants are summarized in Table 3-55 using peak fuel and vessel temperatures as means of comparing outcomes. Although the spread in the predictions is rather large, with the exception of one estimate of peak vessel temperature (France, 605°C), all the

maximum temperatures were within the nominal design limits for accident conditions. One conservatism (for peak fuel temperature) in the reference model is the omission of core block thermal annealing that would in fact occur at the high temperatures experienced here. The resulting increase in core thermal conductivity would lead to lower predicted peak fuel temperatures, but on the other hand would cause the peak vessel temperatures to increase. High peak vessel temperature problems can usually be solved by judicious placement of insulation between the core and the inner surface of the vessel. While this would reduce the RCCS heat removal capacity somewhat, the designer can strike a balance so that the average vessel temperature is still high enough to reject enough heat to keep the fuel temperatures below limits. Peak vessel temperatures for this case occur near the core beltline. In selecting vessel insulation design strategies, it is important to note that to account for the pressurized LOFC case (next benchmark), additional insulation may be needed near the top of the vessel because of the buoyancy forces.

Table 3-55 Comparison of Results for LOFC with Scram and Depressurization*

Country	T-f Max (□C)	@t = (h)	T-v Max (□C)	@t = (h)
China	1590	87	389	97
France	1565	140	605	140
Netherlands	1371	42	463	85
Russia	1425	75	435	85
US	1552	87	420	106

*NOTE: Some values read from graphs.

3.4.7.4. LOFC with Scram and Constant Primary System Pressure

The results of the participants are summarized in Table 3-56, again using peak fuel and vessel temperatures to compare outcomes.

Table 3-56 Comparison of Results for LOFC with SCRAM and Constant Primary System Pressure*

Country**	T-f Max (□C)	@t = (h)	T-v Max (□C)	@t = (h)
China	1379	71	370	90
Netherlands	1256	8	407	75
Russia	1325	65	345	80
US	980	1	553	48

*NOTE: Some values read from graphs.

** France did not do this case, noting that the resulting convection flows „would require a 3-D solution.“

As in the previous benchmark case, there is a rather large spread in the resulting predictions. Because of the additional complexity of the natural circulating convection flows in the core, wider variations would be expected. All temperatures are within accident case design limits. The one lower peak core temperature (US 980°C) is probably because of the higher

circulating flows predicted by the MORECA modelling scheme. More investigation of these differences would be of interest; although in no case does the pressurized LOFC accident prediction lead to prohibitively high fuel temperatures.

3.4.7.5. Sensitivity Studies

Several sensitivity studies were done for the depressurized LOFC case. China and US both calculated the effects of increasing the afterheat power function by 10% (a common assumption for licensing studies). China noted a 115°C increase in peak fuel temperature vs. a 98°C increase for the US calculation. The combination of +10% afterheat and use of a core annealing algorithm that increased core thermal conductivity with increasing temperature led to a net decrease in peak fuel temperature of 25°C (US).

China and Russia both calculated the effect of a 25% decrease in core conductivity on peak fuel temperature, with estimates of +202°C (China) and 130°C (Russia). China, Russia, and US all saw a negligible effect on peak fuel temperature if the RCCS coolant temperature was assumed to be 140°C (in a boiling mode) vs. the reference case values of 65 - 90°C. For the case where metal emissivities were assumed to decrease 25% from their normal value of 0.8 (to 0.6), predicted effects on maximum vessel temperatures by China and Russia were very close (+62°C and +55°C).

3.4.7.6. Conclusions

This benchmark exercise showed that for LOFC accident calculations, the predicted peak responses can vary widely depending on what appear to be reasonable modelling alternative choices and various computational methods. It is likely that at least some of the differences in results are due to differences in modelling insulation and core thermal conductivity. While the code to experiment exercises in the HTTR RCCS mockup benchmarks could be resolved better by comparisons with the "correct answer," that option is not available in this case. Well-planned experiments to provide code-to-actual data comparison opportunities will be valuable in resolving some of the differences seen here.

CHAPTER 4

CODE TO EXPERIMENT BENCHMARK EXERCISES

4.1. HTTR RCCS MOCKUP

4.1.1. Description of the HTTR RCCS Mockup and Benchmark Data

4.1.1.1. Introduction

Gas Cooled Reactor (GCR) has inherent characteristics of negative reactivity coefficient and very slow time response during abnormal transients and accidents because of high heat capacity and low heat generation density in reactor core compared with Light Water Reactor. Future design of High Temperature Gas Cooled Reactor system will be based on passive safety technologies which are relevant for the inherent safety characteristics of GCR.

As decay heat is generated in the core region during accidents, reactor core and other part of the reactor system must be cooled and reactor must safely be shut down. One of the most important cooling systems expected to operate effectively during the accidents is vessel-cooling system (VCS) which surrounds the pressure vessel and removes decay heat. With the operation of VCS during accidents, decay heat would be removed mainly by natural convection and thermal radiation. Therefore, It will be important to obtain operating characteristics of VCS and to develop computer code to predict temperature transients of the reactor system precisely for effective design of VCS.

International Atomic Energy Agency (IAEA) Coordinated Research Program (CRP) on "Heat Transport and Afterheat Removal for Gas Cooled Reactors under Accident Conditions" started in January 1993. In the program, benchmark problems were proposed. Other objectives of the program should include:

– evidence of some design choices over others,

– indications of how the reactor vessel and VCS can be monitored during normal operation so that problems potentially affecting performance during an accident conditions can be detected.

Time response of the reactor internals during conduction cooldown accidents (one of the limiting accident conditions is referred to as a "conduction cooldown″ accident) is much slower than that for the heat removal process of the VCS. Therefore, if the temperature profiles are established for the reactor vessel, the calculation of cooling performance of the passive cooling system can be treated as a steady state problem. Therefore, experimental data of cooling performance of the cooling panel test apparatus (JAERI, Japan) investigating heat transfer performance of the cooling panel system was selected as the benchmark problem between computational codes and experimental data.

4.1.1.2. Characteristics of experimental apparatus

Schematic diagram of experimental apparatus is shown in Figs. 4-1 and 4-2. The apparatus mainly consists of a pressure vessel, gas supply, vacuum pump systems, water supply and cooling panels surrounding the pressure vessel.

Pressure vessel is composed of several parts: upper head, side shell, lower shell, legs and skirts. The upper head is connected to the side shell by a flange shown in Fig.4-2. The pressure vessel is supported by four legs. Four curved steel plates are fixed surrounding the legs as a skirt type support. Nineteen standpipes can be fixed on the upper head. There are four types of standpipes, two different diameters and two different length.

Cooling panels are divided into three parts, upper, side and lower cooling panels. Each cooling panel has 25, 88 and 12 cooling tubes, respectively. Cooling water is supplied from two water supply systems. Water and air can be circulated in the cooling panel. Surfaces of the cooling tubes and the pressure vessel were coated by black paint to unify thermal emissivity. The cooling panels were surrounded by insulation blanket, KAOWOOL (ceramic fiber insulator).

Six segments of electric heaters are installed vertically in the center of the pressure vessel. Each heater segment consists of helical nichrome coils wound around an annular ceramic block. There are blockages at the center of the ceramics blocks, therefore, there is no possibility of natural convection through the center region of the heater segments. Temperature of outer surface of the pressure vessel, the heater, the cooling tube, the insulator and gas are measured by cromel alumel sheathed thermocouples. Water temperature was measured by platinum resistance. For the measurement of gas temperature, radiation was prevented by setting a small plate in front of the thermocouple. Heat removed by the cooling panels is calculated from the enthalpy change of the cooling water.

In the experiment, pressure was varied from vacuum (1.3Pa) to 1.0Mpa. to investigate the effect of gas pressure on heat transfer characteristics. Helium and nitrogen gases are used in the experiments.

Main specifications of the apparatus are as follows:

1) Pressure Vessel

Height of the pressure vessel:	3000 mm
Inner diameter of the shell:	1000 mm
Thickness of the vessel:	12 mm
Radius of the upper shell:	500 mm
Lower head	
Configuration:	2:1 half ellipsoid
Longer radius:	500 mm
Shorter radius:	250 mm
Working fluid:	He, N_2
Pressure:	1.3Pa1.0Mpa

2) Electric heater

Height:	2000 mm
Diameter:	600 mm
Maximum temperature:	600 C
Maximum heat input:	100 kW
Maximum heat input of the segments	
No.1 heater segment:	7 kW
No.2-No.5 heater segments:	21 kW
No.6 heater segment:	7 kW
Heat transfer area of the segments	
No.1 heater segment:	0.283 m^2
No.2-No.5 heater segments:	0.848 m^2
No.6 heater segment:	0.135 m^2

3) Cooling panel

Outer diameter of cooling tube:	31.8 mm
Pitch of the cooling tubes:	60 mm
Maximum flow rate of water:	10 m^3/hour

Comparison of main features of the HTTR vessel cooling system with the out-of-pile test rig of this experiment is shown in Table 4-1. Thermal properties of the materials of the experimental apparatus are shown in Tables 4-2 and 4-3.

4.1.1.3- Experimental conditions of benchmark problems

Six experimental conditions are selected as benchmark problems. They are described as:

A) Pressure vessel without stand pipes cooled by water circulated in the cooling panel

- Vacuum inside the pressure vessel, 6 heater segments are on
- Helium gas inside the pressure vessel, 6 heater segments are on
- Nitrogen gas inside the pressure vessel, 6 heater segments are on

B) Pressure vessel with stand pipes

- Helium gas inside the pressure vessel cooled by water circulated in the cooling panel, 5 heater segments are on (No.5 heater segment is off),
- Helium gas inside the pressure vessel cooled by air circulated in the cooling panel, 5 heater segments are on (No.5 heater is off),
- Helium gas inside the pressure vessel, only No.6 heater segment is on (No.1~No.5 heaters are off). Two cases of experiment with different heat input were performed, (VI)-a and (VI)-b.

Table 4-0 Detailed condition of the experiments described above are shown as follows:

Benchmark Problem	(I)	(II)	(III)	(IV)	(V)	(VI)-a	(VI)-b
Item of gas		He	N_2	He	He	He	He
Pressure(MPa)	$1.3x10^{-6}$	0.73	1.1	0.47	0.64	0.96	0.98
Heat input							
Total input(kW)	13.14	28.79	93.93	77.54	29.71	2.58	7.99
heater segment							
No.1 (kW)	1.01	1.16	5.90	5.63	1.80	0	0
No.2	2.31	3.11	16.05	19.60	5.23	0	0
No.3	2.64	3.52	19.88	21.59	5.68	0	0
No.4	2.46	5.10	22.24	22.70	11.26	0	0
No.5	3.76	10.42	22.13	0	0	0	0
No.6	0.96	5.49	7.72	8.00	5.74	2.58	7.99
Cooling panel	Water	Water	Water	Water	Air	Air	Air
Stand pipes	No	No	No	With	With	With	With

4.1.1.4. Experimental results

Vertical distributions of temperature on components and heat fluxes of the heater segments are shown in Figs. 4-3 to 4-8. In all Figs. 4-3, first Fig. (a) shows schematic model of the pressure vessel, heater and surrounding cooling panel, second Fig. (b) shows vertical temperature distributions of heater, pressure vessel, cooling panel and insulator, the last Fig. (c) shows heat flux distribution on the heater segments.

Figure 4-3 shows the experimental results for the benchmark problem (I), Fig. 4-4 for the benchmark problem (II), Fig. 4-5 for the benchmark problem (III), Fig. 4-6 for the benchmark problem (IV), Figs, 4-7 and 4-8 for the benchmark problem (VI)(a) and (b), respectively.

Table 4-1 Comparison of main features of The HTTR VCS System with the present experimental apparatus

Item	Present apparatus	HTTR
Pressure Vessel		
Height / Diameter	3 m / 1m	13.2m / 5.7m
Temperature	450 C	450 C
Reactor Core (Heater)		
Height / Diameter	2 m / 0.6 m	8 m / 4.3 m
Temperature	600C	860C
Heat Flux (of Decay Heat)	25kW/m^2	17.5kW/m^2
Total Heat (of Decay Heat)	100kW	2400kW
Water Cooling Panel		
Height / Width	3.4m / 2.9m	14.7 m / 8.5 m
Pitch of water tube	60 mm	60 mm
Flow rate of water	10 t/h	90 t/h

4.1.1.5. Material Data

Table 4-2 Conductivities of Materials

Material \Temperature T [K]	300	400	500	600	800	1000
Stainless Steel (SUS304)						
Pressure vessel	14.9	16.7	18.3	19.7	22.6	25.4
Thermocouple holder						
Heater support						
Heater support plate						
Carbon Steel (C-Mn-Si)						
Cooling tubes	41.0	42.2	41.5	39.7	35.0	27.8
Carbon Steel (Plain Carbon)						
Legs	60.6	56.8	52.7	48.0	39.3	30.1
Skirt						
Ceramics (Al_2O_3 Heater block)		36.0		20.2		10.4

Unit: [W/mK]

Table 4-3 Emissivities of materials

Components Temperature T [C]		149	260	538	816	
T [K]		422	533	811	1089	Correlation function
Pressure vessel						
Stainless steel (SUS304)	0.07	0.08	0.10	–	$0.0385+7.612\times10^{-5}T$	
Polished						
Oxidized			0.79	0.79	0.79	– 0.79
Electric heater						
Nichrome Polished	0.66	0.67	0.71	–	$0.603+1.315\times10^{-4}T$	
Oxidized	0.96	0.97	0.98	–	$0.941+4.844\times10^{-5}T$	
Ceramics (Al_2O_3)	0.93	0.93	0.67	0.44	0.93 (T<533[K]) $1.395-8.813\times10^{-4}T$ (T>533[K])	

Unit: [–]

We recommend the value of 0.95 for the emissivity of the black paint which is put on the surface of the pressure vessel and water/air cooling tubes.

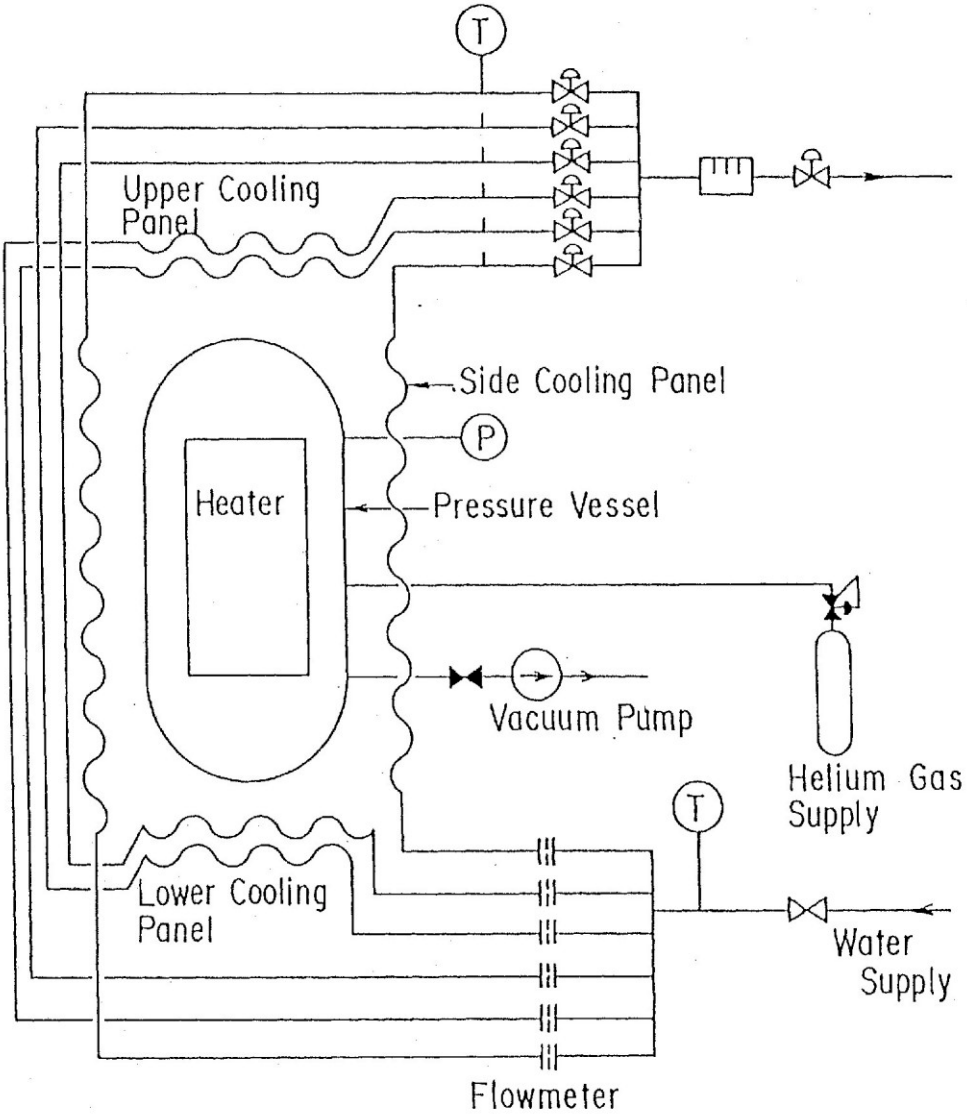

Fig. 4-1 Schematic Diagram Test Apparatus

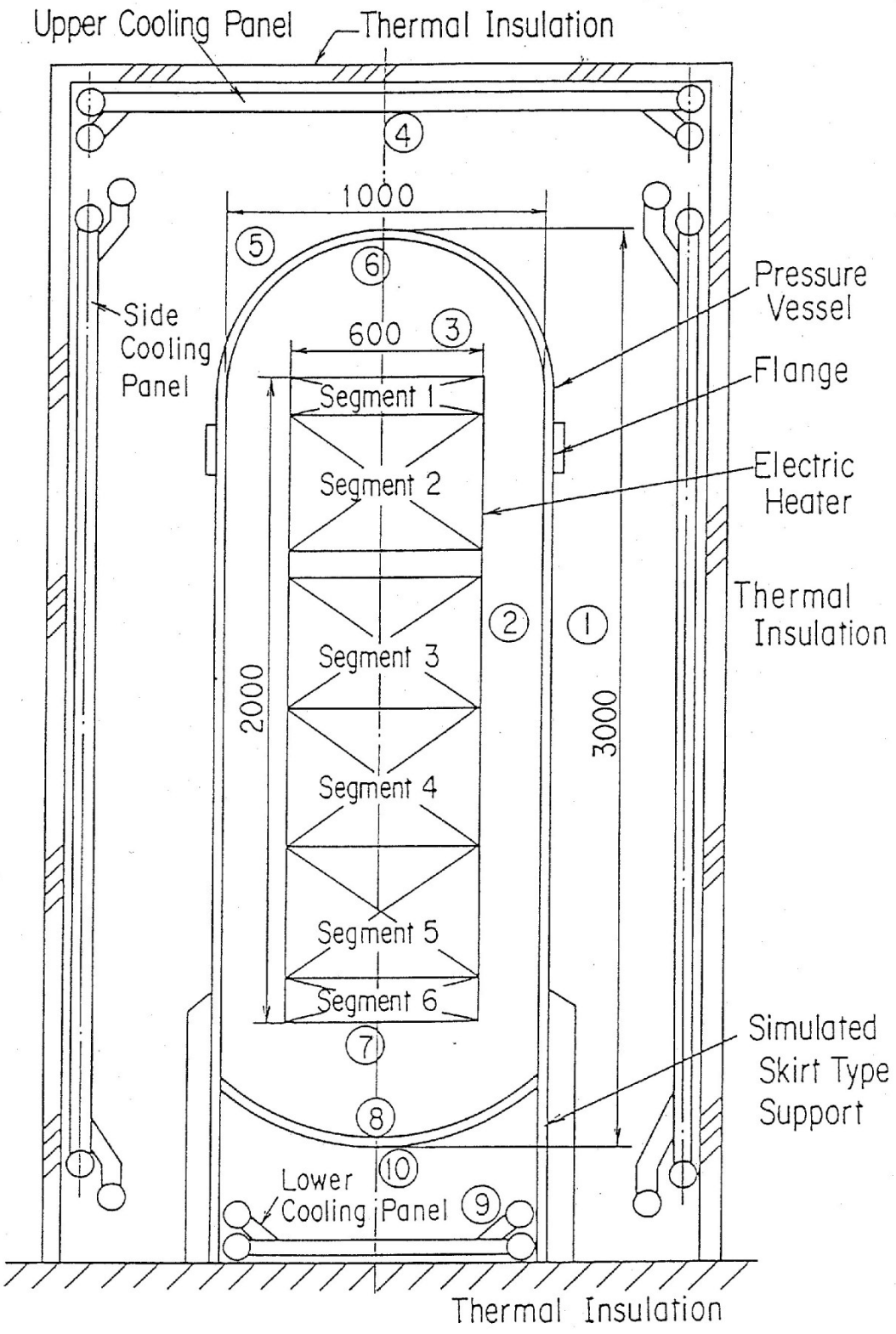

Fig. 4-2 Schematic Diagram of Pressure Vessel and Surrounding Cooling Panel

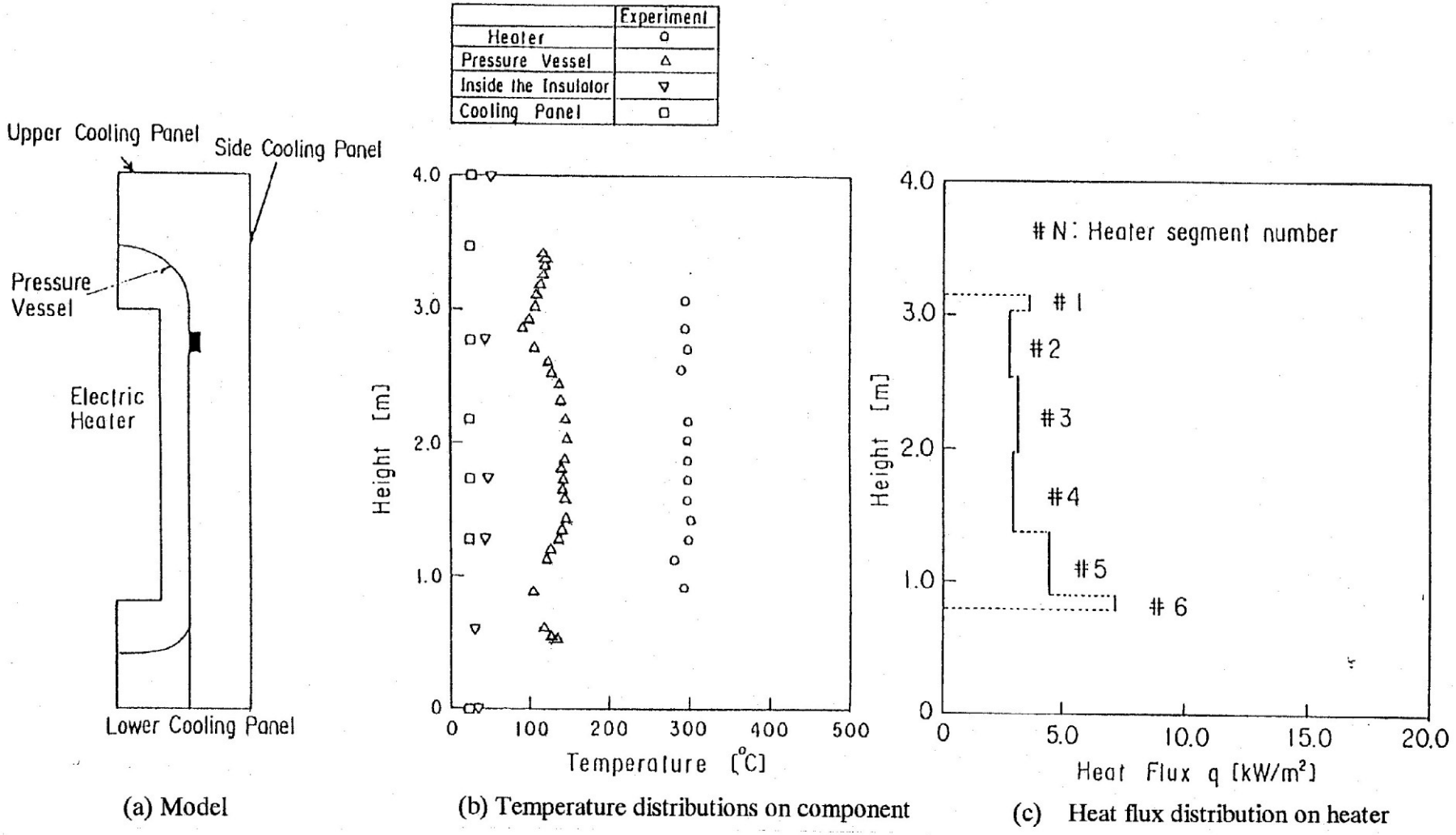

Fig. 4-3 Experimental Results of Benchmark Problem I

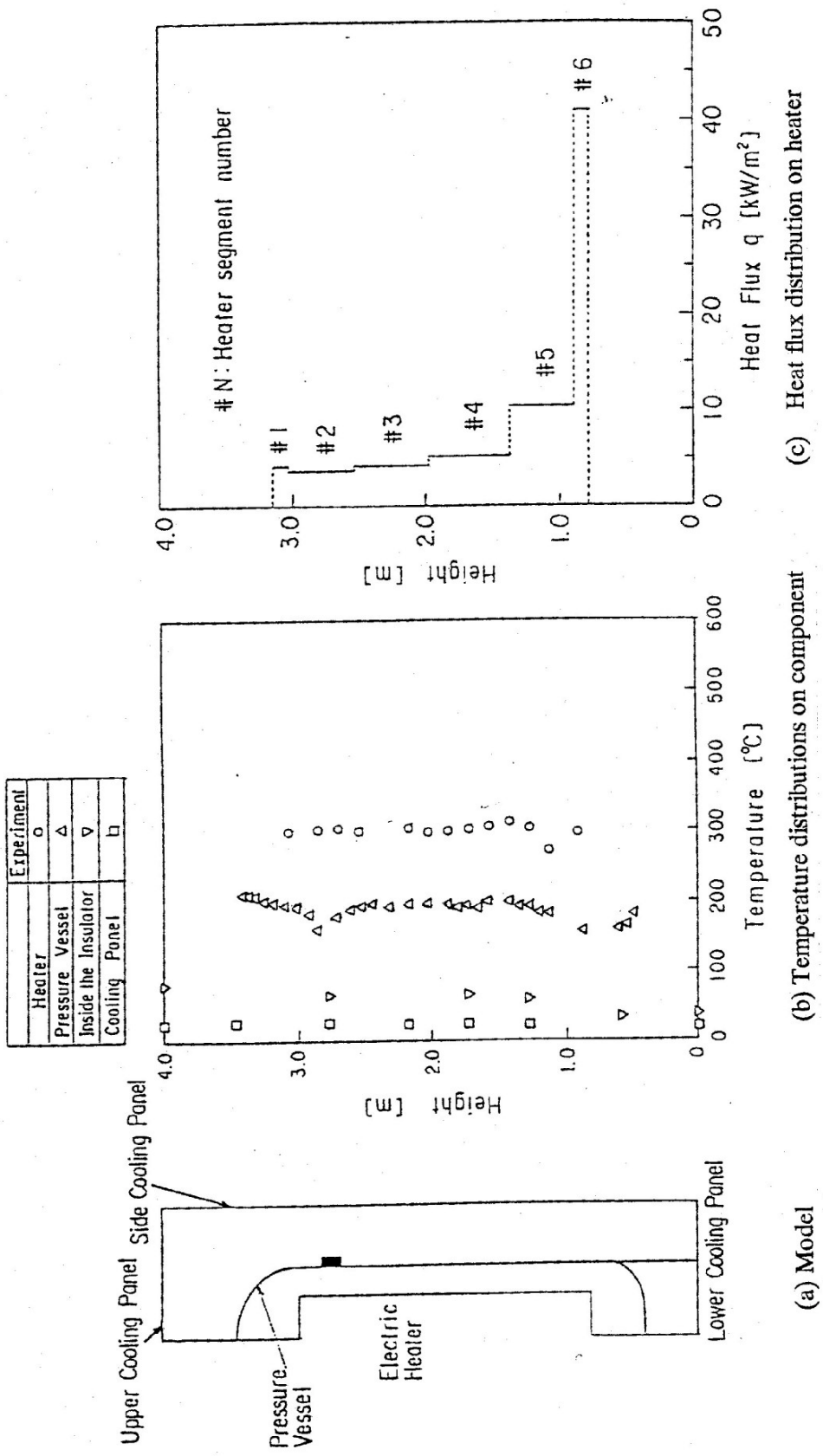

Fig. 4-4 Experimental Results of Benchmark Problem II

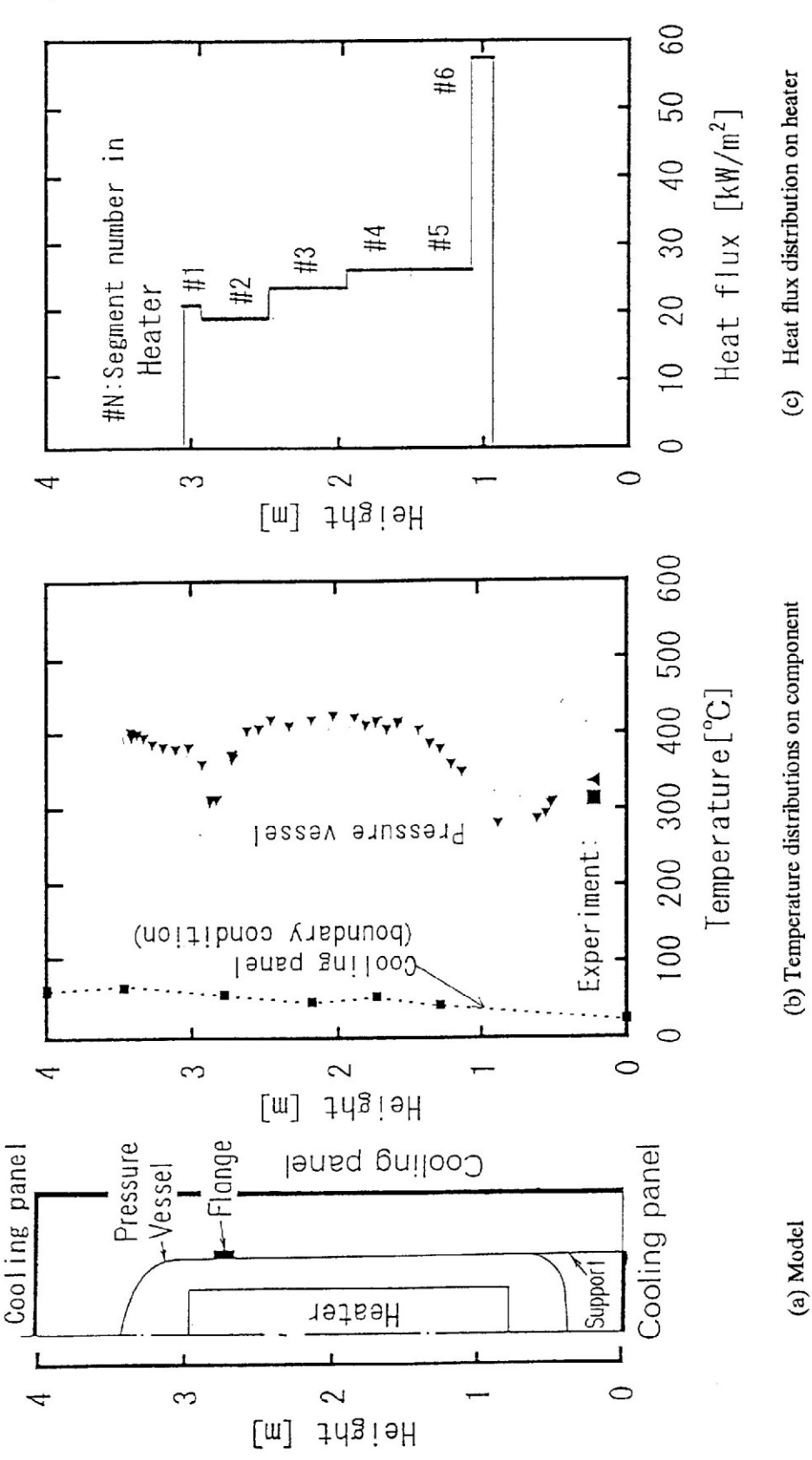

Fig. 4-5 Experimental Results of Benchmark Problem III

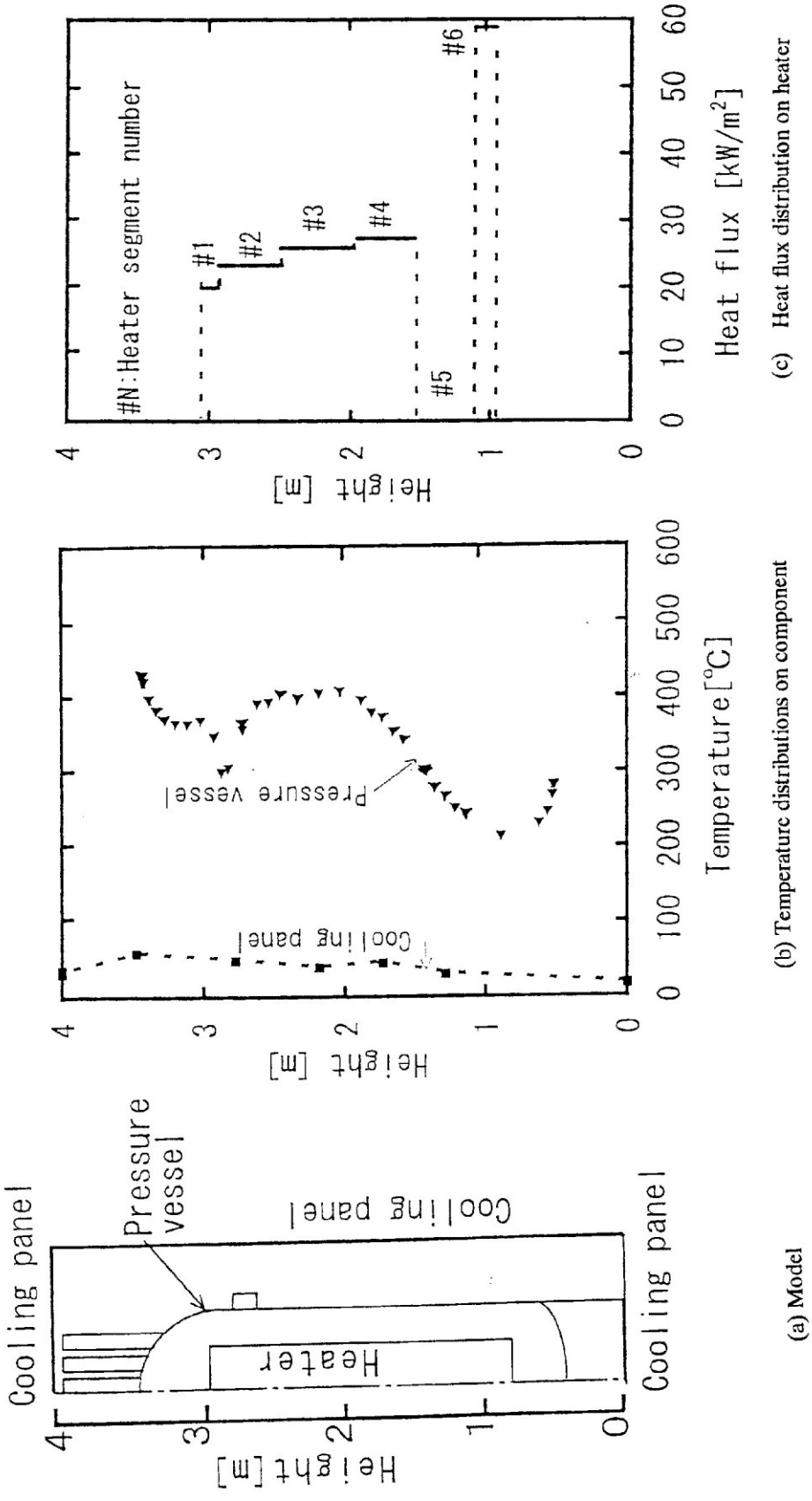

Fig. 4-6 Experimental Results of Benchmark Problem IV

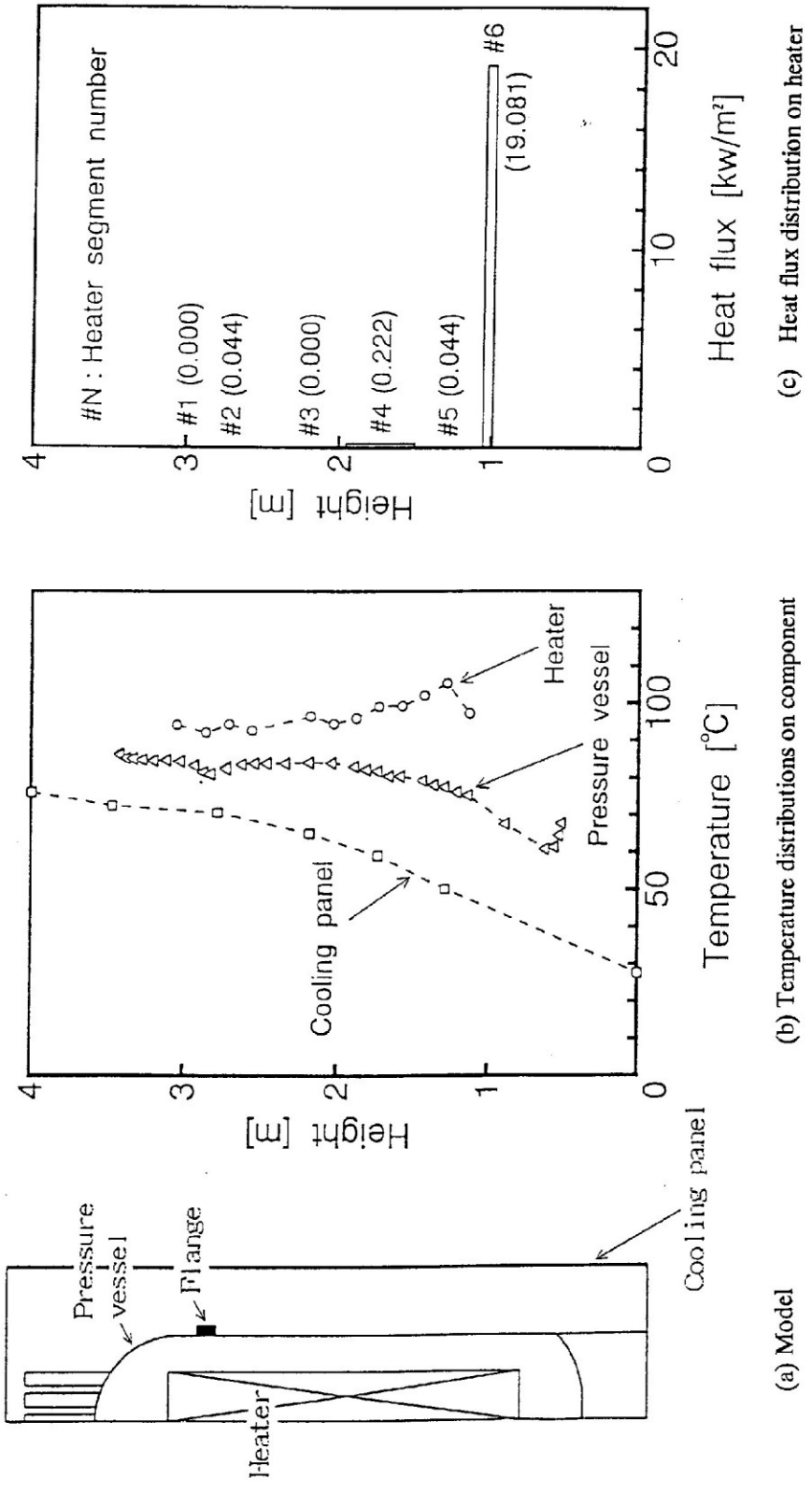

Fig. 4-7 Experimental Results of Benchmark Problem VIa

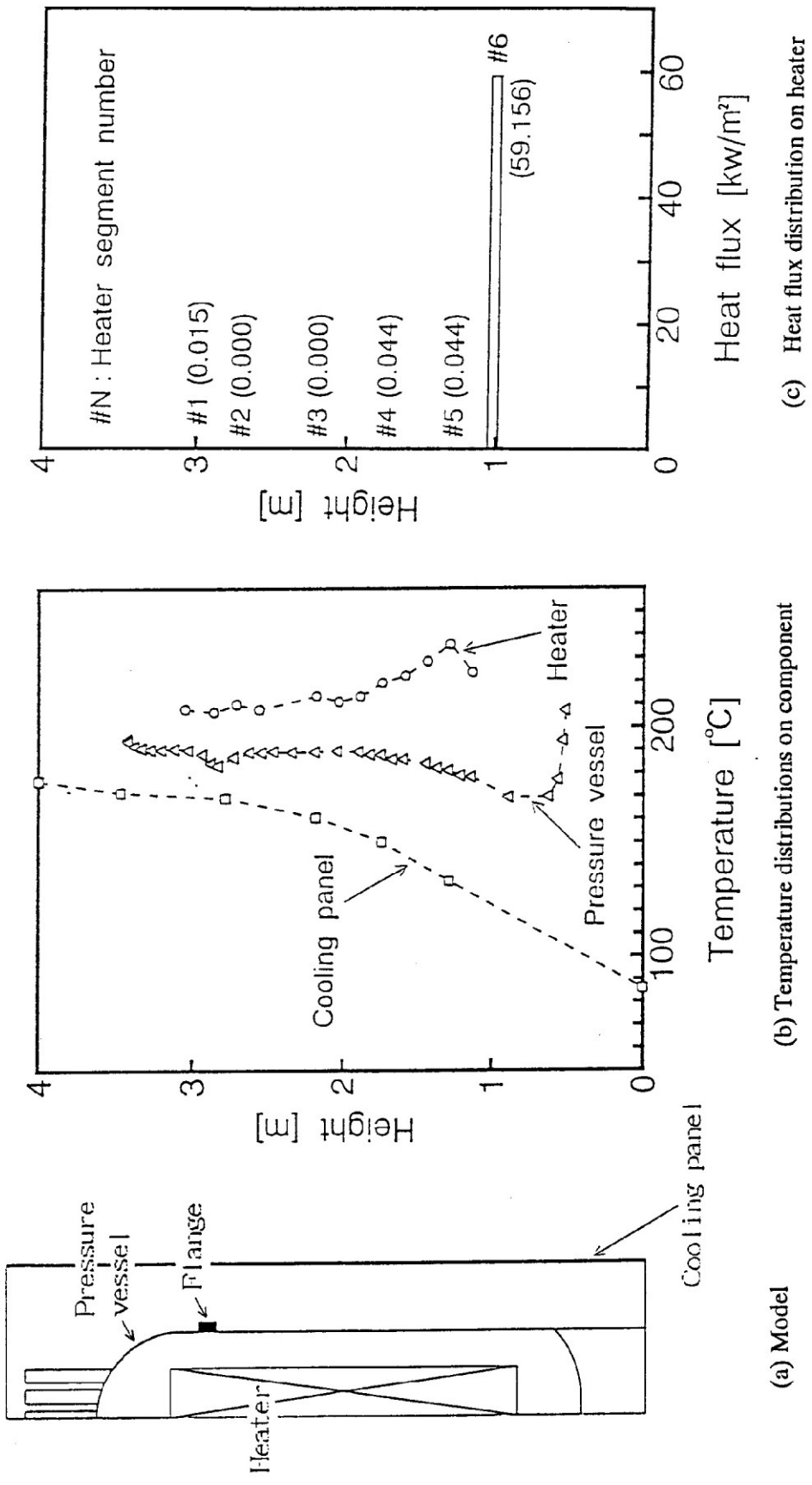

Fig. 4-8 Experimental Results of Benchmark Problem VIb

4.1.2. Results of Simulation of the HTTR RCCS Mockup with the TRIO-EF CASTEM 2000 Code

4.1.2.1. Introduction

The CEA contribution is concerned with the application of general flow codes to the JAERI reactor cavity cooling system experiment.

The decay heat removal system of modular high temperature reactor acts in a passive way, through conduction, radiation heat transfer and natural convection.

The complexity of the system geometry necessitates that the computer models used for performance analysis must be simplified and cannot represent all the details and all the phenomena of the overall system. As an example, natural convection is generally represented by heat transfer correlation, and not calculated directly by resolution of Navier Stokes equations.

This approach, which is profitable for system analysis codes (in terms of simplification, parametric studies and time consumption) must be validated and justified, according to the keyrole of the decay heat removal system.

The decay heat removal is based on the capacity of the core components (fuel particles and graphite) to accept temperatures up to 1600°C without damage, but the surrounding structures (internal components, pressure vessel) are metallic and must be protected against too high temperature resulting from heat transport from the core.

Only general flow codes, including convection, radiation and conduction transports can handle such a complicated situation and provide the necessary detailed information on local flow and resulting temperatures and justify the approximations and simplification used in system analysis codes.

The test configuration, boundary conditions and instrumentation of the JAERI HTTR RCCS test constitutes an excellent basis for this approach.

4.1.2.2. MODEL

4.1.2.2.1. Code

The code TRIO-EF CASTEM 2000 used for the calculation is a 3D flow, conduction and radiation heat transfer code. It uses a finite element method to solve :

– 3D Navier Stokes equations,

– 3D turbulent flow in using K-E or K-L model,

– 3D conduction,

– 3D radiation heat transfer in gray enclosures with hidden parts,

– Detailed informations on the code are given in the appendix 1.

4.1.2.2.2. Geometry and mesh

The description of the JAERI RCCS test is given in Chapter 4.1.1.

The model is based on a 2D axisymmetric geometry, according to the following considerations :

– the geometry of the test facility is axisymmetric, except in the region of the supporting structures of heating elements and pressure vessel.

– the test results (temperature of structures and gas) do not exhibit any major 3D effects and justify (a postierori) a 2D-approach.

For the two regions with 3D geometry, both the heater and pressure vessel supports are represented by an equivalent 2D-cylindrical skirt with adapted properties (heat conductivity, view factors, etc. ....) giving the same thermal behavior as the real geometry. A thermal resistance has been introduced between pressure vessel and support structure in order to take account of the constricted welding areas joining the support legs and the pressure vessel.

The final mesh results from a progressive approach, where the mesh has been iteratively refined in regions of interest (i.e.: boundary layer, large thermal gradient region, change in flow direction) without exceeding a too big number of nodes. The result is presented on Fig. 4-9 with:

– the heater and its six heating regions, the insulating material and the heater support,
– the internal space between heaters and pressure vessel filled with gas (nitrogen or helium),
– the pressure vessel,
– the external space between pressure vessel and cavity filled with ambient air,
– The total number of nodes is 4322.

After checking with JAERI, the initial mesh has been improved to offer a possible communication (for natural convection) between (see Fig. 4-10):

– cavity 1 and 2 (inside the pressure vessel) through the openings of the heater support
– cavity 3 and 4 (outside pressure vessel) through leak paths in the skirt surrounding the vessel support legs.

4.1.2.2.3. Physical model.

4.1.2.2.3.1. Basic assumptions

– Density effect is limited to volume forces (Business approximation),
– Natural convection is considered as laminar. In cavities, the transition from laminar to turbulent flow is characterized by a critical Rayleigh number calculated with the space width and the aspect ratio. The value of the Rayleigh number for the JAERI experiment is never up to $6.5*10^8$ and corresponds to the transition from laminar to turbulent (1). Moreover, the important thermal stratification existing in the cavities has a tendency to stabilize the natural convection and increases the transition laminar to turbulent (2) to a higher Rayleigh number value,
– For radiation heat transfer, the surfaces are diffuse-grey and the filling gas is a non participating-medium.

4.1.2.2.3.2. Material properties

They are provided by JAERI (see Chapter 4.1.1.).

4.1.2.2.3.3. Boundary conditions

– Heat flux is imposed on the six heating elements (input electrical power),
– In the reactor cavity, the section without cooling panels is considered as adiabatic and the sections with cooling panels are assumed to be at constant temperature (mean temperature of the cooling water).

4.1.2.3. Problems Considered

Only three tests have been retained for our calculations in the grid test realized by JAERI. They are all related to the problem « 1 » described in (Chapter 4.1.1.)

The three experiments are concerned with a vessel configuration without standpipes:

– Experiment n°1 « Vacuum conditions »: the helium pressure in the vessel is only 1.3 Pa and heat transfer from the heaters to the pressure vessel is mainly due to radiation and conduction. The reactor cavity is filled with ambient air,

– Experiment n° 2 « Helium gas conditions » with a helium pressure of 0.73 Mpa in the vessel which leads to a limited transport by natural convection flow inside the pressure vessel,

– Experiment n° 3 « Nitrogen gas conditions » with a nitrogen pressure of 1.1 Mpa in the vessel which induces an important natural convection flow inside the pressure vessel.

4.1.2.4. Results

4.1.2.4.1. Experiment 1(Vacuum conditions)

With a helium pressure of 1.1 pa, the natural convection is completely inhibited in the pressure vessel (the Rayleigh number is proportional to pressure^2), but conduction in gas cannot be neglected (according to the Knudsen number).

The main results are presented on Figs. 4-11 to 4-14

The velocity field in the reactor cavity (Fig. 4-11) is a typical natural convection boundary layer flow with ascending flow along the pressure vessel and descending boundary layer along the cooling panels. A by pass flow is induced by buoyancy forces in the cavity under the pressure vessel: it contributes to remove heat by convection from the bottom of the pressure vessel.

Isotherms in the reactor cavity are shown on Fig. 4-12. A large thermal stratification occurs in the cavity bulk due to convective transport. On the bottom head of the pressure vessel, the large temperature gradient in the gas (in the vicinity of the wall) is a consequence of the limited convective flow in this region.

Figure 4-13 shows a comparison of measured and calculated vessel temperatures versus the curvilinear abscissa (origin at the top of the vessel).

– The general shape of the temperature profile is respected, except in the flange region. This flange is not represented in our mesh .In the experiment, its act as a fin both for radiation and convection and the corresponding heat transfer is underestimated in the calculation,

– The calculated temperature is slightly above the measured one, except in the region of the lower head where temperature is strongly dependent upon the estimated leak path in the experiment,

– A discrepancy is also observed in the attachment area of the supporting legs where the local temperature is affected by the heat losses and its simplified representation in our model.

In the balance of heat transfer represented on Fig. 4-15, radiation is predominant and represents 79% of the total heat transfer. As shown on Fig. 4-14, the convective heat transfer is not constant along the wall. At the bottom of the vessel, the combination of cold air and hot wall induces a strong convective heat transfer which decreases at the top, according to the presence of hot air close to the vessel.

4.1.2.4.2. Experiment 2 (Helium conditions)

In this experiment, natural convection is modeled inside the pressure vessel.

The velocity field in the reactor cavity (Fig. 4-16) is similar to the previous experiment.

In the pressure vessel cavity, the flow regime (Fig 4-17) is also a boundary flow regime in the space between heaters and pressure vessel with a counter-flow cell above the top heater.

Isotherms in the two cavities are presented on Figs. 4-18 and 4-19.

In the reactor cavity, the thermal stratification is increased, as a consequence of the higher temperature of the pressure vessel.

In the internal cavity, an important temperature gradient appears under the bottom heater, due to the high level of the input power in this element (see experimental results) and the limited convection flow arising in this restricted area.

Figure 4-20 gives a comparison of measured and calculated vessel temperatures versus the curvilinear abscissa (origin at the top of the vessel).

– The general shape of the two curves are quite similar,
– The calculated temperatures are about 20°C up to the measured ones. This difference can be explained by the effective emissivity used for the calculation, which has been determined from the test by a post-calculation, and not directly measured,
– The previous remark referring to the lack of representivity of the flange region remains applicable.

In this experiment, the effect of natural convection inside the vessel and the coupling between internal (pressure vessel) and external (reactor cavity) natural convection becomes effective:

– The hottest bulk temperature of the helium in the internal cavity is observed in the region of the upper head, despite the fact that the heating power in this region is reduced.(Heat flux on the top heater is ten times less than on the bottom one). This is a direct consequence of heat transport by natural convection,
– The repartition of the convective heat flux along the pressure vessel (Fig. 4-21) is modified, and the external convective heat flux is improved at the top of the pressure vessel, according to the high level of wall temperature in this region, in comparison to the air temperature.

The resulting balance of heat fluxes (Fig. 4-22) shows that about 75% of the total heat flux leaving the pressure vessel is due to radiation.

4.1.2.4.3. Experiment 3 (Nitrogen conditions)

This experiment is characterized by:

– The high level of temperature of the heaters and pressure level,
– The use of nitrogen as filling gas in the pressure vessel. Nitrogen has a very low conductivity and a big density (in comparison to helium) and the natural convection effect will be improved in the inner cavity.

The velocity fields in the two cavities are shown on Figs. 4-23 and 4-24. The flow regime is still a boundary layer flow with high velocities in the upward boundary along the heaters.

Isotherms in the cavity are presented on Figs, 4-25 and 4-26. A large stratification is present in the cavities, with a difference of temperature up to 150°c from the bottom to the top.

The measured and calculated temperatures on the pressure vessel are plotted on Fig. 4-27.

In the central section, the agreement between model and experiment is good. The discrepancy is in the flange region is still present, due to the lack of representativity. But, large errors are recorded at the two extremities of the curve:

– the calculated lower head temperature is 100°C above the measure,

– the calculated upper head temperature is 70°c under the measure.

Such discrepancies must be attributed to the insufficiency of the convective transport from the bottom to the top of the vessel. This fact is certainly relevant to the use of a laminar model for convection, in a situation where local thermal instabilities can exist in the region of upper heater (due to destabilizing temperature gradient above the heater) and lower heater (due to accumulation of hot gas under the heater) and improve the convective heat transport by « turbulent bursts ».

The heat transfer balance (Fig. 4-27a) emphasizes the importance of radiation, which represents now 86% of the total heat flux on the pressure vessel.

4.1.2.5. Conclusions

The JAERI benchmark problems have provided an excellent data basis to validate decay heat removal model for modular high temperature reactor.

The model used for this validation is based on the utilization of a general thermal-hydraulic computer code, which offers the possibility of a complete model of the problem, with the description of the natural convection flow.

The pressurized tests (helium and nitrogen) are of great interest because they give the possibility to model the complete coupling of natural convection, conduction and radiation in two adjacent regions, which is a representative situation of the decay heat removal system of high temperature reactor.

The nitrogen test model has shown that, even with a radiation heat transfer accounting for more than 86% in the total heat transfer, the natural convection cannot be neglected and its contribution to heat transport should be taken into account.

REFERENCES TO SECTION 4.1.2.

[1] Heat Exchange Design Handbook- Paragraph 2-5-8-10. Hemisphere Publishing Corporation 1987

[2] Natural convection in enclosures-C.J.HOOGENDOOM-8th International Heat Transfer Conference-San Fransisco-USA-1986.

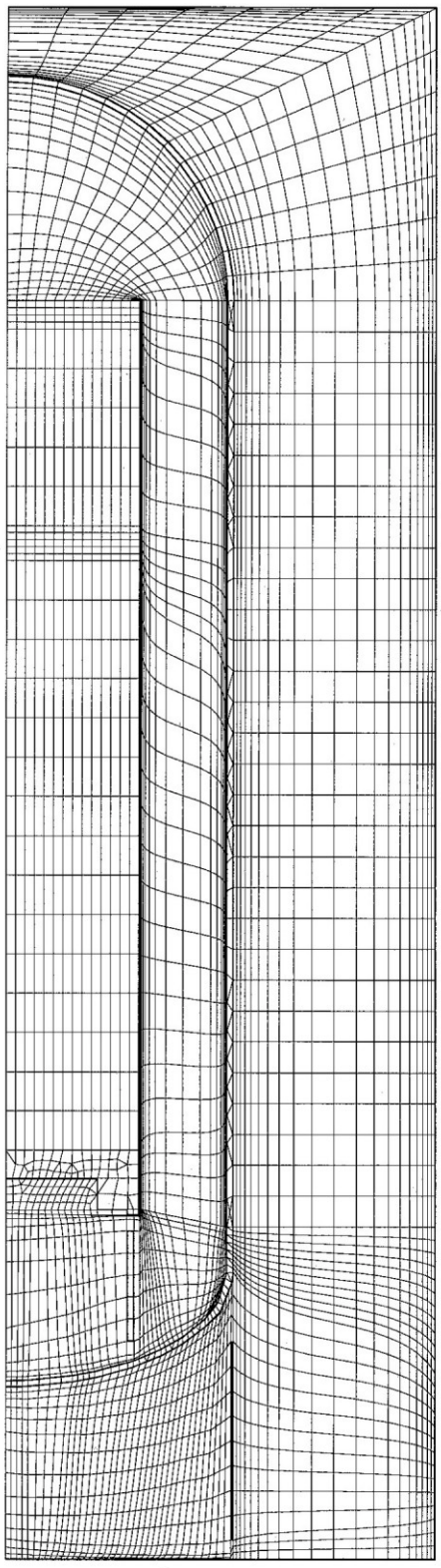

Fig. 4-9 JAERI Experiment Mesh

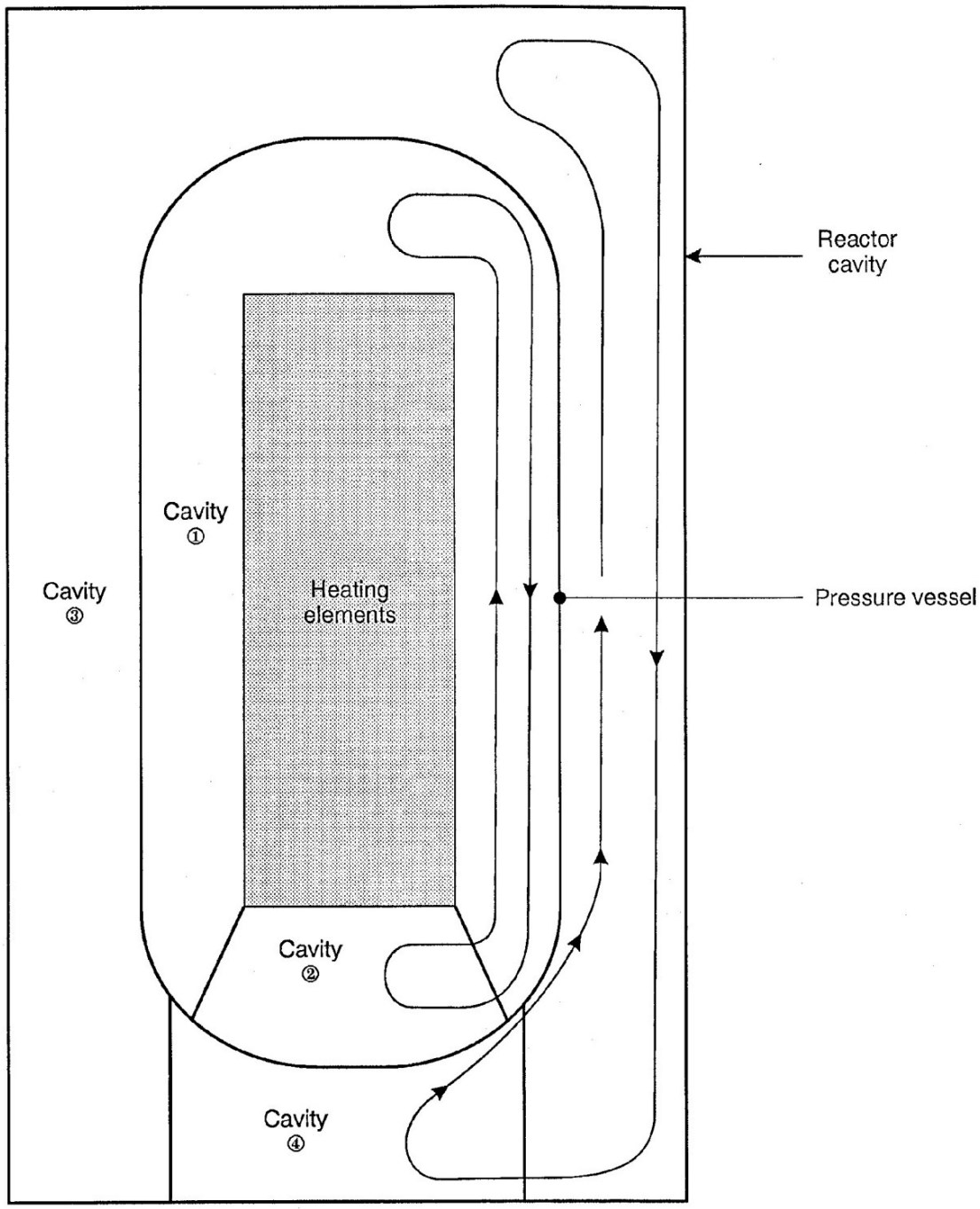

Fig. 4-10 Representation of the JAERI Experiment

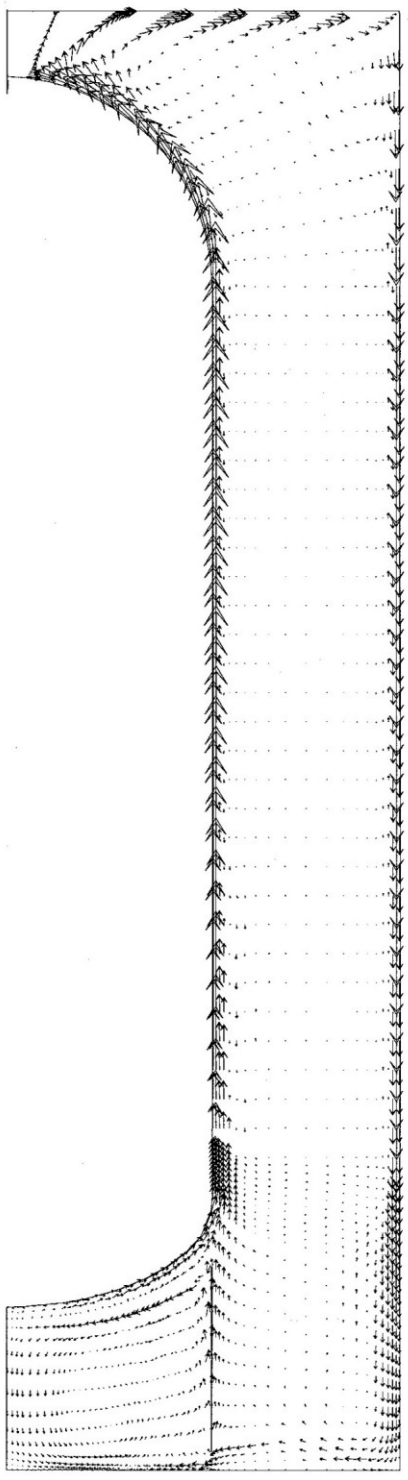

Fig. 4-11 External Cavity – Velocities
Experiment 1 Vacuum Conditions

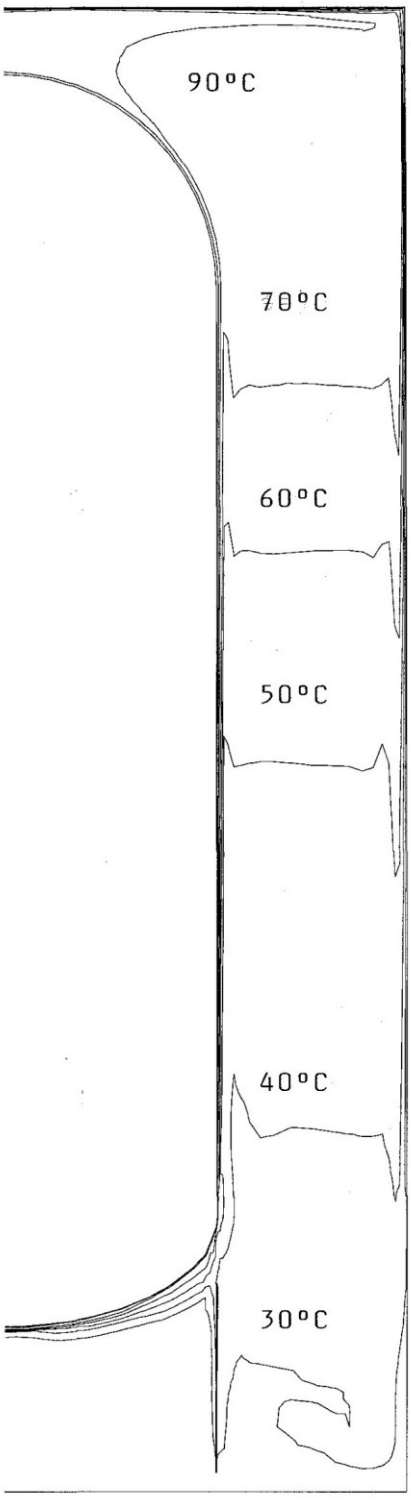

Fig. 4-12 External Cavity – Isotherm
Experiment 1- Vacuum Conditions

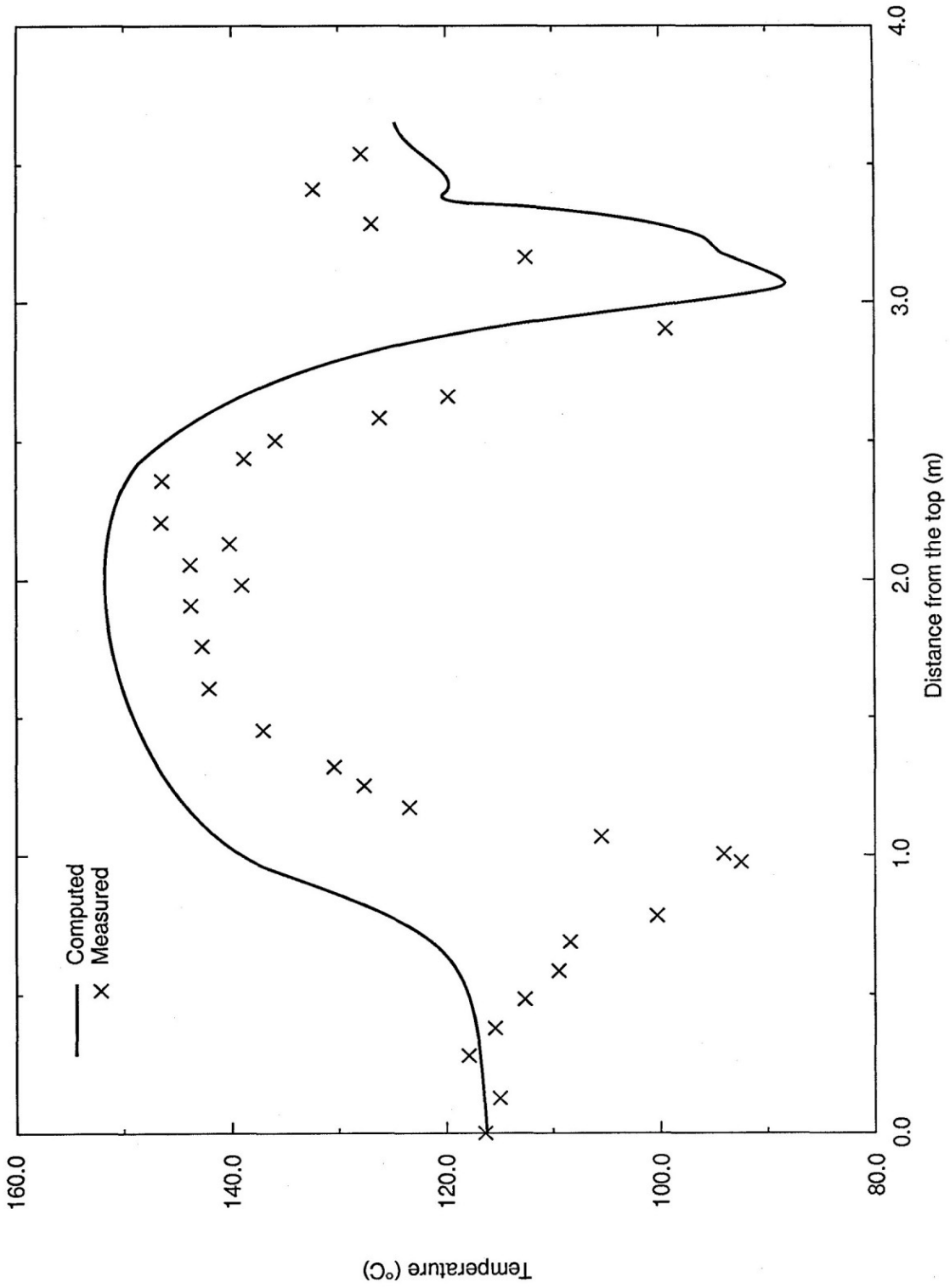

Fig. 4-13 Temperature along the pressure vessel
Experiment 1- Vacuum Conditions

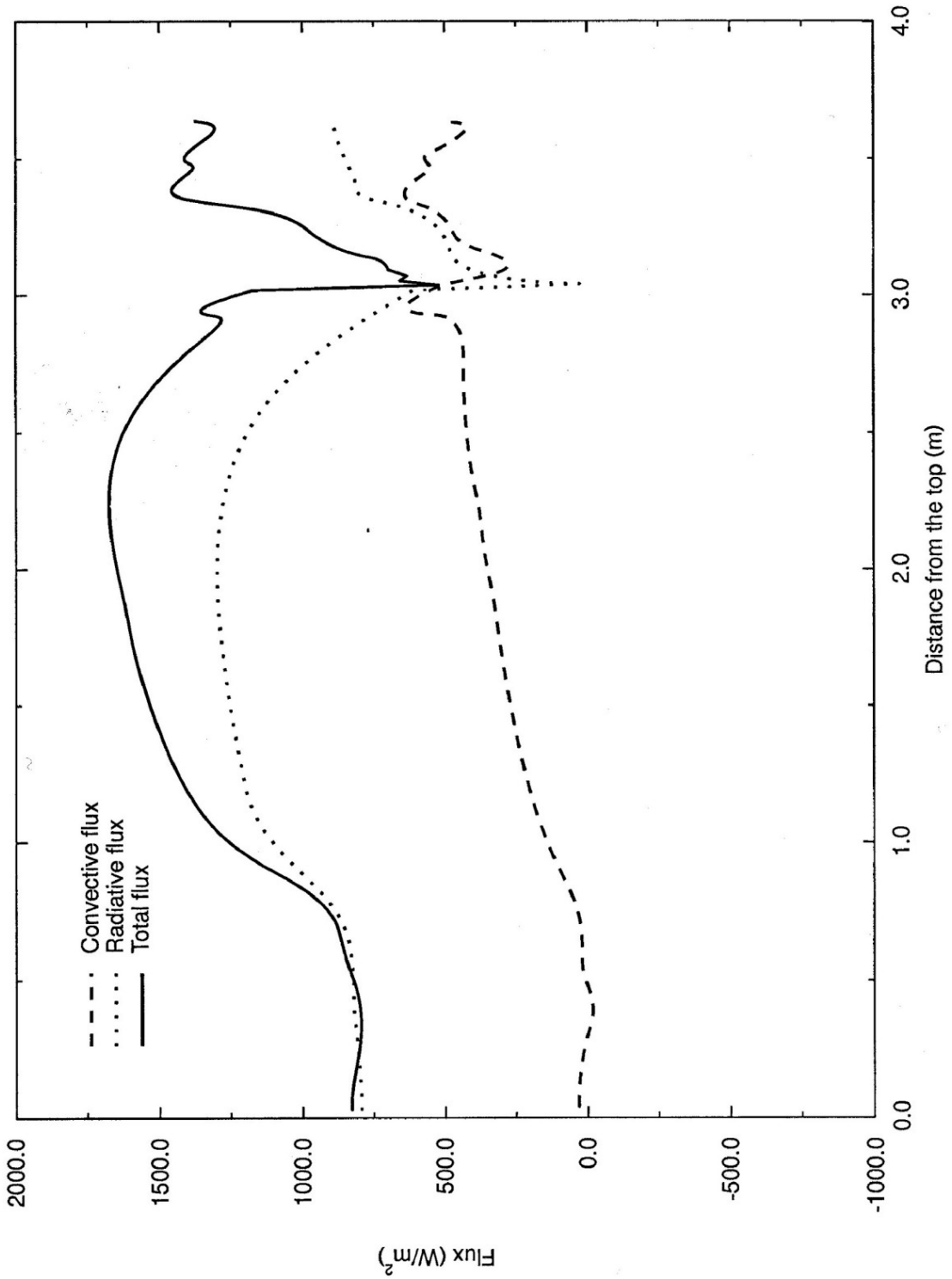

Fig. 4-14 Heat Fluxes along the pressure vessel
Experiment 1 – Vacuum conditions

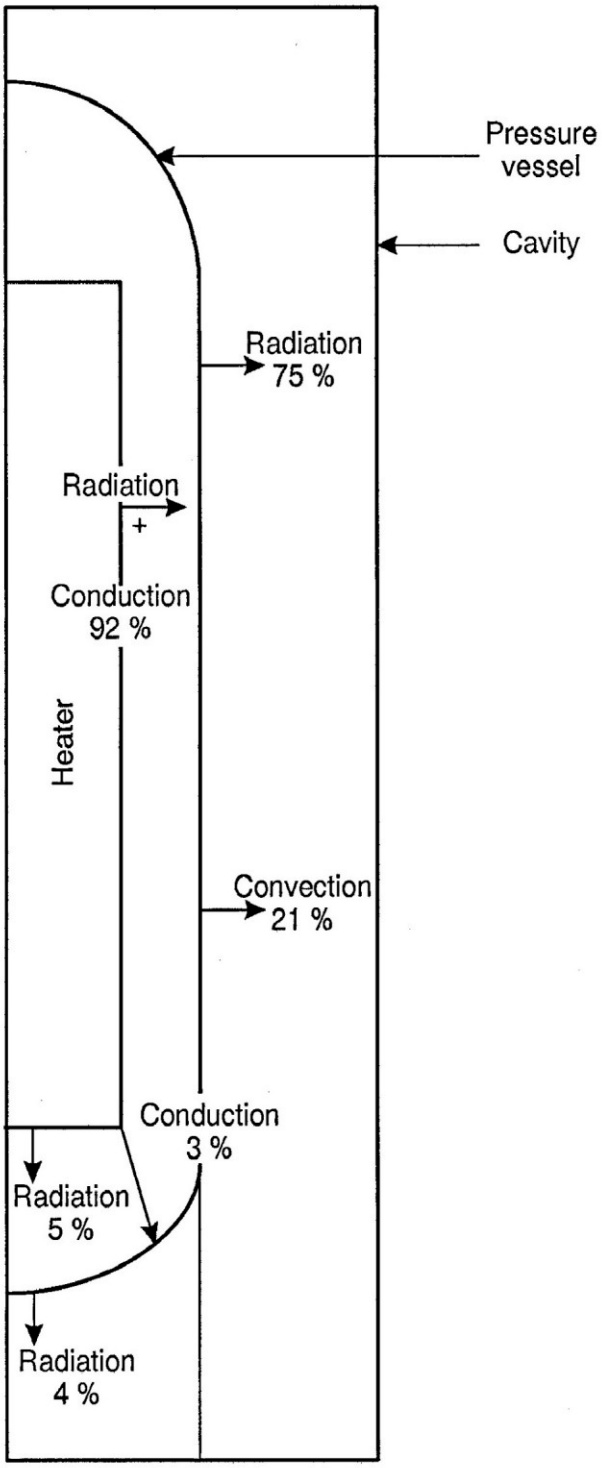

Fig. 4-15 Calculated heat balance
Experiment 1 – Vacuum conditions

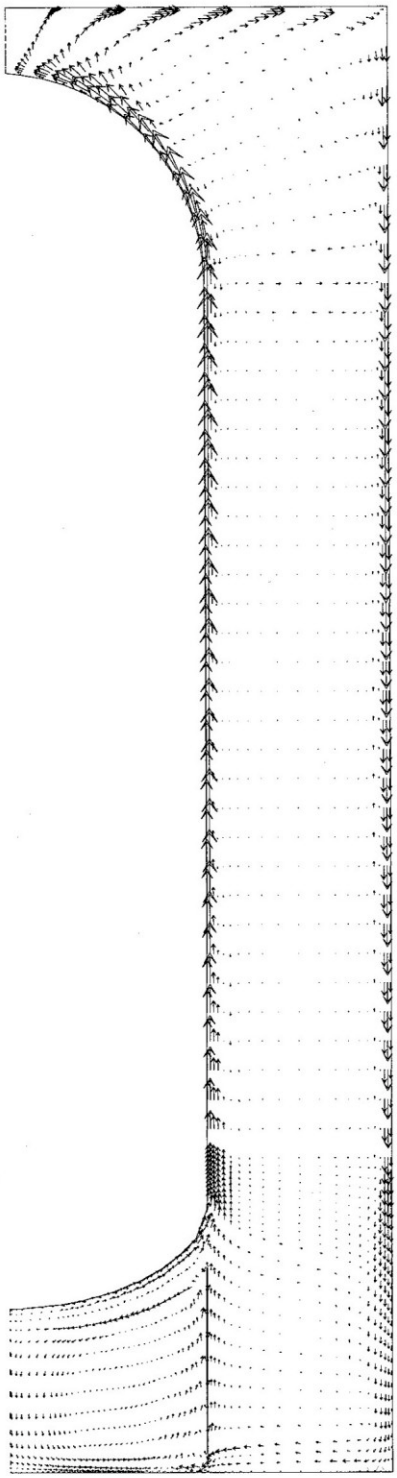

Fig. 4-16 External cavity – Velocities
Experiment 2 – Pressurized conditions
helium gas

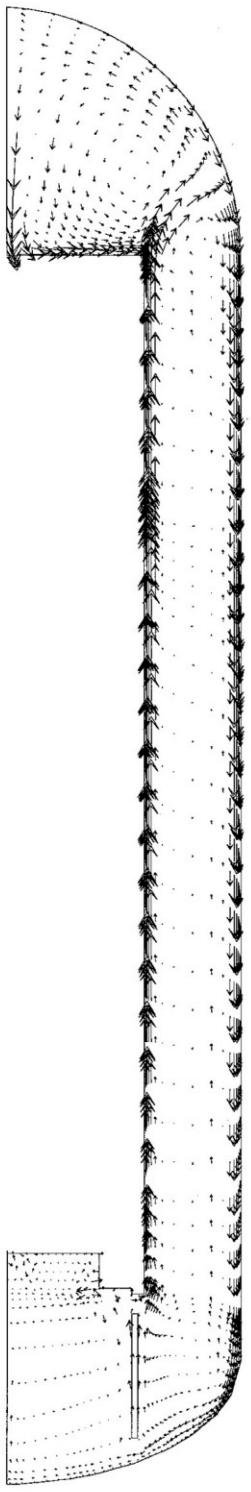

Fig. 4-17 Internal cavity – Velocities
Experiment 2 – presurized conditions
Helium gas

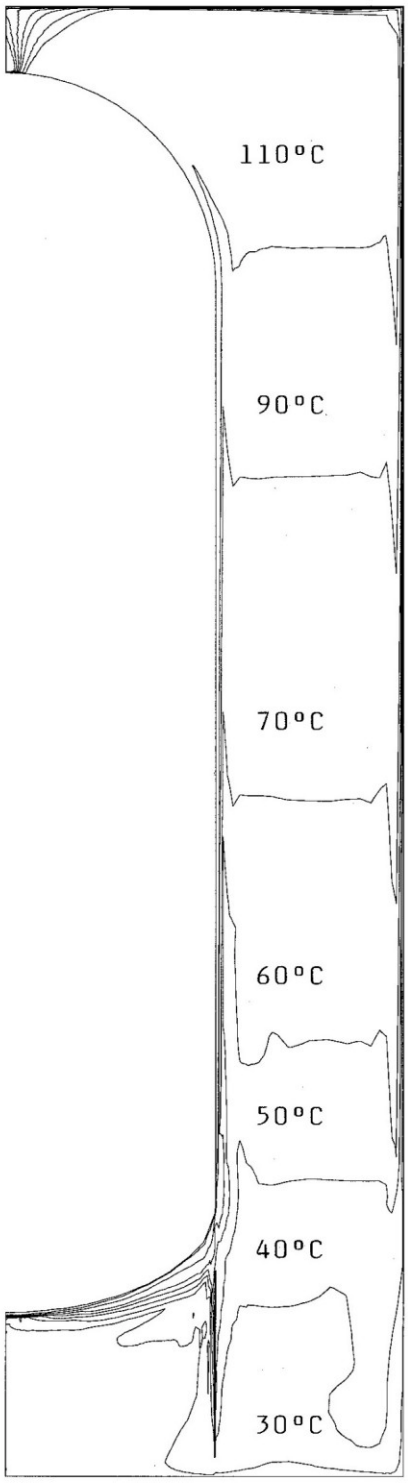

Fig. 4-18 External cavity – Isotherms
Experiment 2 – Pressurized
conditions helium gas

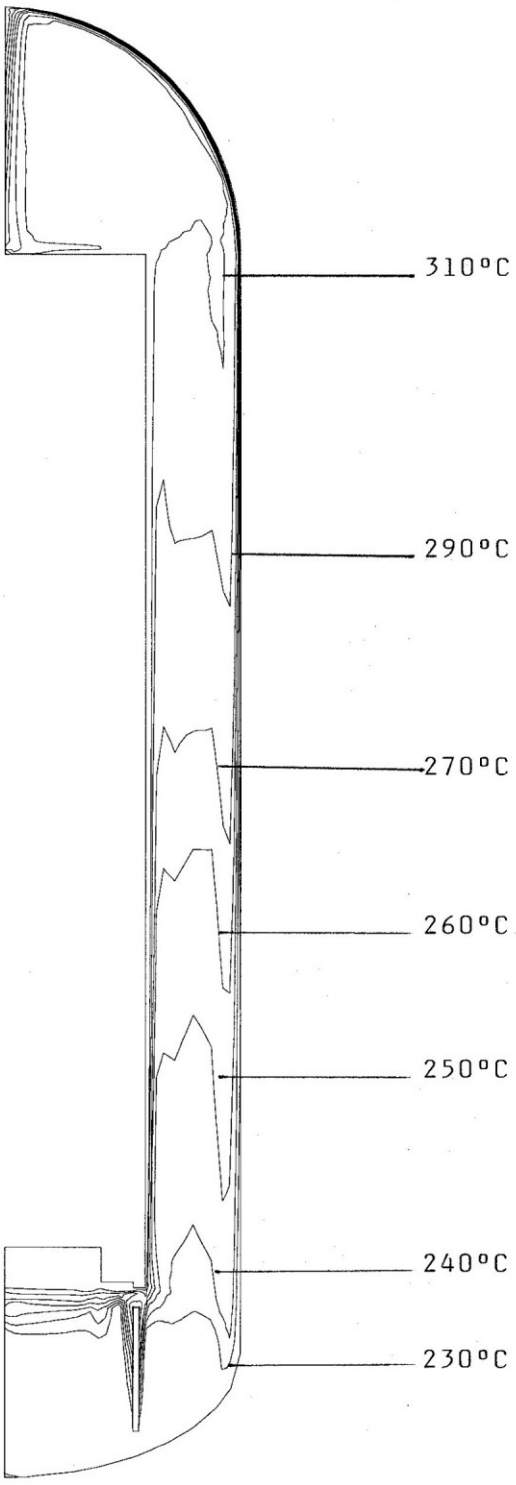

Fig. 4-19 Internal cavity – Isotherms
Experiment 2 – presurrized
conditions –helium gas

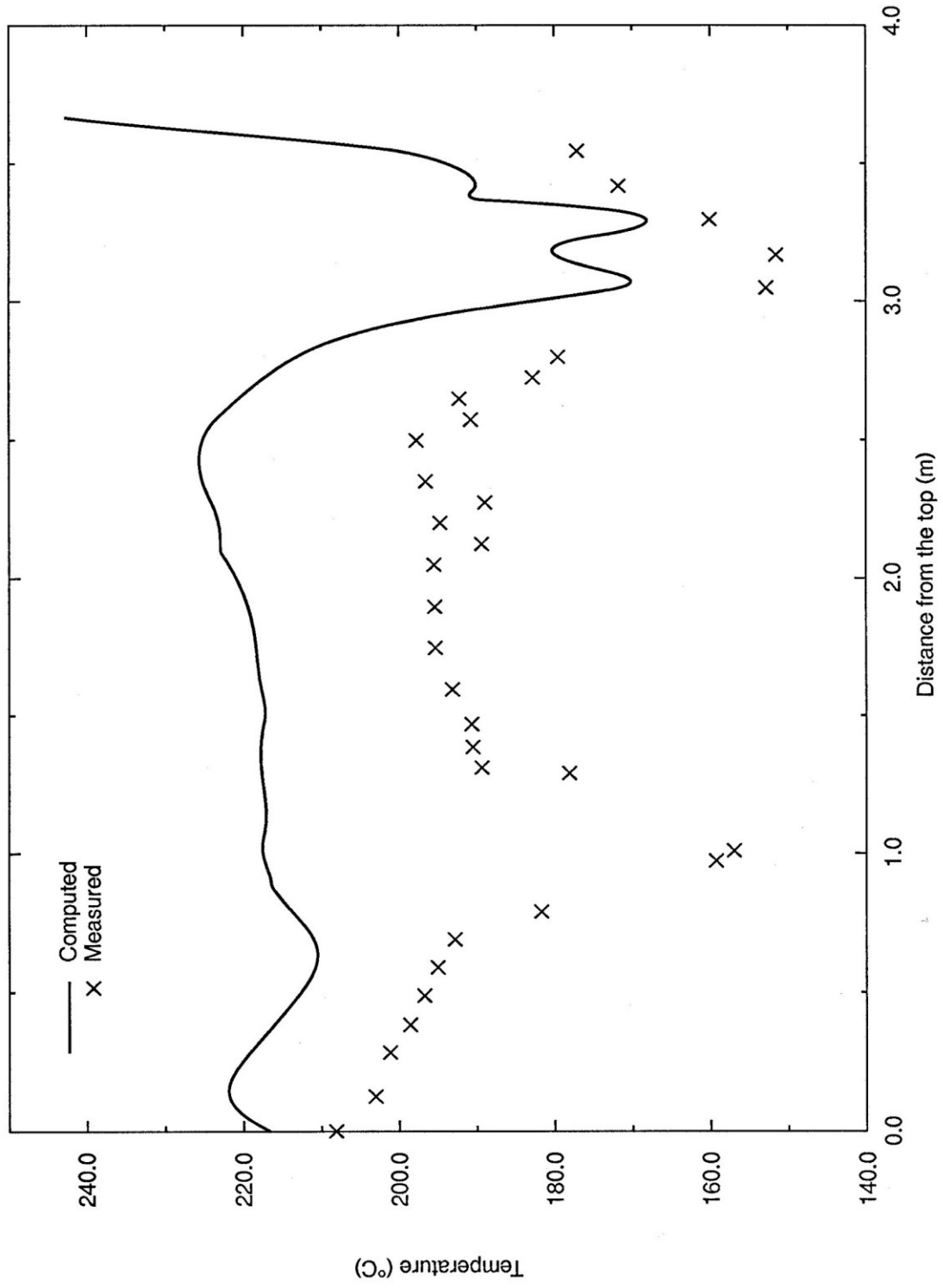

Fig. 4-20 Temperature along the pressure vessel
Experiment 2 – Pressurized conditions – Helium gas

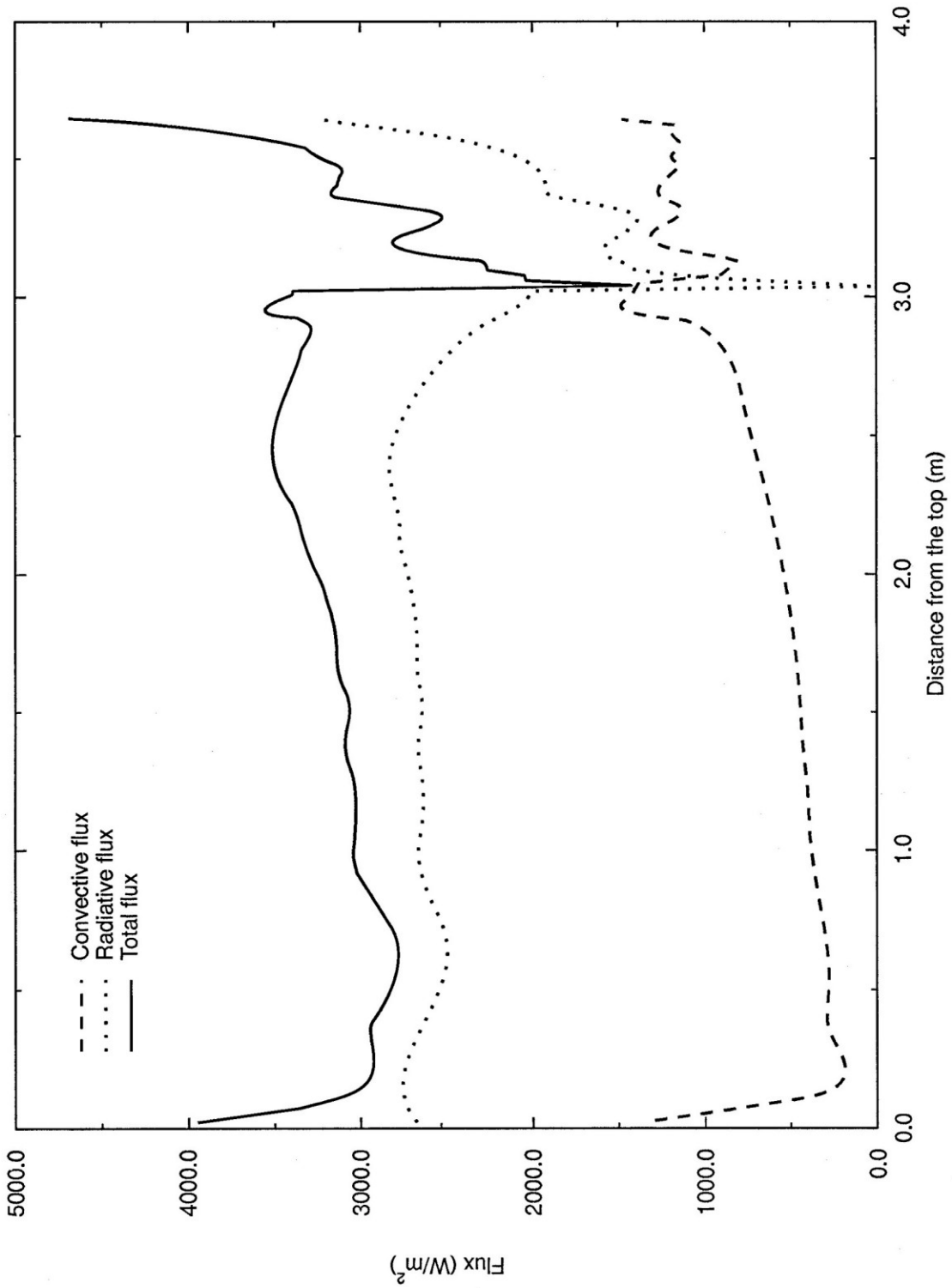

Fig. 4-21 Heat fluxes along the pressure vessel Experiment 2 – pressurized conditions – helium gas

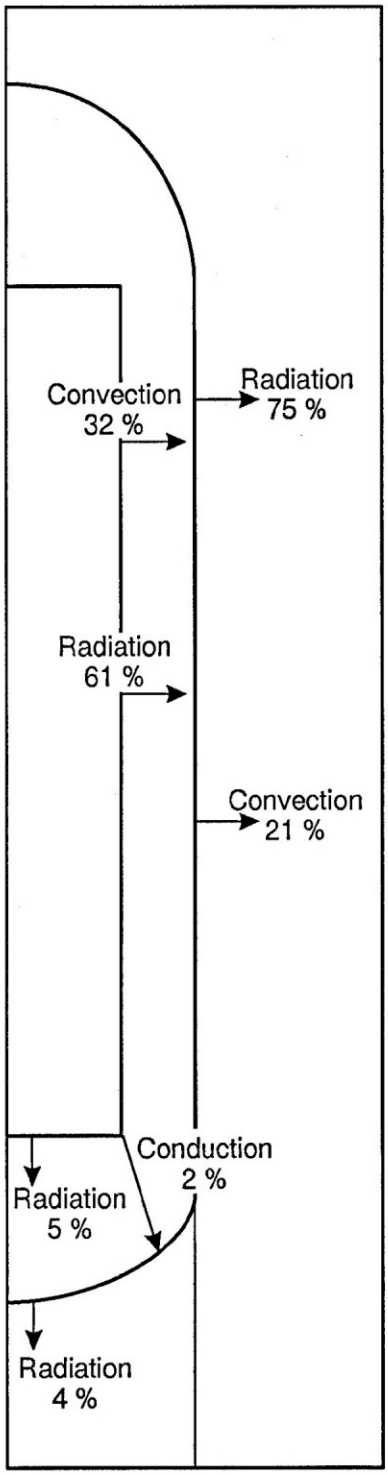

Fig. 4-22 Calcul heat balance Experiment 2 – Pressurized conditions – helium gas

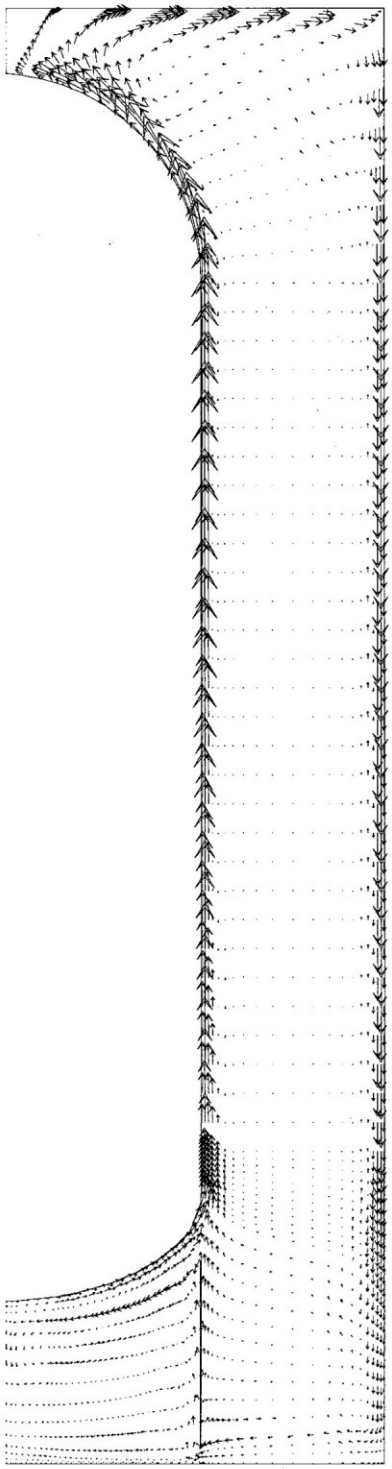

Fig. 4-23 External cavity – Velocities
Experiment 2 – pressurized conditions –
Nitrogen gas

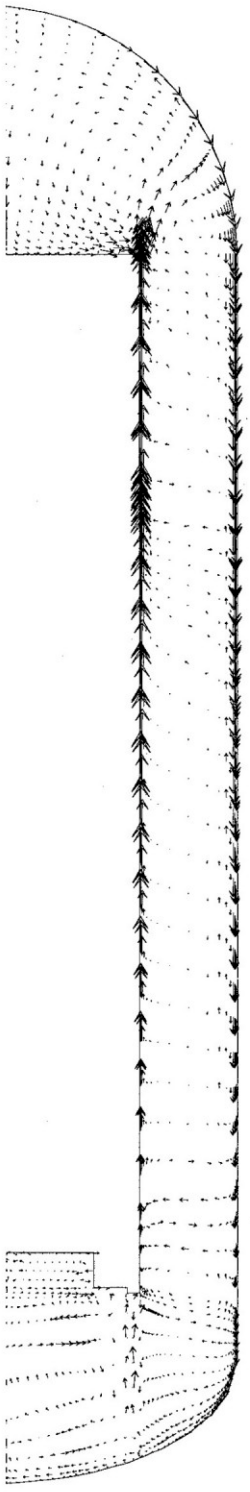

Fig. 4-24 Internal cavity – Velocities
Experiment 2 – Pressurized conditions – nitrogen gas

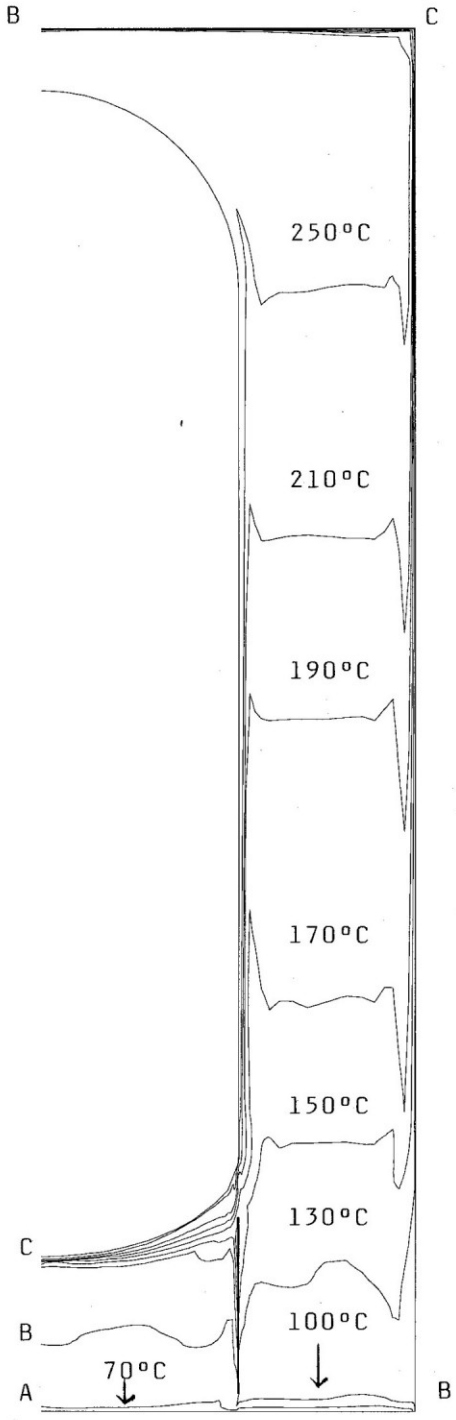

Fig. 4-25 External cavity – Isotherms
Experiment 3 – pressurized conditions – nitrogen gas

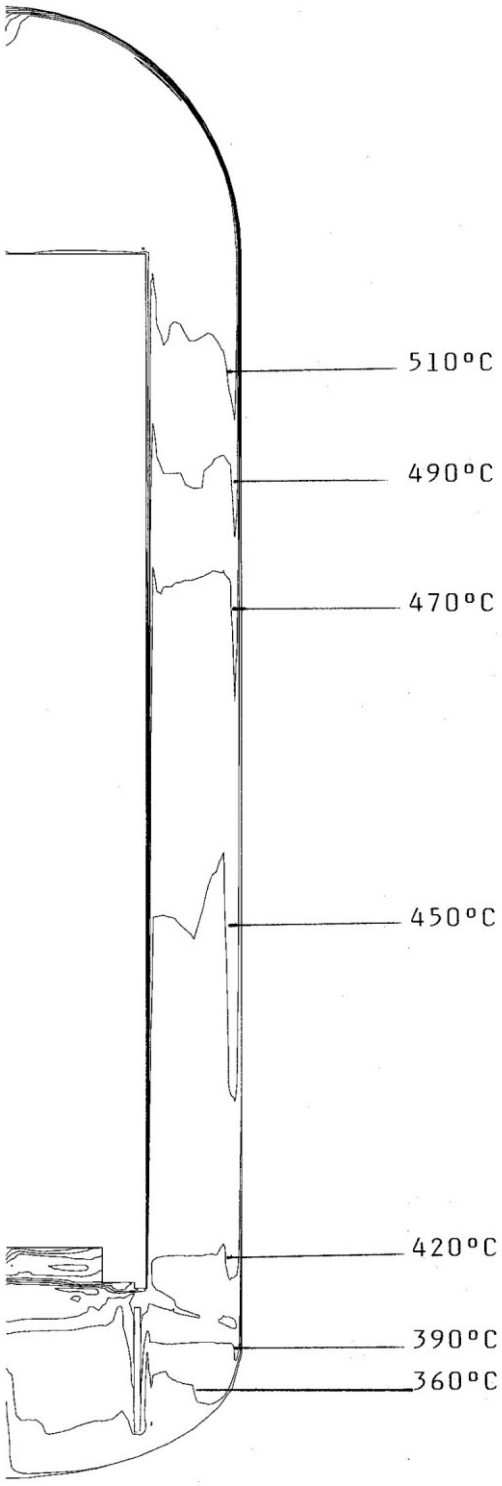

Fig. 4-26 Internal cavity – Isotherms
Experiment 3 – Pressurized conditions
– nitrogen gas

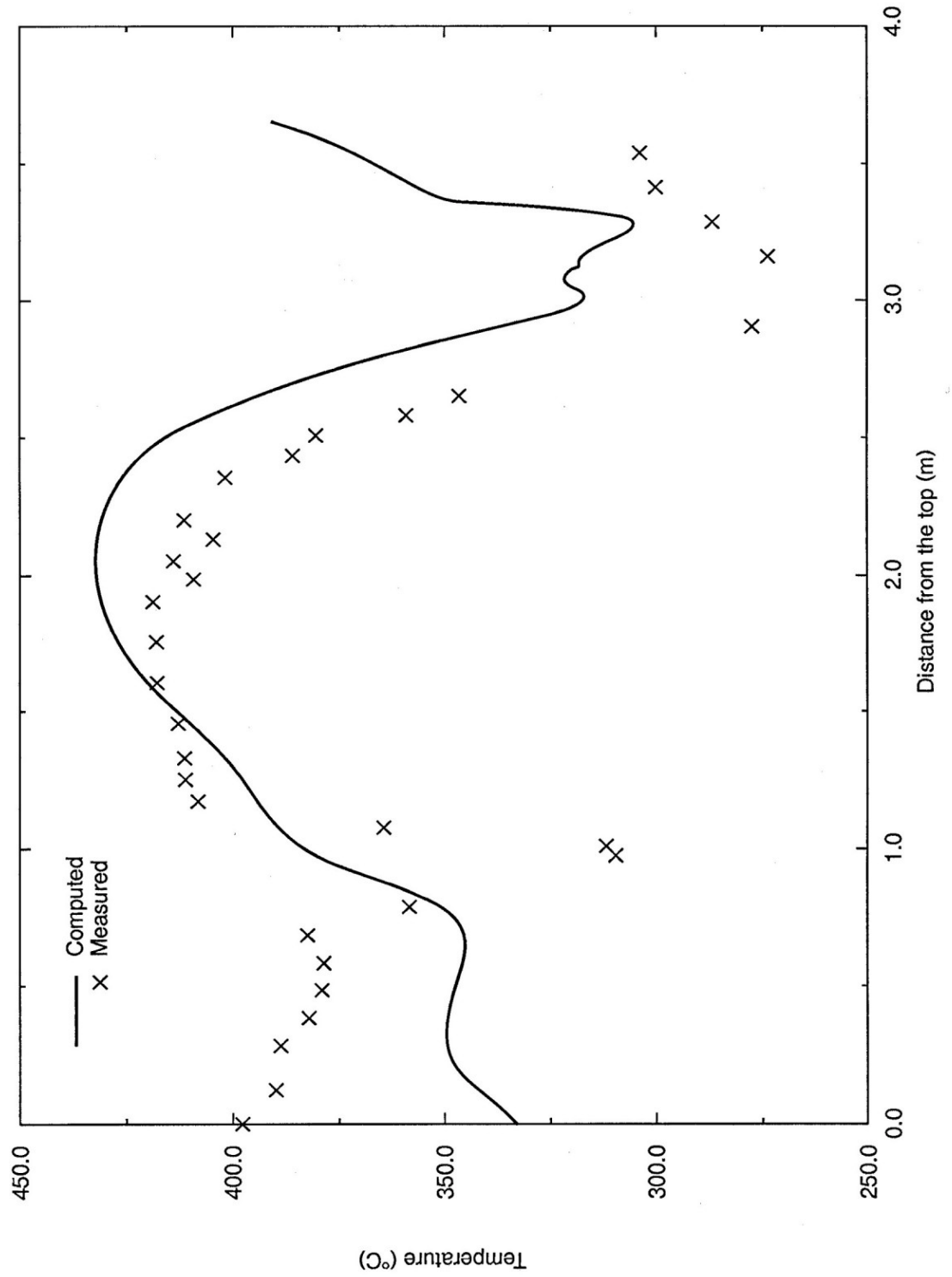

Fig. 4-27 Temperature along the pressure vessel Experiment 3 – pressurized conditions – nitrogen gas

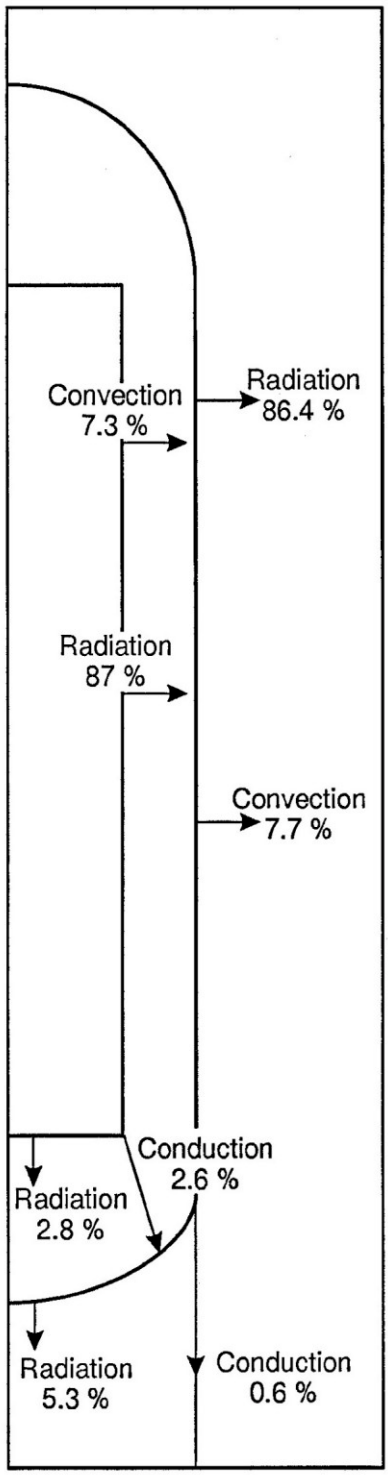

Fig. 4-27a Calculated heat balance Experiment 3 – pressurized conditions – nitrogen gas

4.1.3. Results of Solution of the HTTR RCCS Mockup Benchmarks

4.1.3.1. Introduction

The six benchmark problems provided by Dr. M. Hishida of the Japan Atomic Energy Research Institute (JAERI) with water and air cooling have been analysed in INET as a part of the IAEA Co-ordinated Research Program (CRP) on " Heat Transport and Afterheat Removal for GCRs under Accident Conditions." The HTTR RCCS experimental apparatus and experimental conditions are results of benchmark problems are given in 4.1.1.

4.1.3.2. Analysis Approach and Model

4.1.3.2.1. Analysis Approach and Model of THERMIX

The computer code THERMIX, a two-dimensional heat conduction program, is used for analysis of HTTR benchmark problem. Because of the limitation of the computer code, the reactor pressure vessel is represented as a cylindrical vessel. A simulating model is set up, which is used to calculate the temperature distributions on the pressure vessel and heaters under the given output power of the heater and cooling panel temperatures, which is the problem (1) of the JAREI experiment description. The analytical model consists of 18×49 meshes and 34 components to represent different construction, such as heaters, reactor pressure vessel, insulator and cooling tubes. The insulated upper and lower boundary condition is used considering absent of upper and lower cooling panels from operation. The another simulating model is used to calculate the heated power under the given temperature distributions on the pressure vessel and cooling panels. If the variation of the cooling panels' temperatures with height is large, it was given using linear interpolator. The outer surfaces of cooling tubes and insulator surface are uniformly coated by black paint. Emissivity of the black paint is 0.95. The thermal radiation heat transfers among the pressure vessel, the cooling panels and insulator are considered based on heat equilibrium under the given cooling panels' temperatures and insulator temperatures.

In the annulus cavity between the outer pressure vessel and the cooling panels, there is convective heat transfer, and in the annulus cavity between the core barrel [heaters] and inner pressure vessel, there are also substantial convection driven flows. In simulating model, the convective heat transfers of the annulus (for both inside and outside of the pressure vessel) are approximated by selecting correlation.

The Keyhani equation:

$$Nu = 0.138\ (Gr \cdot Pr)^{0.258}$$

is used for the convective heat transfer in the annulus between the heaters and the pressure vessel, and the annulus between the pressure vessel and the cooling panels.

The key parameters of the simulating model as follows: emissivities of 0.95 for the outer vessel surface and the cooling panels, the emissivities of 0.93 and 0.79 for the heaters and inner vessel surface respectively.

4.1.3.2.2. Analysis Approach and Model of CCRCC

In order to study further the natural convection's effect, the computer code CCRCC, a two-dimensional heat conduction and fluid convection program, is used for analysis of HTTR benchmark problem. The code is developed from SIMPLE (Semi-Implicit Method for Pressure-Linked Equations) through adding functions of dealing with radiation, natural convection. Radiation and natural convection are brought into governing equations as a source term. The equations are discretised with finite difference, and then solved by ADI iterative method. Infinite-length concentric cylinders' model is used to calculate radiation between vis-à-vis radiation surfaces except for top and bottom heater, where a revised method is used. Moreover, the buoyancy forces generated by the variations in fluid density are modeled as a source term in the momentum equation

with $\rho . g$ instead of using the Business approximation considering that large difference of temperatures' exit in the apparatus.

A simulating model is shown in Fig. 4-28. The model is based on an axis-symmetric geometry in order to accommodate a two-dimensional calculation. The outer boundary of the model is located along the inner surface of the cooling panel and adjacent cavity wall section. The region behind the cooling panel is not modelled. It is assumed that total heat generated by the heater is removed by the cooling panels. Because of the limit of two-dimensional model, the standpipes are not accounted. The model is composed of three fluid regions: internal cavity in the pressure vessel, external air cavity and the cavity region below the vessel and inside the support skirt. It is assumed that the cavity below the vessel is isolated from the rest of the cavity. Inside the vessel, it is assumed that the heater support skirt is porous enough so that its impedance to fluid flow is not significant and it is not considered. The analytical model consists of 38×97 meshes and 6 components to represent construction, such as heaters, insulator, pressure vessel, skirt support, and fluid, including air and helium. Under the given output power of the heaters and cooling panel temperatures, the distributions of temperature and fluid velocity can be achieved with the model, which is the problem (1) of the JAREI experiment description.

The cooling panels' temperatures are given through linear interpolation between measured temperatures. The key parameters of the radiation model are as follows: emissivities of 0.95 for the outer vessel surface and the cooling panels, the emissivites of 0.93 and 0.79 for the heaters and inner vessel surface respectively. Very small relaxation factors for pressure, velocity, temperature is used because of the strong non-linearity in order to get convergent solution.

4.1.3.3. Results

4.1.3.3.1. THERMIX Results

The comparisons of the measured heater power with calculated values under the condition of given pressure vessel temperature and cooling panel temperature distribution are shown in Table 4-9. The calculated heat transfer from the pressure vessel to the cooling panels is very close to the measured heater power the relative deviation is less then 5%.

The comparisons of the measured vessel and heater temperature with calculated values under the condition of given heating power are shown in Table 4-4 – 4-6 and Fig. 4-29 - Fig. 4-35. Table 4-4 shows a comparison of the measured and calculated pressure vessel temperatures in the core barrel section, most of the results show good agreements. The figures also shows that the calculated temperatures are somewhat lower than the measured temperature in the upper region of the core barrel, however, in the lower region of the core barrel, the calculated temperatures are slightly higher than the measured temperatures. In general, the results are better when the temperatures are higher, for example, benchmark No.3, No.4 and No.5 which are near HTTR's accidents' situations. The reason is that radiative heat transfer is dominant to natural convection heat transfer when temperatures are high. The overall average calculated temperatures of the pressure vessel are close to the measured average temperature. Table 4-5 shows the comparison for temperatures of the six heaters (Heaters No.1 and No.6 are the top and bottom heaters, No.2 to no.5 are the core barrel section). It predicts that the calculated average temperatures of Heaters No.3 to No.6 is higher than the measured values, and that of heaters No.1 and No.2 are lower than the measured values.

Table 4-6 give the proportions of convection heat transfer in total removal heat. It shows convection heat transfer's proportion decreases with the increase of temperature and radiation heat transfer is dominant for all the benchmark problems.

Table 4-6 give some sensitivity studies on the vacuum condition case Problem 2. Different correlations for natural convection are used in the annulus between the vessel and the cooling panels. For all the correlations the deference of the results are not too large. When accounting for the effect of different temperatures between cooling panels and insulator on the radiative heat transfer the results are better.

In general, the calculated temperatures are lower than the measured values in the upper region of the heaters and the pressure vessel; on the contrary, the calculated temperatures are higher than the measured values in the bottom region of the heaters and the pressure vessel. The reason caused this difference is that the convective correlation of the simulating model does not take into account the heat transfer by natural circulation in the annulus between the heaters and the pressure vessel and the cavity between the pressure vessel and the cooling panels. In the experimental condition, the natural circulation are formed in the annuluses, and the cold gas downflows along the side wall of the annulus that cools the bottom cavity and the hotter gas upflows into the top cavity specially in the benchmark problem 6. It causes the heat redistribution in the region of the upper head and bottom head vessel, and so does in region of the upper heater (heater No.1) and bottom heater (heater No.6). This phenomenon cannot be simulated by the computer code THERMIX.

4.1.3.3.2. CCRCC Results

The two benchmark problems supplied by JAERI in October of 1995 and May of 1996 with air-cooling have been analyzed by making use of the computer code CCRCC. Temperatures measured with the thermocouples designated by the "C" azimuthal position on the vessel outside wall are used as the basis for comparison with the calculated results. Fig. 4-36 - Fig. 4-38 shows a comparison of the measured pressure vessel temperatures with calculated values. The used values summarized in Table 4-9. From these Figures and Tables, it shows that the overall agreement between calculation and experiment is good, especially in the upper. The calculated temperatures are up to the measured values by about average 15.3ºC, 3.6ºC and 0.5ºC for Benchmark No.5, No.6a and No.6b, respectively. Some discrepancy in the bottom head exits. The maximum differences between calculated temperature and experimental value are 66.9ºC, 10.1ºC and 17.9ºC for Benchmark No.5, No.6a and No.6b, respectively. This is possibly due to the imperfect radiation model, especially in the bottom head. The thermal heat transfer by convection is about 2.5%, 23.6% and 9.7% in the pressure vessel and 8.5%, 27.8% and 19.1% in the outside cavity for Benchmark No.5, No.6a and No.6b, respectively. It indicates that convection heat transfer is much less than radiative heat transfer when the temperatures are higher.

For all the three benchmark problems, the velocity field calculated shows that inside the vessel, natural convection causes the helium to flow upward along the heater and down along the inside of the vessel wall and outside the vessel, the air flows upward along the vessel wall and downward alongside cooling panels. The maximum velocity is approximately 0.145 m/s, 0.074m/s and 0.086m/s for Benchmark No.5, No.6a and No.6b. Near side walls, velocities are very larger than other areas, which indicate very thin boundary layer. The temperature fields show that the maximum temperatures in helium and in air appear in the upside of internal cavity and external cavity, respectively. Apparent temperature boundary layers exist near the side cooling panel and side outer pressure vessel.

The calculation results prove that the HTTR benchmark experiment with stands pipes and air-cooling can be simulated well by the code CCRCC. The calculated results are good agreement with the measured values, especially for the cases with No.6 heater segment on. Thus it can be seen that the influence of natural convection can be simulated well by the code CCRCC. Although radiation is the main way of the removal of heat, natural convection has an important effect on the redistribution of temperature. And it can not be neglected in an accurate research of the temperature distribution on the structures. Through ameliorating the radiation model, improvements on the accuracy of results by CCRCC seem possible. Further validation of the code can be carried on through calculating other benchmark problems.

4.1.3.4. Conclusion

- The HTTR RCCS benchmark experiment problems are of great value to provide partial validation of computer code,
- The Mock-up experiments can be simulated by the code THERMIX, and the calculated results are good agreement with the measure values. Under the condition of given pressure vessel temperature and cooling panel temperature distribution, the calculated heat transfer from the pressure vessel to the cooling panels is very close to the measured heater power. Under the condition of given heating power, the calculated pressure vessel temperatures agree well with measured values except for the cases with only bottom heater on, in which natural convection have an important effect on the distribution of heat and temperature on the pressure vessel and code THERMIX can not simulate well these cases,
- The HTTR benchmark experiment with stand pipes and air-cooling can be simulated well by the code CCRCC. The influence of natural convection can be simulated well by the code CCRCC. The calculated results are good agreement with the measured values. The model not using Business approximation gets better results than using it. Moreover, it was found that conduction heat transfer along axis direction has an important effect on the heat distribution along pressure vessel,
- It is better understanding the heat transfer of the experiments of JAREI through the comparisons between calculated and measured results.

REFERENCES TO SECTION 4.1.3.

[1] Gao Zuying, Wang Chunyun, Yang Bin, “Analysis of HTTR Reactor Cavity Cooling System Benchmark Problem in INET”, Institute of Nuclear Energy Technology, Tsinghua University, China, Oct. 29, 1994.

[2] Wang Chunyun, Gao Zuying, “Analysis of HTTR Reactor Cavity Cooling System Benchmark Problem in INET”, Institute of Nuclear Energy Technology, Tsinghua University, China, July 12, 1995.

[3] Wang Chunyun, Gao Zuying, “Analysis of HTTR Reactor Cavity Cooling System Benchmark Problem in INET”, Institute of Nuclear Energy Technology, Tsinghua University, China, Oct. 16, 1995.

[4] Gao Zuying, “INET Analysis of Three HTTR Experiment Benchmark Problem”, Institute of Nuclear Energy Technology, Tsinghua University, China, June 1996.

[5] Zhao Haihua, Gao Zuying, “INET Analysis of HTTR Experiment Benchmark Problem by CCRCC Code”, Institute of Nuclear Energy Technology, Tsinghua University, China, September 1996.

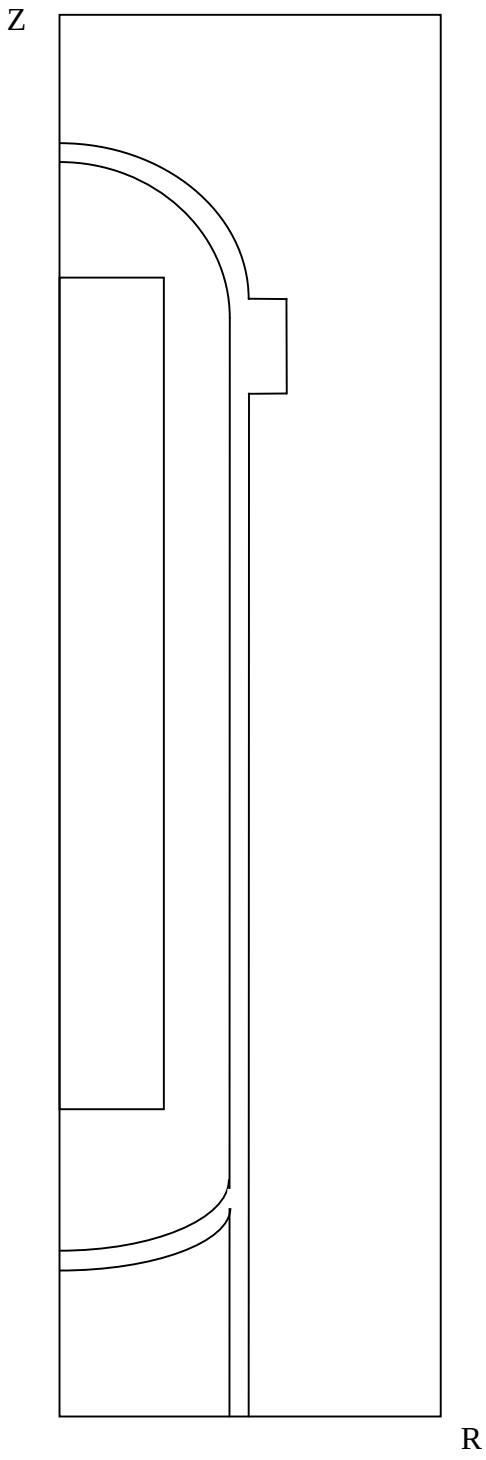

Fig. 4-28 Simulating Model for Code CCRCC

Table 4-4 Comparison of the measured and calculated heater power

Benchmark No.	1	2	3	4	5	6a	6b
Measured power kW	13.14	28.79	93.9	77.5	29.7	2.58	7.99
Calculated power kW	12.93	30.05	93.3	76.4	30.8	2.51	7.83
Relative deviation	-1.6%	4.4%	-0.6%	-1.4%	3.7%	2.7%	-2.%

Table 4-5 Comparison of the measured and calculated pressure vessel temperatures

Bench-mark No.	°C	Upper Head	Upper S. W.	Htr. #2	Htr. #3	Htr. #4	Htr. #5	Lower S. W.	Botto mHead	Ave.
	Measured	115.8	102.8	121.9	142.6	142.3	133.2	99.1	124.8	122.8
1	Calculated	142.2	101.3	128.5	140.4	144.0	135.8	80.4	147.3	127.5
	Deviation	26.4	-1.5	6.6	-2.2	1.7	2.6	--18.7	22.5	4.7
	Measured	202.9	181.8	187.2	195.3	192.7	188.4	152.9	165.2	183.3
2	Calculated	167.1	126.9	147.4	193.9	224.3	238.5	147.4	244.5	186.3
	Deviation	-35.8	-54.9	-39.8	-1.4	31.6	50.1	-5.5	79.3	3.0
	Measured	388.4	359.7	400.0	419.2	411.2	373.5	276.8	290.5	364.9
3	Calculated	341.0	349.9	379.3	396.6	408.5	377.6	283.2	307.1	355.4
	Deviation	-47.4	-9.8	-20.7	-22.6	-2.7	4.1	6.4	16.6	-9.5
	Measured	385.9	346.4	389.4	404.8	366.3	263.6	207.2	246.0	326.2
4	Calculated	338.9	295.6	370.5	385.6	357.8	291.3	228.4	263.1	316.4
	Deviation	-47.0	-50.8	-18.9	-19.2	-8.5	27.7	21.2	17.1	-9.8
	Measured	503.3	497	504	500	484	439	407.6	405	467.5
5	Calculated	496	485	499	495	483	422	390	403	459.1
	Deviation	-7.3	-12.0	-5.0	-5.0	-1.0	-17.0	-17.6	-2.0	-8.4
	Measured	85.5	81.4	83.9	83.2	81	78.1	67.4	63.4	78.0
6a	Calculated	71	71	68.3	67.1	71.6	89.4	105.1	118	82.7
	Deviation	-14.5	-10.4	-15.6	-16.1	-9.4	11.3	37.7	54.6	4.7
	Measured	192	189.9	189.3	188	187.6	182.2	166.8	183	185
6b	Calculated	169.4	166.8	164.8	159	160	186.4	216.6	261	186
	Deviation	-22.6	-23.1	-24.5	-29.0	-27.6	4.2	49.8	78.0	1.0

Table 4-6 Comparison of the measured and calculated heater temperatures

Benchmark	°C	Htr. 1	Htr. 2	Htr. 3	Htr. 4	Htr. 5	Htr. 6
	Measured	287.9	294.1	296.3	296.2	294.9	287.3
1	Calculated	290.6	291.8	305.3	314.2	255.0	322.8
	Deviation	2.7	-2.3	9.	18.	-39.9	35.5
	Measured	269.9	299.0	298.0	300.4	292.0	291.2
2	Calculated	260.5	272.8	316.5	370.4	413.4	508.2
	Deviation	-9.4	-26.2	18.5	70.	121.4	217.
	Measured	582.9	589.5	585.4	576.2	539.0	504.1
3	Calculated	530.6	560.2	622.3	627.1	590.5	555.1
	Deviation	-52.3	-29.3	36.9	50.9	51.5	51
	Measured	576.1	584.9	577.9	527.1	367.6	461.3
4	Calculated	509.4	555.3	586.3	546.1	427.2	476.0
	Deviation	-66.7	-29.6	8.4	19.0	59.6	14.7
	Measured	549.7	541.2	551.3	563.6	460.8	452.9
5	Calculated	534.8	548.2	548.9	547.7	475.8	474.3
	Deviation	-14.9	7.0	-2.4	-15.9	15.0	21.4
	Measured	92.5	94.3	96.4	99.1	105.2	94.8
6a	Calculated	71	70	71	81.8	116	155
	Deviation	-21.5	-24.3	-25.4	-17.3	10.8	60.2
	Measured	206.1	209.7	213.3	219.2	235	292.9
6b	Calculated	167	165.5	163.8	175.8	236.2	400
	Deviation	-39.1	-44.2	-49.5	-43.4	1.2	107.1

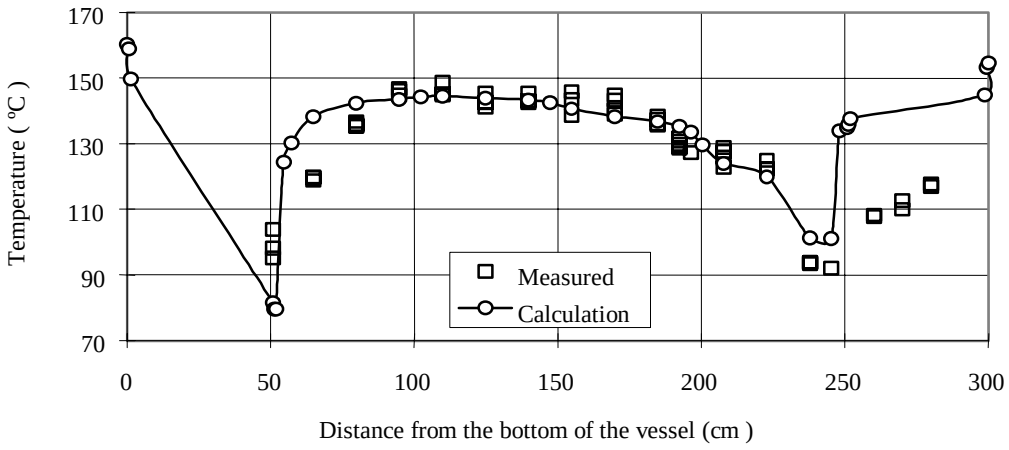

Fig 4-29 Vessel Barrel Section Surface Temperature
(Benchmark No.1)

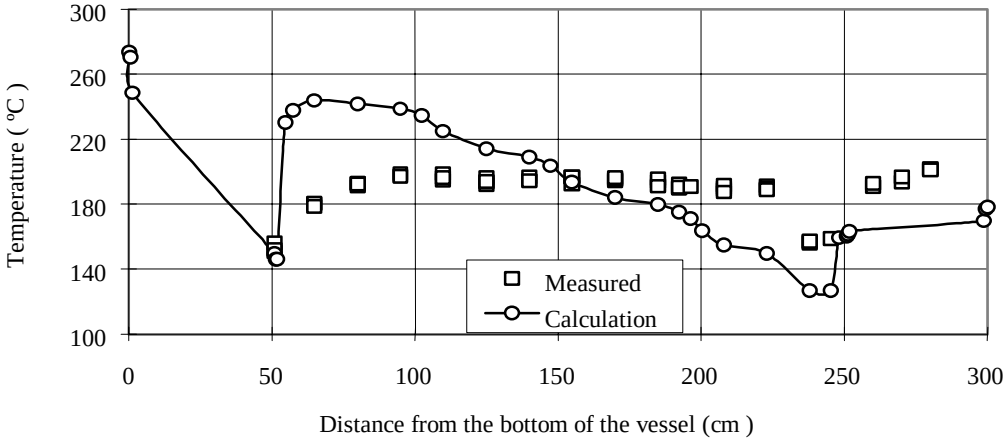

Fig 4-30 Vessel Barrel Section Surface Temperature
(Benchmark No.2)

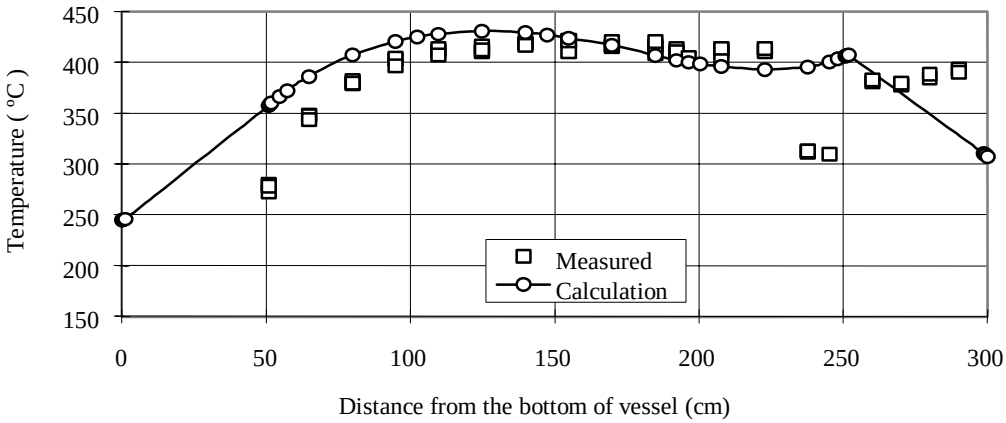

Fig 4-31 Vessel Barrel Section Surface Temprature
(Benchmark No.3)

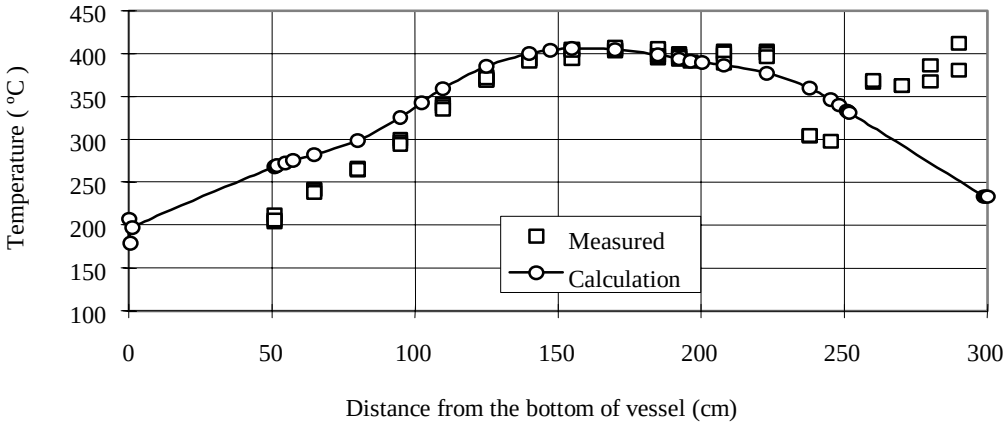

Fig 4-32 Vessel Barrel Section Surface Temperature
(Benchmark No. 4)

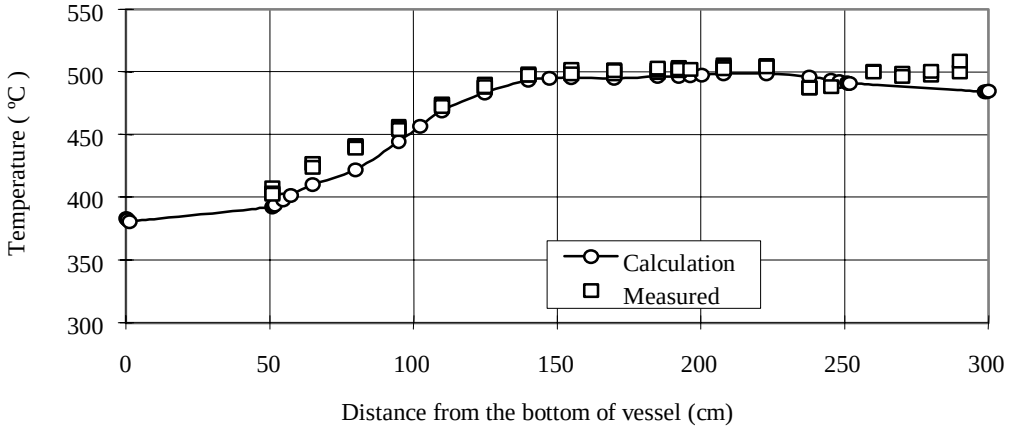

Fig 4-33 Vessel Barrel Section Surface Temperature
(Benchmark No.5)

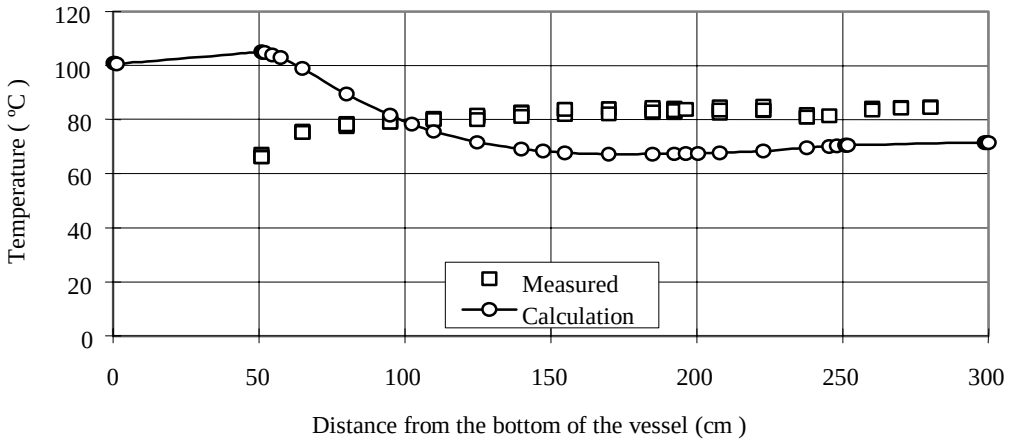

Fig. 4-34 Vessel Barrel Section Surface Temperature
(Benchmark No.6.1)

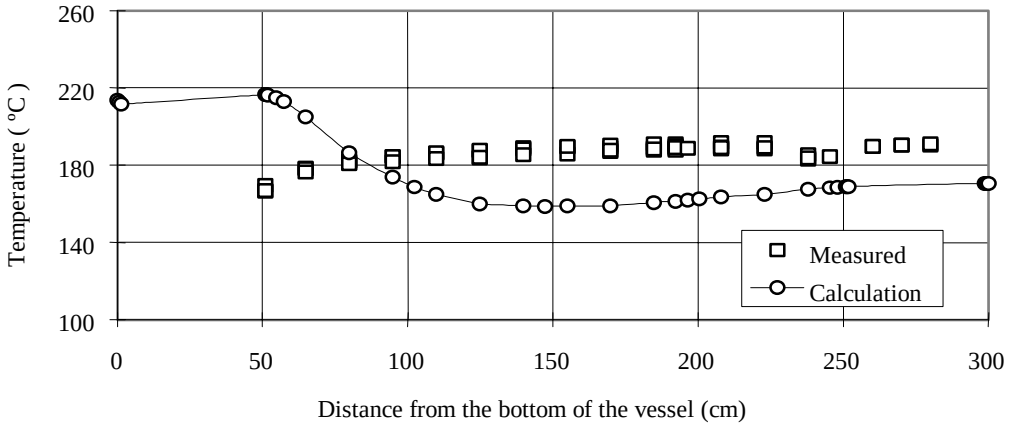

Fig 4-35 Vessel Barrel Section Surface Temprature
(Benchmark No.6.2)

Table 4-7 Proportions of convection heat transfer in total removal heat (%)

Benchmark No.	1	2	3	4	5	6a	6b
Inside of vessel	Vacuum	35	6.5	16	10	40	28
Outside of vessel	15	13	9	14	2	12	6

Table 4-8 Comparison of the heat loss from the vessel to the cooling panels for Problem 2 in the Benchmark No.1 (heat in kW)

	Without considering the insulator' effect on radiation heat transfer		Considering the insulator effect on radiation heat transfer	
	Calculated value	Relative deviation	Calculated value	Relative deviation
Measured:			13.14	
Keyhani Equation	14.42	9.5%	12.93	-1.6%
THERMIX Equation	15.9	20%	14.52	10.5%
Russian Equation	14.63	11%	13.16	0.2%
HTTR Equation	14.86	13%	14.87	13.1%
Max. measured vessel temp.	14.86	13%	13.31	1.3%
Min. measured vessel temp.	14.22	8%	12.74	-3%

Table 4-9 Temperature of outer surface of vessel

Benchmark		5			6a			6b		
Measu-ring tag number	Location (m) *	Measured (ºC)	Calculated (ºC)	error (ºC)	Measured (ºC)	Calculated (ºC)	error (ºC)	Measured (ºC)	Calculated (ºC)	error (ºC)
c28	0.520	390.8	389.4	-1.4	59.9	67.7	7.8	166.1	181.1	15.0
c27	0.630	401.5	468.4	66.9	62	72.1	10.1	189.9	207.8	17.9
c19	0.910	403.4	457.2	53.8	66.3	68.9	2.6	166.6	176.7	10.1
c18	1.160	426.7	466.7	40.0	75.8	78.4	2.6	178.2	192.1	13.9
c17	1.310	440.8	469.9	29.1	78.4	78.4	0.0	182.2	187.4	5.2
c16	1.460	455.6	474.5	18.9	79.6	77.7	-1.9	184.7	184.8	0.1
c15	1.610	473.9	496.3	22.4	80.5	76.3	-4.2	186.5	181.7	-4.8
c14	1.760	490.1	510.9	20.8	81.7	75.5	-6.2	187.6	181.2	-6.4
c13	1.910	498.6	513.2	14.6	82.7	75.3	-7.4	188.4	181.6	-6.8
c12	2.060	502.1	509.4	7.3	83.8	75.5	-8.3	189.9	183.3	-6.6
c11	2.210	501.7	509.0	7.3	84.1	75.7	-8.4	190.5	184.4	-6.1
c10	2.360	503.1	511.0	7.9	84.6	76.5	-8.1	191.2	186.5	-4.7
c8	2.485	503.3	511.8	8.5	84.4	76.9	-7.5	191.1	187.3	-3.8
c6	2.565	505.9	512.4	6.5	84.8	77.3	-7.5	191.6	188.	-3.6
c5	2.645	505.8	512.0	6.2	84.9	78.1	-6.8	191.7	188.7	-3.0
c3	2.763	499.0	511.3	12.3	84.	78.7	-5.3	189.4	189.3	-0.1
c1	2.783	488.0	498.0	10.0	82.1	78.7	-3.4	185.5	187.7	2.2
c26	3.000	497.0	508.5	11.5	84.3	80.1	-4.2	189.8	191.1	1.3
c25	3.191	499.1	507.4	8.3	86.1	81.	-5.1	192.8	192.8	0.0
c24	3.324	497.1	509.8	12.7	86.2	81.4	-4.8	193.1	193.1	0.0
c23	3.430	502.7	499.5	-3.2	86.2	80.8	-5.4	193.	190.5	-2.5
c22	3.474	512.2	509.5	-2.7	86.3	81.1	-5.2	194.4	191.3	-3.1
c21	3.480	513.4	508.4	-5.0	86.3	81.	-5.3	194.6	191.2	-3.4
average value		478.8	494.1	15.3	80.7	77.1	-3.6	187.3	187.8	0.5

* location is the distance from the bottom cooling panel

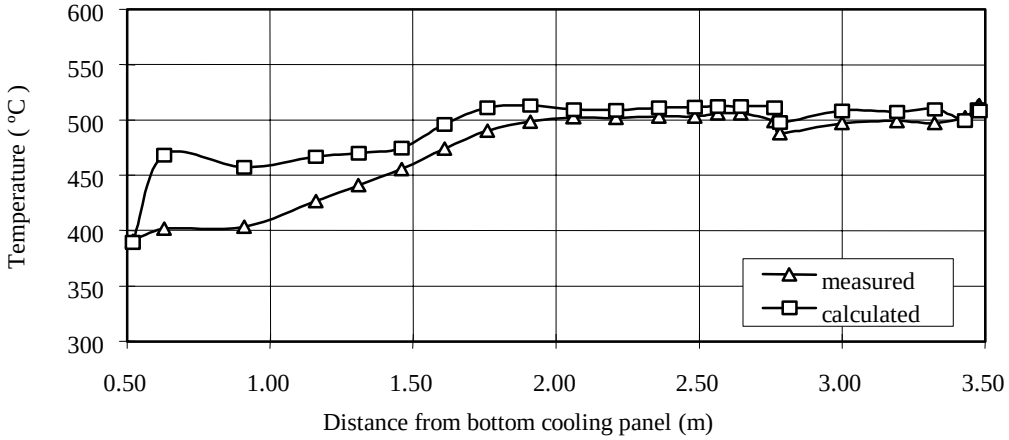

Fig. 4-36 Temperature of outer surface of vessel for case crp-3 (95.10)

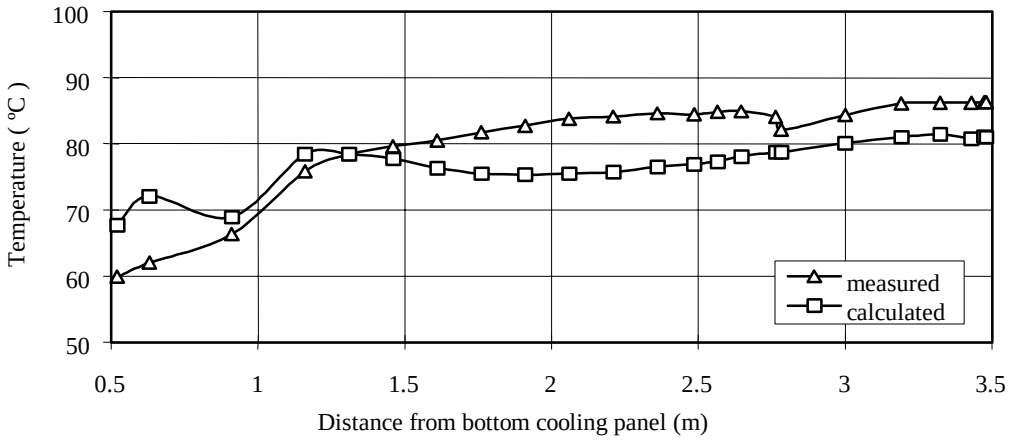

Fig. 4-37 Temperature of outer surface of vessel for case crp-3 (96.5,e1)

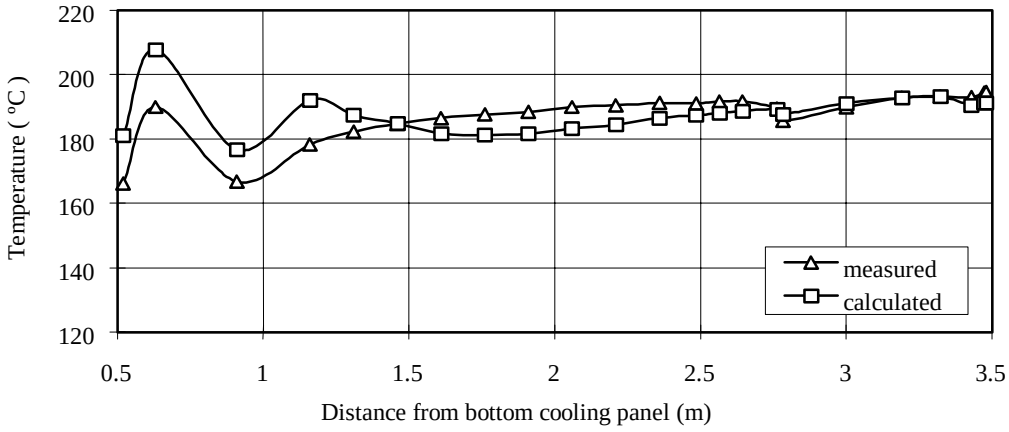

Fig. 4-38 Temperature of outer surface of vessel for case crp-3 (96.5,e2)

4.1.4. Calculations of the HTTR Reactor Cavity Cooling system Benchmark Problems with the DUPT - and SM1 – codes

4.1.4.1. Introduction

In HTGRs afterheat is transferred from the reactor vessel to the reactor cavity cooling system (RCCS) by radiation, natural convection and conduction in condition of complex shape of surfaces. Therefore, comparison of computed results with experimental data is very important for codes validation. Experiments provided by JAERI on HTTR mockup allowed for the first time to get data on heat transfer from the vessel to the RCCS. The data are an excellent basis for benchmark exercises which lead to better understanding of heat transfer process, limitations and approaches.

4.1.4.2. Model features and limitations

The OKBM benchmark analysis was done by using DUPT-and SM1-codes (brief description is given in Appendix A.2.2).

Descriptions of the HTTR RCCS mockup and benchmark data are presented in Chapter 4.1.1.

The mockup is axisymmetric except supporting structures of the heater and the pressure vessel. For 2D-calculations the supporting structures were transformed into symmetric cylindrical skirts.

The computational grid is shown in Fig. 4-39. The total number of nodes is 4104.

It is to be noted that the region inside the heater support is available for natural convection through the openings in the support. The region inside the vessel support may also communicate to the cavity through leak paths in the skirt.

Heat transfer by conductivity along the heater support and the support skirt is not taken into account.

4.1.4.2.1. Boundary conditions

Heat flux on the heater surface was given to provide calculations on DUPT-code inside the pressure vessel. For calculations on SM1-code, measured temperature distributions along the heater were used.

Outside the pressure vessel the heat sink temperature was adopted as average between the measured cooling tube and wall temperatures with account for their area.

For the benchmark problems (BPs) I, II, III, IV the insulated wall surface was assumed to be adiabatic, for BPs V, VI-a, VI-b heat losses through the insulation were accounted for.

4.1.4.3. Results

Calculations with using DUPT-code were performed for all BPs.

BPs VI-a and VI-b in which there is a significant axial convective heat transport were not computed on SM1-code having simplified model for calculation of heat transfer by convection.

Temperature distributions on the vessel outer surface are presented in Figs. 4-40-4-46.

Computed fractions of heat transferred by convection and radiation inside and outside vessel, and also heater power calculated by using SM1-code are presented in Table 4-10.

Table 4-10 Fractions of radiative and convective heat

Experiment	Code	Fraction of radiative and convective heat inside vessel, %		Fraction of radiative and convective heat outside vessel, %		Ratio of computed/measured heater power (first benchmark problem)	Ratio of computed/measured heater power (second benchmark problem)
		Radiation	Convection	Radiation	Convection		
	DUPT	100	0	78.4	21.6	-	-
I	SM1	100	0	79.7	20.3	14.24/13.14 1.83	-
	DUPT	58.3	41.7	81.9	18.1	-	-
II	SM1	65.6	34.4	80,0	20.0	20.2/28.79 0.70	-
	DUPT	90.3	9.7	90.1	9.9	-	-
III	SM1	88.5	11.5	81.2	18.8	90.6/93.9 0.965	95.74/93.9 1.02
	DUPT	73.1	26.9	89.7	10.3	-	-
IV	SM1	89.0	11.0	88.5	11.5	71.4/77.54 0.935	-
	DUPT	78.2	21.8	94.5	5.5	-	31.2/29.7 1.05
V	SM1	93.3	6.7	98.1	1.9	27.3/29.7 0.92	33.32/29.7 1.12
VI-a	DUPT	41.2	58.8	71.8	28.2	-	2.67/2.6 1.027
VI-b	DUPT	60.9	39.1	81.7	18.3	-	-

Comparison of the computed temperatures on SM1-code and measured distribution shows a good agreement for the side wall. More significant difference takes place for the lower and upper heads. Moreover, computed temperatures on lower and upper heads in all BPs are lower than measured values.

This is a result of simple modeling of heat exchange by radiation between surface of intricate shape and not taking into account heat transport by gas in axial direction.

Temperature distribution in the experiment on BPI shows computed values to be higher than the measured ones almost along all height of the vessel. In this experiment vacuum inside the vessel created, therefore influence of gas convection on heat transport was excluded.

Consequently, thermocouple measurements which are used as input data for calculations are close to real heater temperatures. The temperature distribution along the vessel confirms overestimation of power transferred from the heater to the vessel (+8%).

In the rest experiments (BP II-V) computed temperature distributions along the vessel displaced comparatively measured temperatures with simultaneous reduction of power transferred (from - 3.5% to - 30%).

This can be explained by the fact that measured heater temperatures lower than temperatures on its surface due to temperature gradient between the heater surface and thermocouples and influence of gas convection.

Moreover, reduction of computed heater power compared to measured one for experiment on BP III in which significant fraction of power is transferred by convection, is maximum and equal to 30%.

Temperature distribution obtained by using DUPT-code corresponds in great extent to measured values that says about more correct model of heat transfer by convection and radiation.

It is to be noted that the computed temperatures of the heater higher than the measured values in all experiments.

Figures 4-47 and 4-48 shows computed and measured temperatures along the heater for.

Experiments respectively with maximum (BP VI-a) and minimum (BP III) fractions of heat transferred by convection inside the vessel. The result tells as the calculation on SM1-code, that heater temperatures measured by the thermocouples are lower than real average heater temperatures.

Calculation of heat fraction on DUPT-code (Table 4-10) gives maximum values of heat fraction transferred by convection inside the vessel for the experiments on BP II, VI-a, VI-b.

Apparently, this is due to influence of two major factors:

– level of heater temperature which in these experiments is lower than in others, thus it results in decreasing fraction of heat transferred by radiation,

– fraction of power generated in lower segments of the heater that is 100% in the experiments on BP VI-a, VI-b and more than 50% in the experiment on BP II. This leads to more intensive heat transport by convection from lower to upper part of the vessel.

Fraction of power transferred by convection outside the vessel is in the range of 18-28% and 5-10% accordingly in experiments on BP I, II, VI-a, VI-b and BP III, IV, V. The result is in correspondence with the calculation inside the vessel. More lower fraction in experiments on BP III, IV, V is apparently explained by high level of temperature compared to the other experiments hence heat transport by radiation increases. Influence of change of other factors tells on the fraction more weakly (temperature distribution along the vessel and cooling panels, ratio of difference between cooling surfaces and gas to average gas temperature - Gr number).

Calculated results of heat fractions obtained by using SM1-code are qualitatively agreed with calculations on DUPT-code.

To illustrate flow patterns, Figs. 4-49 and 4-50 show velocity vectors inside and outside the vessel for experiments with minimum (BP) and maximum (BP VI-a) convective heat fraction in the annulus between the vessel and panels.

In annulus between the heater and vessel there are pronounced upward and downward flows along cylindrical surfaces. In the lower part gas flows only upward, in the upper region the flow is divided and turns downwards and upwards.

In annulus between the vessel and panels, together with upward and downward flows along cylindrical surfaces there are flows in horizontal direction that more pronounced in the experiment on BP V due to more temperature difference between the vessel and panels. Recirculation zones are formed only in the lower and upper parts of the cavity.

For the second BP, calculation of power transferred from vessel to cooling panels giving measured temperature distribution along the vessel was performed. The calculation included experiments only with maximum (BP III - DUPT, SM1) and minimum (BP VI-a - DUPT, BP V - SM1) heater power. The results are presented in Table 1.

Difference between computed and measured values is in a range from +3% to -5% for DUPT- code and from -2% to -12% for SM1- code. More error for SM1-code calculation is

explained by less prediction of temperature distribution along the vessel, particularly in the lower and upper parts.

Summarizing the results one can say about acceptable correspondence between calculated and measured temperature distributions along the vessel. SM1-code is convenient to use for calculation of transient removal from a core to ultimate sink. More accurate temperature distribution of structures in axial and radial directions may be obtained on DUPT-code at characteristic instants of time.

4.1.4.4. Conclusions

- SM1-code gives satisfactory results of temperature distributions along the cylindrical part of the vessel. The difference between measured and calculated values is higher for the lower and upper heads of the vessel. This is particularly seen for BP I, II with low vessel temperatures when heat transfer by convection is rised,
- Values of total power computed on SM1 code for BP III, IV, V with high vessel temperatures differs from the measured heater power not more than 8 %. If the vessel temperatures are low and there is a significant effect of convection on heat transfer (BPII), the code doesn't allow to provide appropriate results,
- DUPT-code gives more correct temperature distributions along the vessel compared to SM1-code. The worst agreement of the calculated and measured temperatures is for BPs I, II with a low level of the vessel temperatures and appreciable fraction of convective heat transfer in the annulus outside the vessel,
- Heat losses from the vessel to the cooling panels are in a range of 18-28 % for BP with low vessel temperatures (BP I, II, VI-a, VI-b) and drops up to 10 % in experiments with vessel temperatures matching reactor conditions (BP III, IV),
- Though, at high level of vessel temperatures the convection fraction is not so large, effect of heat transfer by convection must be taken into consideration especially from view point of its influence on temperature distribution along the reactor vessel.

REFERENCES TO SECTION 4.1.4.

[1] S. Takada, Y.Shiina, Y.Inagaki, and M.Hishida, “Benchmark Problem for LAEA Coordinated Research Program (CRP-3) on GCR Afterheat Removal,” JAERI Dept. of High Temperature Engineering Research, Feb. 1994, (IAEA Reference 622-13-RC-503).

[2] S. Takada, Y.Shiina, Y.Inagaki, M.Hishida, and Y.Sudo, “Benchmark Problem for IAEA Co-ordinated Research Program (CRP-3) on GCR Afterheat Removal,” JAERI Dept. of High Temperature Engineering Research, Feb. 1995, (LAEA Reference 622-13-RC-503.2).

[3] S. Takada, Y.Shiina, Y.Inagaki, M.Hishida and Y.Sudo, “Benchmark Problem for IAEA Co-ordinated Research Program (CRP-3) on GCR Afterheat Removal - Pressure vessel with stand pipes,” JAERI Dept. of High Temperature Engineering Research, June 1995.

[4] S. Takada, K.Suzuki, I.Terunima, Y.Shiina, M.Hishida, and Y.Sudo, “Benchmark Problem for IAEA Coordinated Research Program (CRP-3) on GCR Afterheat Removal - Air cooling panel,” JAERI Dept. of High Temperature Engineering Research, October 1995.

[5] S. Takada, Y.Shiina, M.Hishida, and Y.Sudo, “Benchmark Problem for IAEA Coordinated Research Program (CRP-3) on GCR Afterheat Removal”, JAERI Dept. of High Temperature Engineering Research, October 1995. (power only to bottom heater).

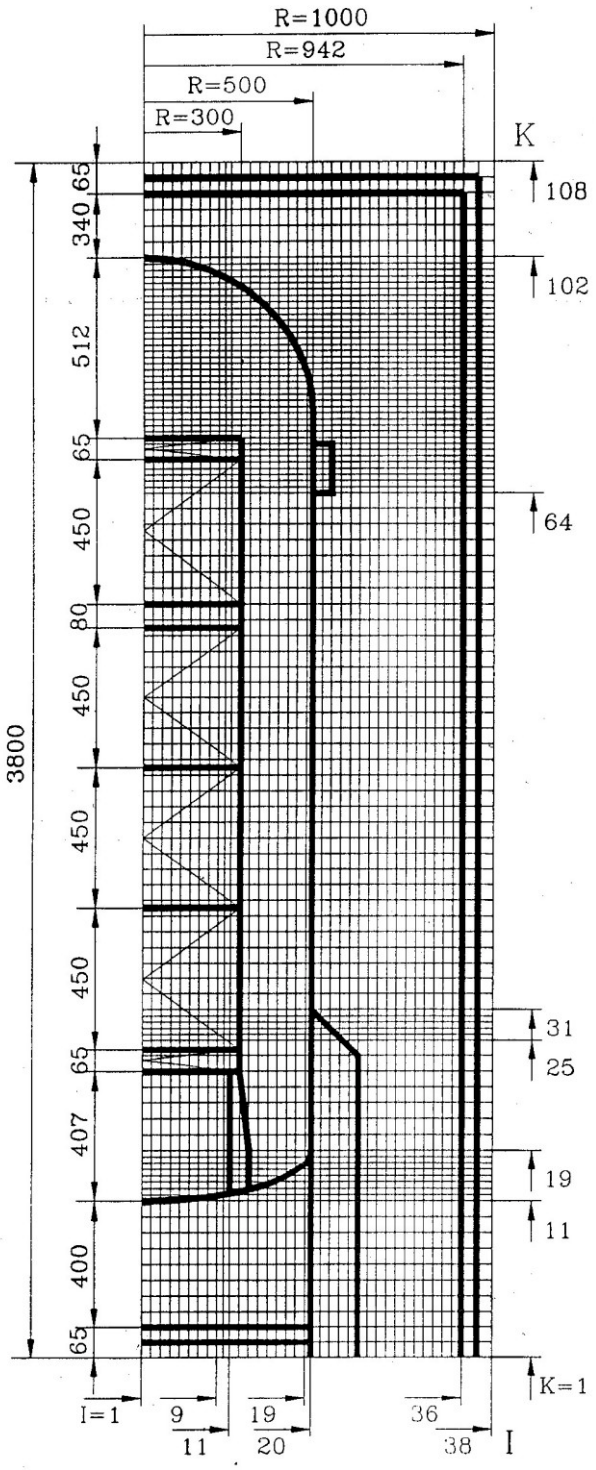

Fig. 4-39 DUPT code computation grid

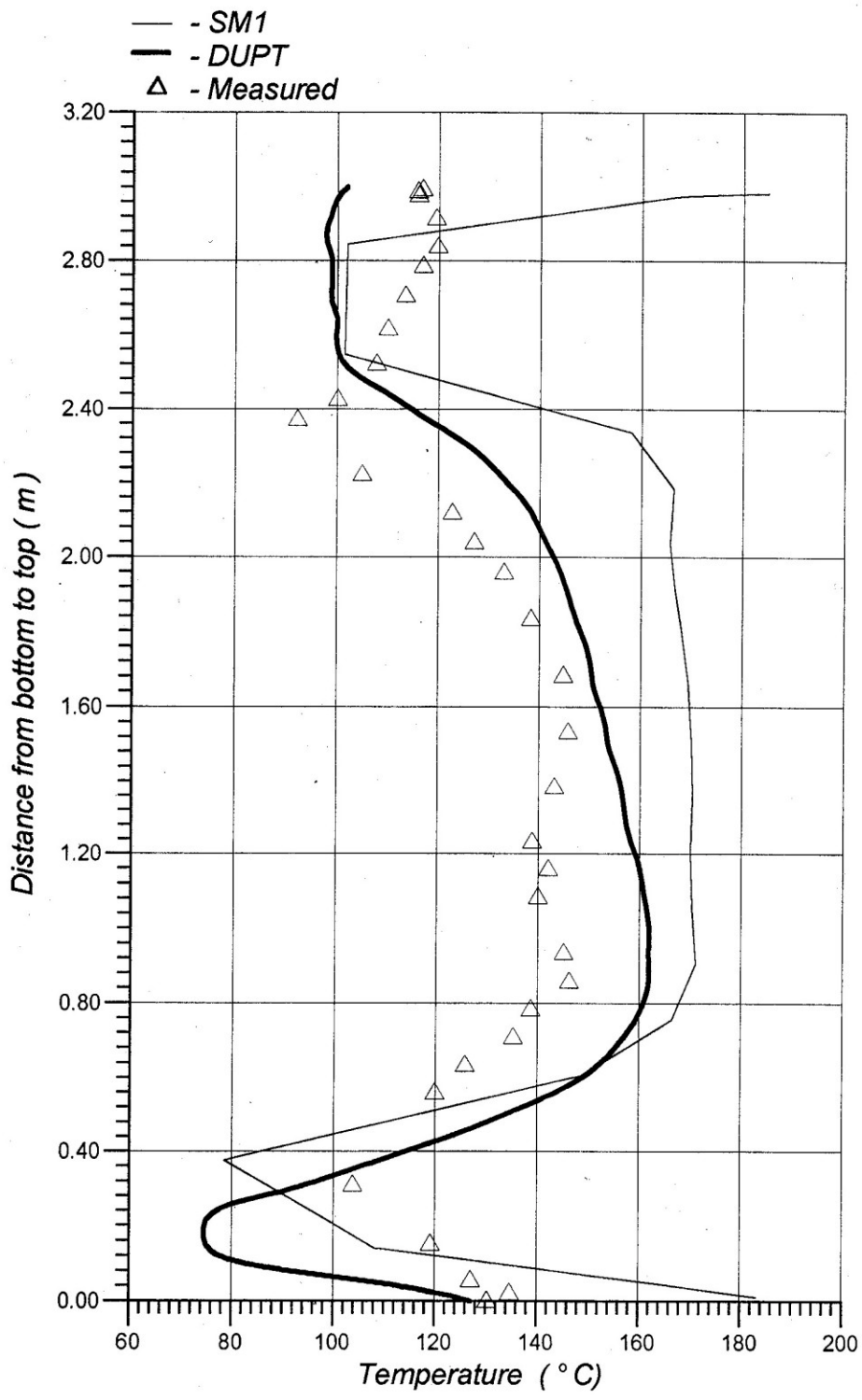

Fig. 4-40 Vessel outside surface temperature (Benchmark problem I)

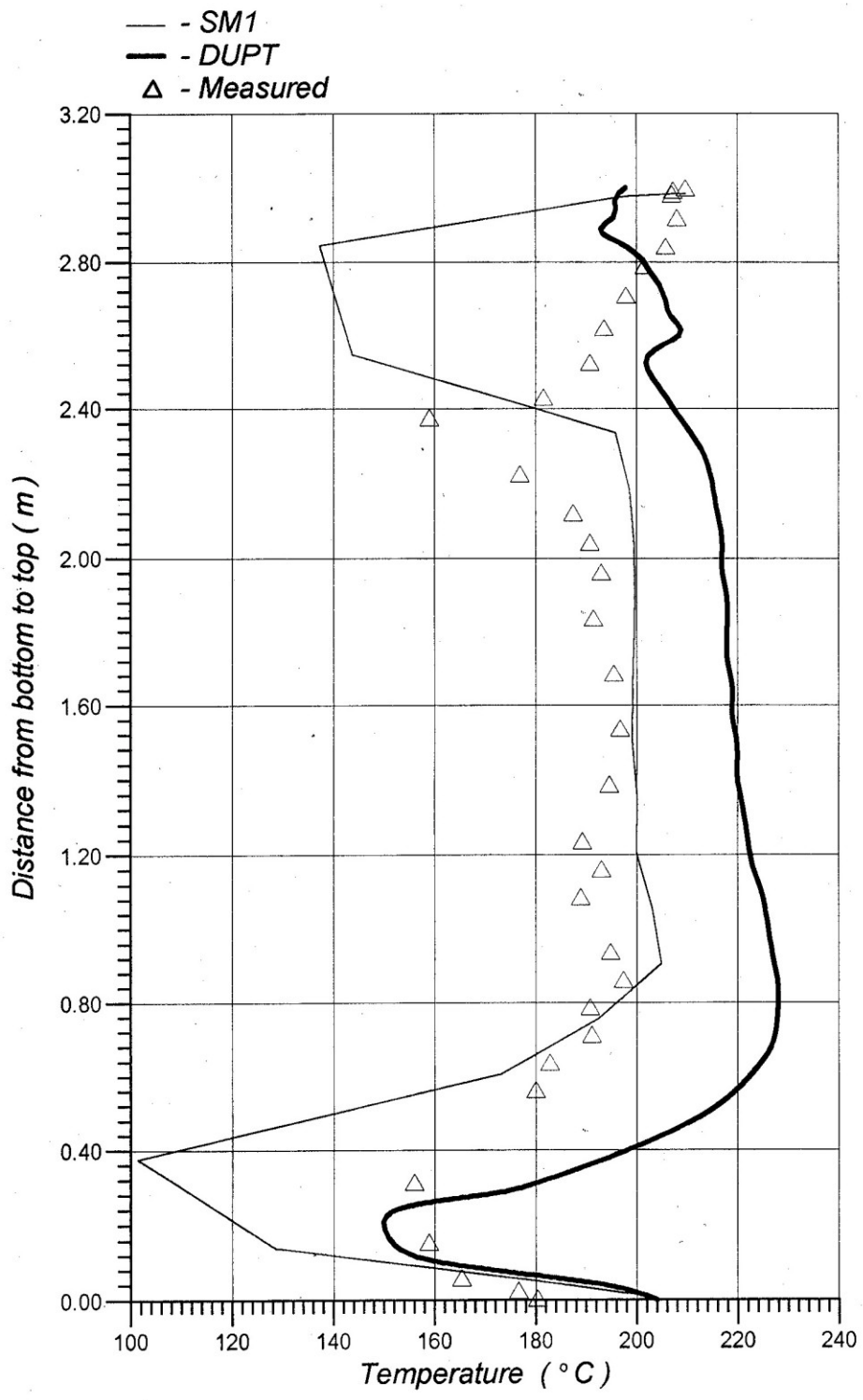

Fig. 4-41 Vessel outside surface temperature (Benchmark problem II)

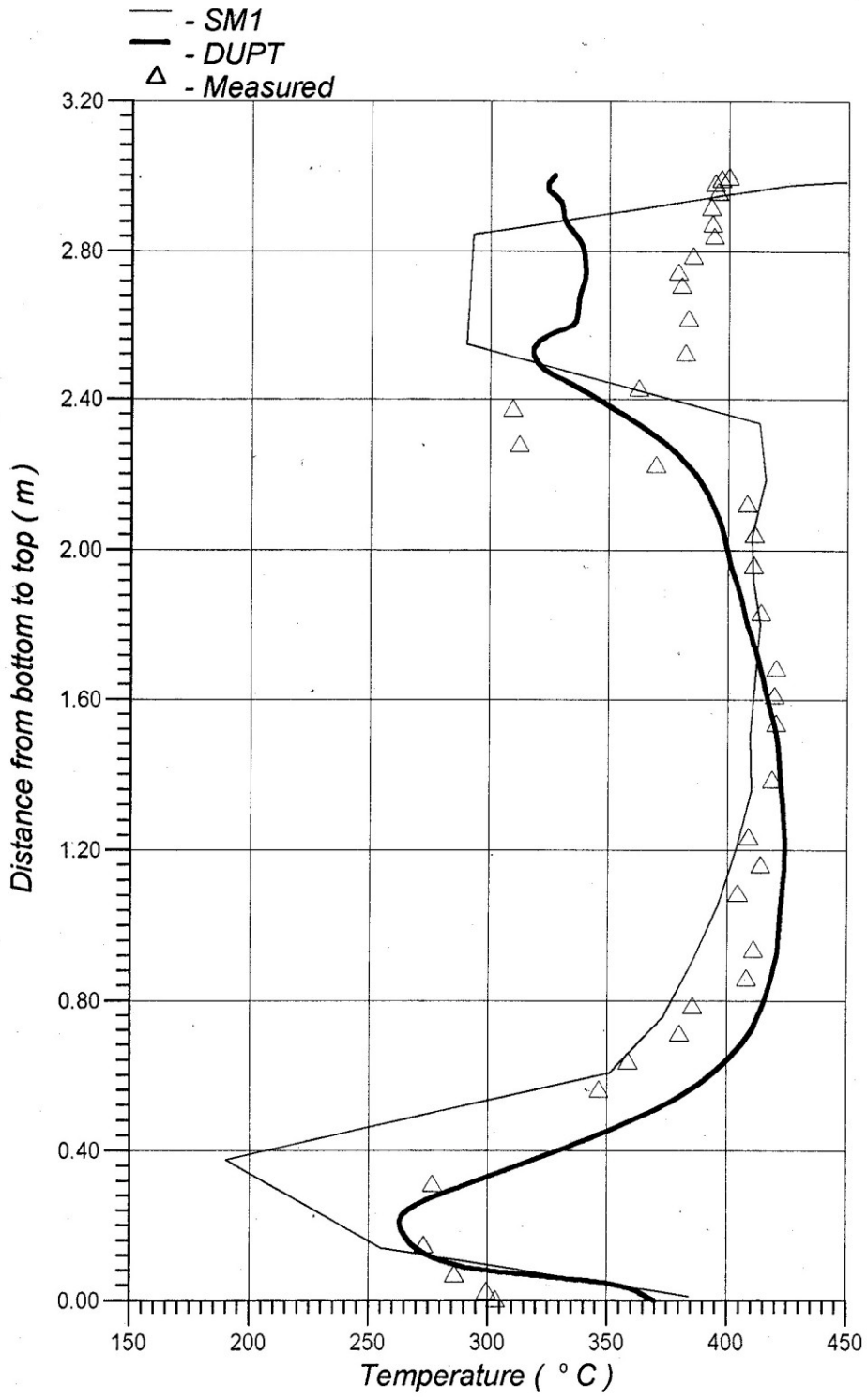

Fig. 4-42 Vessel outside surface temperature (Benchmark problem III)

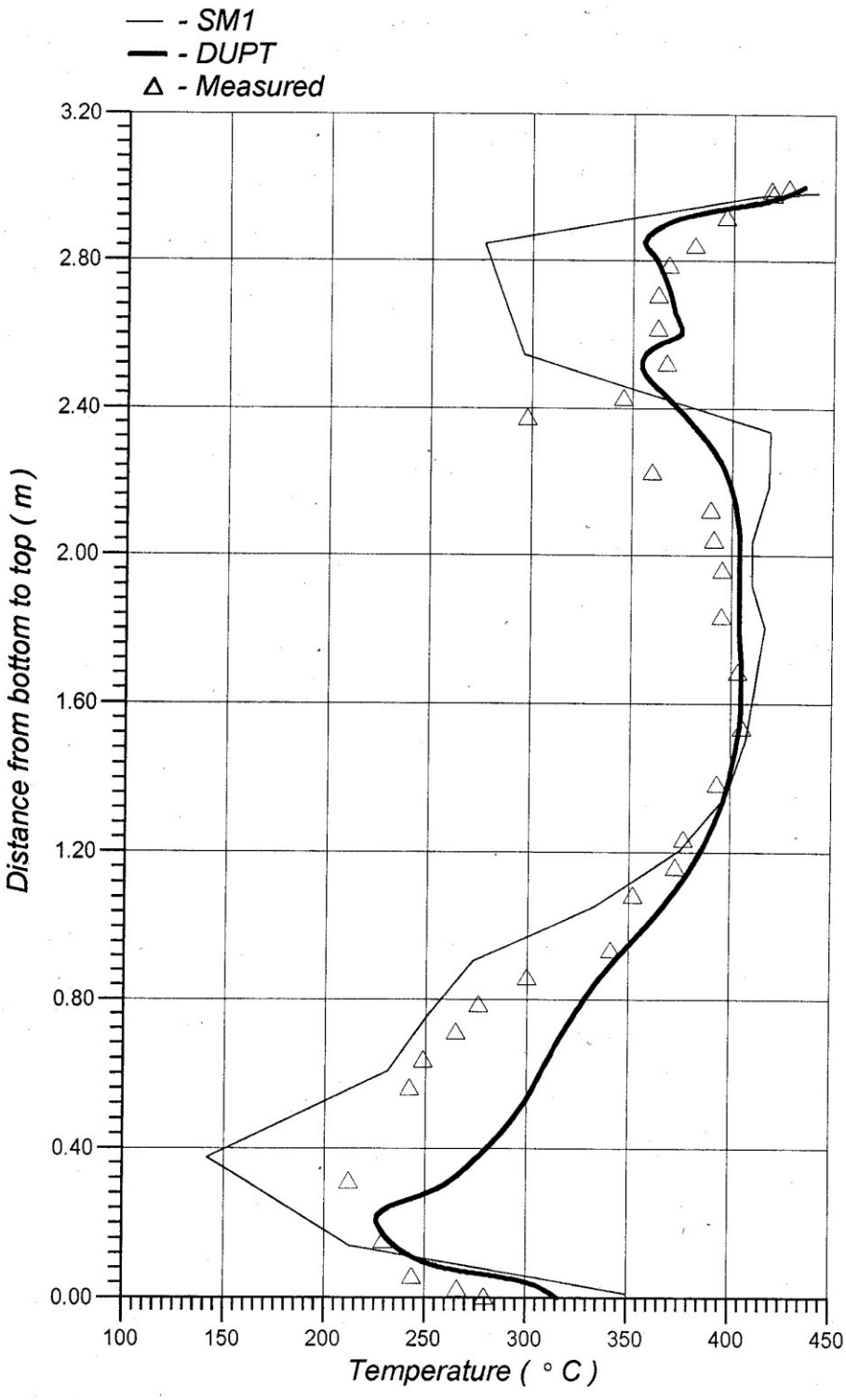

Fig. 4-43 Vessel outside surface temperature (Benchmark problem IV)

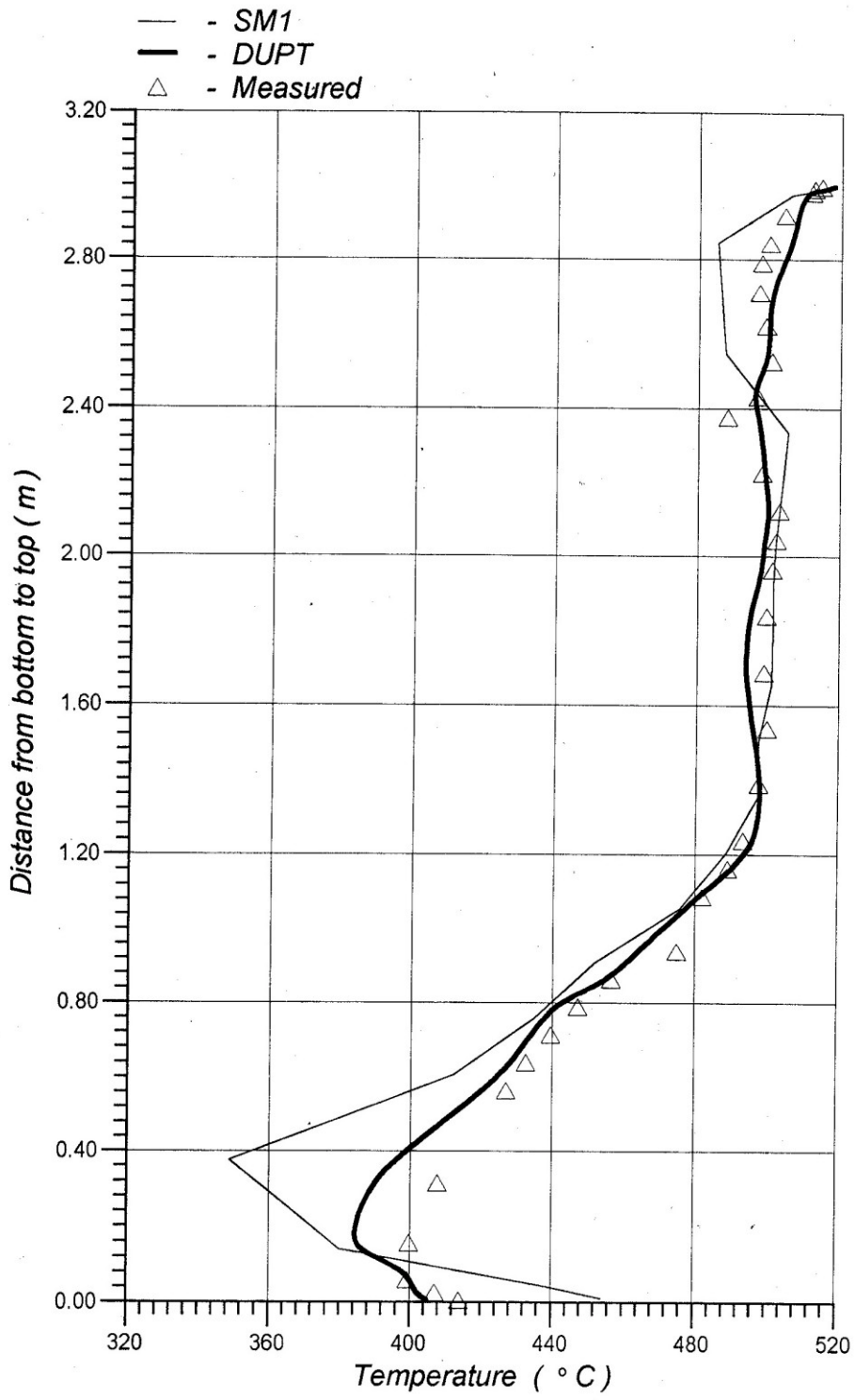

Fig. 4-44 Vessel outside surface temperature (Benchmark problem V)

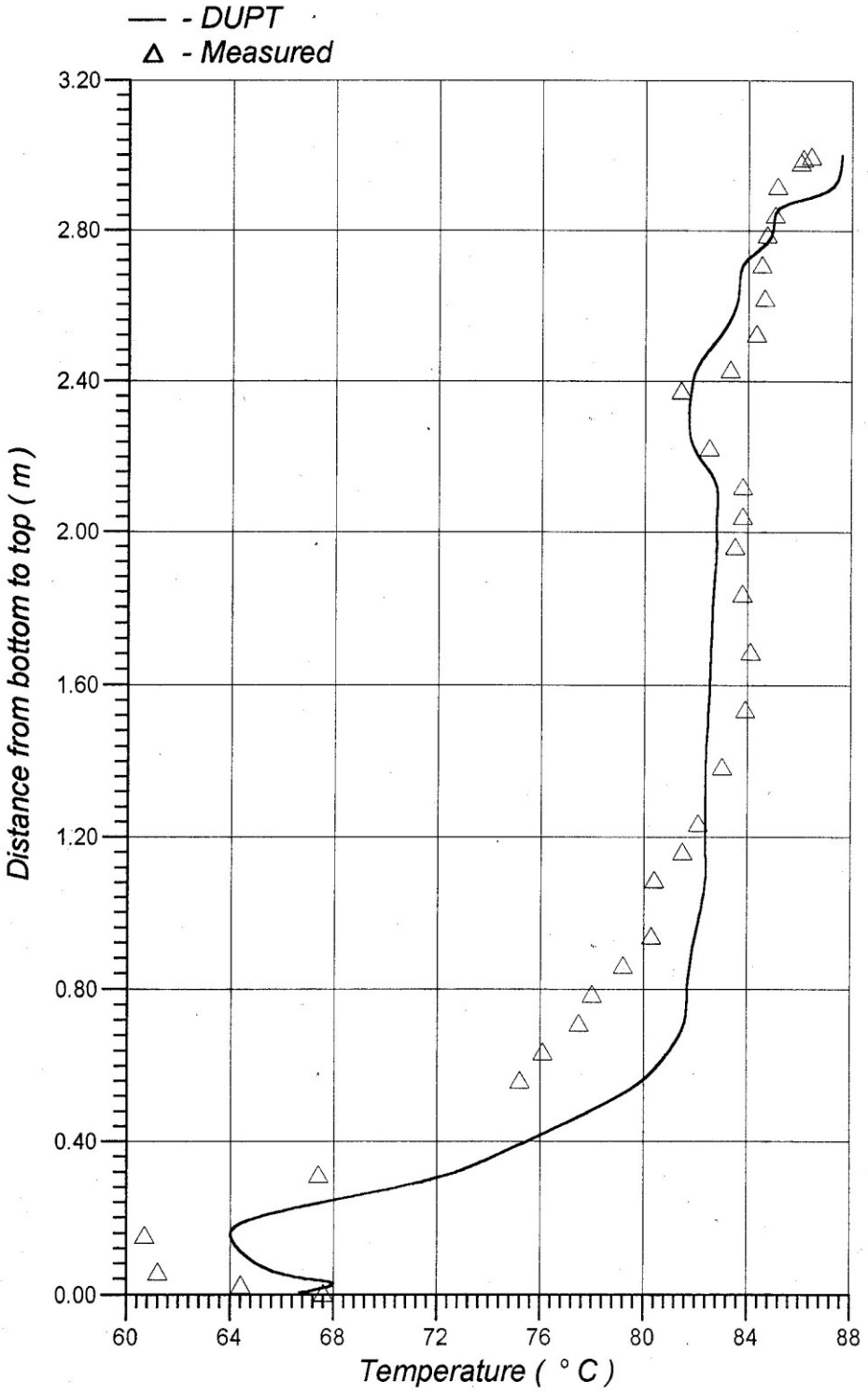

Fig. 4-45 Vessel outside surface temperature
(Benchmark problem VI-a)

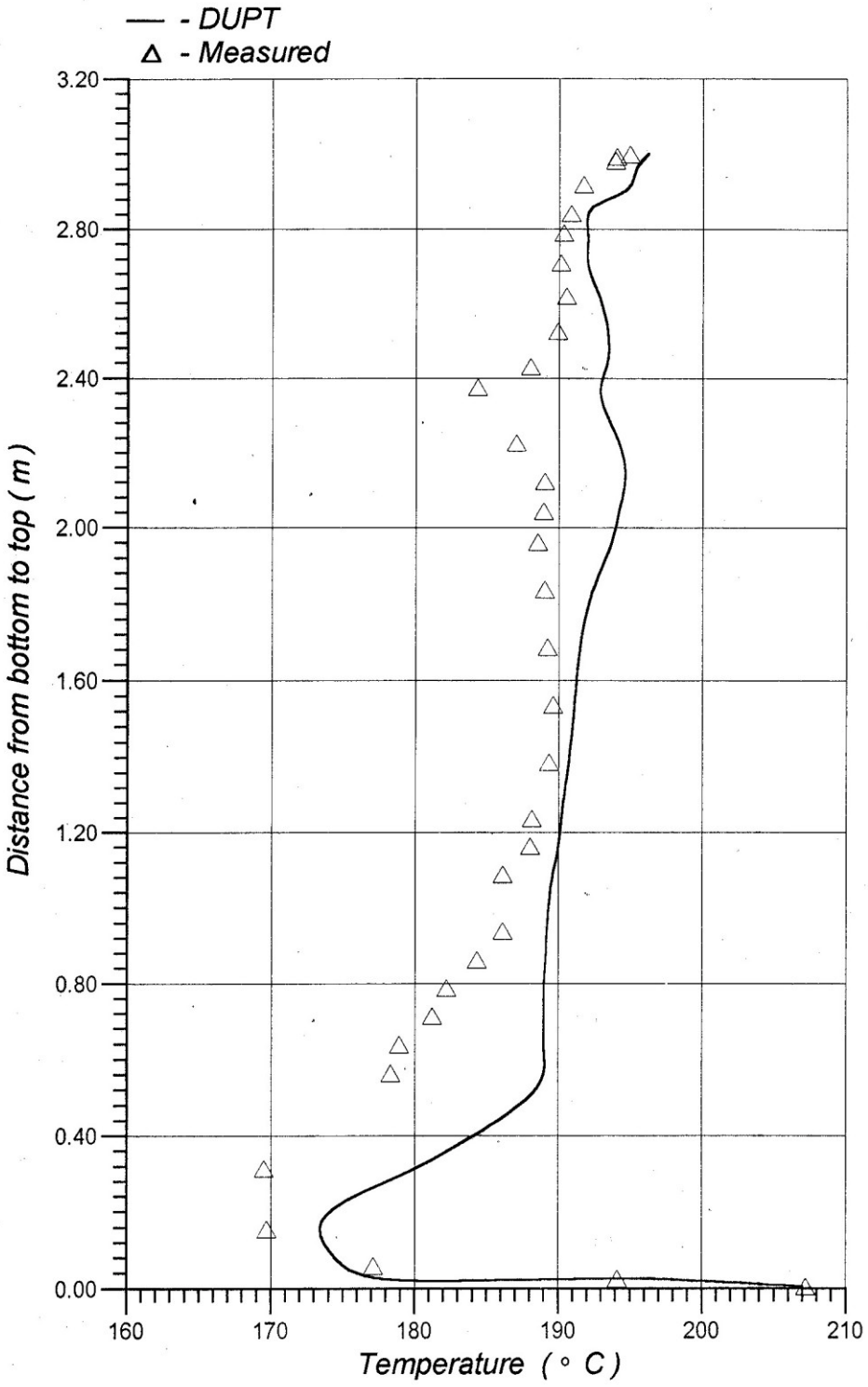

Fig. 4-46 Vessel outside surface temperature
(Benchmark problem VI-b)

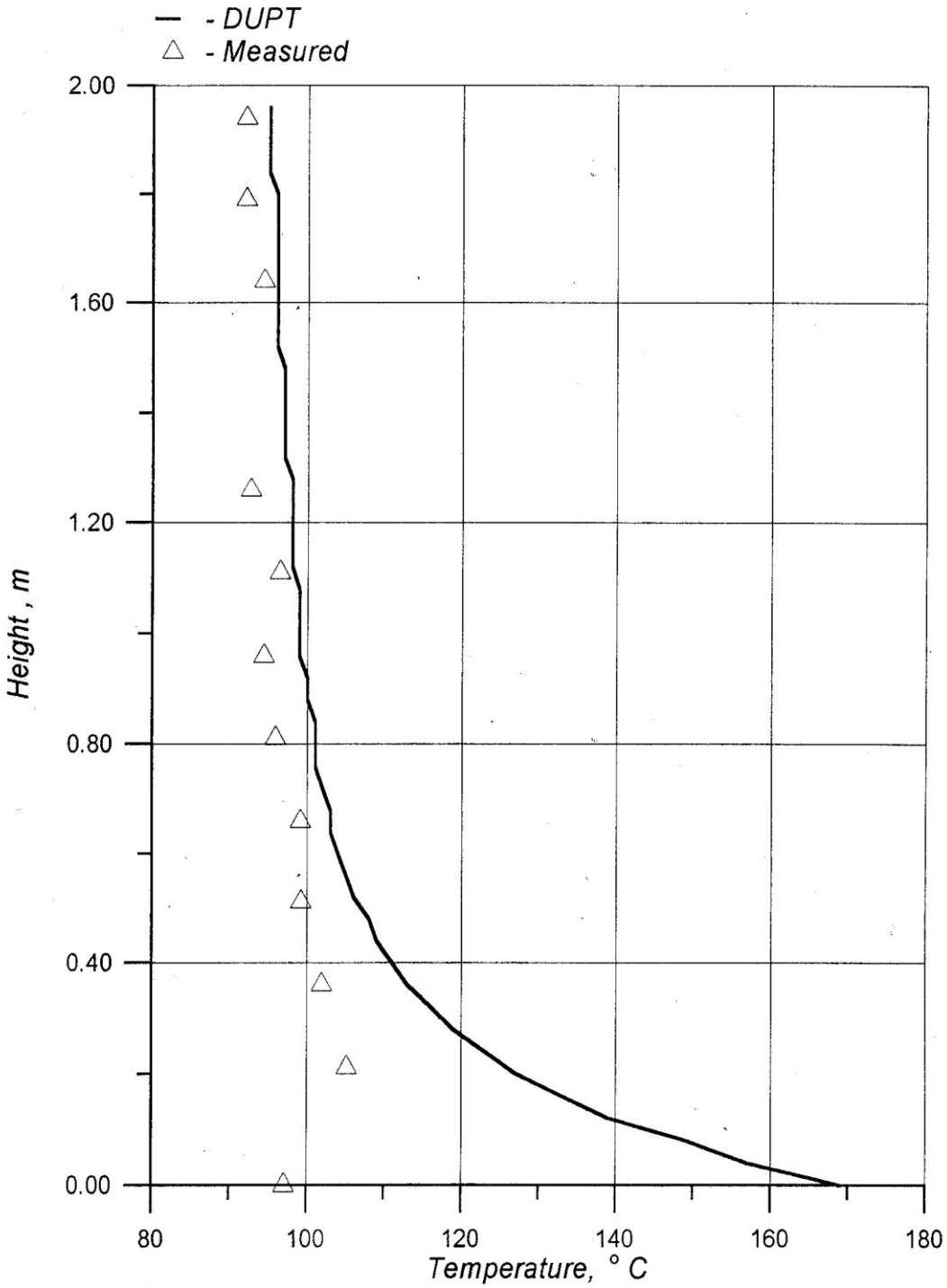

Fig. 4-47 Heater outside surface temperature
(Benchmark problem VI-a)

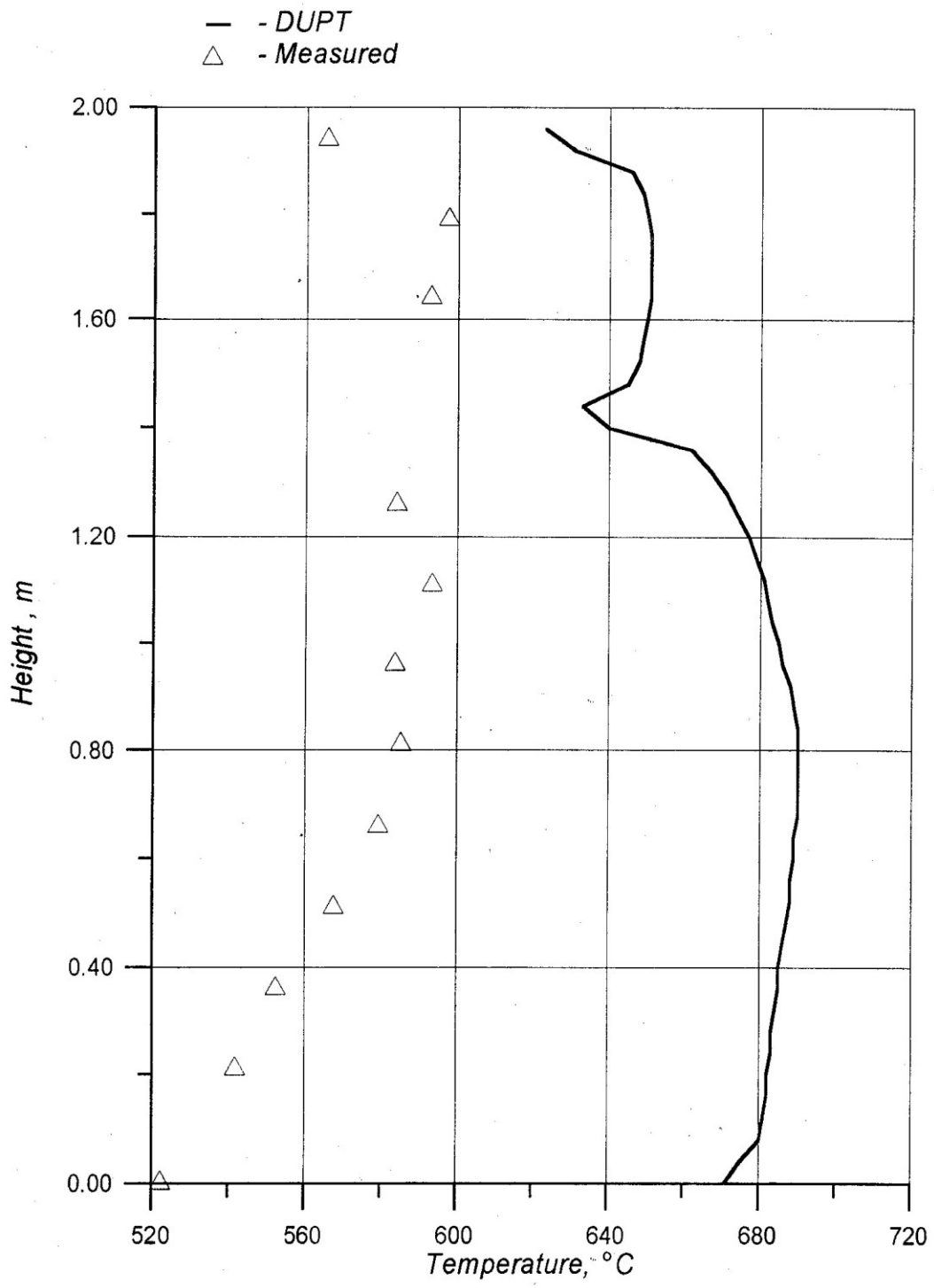

Fig. 4-48 Heater outside surface temperature (Benchmark problem III)

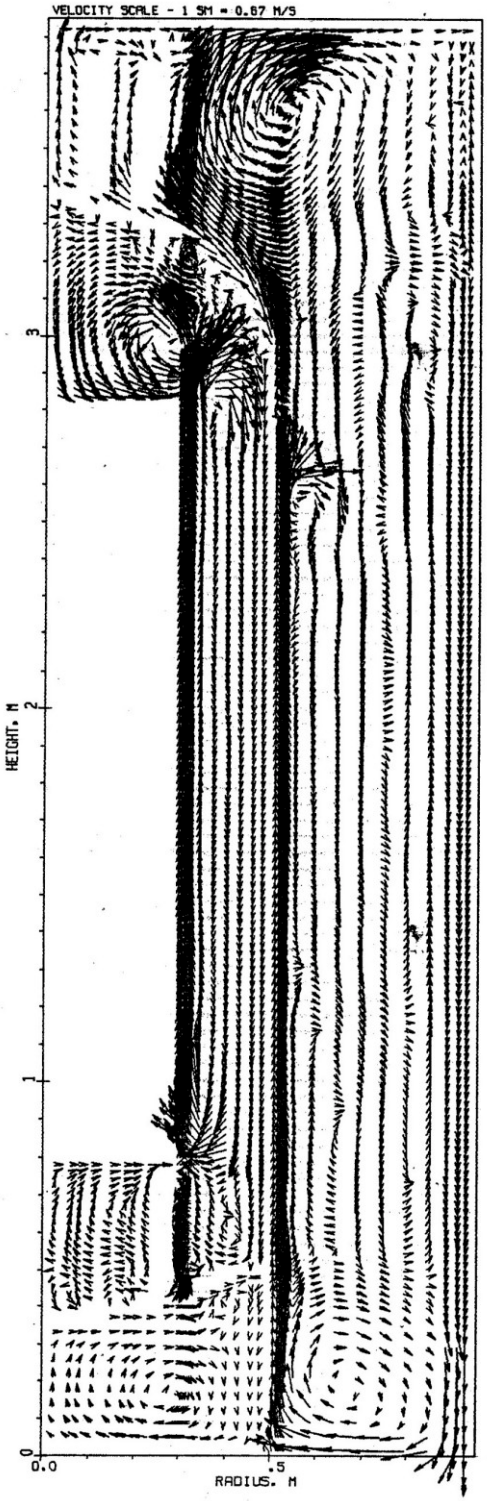

Fig. 4-49 Velocity vectors inside and outside vessel (Benchmark problem V)

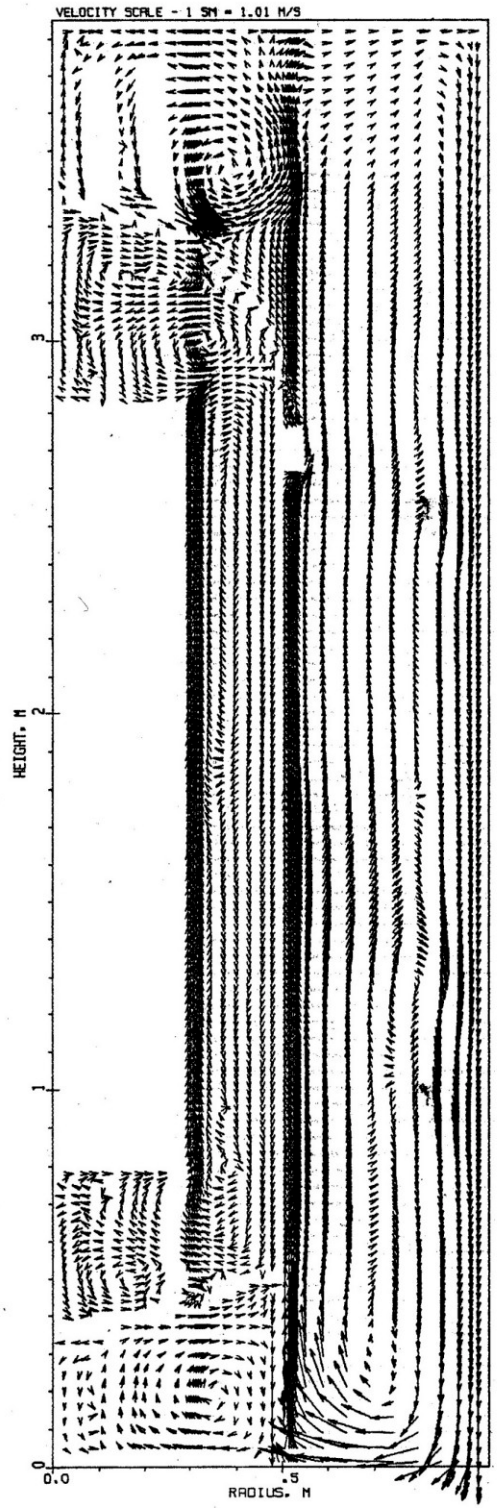

Fig. 4-50 Velocity vectors inside and outside vessel
(Benchmark problem VI-a)

4.1.5. Analysis of HTTR Reactor Cavity Cooling System Benchmark Problem with the MORECA–Code

4.1.5.1. Introduction

The benchmark problems [1]-[5] provided by Dr. M. Hishida of the Japan Atomic Energy Research Institute (JAERI) were analyzed at ORNL as a part of the IAEA Coordinated Research Program (CRP) on "Heat Transport and Afterheat Removal for GCRs under Accident Conditions." The purpose of the exercise is to provide partial validation of analytical methods used to predict the response of Reactor Cavity Cooling System (RCCS) designs used by CRP participants for their respective GCR plant designs. It is also useful in that comparisons of results and techniques will lead to a better understanding of the strengths and limitations of the various models and approaches used. Sensitivity studies performed as part of the analyses will also indicate any special requirements for R&D or design studies to ensure that critical parameters stay within prescribed limits.

The HTTR RCCS experimental data generously supplied by JAERI is particularly useful to this exercise, as it is the result of very carefully designed and executed experiments. The experimental apparatus consists of a partial-scale vessel test section with 6 individually-controlled heaters corresponding to the GCR's core barrel (4) and top and bottom reflectors (1 each), with water-cooled panels surrounding the vessel (Fig. 4-51).

4.1.5.2. ORNL Analysis Approach

The model used in the ORNL MORECA code for vessel-to-RCCS heat transport is a multi-node dynamic representation of about 100 nodes each for the RCCS and vessel. It includes "textbook" approximations for radiation heat transfer view (or shape) factors and net heat transport, with Rayleigh or Grashof Number-based correlations for estimating overall convection heat transfer in the annulus between the vessel and the cooling panels. Since the model is a small part of an overall reactor (dynamic) accident simulator, it must be "efficient" and hence does not attempt to provide fine-structure temperature profiles like those obtained from multi-thousand-node-type finite difference or finite element codes.

The main questions to be answered in this exercise are, given the differences in the HTTR and other HTGR RCCS designs, and other limitations imposed by the nature of the experimental data provided, what aspects of the MORECA-like model can be evaluated and validated, and are the models used "satisfactory?"

4.1.5.3. ORNL Analysis Model Features and Limitations

The model used for benchmark problem analysis, adapted from the MORECA code, predicts vessel and core barrel (heater) temperature profiles (vs. time) for input values of heater power and cooling panel temperatures. The models used for heat transfer between the core barrel and vessel utilize 12 azimuthal segments (30° each) corresponding to each of the 4 core barrel heater sections. Currently, with no azimuthal asymmetry indicated in the experimental setup, there will be no azimuthal temperature variations predicted; however, this feature would be of use if azimuthal asymmetry were introduced into the experiments. The top heater (corresponding to the top reflector) is represented by 9 equal-area concentric rings with a corresponding 9-ring model for the top vessel head area. The vessel upper and lower side wall areas are represented by one cylindrical ring each. Since there is (typically) relatively little interest in the bottom temperatures, the bottom heater, bottom vessel, and bottom cooling panel areas are assigned only one node each.

In the initial HTTR experiments, the forced-flow water-cooled panel spatial temperature variations were very small (3°C maximum), and thus the panels were represented as a uniform-temperature heat sink. However, with the vessel heat sink at a nearly uniform temperature, the capability of the radiant heat transfer model for predicting heat losses to non-uniform temperature heat sinks is not readily validated. A better check on radiation heat transfer modeling is provided by

the temperature distributions resulting from heater (core barrel) to vessel heat transfer, especially for the vacuum case, where convective heat transfer in the vessel is nil.

In the first two test runs (LTV & LTP), the vessel temperatures are significantly lower than those typical of HTGR LOCA scenarios, so the radiative component of heat transfer is proportionally smaller than in the reactor case. Hence, the selection of an optimum correlation for convective heat transfer in the annulus would be much less critical for the reactor case.

Subsequent runs were submitted to the CRP by JAERI for higher average vessel temperatures (~367 and 329°C), which were the high-temperature pressurized case (HTP) and the high-temperature standpipe case (HTSP), respectively. In the standpipe case, 19 pipes were welded to the top vessel head to simulate the control rod drive housings; in addition, the temperature in the core barrel region was less uniform than usual because one of the heaters (No. 5) was broken.

Three additional cases were submitted with air, rather than water, cooling in the RCCS panels. In the first of these (HTAC), the vessel temperature was considerably higher (~467°C), though due to limitations in panel heat removal capability, the total power removed was small. The other two cases (LTH6 & MTH6) were at lower temperatures with only the bottom heater turned on, and were designed to help with the understanding of the natural convection within the pressure vessel. The standpipes were still in place.

The analysis code used in the HTSP and air-cooled panel cases was modified to treat the three RCCS cooling panel temperatures (top, side, and bottom) individually. Previously, the three panel temperatures were nearly equal, and so a uniform sink temperature was assumed. Also, the effective area of the vessel upper head was augmented by 50% to account for the "extended heat transfer surface" of the standpipes.

For the HTTR RCCS benchmark experiment cases in which the vessel is pressurized, there are substantial convection-driven flows between the core barrel (heaters) and vessel walls. These flows cause a significant redistribution of heat within the vessel. While large (pressurized) convection flows are characterized in the MORECA code's core model, the specially adapted RCCS model does not accommodate this phenomenon; instead, annulus convection heat transfer (for the annuli both inside and outside the vessel) is approximated by selected Rayleigh or Grashof-based correlations. An effective annulus convective heat transfer coefficient derived from the selected correlation is used both in the annulus (core barrel [heater] to vessel) and between the top (and bottom) heaters and the top (and bottom) vessel head. Likewise, outside the vessel, the heat transfer coefficient derived for the annulus between the vessel and cooling panels is used in the top and bottom areas.

While the use of approximate annulus (convective) heat transfer coefficients appears to result in reasonable agreement for all benchmark problem cases of annulus heat transfer, as well as for the top and bottom vessel areas for atmospheric pressure (or less), it does not adequately model the pressurized vessel case. There the data clearly indicate that the cooler downflow of pressurized helium along the vessel wall that cools the bottom cavity and the hotter upflow into the top cavity cause major heat redistributions in the top and bottom areas that are not accounted for by the correlations. Since these effects were not judged to be crucial to accident modeling in the MORECA code, which does account for the large convection flows in the core regions, no attempt was made to model these complex phenomena solely for the benchmark exercise.

Another feature added to the special RCCS model for the HTTR benchmark cases was an "optional" heat loss calculation. The heat transfer through the 100-mm-thick Kaowool-insulated shell surrounding the experiment was difficult to infer because most of it is shielded from the vessel by the cooling panels. An approximate heat loss was derived by using an average (measured) outer shell temperature as the ultimate sink temperature, and then calculating (by iteration) a radiation plus convection heat transfer rate using averaged vessel and insulator inner shell temperatures, which must then equal the heat conduction rate through the insulation. The major unknown in this calculation is the effective heat transfer area of the insulator shell as seen by the vessel.

4.1.5.4. Results of Benchmark Studies

Results are presented for the 7 test cases submitted by JAERI. In each case, "Problem 1" is to calculate the vessel temperatures given the heater powers and the vessel internal pressure, and "Problem 2" is to calculate the heat transfer rate from the vessel to the cooling panels given the vessel temperatures. The given vessel temperature data also serve as the "answers" to Problem 1. As noted in the previous section, the calculation of vessel temperatures for the pressurized vessel conditions is not complete in that the convection-driven flows heating and cooling the top and bottom vessel areas are not accounted for in the Rayleigh or Grashof Number-based annular heat transfer correlations.

Since the HTTR RCCS experiment has no intrinsic azimuthal asymmetries, the temperature data at given elevations around the circumference were averaged to obtain mean values that could be applied to the comparisons with calculations. Temperature data were also typically recorded at several axial levels for each of the axial nodes in the model, which correspond directly to individual heater segments. These were also averaged to make further comparisons. More modeling detail is included in the upper vessel head region, which includes 9 equal-area concentric ring segments each for the top heater and the vessel head. Single nodes were used for the bottom heater and vessel areas.

Key values typically used in the "best estimate" Reference case model calculations include emissivities of 0.95 for the (blackened) vessel outer surface and the cooling panels, and emissivities of 0.66 and 0.79, respectively, for the heaters and vessel inner surfaces (the latter being measured values given in the JAERI experiment description).

The Eckert-Carlson Grashof Number-based correlation[8] for annulus convective heat transfer is used for Reference case calculations (for both inside and outside the vessel). When the experiment heat loss calculation is included, the Reference case assumption is that, due to the spacing of the tubes in the cooling panels, the vessel effectively sees 10% of the surface area of the insulation located behind the cooling panels. Correspondingly, the effective cooling panel heat transfer area is reduced to 90% of the total circumscribed by the panels.

Sensitivity studies are also described which indicate the effects of variations in these baseline assumptions.

4.1.5.4.1. Low-Temperature Vacuum Condition (LTV) Reference Case

Figures 4-52 through 4-54 show comparisons of the measured vessel temperatures for the vacuum condition case with the model's Reference case calculated values (Problem 1) for the top head, core barrel section and bottom regions. The error bands shown on some of the temperature data points correspond to the RMS values of the spread in measured values around the circumference of the vessel. In Fig. 4-52 (top head), calculations for the 9-ring head model show a steeper gradient than measured, but the same average temperature, as well as very close agreement on the upper sidewall average. Fig. 4-53 (core barrel region) shows good agreement in the middle sections, with high predictions for the ends. The measured temperatures in the flange area (for both the vacuum and pressurized cases) are much lower than the region temperature predictions, since the radial heat conduction from the vessel to the outer portion of the (low-conductivity) steel flange is not modeled. The calculated bottom area average temperature (Fig. 4-54) is close to the measured value.

The RMS value of the temperature differences (measured vs. calculated) for the eight vessel sections, which is used as a figure of merit for sensitivity study comparisons, is 11.5°C for the Reference case. The overall average measured vessel temperature is 122°C vs. a calculated average of 129°C. At these temperatures the (calculated) distribution of radiant vs. convective heat losses is roughly 65% to 35%. Nominally, this ratio for the HTGR heatup accident cases is more in the range of 90% to 10%.

For Problem 2, with the averaged measured values for vessel temperature inserted into the model, the calculated (Reference case) heat loss to the cooling panels is 11.57 kW, compared to 13.14 kW total heater power (12% low). However, including the Reference model calculation for heat loss through the insulated experiment enclosure (1.69 kW), the total losses calculated are 13.26 kW (vs. 13.14 kW input), or <1% high.

4.1.5.4.2. Low-temperature vacuum condition (LTV) sensitivity studies

Sensitivity studies done for the vacuum condition case included:

a) An increase in the emissivity value assumed for the blackened outer vessel surface and the cooling panels from 0.95 to 1.0 resulted in decreasing the calculated average vessel temperature to 125°C (Problem 1), vs. the measured average of 122°C,

b) Using different correlations for convection heat losses in the annulus between the vessel and the cooling panels had some effect on calculated vessel temperatures (Problem 1) and power losses (Problem 2), more so than would be the case for higher temperature vessels. Using the Rayleigh-Number-based Keyhani equation[9], the calculated average vessel temperature was 123°C (6°C lower than the Reference case and 1°C higher than the measured average). The calculated power loss to the cooling panels for Problem 2 was 12.67 kW (vs. 11.57 kW for the Reference case),

c) Assuming 100% effective heat transfer area for the cooling panels (vs. 90% Reference case), the calculated mean vessel temperature was reduced by 6°C to 123°C (Problem 1) and the heat loss to the cooling panels using vessel temperature data (Problem 2) increased to 12.75 kW (up 10.2%),

d) In a variation on the Problem 2 calculation, the input for the measured vessel temperatures was varied +/- 5°C around the measured average values. The resulting heat loss rates to the cooling panels, 12.35 kW for +5°C and 10.82 kW for -5°C (vs. 11.57 kW Reference case), are +/- 6.5% changes, which are proportional to appropriately weighted changes in the 4th-power and arithmetic-average temperature differences between the vessel and the panel cooling water,

e) The Reference model uses an expression for net radiation exchange for convex gray surfaces in a radiation-free space (i.e., no external irradiation is present). In a variation which used the expression for gray surfaces enclosed by a single reradiating surface, the differences were insignificant.

4.1.5.4.3. Low-Temperature Helium Pressurized Condition (LTP) Reference Case

Figure 4-55 shows a comparison of the measured and calculated vessel temperatures in the core barrel region for the pressurized condition case using the Reference model (Problem 1). As noted previously, the model does not account for the relatively large buoyancy-driven convection flows that cause additional heating in the upper head area and additional cooling in the lower vessel area, so these comparisons are not shown. As before, the error bands shown on some of the temperature data points correspond to the RMS for measured values around the circumference of the vessel. Calculated values of vessel temperatures in the core barrel heater region are reasonably close to the measured values in the top and middle sections, but diverge near the bottom as the effects of the convection cooling flows, not accounted for, become more important. The overall average measured vessel temperature is 183°C, and at this temperature, the (calculated) distribution of radiant vs. convective heat losses is roughly 70% to 30% as opposed to 90% to 10% for HTGR cases of interest.

For Problem 2, with the averaged measured values for vessel temperature inserted into the model, the calculated (Reference case) heat loss to the cooling panels is 22.21 kW, compared to 28.79 kW total heater power (22.9% low). Including the heat loss through the insulated experiment enclosure (2.78 kW), the total losses calculated are 24.99 kW (vs. 28.79 kW input), or 13.2% low.

While no explanations for this difference are offered, it is noted that the error is conservative (i.e., the model predicts less-than-actual heat transfer rates).

4.1.5.4.4. Low-Temperature Pressurized Condition (LTP) Sensitivity Studies

One of the sensitivity studies done for the pressurized condition case included alternative correlations for convection heat losses in the annulus between the vessel and the cooling panels were used. For the Keyhani equation, the calculated power loss to the cooling panels (Problem 2) was 24.03 kW, and with the heat loss to the shell (2.87 kW), the total computed power output is 26.9 kW (6.6% low, vs. 13.2% low in the Reference case). Hence, it appears that the Rayleigh-based convection heat transfer equation may be superior under these conditions.

4.1.5.4.5. High-Temperature Pressurized (HTP) Reference Case

Because the vessel is pressurized in the subsequent cases, and due to the limitations of the model noted previously, only Problem 2 solutions are presented.

Table 4-11 shows the averages of the measured vessel temperatures and their standard deviations for the high-temperature case (HTP), and comparisons of the calculated heat losses with the measured input power, along with a case using the Keyhani correlation. The calculated heat loss from the vessel to the cooling panels for the Eckert-Carlson case is 87.92 kW. With the heat loss to the insulated shell, the total is 94.48 kW, compared to 93.93 kW total heater power (calculated losses 0.6% high). In this case, the Keyhani correlation results in an overprediction of the total heat loss by 4.8%. The right-hand column (Conv/Total) shows the ratio of calculated convection losses to the cooling panel to the total (convection plus radiation) losses.

Table 4-11: Measured vessel temperatures for the high-temperature pressurized case (HTP) (temperatures in °C) and comparisons of measured and calculated heat losses (powers in kW)

Core Barrel Section

	Vessel Head	Upper S.W.	Htr. 2	Htr 3	Htr. 4	Htr. 5	Lower S.W	Lower Head	Average Temp
Measured	392.0	374.9	399.9	415.8	413.6	376.0	276.7	289.1	367.2
Std Dev.	6.7	10.6	20.2	3.0	4.6	27.7	3.8	14.6	11.4

JAERI: Heater power in = 93.93 (estimated loss to cooling panels = 84.61; estimated loss to insulation = 9.32)

ORNL Heat-Loss Calculations:

	Total	Total/JAERI	Cooling Panel	Insul.	Conv/Total
Eckert-Carlson	94.48	1.006	87.92	6.56	0.160
Keyhani	98.48	1.048	91.91	6.57	0.196

4.1.5.4.6. High-temperature stand-pipe (HTSP) reference case

Table 4-12 shows the averages of the measured vessel temperatures and their standard deviations for the stand-pipe case, along with comparisons of the calculated heat losses with the measured input power as the results for "Problem 2" plus a variation using the Keyhani correlation. The calculated heat loss from the vessel to the cooling panels for the Eckert-Carlson case is 73.7 kW, plus a heat loss to the insulated shell, for a total of 79.54 kW, compared to 77.54 kW total heater power (calculated losses 2.6% high). Once again, the Keyhani correlation gives somewhat higher results (calculated losses 7.3% high).

Table 4-12 Measured vessel temperatures for the high-temperature standpipe case (HTSP) (temperatures in °C) and comparisons of measured and calculated heat losses (powers in kW)

		Core Barrel Section							
	Vessel Head	Upper S.W.	Htr. 2	Htr. 3	Htr. 4	Htr. 5	Lower S.W.	Lower Head	Average Temp
Measured	399.7	360.1	389.6	402.4	363.7	264.7	207.2	243.3	328.8
Std. Dev.	24.8	9.2	16.8	2.4	23.5	25.9	4.2	25.2	16.5

JAERI: Heater power in = 77.54 (estimated loss to cooling panels = 69.15; estimated loss to insulation = 8.39)

ORNL Heat Loss Calculations:

	Total	Total/JAERI	Cooling Panel	Insulation	Conv/Total
Eckert-Carlson	79.54	1.026	73.70	5.84	0.171
Keyhani	83.20	1.073	77.35	5.85	0.210

4.1.5.4.7. High-Temperature Air-Cooled RCCS Panel (HTAC) Reference Case

Since the cooling panels were not designed for air cooling, the RCCS heat removal capability was not as efficient as it would be normally. However, this test provided a good benchmark point for both a high-temperature vessel and a high-temperature cooling panel (e.g., for a degraded system). For both the Reference (Eckert-Carlson) and Keyhani cases (Table 4-13), the predicted heat losses were low; however, convection losses are a minor part of the total. The discrepancies are more likely due to an underestimation of the losses through the insulation.

Table 4-13 Measured vessel temperatures for the high-temperature air-cooled panel case (HTAC) (temperatures in °C) and comparisons of measured and calculated heat losses (powers in kW)

		Core Barrel Section							
	Vessel Head	Upper S.W.	Htr. 2	Htr. 3	Htr. 4	Htr. 5	Lower S.W.	Lower Head	Average Temp
Measured	505.7	498.2	501.6	500.3	487.7	440.3	404.4	398.9	467.1
Std. Dev.	7.1	1.5	2.3	1.3	8.1	11.9	2.8	8.7	5.5

JAERI: Heater power in = 29.79

ORNL Heat Loss Calculations:

	Total	Total/JAERI	Cooling Panel	Insulation	Conv/Total
Eckert-Carlson	27.78	0.927	20.75	7.03	0.032
Keyhani	28.04	0.941	21.00	7.04	0.043

4.1.5.4.8. Low/Medium Temperature Single-Heater (LTH6/MTH6) Reference Cases

While the MORECA code RCCS model does not account for the convection flow and heat transfer within the pressure vessel, and hence doesn't address the issue of heat redistribution in the vessel, solutions of Problem No. 2 provide additional useful validation of the vessel to RCCS panel heat transfer models. Table 4-14 shows the results for both cases, each with the Reference (Eckert-Carlson) and Keyhani convection heat loss models. While the percentagewise agreement is not as good as in previous cases (7.9 and 13.7% high for predicted heat loss), the absolute values of the errors for such a large experiment (~200-350 W high) are quite small.

Table 4-14 Measured vessel temperatures for the low- and medium-temperature single-heater cases (LTH6/MTH6) (temperatures in °C) and comparisons of measured and calculated heat losses (powers in kW) [L=low, M=medium]

Core Barrel Section

		Vessel Head	Upper S.W	Htr. 2	Htr. 3	Htr. 4	Htr. 5	Lower S.W.	Lower Head	Average Temp
Measured	L	85.5	84.1	83.4	83.3	81.5	77.6	66.6	61.9	78.0
Std. Dev.	L	0.8	0.9	0.7	0.9	1.0	1.6	0.7	2.7	1.2
Measured	M	192.7	189.7	188.7	188.7	186.7	180.0	167.6	181.3	184.5
Std. Dev.	M	1.8	1.4	1.4	1.6	1.8	2.5	1.6	15.5	3.5

JAERI: Heater 6 (bottom) power in = 2.576 (L); 7.986 (M)
ORNL Heat Loss Calculations:

		Total	Total/JAERI	Cooling Panel	Insulation	Conv/Total
Eckert-Carlson	L	2.78	1.079	1.72	1.06	0.255
Keyhani	L	2.93	1.137	1.87	1.06	0.315
Eckert-Carlson	M	8.32	1.042	5.45	2.87	0.146
Keyhani	M	8.60	1.077	5.72	2.88	0.187

4.1.5.5. Conclusions

– We have found this to be a very useful validation exercise, and are very grateful to Dr. Hishida and his colleagues at JAERI for their generosity in supplying this data to the CRP,

– At the relatively low temperatures, the annular convection heat transfer is 30-35% of the total heat transfer from the vessel to the cooling panels, which is ~4 times more than its contribution in the higher temperature ranges typically seen in HTGR loss of coolant accident scenarios. Use of the Eckert-Carlson correlation (Reference model) gives more pessimistic results (smaller heat transfer coefficients and higher vessel temperatures) than

does the Keyhani correlation (as used originally in the MORECA-2 code). The differences in these correlations become less important at the higher temperatures,

- Variations in emissivity values for the vessel-to-cooling panel radiant heat exchange process have a direct proportional effect on heat loss (at given vessel temperatures). Computed changes in heat losses for variations in average vessel temperatures were in direct proportion to weighted changes in the 4th-power and arithmetic-average temperature differences between the vessel and the panel cooling water. Hence in spite of the relatively wide variations in vessel temperatures, the overall heat removal capabilities appear to be fairly simply related to key heat exchange factors (emissivities) and average temperature differences,

- When the vessel is surrounded by cooling panels at a uniform temperature and the emissivities are very high, the calculated radiant heat transfer to the panels would not be sensitive to view factor or net radiation exchange modeling distinctions, and hence would not provide validation for the models used. However, comparisons made for heat transfer models from the core barrel (heaters) to the vessel, where the sink temperature (vessel) is non-uniform, showed a distinct advantage to using the view factors and net radiant exchange expressions for finite-length concentric cylinders,

- Certain aspects of "simplified RCCS models" (i.e., those using relatively few nodes and textbook equations for macro-scale radiative and convective heat transfer) were not validated in this benchmark problem exercise. However, those that were tested ("challenged") were shown to be of sufficient accuracy for the purposes of GCR accident simulations, and the errors seen were generally in the conservative direction (i.e., models predicted less-than-actual RCCS heat removal). For example, since predicted total heat removal from the vessel was typically within 10% of actual, the effects on maximum fuel temperature predictions in heatup accident scenarios would be within acceptable bounds. The accuracy of bulk vessel temperature predictions was also acceptable for limiting temperature conditions within the limits, as noted, of the model's capability,

- At the higher vessel temperatures, the ratio of annular convection temperature to the total is in the range of 5-10%, compared to those of the relatively low temperatures in the initial benchmark calculations (30-35%). Ratios typical of HTGRs in loss of coolant accident scenarios are in the 10% range. Differences in the convection correlations become less important at the higher vessel temperatures,

- The wider variation in vessel and sink temperatures for HTP and later cases with stand-pipes and air cooling provided a better test of the validity of the view factor and net radiation exchange models. Also, the accuracy of the predictions of total heat loss from the vessel was very good. The simplified models used in this case were shown to be of sufficient accuracy for the purposes of GCR accident simulations, and the errors (with the Eckert-Carlson convection model) were generally in the conservative direction (i.e., models predicted less-than-actual RCCS heat removal),

- Other experiments could give useful validation data for the radiative heat transfer models by making the effective cooling panel heat sink non-uniform, for example:

    a) putting insulating material in front of a sector of the side panel (e.g., 30°) to test the model's sensitivity to azimuthal variations in radiative heat transfer; and

    b) cutting off one of the two cooling water supplies for the side panel to test the approximation for effective panel and insulated shell heat transfer areas.

REFERENCES TO SECTION 4.1.5.

[1] S. Takada, Y. Shiina, Y. Inagaki, and M. Hishida, "Benchmark Problem for IAEA Coordinated Research Program (CRP-3) on GCR Afterheat Removal," JAERI Dept. of High Temperature Engineering Research, Feb. 1994, (IAEA Reference 622-I3-RC-503).

[2] S. Takada, Y. Shiina, Y. Inagaki, M. Hishida, and Y. Sudo, "Benchmark Problem for IAEA Coordinated Research Program (CRP-3) on GCR Afterheat Removal," JAERI Dept. of High Temperature Engineering Research, Feb. 1995, (IAEA Reference 622-I3-RC-503.2).

[3] S. Takada, Y. Shiina, Y. Inagaki, M. Hishida, and Y. Sudo, "Benchmark Problem for IAEA Coordinated Research Program (CRP-3) on GCR Afterheat Removal - Pressure vessel with stand pipes," JAERI Dept. of High Temperature Engineering Research, June 1995.

[4] S. Takada, K. Suzuki, I. Terunima, Y. Shiina, M. Hishida, and Y. Sudo, "Benchmark Problem for IAEA Coordinated Research Program (CRP-3) on GCR Afterheat Removal - Air cooling panel," JAERI Dept. of High Temperature Engineering Research, October 1995.

[5] S. Takada, Y. Shiina, M. Hishida, K. Suzuki, and Y. Sudo, "Benchmark Problem for IAEA Coordinated Research Program (CRP-3) on GCR Afterheat Removal," JAERI Dept. of High Temperature Engineering Research, October 1995. (power only to bottom heater)

[6] S. J. Ball and D. J. Nypaver, MORECA-2: Interactive Simulator for Modular High-Temperature Gas-Cooled Reactor Core Transients and Heatup Accidents with ATWS Options, NUREG/CR-5945 (ORNL/TM-12233), Oak Ridge National Laboratory, October 1992.

[7] J. C. Conklin, Modeling and Performance of the MHTGR Reactor Cavity Cooling System, NUREG/CR-5514 (ORNL/TM-11451), Oak Ridge National Laboratory, April 1990.

[8] E. R. G. Eckert and W. O. Carlson, "Natural Convection in Air Layer Enclosed Between Two Vertical Plates with Different Temperatures," Intl. J. Heat and Mass Trans., Vol. 2, p. 106, 1961.

[9] Keyhani et al., "Free Convection in a Vertical Annulus with Constant Heat Flux on the Inner Wall," J. Heat Trans., Vol. 105, pp. 454-459, 1983.

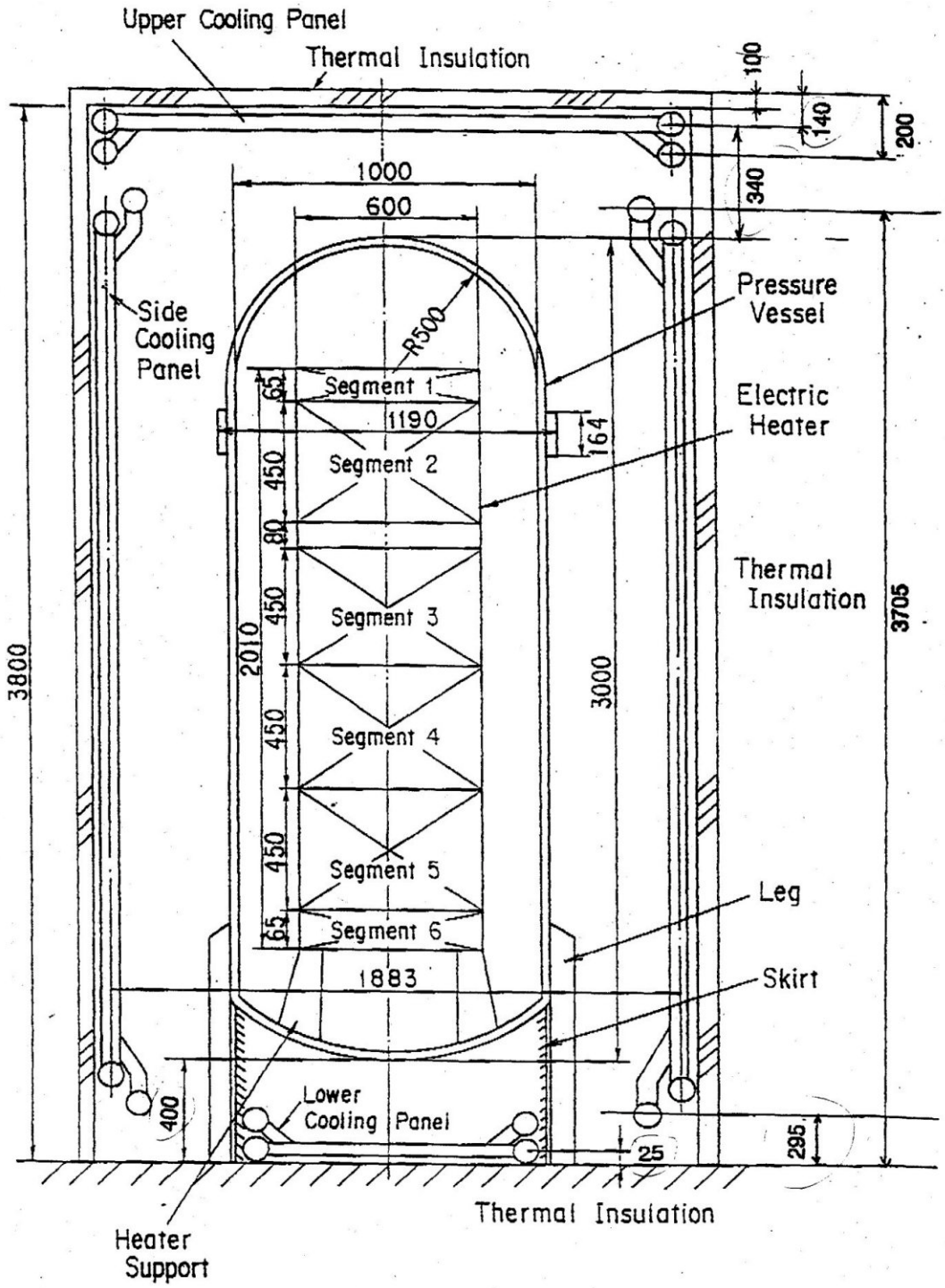

Fig. 4-51 Schematic Diagram of the Test Apparatus

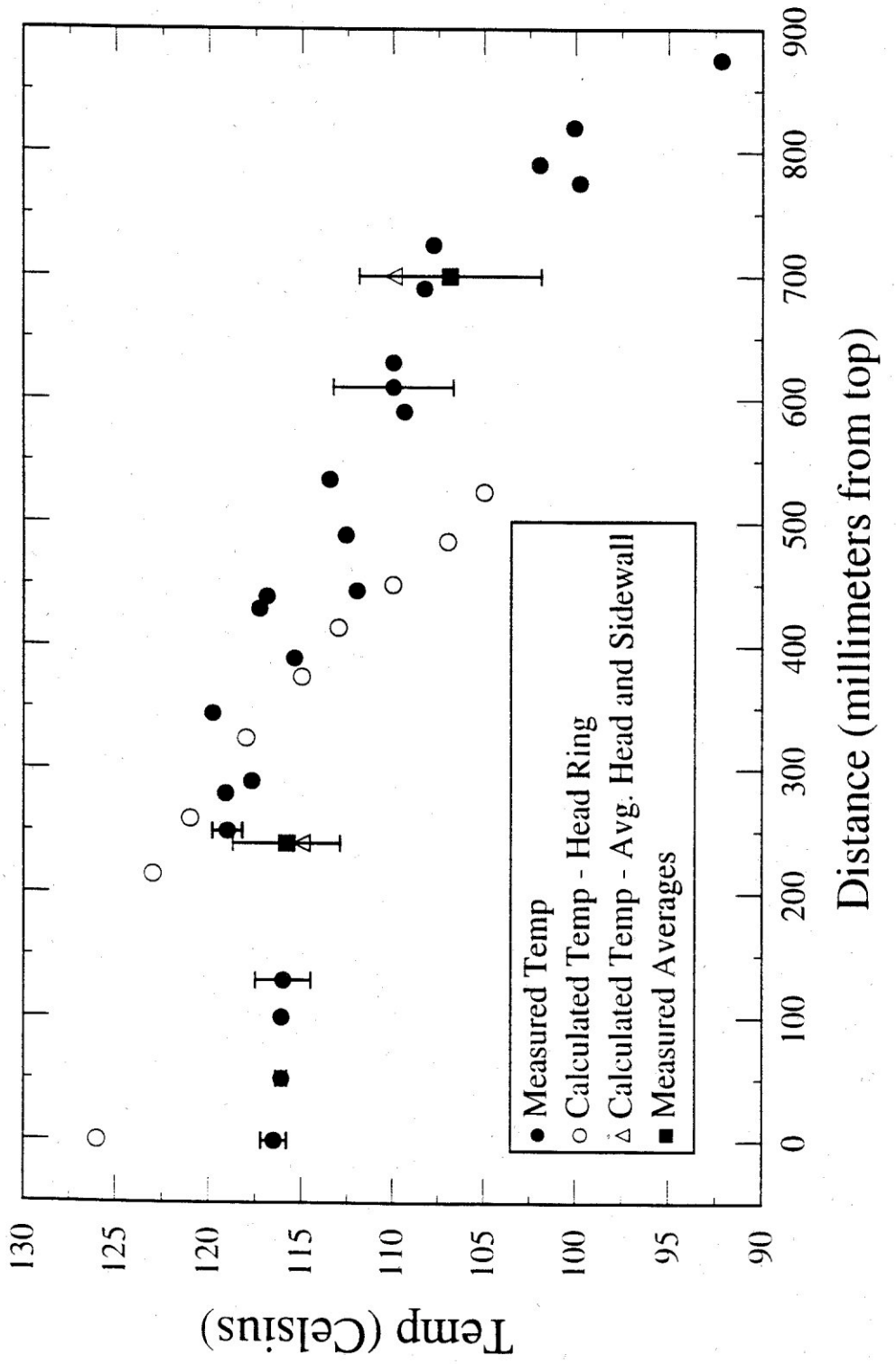

Fig. 4-52 Pressure vessel upper head surface temperature – vacuum conditions

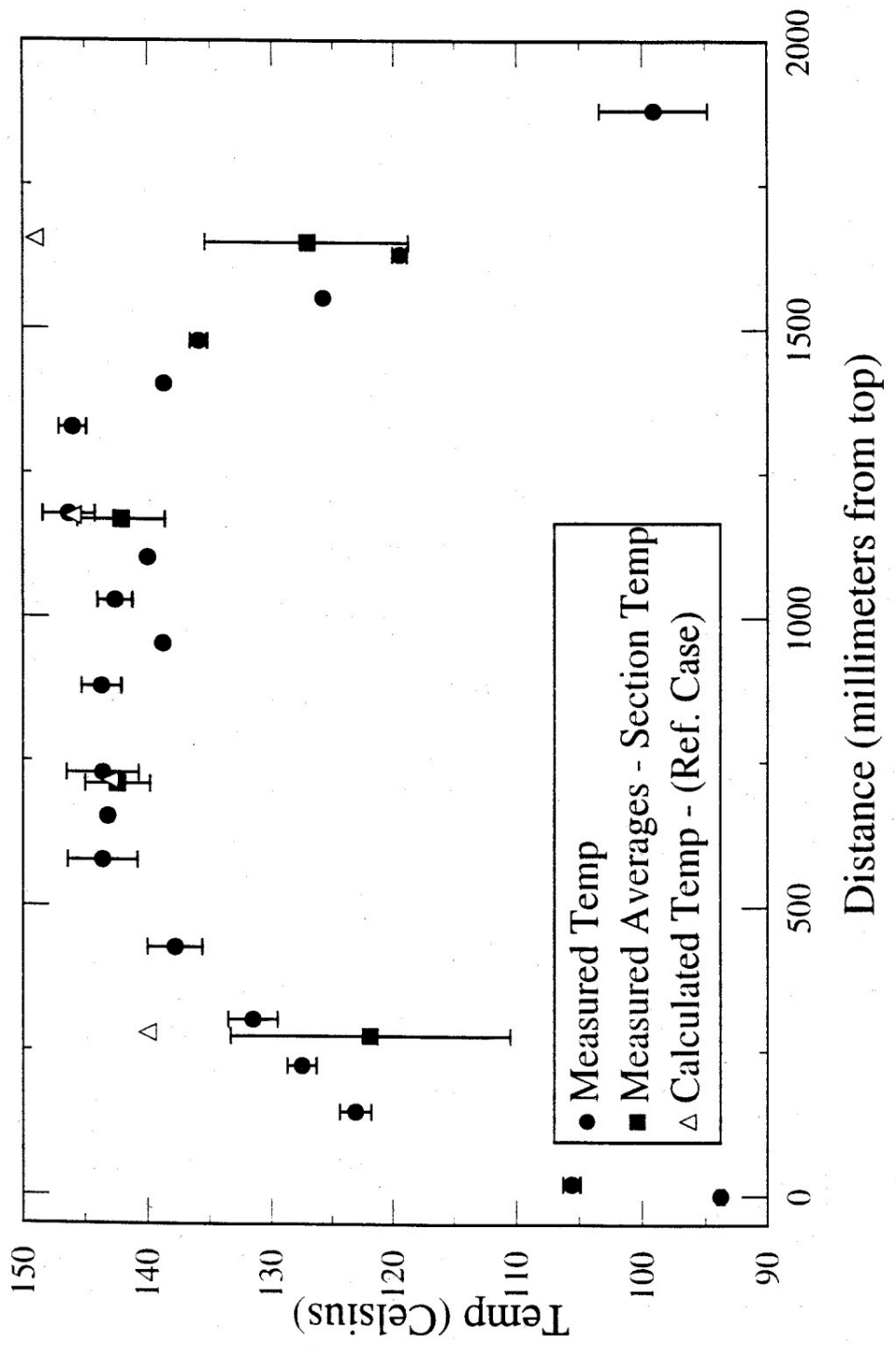

Fig. 4-53 Pressure vessel core barrel section surface temperature – vacuum conditions

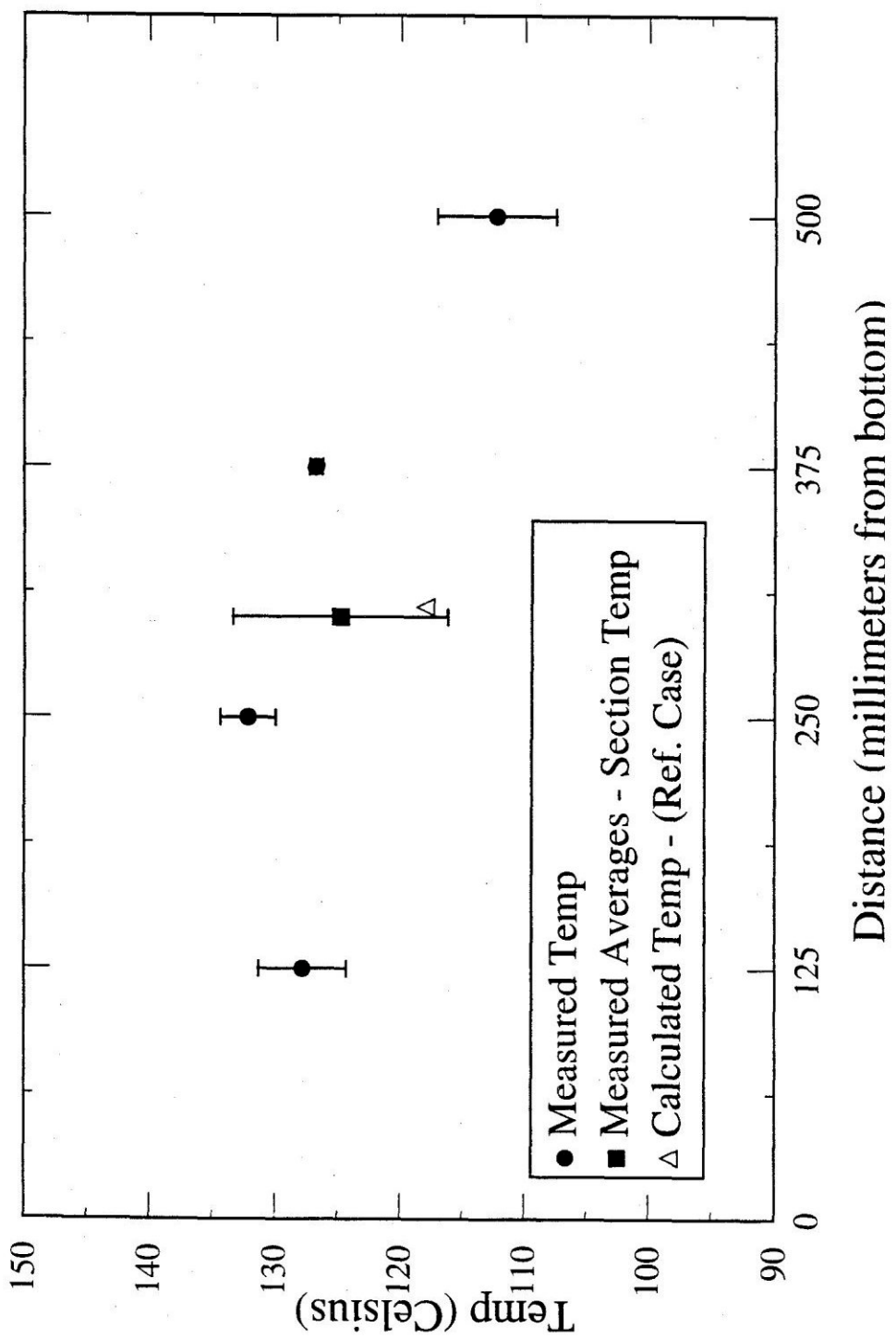

Fig. 4-54 Pressure vessel – bottom section surface temperature – vacuum conditions

Fig. 5

Pressure Vessel Core Barrel Section Surface Temperatures - Pressurized Conditions

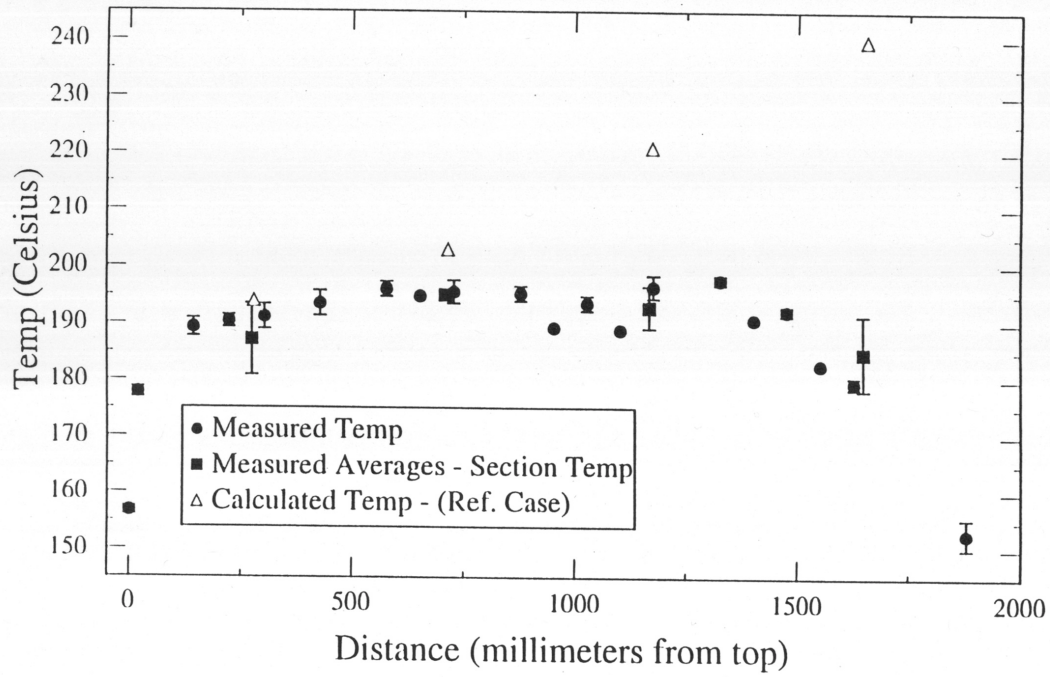

4.1.6. Analysis of HTTR Reactor Cavity Cooling System Benchmark Problem with the Fidap–Code

4.1.6.1. Introduction

The two key issues addressed by this exercise are:

– The degree of computational complexity required to simulate the passive heat removal mechanisms in the GCRs, specifically radiation and natural (free) convection, which facilitate heat transfer from the reactor core to the reactor cavity cooling system (RCCS); and,

– The sensitivity of the GCR decay heat removal analytical predictions to variations in analysis methodology and modeling approaches.

The analysis performed by Bechtel Research and Development in support of this effort used computational fluid dynamics (CFD) model developed to simulate the heat transfer and associated temperatures for the test model.

Data from the HTTR mockup were provided by JAERI for a heat transfer experiment using high heat fluxes from the simulated reactor heater surface representing a heater temperature condition close to that inside actual GCRs. The high temperature condition was analyzed using a model with a strong focus on issue 1 described above. Several model variations were investigated to evaluate the degree of computational detail required to achieve accuracy in comparison to the experiment measurements.

4.1.6.2. Analysis Methology

Computational Fluid Dynamics (CFD) involves the numerical solution of the governing equations of fluid mechanics and heat transfer using iterative methods based on the finite difference or the finite element technique. CFD utilizes the construction of a computational grid, or mesh, which comprises the physical domain of the problem geometry, and solves the governing equations of mass, momentum, and energy conservation (i.e., Navier-Stokes) at each intersecting node of the mesh.

The mathematical modeling of benchmark problem was performed using the FIDAP Fluid Dynamics Analysis Package [1] a commercially available software program developed by Fluid Dynamics International, Inc. FIDAP is based on the finite element method and utilizes unstructured meshing techniques for grid generation.

4.1.6.3. The Model

The HTTR RCCS experimental data generously supplied by JAERI[2] was particularly useful to this exercise, as it resulted from very carefully designed and executed experiments. The experimental apparatus, shown in Fig. 4-56, consists of a partial-scale pressure vessel test section with 6 individually controlled heaters located along the core barrel and top/bottom reflectors, with water-filled RCCS cooling tubes surrounding the vessel. Experimental data was provided for a wide variety of conditions. The one selected for analysis in this paper is a case of a pressurized gas condition to incorporate the effect of helium natural convection inside the pressure vessel (i.e., pressurized conduction cooldown accident) which is a more challenging analysis since it requires the additional modeling of helium natural convection inside the vessel combined with thermal radiation. Also the vessel temperatures for this case were higher than those for others and closer to the temperatures characteristic of the actual GCRs.

The model was based on an axis-symmetric geometry in order to accommodate a two-dimensional calculation. The dimensions used in the model replicate the physical experiment to a high degree of accuracy, while at the same time incorporating simplicity in several key areas. The inner boundary of the model is located along the outer surface of the heater and the outer boundary is located along the inner surface of the cooling tubes and adjacent cavity wall section. To simplify the model, the region behind the cooling tubes was not modeled. The spacing between the tubes

cannot be replicated with a 2-D model, so this effect was accounted for by adjusting the effective sink temperature of the modeled cavity wall surfaces using an area-weighted average between the measured cooling tube and insulated wall temperatures.

The model was comprised of two fluid regions–inside the vessel (nitrogen at specified pressure) and outside the vessel (air at atmospheric pressure)–separated by the pressure vessel. It was assumed that the reactor cavity region below the vessel and inside the support skirt is isolated from the rest of the cavity–in effect, the air in this region is trapped. Inside the vessel, it was assumed that the heater support skirt is porous enough so that its impedance to fluid flow and heat transfer is not significant–thus, it was not modeled.

At the top and bottom of the heater, the wall surrounding the heater is extended to account for the effect of the structural "ring" around the heater used to support the heater. Thus the heater surface (heaters 1 and 6) is "indented" at the top and bottom of the vessel to incorporate more realistic geometry at these locations.

The heater output was specified in terms of surface heat flux at the locations indicated based on the reported heater power values. The segments along the heater surface where heat is not applied were modeled as adiabatic. The cooling panel boundaries were maintained at constant temperature. The sections along the cavity wall not bounded by cooling panels were modeled as adiabatic.

Grey-body radiation heat transfer is computed at specified radiating surfaces. The geometric view factors between the radiating surfaces were computed by FIDAP, accounting for shadowing effects in the view factor calculation. Surface emissivity values are shown in Table 4-15. The heat sink temperatures used for the cooling panel model boundary surfaces were derived from taking the mean value between the measured cooling tube and wall temperatures as reported in Reference 2 and are shown in Table 4-16.

Table 4-15 Prescribed Surface Emissivities

Location	Emissivity
Heater surface	0.79
Vessel inner surface	0.8
Vessel outer surface and skirt	0.95
Side cooling panel	0.95
Top/ bottom cooling panel	0.95 0.95

Table 4-16 Cooling Panel Heat Sink Temperatures

Cooling tube position (Thermocouple identification number)	Temperature (C)	Wall position (Thermocouple identification number)	Temperature (C)	Mean temperature (C)
1	67	14	160	113.5
2	58	15	169	113.5
3	47	16	143	95
4	54	17	165	109.5
5	43	18	172	107.5
6	55	19	149	102
7	66	20	168	117
8	54	21	179	116.5
9	65			
10	61	23	176	118.5
11	24			
12	25	24	70	47.5

The buoyancy forces generated by the variations in fluid density are modeled in FIDAP as an additional term in the momentum equation by use of the Business approximation, in which the density term in the hydrostatic head is varied in proportion to the temperature of the fluid and its volume expansion coefficient.

In free convection, the description of flow as turbulent or laminar is determined by its characteristic Grashof or Rayleigh (Gr*Pr) numbers. The division between turbulent and laminar regimes is dependent on the geometry of the domain and can vary within the flow field itself. Typically, the transition between laminar and turbulent occurs at Rayleigh numbers between 10^8 and 10^{11}. For the HTTR experiment, the Rayleigh number inside the pressure vessel is on the order of 1.4×10^{12}, so the turbulent flow model was used for the base case calculations.

The model typically used for confined flows involving natural convection is the "K-epsilon" model, in which the turbulent viscosity is related to the turbulent kinetic energy and turbulent dissipation in the fluid, which are used to describe the time-averaged scale of the turbulent eddies.

The finite element mesh was designed with element density concentrated along all surfaces to capture the thin thermal boundary layers as characterized by turbulent natural convection conditions, particularly along the vessel wall and heater surface. In order to investigate the sensitivity of the solution to the mesh concentration, several models were constructed with different grid distributions. The finite element mesh for the grid referred to as Case 2 is shown in Figs. 4-57. Typical element thicknesses are shown below in Table 4-17. The changes were made from Case 1 to Case 2 were in the mesh concentration along the heater and inside vessel surface, while maintaining the same mesh outside the vessel. The changes made from Case 2 to Case 3 were in the mesh concentration outside the vessel, while maintaining the mesh inside the vessel the same. In this way an attempt was made to investigate the mesh sensitivity inside and outside the vessel separately. The resulting grids for the models used in this analysis ranged between 18,000 and 20,000 elements.

Table 4-17 Element Thickness (mm) Along Walls

	Case 1	Case 2	Case 3
Vessel sidewall (out)	3.5	3.5	1.4
Vessel sidewall (in)	1.0	0.4	0.4
Vessel head (out)	2.6	2.6	0.8
Vessel head (in)	3.5	0.4	0.4
Heater (top)	2.0	0.7	0.7
Heater (bottom)	3.5	0.7	0.7
Heater (side)	1.0	0.4	0.4
Cooling panel (top)	3.2	3.2	3.2
Cooling panel (side)	7.5	7.5	4.5
Cooling panel (bottom)	7.2	7.2	7.2

4.1.6.4. Results

Results are presented for the steady state calculation of temperatures based on the heater power, RCCS cooling panel and insulated wall temperatures, and vessel internal pressure (with nitrogen). To simplify the compilation of test data, temperatures measured with the thermocouples designated by the "C" azimuthal position on the vessel outside wall were used as the basis for comparison with the CFD model.

4.1.6.4.1. Velocity Field

The velocity profile shown in Fig. 4-58 and the streamline contour plot shown in Fig. 4-59 permit visualization of the flow patterns generated inside and outside the vessel and around the upper head region. The Figures shown are derived from the analysis for Case 2 mesh. Inside the vessel, buoyancy-driven natural convection causes the nitrogen to flow upward along the heater and down along the inside of the vessel wall. Outside the vessel, the air flows upward along the vessel wall and downward alongside cooling panels. The maximum velocity inside the vessel is approximately 0.4 m/s and outside the vessel is around 0.8 m/s. It is interesting to note the relatively thin boundary layers predicted by the model along the vessel sidewall and side cooling panel, which is characteristic of natural convection in the high Rayleigh number regime, particularly with the presence of a significant radiation heat transfer component. It is also interesting to see the increasing thickness of the boundary layer develop at higher elevations. The streamline contour plot shows that there is predominantly one main recirculation loop inside the vessel and in the surrounding reactor cavity, although the obstruction caused by the flange does cause a small portion of the air flow to turn around in that region.

4.1.6.4.2. Temperature Profile

The calculated vessel (outside) temperature is shown in Fig. 4-60 for three model meshes along with the test measurements (values summarized in Table 4-17). A color profile of the wall temperatures in the model is shown in Fig. 4-60. Along the vessel sidewall, the agreement between model and experiment is excellent, particularly in the lower part. At the upper sidewall elevation, the model slightly under predicts the temperature. This trend is continued in the upper vessel head,

where the predicted temperatures are around 40°C to 50°C less than the experimental values. The results for Case 2 are most accurate in this region, which indicates that the highest concentration of elements near the surface is appropriate for inside the vessel in order to obtain the highest accuracy for the surface heat transfer calculation, while outside the vessel the elements along the wall do not have to be as concentrated.

Along the lower vessel head, all models predict significantly higher temperatures than the data. This portion of the vessel is opposite the bottom heater, which has a disproportionately high heat flux. The high heater surface temperature suggests that heat transfer is predominantly driven by radiation. The large differences between the model and the data indicate that the model does not incorporate all of the heat removal mechanisms, probably due to insufficient representation of the heat source profile and lack of features to account for all of the convective flow paths.

Fig. 4-61 shows a distribution of temperatures for the nitrogen inside the vessel, the air inside the surrounding cavity, and the steel components (vessel, flange, and support skirt). The mixing effects of natural convection within the pressurized nitrogen are illustrated by this plot. As a result of buoyancy, the hottest gas temperatures occur in the upper head region, with temperatures inside the dome calculated between 450°C and 550°C. The temperature difference between the upper plenum and lower plenum generated by the buoyant nitrogen convection is on the order of 200°C. Consequently, the peak temperature on the upper head is nearly as high as the peak sidewall temperature, despite the fact that the heater output in this region is much less. These nitrogen temperatures show very good agreement with the thermocouple measurements, which were provided in the upper head only.

Inside the vessel lower head, the nitrogen gas is somewhat stagnated, as the sharp turn below the annulus somewhat disconnects this region from the primary recirculation flow (see Fig. 4-59). In the vicinity of the bottom heater, a region of extremely high temperature is shown below heater 6. This occurs as a result of the relatively large amount of heat rejected which is trapped and cannot be convected and recirculated. The indentation of the heater surface has little effect on this result, as a model calculation without the indentation (not shown) produced a similar result. This high temperature condition creates a significant radiation heat transfer component from the bottom heater to the lower vessel head which results in the high surface temperatures previously shown in Fig. 4-60.

Outside the vessel, the highest temperatures also occur around the upper head. Due to buoyancy effects, the highest air temperatures are found at the top of the cavity, with maximum temperatures of around 250°C and minimum temperatures on the order of 120°C. At the bottom of the cavity, the temperatures are a bit higher due to the absence of cooling tubes. Thus, the temperature difference inside the reactor cavity from top to bottom due to natural convection is around 130°C. Also found are localized heating effects due to the flow separation around the vessel flange.

4.1.6.5. Conclusions

In GT-MHR designs, the vessel temperatures during conduction cooldown conditions exceed 400°C and radiative heat transfer accounts for more than 90% of the heat transfer. These conditions were replicated very well in the CRP HTTR experiment, which produced similar vessel temperature conditions. Thus, the CRP benchmark model represents an excellent validation exercise for the analysis tools used to predict temperature conditions during post-accident passive decay heat removal. Although radiation is the dominant mechanism for heat transfer from the reactor to the RCCS, natural convection plays a significant role in producing the localized temperature distributions which are essential for confirming cooling system performance. Because of the significant natural convection component, the applicability of empirical correlations is very limited, and the use of experiments to validate the models becomes even more necessary. In contrast, radiation heat transfer calculations tend to be very robust [in the absence of convection] as long as the geometric view factors and shadowing effects are computed properly.

Based on the preceding analysis and the analysis performed in 1994 [3], it appears that in order to accurately simulate the complex geometry and combined radiation/free convection modes of heat transfer of an experiment such as the HTTR, and consequently in order to model the decay heat removal conditions inside an actual gas-cooled reactor such as the GT-MHR, a thorough preliminary evaluation of the following key parameters is essential:

– mesh grading/density,

– buoyancy/turbulence modeling,

– geometry details.

This investigation provided an excellent starting point towards the validation of modeling decay heat removal in the GCR with computational fluid dynamics models and the higher temperature conditions confirm that [particularly inside the vessel] certain geometry details can affect the heat transfer performance and produce local temperature variations of significance. In addition, accurate simulation of combined radiation/convection heat transfer along surfaces with high Rayleigh number requires a high level of mesh detail in any CFD model, unless empirical correlations are substituted. The problem with empirical correlations is that they can be effective for some configurations (usually very simple geometries) and inappropriate for others. Thus, the use of the finite-element technique holds great promise for simulation of problems such as the CRP Benchmark model. In terms of confirming/validating the applicability of various buoyancy and turbulence models, which are to varying degrees semi-empirical, the use of an experiment such as the HTTR is essential because the accuracy of these models [like any empirical model] is dependent on the particular configuration and conditions, and fine-tuning of the models may ultimately be necessary to obtain optimum performance and to achieve validation prior to construction of a full-scale prototype.

RERERENCES TO SECTION 4.1.6.

[1] FIDAP User Manuals, Fluid Dynamics International, Inc., 1991.

[2] S. Takada, et.al. “Benchmark Problem for IAEA Coordinated Research Program (CRP-3) on GCR Deacy Heat Removal,” JAERI Dept. of High Temperature Engineering Research, February 1995 (IAEA Reference 622-I3-RC-503.2).

[3] Bechtel National Inc., “Bechtel Analysis of HTTR Reactor Cavity Cooling System Benchmark Problem,” October 1994

.

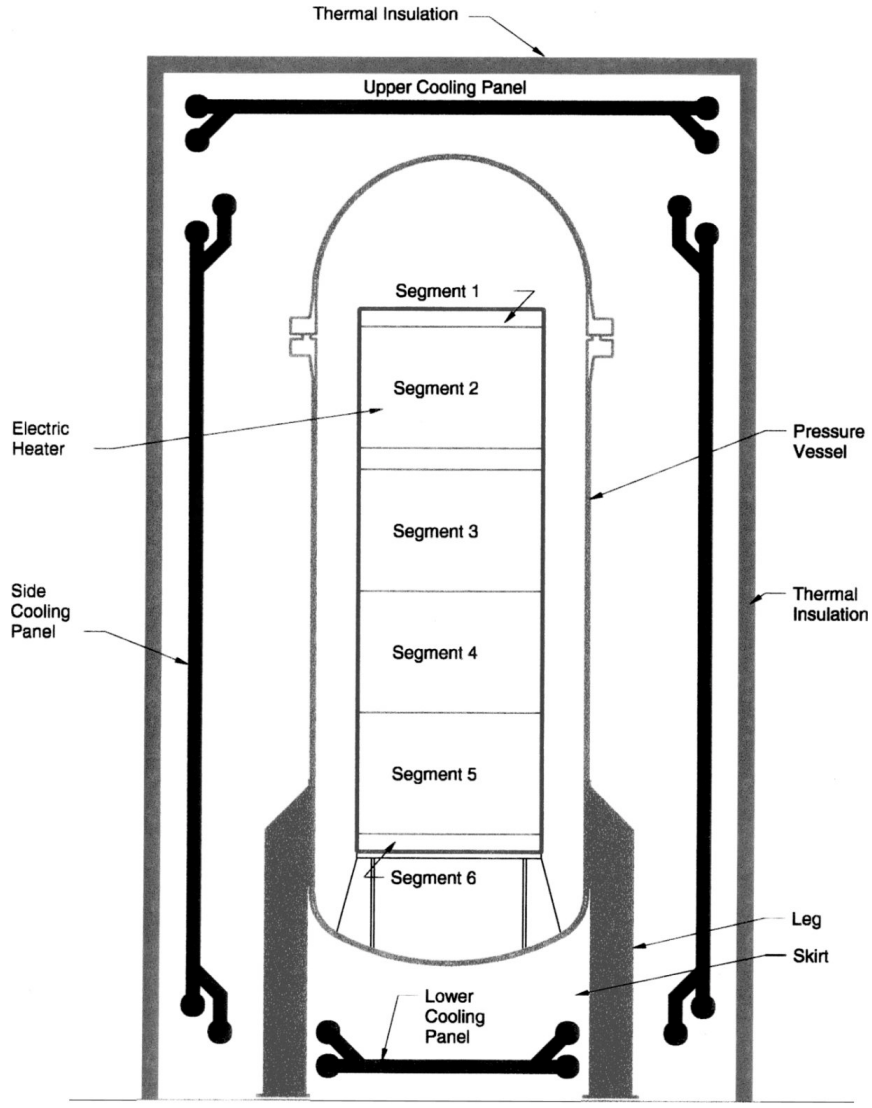

Fig. 4-56 Schematic Diagram of Test Apparatus

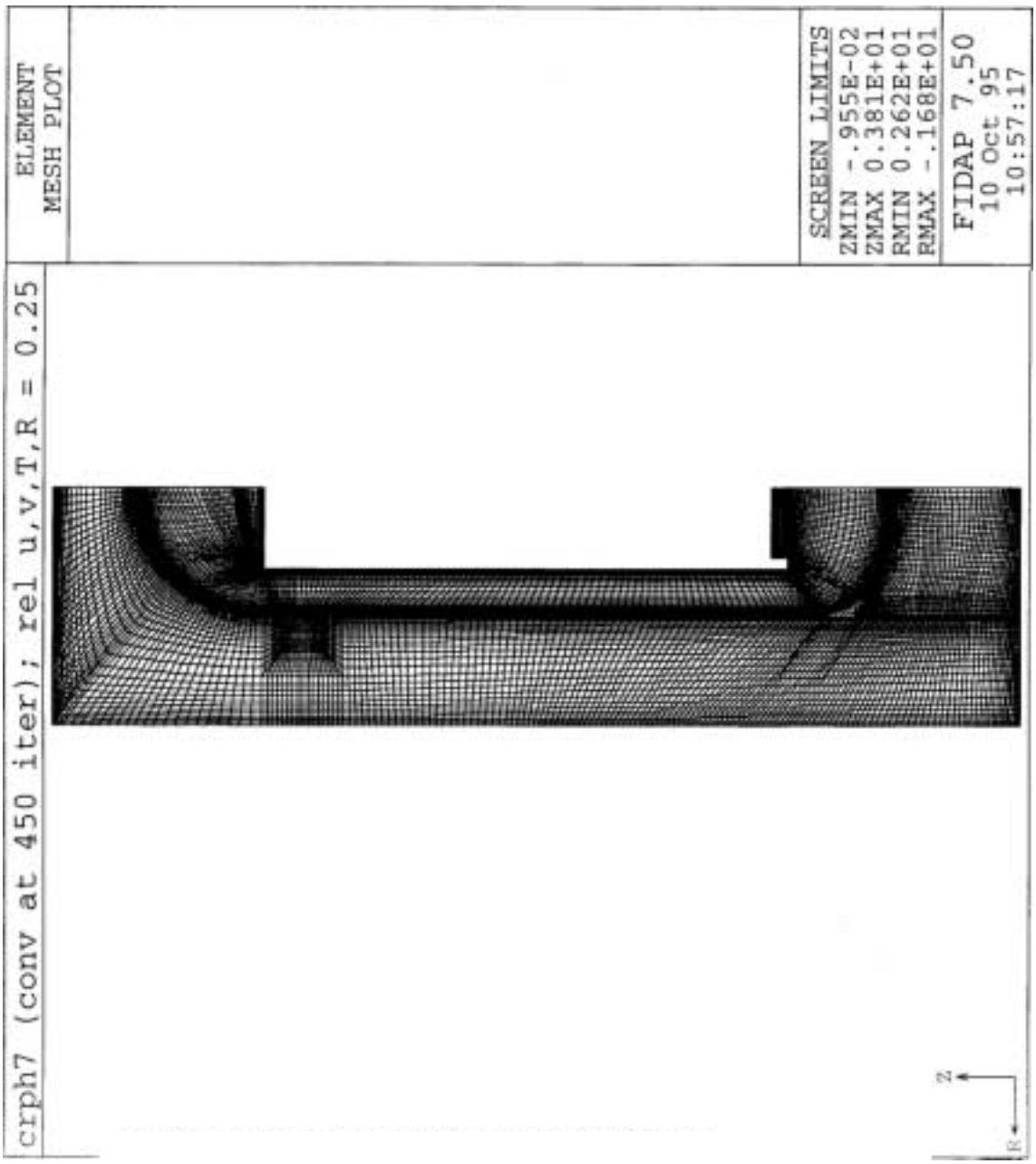

Fig. 4-57 CFD Model Axi-symmetric computational grid (complete)

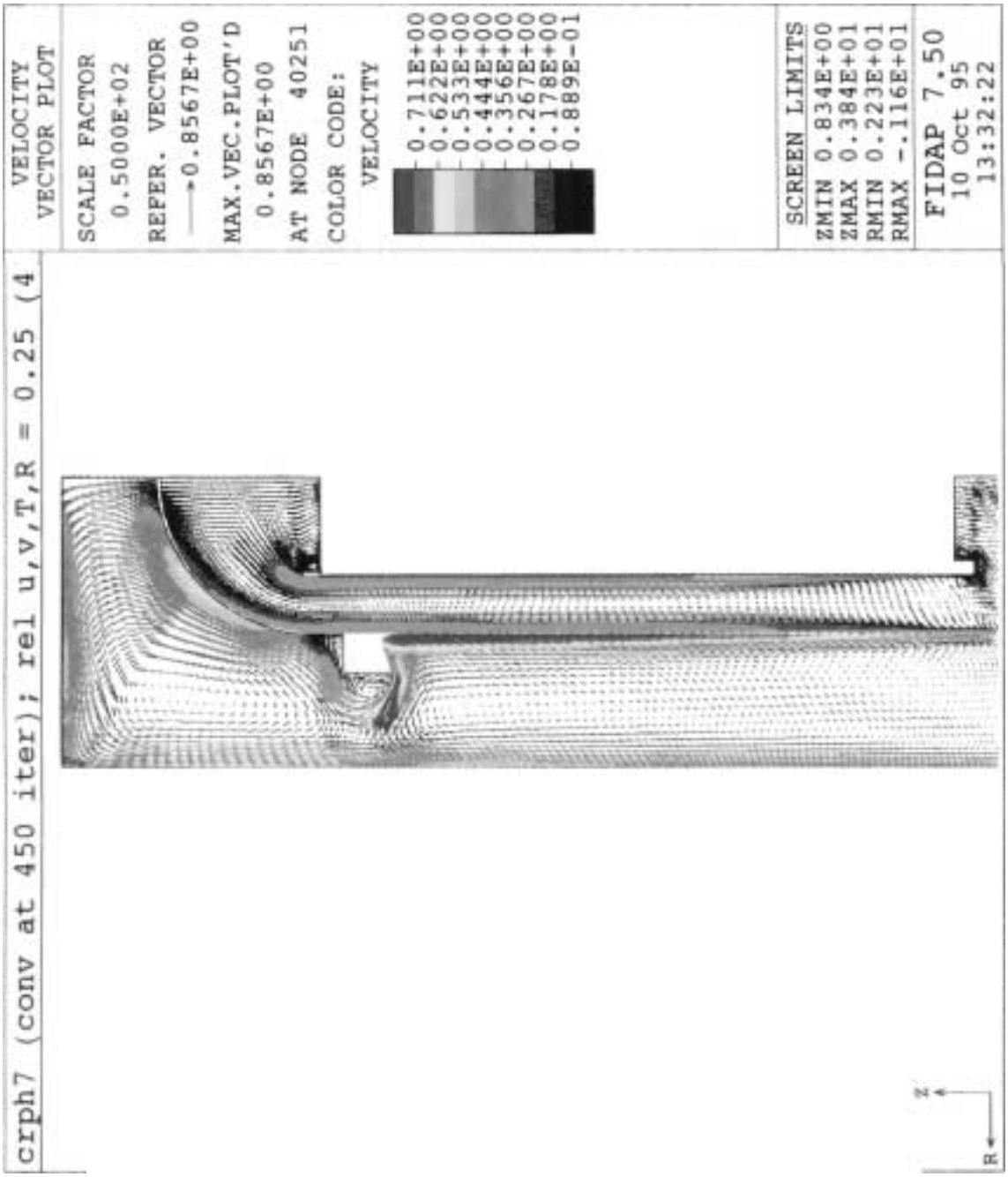

Fig. 4-58 Velocity vcctors inside and outside vessel

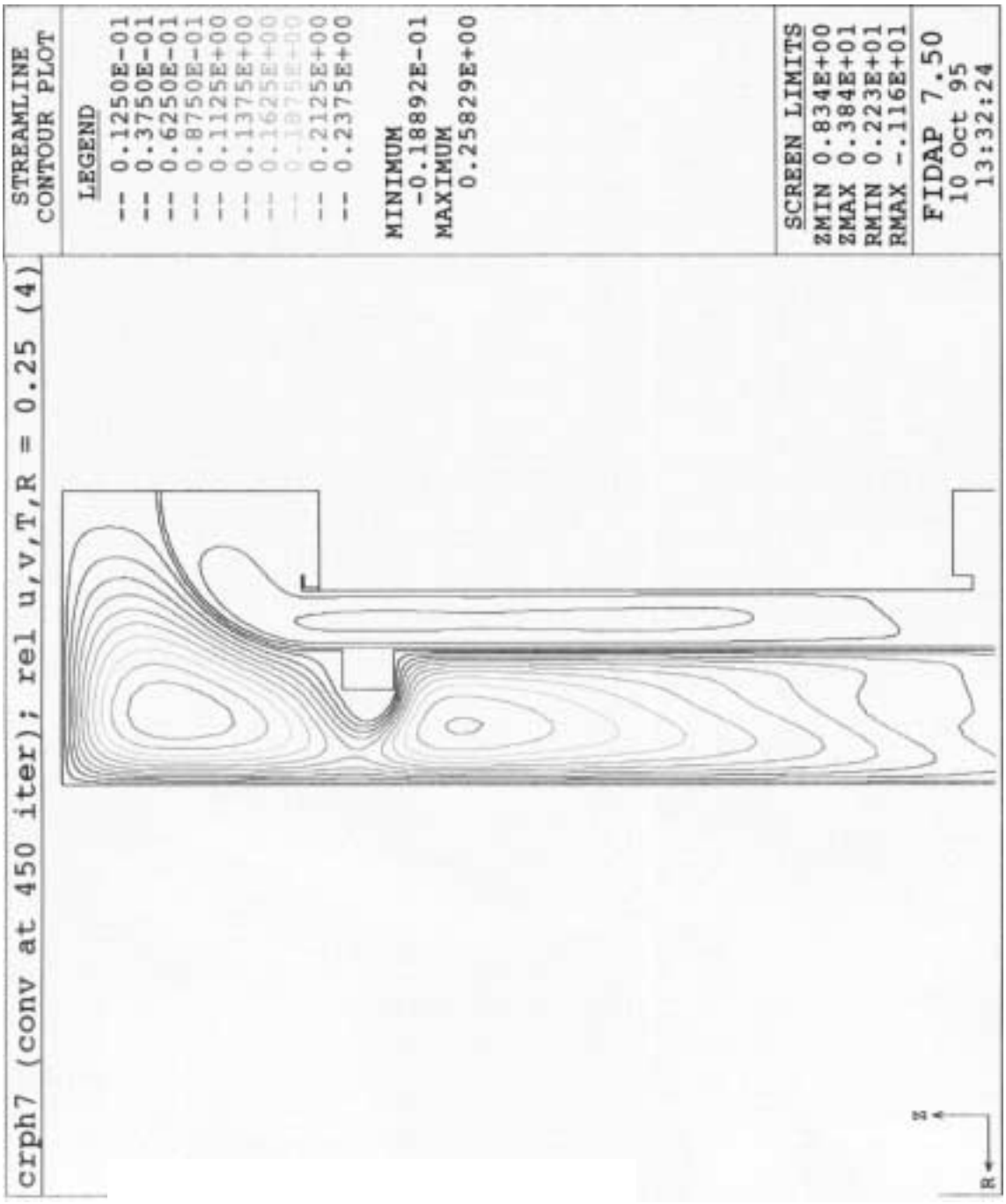

Fig. 4-59 Streamline contours inside and outside vessel

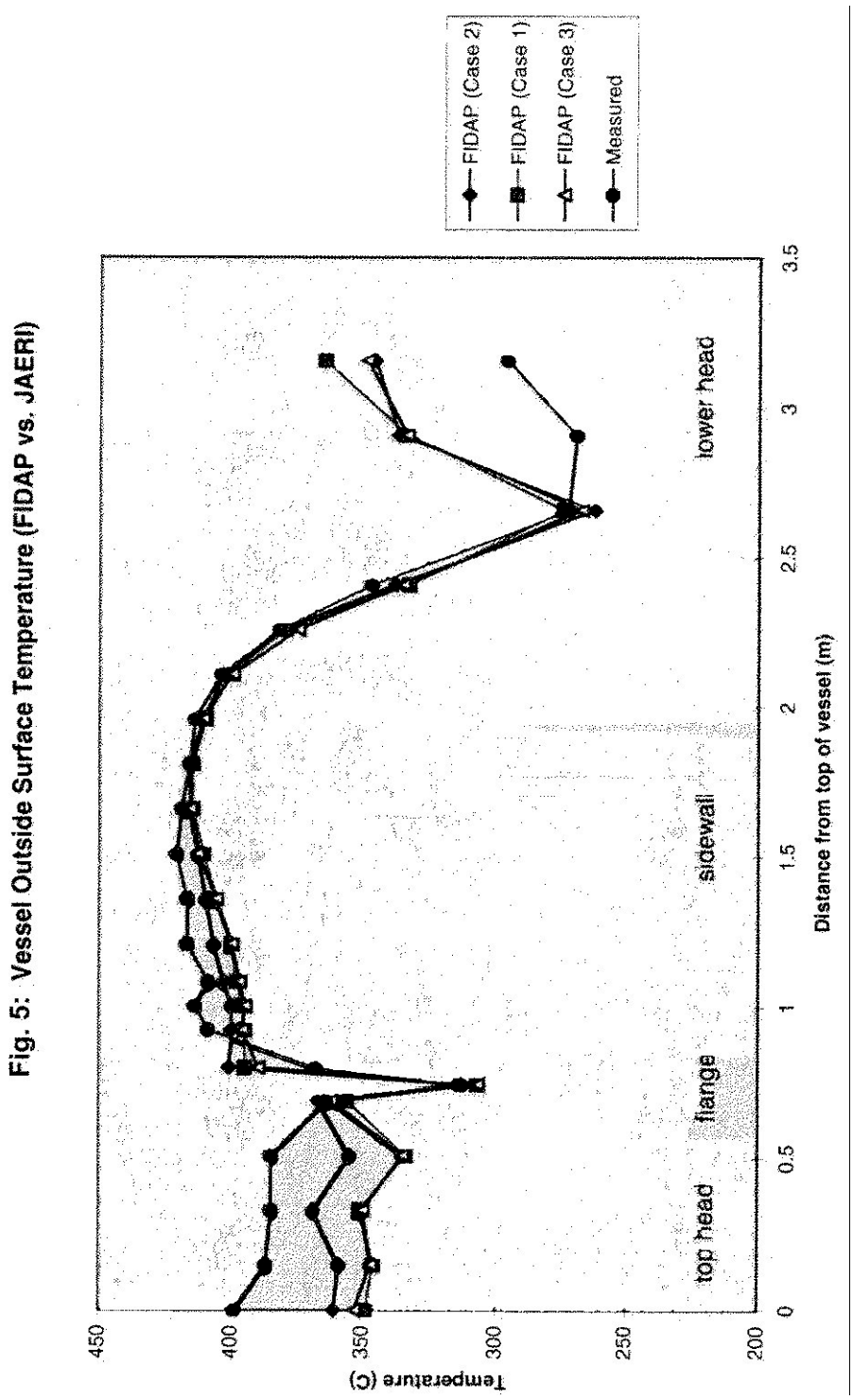

Fig. 4-60 Vessel outside surface temperature (FIDAP vs. JAERI)

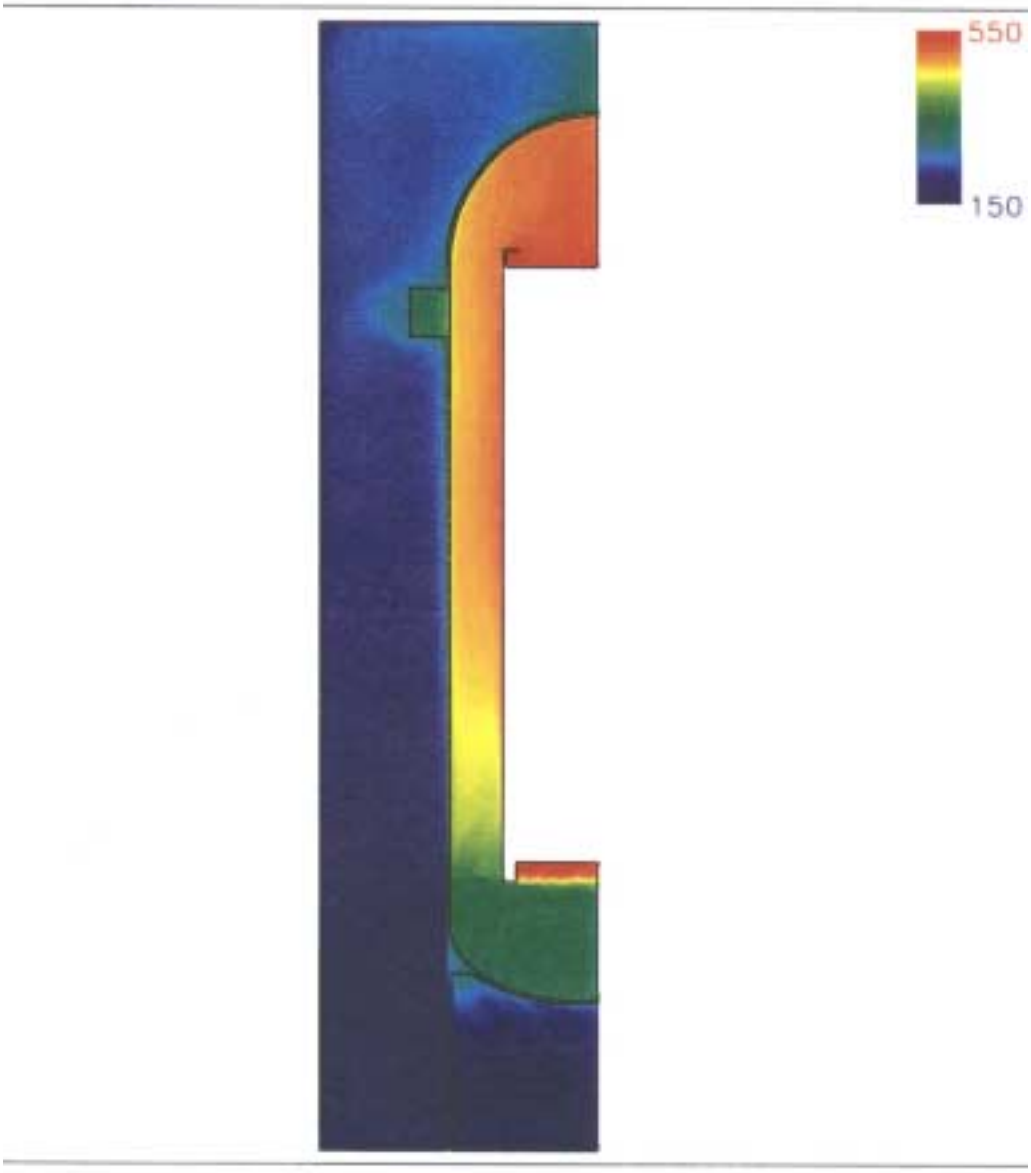

10. Temperature Profile for Inside and Outside Vessel (Including Structures)

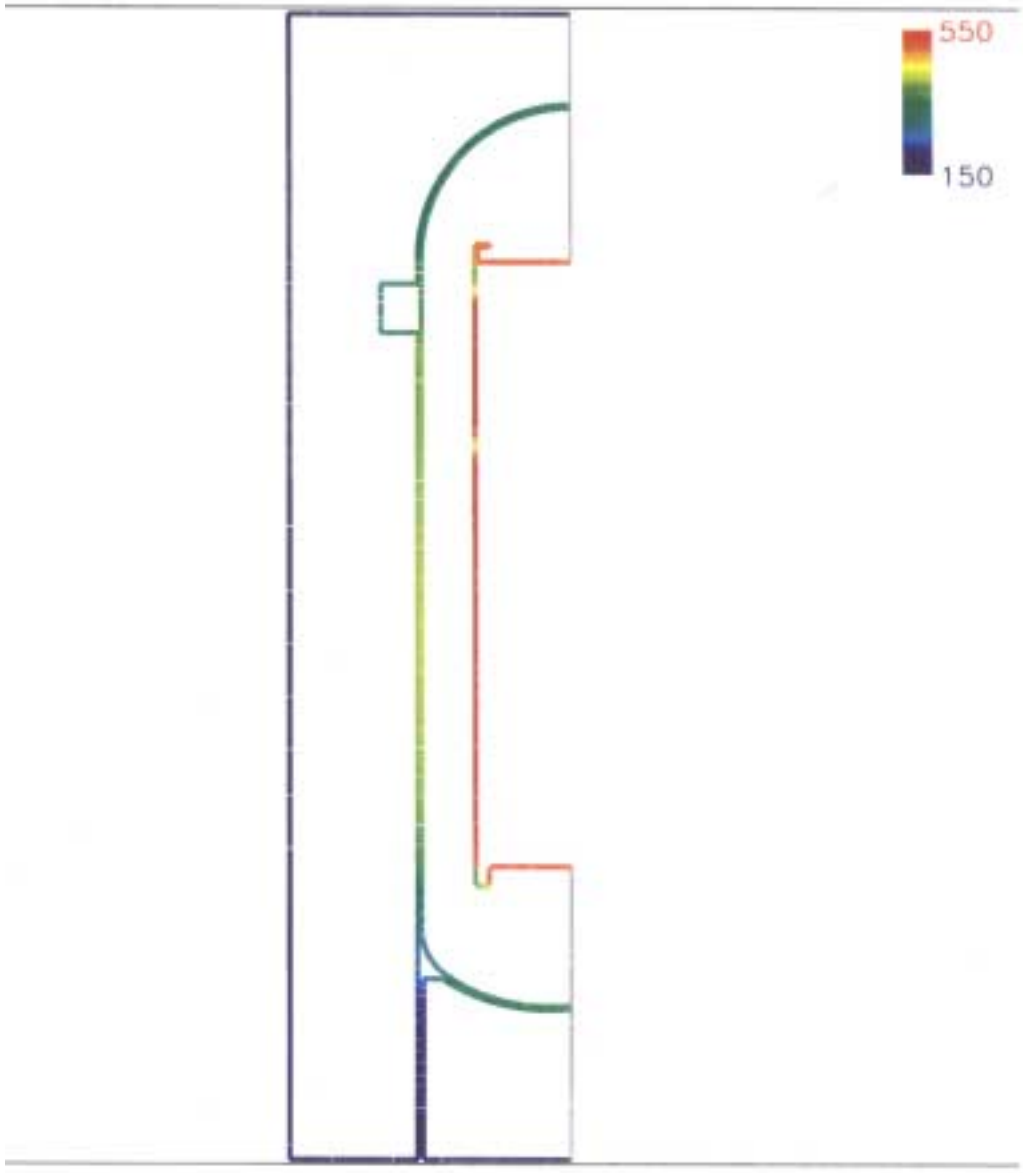

9. Temperature Profile of Model Surfaces

4.1.7. Results of Simulation of the HTTR RCCS Mockup with the THANPACST2 code

4.1.7.1. Introduction

Six benchmark problems are presented by JAERI with various experimental conditions. Four problems were solved numerically by the use of computer code THANPACST2 which were developed for the numerical simulation of the HTTR mockup experiments. Description of the code and comparison of the results between the experiment and the numerical simulation are presented.

4.1.7.2. Analysis

4.1.7.2.1. Computational code THANPACST2

Transfer of momentum and energy in the pressure vessel and surrounding cooling panels were numerically solved by a computer code THANPACST2. The code solves time dependent flow and temperature fields in a two dimensional cylindrical coordinate system considering natural convection and thermal radiation. Basic equations are expressed as follows:

(Continuity and Momentum)

$$\nabla \cdot \mathbf{u} = 0$$

$$\frac{\partial \mathbf{u}}{\partial t} = -\frac{1}{\rho}\nabla p + \nu \nabla^2 \mathbf{u} - (\mathbf{u} \cdot \nabla)\mathbf{u} - \mathbf{Res} - \mathbf{g}\beta(T - T_{ref})$$

(Energy)

Fluid

$$\frac{\partial T}{\partial t} = \frac{1}{\rho C_p}\left(\kappa \nabla^2 T + q_s\right) - (\mathbf{u} \cdot \nabla)T$$

Structure component

$$\frac{\partial T_s}{\partial t} = \frac{1}{\rho C}\left(\kappa \nabla^2 T_s - q_s + q_{rad} + q_p\right)$$

where **Res**, T_{ref}, T_s, q_s, q_{rad} and q_p are pressure drop induced by inlet and outlet configuration, reference temperature, temperature of structure component, heat from component cell to fluid, heat transferred by radiation and generated heat in structure, respectively.

During loss of forced cooling accident, heat is removed by natural convection, thermal radiation and heat conduction. Heat transfer coefficient by natural convection between the cell surface of structure component and fluid was calculated from a fixed local Nusselt number Nu_c. The local Nusselt number Nu_c was given from empirical correlation of local Nusselt number Nu_m which have been proposed by several investigators. Heat transferred from a surface 1 to a surface 2 by thermal radiation is obtained by the following equations.

$$Q_{12} = A_1 \cdot \varepsilon \cdot F_{12} \cdot \left(T_1^4 - T_2^4\right)$$

$$\varepsilon = 1 \Big/ \left(1/\varepsilon_1 + A_1/A_2 \cdot (1/\varepsilon_2 - 1)\right)$$

where Q_{12}, A, ε, σ, T designate radiated heat from surfaces 1 to 2, surface area, emissivity, Stefan–Boltzmann constant and surface temperature, respectively, and subscripts 1 and 2 denote the surfaces 1 and 2. Geometric factor F_{12} for each surface is obtained by using the unit-sphere method. Thermal radiation from one surface to maximum 30 surfaces could be treated in the computer code.

Staggered grid system is used to describe the velocity and temperature fields. Scalar variables such as temperature and pressure are defined at the center of the grid cell. Vector variables

such as velocity components are defined at the surface of the grid. Basic equations are solved by using control volume method. Time derivative term was differentiated by forward difference, convection term upwind difference and diffusion term central difference. Pressure correction method is adopted to determine the variables on the finite volume surface and nodes. In the pressure correction method, fluid velocity which is calculated explicitly from the equation of motion is corrected in consideration of the pressure to satisfy the equation of continuity. Properties of the fluid, such as density, viscosity, thermal conductivity and Prandtl number are estimated considering the local temperature and pressure. Thermal conductivities of structure components are assumed to be constant, which are shown in Table 1. Surface temperatures of the structure components are calculated from the heat balance of thermal radiation, heat conduction and natural convection.

Convergence was judged by the criterion that the difference between heat input and calculated heat transferred to the cooling panel became less than 1%.

4.1.7.2.2. Analytical model

Experimental apparatus is simulated by an analytical model of cylindrical geometry. Fig. 4-63 shows the grid system of the experimental apparatus. Two-dimensional cylindrical geometry (23×39 grid system) is used to discretize the heater, pressure vessel supported by legs, skirt and cooling panels.

There are airflow channels between inside and outside the cavity under the lower head of the pressure vessel, which is surrounded by skirt type support. Air flows in the cavity from outside through a clearance between the skirt and the floors, and flows out through the clearance of H-type steel legs. The air channels are expressed by porous body cells which have properties of both solid and fluid cells at the upper and lower edges of skirt type support in the analytical model.

All of the heat input in the pressure vessel is assumed to be removed by the cooling panels. Heat loss from the cooling panels to the outside is assumed to be zero.

In the analytical model of the experimental apparatus, standpipes could not be simulated because they are three-dimensional. Due to the existence of standpipes, heat transfer area at the outer surface of the upper head of the pressure vessel is reduced. Configuration factor F is introduced in the analysis from top of the pressure vessel to the cooling panel and the factor F was parametrically varied from 0.1 to 1.0.

4.1.7.2.3. Empirical correlation of heat transfer coefficients used in the analysis

Thermal radiation is considered between the pressure vessel and the surfaces of electric heater, between the pressure vessel and the cooling panels and between cooling panels and skirt type support.

Heat transfer coefficients by natural convection between outer surface of the side pressure vessel and side cooling panel and between the side surface of the heater and the inner surface of the pressure vessel are calculated from an empirical correlation proposed by Thomas and de Vahl Davis [1] for concentric cylinder,

$$\mathrm{Nu}_m = 0.286 \cdot \mathrm{Ra}^{0.258} \cdot \mathrm{Pr}^{0.006} \cdot \mathrm{H}^{-0.238} \cdot \mathrm{K}^{0.442}$$

where Ra, H and K are Rayleigh number, aspect ratio and ratio of outer and inner radii of cylinders, respectively.

Heat transfer coefficient by natural convection at the top surface of heater, upper cooling panel and outer surface of upper head of pressure vessel are calculated from empirical correlations proposed by Fishenden and Saunders [2] for case of upward-faced hot surface or downward-faced cold surface,

$$\mathrm{Nu_m} = 0.54 \cdot \mathrm{Ra}^{0.25} \qquad \left(1\times10^5 \le \mathrm{Ra} \le 2\times10^7\right)$$

$$\mathrm{Nu_m} = 0.14 \cdot \mathrm{Ra}^{0.33} \qquad \left(2\times10^7 \le \mathrm{Ra} \le 3\times10^{10}\right)$$

Heat transfer coefficient by natural convection on the inner surface of upper head of the pressure vessel is calculated from empirical correlations proposed by Shiina [3]

$$\mathrm{Nu_m} = 0.1974 \cdot \mathrm{Ra}^{0.25} \qquad \left(1\times10^6 \le \mathrm{Ra} \le 1\times10^8\right)$$

$$\mathrm{Nu_m} = 0.312 \cdot \mathrm{Ra}^{0.33} \qquad \left(1\times10^9 \le \mathrm{Ra} \le 5.5\times10^{10}\right)$$

Heat transfer coefficient by natural convection on the bottom surface of heater, inner surface of lower head of pressure vessel and lower cooling panel are calculated from an empirical correlation proposed by Fishenden and Saunders for case of upward-faced cold surface or downward-faced hot surface,

$$\mathrm{Nu_m} = 0.27 \cdot \mathrm{Ra}^{0.25}$$

Heat transfer coefficient by natural convection on the outer surface of the lower head of the pressure vessel was estimated to be Nu_c=45 which was obtained by an experiment with vacuum condition inside the pressure vessel.

4.1.7.2.4. Emissivity

Emissivity was assumed to be 0.79 for the inner surface of the pressure vessel, 0.66 for the heater. Emissivity of the black paint coated on the outer surface of the pressure vessel, the skirt type support and the cooling panels was assumed to be 0.95.

4.1.7.3. Comparison of the results between experiment and analysis

Comparison of the numerical results of benchmark problem (I)~(IV) with experiments are discussed as follows.

4.1.7.3.1. Benchmark problem (I)

(Vacuum, Heat input;13.14kW, Fluid of cooling panel; water, No stand pipes)

Figures 4-64 and 4-65 show results of numerical analysis and comparison with the experiment. Fig. 4-64 shows surface temperature of structure components and heat flux distribution on the heater. In the Fig. 4-64b, solid lines indicate the numerical results. Measured temperature distribution shows almost uniform profile on the shell of the pressure vessel. Numerical results in temperature are slightly lower on the upper head of the pressure vessel, higher on the flange and the connecting region of legs and skirts than the experimental results. Reason for low temperature at the upper head of the pressure vessel in the analysis would be due to that the surface area of the upper head is 1.2 times larger in the numerical model than in the experiment. Two reasons could be considered for high temperature in numerical results at the region of legs and skirt. One would be that since the analytical model was simulated by cylindrical configurations, three-dimensional structure of legs and skirt and their effects on heat transfer, i.e. expansion of surface area and fin effect, are not considered. Surface area of the experimental apparatus near the legs and skirt is 40% larger than that of the numerical model. Another would be due to the existence of airflow path from inside under the lower head to outside through H-type steel which is three-dimensional structure and also the effect is not considered. In spite of the differences in temperature described above, agreement between numerical and experimental results in temperature on the pressure vessel is rather well. Temperature of No.5 heater segment is about 100C higher in the analysis than in the experiment as shown in Fig. 4-64c. The reason would be same as described above that heat removed by legs and airflow in H-type steel is not considered in the analysis. Heater temperatures,

however, are not measured correctly because thermocouples are not fixed just on the heater segment but on support near the heaters, therefore, detailed discussion on the heater temperatures is not profitable.

Figure 4-65 shows isothermal contour and velocity vector outside of the pressure vessel. Temperature gradient is steep around the pressure vessel. Main flow of air is upward flow along the pressure vessel and downward flow along the side cooling panels. Air flowing up along the shell is partially disturbed by the flange. Numerical results show the existence of airflow under lower head of the pressure vessel from inside to outside. Effect of the airflow on the temperature of lower part of the pressure vessel could not be negligible.

4.1.7.3.2. Benchmark problem (II)

(Helium gas, Pressure;0.73Mpa., Heat input;28.79kW, Fluid of cooling panel; Water, No standpipes)

Figures 4-66 and 4-67 show comparison of the results between numerical analysis and experiment. Figure 4 shows surface temperature of structure components and heat flux distribution of the heater segments. Temperature distributions on the pressure vessel show similar profile to the case of Benchmark (I). Numerical results in temperature agree with experimental results except upper head and lower part of the pressure vessel. Reasons for the discrepancy in the temperature distribution would be qualitatively same as described in the previous section.

Fig. 4-67 shows isothermal contour and velocity vector. Helium gas flows upward along the side shell of the pressure vessel. Helium gas temperature at the top region inside the upper head of the pressure vessel was about 70 C lower in the numerical analysis than in the experiment. This would be due to stepwise wall used in the numerical model instead of spherical wall, which prevents hot gas flow rising up along the inner wall of upper pressure vessel and also due to the surface area used in the analysis which is 1.2 times larger than in the experiment. Temperature profiles of the heater segment is similar to the Benchmark problem (I). Difference in the temperature of No.5 heater segment between numerical and experimental results is increased. This would be due to that helium temperature is the lowest in the lower part of the pressure vessel and the thermocouple measuring No. 5 heater temperature would be affected rather by this low temperature helium than No.5 heater. Transferred heat by thermal radiation is estimated to be 60.1% of total heat input.

4.1.7.3.3. Benchmark problem (III)

(Nitrogen gas, Pressure;1.1Mpa., Heat input;93.93kW, Fluid in the cooling panel; Water, No standpipes)

Figures 4-68 and 4-69 show comparison of the results between numerical analysis and the experiment. Figure 4-68 shows temperature distributions of the pressure vessel and cooling panel and heat flux distributions on the heater segments. Temperature distribution of the cooling panel is almost uniform but slightly increasing with height from floor. Temperature obtained by the numerical result show lower values on the upper part of the pressure vessel. Temperature on the pressure vessel near the legs and skirts is considerably higher than the experiment. Difference in temperature on the pressure vessel between numerical and experimental results is increased, i.e. -72 to 128C. Reason of this increase would be mainly due to the increase in heat input.

Numerical results of isothermal contour and velocity vector are shown in Fig. 4-69. Circulating flow is formed in the pressure vessel. Weak flow circulation could be observed in the upper and lower head. Maximum flow velocity of the upward and downward flow inside the pressure vessel were 0.6m/s and 0.3m/s, respectively. Outside the pressure vessel, flow is rather complex. Nitrogen gas flows upward along lower side wall of the pressure vessel and it separates. Just above the separation, downward flow could be observed along the sidewall of the outer pressure vessel. Near the top inside the upper head, gas temperature was 70C lower in the analysis

than in the experiment. This value seems not very large compared with the Benchmark problem (II) considering large heat input in this case. Airflow below the lower head of the pressure vessel is increased. The maximum velocities of upward and downward flow were 0.7 m/s and 0.6 m/s, respectively.

4.1.7.3.4. Benchmark Problem (IV)

(Helium gas, Pressure;0.47Mpa., Heat input;77.5kW, Fluid of cooling panel; Water, with stand pipes)

As is described before, standpipes could not be simulated directly in the analytical model. Instead, configuration factor F was introduced and varied from 0.1 to 1 in the numerical simulation. Figs 4-70 and 4-71 show comparison of the results between numerical analysis and the experiment. Fig. 8 shows temperature distribution of the pressure vessel and cooling panel and heat flux distributions on the heater segments. Temperature of the pressure vessel obtained by numerical calculation is higher near the flange region than the experiment. Temperature of the upper head surface increases with increase in height. Temperature on the top of the pressure vessel increases with decrease in the configuration factor F, but dependence of F on the temperature is very small.

Figure 4-71 shows isothermal contour and velocity vector map. Large circulating flow can be observed in the pressure vessel. Maximum velocities of upward and downward flows are 0.8 m/s and 0.6 m/s, respectively. Outside the pressure vessel, large circulating flow was also formed from the bottom to the top of the region. The circulating flow around the side shell of the pressure vessel is different from the case of the benchmark problem (III), this would be due to small heat input compared to the case (III) because No.5 heater segment was broken and the temperature of lower part of the pressure vessel was lower than the benchmark problem (III). Maximum velocities of upward and downward airflow were 0.8 m/s and 0.4 m/s respectively. Agreement in temperature between numerical analysis and experiment is well.

REFERENCES TO SECTION 4.1.7.

[1] Keyhani,M. et al., Trans. ASME, **105**, 454(1983)

[2] Fishenden, M. et al., „Introduction to Heat Transfer“, Clarendon Press, 180(1950)

[3] Shiina,Y. et al., Trans JSME, **55**, 518(1989)

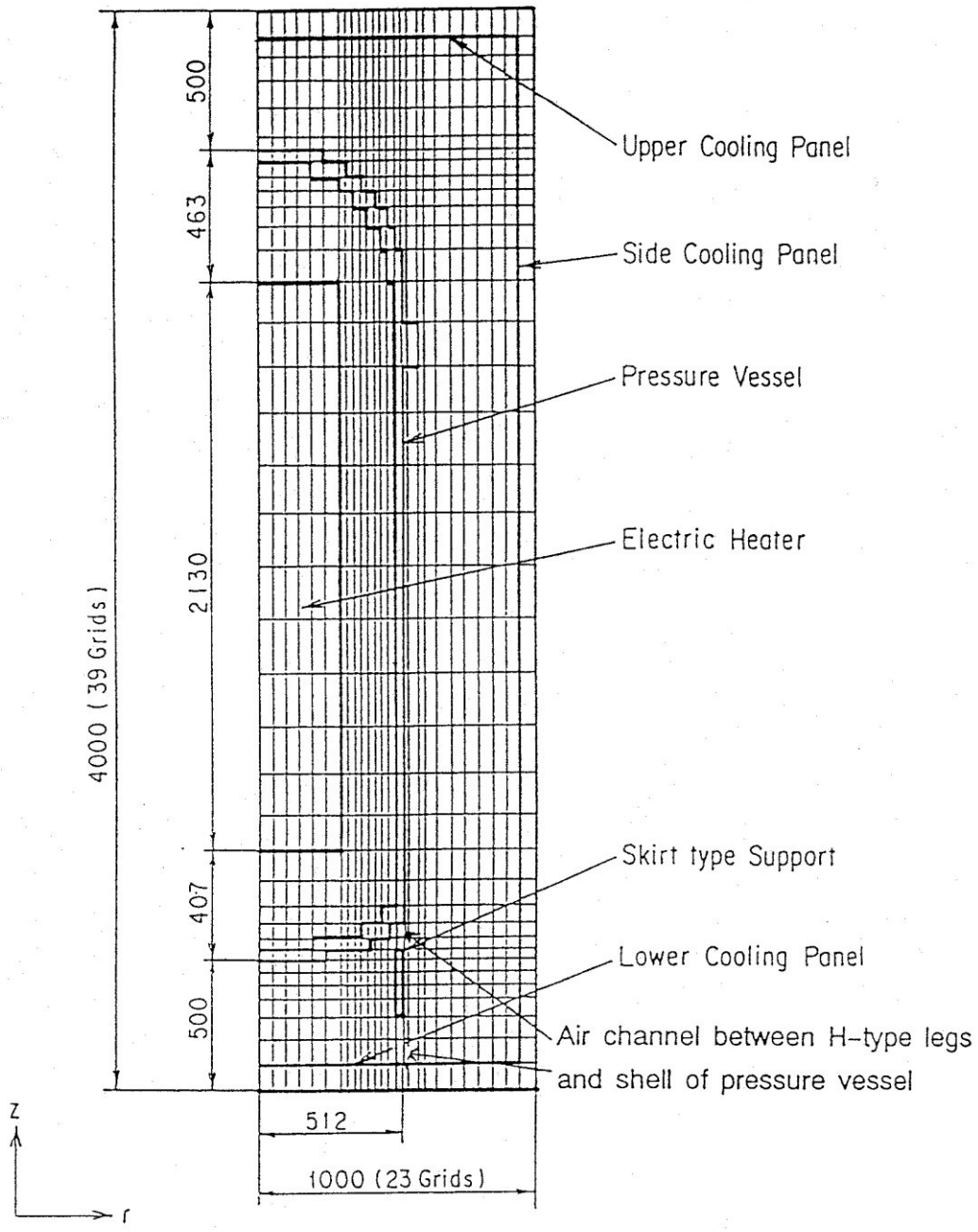

Fig. 4-63 Grid system of simulation model

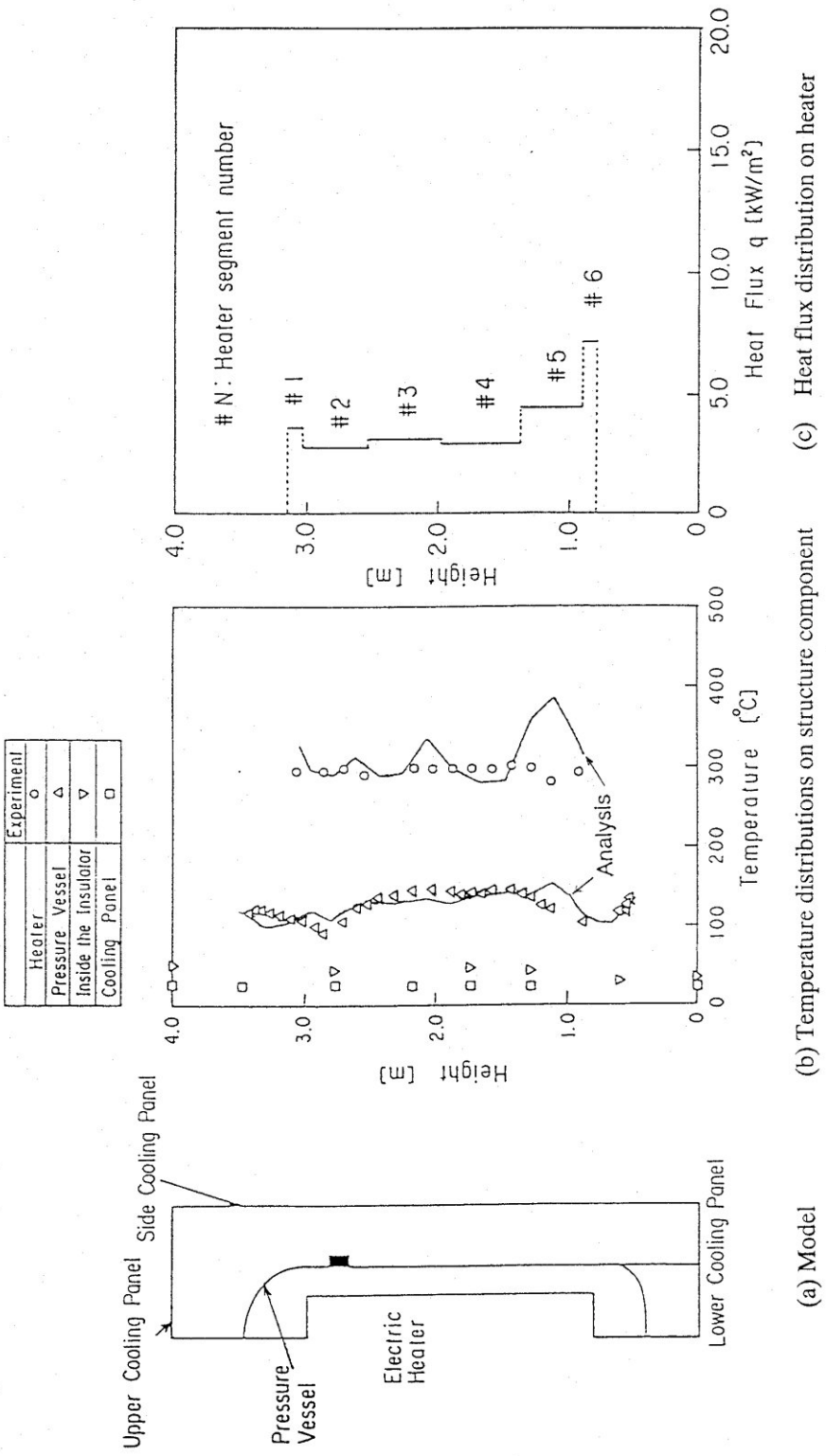

Fig. 4-64 Comparison of the results between numerical calculation and experiment for benchmark problem (I)

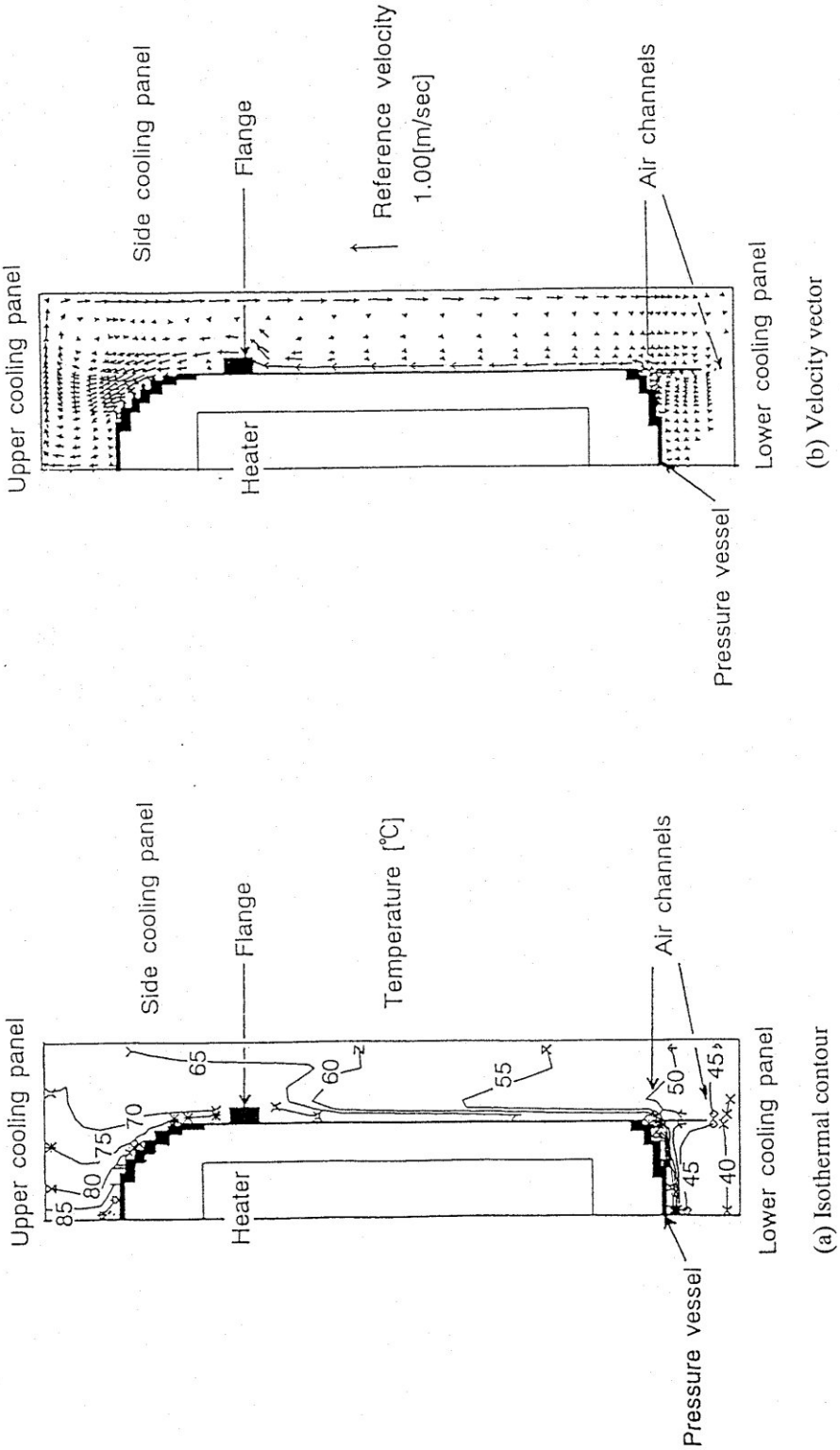

Fig. 4-65 Numerical results of isothermal contour and velocity vector for benchmark problem (I)

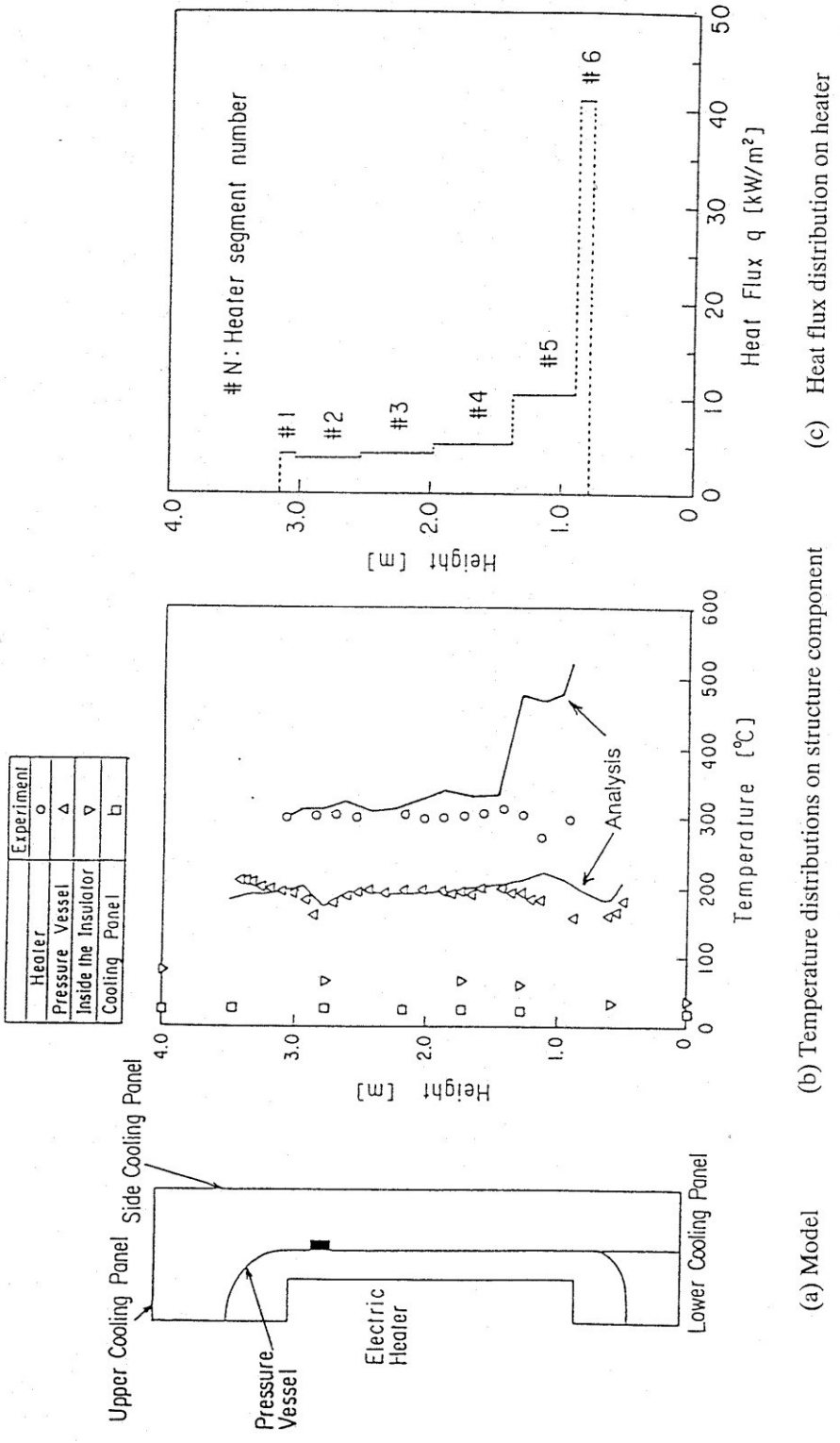

Fig. 4-66 Comparison of the results between numerical calculation and experiment for benchmark problem (II)

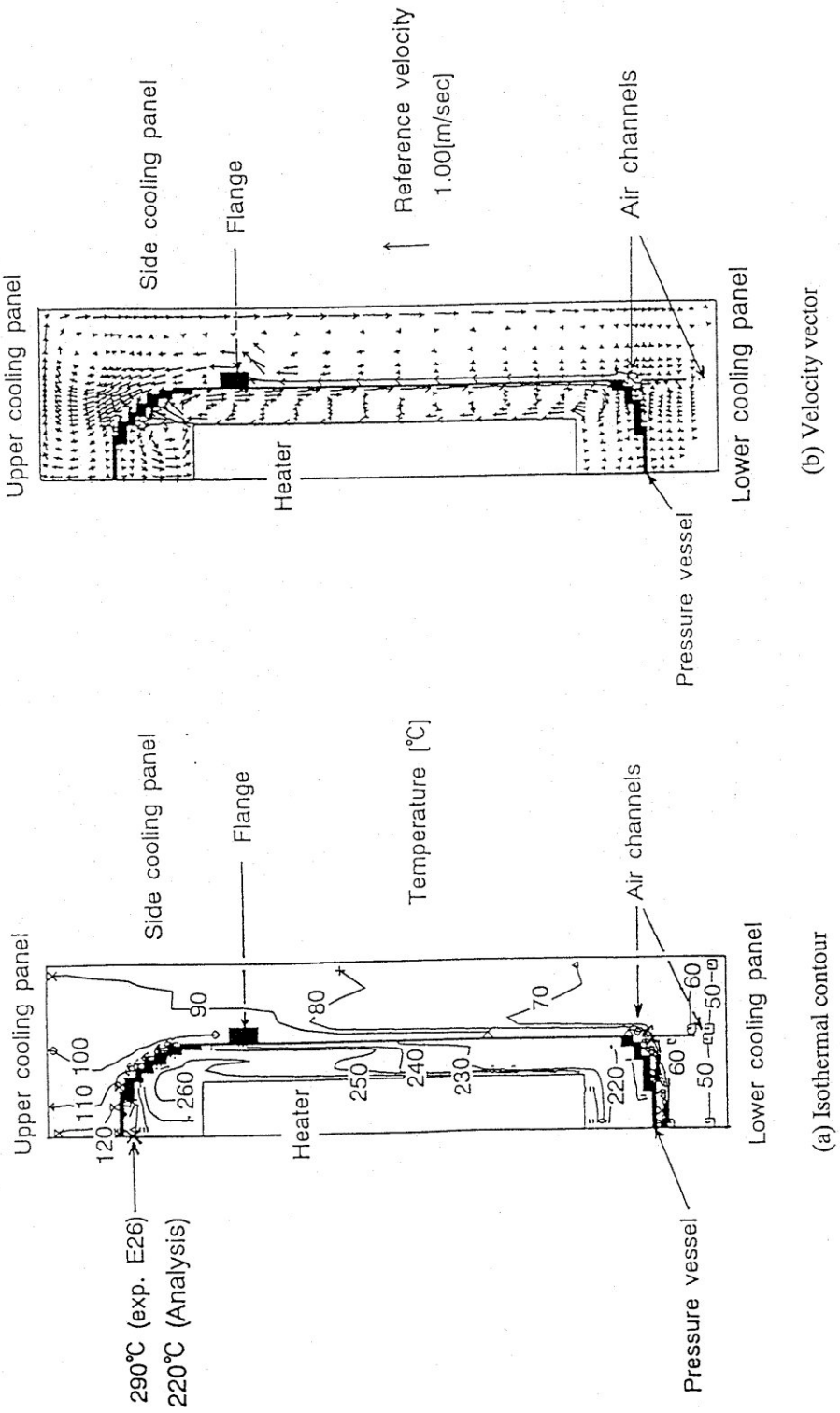

Fig. 4-67 Numerical results of isothermal contour and velocity vector for benchmark problem (II)

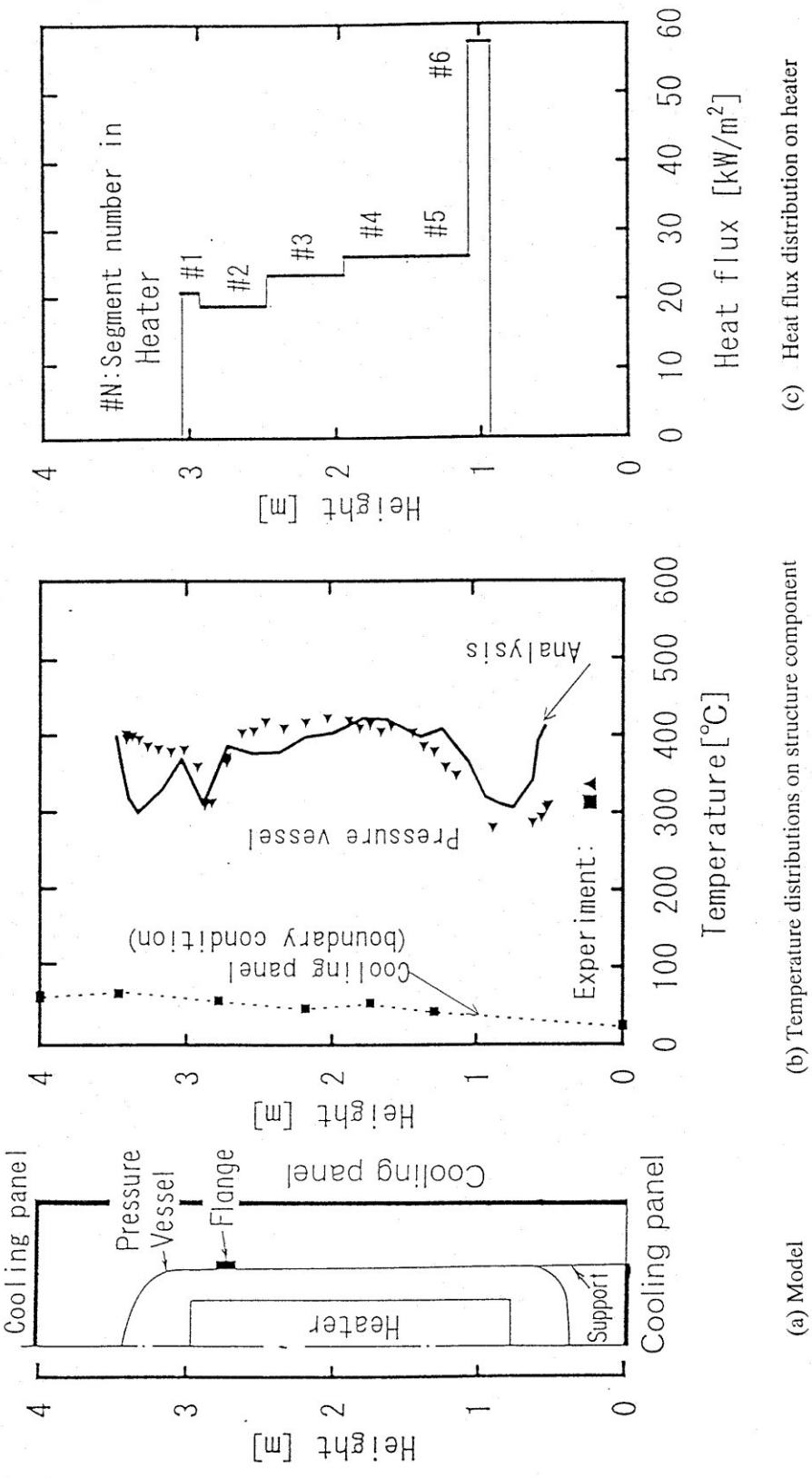

Fig. 4-68 Comparison of the results between numerical calculation and experiment for benchmark problem (III)

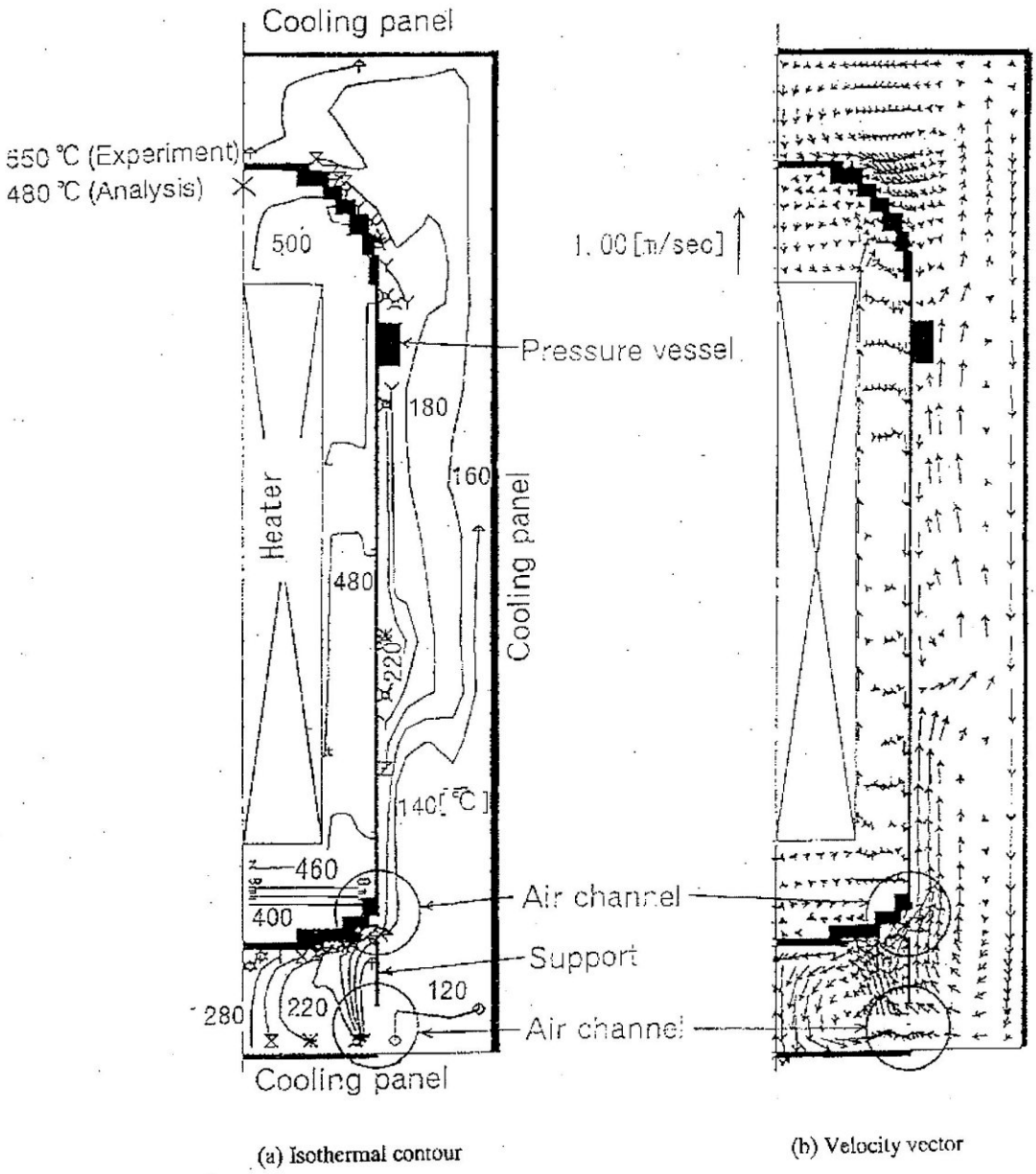

Fig. 4-69 Numerical results of isothermal contour andvelocity vector for benchmark problem (III)

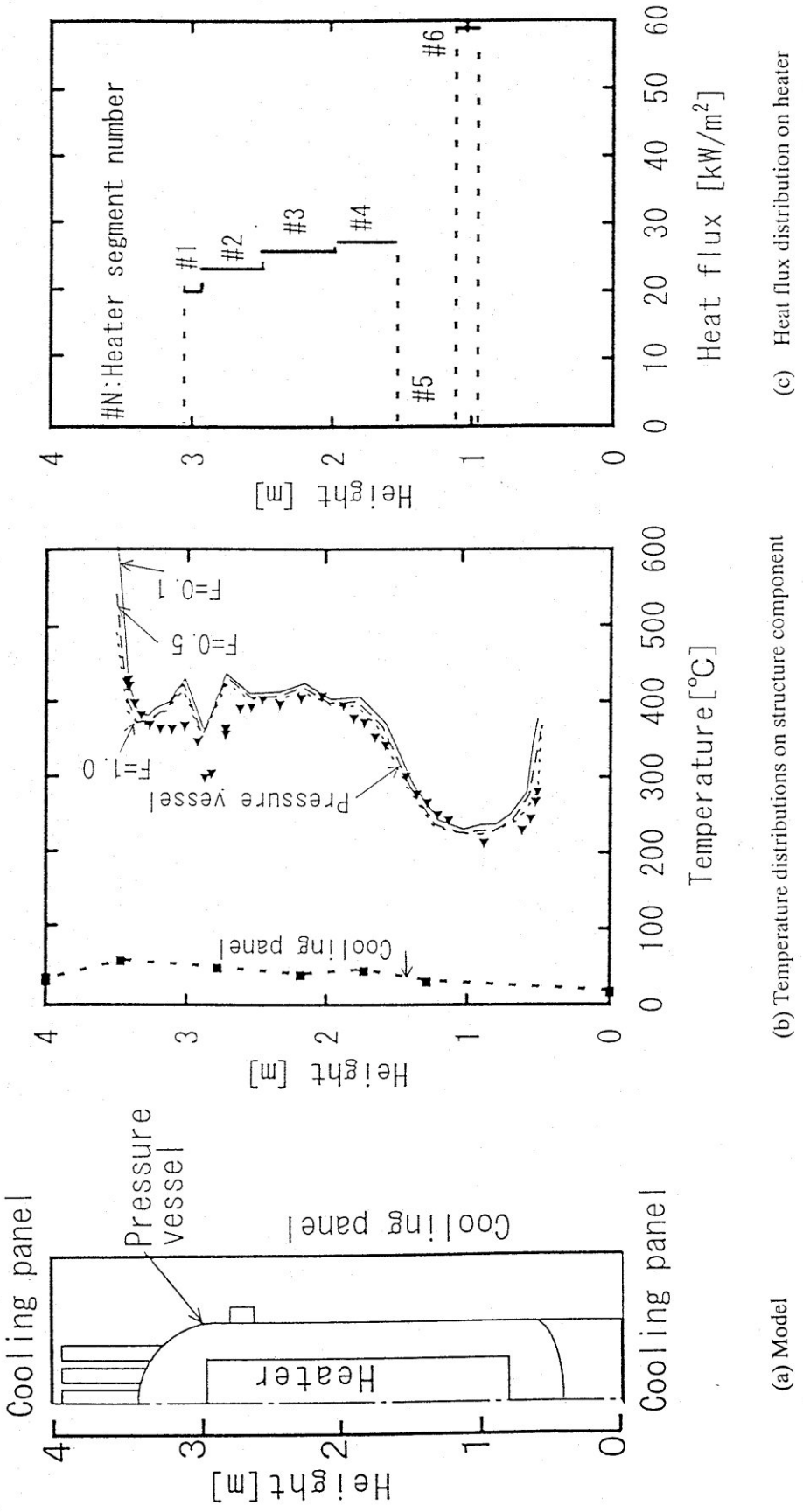

Fig. 4-70 Comparison of the results between numerical calculation and experiment for benchmark problem (IV)

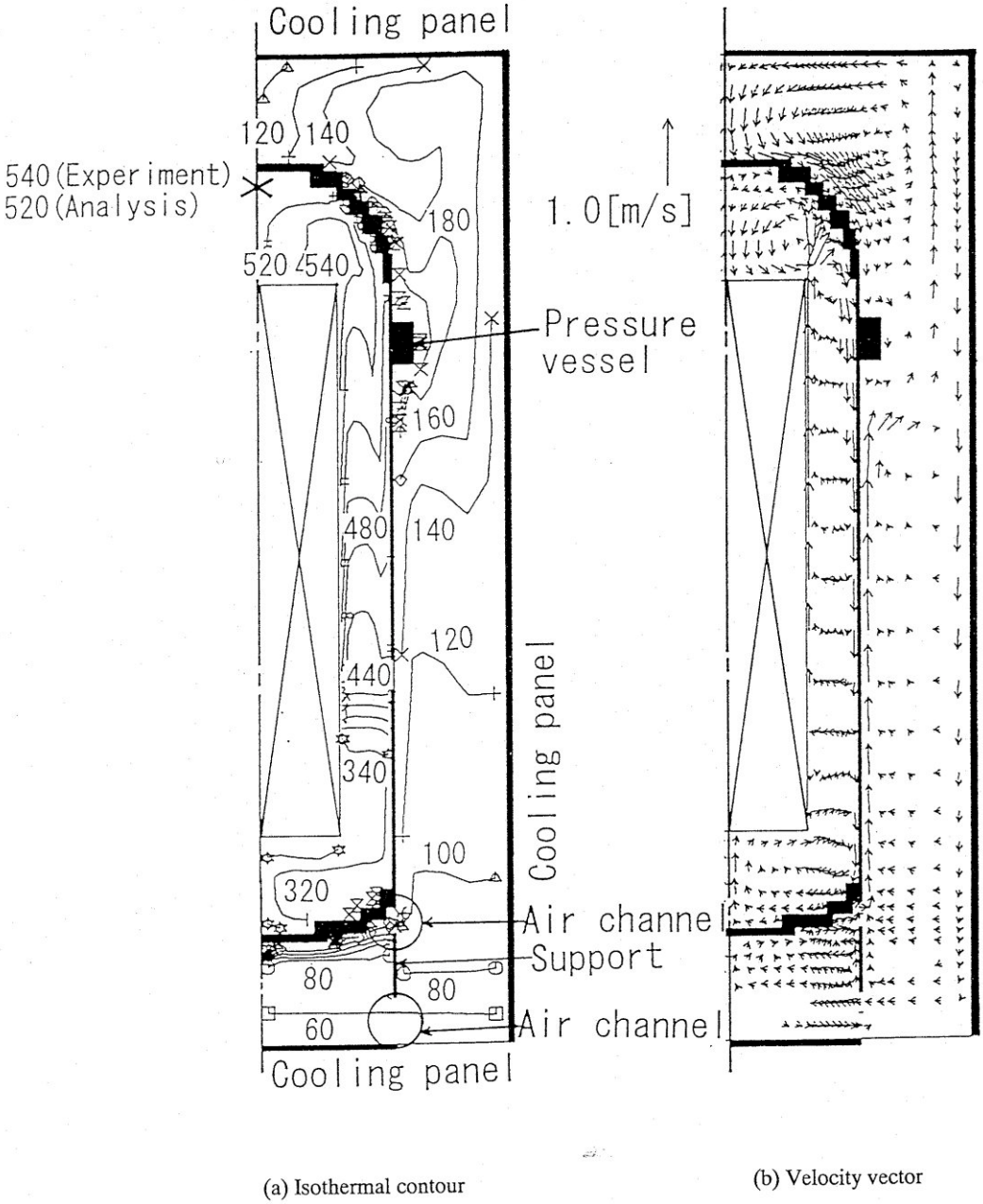

Fig. 4-71 Numerical results of isothermal contour and velocity vector for benchmark problem (IV)

4.1.8. Comparison and conclusions

4.1.8.1. Results comparison and discussion

Experiment of HTTR RCCS Mockup, which were performed at JAERI, were selected as a code to experiment benchmark problem. Six experimental results were offered from JAERI and the results were compared with the analytical results obtained by TRIO-EF CASTEM2000 code (France), THERMIX and CCRCC codes (China), SM1 and DUPT codes (Russia), MORECA and FIDAP codes (USA) and THANPACT2 code (Japan). Benchmark points are to evaluate heat transfer performance and temperature distribution of the pressure vessel. Comparisons of the results are summarized in Tables I- VII.

Temperature distribution of the pressure vessel

Surface temperature distributions were obtained by numerical works. Temperature differences, ΔT_{max} and ΔT_{min} (nomenclature should be referred at the bottom of the Table I) were compared in the Tables I-VII. Generally, sidewall temperature of the pressure vessel agreed well with the experimental values. However, difference was large at the top and bottom heads and flange region. At the flange region, calculated temperature normally showed higher values than experiment. This would be due to ignorance of the fin effect of the flange. The differences in temperature at the top and bottom heads are due to the effect of natural convection. Therefore, the results obtained by the codes which can solve flow fields inside and outside the pressure vessel would show qualitatively similar temperature distribution as the experiments and the differences were relatively small. Temperature profiles at the top and bottom heads obtained by conduction codes showed different profiles from the experiments. These results show that estimation of the flow fields is very important to obtain correct temperature fields.

In the HTGR LOCA scenarios, as radiation heat transfer exceeds 90% of total heat transfer, the role of natural convection becomes relatively small and the results will agree well independent on the Codes

Heat transfer by radiation and natural convection

The ratios of the heat transferred by radiation and natural convection to total heat input are shown in Tables 4-18-4-24. The results show that radiation heat transfer is dominant. Radiation heat occupies about 50-98% of total heat input and increases with the increase in temperature and pressure. Especially, in case of air cooling, pressure vessel temperature becomes high and the ratio of radiation becomes high.

Calculated total heat inputs agree well with the experimental values, although the differences in the temperatures at the top and bottom heads are rather high.

4.1.8.2. Conclusions

Temperature distribution on the pressure vessel agreed well on the sidewall, however, there were some differences in the top and lower heads temperatures, which would be due to the effect of natural convection.

– Temperature results obtained by the codes which can solve flow fields showed qualitatively good agreement with the experiments. The results of conduction code showed larger errors,

– Radiation heat transfer was dominant in the experimental temperature range. The ratios of transferred heat by radiation to total heat input were estimated in the range of 50-98%. Comparison of total heat input showed good agreement between experiment and analysis,

– Considering that temperatures during HTGR LOCA scenarios will be higher than the experiments, the role of natural convection will be comparatively small. Therefore, temperature estimation will be good enough by the conduction codes with improved heat

transfer correlation. However, it will be necessary to consider solving flow fields to improve the correctness of the codes and the occurrence of hot spots.

Table 4-18 Comparison of the experimental and analytical results (Benchmark I)

Code name (Nation)	Calculated Q_{rad}/Q_{total} and Q_{conv}/Q_{totl} (inside P.V.)	Calculated Q_{rad}/Q_{total} and Q_{conv}/Q_{totl} (outside P.V.)	$\frac{\Delta Q_{total}}{(Q_{total})_{exp}}$	$\Delta T_{max} = (T_{max})_{calc} - (T_{max})_{exp}$ $\Delta T_{min} = (T_{min})_{calc} - (T_{min})_{exp}$
TRIO-EF CASTEM 2000 (France)		Rad: 0.79 NC : 0.21		ΔT_{max} = + 6°C ΔT_{min} = -5°C
THERMIX (China)		Rad: 0.85 NC : 0.15	-0.016	ΔT_{max} = + 5°C ΔT_{min} = +18°C
SM1 (Russia)		Rad: 0.80 NC : 0.20	0.083	ΔT_{max} = +24°C ΔT_{min} = -14°C
DUPT (Russia)		Rad: 0.78 NC : 0.22		ΔT_{max} = +16°C ΔT_{min} = - 8°C
MORECA (USA)		Rad: 0.65 NC : 0.35	0.009	ΔT_{max} = + 5°C ΔT_{min} = +11°C
THANPACT2 (Japan)		Rad: 0.71 NC : 0.29	-0.028	ΔT_{max} = +10°C ΔT_{min} = +10°C

Q_{rad} =heat transferred by radiation, Q_{conv} =heat transferred by natural convection, $Q_{total} = Q_{rad} + Q_{conv}$, $\Delta Q_{total} = (Q_{total})_{cal} - (Q_{total})_{exp}$, $(Q_{total})_{calc}$ =calculated total heat input, $(Q_{total})_{exp}$ =measured heat input, $(T_{max})_{calc}$ =calculated maximum temperature on the pressure vessel, $(T_{max})_{exp}$ =measured maximum temperature on the pressure vessel.

P.V.; Pressure vessel, Rad: Radiation, NC; Natural convection

Table 4-19 Comparison of the experimental and analytical results (Benchmark II)

Code name (Nation)	Calculated Q_{rad}/Q_{total} and Q_{conv}/Q_{totl} (inside P.V.)	Calculated Q_{rad}/Q_{total} and Q_{conv}/Q_{totl} (outside P.V.)	$\frac{\Delta Q_{total}}{(Q_{total})_{exp}}$	$\Delta T_{max} = (T_{max})_{calc} - (T_{max})_{exp}$ $\Delta T_{min} = (T_{min})_{calc} - (T_{min})_{exp}$
TRIO-EF CASTEM 2000 (France)	Rad: 0.66 NC: 0.32 (conduction 0.02)	Rad: 0.79 NC : 0.21		ΔT_{max} = +32°C ΔT_{min} = +16°C
THERMIX (China)	Rad: 0.65 NC : 0.35	Rad: 0.87 NC : 0.13	0.044	ΔT_{max} = +70°C ΔT_{min} = +30°C
SM1 (Russia)	Rad: 0.66 NC : 0.34	Rad: 0.80 NC : 0.20	-0.30	ΔT_{max} = + 7°C ΔT_{min} = -55°C
DUPT (Russia)	Rad: 0.58 NC : 0.42	Rad: 0.82 NC : 0.18		ΔT_{max} = +29°C ΔT_{min} = - 5°C
MORECA (USA)	Rad: NC:	Rad: 0.70 NC : 0.30	-0.132	ΔT_{max} = ΔT_{min} =
THANPACT2 (Japan)	Rad: 0.60 NC : 0.40	Rad: 0.74 NC : 0.26	-0.114	ΔT_{max} = +18°C ΔT_{min} = +14°C

Table 4-20 Comparison of the experimental and analytical results (Benchmark III)

Code name (Nation)	Calculated Q_{rad}/Q_{total} and Q_{conv}/Q_{totl} (inside P.V.)	Calculated Q_{rad}/Q_{total} and Q_{conv}/Q_{totl} (outside P.V.)	$\frac{\Delta Q_{total}}{(Q_{total})_{exp}}$	$\Delta T_{max} = (T_{max})_{calc} - (T_{max})_{exp}$ $\Delta T_{min} = (T_{min})_{calc} - (T_{min})_{exp}$
TRIO-EF CASTEM 2000 (France)	Rad: 0.90 NC : 0.07 (conduction 0.03)	Rad: 0.92 NC : 0.08		ΔT_{max} = +15°C ΔT_{min} = +32°C
THERMIX (China)	Rad: 0.93 NC : 0.07	Rad: 0.91 NC : 0.09	-0.006	ΔT_{max} = +10°C ΔT_{min} = +30°C
SM1 (Russia)	Rad: 0.89 NC : 0.11	Rad: 0.81 NC : 0.19	-0.035	ΔT_{max} = - 6°C ΔT_{min} = -86°C
DUPT (Russia)	Rad: 0.90 NC : 0.10	Rad: 0.90 NC : 0.10		ΔT_{max} = + 3°C ΔT_{min} = -14°C
MORECA (USA)	Rad: NC :	Rad: 0.90 NC : 0.10	+0.048	ΔT_{max} = ΔT_{min} =
THANPACT2 (Japan)	Rad: 0.90 NC : 0.10	Rad: 0.85 NC : 0.15	-0.164	ΔT_{max} = + 5°C ΔT_{min} = +20°C

Table 4-21 Comparison of the experimental and analytical results (Benchmark IV)

Code name (Nation)	Calculated Q_{rad}/Q_{total} and Q_{conv}/Q_{totl} (inside P.V.)	Calculated Q_{rad}/Q_{total} and Q_{conv}/Q_{totl} (outside P.V.)	$\frac{\Delta Q_{total}}{(Q_{total})_{exp}}$	$\Delta T_{max} = (T_{max})_{calc} - (T_{max})_{exp}$ $\Delta T_{min} = (T_{min})_{calc} - (T_{min})_{exp}$
THERMIX (China)	Rad: 0.84 NC : 0.16	Rad: 0.86 NC : 0.16	-0.014	ΔT_{max} = -20°C ΔT_{min} = -25°C
SM1 (Russia)	Rad: 0.89 NC : 0.11	Rad: 0.89 NC : 0.11	-0.065	ΔT_{max} = +15°C ΔT_{min} = -70°C
DUPT (Russia)	Rad: 0.73 NC : 0.27	Rad: 0.90 NC : 0.10		ΔT_{max} = + 7°C ΔT_{min} = +13°C
MORECA (USA)	Rad.: NC:	Rad: 0.79 NC : 0.21	+0.073	ΔT_{max} = ΔT_{min} =
THANPACT2 (Japan)	Rad: 0.84 NC : 0.16	Rad: 0.82 NC : 0.18	-0.19	ΔT_{max} = +100°C ΔT_{min} = + 8°C

Table 4-22 Comparison of the experimental and analytical results (Benchmark V)

Code name (Nation)	Calculated Q_{rad}/Q_{total} and Q_{conv}/Q_{totl} (inside P.V.)	Calculated Q_{rad}/Q_{total} and Q_{conv}/Q_{totl} (outside P.V.)	$\frac{\Delta Q_{total}}{(Q_{total})_{exp}}$	$\Delta T_{max} = (T_{max})_{calc} - (T_{max})_{exp}$ $\Delta T_{min} = (T_{min})_{calc} - (T_{min})_{exp}$
THERMIX (China)	Rad: 0.90 NC : 0.10	Rad: 0.98 NC : 0.02	+0.035	ΔT_{max} = -12°C ΔT_{min} = - 7°C
CCRCC (China)	Rad: 0.98 NC : 0.02	Rad: 0.92 NC : 0.08		ΔT_{max} = +10°C ΔT_{min} = - 5°C
SM1 (Russia)	Rad: 0.93 NC : 0.07	Rad: 0.98 NC : 0.02	+0.12	ΔT_{max} = + 4°C ΔT_{min} = -51°C
DUPT (Russia)	Rad: 0.78 NC : 0.22	Rad: 0.95 NC : 0.05		ΔT_{max} = + 4°C ΔT_{min} = -15°C
MORECA (USA)	Rad: NC :	Rad: 0.96 NC : 0.04	+0.043	ΔT_{max} = ΔT_{min} =

Table 4-23 Comparison of the experimental and analytical results (Benchmark VI **(a)**)

Code name (Nation)	Calculated Q_{rad}/Q_{total} and Q_{conv}/Q_{totl} (inside P.V.)	Calculated Q_{rad}/Q_{total} and Q_{conv}/Q_{totl} (outside P.V.)	$\frac{\Delta Q_{total}}{(Q_{total})_{exp}}$	$\Delta T_{max} = (T_{max})_{calc} - (T_{max})_{exp}$ $\Delta T_{min} = (T_{min})_{calc} - (T_{min})_{exp}$
THERMIX (China)	Rad: 0.60 NC : 0.40	Rad: 0.88 NC : 0.12	+0.027	ΔT_{max} = +20°C ΔT_{min} = - 3°C
CCRCC (China)	Rad: 0.76 NC : 0.24	Rad: 0.72 NC : 0.28		ΔT_{max} = - 5°C ΔT_{min} = + 8 °C
DUPT (Russia)	Rad: 0.41 NC : 0.59	Rad: 0.72 NC : 0.28	+0.027	ΔT_{max} = + 1°C ΔT_{min} = + 3°C
(USA) MORECA	Rad: NC :	Rad: 0.69 NC : 0.31	+0.137	ΔT_{max} = ΔT_{min} =

Table 4-24 Comparison of the experimental and analytical results (Benchmark VI (b))

Code name (Nation)	Calculated Q_{rad}/Q_{total} and Q_{conv}/Q_{totl} (inside P.V.)	Calculated Q_{rad}/Q_{total} and Q_{conv}/Q_{totl} (outside P.V.)	$\frac{\Delta Q_{total}}{(Q_{total})_{exp}}$	$\Delta T_{max} = (T_{max})_{calc} - (T_{max})_{exp}$ $\Delta T_{min} = (T_{min})_{calc} - (T_{min})_{exp}$
THERMIX (China)	Rad: 0.72 NC : 0.28	Rad: 0.94 NC : 0.06	-0.02	ΔT_{max} = +10°C ΔT_{min} = -10°C
CCRCC (China)	Rad: 0.90 NC : 0.10	Rad: 0.81 NC : 0.19		ΔT_{max} = +15°C ΔT_{min} = +10°C
DUPT (Russia)	Rad: 0.61 NC : 0.39	Rad: 0.82 NC : 0.18		ΔT_{max} = + 2°C ΔT_{min} = + 4°C
MORECA (USA)	Rad: NC :	Rad: 0.81 NC : 0.19	+0.077	ΔT_{max} = ΔT_{min} =

4.2. THE SANA-1-EXPERIMENTS FOR SELF-ACTING REMOVAL OF THE AFTERHEAT FROM A PEBBLE BED

4.2.1. Sana-1 Code-To-Experiment Summary Description of the Benchmark

4.2.1.1. Motivation

The high temperature reactor offers the possibility at a suitable design and dimensions to master heaviest accidents. The produced decay heat is removed safely from the reactor core at this as hypothetically classified accident, failure of all heatsinks at simultaneous depressurization. No temperatures occur that lead to an increased fission product release or to a damage of the reactor structures, what is possible at core melting capable reactors. The heat transport is based on at any time available mechanisms: heat conduction, heat radiation and natural convection. Active technological facilities aren't required.

The after-heat is removed self-acting safely.

To confirm this striking safety quality, the considerable heat technical parameters of the self-acting after-heat removal are examined in the experiment SANA.

Tasks:

– Measurement of time dependent three-dimensional temperature distribution,

– Determination of effective heat conductivity as a function of the temperatures in the core structures,

– Evaluation of permitted heat flux densities at different boundary conditions,

– Provision of data sets for the program validation (THERMIX / DIREKT, TINTE),

– Statements concerning natural convection phenomena.

4.2.1.2. Structure of the pilot plant

For the examinations in the context of the SANA experiments a bed of graphite pebbles in cylindrical arrangement is selected. The part of the core of the pebble bed reactor has a diameter of 1,5m as well as a height of 1m. Approximately 9500 graphite pebbles with a diameter of 6cm in irregular arrangement find space in the volume of 1,77m^3.

The heat production is carried out in at maximum 4 electrical resistance heating elements, which are ordered vertically in the bed. The installed maximum power of 50kW facilitates a maximum power density of 28kW/m^3. That means 0,93% of the full power transferred to the module reactor and corresponds to a time of 3h to 4h after admission of the depressurization accident. To guarantee a considerable radial heat flux, insulation systems limit the bed at the top and the bottom.

SANA main data

–	Maximum bed temperature	1600°C
–	Installed electrical power	50kW
–	Diameter of the pebble bed	1,5m
–	Height of the pebble bed	1,0m
–	Complete height	3,2m
–	Pebble diameter	60mm

Thermocouples, which are used for the recording of the temperature profiles, are distributed over the test stand. To prevent corrosion at the graphite installations, the plant is operated among

inert gas atmosphere. The heating element connections get cooled with water. The power supply is carried out from the three phase mains. The data acquisition system and the control of the experiments can occur with a personal computer.

Fig. 4-72 Photo of the test facility

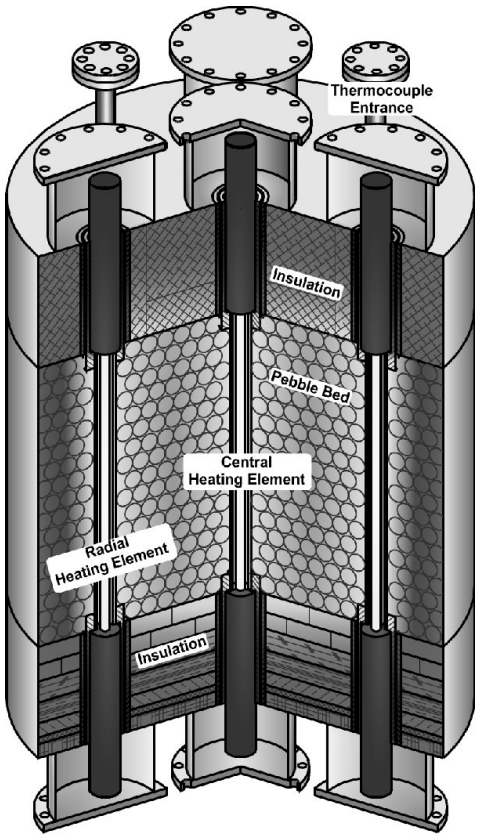

Fig. 4-73 SANA-I

4.2.1.3. Data acq uisition system and computer

The thermocouples are connected to a 60-channel hybrid recorder which has a built-in comparison point. The thermoelectric characteristics for a number of common combinations, among this type N and type W, are integrated in the device. It is able to convert the measured thermoelectric voltages to °C and to show them on the display and the built-in printer. For the MoRe elements at first only the recording of the thermoelectric voltage is carried out in the hybrid recorder. A PT100 resistance element is used as an external comparison point temperature. The maximum scanning rate of the recorder lies at 2 seconds. A further hybrid recorder with 30 channels is available to scan the analogue exits of the gas analysis devices as well as the actual value outputs of the thyristor. This recorder works with a maximum scanning rate of 30 channels in 6 seconds. The recorders are equipped with a parallel IEEE-488-interface to enable the both direction data exchange and over this with a personal computer which has also an IEC bus interface. The measured data received by the computer can be saved on the built-in hard disk. A serial interface (RS 232) connects the computer with the power giver. The computer can be used to the control of the heating facilities with it. The imbedding of the measurement hardware into the test stand is represented in the illustration. (Fig. 4-74)

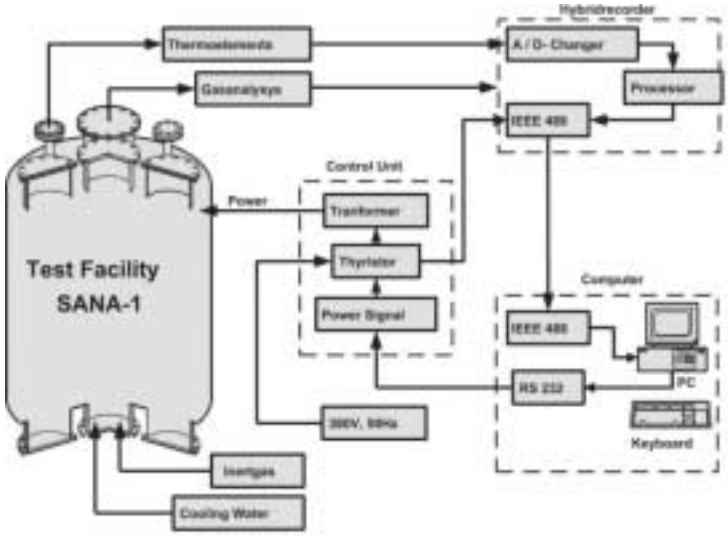

Fig. 4-74 Flow sheet of electrical power and data

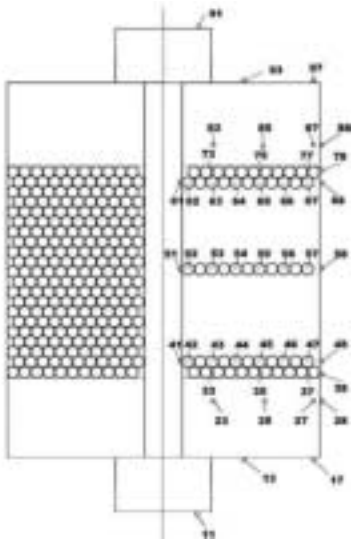

Fig.4-75 Arrangement of the thermocouples in the test stand SANA I

4.2.1.4. Plant Data

Tests were executed with one or four heating elements in 15000 hours. Nitrogen (representative for air), helium and argon came to the use as inert gases. To accomplish the highest temperature region (above of 1200 °C), an insulation is brought in between the vessel wall and the pebble bed at a part of the tests. The influence of natural convection explains the more distinctive vertical arrangement in the temperature layers at the tests with nitrogen in comparison with those with helium. Both, stationary and non steady tests were executed

The bed is heated by an electrical resistance heater. The heating is executed by a graphite tube with 32 mm outside diameter and attached centrally in the bed. A protection tube of 141mm outside diameter protects the heating tube against the direct touch with the pebbles. The heating element is lasted at the top and the bottom by the connection electrodes, which are also made from graphite. Because of their clearly larger crossways cut area (diameters 80 mm) and therefore clearly lower resistance, only a low heat production has to be removed there. This, by the connection electrodes passed on heat flux, is removed by a water-cooling installed into the cover hoods of the connection electrodes.

To reach that the heat flux is removed mainly radial from the bed became above and below the bed with different materials insulated. The upper insulation passes CERACHEM-Blanket

material from a 400 mm thick layer (data see table). The lower insulation is, because it carries the weight the bed, built of several layers with various stability and heat conducting properties. These layers are from top to the bottom:

Fire light brick RI 30 B, company Savoie Feuerfest (fireproof) 128 mm thick,

– CERAFORM 1000, company Gossler 75 mm thick,
– CERAFORM 100, company Gossler 75 mm thick,
– THERMOSIL 1100, company Gossler 50 mm thick,
– THERMOSIL 1000, company Gossler 25 mm thick,
– GOSSLEROC GMP 150, company Gossler 50 mm thick.

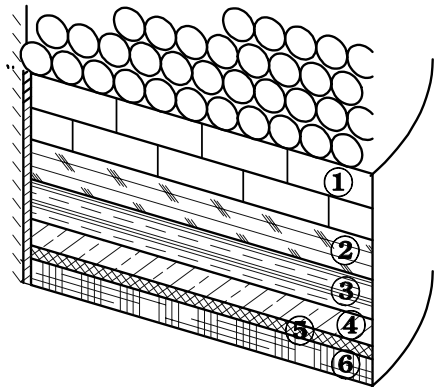

Fig. 4-76 Bottom insulation of the test facility

The whole arrangement is put in a steel vessel which is provided with a touch protective barrier on the outside to avoid injuries by the hot surface. An inert gas atmosphere, either helium, nitrogen or argon, protects the inside graphite materials against corrosion reactions.

The resistance heater is provided with electrical power by the 380V 50 Hz three phase mains. The power is settled about a communication capable thyristor powergiver. The voltage is reduced by a transformer behind the thyristor. At most the current on the secondary side has a value of 1220A. Coated thermocouples of type N (DIN IEC 584) are used for the measuring of the temperature-profiles within the test facility. The arrangement of the thermocouples is shown in the figure.

In addition were measured:

– The pressure in the test stand,
– The pressure in the bottle of gas bundles and in the gas inlet line,
– The gas mass flow,
– The composition of the waste gas,
– Temperatures and flow of the cooling water.

A large portion of these measured data was by a computer directly continuously taken and saved.

4.2.1.5. Benchmark Description

For the benchmark typical steady state runs of the test facility are given. The variation is made with power, which is equivalent to the temperature level. Two representative gases are chosen:

– Helium as the normal cooling gas,

– Nitrogen as the representative of air.

The kind of heating is changed:

– Heating of the full height,

– Heating of the lower half of the pebble bed,

– Heating of the upper of the pebble bed.

Additionally tests are included with 30mm pebbles instead of the standard diameter of 60mm.

In one test series the vessel is only filled partly to simulate an upper gas plenum. The data for the tests are given at Appendix A.1.1

4.2.2. INET Analysis of SANA-1 Experiment Benchmark Problems

4.2.2.1. Introduction

The SANA benchmark problems which are provided by Dr. H.F.Nieβen of the Institute for Safety Research and Reactor Technology Research Centre Jülich Gmbh (KFA) in Germany [1], are a part of the IAEA Coordinated Research Program (CRP) on "Heat Transport and Afterheat Removal for GCRs under Accident Conditions". This paper gives the analytic results and the comparison with the measured data.

The SANA experimental apparatus consists of a graphite pebble bed core with a diameter of 1.5 m as well as a height of 1 m, four electrical resistance heating element inside the pebble bed, insulator at the top and the bottom and a steel vessel. About 9600 graphite spheres with diameter of 6 cm are arranged in the core. Four experimental data with long central heating element (including temperature, heating powers) of SANA benchmark have been supplied by Dr. H.F.Nieβen to determinate the effective heat conductivity of pebble bed as a function of temperature and to validate the computer code through comparison between calculations and experiments data. These four experiments are following:

– Nitrogen 30 kW nominal heating power with long heating element,

– Nitrogen 10 kW nominal heating power with long heating element,

– Helium 30 kW nominal heating power with long heating element,

– Helium 10 kW nominal heating power with long heating element.

The INET analysis for SANA benchmark includes determination of effective conductivity of pebble bed as a function of temperature, the comparison of effective conductivity with measured data and temperature distribution calculations in the pebble bed with and without natural convection.

4.2.2.2. Analysis Approach and Model
Computer Code and Analytical Model

The computer code THERMIX, a computer program used for two dimensional, thermal hydraulic analysis of a pebble bed in HTGR, is used for analysis of SANA benchmark problems.

A simulating model is shown in Fig. 4-77, which is used to calculate the distribution of the pebble bed temperatures under the given output power of the heating element and vessel temperature as boundary condition. The analytical model consists of 18×35 meshes and 20 components to represent different construction, such as heating element, pebble bed, pressure vessel, insulator et, al. The heating element has the upper and bottom insulator as well as pebble bed.

– Effective Thermal Conductivity

The core of the HTGRs is a packed bed of spherical fuel elements, the heat is transported simultaneously by these types of mechanisms: radiation in void region, conduction of gas, conduction of spherical and convection of gas. The heat flux is considered to consist of three parts except convection: The first is a solid conduction—void radiation—solid conduction process, the second is solid conduction—gas conduction—solid conduction process and the third is solid conduction—contact area conduction—solid conduction process. So the following three different types of effective conductivity must be evaluated:

1. Void radiation + solid conduction

This type effective conductivity is based on the cell model defined by Zehner and Schluender. In the cell model the pebble bed is replaced by an arrangement of unit cells, and the heat transfer is the combination of radiation in the voids and conduction within the spheres. The formula of the cell model is modified by G. Breitbach and H. Barthels[2]:

$$\lambda_e = \left\{ \left[1-(1-\varepsilon)^{1/2}\right]\varepsilon + \frac{(1-\varepsilon)^{1/2}}{2/\varepsilon_r - 1} \cdot \frac{B+1}{B} \cdot \frac{1}{1+\dfrac{1}{(2/\varepsilon_r - 1)\Lambda}} \right\} 4\sigma T^3 d$$

(1)

where:

$$B = 1.25\left(\frac{1-\varepsilon}{\varepsilon}\right)^{10/9}$$

(2)

$$\Lambda = \frac{\lambda_s}{4\sigma T^3 d}$$

(3)

The first term in the brackets represents the radiation and is the dominating term at high temperature.

2. Gas conduction + solid conduction

This type of effective conductivity is the prediction of the stagnant thermal conductivity of the working medium in porous media. Based on a one-dimensional heat flow model for conduction through a packed bed of spherical particles, Zehner and Schlunder presented a correlation for the stagnant thermal conductivity which was tested by V. Prasad et, al.[3]:

$$\frac{\lambda_e}{\lambda_f} = 1-\sqrt{1-\varepsilon} + \frac{2\sqrt{1-\varepsilon}}{1-\lambda B}\left[\frac{(1-\lambda)B}{(1-\lambda B)^2}\ln\left(\frac{1}{\lambda B}\right) - \frac{B+1}{2} - \frac{B-1}{1-\lambda B}\right]$$

(4)

where: B is the same as Eq. (2).

3. Contact conduction + solid conduction

This type of effective conductivity is the prediction of area contact conduction for beds made of spherical particles where the particles are subject to a compressive load (for example, weight of particles). The radius of the contact area between two spheres is given by Hertzian elastic

deformation[4]. Chen and Tien analysed the conductive heat flow for the three close-pack cubic arrangements and gave the contact resistance. The final result is:

$$\frac{\lambda_e}{\lambda_s} = \left[\frac{3\left(1-\mu_p^2\right)}{4E_s} fR\right]^{1/3} \frac{1}{0.531S}\left(\frac{N_A}{N_L}\right)$$

(5)

where:

$$f = p\frac{S_F}{N_A}$$

(6)

In Eq. (5) and (6), NA and NL are the number of particles per unit area and length, respectively. For the simple cubic arrangement the constants S, SF, NA and NL are given as S = 1, SF = 1, NA = $1/(4R^2)$, NL = 1/(2R), R is sphere radius which value is 0.03m here. The Poisson ratio $\mu_p = 0.136$ and the Young modules Es = 9.0×10^9 (N/m^2) are used. The external pressure p is estimated by the weight of particles in the pebble bed.

The total effective conductivity, marked as formula 35, is the sum of these three parts:

Formula 35:

$$\lambda_e^t = \lambda_e^r + \lambda_e^g + \lambda_e^c$$

(7)

The porosity of 0.41 in pebble bed is used. At the boundary areas of a half pebble diameter the porosity of 0.65 and 0.50 are used for protection tube and furnace wall. The pebble emissivity of 0.8 is selected. The temperature dependent heat conductivity of the materials are known in [1].

In Eq. (7) the effect of gas convection on heat transfer is not included. Since the computer code THERMIX has the function of simulating the process of natural convection, the model of natural convection in the core is included in the calculation of temperature distribution of the pebble bed in order to take the influence of natural convection into account. Therefore the heat transported by natural convection can be evaluated according to the calculating results.

4.2.2.3. Results and Comparison with Experiment

– Effective Thermal Conductivity

The effective heat conductivity calculated by Eqs (1), (4) and (5) are shown in Fig. 4-78 and Fig. 4-79. The measured conductivity based on the experimental temperatures in pebble bed of SANA experiment is also shown in Figs. 4-78 and 4-79 for nitrogen and helium condition respectively.

The comparison of effective conductivity between the correlation and measured data show that the total effective conductivity is a bit lower than measured value. The reason is that in SANA experiments the heat is transported not only by radiation and conduction, but also by convection of gas in pebble bed. While in Eq. (7) the convection of gas is not concerned.

The comparison also shows that in the lower temperature region of nitrogen condition the measured value is much higher. In view of these three types of heat transfer the radiation is much more important than the others as the temperature increasing. Only in lower temperature region the stagnant thermal conductivity and contact conductivity occupy the major parts of total conductivity.

The contact conductivity is estimated using the parameters related to a simple cubic arrangement and the result is $\lambda e/\lambda s = 0.0166$.

– Temperature Distribution

The calculated temperature distribution without natural convection using the effective heat conductivity (formula 35) and its comparison with measured data are shown in Figs. 4-79 – 4-83 for the four different SANA experiments. The calculated results are a bit higher than measured data in centre pebble bed region and lower in outer region.

The calculated temperature distributions with natural convection are also shown in Figs. 4-79 – 4-82 for the four SANA experiments. The temperature discrepancy among top, middle and bottom of pebble bed at the same radius with natural convection is larger than that without convection. This phenomena satisfies the actual state of natural convection, meanwhile the temperature distribution with natural convection is much closer to the measured data.

Apparently the natural convection takes a greater effects on the heat transfer for the nitrogen condition than that for helium condition, and it occupies a greater proportion in heat transport for the low heating power condition than for high power condition.

4.2.2.4. Conclusions

– The SANA benchmark experiments are very valuable and useful for understanding of complex heat transfer phenomena in pebble bed and for verification and validation of computer code,

– Three types of effective thermal conductivity are evaluated. The total effective conductivity by the correlation is a bit lower than the measured value because the effect of convection on the heat transfer is not included in the correlation. The calculated temperature distributions show good agreement with the measurement data. The comparison shows that, the SANA benchmark experiment can be accurately simulated by the THERMIX code using the effective conductivity correlation,

– In the calculations the influence of natural convection must be to take into account more accurately for nitrogen condition, especially under lower heating power. The SANA benchmark experiments are also useful to understand the effects of heat transportation by natural convection on the temperature distribution of the pebble bed. The natural convection phenomena can be simulated by the THERMIX code,

– The SANA benchmark experiments validate the THERMIX code and the effective conductivity correlation in modelling the heat transfer mechanisms in pebble bed. Therefore the THERMIX code can be suitably used in designing of pebble bed for GCRs or other analysing options.

Nomenclature

B	form factor [see Eq.(3)]	ε	Porosity
d	particle diameter (m)	ε_r	Emissivity
E_s	Yang modules (N/m^2)	λ	conductivity ratio, λ_f/λ_s
f	force (N)	λ_e	effective thermal conductivity (W/m·K)
p	pressure (Pa)	λ_f	thermal conductivity of gas (W/m·K)
R	radius (m)	λ_s	thermal conductivity of particles (W/m·K)
T	temperature (K)	μ_p	Poisson ratio
		σ	Stephan-Boltzmann constant = 5.67×10^{-8} ($W/m^2\cdot K^4$)

REFERENCES TO SECTION 4.2.1.

[1] H. F. Nießen, and B. Stöcker, “Sana-1 Code-to-experiment Summary Description of Benchmark”, 3rd IAEA Research Co-ordination Meeting on “Heat Transport and Afterheat Removal for Gas-cooled Reactors under Accident Conditions”. 14-17 November 1995, Vienna.

[2] G. Breitbach and H. Barthels, “The Radiant Heat Transfer in the HTR Core After Failure of the Afterheat Removal Systems”, Nuclear Technology, 49, pp392-399, August 1980.

[3] V. Prasad, N. Kladas, A. Bandyopadhaya and Q. Tian, “Evaluation of Correlations for Stagnant Thermal Conductivity of Liquid-Saturated Porous Beds of Spheres”, International Journal of Heat and Mass Transfer, 32, pp1783-1796.

[4] “Principles of Heat Transfer in Porous Media”, Springer (Mechanical Engineering Series), 1991, pp128.

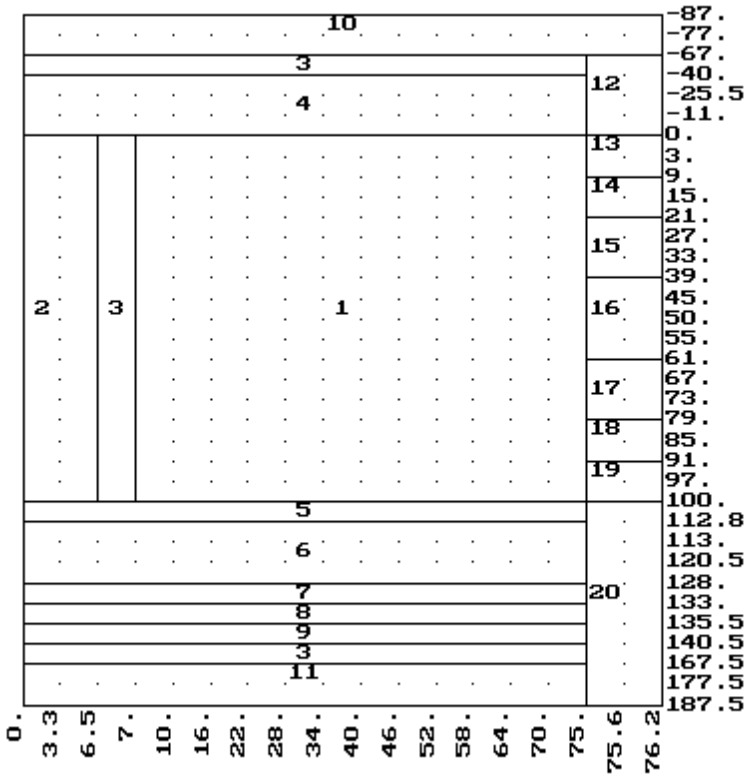

Fig.4-77 Numerical Simulating Model for SANA Benchmark Problems

1. Pebble bed
2. Heating element
3. Steel
4. Top insulation
5-9. Bottom insulation
10. Upper boundary
11. Bottom boundary
12-20. Side Boundary

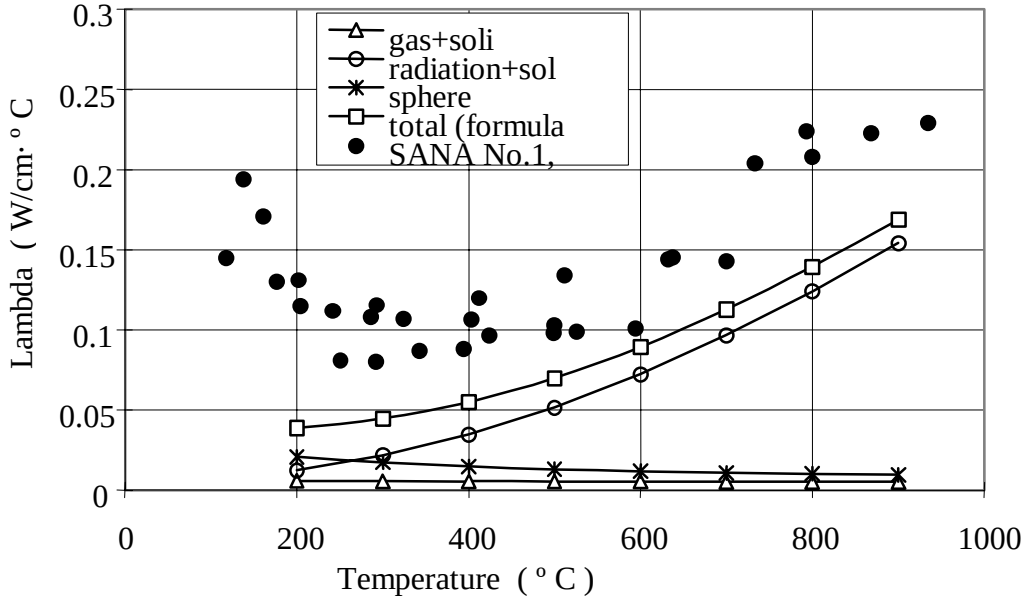

Fig. 4-78 Effective conductivity comparison among correlations and measured data for nitrogen condition

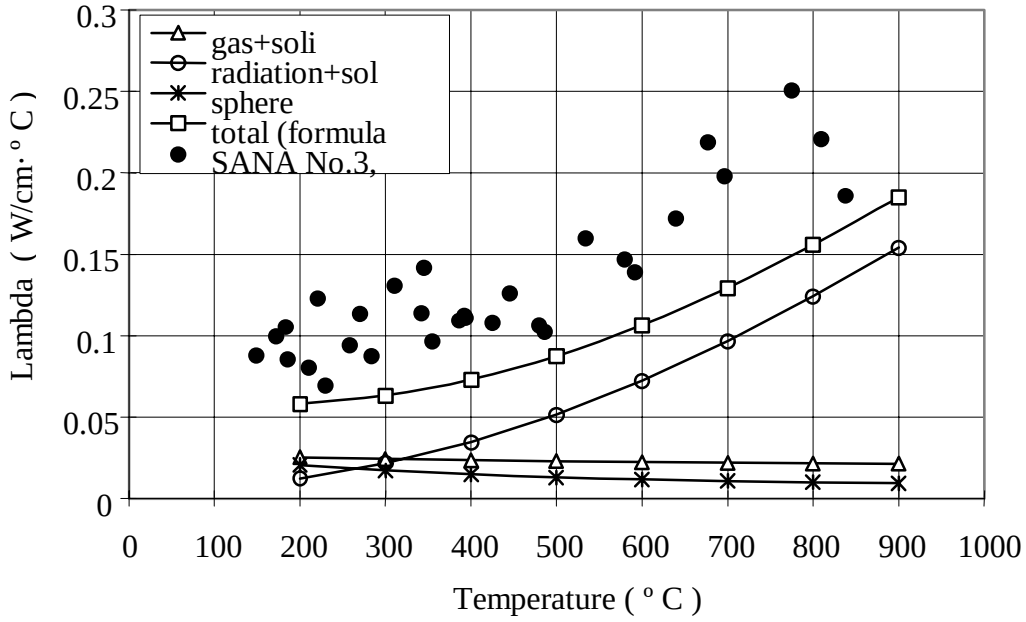

Fig 4-79 Effective conductivity comparison among formulas and measured data for helium condition

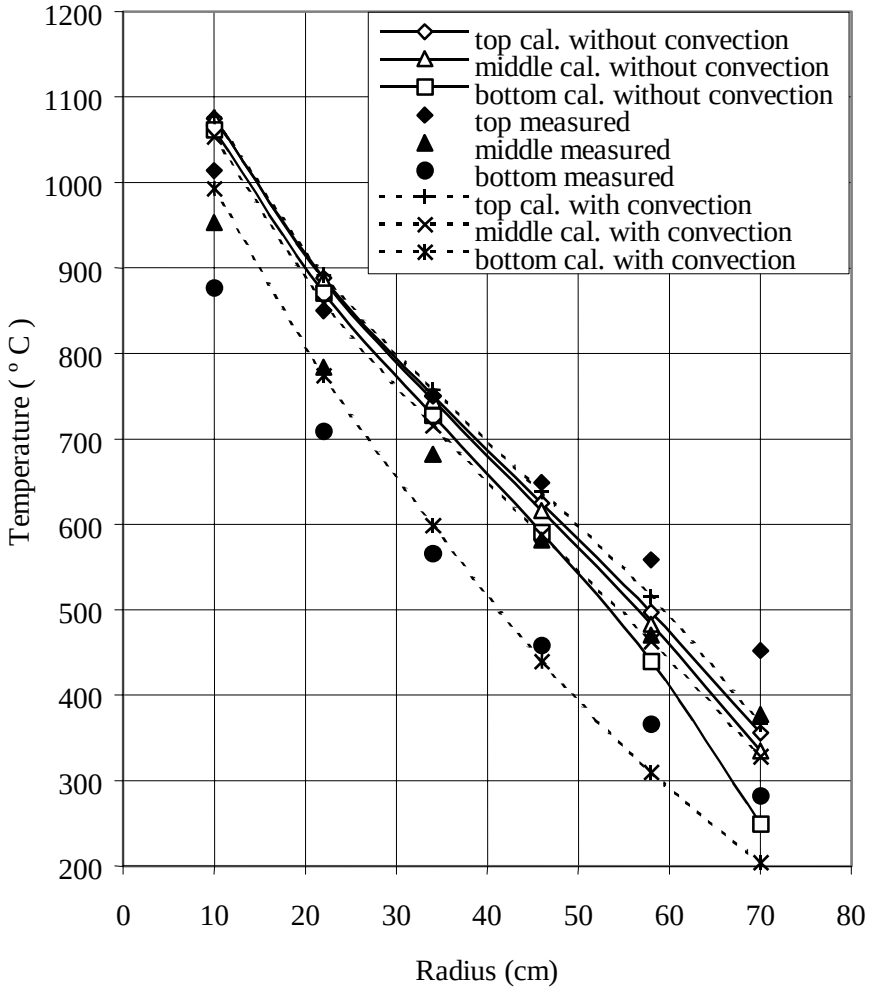

Fig. 4-80 Temperature comparison between calculations (with formula 35) for SANA No.1

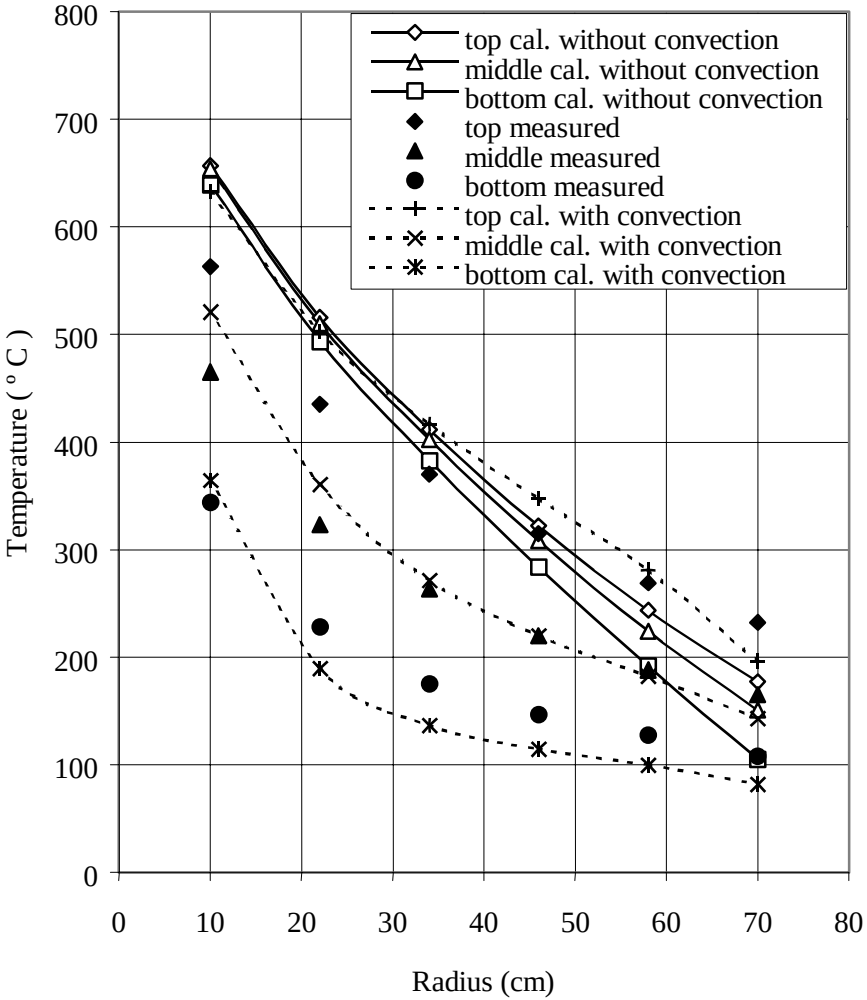

Fig 4-81 Temperature comparison between calculations (with formula 35) for SANA No.2

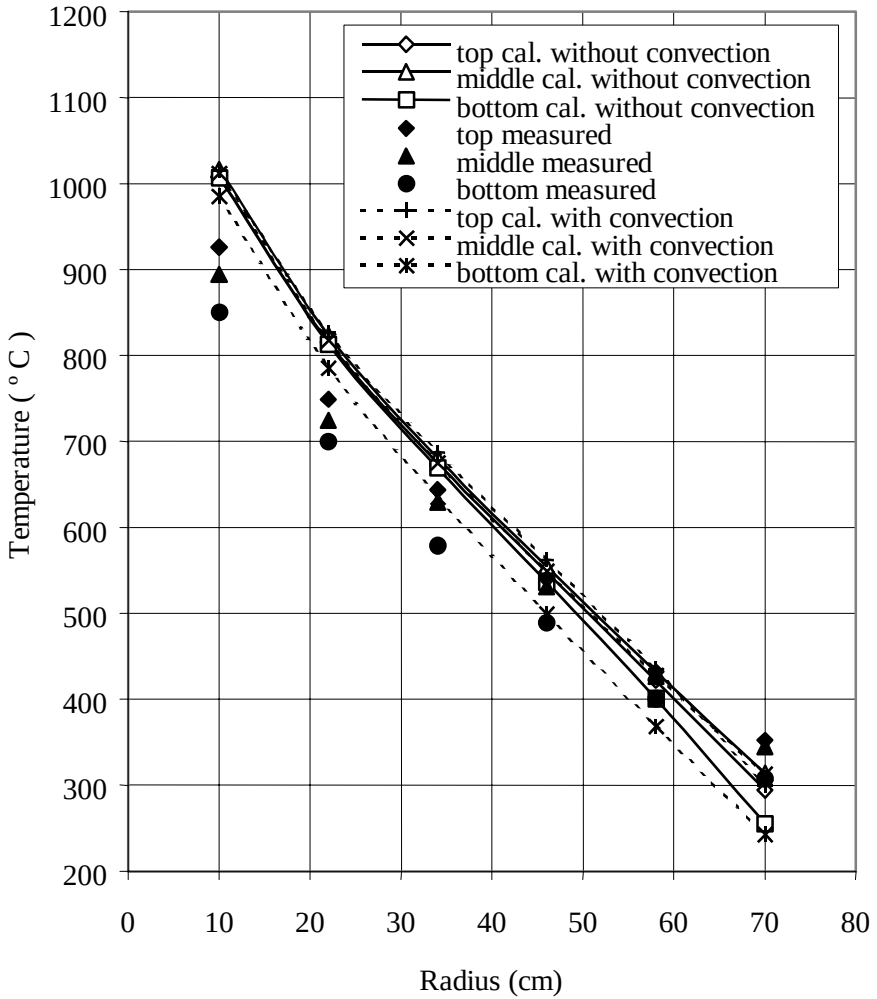

Fig 4-82 Temperature comparison between calculations (with formula 35) for SANA No.3

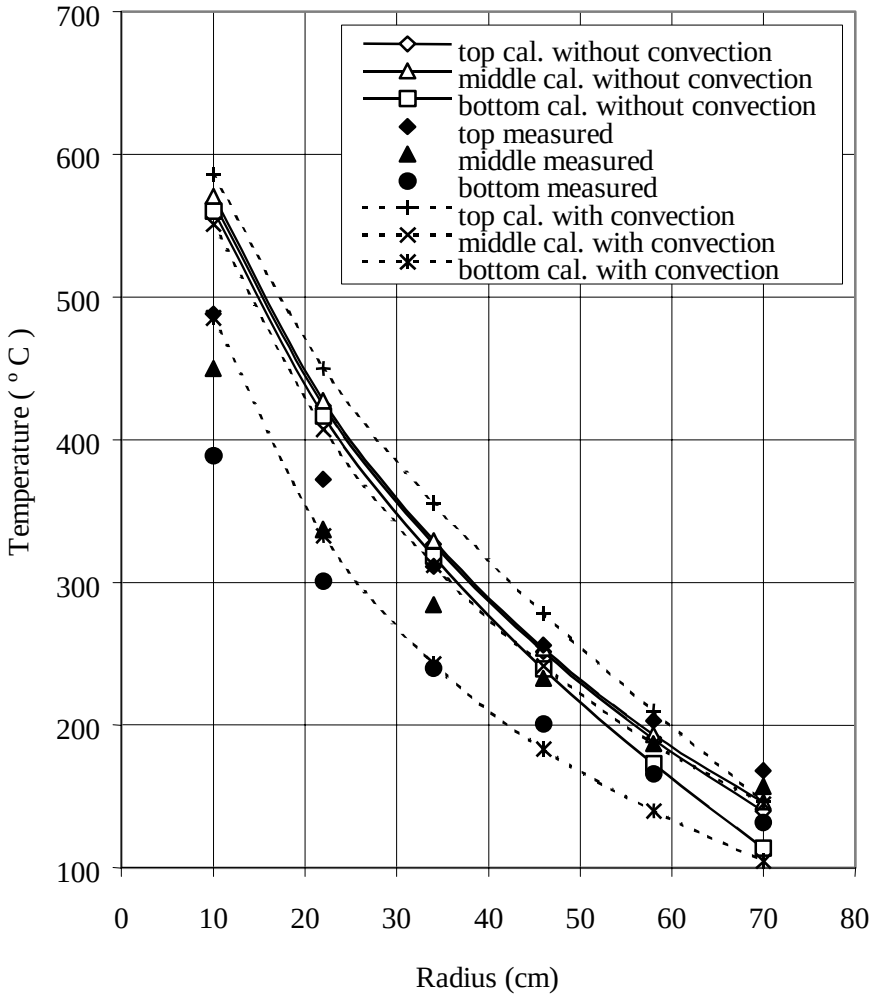

Fig 4-83 Temperature comparison between calculations (with formula 35) for SANA No.4

4.2.3. TRIO-EF Model of SANA-1 Experimental Set-Up

4.2.3.1. Summary

This benchmark problem is part of an AIEA Coordinated Research Program on « Heat Transport and After Heat Removal for Gas Cooled Reactors under Accident Conditions ». It was presented during the 4th RCM as part of the French contribution to the validation of general codes on experimental dates:

– JAERI for HTTR Reactor Cavity Cooling System,

– SANA - 1 for Self-Acting Removal of the After Heat from a Pebble Bed.

This paper concerns the experiments on SANA - 1 which datas were provided by H. F. Niessen and B. Stöcker from the Institute for Safety Research and Reactor Technology Research Center Jülich Gmbh (KFA), Germany.

4.2.3.2. Introduction

A model of SANA-1 test facility experiments [1] was built by using a porous media formulation. It was developed with a finite element code [2]. After a description and the comparison with the experimental data, a sensitivity analysis is presented.

4.2.3.3. Model

4.2.3.3.1. Geometry

The axial symmetry of the pebble bed, insulation materials and heating element allows for a two-dimensional modelling in cylindrical coordinates.

As the amounts of heat removed from the electrodes and the resistance are known from the experiments [1], the related heat fluxes are imposed at the boundaries of the protection tube; the inside parts are not described.

4.2.3.3.2. Code

Within the bed, the porous media formulation includes all heat transfer participation in conductive and convective terms (radiation being linearized). The problem is only conductive in solid parts (insulation, vessel). True radiant heat transfer calculation is added for the cases with a cavity on top of the pebbles. Thus, the equations to be solved in cylindrical coordinates are:

– Energy transport,

– 2D Momentum transport (Mass conservation is solved by a penalty method [2]),

– 2D Radiation in cavity.

The steady state solution is reached using an implicit scheme for both scalar and vectorial equations while transient terms are included for more stability.

4.2.3.3.3. Equations

Darcy, Brinkman and Forchheimer hypothesis [3] are considered for the momentum conservation (see Equation 1). Brinkman viscous drag term enables to impose a no-slip boundary condition at walls while Forcheimer inertial component of pressure drop describes the non-linear

effects on pressure drops at increasing Reynolds number. The recommended effective viscosity is the one of the fluid [4].

$$\frac{1}{\varepsilon}\frac{\partial V_D}{\partial t}+\frac{1}{\varepsilon^2}V_D.\nabla V_D=-\frac{1}{\overline{\rho}_f\varepsilon}\nabla p+\nu_e\nabla^2 V_D-\left[\frac{\nu_f}{K}+\frac{C}{K^{1/2}}|V_D|\right]V_D+\frac{\Delta T}{\overline{T}}g$$
$$\nabla V_D=0$$
$$(\varepsilon\rho_f C_p^f+(1-\varepsilon)\rho_S C_p^S)\frac{\partial T}{\partial t}+\rho_f C_p^f V_D.\nabla T=\lambda_e\nabla^2 T$$

Equation 1 Conservation equations using Darcy, Brinkman and Forcheimer formulations; constant mass density and thermal equilibrium are assumed.

The equilibrium approximation is assumed between the solid and the gas phases [5] (see Eqs 1 and 2) so that a unique energy conservation relation is needed.

Because the Business approximation is only valid for small density variations a model was developed which solves the conservation of the momentum vector defined from the Darcian velocity by:

$$\vec{G}=\rho_f\vec{V}_D \text{ (see Eq. 2).}$$

The differential operators and coefficients are applied distinctly to each area according to its characteristical properties like conductivity, permeability or viscosity. For example, the convection term in the energy conservation only concerns the pebble bed area.

$$\frac{1}{\varepsilon}\frac{\partial G}{\partial t}+\frac{1}{\rho_f\varepsilon^2}G.\nabla G=-\frac{1}{\varepsilon}\nabla p+\nu_e\nabla^2 G-\left[\frac{\nu_f}{K}+\frac{C}{K^{1/2}}|V_D|\right]G+\rho_f g$$
$$\nabla G=0$$
$$(\varepsilon\rho_f C_p^f+(1-\varepsilon)\rho_S C_p^S)\frac{\partial T}{\partial t}+C_p^f G.\nabla T=\lambda_e\nabla^2 T$$

Equation 1 Conservation equations using Darcy, Brinkman and Forcheimer formulations; variable mass density and thermal equilibrium are assumed.

4.2.3.3.4. Boundary conditions

Outside limits of the vessel

The vessel walls exchange energy by radiation and natural convection with the surrounding environment; a heat flux condition is then imposed:

$$\lambda_i\left(\frac{\partial T}{\partial y}\right)_{Y^-}=\phi_R+\phi_C \text{ , with } \phi_R=\sigma\varepsilon_{Vessel}(T_{Y^-}^4-T_\infty^4) \text{ and } \phi_C=h(T_{Y^-}-T_\infty)$$

Limits of the pebble bed: no-slip relation (zero velocity at walls).

4.2.3.4.1. Physical properties

Statistical bed porosity, insulation and graphite conductivities are known ([1] and [6]). Pebbles and surfaces in the cavity (for the tests with a plenum) are first assumed to have the same emissivity (0,8) but distinct values were considered in the sensitivity analysis in 4.

4.2.3.5. Pebble bed effective properties

Pressure drop in the packed bed

Permeability and inertial coefficients (*K* and *C* in Equation 1 and 2) of SANA-1 bed were previously determined [7]. They are slightly different from Ergun formula which are commonly used for packed beds of spherical particle [3].

$$K = \frac{\varepsilon^3 d^2}{160(1-\varepsilon)^2} \quad \text{and} \quad C = \frac{3}{\varepsilon^{3/2}\sqrt{160}}\left(\frac{\nu(1-\varepsilon)}{d}\right)^{0,1}$$

Porosity in the packed bed

In order to take in account the channelling effect of the flow near the wall, explained by the variation of porosity [8], it is assumed that it varies exponentially as a function of the distance from the boundary (Y^-) [9] ($\varepsilon = \varepsilon_\infty[1 + C_1 \exp(-N_1 Y^- / d)]$, with C_1=1,4 and N_1=5).

Effective conductivity

Three different types of heat transfer can be assumed in the stagnant bed: *radiation + solid conduction*, *gas + solid conduction'* ,*sphere contacts + solid conduction*. Zehner and Schlünder cell model is used for radiant transfers [10]. The second is modelled by a weighted average formula [11] tested by Prasad et al. [12]. The last type uses the Hertzian elastic deformation [13] to approximate the contact radius of a sphere in the bed as a function of structural parameters. The boundary conductivity is lower than the statistical bed: the multiplication by a coefficient (0,5) is used in the areas at a half diameter distance from the walls.

4.2.3.5. Comparison with experiments

Situation	Sphere diameter	Heating element / Type of Bed	Gas	Nominal Power [kW]
(1)	60 mm	Long heating element	N2 , He	10 , 30
(2)	30 mm	Long heating element	N2 , He	10 , 30
(3)	60 mm	Half element at the top	N2 , He	20
(4)	60 mm	Half element at the bottom	N2 , He	20
(5)	60 mm	(4) + Plenum	N2 , He	20

Figures 4-84 to 4-85 show the predictions for situation (1). The convective heat transfer is responsible for the stratification of temperatures: higher at the top and lower at the bottom of the bed. Meanwhile, this effect depends on the gas and power input: it is clearly enhanced by nitrogen or by decreasing the power while it decreases or disappears with Helium or by increasing the power. The model reproduces all these tendencies and the results are closed to the test data. Meanwhile, the discrepancy for the 10 kW test in Helium (Fig. 4-87) reveals that the model predicts correctly the magnitude of the vertical temperature gradients in the statistical bed but over-estimate the temperatures, mainly near the central cylinder.

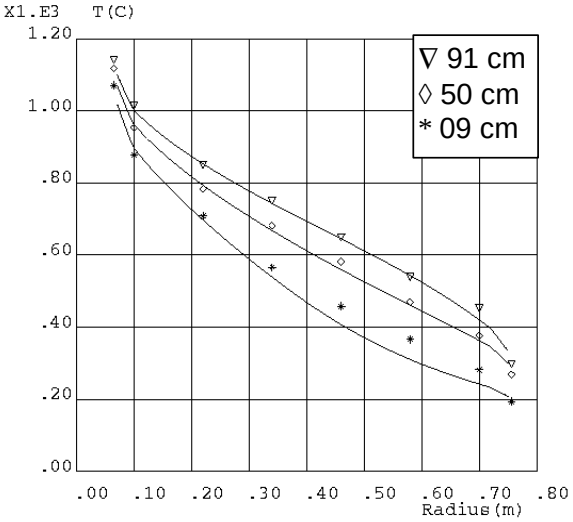

Fig. 4-84 L.H.E. / 60 mm pebbles / 30 kW / Nitrogen

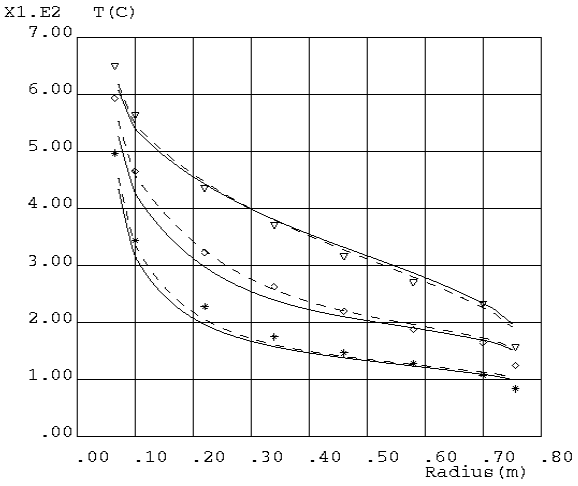

Fig. 4-85 L.H.E. / 60 mm pebbles / 10 kW / Nitrogen. Influence of mass density : constant and variable model (dashed line)

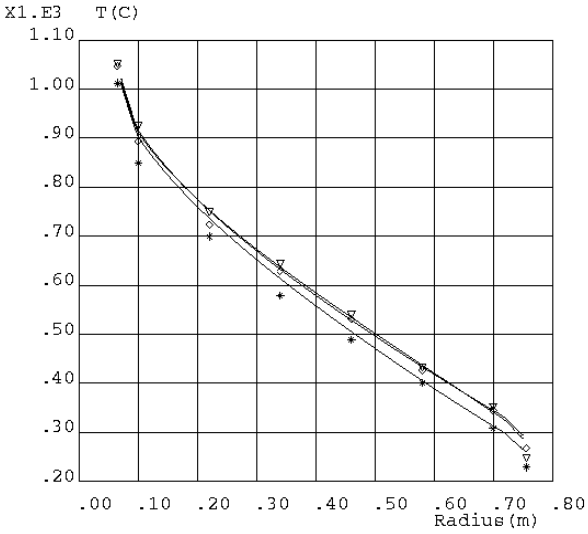

Fig. 4-86 L.H.E. / 60 mm pebbles / 30 kW / Helium

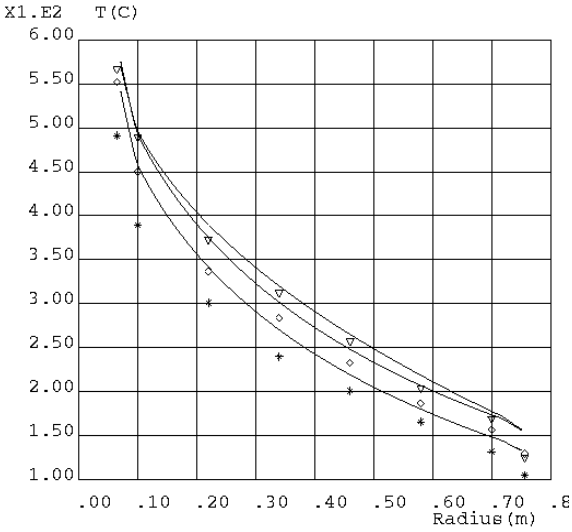

Fig. 1-87 L.H.E. / 60 mm pebbles / 10 kW / Helium

Figures 4-88 to 4-91 show the situation (2). In comparison with the previous (1), the magnitude of the temperature vertical gradient is sensibly reduced (unless for the test in Nitrogen at 10 kW input (Fig. 4-89) where the differences of temperatures at a same radius can even be higher than for 60-mm pebbles). This would be the additional effect of a higher conductivity and a lower permeability (see section 4.2.4). The calculation reproduces this tendency for the three

other cases: a significant reduction of the stratification and an increase of the temperature near the heating element.

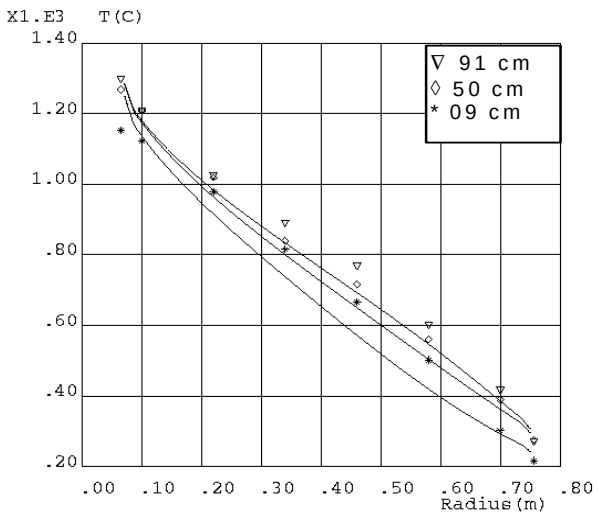

Fig. 4-88 L.H.E. / 30 mm pebbles / 30 kW / Nitrogen

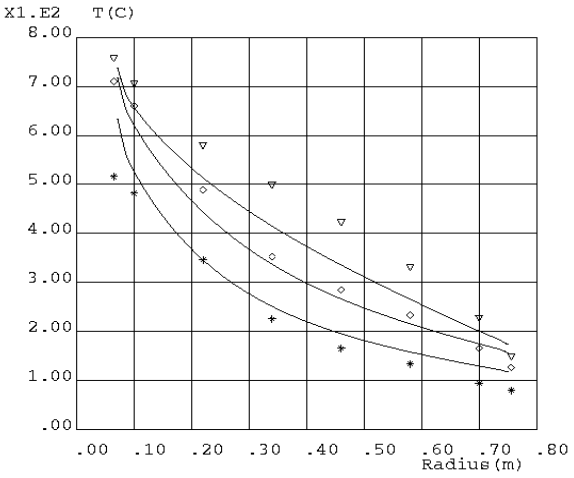

Fig. 4-89 L.H.E. / 30 mm pebbles / 10 kW / Nitrogen

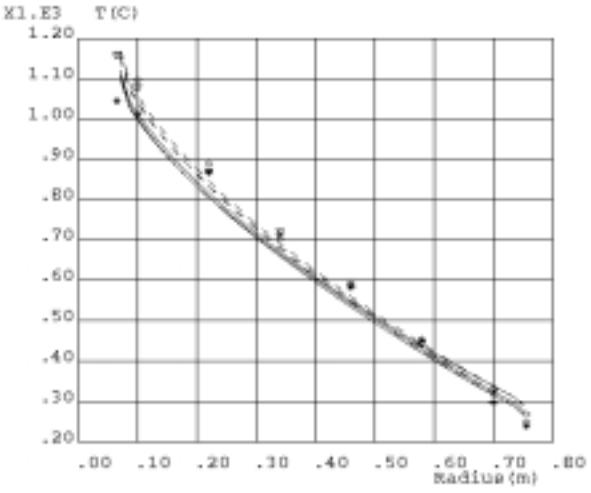

Fig. 4-90 L.H.E. / 30 mm pebbles / 30 kW / Helium Influence of pebbles emissivity on case (B) : 0,9 and 0,8 (dashed line)

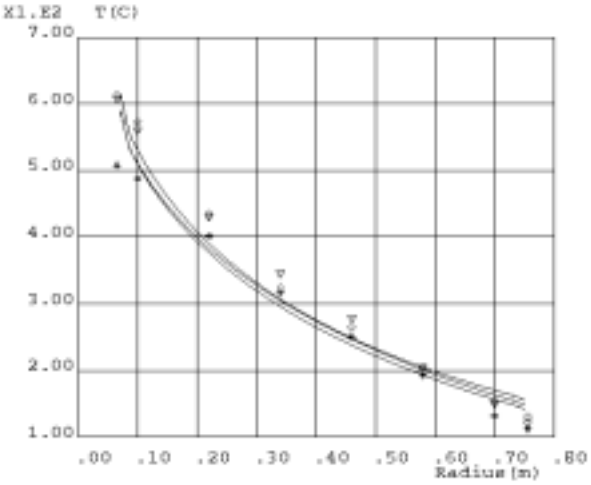

Fig. 4-91 L.H.E. / 30 mm pebbles / 10 kW / Helium

Figures 4-92 and 4-93 show the situation (3). The type of gas do not influence as much as in situations (1) and (2) the heat transfer because the stratification magnitude is nearly the same for both as well as the temperatures near the protection cylinder. This would mean that conduction related to gas conductivity is not as influent as in previous situations: convective

transport is predominant. The top position of the heat flux also explains the vertical distribution of the temperatures. All these features are accurately predicted by the model.

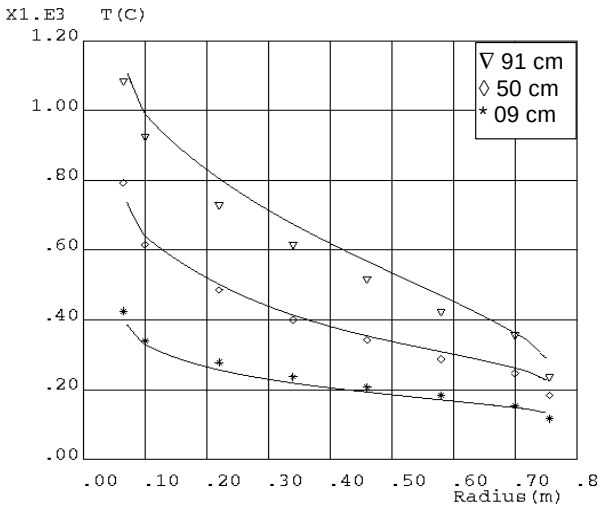

Fig. 4-92 Half top heating element / 60 mm pebbles / 20 kW / Nitrogen

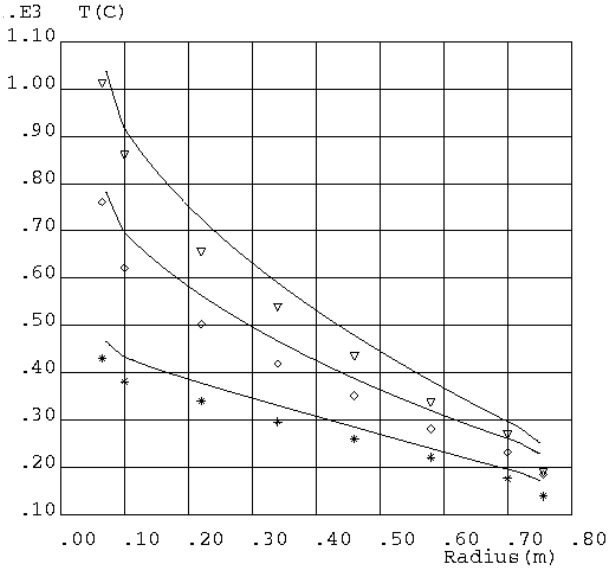

Fig. 4-93 Half top heating element / 60 mm pebbles / 20 kW / Helium

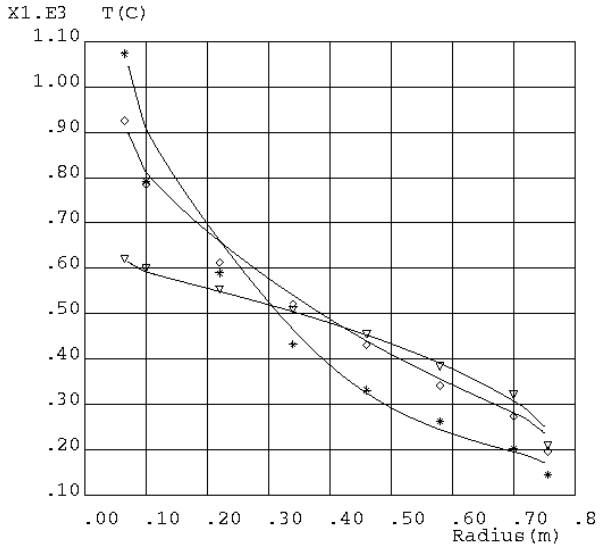

Fig. 4-94 Half bottom heating element / 60 mm pebbles / 20 kW / Nitrogen

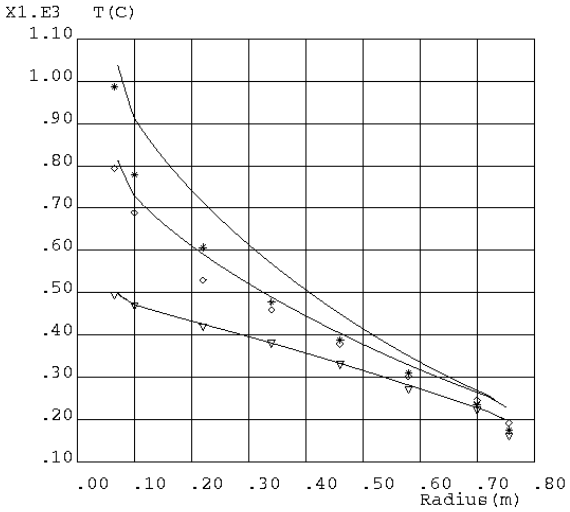

Fig. 4-95 Half bottom heating element / 60 mm pebbles / 20 kW / Helium

Figures 4-94 and 4-95 show the situation (4). In the Helium test (Fig. 4-95) the vertical distribution is changed with higher temperatures at the bottom than at the top. Along the central cylinder and the vessel wall these are reversed perfectly, in comparison to situation (3) in Helium (Fig. 4-93), between the levels 91cm and 09cm. These effects are also reproduced by the calculation. The under-estimation of the convective heat transfer could explain the discrepancy in the radial distribution at the mid-height and at the bottom (09cm) levels. The test in Nitrogen (Fig

4-94) is almost perfectly predicted: the temperatures are reversed near the central cylinder but not at the vessel wall, creating cross sections of the three radial distributions:

– levels 09cm and 50cm between radii[cm] 10 and 20,

– levels 09cm and 91cm between radii[cm] 20 and 30,

– levels 50cm and 91cm between radii[cm] 30 and 40.

Figures 4-96 and 4-97 show the situation (5). It has to be noticed that the higher level of thermocouples is at 63cm. The Nitrogen test (Fig. 4-96) reveals a similar distribution of the temperatures to the situation (4) and is accurately predicted by the calculation.

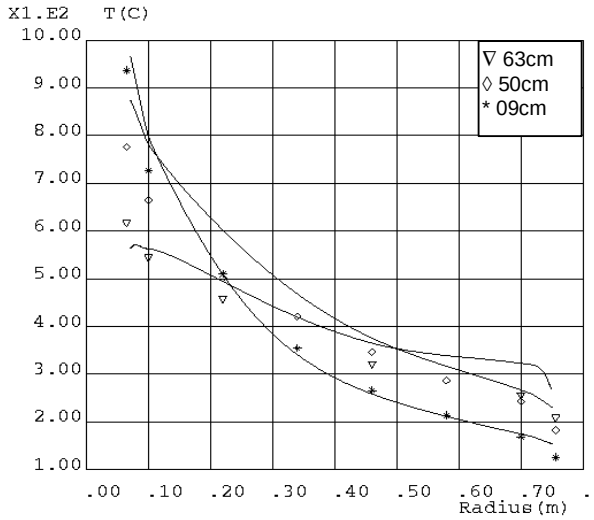

Fig. 4-96 Half bottom heating element and Plenum / 60 mm pebbles / 20 kW / Nitrogen

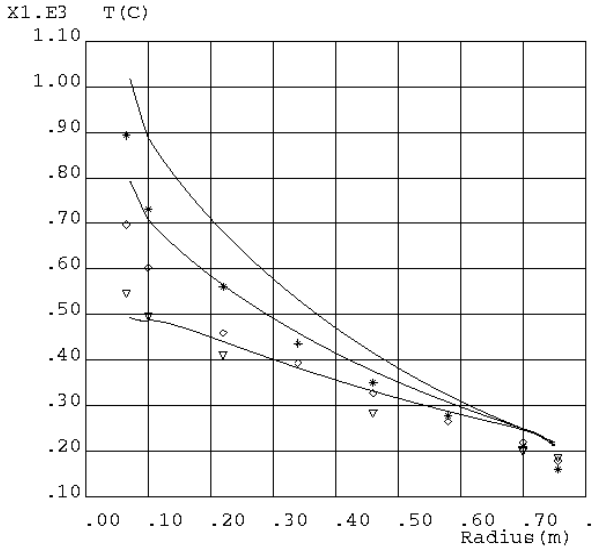

Fig. 4-97 Half bottom heating element and Plenum / 60 mm pebbles / 20 kW / Helium

More discrepancy than in situation (4) is observed between the predictions and the experimental data for the Helium test (Fig. 4-97): the temperatures near the central cylinder are over-estimated at the levels 50 cm and 09cm but not at 63cm, near the surface of the bed. The exchanges of heat in this area are dominated by radiation in the cavity which seems to be satisfactorily described by the model for both Helium and Nitrogen tests. Below this level, coupled conduction and convection are dominant. Like in situation (4) for the Helium (Fig. 4-95), the convective effects would be under-predicted by the calculation. The use of different emissivities for radiating surfaces and of a 'turbulent' viscosity did not improve the results (see 4.).

4.2.3.4. Sensitivity analysis

The sensitivity analysis is mainly based on two opposite situations for heat exchange within the bed: (A) and (B), the former shows in experiments a strong coupling of convection and conduction and the latter inhibits most of the convective participation. The plenum tests (C and D for Nitrogen and Helium) are also the opportunity to analyse the sensitivity to the surfaces emissivities in the cavity and to a pseudo-turbulent viscosity for the gas in the plenum.

– (A): 10 kW and 60mm pebbles for the Long Heating Element Nitrogen run,

– (B): 30 kW and 30mm pebbles for the Long Heating Element Helium run.

	A	B
Mass density modelling	constant or **variable**	*no influence*
Porosity variation	step or **exponential**	*no influence*
Pebbles emissivity	**0,8** or 0,9	0,8 or 0,9
Effective contact conductivity ratio	0,013 or **0,025**	*see pebbles emissivity*

	C	D
Emissivities in the cavity	*no influence*	*no influence*
Viscosity in the plenum	*no influence*	*no influence*

Table 4-25 -Sensitivity analysis (only temperature effects are notified)

1. The relative variation of the mass density can be higher than 100% according to the temperature distribution within the bed. Taking in account this phenomenon in the model creates a different spatial distribution of temperatures which is negligible on case (B) and of a low magnitude (Fig.4-85) on case (A).

2. Since the different curvature radii of the central cylinder and the vessel surfaces influence the spatial distribution of the pebbles they determine the porosity near the walls as much as the radius of the particles. A step function has been proposed for SANA-1 [6] experiment with a larger porosity (0,65) near the protection tube of the heating element than near the external boundary of the bed (0,50). This function and the exponential evolution were compared on (A) where convective effects are important. The exponential form seems to over-estimate the stratification of temperatures, thus, the convection in comparison with the step function (Fig. 4-98), but the differences are not significant.

3. Reducing the pebbles emissivity (0,9 to 0,8) decreases the solid effective conductivity due to radiant exchanges which produces a very low increase of the temperatures in (B) where only conduction occurs (Fig. 4-90) and has small effects on (A) as this enhances the convection, which explains the increased vertical gradients of the temperature (Fig. 4-99). The effect of the emissivity assumed for the surfaces in the cavity was analysed by giving the following values: 0,8 for the central cylinder - 0,6 for the vessel - 1 for the top of the bed and the insulation layer. Previously, 0,8 were assumed for all of them. Nevertheless, no difference of temperatures was noticed for C or D cases.

4. The ratio between the estimated conductivity due to contact among pebbles and the effective conductivity of the solid depends on the material properties and on structural parameters. A lower and an upper bound are obtained for the ratio $\lambda_e^c / \lambda_e^S$ by using the parameters related to a simple cubic and a body-centered cubic matrix:
   $\lambda_e^c / \lambda_e^S = 0{,}013$ for the simple cubic ($porosity = 0{,}476$)
   $\lambda_e^c / \lambda_e^S = 0{,}025$ for the body-centered cubic ($porosity = 0{,}32$)

   The effects are similar to a change of emissivity (Fig. 4-100) as it is assumed that the ratio is constant in the bed, which is not true because the constraint at the basis is higher than at the top, involving larger contact radii.

1. The convection in the plenum is more important which would enhance the turbulence, creating more dispersion of the momentum: this effect was investigated by multiplication of the gas viscosity by 100 in this area but it had no influence on the temperature distribution.

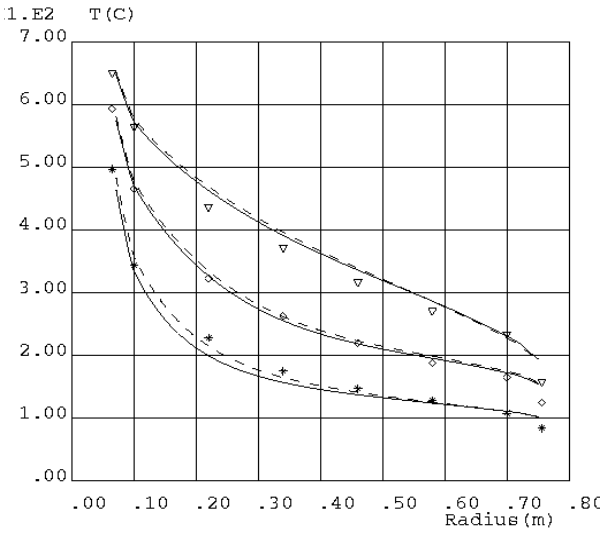

Fig. 4-98 Influence of porosity function type on case (A) : exponential and step (dashed line)

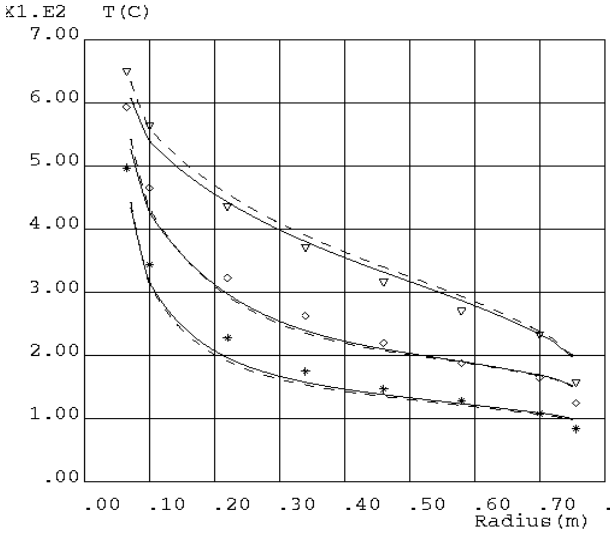

Fig. 4-99 Influence of pebbles emissivity on case (A) : 0,9 and 0,8 (dashed line)

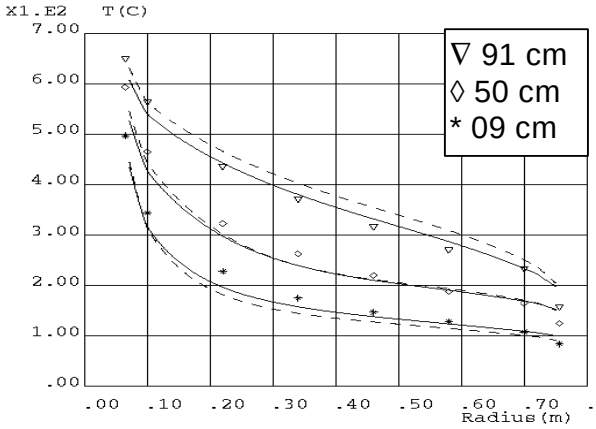

Fig. 4-100 Influence of contact effective conductivity ratio with solid effective conductivity on case (A) : 0,025 and 0,013 (dashed line)

4.2.3.5. Conclusion

This result show that the heat transfer in pebbles bed High Temperature Reactors is accurately described by means of a porous media calculation using the available correlations required for the effective properties.

The SANA-1 test parameters allowed to qualify the overall description of each heat transport phenomenon modelisation, even considering the uncertainty related to some characteristics of the bed. Therefore, this could be readily used as a prediction tool or for investigating other design options, including different bed geometries, packings or volumetric heat sources.

NOMENCLATURE

C	Forcheimer coefficient	ε	packing porosity
Cp	specific heat at constant pressure	ε_∞	statistical packing porosity
d	pebbles diameter	ε_{Vessel}	vessel total emissivity
g	gravitational acceleration	λ_e	packing effective thermal conductivity
G	impulsion density	λ_f	fluid thermal conductivity
h	heat transfer coefficient	ν	fluid viscosity
K	permeability of the packing	ρ_f , ρ_S	fluid and solid mass density
N_1 , C_1	constants in porosity wall function	σ	Stefan-Boltzman constant
V_D	Darcian velocity	ϕ_R , ϕ_C	radiant and conductive heat fluxes
Y	distance coordinate		

REFERENCES TO SECTION 4.2.3.

[1] SANA-1 code-to-experiment summary description of benchmark. H.F. Niessen, B. Stöcker. Institute for Safety Research and Reactor Technology Research Center Jülich, Gmbh (KFA), Germany.

[2] J.P. Magnaud, S. Goldstein. The finite element version of TRIO code. 7th International Conference in Fluid Mechanics, Huntsville, USA (1989).

[3] V. Prasad, G. Lauriat, N. Kladias. Non-Darcy Natural Convection in a Vertical Porous Cavity. Heat and Mass Transfer in Porous Media. Ed. M. Quintard, M. Todorovic'. Elsevier 1992, pp 293-314.

[4] G. Neale and W. Nader, 1974, Practical Significance of Brinkman's Extension of Darcy's Law. The Canadian Journal of Chemical Engineering, Vol. 52, pp 475-478.

[5] N. Wakao and S. Kaguei, 1982, Heat and Mass Transfer in Packed Beds, Gordon and Breach Science Pub.

[6] 23-08-96 Fax from Dr. Niessen. Numerical Simulation of the SANA-1 Experiments by using the TINTE-Code.

[7] 21-11-95 Fax from Dr. Niessen.

[8] E. David, G. Lauriat, P. Cheng. A Numerical Solution of Variable Porosity Effects on Natural Convection in a Packed-Sphere Cavity. Journal of Heat Transfer. Transaction of the ASME, May 1991. Vol. 113, pp 391-399.

[9] P. Cheng, C. T. Hsu, A. Chowdhury, 1988. Forced Convection in the Entrance Region of a Packed Channel with Asymmetric Heating. ASME Journal of Heat Transfer, Vol. 110, pp 946-954.

[10] G. Breitbach and H. Barthels. The Radiant Heat Transfer in the HTR Core After Failure of the Afterheat Removal Systems. Nuclear Technology, 49, pp 392-399, August 1980.

[11] G.R. Hadley, 1986, Thermal Conductivity of Packed Metal Powders, International Journal of Heat and Mass Transfer, 29, pp 909-920.

4.2.4. Numerical Simulation of the SANA-1 Experiments with the TINTE-Code

4.2.4.1. Modelling of the test facility

4.2.4.1.1. Tinte

During the last decade the program TINTE has been developed at KFA-ISR [1, 2]. It is a two-dimensional time dependent nuclear, thermal-hydraulic and graphite corrosion calculation program. It can be used for design and analysis of an HTGR under normal operation or accident conditions. It has been tested by the experiments performed on the AVR reactor, and successfully used for design and analysis of other reactors. Without being coupled to the program-module for nuclear calculations, it can be used for thermal-hydraulic calculations alone.

Due to the axis symmetry of the main part of the SANA test facility geometry (and therefore to the axis symmetric temperature field), the thermohydraulic module of TINTE can be used to simulate the experiments. Only the vessel surface cannot be modelled exactly because of its three-dimensional geometry (cooling equipment, outlet of the thermocouples). Nevertheless, this geometry has no perceptible effect on measured or calculated data, as measurements and parameter studies show.

4.2.4.1.2. Modelling of the Geometry

An r-z geometry was composed (Fig. 4-101) for the numerical calculation of the axis symmetric temperature fields. The heating element and the connection electrodes are defined as areas of heat production. The cooling of the electrodes is modelled as areas of constant temperature, which are coupled with the surrounding materials by a surface-heat-transfer coefficient. The heat exchange between heating element and protection tube results mainly from radiation. Heat conduction in the inert gas is also considered, though it could be neglected. The pebble bed, which surrounds the protection tube, is considered as a homogenous medium with an effective heat conductivity, according to the cell-model of Zehner / Bauer / Schlünder. This conductive heat transport is superposed by a convection field which simulates the gas flow in the void of the pebble bed. The heat transport between the pebbles and the inert gas is calculated by using a Nußelt law. For the main part of the pebble bed a void fraction of 41 % is used. At the boundary areas of a half pebble diameter corrected values of the void fraction are assumed (protection tube/pebble bed: 65 %, pebble bed/furnace wall: 50 %). The heat transport between furnace wall and environment is simulated by radiation and a (constant) surface-heat-transfer coefficient. The temperature dependent heat conductivity of the material data library of TINTE is used for the modelling of the axial insulation of the pebble bed. These data are based on measurements of the manufacturer and are valid for fibre materials under air atmosphere. Due to the similarity of the thermodynamic values of air and nitrogen these data are used for the experiments under nitrogen atmosphere as well. For the simulations of the tests with helium the effective conductivity of the fibre-insulation must be increased by the factor 2,5 - 3. The material data library contains also the material data of gases and solids.

4.2.4.1.3. Boundary conditions

Apart from the known material data there are further necessary data which can only be specified with some uncertainties, because no own experimental values are available. But from literature and parametric studies these values are estimated in physical suitable limits. The data could be specified by comparison of parametric studies with all experiments. Other parametric studies showed that the thermal conductivity in the boundary areas of the pebble bed is not

simulated correctly by the cell-model of Zehner Bauer / Schlünder, which is only valuable for the statistic pebble bed, but not for the boundaries. Therefor at these boundary areas with a thickness of a half pebble diameter a correction coefficient is introduced to compensate this effect.

In addition to this, it is necessary to estimate for every test the amount of heat which is produced in the heating rod and the connection electrodes. These values are calculated by an estimation of the electrical resistance of heating rod, connection electrodes, transformer and conductors. Due to the different temperatures in the heating rods and connection electrodes when using different gases and / or pebble diameters there is a possibility to get different heating power in these components at the same nominal electric power because of the temperature dependent electrical resistance of graphite. In reality this effect can be neglected as simulations have shown.

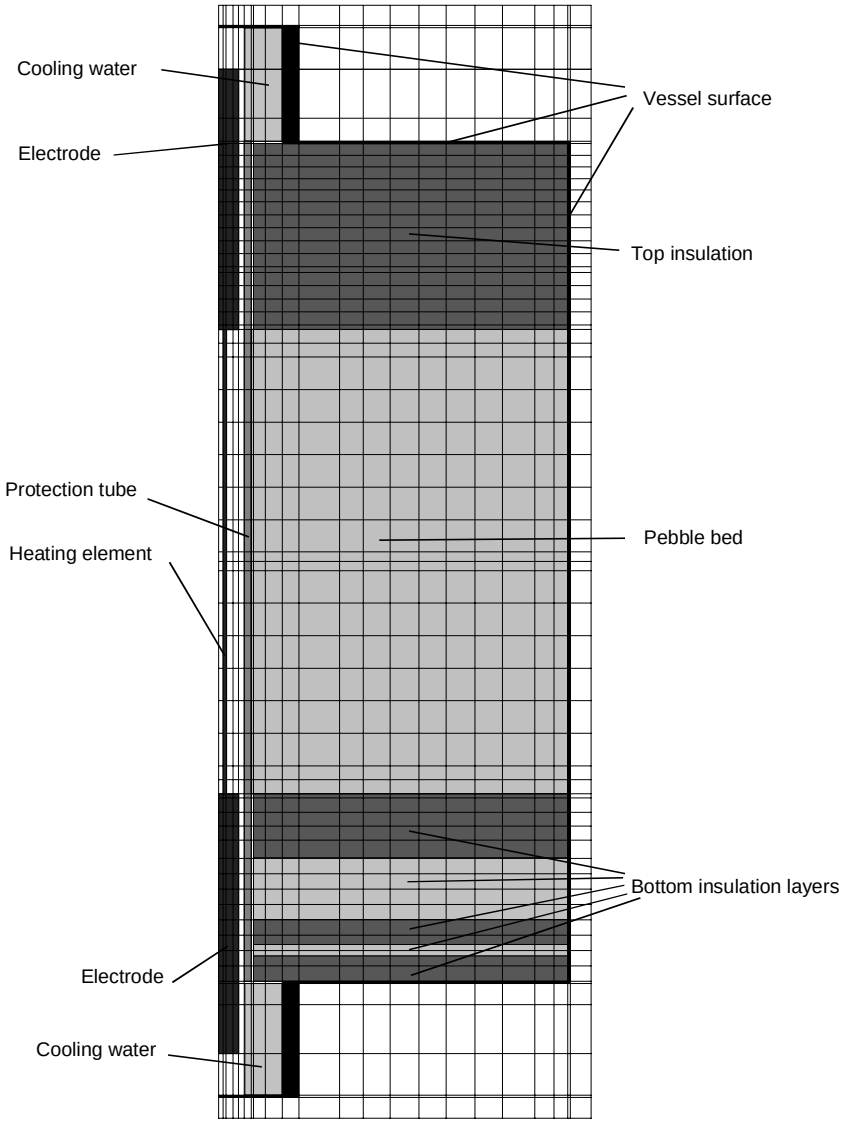

Fig. 4-101 Geometry of the TINTE-simulations of the SANA experiment

Table 4-26 Material data

total emissivity coefficient of graphite	e	0,9
relative area of contact	s	0,08
surface-heat-transfer coefficient of the vessel	a	8 W/(m^2K)
coefficient protection tube/pebble bed	-	0,6
coefficient protection tube/pebble bed	-	0,5

Table 4-27 Heat production in heating element and electrodes, heat loss (amount and fraction) in transformer and conductors

geometry of the heating rod	$P_{nominal}$ [kW]	$P_{heating\ rod}$ [kW]	$P_{elektrodes}$ [kW]	P_{loss} [kW]	P_{loss} [%]
long	10	8,91	0,62	0,47	4,66
	30	27,36	1,70	0,94	3,13
short (half)	20	16,17	2,78	1,05	5,24

4.2.4.2. Comparison of the simulations with the experiments

All steady state experiments of the five series considered have been simulated:

Table 4-28 Simulated experiments

No.	pebble diameter [mm]	heating rod/pebble bed geometry	gas	heating power [kW]
(1)	60	long heating element	N_2, He	10 , 30
(2)	60	half heating element at the top	N_2, He	20
(3)	60	half heating element at the bottom	N_2, He	20
(4)	60	half heating element at the bottom with gas plenum above the pebble bed	N_2, He	20
(5)	30	long heating element	N_2, He	10 , 30

The simulation of the 4th series did not give a satisfying agreement to the experimental data. This may be probably explained with an inaccurate simulation of the high turbulent free convection in the void by the TINTE code. The other four series are presented in the following sections.

The diagrams of the comparison of the measurements and the calculated data are divided in two parts. The left diagram shows the radial temperature distribution in the three completely with thermocouples equipped pebble layers (at the height of 9 cm, 50 cm and 91 cm). The diagram on the right side shows the axial temperature distribution at constant radius. In both types of diagrams the symbols represent the measured data, while the curves show the calculated values.

4.2.4.2.1. Long heating element, 60 mm pebbles

In Figs 4-102 and 4-103 the comparison of measurement and calculated data of the tests with 10 kW and 30 kW heating power under helium and nitrogen atmosphere are displayed. The radial temperature distributions show in all experiments a dependency from the height in such a way, that the highest temperatures are in upper layer and the smallest in the lower layer, due to the free convection in the pebble bed. The relative temperature difference between these layers is larger with nitrogen as inert gas than with helium, and for lower heating power it is larger than for higher heating power. Altogether the simulations show a very satisfying consistency with the measured values. The largest difference can be observed in the protection tube and the first pebble layer. This can be explained by the insufficient modelling of this strongly diluted area by the cell-model of Zehner/Schlünder, which is, as already mentioned, only valuable for the statistic pebble bed, not for the boundaries.

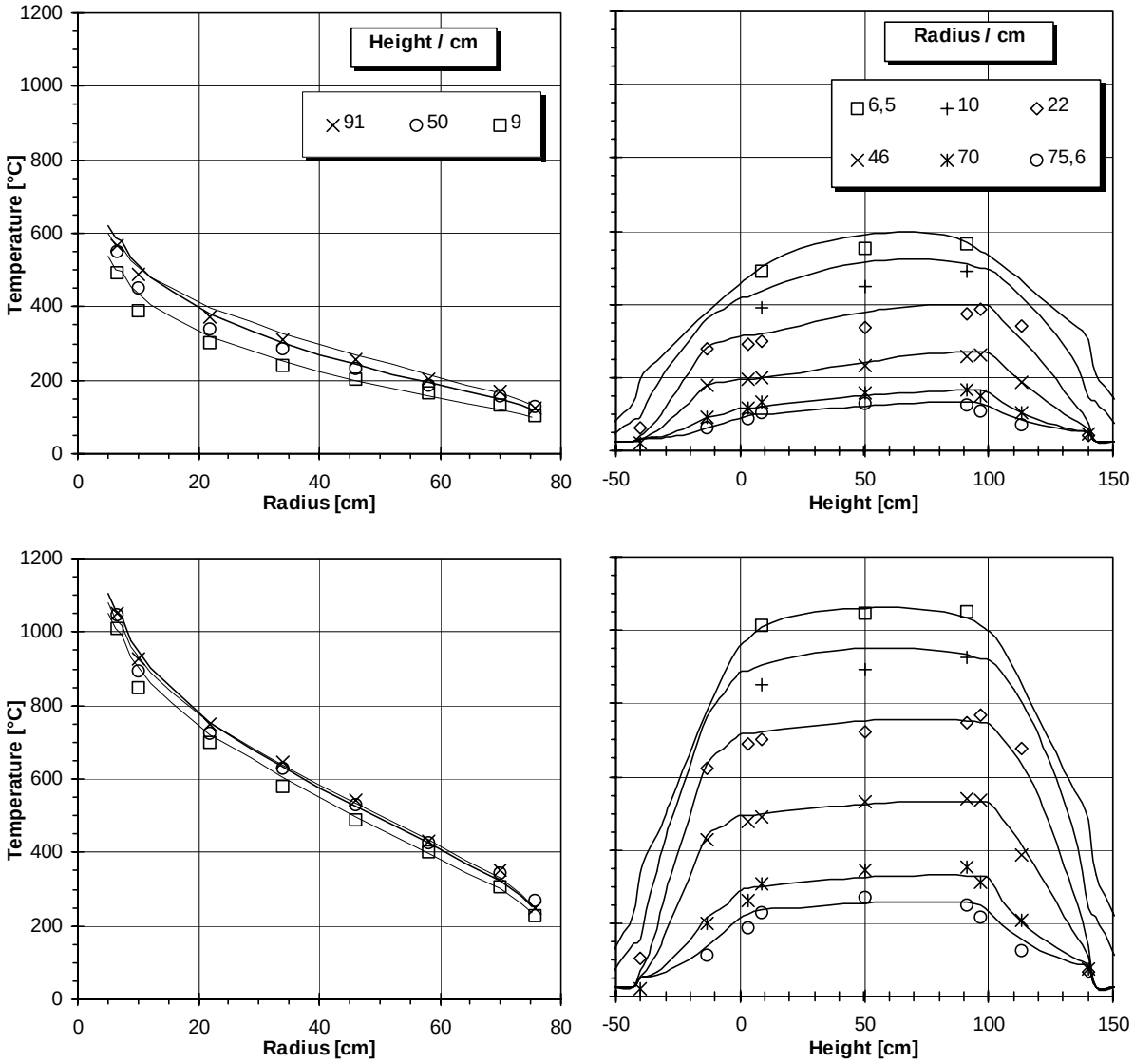

Fig. 4-102 Measured and calculated temperature distribution (TINTE), helium, long heating element
top : 10 kW nominal heating power,
bottom : 30 kW nominal heating power

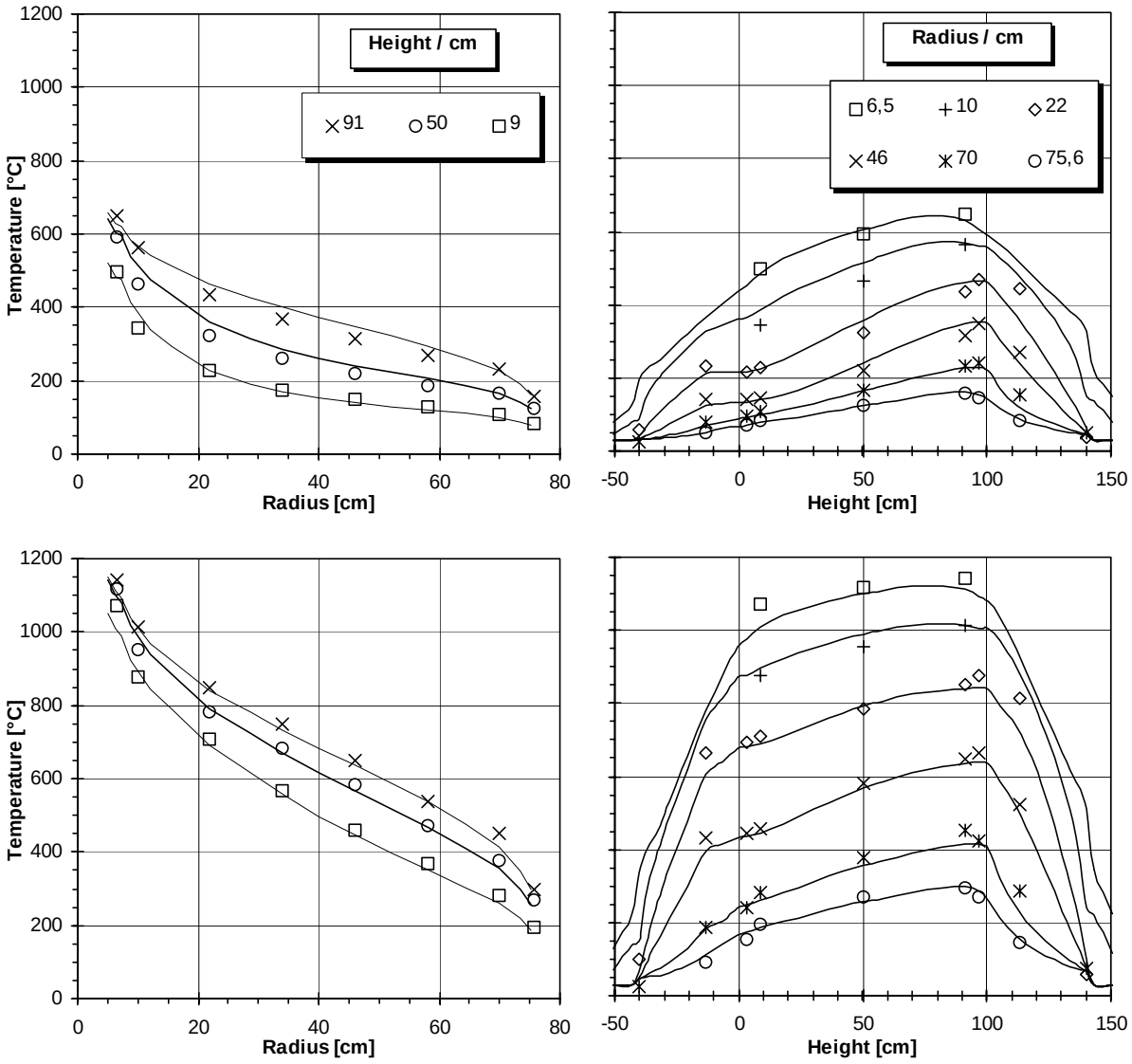

Fig. 4-103 Measured and calculated temperature distribution (TINTE), nitrogen, long heating element
top : 10 kW nominal heating power,
bottom : 30 kW nominal heating power

4.2.4.2.2. Short heating element

In this section the comparison of measurement and calculated data of the tests with 20 kW heating power under helium and nitrogen atmosphere with short heating element are displayed. In these experiments either the top or the bottom of the pebble bed was heated.

The radial temperature distributions of the experiments with the heating element at the top (Fig. 4-104) show a similar arrangement of temperature layers in that way that the highest temperatures are in upper layer and the smallest in the lower layer due to the local heating of the pebble bed's upper part. The diagrams are quite similar for both gases, although the temperature

differences for nitrogen are a little higher, as a consequence of the lower thermal conductivity of nitrogen and its higher tendency towards natural convection.

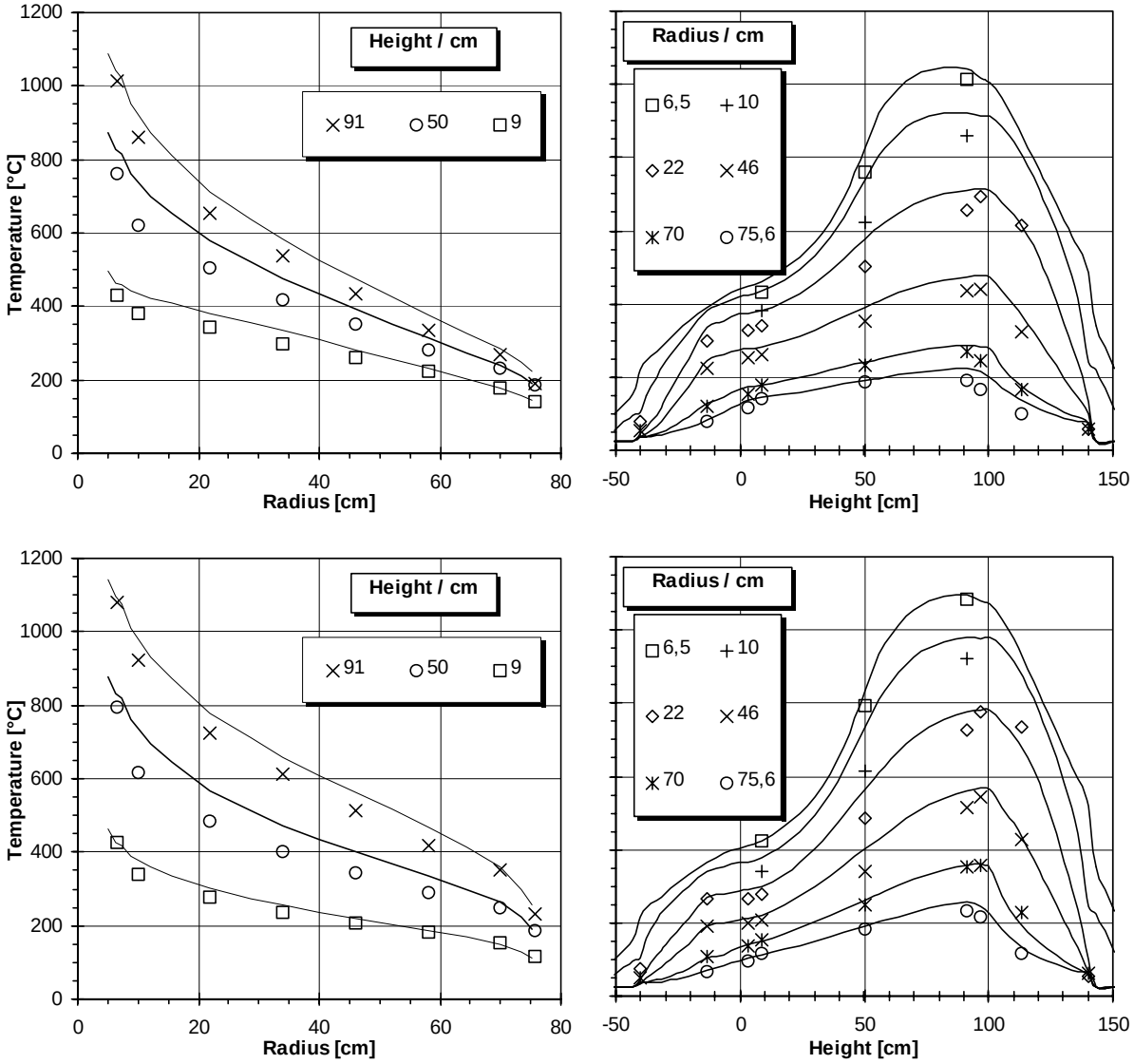

Fig. 4-104 Measured and calculated temperature distribution (TINTE), 20 kW heating power, short heating element at the top
top : Helium
bottom : Nitrogen

In contrast to this the results of the test with the heating element at the bottom show a considerable difference between the two gases. With helium as inert gas a temperature difference between the layers is built up in the inner part of the pebble bed, so the highest temperatures are in the lower layer. This effect decreases continuously with increasing radius. In the outer part the temperatures are almost homogeneous at a constant radius. Under nitrogen atmosphere the inner temperature difference with the highest temperature in the lower area is similar to helium, while this is reversed completely in the outer part of the pebble bed, i.e. the higher temperatures are now found in the upper layer. The simulation yields a "turning point" at about 25cm radius, which is in accordance to the measurement.

These simulations show altogether a good conformity with the measurement data, although all simulations tend towards too high temperatures. The highest differences (max. 100K) can be observed in the central layer at a height of 50cm.

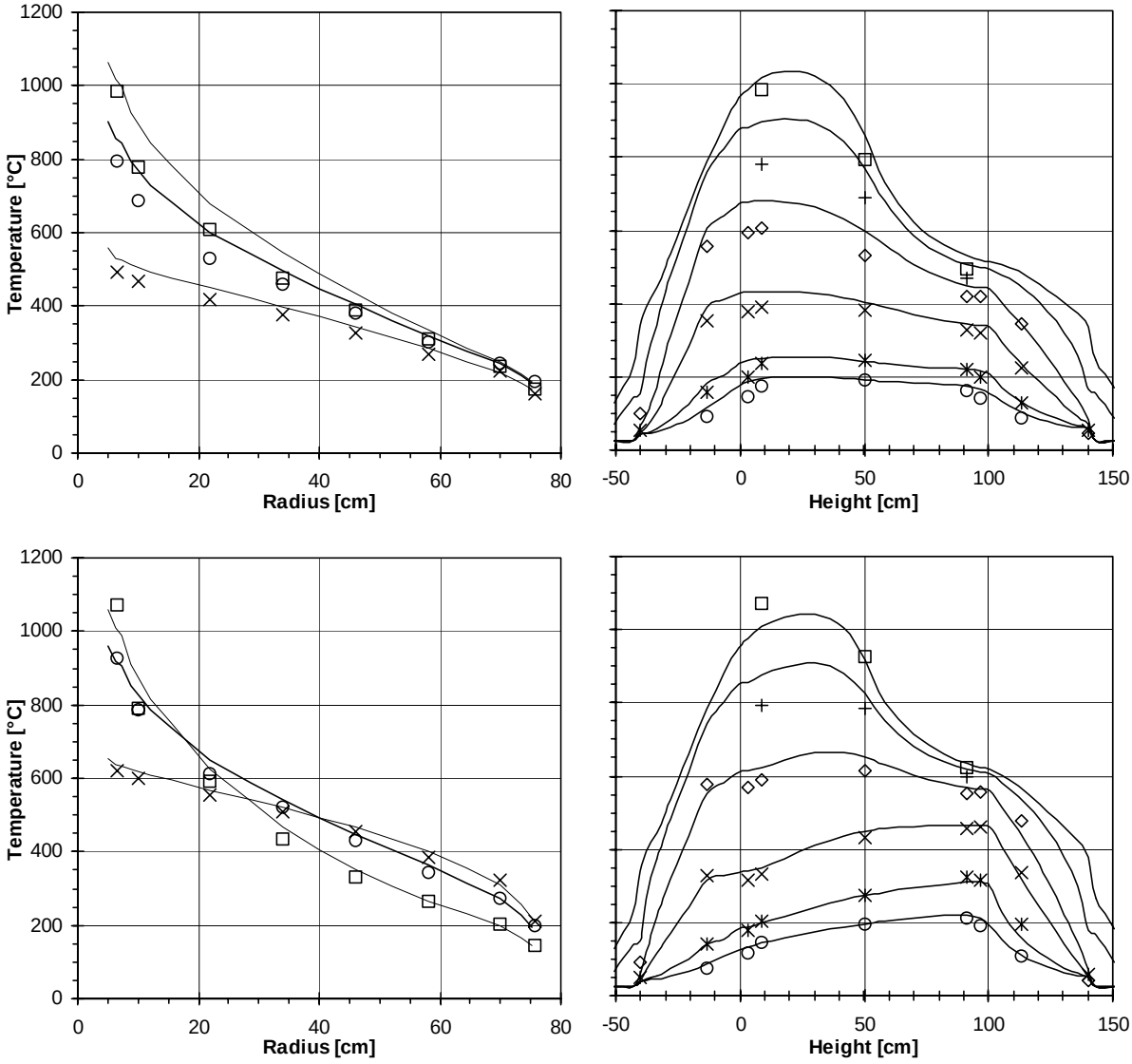

Fig. 4-105 Measured and calculated temperature distribution (TINTE), 20 kW heating power, short heating element at the bottom
top : Helium
bottom : Nitrogen

4.2.4.2.3. Long heating element, 30 mm pebbles

In Figures 4-106 and 4-107 the comparison of measurement and calculated data of the tests with 10 kW and 30 kW heating power under helium and nitrogen atmosphere are shown. The conformity of measurement and simulation data is similar to section 1.2.1. Only for 30 kW nominal heating power and nitrogen as inert gas some of the calculated temperatures are

significantly lower in comparison to the experiments (Fig. 4-107). At the same heating power under helium atmosphere a significant temperature difference between the layers cannot be located anymore, what is in accordance to the experiments: In this case the natural convection has no effect any more in contrast to the experiments with bigger pebbles (Fig 4-103).

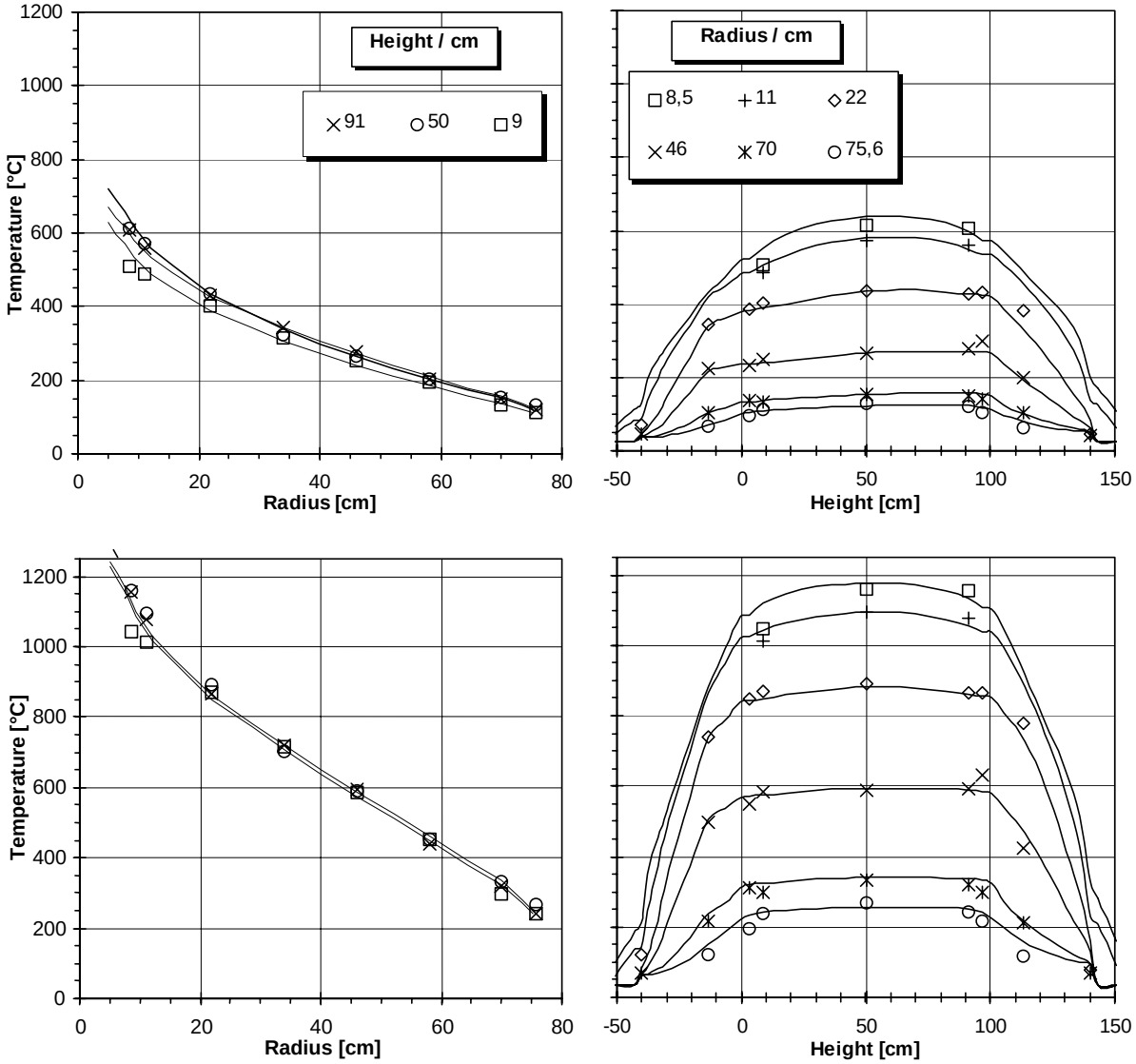

Fig. 4-106 Measured and calculated temperature distribution (TINTE), helium, long heating element, 30 mm pebble diameter
top : 10 kW nominal heating power,
bottom : 30 kW nominal heating power

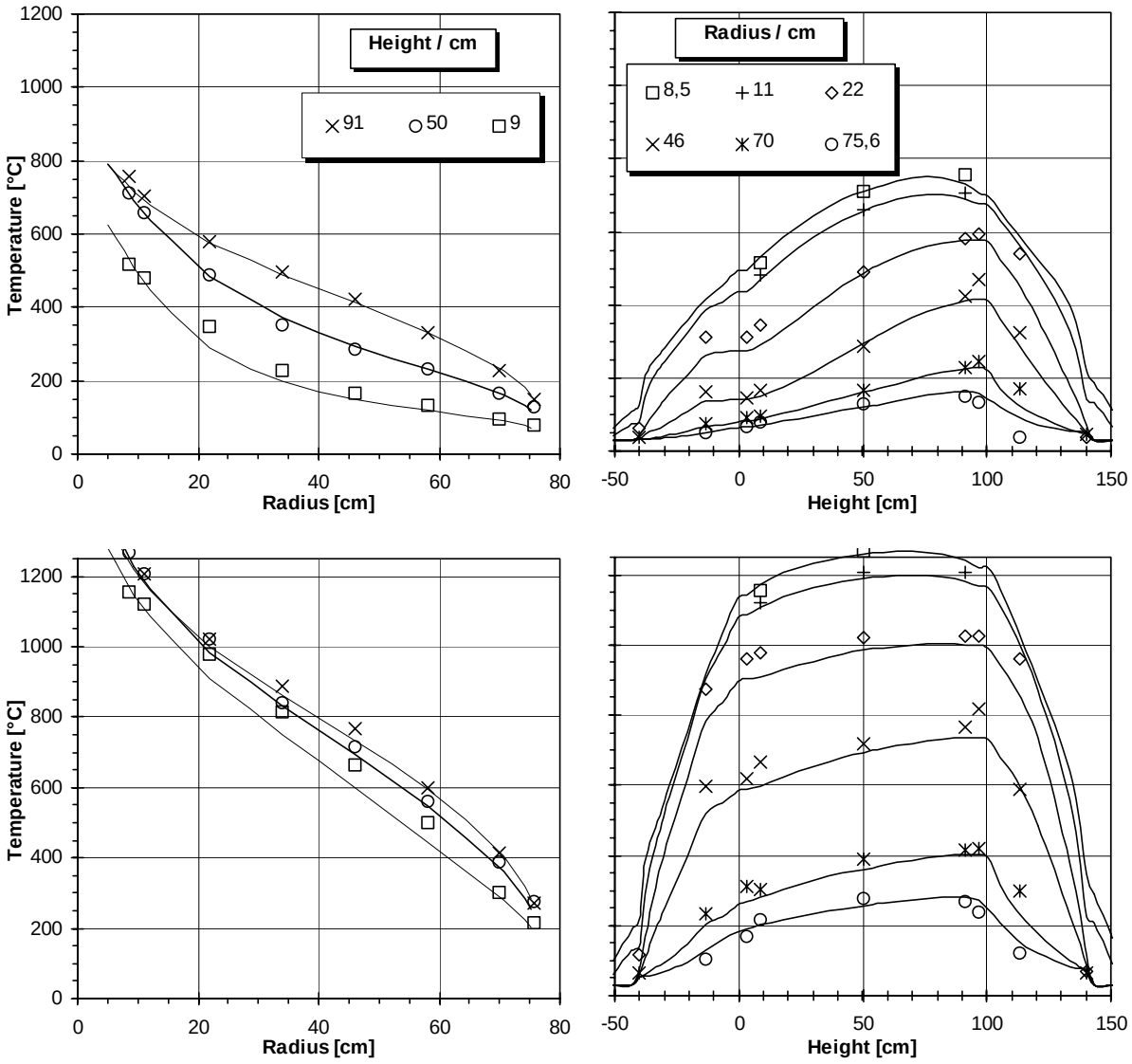

Fig. 4-107 Measured and calculated temperature distribution (TINTE), nitrogen, long heating element, 30 mm pebble diameter
top : 10 kW nominal heating power,
bottom : 30 kW nominal heating power

4.2.4.2.4. Numerical behaviour

The simulations did not lead to any numerical divergence. Nevertheless it must be mentioned that the simulation of all the experiments under nitrogen atmosphere did not converge to the end. The maximum gas temperature differences between two iterations oscillated within 3K. This phenomenon could have an influence on the local convection currents, but not on the temperatures of the solid. This effect could be observed especially at low nominal heating power. The problem never occurred at simulations of the helium experiments. It seems that the numerical stability decreases by an increasing amount of natural convection on the total heat transport.

4.2.4.3. Summary

The simulations of the SANA-1 experiments with central long heating geometry and different pebble diameter made with the computer code TINTE show a good accordance to the measured temperature fields in a wide temperature range (100 - 1200 °C). The heat transport by conduction and radiation (represented by the temperatures in the central radial layer) and the natural convection phenomena (represented by the temperature differences between the different radial layers) both are simulated correctly in quality and quantity. The experiments with short heating element are simulated well with some reservations. These tests set strong requirements on the computer code due to the fact of varying heat-flux densities in the central layers as a consequence of the non-symmetrical heating either in the upper or the lower part of the pebble bed.

In total the simulations prove a successful, integral validation of the thermohydraulic module of TINTE in a large part of the representative temperature spectrum of a pebble bed HTGR.

REFERENCES TO SECTION 4.2.4.

[1] H. F. Nießen, B. Stöcker “SANA-1 code-to-experiment summary description of the benchmark” 3rd IAEA Research Co-ordination Meeting on "Heat Transport and Afterheat Removal for Gas-cooled Reactors under Accident Conditions", 14-17 November 1995, Vienna.

[2] H.Gerwin, W. Scherer, E. Teuchert, “The TINTE Modular Code Sytem for Computational Simulation of Transient Processes in the Primary Circuit of a Pebble-Bed High-Temperature Gas-Cooled Reactor”Nuclear Science and Engineering, Vol. 103, pp. 302 - 312, 1989.

[3] H. Gerwin, “Das zweidimensionale Reaktordynamikprogramm TINTE, Teil 1: Grundlagen und Lösungsverfahren”.

[4] R. Bauer, E. U. Schlünder, “Effective radial thermal conductivity of packings in gas flow. Part I. Convective transport coefficient, Part II. Thermal conductivity of the packing fraction gas flow “ International Chemical Engineering Vol. 18, No. 2 pp. 189 - 204, 1978.

4.2.5. Comparison and Conclusions of the SANA Benchmark

For the confirmation of self-acting afterheat removal under hypothetical accident conditions from pebble bed reactors at the Research Centre Jülich a test facility with in electrical heating input up to 30kW was erected and operated. A description of the test facility is given. Within the different tests the pebble diameter, the pebble material, the gas in the pebble bed, the heating-power and the arrangement of the heating were changed. Parts of the data were used within an IAEA Co-ordinated Research Program as benchmark problems for the code validation.

In the benchmark participated China [1], France [2] and Germany [3]. Three different computer codes were used:

– THERMIX (China),

– TRIO-EF (France),

– TINTE (Germany).

All computer codes could simulate the test results with a sufficient good agreement, when the tests were executed with helium. For the tests with nitrogen the natural convection has to be taken into account.

This results show that the heat transfer in pebbles bed High Temperature Reactors is accurately described by mean of a porous media calculation using the available correlation required for the effective heat conductivity.

The SANA-1 test parameters allowed to qualify the overall description of each heat transport phenomenon modelisation, even considering the uncertainty related to some characteristics of the bed. Therefore, this could be readily used as a prediction tool or for investigating other design options, including different bed geometry, packing or volumetric heat sources.

The simulations of the SANA experiments with central long heating geometry and different pebble diameter made with different computer codes show a good accordance to the measured temperature fields in a wide temperature range (100 - 1200 °C). It can be supposed, that both the heat transport by conduction and radiation (represented by the temperatures in the central radial layer) and the natural convection phenomena (represented by the temperature differences between the different radial layers) in quality and quantity are simulated correctly. The experiments with short heating element are simulated well with reservations. These tests set exacting requirements on the computer code due to the strong different heat-flux densities in the central layers as a consequence of the unsymmetrical heating either in the upper or the lower part of the pebble bed.

A summarize not only of the bench mark tests but of all SANA tests made with graphite pebbles at KFA is shown in the Figs. 4-108 and 4-109.

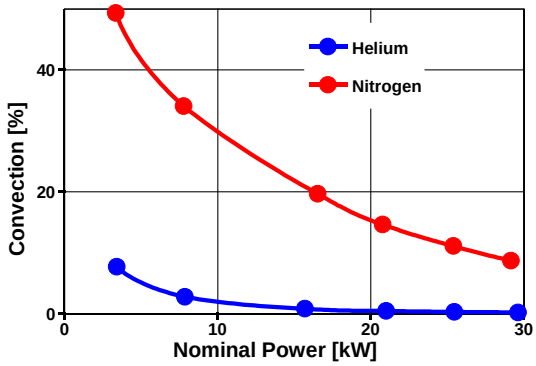

Fig. 4-108 Heat transported by natural convection

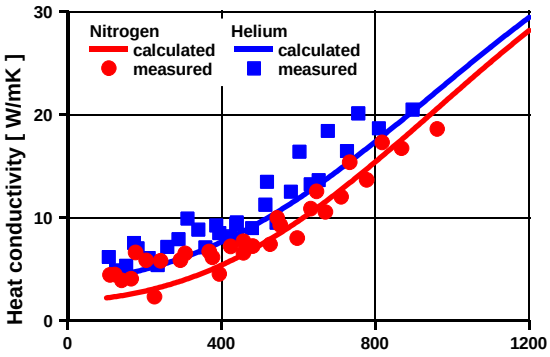

Fig. 4-109 Comparison of heat transfer calculated with Zehner Bauer Schlünder and measured heat transfer

REFERENCES TO SECTION 4.2.5.

[1] Zuying Gao, Jie Liu “INET Analysis of SANA-1 Experiment Benchmark Problems”; Institute of Nuclear Energy Technology Tsinghua University, Beijing 100084, China.

[2] Olivier Amoignon “TRIO-EF Model of SANA-1 Eperimental Set-up” COMMISSARIAT A L’ENERGIE ATOMIQUE Direction of Nuclear Reactors, Department of Mechanics and Technology, Thermal and Mechanical Engineering Service, Systems Studies Laboratory Saclay, France.

[3] B. Stöcker, H. Gerwin, H. F. Nießen, W. Scherer “ Numerical Simulation of the SANA-1 Experiments with the TINTE-Code” Institute for Safety Research and Reactor Technology Research Centre Jülich GmbH (KFA), Jülich Germany.

APPENDIX A1

DETAILED EXPERIMENTAL DATA SETS FOR THE BENCHMARKS

A.1.1. SANA–1

A.1.1.1. Material Data

The pebbles within the test facility are made of non–irradiated graphite Type: Sigri/AL 2–500, with a heat conductivity of:

ϑ in [°C];

λ in $\left[\frac{W}{m \cdot K}\right]$;

$$\lambda_{AL\,2-500} = 186{,}021 - 39{,}5408 \cdot 10^{-2} \cdot \vartheta + 4{,}8852 \cdot 10^{-4} \cdot \vartheta^2 - 2{,}91 \cdot 10^{-7} \cdot \vartheta^3 + 6{,}6 \cdot 10^{-11} \cdot \vartheta^4$$

The heat conductivity data of the fibre insulation modules at the top are represented in air by the formula:

CERACHEM - Blanket; Fa. Gossler:

$$\lambda_{IOB} = 0{,}0984 - 2{,}02 \cdot 10^{-4} \cdot \vartheta + 4{,}1 \cdot 10^{-7} \cdot \vartheta^2 + 10^{-10} \cdot \vartheta^3;$$

For the bottom insulation the thermal conductivity in air is represented by the following formulas:

Light fire brick RI 30 B; Savoie Feuerfest:

$$\lambda_{IU1} = 0{,}396 + 2{,}46 \cdot 10^{-4} \cdot \vartheta + 2{,}5 \cdot 10^{-7} + 10^{-10} \cdot \vartheta^3;$$

CERAFORM 1000 and CERABORD 100; Gossler:

$$\lambda_{IU2,3} = 0{,}0437 + 7{,}1 \cdot 10^{-5} \cdot \vartheta + 5 \cdot 10^{-8} \cdot \vartheta^2 + 7 \cdot 10^{-11} \cdot \vartheta^3;$$

THERMOSIL 1100; Gossler:

$$\lambda_{IU4} = 0{,}0803 + 4 \cdot 10^{-5} \cdot \vartheta + 7 \cdot 10^{-8} \cdot \vartheta^2;$$

THERMOSIL 1000; Gossler:

$$\lambda_{IU5} = 0{,}041 + 4{,}5 \cdot 10^{-5} \cdot \vartheta + 1{,}1 \cdot 10^{-7} \cdot \vartheta^2 + 5{,}5 \cdot 10^{-11} \cdot \vartheta^3;$$

GOSSLEROC GMP 100; Gossler:

$$\lambda_{IU6} = 0{,}058 + 10^{-6} \cdot \vartheta + 4 \cdot 10^{-7} \cdot \vartheta^2;$$

NOTE: Following KFA–experiments the values for the fibre insulation (layer (6) at the bottom and at the top-insulation) are in helium–atmosphere three times higher than those in air!!!

A.1.1.2. Data for The Stationary Tests with Long Heating Element 60mm Pebble Diameter

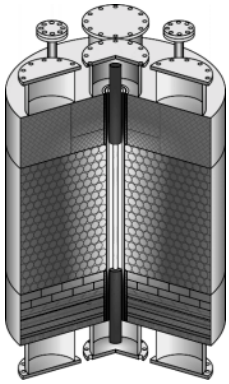

1. Nitrogen 30kW nominal heating power 60mm pebble diameter
2. Nitrogen 10kW nominal heating power 60mm pebble diameter
3. Helium 30kW nominal heating power 60mm pebble diameter
4. Helium 10kW nominal heating power 60mm pebble diameter

Fig. 1: Arrangement of the heating element 〈

1. Nitrogen 30kW nominal heating power with long heating element

P heating element/kW	27,189
P electrodes/kW	1,817

Date	20.10.95
Zeile	92
P / kW	30,0
CO / Vol.%	0,58
OXOR 6N / Vol.%	-0,08
TU / °c	26,2
Dewpoint	-43,5

Cooling Water Instrumentation

Thermocouple-	Top		Bottom	
Position	Inlet	Outlet	Inlet	Outlet
Temperature / °C	16,5	25,4	16,2	25,0
Throughput / l/h	220	240	210	210

Arrangement of the Thermocouples

Height / Radius [cm]	6,5	10	22	34	46	58	70	75,6
167	99							
140			60				76	
113			815		523		288	145
97			877		663		424	272
91	1141	1014	850	750	649	539	452	297
50	1118	953	784	682	582	470	377	269
9	1071	877	709	566	458	366	282	194
3			692		446		240	152
-13			665		433		189	93
-40			101				24	
-67	49							
Protection Tube		Pebble Bed		Insulation		Vessel Surface		

2. Nitrogen 10kW nominal heating power with long heating element

P heating element /kW	8,855
P electrodes /kW	0,662

Date	13.10.95
Zeile	120
P / kW	10,0
CO / Vol.%	0,04
OXOR 6N / Vol.%	-0,04
TU / °c	26,3
Dewpoint	-31,5

Cooling Water Instrumentation

Thermocouple-	Top		Bottom	
Position	Inlet	Outlet	Inlet	Outlet
Temperature / °C	17,1	22,0	16,9	21,0
Throughput / l/h	200	210	200	220

Arrangement of the Thermocouples

Height / Radius [cm]	6,5	10	22	34	46	58	70	75,6
167	67							
140			39				49	
113			443		268		153	85
97			470		347		243	144
91	648	563	435	370	315	269	232	156
50	593	465	323	263	220	188	165	125
9	497	344	228	175	147	128	108	84
3			214		141		97	70
-13			232		139		78	51
-40			59				24	
-67	31							
Protection Tube		Pebble Bed		Insulation		Vessel Surface		

3. Helium 30kW nominal heating power with long heating element

P heating element /kW	27,189
P electrodes /kW	1,817

Date	08.11.95
Zeile	90
P / kW	30,1
CO / Vol.%	0,70
OXOR 6N / Vol.%	0,26
TU / °c	26,0
Dewpoint	-48,4

Cooling Water Instrumentation

Thermocouple-	Top		Bottom	
Position	Inlet	Outlet	Inlet	Outlet
Temperature / °C	14,7	26,8	15,3	25,5
Throughput / l/h	215	170	235	190

Arrangement of the Thermocouples

Height / Radius [cm]	6,5	10	22	34	46	58	70	75,6
167	104							
140			67				74	
113			678		388		206	126
97			768		538		310	216
91	1052	926	749	644	540	432	352	247
50	1047	894	724	629	531	427	345	268
9	1012	850	700	579	489	401	308	229
3			688		479		262	188
-13			624		426		199	113
-40			105				21	
-67	45							
Protection Tube		Pebble Bed		Insulation		Vessel Surface		

4. Helium 10kW nominal heating power with long heating element

P heating element /kW	8,855
P electrodes /kW	0,662

Date	27.10.95
Zeile	97
P / kW	10,0
CO / Vol.%	0,02
OXOR 6N / Vol.%	0,25
TU / °c	23,0
Dewpoint	-44

Cooling Water Instrumentation

Thermocouple-	Top		Bottom	
Position	Inlet	Outlet	Inlet	Outlet
Temperature / °C	16,3	21,3	16,2	20,9
Throughput / l/h				

Arrangement of the Thermocouples

Height / Radius [cm]	6,5	10	22	34	46	58	70	75,6
167	66							
140			40				45	
113			341		188		104	69
97			387		262		151	110
91	565	488	372	311	256	203	168	124
50	552	450	337	284	233	187	157	130
9	491	389	301	240	201	166	132	105
3			290		194		116	89
-13			276		180		92	62
-40			62				22	
-67	29							
Protection Tube		Pebble Bed		Insulation		Vessel Surface		

A.1.1.3. Data for The Stationary Tests with Short (Half) Heating Element on The Bottom Side

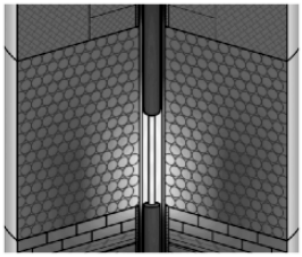

1. Nitrogen 20kW nominal heating power
2. Helium 20kW nominal heating power

Fig. 2: Arrangement of the heating element 〈

1. Nitrogen 20kW nominal heating power with short (half) heating element on the bottom side

P heating element /kW	16,17
P electrodes /kW	2,783

Date	27.02.96
Zeile	39
P / kW	20,1
CO / Vol.%	0,33
OXOR 6N / Vol.%	-999,99
TU / °c	27,5
Dewpoint	-48,1

Cooling Water Instrumentation

Thermocouple-	Top		Bottom	
Position	Inlet	Outlet	Inlet	Outlet
Temperature / °C	10,5	17,7	11,2	22,0
Throughput / l/h				

Arrangement of the Thermocouples

Height / Radius [cm]	6,5	10	22	34	46	58	70	75,6
167	40							
140			43				59	
113			479		336		195	107
97			555		459		315	192
91	621	600	554	509	455	384	322	210
50	925	785	613	522	432	342	274	197
9	1073	792	590	433	332	263	203	146
3			567		316		177	117
-13			575		328		141	75
-40			93				50	
-67	46							
Protection Tube		Pebble Bed		Insulation		Vessel Surface		

2. Helium 20kW nominal heating power with short (half) heating element on the bottom side

P heating element /kW	16,17
P electrodes /kW	2,783

Date	10.02.96
Zeile	87
P / kW	20,0
CO / Vol.%	-0,02
OXOR 6N / Vol.%	999,99
TU / °c	24,3
Dewpoint	-21

Cooling Water Instrumentation

Thermocouple-	Top		Bottom	
Position	Inlet	Outlet	Inlet	Outlet
Temperature / °C	11,4	18,4	12,0	23,0
Throughput / l/h				

Arrangement of the Thermocouples

Height / Radius [cm]	6,5	10	22	34	46	58	70	75,6
167	35							
140			44				53	
113			344		222		129	86
97			418		320		200	140
91	493	468	419	379	329	270	222	160
50	794	689	530	460	380	303	246	193
9	986	779	607	478	389	310	235	175
3			595		380		201	146
-13			555		352		158	92
-40			98				55	
-67	40							
Protection Tube		Pebble Bed		Insulation		Vessel Surface		

A.1.1.4. Data for The Stationary Tests with Short (Half) Heating Element on The Top Side

1. Nitrogen 20kW nominal heating power
2. Helium 20kW nominal heating power

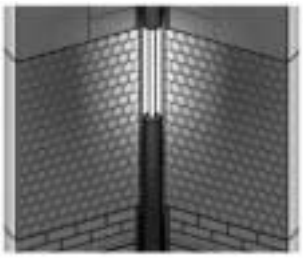

Fig. 3: Arrangement of the heating element 〈

1. Nitrogen 20kW nominal heating power with short (half) heating element on the top side

P heating element /kW	16,17
P electrodes /kW	2,783

Date	18.12.95
Zeile	7
P / kW	20,0
CO / Vol.%	0,36
OXOR 6N / Vol.%	0,04
TU / °c	28,0
Dewpoint	-49

Cooling Water Instrumentation

Thermocouple-	Top		Bottom	
Position	Inlet	Outlet	Inlet	Outlet
Temperature / °C	13,5	22,7	13,6	19,2
Throughput / l/h				

Arrangement of the Thermocouples

Height / Radius [cm]	6,5	10	22	34	46	58	70	75,6
167	92							
140			53				63	
113			734		428		229	118
97			775		546		356	217
91	1082	923	726	613	514	420	353	233
50	793	616	486	400	343	288	247	184
9	425	341	278	237	207	183	154	117
3			265		199		137	95
-13			264		189		106	66
-40			73				48	
-67	32							
Protection Tube		Pebble Bed		Insulation		Vessel Surface		

2. Helium 20kW nominal heating power with short (half) heating element on the top side

P heating element /kW	16,17
P electrodes /kW	2,783

Date	19.01.96
Zeile	77
P / kW	20,0
CO / Vol.%	0,55
OXOR 6N / Vol.%	-999,99
TU / °c	24,2
Dewpoint	-47,6

Cooling Water Instrumentation

Thermocouple-	Top		Bottom	
Position	Inlet	Outlet	Inlet	Outlet
Temperature / °C	11,7	21,8	12,4	19,3
Throughput / l/h				

Arrangement of the Thermocouples

Height / Radius [cm]	6,5	10	22	34	46	58	70	75,6
167	96							
140			56				58	
113			613		323		164	99
97			695		441		247	168
91	1012	860	655	539	435	337	269	190
50	761	622	503	420	352	282	233	186
9	431	382	341	297	261	222	177	140
3			330		252		154	117
-13			298		223		119	78
-40			78				52	
-67	31							
Protection Tube		Pebble Bed		Insulation		Vessel Surface		

A.1.1.5. Data for The Stationary Tests with Short (Half) Heating Element on The Bottom Side and a Gas Plenum above The Pebble Bed

1. Nitrogen 20kW nominal heating power
2. Helium 20kW nominal heating power

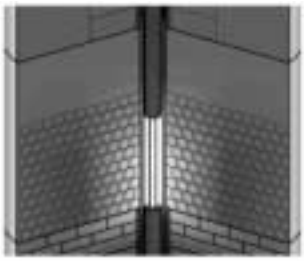

Fig. 4: Arrangement of the heating element and the pebble bed 〈

1. Nitrogen 20kW nominal heating power with short (half) heating element on the bottom side and a gas plenum above the pebble bed

P heating element /kW	16,17
P electrodes /kW	2,783

Dateiname: sn20o109

Date	24.07.95
Zeile	23
P / kW	20,1
CO / Vol.%	0,20
OXOR 6N / Vol.%	-0,05
TU / °c	31,9
Dewpoint	-33,5

Cooling Water Instrumentation

Thermocouple-	Top		Bottom	
Position	Inlet	Outlet	Inlet	Outlet
Temperature / °C	20,6	26,0	20,7	29,2
Throughput / l/h				

Arrangement of the Thermocouples

Height / Radius [cm]	6,5	10	22	34	46	58	70	75,6
167	69							
140			45				63	
113			346		241		165	113
91								194
63	615	543	456		319		254	207
50	776	665	502	421	347	287	243	183
9	937	727	510	355	266	214	169	126
3			487		252		148	103
-13			495		267		120	74
-40			100				57	
-67	31							
Protection Tube		Pebble Bed		Insulation		Vessel Surface		

2. Helium 20kW nominal heating power with short (half) heating element on the bottom side and a gas plenum above the pebble bed

P heating element /kW	16,17
P electrodes /kW	2,783

Date	8.8.95
Zeile	23
P / kW	20,0
CO / Vol.%	-0,01
OXOR 6N / Vol.%	2,09
TU / °c	30,2
Dewpoint	-3,1

Cooling Water Instrumentation

Thermocouple-	Top		Bottom	
Position	Inlet	Outlet	Inlet	Outlet
Temperature / °C	22,2	29,8	22,4	35,6
Throughput / l/h				

Arrangement of the Thermocouples

Height / Radius [cm]	6,5	10	22	34	46	58	70	75,6
167	73							
140			50				62	
113			287		201		138	104
91								164
63	546	496	411		283		200	185
50	697	603	460	394	328	266	220	180
9	893	732	561	437	351	278	211	161
3			553		341		180	137
-13			519		321		147	94
-40			107				64	
-67	31							
Protection Tube		Pebble Bed		Insulation		Vessel Surface		

A.1.1.6. Data for The Stationary Tests with Long Heating Element,30mm Pebble Diameter

1. Helium 30kW nominal heating power 30mm pebble diameter
1. Helium 10kW nominal heating power 30mm pebble diameter
2. Nitrogen 30kW nominal heating power 30mm pebble diameter
3. Nitrogen 10kW nominal heating power 30mm pebble diameter

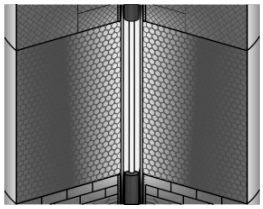

Fig. 5: Arrangement of the heating element and the pebble bed ⟨

1. Nitrogen 30kW nominal heating power with long heating element and 30mm pebble diameter

$P_{heating\ element}$ /kW	27,189
$P_{electrodes}$ /kW	1,817

Date	03.05.96
Zeile	16
P / kW	30,0
CO / Vol.%	0,34
OXOR 6N / Vol.%	0,01
TU / °c	30,5
Dewpoint	-42,1

Cooling Water Instrumentation

Thermocouple-	Top		Bottom	
Position	Inlet	Outlet	Inlet	Outlet
Temperature / °C	16,8	36,8	17,9	32,4
Throughput / l/h		200		200

Arrangement of the Thermocouples

Height / Radius [cm]	8,5	11	22	34	46	58	70	75,6
167	64							
140			68				67	
113			960		589		299	122
97			1026		816		419	238
91	1296	1207	1023	889	767	600	416	270
50	1269	1208	1019	840	717	561	390	276
9	1153	1122	979	816	666	502	302	217
3			958		617		313	171
-13			875		599		235	106
-40			116				63	
-67	70							

1. Pebble to Protection Tube	Pebble Bed	Insulation	Vessel Surface

2. Nitrogen 10kW nominal heating power with long heating element and 30mm pebble diameter

$P_{heating\ element}$ /kW	8,855
$P_{electrodes}$ /kW	0,662

Date	28.03.96
Zeile	22
P / kW	10,0
CO / Vol.%	0,18
OXOR 6N / Vol.%	-0,1
TU / °c	27,3
Dewpoint	-29,5

Cooling Water Instrumentation

Thermocouple-	Top		Bottom	
Position	Inlet	Outlet	Inlet	Outlet
Temperature / °C	14,9	20,3	14,6	19,5
Throughput / l/h		200		200

Arrangement of the Thermocouples

Height / Radius [cm]	8,5	11	22	34	46	58	70	75,6
167	41							
140			39				45	
113			538		325		168	35
97			592		471		245	133
91	756	705	579	498	422	331	227	148
50	710	660	489	353	285	234	166	127
9	516	482	346	226	166	134	95	80
3			310		145		93	65
-13			310		161		75	49
-40			62				39	
-67	37							

1. Pebble to Protection Tube	Pebble Bed	Insulation	Vessel Surface

3. Helium 30kW nominal heating power with long heating element and 30mm pebble diameter

P heating element /kW	27,189
P electrodes /kW	1,817

Date	30.04.96
Zeile	18
P / kW	30,0
CO / Vol.%	0,38
OXOR 6N / Vol.%	0,09
TU / °c	30,0
Dewpoint	-38,5

Cooling Water Instrumentation

Thermocouple-	Top		Bottom	
Position	Inlet	Outlet	Inlet	Outlet
Temperature / °C	17,2	36,6	18,2	33,1
Throughput / l/h		200		200

Arrangement of the Thermocouples

Height / Radius [cm]	8,5	11	22	34	46	58	70	75,6
167	68							
140			78				69	
113			778		425		214	115
97			866		632		300	215
91	1155	1076	867	719	594	442	320	243
50	1159	1096	890	705	590	454	332	269
9	1045	1014	869	715	584	452	298	240
3			846		548		313	194
-13			738		497		218	122
-40			119				71	
-67	63							

1. Pebble to Protection Tube	Pebble Bed	Insulation	Vessel Surface

4. Helium 10kW nominal heating power with long heating element and 30mm pebble diameter

P heating element /kW	8,855
P electrodes /kW	0,662

Date	20.02.95
Zeile	98
P / kW	10,0
CO / Vol.%	-0,01
OXOR 6N / Vol.%	2,08
TU / °c	26,5
Dewpoint	-15,1

Cooling Water Instrumentation

Thermocouple-	Top		Bottom	
Position	Inlet	Outlet	Inlet	Outlet
Temperature / °C	18,9	28,3	19,6	26,7
Throughput / l/h		200		200

Arrangement of the Thermocouples

Height / Radius [cm]	8,5	11	22	34	46	58	70	75,6
167	41							
140			45				43	
113			382		199		104	63
97			430		299		141	106
91	606	559	429	344	277	203	149	119
50	614	573	435	324	265	203	153	131
9	508	488	402	316	251	193	132	112
3			384		233		137	94
-13			347		223		104	67
-40			72				46	
-67	39							

1. Pebble to Protection Tube	Pebble Bed	Insulation	Vessel Surface

A.1.2. OKBM EXPERIMENTAL FACILITIES FOR TESTING OF HTGRS COMPONENTS

A.1.2.1. St-1312 High Temperature Gas Test Facility (Fig. 1)

– Purpose

Testing of full-scale models of steam generator and high temperature heat exchangers under operating parameters. Hydraulic and vibrational characteristics of helium and steam-water circuits of steam generators and heat exchangers and thermal state of the structural elements can be studied.

Besides, the facility is used for the development of control and instrumentation system for different types of reactors.

– Main Engineering Data

Coolant	helium
Coolant temperature, ^{o}C	up to 965
Coolant pressure, MPa	5,0
Coolant flowrate, kg/s	up to 6,48
Heaters power, MW	15
Steam generator model heat transfer, MW	10
Coolant temperature at steam generator model inlet, ^{o}C	up to 750
Coolant temperature at steam generator model outlet, ^{o}C	up to 540
Steam pressure at steam generator model outlet, MPa	17,6
Heat exchanger model thermal heat transfer, MW	0-5

The facility consists of the following main systems:

– gas circuit ;

– steam-water circuit ;

– circuit for equipments cooling ;

– control and instrumentation system;

– TV supervision system.

Coolant circuit includes circulator, recuperator, heater, cooler. heat exchanger and steam generator models.

– Status of the facility

Commissioning phase was completed in 1991. The first stage of steam generator model testing at power level up to 20 % was carried out. At present putting of the facility in prolonged storage has been completed.

A.1.2.2. Main Circulator Test Facility St-1383 (Fig. 2)

– Purpose

Testing of a full-scale prototype of the primary circuit gas circulator. The facility serves for testing of gas circulators, valves and equipment used in HTGRs.
Main Engineering Data

Coolant	helium
Maximum coolant flowrate, kg/s	95
Coolant pressure, MPa	4,9
Coolant temperature, ^{o}C	345
Coolers heat transfer, kW	1010,0

The facility consists of a circulating gas circuit of 41,5 m3 volume, in a form a cylindrical tank with a built-in gas circulator, and auxiliary systems (of heat removal, lubrication and so on).

– Status of the facility

A full-scale prototype of the gas circulator is fabricated. Start-up and trial operation of the facility under partial loads was performed. At present putting of the facility in prolonged has been completed.

A.1.2.3. St-1565 High Temperature Helium Test Facility (Fig. 3)

– Purpose

Testing of fitting, thermal insulation, relief valve, helium mixer models; study of helium coolant technology, study of thermal and hydraulic parameters of steam generators and heat exchanges models.
Simulation of residual heat removal from the core in the emergencies. Study of heat and mass transfer under depressurization of the primary circuit.
Study of thermal processes under water ingress into the primary circuit. Validation of appropriate codes on the test results will be performed.

– Main Engineering Data

Coolant	helium
Coolant pressure, MPa	up to 5,0
Coolant temperature, ^{o}C	up to 1000,0
Coolant flowrate, kg/s	0,1
Electric heater power, kW	up to 500

– Status of the facility

The test facility was put into operation in 1979. A steam generator model was tested. By the present, tests of the prototype shut-off valves (equivalent diameter of 65 mm) used in the pipelines of HTGR refuelling system, of insulation and relief valve have been finished. During the whole period of the facility operation the purification system and control systems of coolant quality are tested. Preliminary tests and analysis of the possibility for investigations of heat and mass transfer in the emergencies were carried out. At present the facility is out of operation.

A.1.2.4. Control Rod Drive Mechanism Test Facility

– Purpose

Testing of the system: “drive mechanism-control rod-drive mechanism guideline”.

– Main Engineering Data

Prototype drive mechanism	full-scale
Operating travel, m	up to 5
Drive mechanism type	electro-mechanic (facility can be adopted for testing another type of drive mechanism - pneumatic, hydraulic)
Medium	atmospheric air

– Status of the facility

The facility is in operation since 1980. Testing of drive mechanisms of different types carried out. At present the facility is out of operation.

A.1.2.5. Masex Test Facility (Fig. 4)

– Purpose

Investigation of heat and mass transfer through penetrations, orifices and tubes. Calculational codes validation.

– Main Engineering Data

Tank volume, m^3	0,4
Tubes length, m	up to 1,6
Media taking part in mass exchange	helium-air
Built-in fan’s flowrate, m^3/h	300,0

– Status of the facility

Since 1991 mass exchange of helium-air for tubes of different length and slope to the horizon was investigated. Influence of gas circulator operation upon mass exchanger was also investigated. Calculational codes were validated. At present the facility is out of operation.

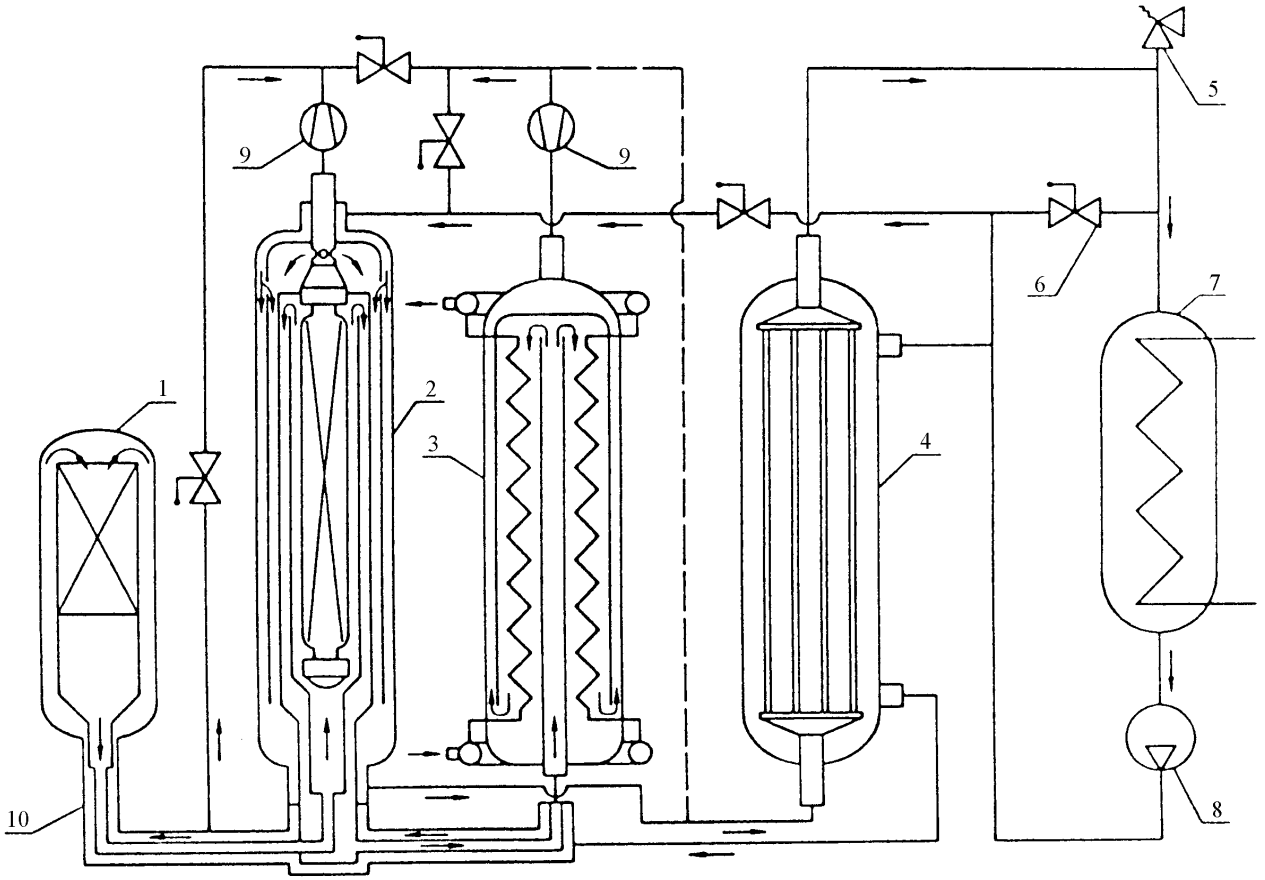

1. High temperature heater
2. High temperature heat exchanger
3. Steam generator
4. Recuperator
5. Relief valve
6. Adjusting valve
7. Cooler
8. Gas circulator
9. Flowmeter
10. Double duct

Fig. 1 (A.1.2.1.) High temperature gas test facility ST-1312 circuit diagram

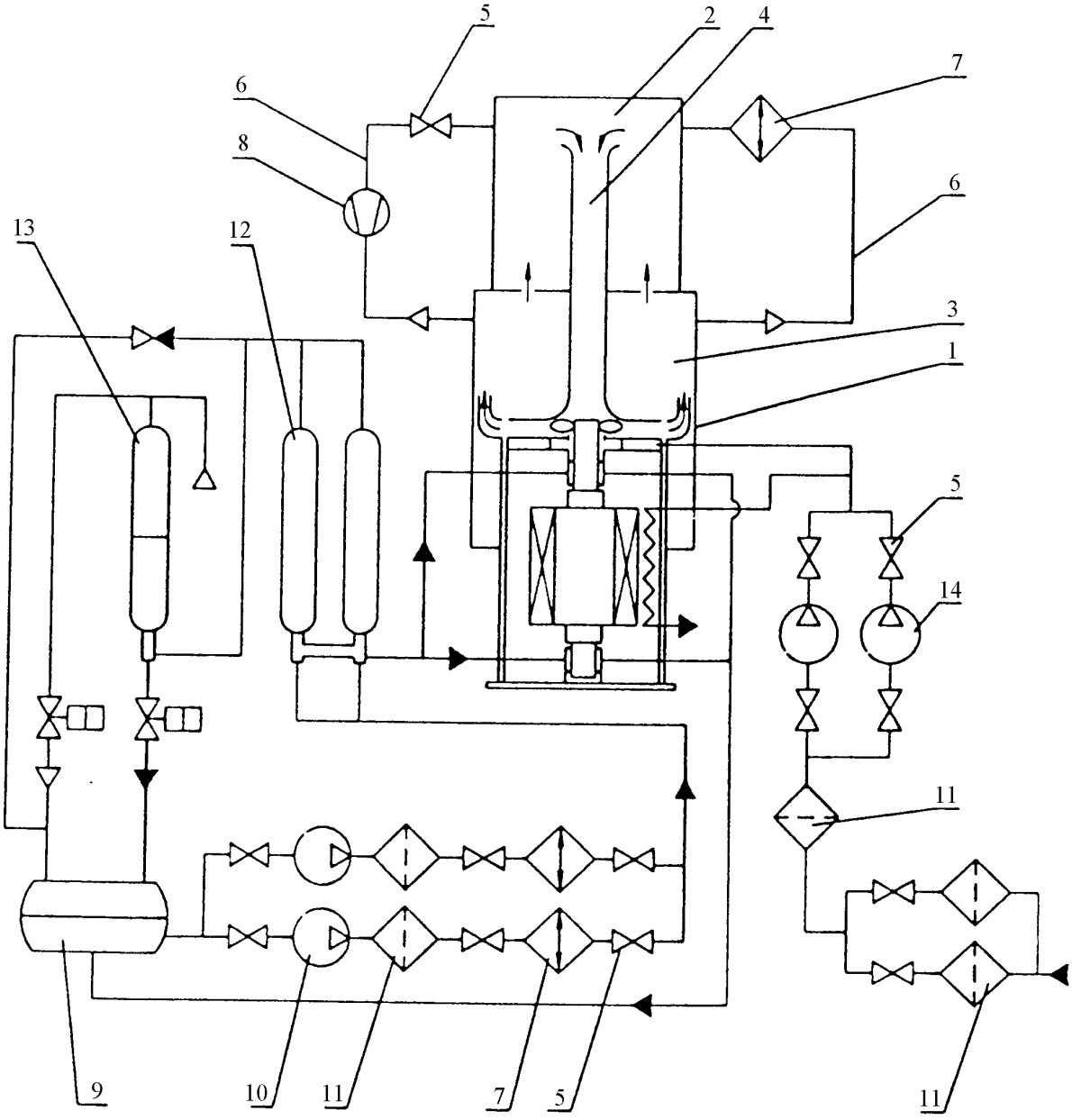

1. Vessel
2. Suction plenum
3. Pressure plenum
4. Central duct
5. Valve
6. Bypass
7. Cooler
8. Flowmeter
9. Oil tank
10. Oil pump
11. Filter
12. Oil cylinder
13. Gas-oil accumulator
14. Pump

Fig. 2 (A.1.2.2.) Diagram of the main circulator test facility ST-1383

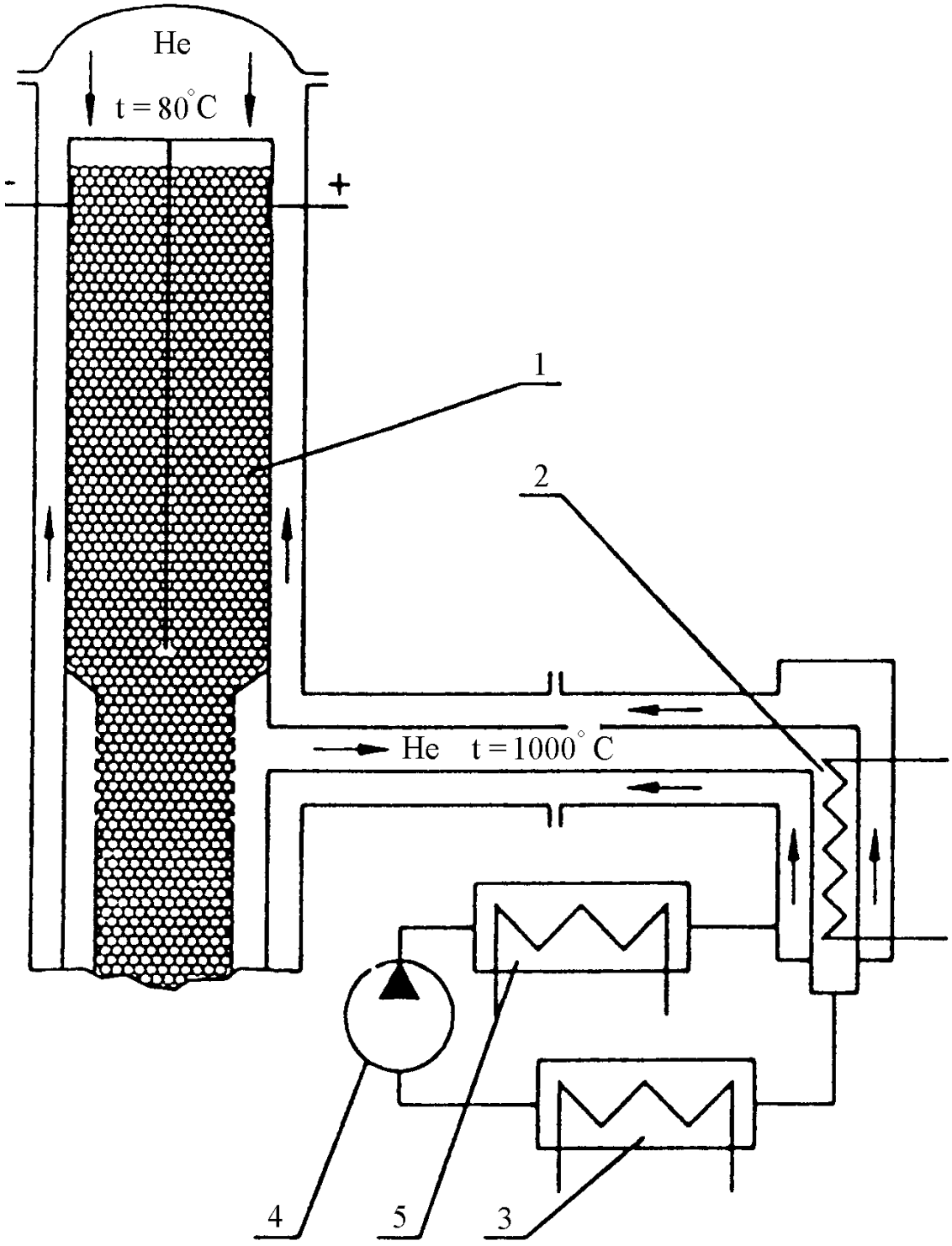

1. High temperature electric heater
2. Main cooler
3. Cooler
4. Circulator
5. Heater

Fig. 3 (A.1.2.3.) Outline of high temperature helium test facility ST-1565

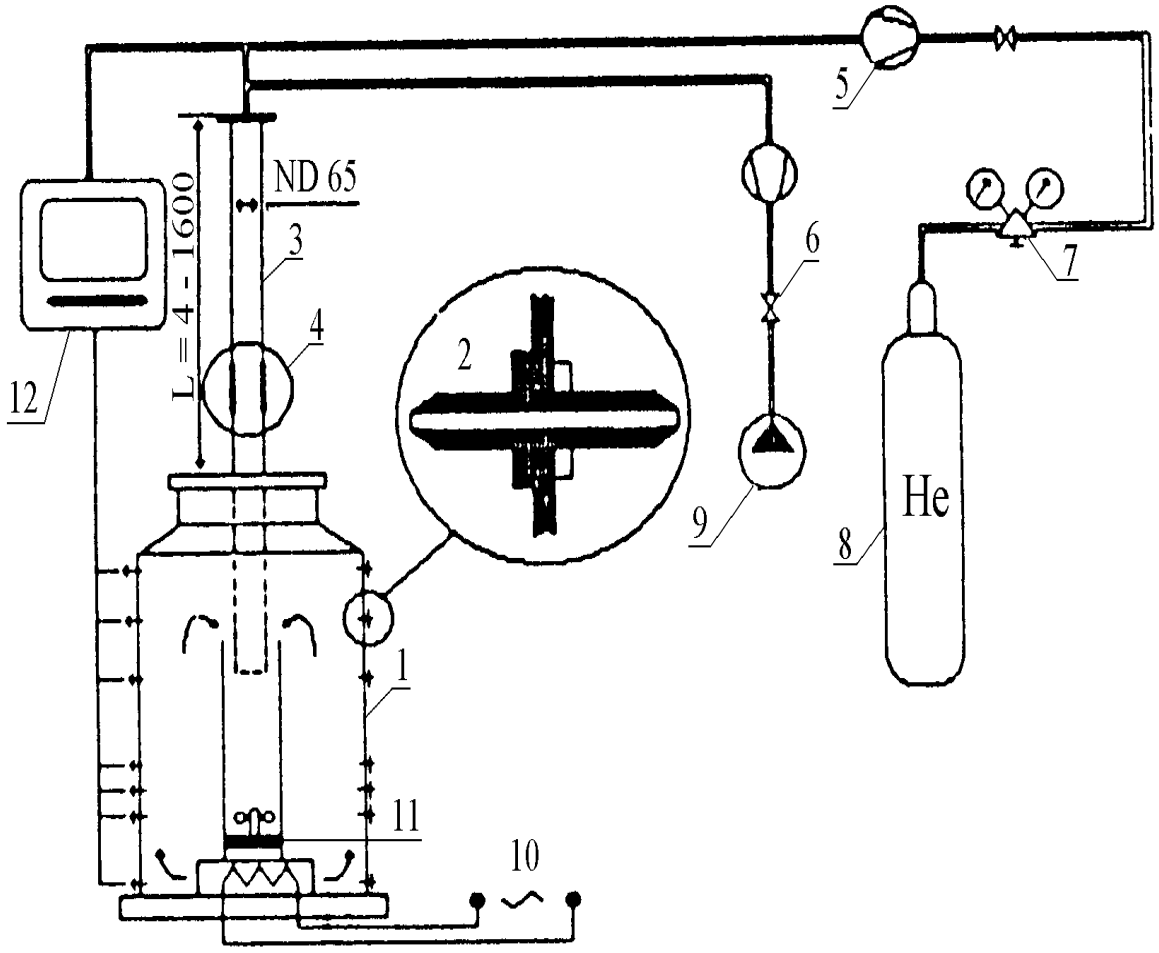

1. Vessel	4. Flexible insert	7. Pressure regulator	10. Heater
2. Sample pipe	5. Flowmeter	8. Cylinder	11. Gas circulator
3. ND 65 pipe	6. Valve	9. Air circulator	12. Measuring complex

Fig. 4 (A.1.2.5.) MASEX Experimental facility for mass transfer investigation

APPENDIX A2

CODE DESCRIPTION

A.2.1. DESCRIPTION OF THE CEA TRIO-EF CODE

A.2.1.1. Introduction

TRIO-EF is a general purpose Fluid Mechanics 3D Finite Element Code. The system capabilities cover areas such as steady state or transient, laminar or turbulent, isothermal or temperature dependent fluid flows; it is applicable to the study of coupled thermo-fluid problems involving heat conduction and possibly radiative heat transfer.

The code is widely used for applications in reactor design, safety analysis and final nuclear waste disposal. More recently, it has been used to study the thermal behaviour of the AVLIS process separation module.

A.2.1.2. Physical Models

TRIO-EF is a general purpose finite element code for flow analysis:

– in industrial scale 3 D geometries,

– with or without distributed internal obstacles,

– with incompressible Newtonian fluid with low thermal expansion,

– steady or unsteady,

– under laminar or turbulent (K-$\in$ model) conditions,

– through porous media,

– with or without energy coupling

– with phase change: liquid-solid.

Furthermore, TRIO-EF is able to deal with nonlinear heat transfer analysis:

– temperature dependent properties,

– forced, natural and mixed convection,

– radiation exchange in enclosures through non participating media, 2 D and 3 D view factor computation.

A.2.1.3. Salient Features

TRIO-EF is based on a macro-language allowing the user to handle data through named and typed objects such as nodal coordinates, fluid properties, thermal or vector fields. An interpreter translates the user-oriented commands into a coordinated set of operator library management instructions which are transparent to the user. Basically TRIO-EF is a set of independently executable modules and computing tools acting on the objects.

All data items can be defined as parameters, enabling the user to develop his own algorithms through the macro-language. Therefore TRIO-EF is ideally suited to parametric and optimization studies.

TRIO-EF takes advantage of the state of the art software development techniques and Quality Assurance Methodology.

A.2.1.4. Numerical Schemes for Flow Computation

a) Governing equation

The equations solved by TRIO-EF comprise the full set of Navier-Stokes equations using the Business approximation

$$\text{continuity:} \quad \text{div } U = 0 \tag{1}$$

$$\text{Momentum:} \quad DU/Dt = 1/\rho \text{ grad } p + \text{div } (\nu \text{ grad } U) + g\beta\,(T-T0) \tag{2}$$

$$\text{Energy:} \quad DT/Dt = \text{div } (\alpha \text{ grad } T) \tag{3}$$

where U, P and T are respectively the velocity, pressure and temperature,

and ρ, ν, α, β the density, kinematic viscosity, thermal diffusivity and volumetric thermal expansion coefficient.

g : gravitational acceleration

b) spatial discretization

The equations listed above are discretized by a finite element method for the spatial approximation using the bilinear 4 nodes elements (in 2 D) and trinilear 8 nodes brick (in 3 D) for velocity and temperature. The pressure is constant over an element.

After discretization of the continuity and momentum equations, we obtain the following linear system at time step "n":

$$M\,U^n - M\,U^{m-1} + A\,U^n m - C^T P^n = F \tag{4}$$

$$Cu^n = 0 \tag{5}$$

where:

- U is the global vector of the nodal velocity components at time n or n-1,
- p is the global vector of the element pressure,
- m depends on the algorithm used,
- M is the consistent mass matrix,
- A contains the advection and diffusion operators (the advection operator can be built in various ways).

c) penalty algorithm

If we take m = n, the system is solved implicitely. In order to eliminate the pressure, we modify ν by writing:

$$P^n = \varepsilon\, C\, U^n \tag{6}$$

which leads to:

$$(M/\Delta t + A + \varepsilon C^T C)\, U^n = F + M/\Delta t\, U^{n-1} \qquad (7)$$

where Δt is the time step

Note: for discontinuous pressure elements, the $C^T X$ matrix can be computed at the element level.

The incompressibility constraint is obtained when ε is large enough, but not too large (because of round off errors). Typically for 2 D flows, we have: $10^6 < \varepsilon L^2/v < 10^{10}$. For 3 D flows, we replace L^2 by L^3 in the above formula.

d) The semi-implicit algorithm

If we take m = n- 1 and if we diagonalize the mass matrix (using for example a Gauss Lobatto quadrature) the algorithm becomes explicit in the momentum equation. Using the continuy equation, we can eliminate the velocity at the time n and get the following linear system:

$$(CD^{-1}C^T)\, P^n = -\Delta t\, CD^{-1} (F - Au^{n-1}) \qquad (8)$$

Where D is the lumped mass matrix, which takes into account the Dirichlet boundary conditions on the velocity.

This scheme is conditionally stable.

A.2.1.5. Diffuse Radiative Heat Transfer: Formalism

In many thermal engineering applications, surfaces are separated by radiatively non-participating media and may be idealized as diffuse emitters and reflectors. Consequently, the net radiant energy fluxes are intimately related to purely geometrical quantities called shape factors, that take into account hidden parts: the problem is mainly the shape factor evaluation.

a) Formalism for radiative enclosures

Radiative enclosure are decomposed into elementary surfaces (finite planar polygonal surfaces). The standard radiosity method gives the matrix relationship between the mean radiant fluxes ϕ and the mean temperatures T over the elements, the matrix depending upon the shape factors and the wall total emissivities:

$$\phi = (I - F)\,(I - (I - \varepsilon)\, F)^{-1}\, \varepsilon\, \sigma\, T^4 \qquad (10)$$

where:

- I is the identity matrix
- F is the shape factor matrix
- ε is the diagonal matrix of the element total emissivities
- σ is the Stefan-Boltzman constant

this relation constitutes a nonlinear boundary condition to the heat conduction equation. The radiant operator is obtained by linearizing equation 10 and by using the relation between nodal temperature and mean temperature.

If T(i) is the nodal temperature at step i, the iterative process which leads to the solution, is as follows:

$$T(i) = K\,T(i) \tag{11}$$

$$(\phi\,'i+1) = R(\varepsilon, F, T(i)\,K\,T(i+1) \tag{12}$$

with:

$$R(\varepsilon, F, T(i)) = (I - F)\,(I - (I - \varepsilon)\,F)^{-1}\,\varepsilon\,\sigma\,T(i)^3 \tag{13}$$

then, the radiant operator is introduced into the conductivity operator.

b) Hidden-surface algorithm of shape factors

The method employed for the computation of 3-D shape factors is derived from an algorithm established for synthetic image generation.

The shape factor between two surfaces i and j is defined as the fraction of the radiant energy leaving surface i which strikes surface j. According to the radiative properties of the surface, assumed to be isothermal, the shape factor is reduced to:

$$F_{ij} = \frac{1}{S_{ij}} \int_{Si} \frac{\cos\Theta_i \cos\Theta_j}{\pi(r_{ij})^2} v_{ij} d_{Si} d_{Sj} \tag{14}$$

where ni, nj, Si, Sj denote the surface local normals and areas, θi and θj the angles between the local normals and local direction MiMj. The vij term takes into account the possible occlusion of surface j due to intervening surfaces in direction MiMj defined by two current points Mi on surface i and Mj on surface j : vij = 0 if there is an occlusion in the local direction MiMj, vij = 1 if not.

The difficulty stems from the fact that the evaluation of shape factors requires for any pair of surface to sort all other surfaces in order to predict whether they see each other entirely, partially or not at all. The number of operations to perform would thus grow as the cube of the number of elements, which is prejudicial to the method efficiency when this number is high. This is the main reason for working out a more efficient sorting algorithm.

The visibility problem can be tackled as follows: consider a surface i and a current point Mi on this surface. This surface has, from point Mi, a view of its environment across the hemisphere of directions surrounding its normal. The problem is to determine for each direction which surface is visible from point Mi and calculate the corresponding elementary shape factors.

The numerical implementation for this method requires:

– the subdivision of surfaces, defining within each surface a set of view points and corresponding sub-elements,

– the approximation of the hemisphere of directions.

The algorithm is greatly simplified by considering a cubic surface, the center of which is the current view point. Each face of the cube is divided into square regular cells, each cell defining a viewing direction and an elementary solid angle. The number of cells per face is called resolution.

For all surfaces and for each view point on that surface, the algorithm consists in projecting all other surfaces on the projection cube (figure 1). The depth "3" of each corresponding cell, that is the distance between the projected cell and the view point along the cell direction is calculated. The

projection of the entire environment solves simultaneously the problems of visibility in each cell thanks to the depth and numerical calculation of shape factors.

The method warrants the energy conservation principle, with accuracy checked by the resolution and the subdivision of the elements.

A.2.2. DESCRIPTION OF THE VGM-, DUPT-, SM1- AND GTAS-CODES

N.Kuzavkov

OKB Mechanical Engineering
Nizhny Novgorod
Russia

A.2.2.3. VGM-CODE

VGM-code is intended for calculations of normal and emergency transients in nuclear power plants with two circuits and reactors cooled by helium.

Simulating regimes include:

- normal operation,
- urgent drop in power due to failure of equipment,
- emergency regimes (inadvertent withdrawal of control rods, inadvertent action of absorber ball
- reactivity system, loss of station service power, violation of heat removal).

Simulating circuits and systems include main equipment having an effect on transients. The mathematical simulation comprises neutronic process, thermal-hydraulic process in the primary, secondary circuits and emergency decay heat removal system, heat transfer in fuel elements, a model of reactivity control system.

The simulation of neutronic process is based on the point kinetics method in 6-group approximation.

Thermal-hydraulic process is simulated in the frame of 1-D model with account of natural convection of the coolant and possibility to change a direction of the circulation. Mixing of flowrates with different temperatures is assumed to be ideal.

The core thermal model allows to compute coolant and moderator temperatures in axial and radial directions versus core inlet temperature, flowrate distribution and power.

Coefficients of heat transfer between gas, fuel and moderator are calculated. Temperature distribution across the moderator due to heat conduction is taken into consideration.

Mass of kernels in every calculating mesh is reduced to point mass of the mesh. Fuel temperature is computed with account of fuel heat capacity and heat exchange with coolant and moderator.

Total reactivity covers temperature effects of fuel and moderator, reactivity of control system and other reactivity perturbation given by piecewise-linear functions. Core power density distribution, reactivity coefficients, characteristics of control rods are derived from neutronic calculations as input data.

Fuel, moderator and coolant temperatures are averaged on corresponding formulae.

Mathematical model of reactor control and protection system simulates operation of automatic regulator on relay principle. Mathematical model of protection system takes account of possible time delay at formation of shutdown signals, acceleration time of absorber rods and balls.

Differential equations in partial derivatives to provide computation of heat transfer in the core are approximated by stable monotonous difference schemes. After manipulations the closed set of algebraic equations are solved by a run method.

To obtain a level of neutron flux, the set of differential equations of neutron kinetics is solved by the finite difference method. Change of decay heat versus time is given in the form of a Table.

To compute heat transfer and friction coefficients approved formulae are applied. The range of definition of coolant properties is from 280K to 1800K and from 0.01 MPa to 100 MPa.

Input data for the code is a nuclear power plant configuration, thermal properties of materials, core power density distribution, local coefficients of reactivity, distribution of hydraulic resistance, characteristics of control and other systems.

Emergency transients are simulated by violation of reactivity and (or) position of control rods, the given power in the control system of neutron power, temperature and flowrate of the coolant at the inlet of the secondary circuit equipment, temperature and flowrate of the coolant at the inlet of emergency heat exchangers in the secondary circuit.

VGM-code allows to get core power density, temperature distribution in fuel elements, coolant temperatures and flowrates in primary, secondary and emergency cooling circuits.

The code consists of units what are convenient for further improvement. The data bank contains separate blocks and every software module has own input data.

A.2.2.2. DUPT-code

Analysis of temperature and velocity distributions in gas cavities is carried out on two-dimensional DUPT-code. The code includes heat and mass transfer equations on the basis of Business approximation for two-dimensional and axis symmetrical geometries using numerical method of longitudinal and transverse run with variable coefficients. To provide calculations for regions tight-packed with equipment, the code applies porosity body method. In accordance with this method thermal properties of a mesh medium are calculated proportionally with volume parts of the mesh components, cross section for fluid is proportional to the mesh fluid part.

To solve hydrodynamic problem, axial and radial components of fluid velocities on hard boundary are assumed to be equal zero. At initial moment of time the fluid is stationary and velocities in all points of the region are equal to zero. To solve heat problem, temperature of the surroundings and heat transfer coefficients on the boundaries are given.

The heat transferred from one surface to another is determined on the following equation:

$$Q_{12} = eC_o\left[\left(\frac{T_1}{100}\right)^4 - \left(\frac{T_2}{100}\right)^4\right]\int_{F_1} dF_1 \int_{F_2} \frac{\cos\varphi_1 \cos\varphi_2}{\pi r^2} dF_2$$

e - emissivity;
C_o - emissivity of black surface;
T_1, T_2 - temperatures of the surfaces;
w - angle at a point of surface 1 for dF of the surface 2;
j_1, j_2 - angles between normals and lines connecting two points on the surfaces 1 and 2;
r - distance between the two points on the surfaces 1 and 2.

A.2.2.3. SM1-code

The code is based on solution of the energy equation for elements with boundary conditions of the third type. Fluid flow is not computed, account for heat transport by the fluid is provided by means of boundary conditions.

The region to be calculated is divided into elements for which the energy balance equation is solved:

$$m_i c_i \frac{dT_i}{d\tau} = \sum_j k_{i,j} F_{i,j} \Delta T_{i,j} + \sum_n \alpha_{eff\,i,n} F_{i,n} \Delta T_{i,n} + N_i$$

where

m - mass of an element, kg
c - specific heat, J/kgK
T - temperature, ^oC
t - time, s
k - heat transfer coefficient, W/m^2K
F - area, m^2
dT - temperature difference, K
a_{eff} - coefficient of effective heat transfer conductance, W/m^2K
N - power, W
i - index of an element
j - index of an element adjacent to i-th element
n - index of a boundary adjacent to i-th element.

Coefficient of effective heat transfer conductance includes radiative and convective partials

$$a_{eff} = a_r + a_c$$

During computation of heat transfer by radiation interacting surfaces is assumed to be at right angles to each other, therefore angle distribution of radiative heat is ignored.

a_r is given by

$$a_r = \frac{C_{o\varepsilon}}{\Delta T_{1,2}} \left(T_1^4 - T_2^4 \right),$$

where

C_o - Stefan - Boltzmann constant, W/m^2K^4
e - effective emissivity
T - temperature, ^oC

$$e = \frac{1}{\frac{1}{\varepsilon_1} + \left(\frac{1}{\varepsilon_2} - 1 \right) \frac{F_1}{F_2}}$$

$e_{1,2}$ - emissivity of the surface
$F_{1,2}$ - area of the surface, m^2
1,2 - surface number.

Heat transfer by convection is described by

$$\alpha_c = \frac{1}{\left(\frac{1}{\alpha_{m,1} F_1} + \frac{1}{\alpha_{m,2} F_2}\right) F_{1(2)}}$$

where

a - heat transfer conductance coefficient, W/m^2K
m - index of media adjacent to surfaces 1,2.

For calculation of heat transfer coefficient under natural convection at vertical and horizontal surfaces the equation is used

$$N_{uf} = a(Gr_f Pr_f)^b (Pr_f/Pr_s)^{0,25},$$

where

Nu - Nusselt number
Gr - Grashof number
Pr - Prandtl number
a,b - coefficients depending on surface orientation and magnitude of Gr_fPr_f
f - index of fluid (Nu, Gr, Pr at parameters of the fluid)
s - index of surface (Pr at temperature of the surface).

A.2.2.4. GTAS code

The core thermohydraulic calculation was performed using "GTAS" code.

The code is intended for calculation of a temperature state of core and reactor structures in stationary and dynamic modes in two-dimension (R-Z geometry) approximation.

The following data are used as initial data:

– geometric characteristics in the field under consideration;
– distribution of energy releases in structural materials;
– thermophysical properties of structural materials and gas media;
– change of mode parameters.

When developing the program the equation of energy for a porous body was used which without account of the coolant motion energy is of a form:

$$c\rho\frac{\partial T}{\partial \tau} = \mathrm{div}(\lambda_э \mathrm{grad} T) + q_v - c_2\rho_2(\vec{w}\cdot \mathrm{grad} T_2)$$

where:
c - specific heat capacity of porous body;
ρ - density of porous body;
T - temperature of porous body;
τ - time;
λ_{ef} -effective coefficient of heat conductivity of porous body;
q_v - density of volumetric energy release;
c_g - specific heat capacity of gas at constant pressure;
ρ_g - density of gas;
T_g - temperature of gas;

$(\vec{w} \cdot \mathrm{grad} T_2)$ - scalar product of velocity gradient of gas temperature.

Volumetric heat conductivity of porous body is determined from the ratio:

$$c\rho = c_g \cdot \rho_g \cdot \varepsilon + c_o \cdot \rho_o (1 - \varepsilon),$$

where:

ε - relative fraction of gas;
c_o - specific heat capacity of solid component;
ρ_o - density of solid component of porous body.

In the structure of graphite blocks considered as a porous body, $c_o \cdot \rho_o >> c_2 \cdot \rho_g$. Volumetric heat capacity of a porous body depends insignificantly on the kind of gas, density of gas is determined by a density and heat capacity of solid component.

The effective coefficient of heat conductivity of a porous body corresponds to coefficient of heat conductivity for joint heat transfer of energy by radiation between surfaces and by heat conductivity for solid phase and gas.

The equation of energy is solved by a method of balance in two-dimensional approximation. Volume of a region under consideration is divided into calculation elements which have a form of cylinder or a hollow cylinder.

Each calculation element is described by three numerals. The first numeral denotes the type of a calculation element, other numerals denote the number of material in the Table where thermophysical properties are given.

The following types of calculation elements are envisaged:

1 - structure of fuel element;
2 - structure of graphite blocks;
3 - solid body;
4 - stagnant transparent gas;
5 - stagnant liquid;
6 - moving transparent gas;
7 - moving liquid.

In the Table of thermophysical properties of materials values of the following parameters are specified for each of the solid porous media depending on the level of temperature:

- coefficient of heat conductivity;
- specific heat capacity;
- density.

For liquid and gases the following is specified:

- coefficient of heat conductivity;
- specific heat capacity at constant pressure;
- density at normal pressure;
- coefficient of dynamic viscosity;
- coefficient of volumetric thermal expansion.

Determination of values of thermophysical parameters is performed using linear interpolation of tabulated values.

Variation of temperature in an annular element under consideration given in Fig. 1 is found from a ratio:

$$\Delta T = (Q1 - Q2 + Q3 - Q4 + Q0 - Q5) \cdot \Delta\tau/(c\rho\Delta V)$$

where:

ΔT - variation of temperature of element;
Q1 - power delivered through upper boundary of element;
Q2 - power removed through lower boundary of element;
Q3 - power delivered through inner (small) boundary of element;
Q4 - power removed through outer (large) boundary of element;
Q0 - power released in the bulk of element;
Q5 - power removed from the coolant element;
$\Delta\tau$ - count interval for time;
$c\rho$ - specific heat capacity and density of material;
ΔV - volume of element.

Power removed through boundary is determined from the ratio:

$$Q_H = q_{s,k} \cdot F_k$$

where:

$q_{s,k}$ - density of heat flux through boundary;
F_k - area of a boundary.

A procedure for calculation of density of heat flux through a boundary is chosen depending on the type of a cell under consideration.

In the case when the cell under consideration and the cell adjoining it consist of porous and solid body the density of heat flux is determined by a ratio:

$$q_{s3} = \frac{2 \cdot \left(T_{i-1,j} - T_{i,j}\right)}{\left(\frac{\Delta R_{i-1}}{\lambda_{i-1,j}} + \frac{\Delta R_i}{\lambda_{i,j}}\right)}$$

where:

i - number of element along radius;
j - number of element along height;
i-1 - number of adjoining element;
T - temperature;
ΔR - step of element along radius;
λ - coefficient of heat conductivity of a material.

For calculation elements consisting of stagnant gas or liquid the density of heat flux is chosen from the ratios:

$$qs_3 = \frac{2 \cdot \left(T_{i-1,j} - T_1\right)}{\left(\Delta R_{i-1} / \lambda_{i-1,j}\right)},$$

$$qs_4 = \frac{2 \cdot \left(T_2 - T_{i+1,j}\right)}{\left(\Delta R_{i+1} / \lambda_{i+1,j}\right)},$$

$$qs_{34} = \varepsilon_g \cdot \lambda_g \cdot \frac{T_1 - T_2}{\Delta R_i} + \sigma_0 \cdot \varepsilon_n \cdot \left(T_1^4 - T_2^4\right),$$

$$qs_3 \cdot \left(1 - \frac{\Delta R_i}{2 \cdot R_i}\right) = qs_{34} = qs_4 \cdot \left(1 + \frac{\Delta R_i}{2 \cdot R_i}\right),$$

where:

T_1, T_2 - temperature of left and right boundaries of an element under consideration;
qs_3 - density of heat flux between boundaries of element;
ε_g - coefficient taking into account the impact of convection onto gas layer heat conductivity;
λg - coefficient of heat conductivity of gas;
$\sigma 0$ - Stefan-Bolzmann constant;
εn - emissivity;
Ri - radius on which the element under consideration is set.

Coefficient taking into account the impact of convection in gas layer is determined from a ratio:

$$\varepsilon_c = 0{,}18 \cdot (Gr \cdot Pr)^{0{,}25},$$

where:

Gr - Grashof number;

Pr - Prandtl number.

For calculation elements consisting of block structure the coefficient of effective heat conductivity in radial direction was determined by the ratio that is used for small temperature fluctuations in structure which thickness is one block:

$$\lambda_{ef} = \frac{\delta_c + \delta_{bl}}{\left(\frac{\lambda_\Gamma}{\delta_c}\varepsilon_c + \sigma_0 \cdot \varepsilon_\Pi \cdot 4 \cdot T^3\right)^{-1} + \delta_{bl}/\lambda_{bl}}$$

where:

δ_c - clearance between blocks;

δ_{bl} -flat-to-flat block dimensions;

T - temperature;

λ_{bl} - block heat conductivity coefficient in radial direction.

In the code heat transfer in axial direction by conductivity is taken into account.

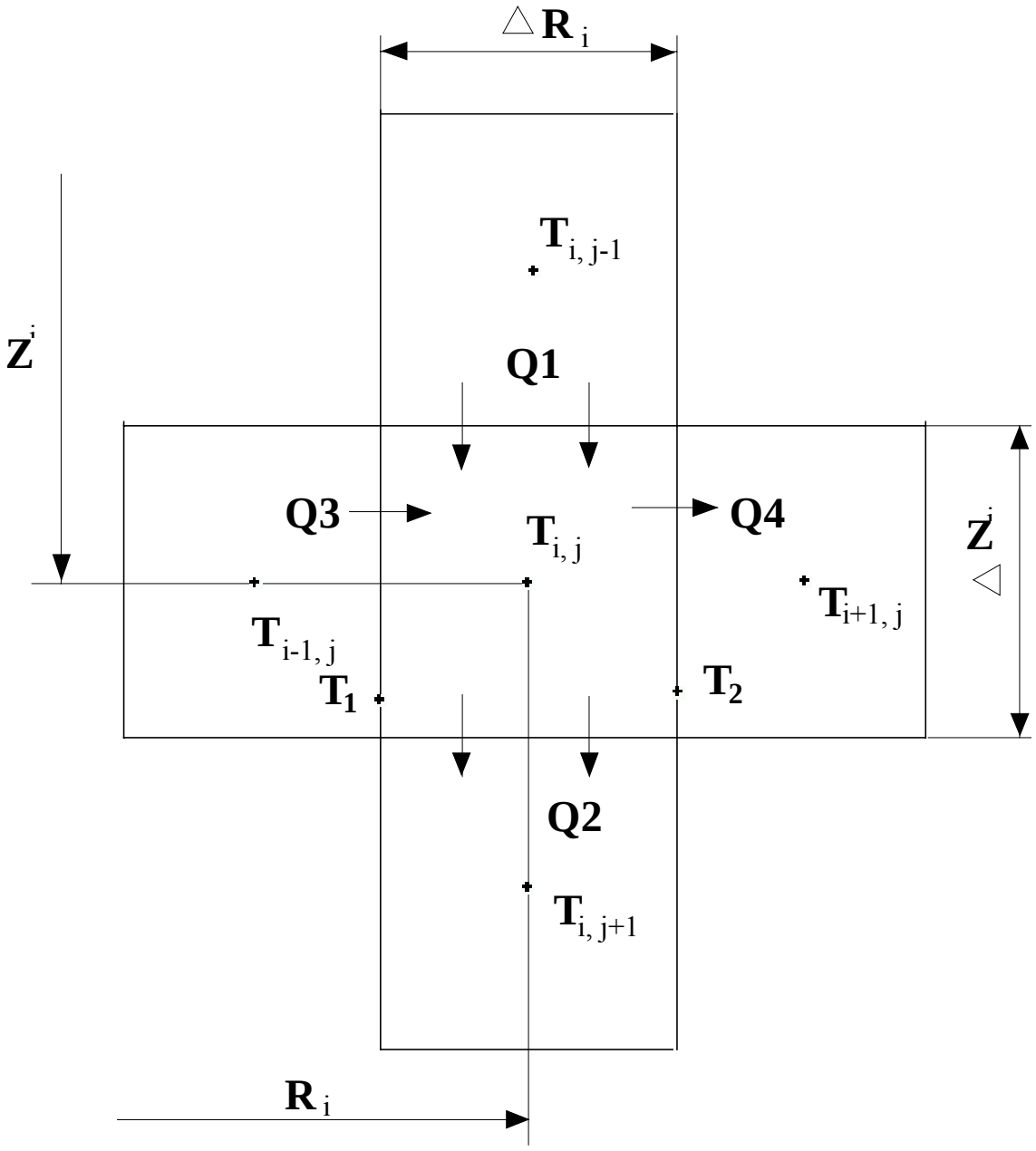

Fig. 1 (A.2.2.) Diagram of calculation element

When the medium under consideration is moving gas the densities of heat flux are determined using the ratios:

$$qs_3 = \frac{2 \cdot \left(T_{i-1,j} - T_1\right)}{\left(\Delta R_{i-1} / \lambda_{i-1,j}\right)} = \alpha \cdot \left(T_1 - T_g\right) + \sigma_0 \cdot \varepsilon_n \left(T_1^4 - T_2^4\right),$$

$$qs_4 = \frac{2 \cdot \left(T_2 - T_{i+1,j}\right)}{\left(\Delta R_{i+1} / \lambda_{i+1,j}\right)} = \alpha \cdot \left(T_g - T_2\right) + \sigma_0 \cdot \varepsilon_n^0 \left(T_1^4 - T_2^4\right)\left(1 - \frac{\Delta R_i}{R_i}\right),$$

where:

α - coefficient of heat removal from the surface of solid medium to gas;
T_g - temperature of gas.
Power released in the bulk of the element is determined using the ratio:

$$Q0 = q_v \cdot \Delta V = N_{rel}(\tau) \cdot N_{nom} \cdot K_v(\tau) \cdot \frac{\Delta V}{V},$$

where:

Nrel(τ) - relative variation of power versus time;
Nnom - nominal power of reactor;
Kv(τ) - relative specific heat release in calculation element;
ΔV - volume of an element under consideration.

For calculation of power removed by coolant from the element under consideration the following ratio for heat exchange at constant temperature of porous body solid component is used:

$$Q5 = \left(T_s - T_{g_{in}}\right) \cdot \left(1 - e^{-\frac{kS}{c_g \cdot G_i}}\right) \cdot c_g \cdot G_i,$$

where:

Ts - mean temperature of porous body solid component;
Tgin - temperature of gas at the inlet into element;
S - heat exchange surfuel element in the element;
k - coefficient of heat transfer from solid component of porous medium to gas;
cg - specific heat capacity of gas at constant pressure;
Gi - mass flow of gas through the element.

Two schemes for calculation of heat exchange between porous body solid component and the coolant are intended to be used in the program:

1. When the internal channels are not indicated the heat removal is effected only from the external side of the block by helium flowing through the gaps. Heat transfer coefficient from the graphite of hexagonal block to helium is specified to be equal to heat transfer coefficient of equivalent in area cylinder rod cross section with even energy release distribution from radius with mean temperature along the section.;

2. When coolant channels are specified the heat removal is effected by both helium in gaps with heat transfer coefficient for the first scheme, and helium in channels. The coefficient of heat transfer through the graphite of block to helium in channels is assumed analogous to coefficient of heat transfer through a hollow cylinder without energy releases with inner cooling. Its cross section area is 0.5 of the cell graphite cross section area.

The distribution of flowrate in the slots of graphite structure and cooling channels is found from the solution of a set of equations:

$$\frac{G_i^2}{2F_i^2}\left(\sum_j \frac{\lambda_{ij}\cdot\Delta Z_j}{\rho_{ij}\cdot d_{ij}}+\frac{\xi_i}{\rho_i}\right)+g\sum_j \rho_{ij}\cdot\Delta Z_j = \text{idem},$$

$$\sum_i G_i = G_0,$$

where:

G_i - coolant flow rate in respective channels;
F_i - area of horizontal boundary of calculation element;
λ_{ij} - coefficient of friction resistance in respective channel, related to Fi;
ρ_{ij} - density of gas;
ΔZ_j - height of calculation element;
d_{ij} - hydraulic diameter;
ξ_i - coefficient of local hydraulic resistance at inlet and outlet from a channel;
G_0 - total flow rate through reactor.

Mass exchange between helium circulating in cooling channels and in gaps is not taken into account.

A.2.3. THE ORNL GRSAC CODE FOR GAS-COOLED REACTOR SIMULATIONS

A.2.3.1. Abstract

An interactive workstation-based simulation code for studying postulated severe accidents in gas-cooled reactors has been developed to accommodate user-generated plant design input with "smart front-end" checking. New code features include on- and off-line plotting, on-line help and documentation, and an automated sensitivity study option. The code and its predecessors have been validated using comparisons with a variety of experimental data and similar codes.

A.2.3.2. Introduction

The GRSAC (Graphite Reactor Severe Accident Code) software is a new general-purpose program developed at Oak Ridge National Laboratory (ORNL). It is based on the ORNL MORECA [1],[2] code for simulating accident scenarios for selected gas-cooled reactor (GCR) design types. The MORECA code and its predecessors were originally developed at ORNL under the sponsorship of the U.S. Nuclear Regulatory Commission (NRC) to perform confirmatory licensing-related studies of a variety of High-Temperature Gas-Cooled Reactor (HTGR) designs, including the Fort St. Vrain HTGR and subsequently the 350-MW(t) steam-cycle Modular HTGR (MHTGR). MORECA was later developed - under U.S. Department of Energy (DOE) sponsorship - to simulate the MHTGR design for the 600 MW(t) direct cycle gas turbine modular helium reactor (GT-MHR).

Since MORECA is a "hard-wired" code, configured only for a particular reactor design, the conversion of MORECA to GRSAC was motivated by the need to generate the connectivities necessary to assemble, verify, and run simulations for a wide variety of graphite-moderated GCR designs.

GRSAC features of particular interest are: three-dimensional core representation, fast-running (typically >2000 times faster than real time on a SUN SparcStation-20 workstation), interactive user interface with on-line and off-line plotting options, automated sensitivity study capabilities, on-line documentation and help screens, and optional ATWS (anticipated transients without scram) capabilities. The basic designs that can be simulated using GRSAC, which the user may modify via the interface to a large (but limited) extent, include the British and French Magnox types (including the Calder Hall, G-2/3, and Bugey-2), Windscale (U.K.), and the HTTR (Japan). Adaptations and analyses are planned for the HTR-10 (China) and the GT-MHR Plutonium burner (U.S.-Russia).

A.2.3.3. Grsac Code Features

A. Reactor Design Setup

Specific design features for a chosen reactor type can be input by the user via design screen selections in the following categories: fuel element, nuclear parameters, core layout and reflector design, primary coolant system, vessel design, reactor cavity, and oxidation parameters. A program setup screen allows the user to activate or deactivate oxidation, Wigner energy, or ATWS features, and to select the coolant gas, core flow direction and computation time parameters. In some cases, such for as the radial and axial power peaking factor inputs and flow coastdown curves, graphical displays and automated consistency check features are included. For all of the user input screens in GRSAC, pop-up HELP windows and a choice of metric or English unit entries are available. The user can also select a "run with validation" option, which is a smart front end check of the entire set of inputs for data inconsistencies.

B. Initial Condition Runs

GRSAC accident sequence analyses require a large set of initial condition values which are created automatically via the Initial Condition mode. The user can select operational inputs such as power level, flow, pressure, etc., and observe the resulting detailed temperature and flow distributions attain steady state conditions. At any point in the run, one can store initial condition values in a RUN file.

C. Programmed Inputs

The interactive input screen for accident simulations allows for user inputs (scram, depressurization, changes in emergency and/or cavity cooling, etc.) at any time during a run. Such inputs can be pre-programmed, however, via a programmed input screen that is available to the user during the run setup procedure.

D. Accident Sequence Runs

Long-term Loss of Forced Convection (LOFC) accidents begin with a programmed flow coastdown transient. They may be simulated both with and without total or partial depressurization of the primary coolant and with or without scram. Optionally, both the active or passive shutdown cooling systems can be made to be either unavailable or available only intermittently in degraded states. For helium or CO_2-cooled cores, there is an option to allow air ingress following a depressurization, and subsequently to initiate (or not) oxidation models for graphite (and clad and metal fuel, if applicable).

LOFC transients in GCRs are generally characterized by slow heatups because of the low power densities and large heat capacities associated with the core.

E. Sensitivity Study Option

Many variations of transient and LOFC accident scenarios have been studied to observe the sensitivities of the predictions to parametric and operational assumptions. These provide guidance in design studies for determining plant operating parameters (including design power level) and in identifying which physical properties and correlations are most crucial to the outcome of postulated accidents.

In the GRSAC automated sensitivity study feature, the rationale is to seek out a set of parameters within user-specified uncertainty bands that result in the worst (or best) case accident consequences using a gradient search algorithm. Sets of 13 model or design parameters (such as heat transfer correlations, etc.) and 12 operational/run parameters (such as time of scram) have been set up to be available for automatic variation (from run to run). The program allows the user to select up to 10 from this set for any given study. To study the effects of a single parameter variation in more detail, a single-parameter option can be used. That parameter is varied uniformly within the uncertainty band (reference run plus 4 others).

A report generator, the results of which are available after the runs are completed, gives a summary of the run results.

A.2.3.4. Description of Selected Grsac Models

A. Reactor Core and Primary Cooling System

In GRSAC, the 3-D, hexagonal geometry core model uses one node each for 163 fuel and 42 reflector element radial regions in each of 14 axial regions. The annular core representation (205 x 14 = 2870 nodes) thus allows for detailed investigations of azimuthal temperature asymmetries in addition to axial and radial profiles. Variable core thermal properties are computed functions of temperature and are dependent on orientation and radiation damage. An annealing model for graphite accounts for the increase in thermal conductivity that may occur during heatup accidents.

The primary coolant flow models cover the full ranges expected in both normal operation and accidents, including a full range of pressurized and depressurization accidents, for forced and natural circulation, for upflow and downflow, and for turbulent, laminar, and transition flow regimes. The primary loop pressure calculation considers variable inventory (due to depressurization actions) and loop temperature changes and uses a simplified model of balance-of-plant gas temperatures.

B. Anticipated transient without Scram (ATWS) model

In an ATWS event, the expected scram would not occur at the start of an LOFC accident but instead could occur at an arbitrary later time or not at all. Slow rod withdrawal accidents can also be simulated if they are in conjunction with an LOFC accident. The model for fuel (as distinct from moderator) temperature is a quasi-steady state approximation valid only for slow transients characteristic of LOFC accidents. The point kinetics approximation for the neutronics is a prompt-jump, single-precursor-group model that compares favorably, for transients of the appropriate rate and magnitude, with calculations using a "full" model with prompt neutron generation time and six delayed neutron precursor groups included. Temperature-reactivity feedback from the 3-D modeling of fuel, moderator, and reflectors utilizes nuclear importance weighting. Models for xenon and samarium poisoning are included.

C. Graphite oxidation models

At the start of an air ingress oxidation transient, both inlet and outlet plena are assumed to be 100% air (i.e., early diffusion between air and the helium or CO_2 coolant is neglected). Thereafter, oxygen concentrations in the plena are calculated assuming well-stirred tank models. Subsequent inlet gas flow is assumed to be air, which mixes with any oxygen-depleted reverse flows there may be from the core.

Oxygen concentrations are calculated for each node at each time step, accounting for depletion occurring upstream in each flow channel, as well as for oxygen depletion within the time step for each node. All heat from oxidation goes directly into the graphite node. It is assumed that only CO2 is produced from the oxidation reaction; any CO that is produced would be burned anyway (though perhaps at a different location).

Two alternative oxidation regimes are assumed to exist, and are referred to as Zone I and Zone III oxidation. The Zone I graphite oxidation rate is governed primarily by the intrinsic chemical reactivity of the graphite according to the Arrhenius relationship, exp(-E/RT). The reaction occurs uniformly throughout an Active Oxidation Zone (AOZ) near the exposed surface. Zone III rates are governed by mass transfer to the exposed surface, where the oxidation occurs. The calculated mass transfer rate is dependent on the degree of turbulence (laminar, transition, and turbulent regimes) and on the diffusion coefficient, which is assumed proportional to the absolute temperature to the 1.8 power. The lesser of the two rates (Zone I or III) is controlling. Oxygen and CO2 concentration changes in the direction of flow are assumed not to affect air transport properties used for flow and heat/mass transfer correlations.

Experimental data have shown variations of up to a factor of 6 in oxidation rates due to differences in graphite "purity" (the higher the purity, the lower the oxidation rate), and even larger variations due to irradiation and effects of contaminants.

Clad and fuel oxidation modeling, for metal fuel reactor designs, was done in a similar manner to the graphite, but without the AOZ feature.

Iv. Code Verification and Validation Activities

Benchmark cases for steady state conditions, transients, and accidents have been run for comparisons with plant data and with similar codes and simulations developed by others and have shown generally good agreement. Earlier validation exercises using ORECA, a forerunner of MORECA, showed good results in comparisons with transient data from the Fort St. Vrain HTGR [3]. Additional validation efforts are currently under way via international cooperative efforts under the guidance of International Atomic Energy Agency Coordinated Research Programs in the areas of passive decay heat removal, neutronics, and fuel performance.

A.2.3.5. Conclusions

The new ORNL GRSAC code can readily be adapted to simulate a wide variety of GCR designs, and then be used to study a wide range of accidents up through very unlikely, severe accident scenarios. The new enhancements include user-definition capabilities for specific plant designs, "smart front-end" checking of input data, on-line help and documentation, on- and off-line plotting, and an automated sensitivity study option. Continuing work on verification and validation has included both use of experimental data and code-to-code benchmarking.

REFERENCES TO SECTION A.2.3.

[1] S. J. Ball, MORECA: A Computer Code for Simulating Modular High-Temperature Gas-Cooled Reactor Core Heatup Accidents, NUREG/CR-5712 (ORNL/TM-11823), Oak Ridge National Laboratory, October 1991.

[2] S. J. Ball and D. J. Nypaver, MORECA-2: Interactive Simulator for Modular High-Temperature Gas-Cooled Reactor Core Transients and Heatup Accidents with ATWS Options, NUREG/CR-5945 (ORNL/TM-12233), Oak Ridge National Laboratory, October 1992.

[3] S. J. Ball, "Dynamic Model Verification Studies for the Thermal Response of the FSV HTGR Core," Proceedings of the 4th Power Plant Dynamics, Control, and Testing Symposium, The University of Tennessee, Knoxville, 1980.

A.2.4. CFX-F3D Software

A.2.4.1. Description

CFX-F3D [1] flow modelling software performs CFD (Computational Fluid Dynamics) calculations. This software has been developed by AEA technology and solves partial differential conservation equations together with their boundary conditions. For this purpose, the software uses the finite volume method for the discretisation of the Navier-Stokes equations for mass, momentum and energy. A computational grid subdivides the physical domain of the problem geometry into a large number of cells. The governing equations of mass, momentum, and energy conservation are solved for the cell centres. The CFX-F3D software consists of a number of modules. These modules can perform the following tasks:

- the geometry and grid generator may be used to define the finite difference grid;
- the interactive front-end module constructs the data file via a series of menus. The output of this module is a single data file using the command language which represents the problem definition. The command language is a set of English-like commands, subcommands, and associated keywords;
- the front-end module takes the input specification of the problem and converts it into a form designed for efficient execution;
- the solution module solves the discretised representation of the problem;
- the graphics module produces the graphic output.

Release 4.1 of CFX-F3D software has the following features of interest for the present problem:

- multi-block grid capability. This capability involves the use of a set of blocks, which are 'glued' together. For each block there is a structured grid. Boundary conditions, solid regions, and porous regions within the domain are described using the concept of a 'patch';
- heat transfer capabilities. Flows with heat transfer are calculated by adding the equation describing the conservation of energy. However, boundary conditions are defined in terms of temperature or heat flux;
- compressible flow options. The program can solve the equation for the stagnant enthalpy and is therefore valid at all Mach numbers. For flows with Mach number less than about 0.3, there is an option that allows the user to designate the flow to be 'weakly compressible'. This invokes two approximations: the energy equation ignores the kinetic terms, and the speed of sound is assumed to be infinite. These approximations have been found to enhance convergence;
- turbulence models. In addition to the k-ε turbulence model which is suitable for high Reynolds number flows, there is a low Reynolds number model. Higher order turbulence models are also available in the software;
- transient flows. Flows varying with time can be modelled.

The radiative heat transfer is modelled in a separate package, called CFX-RADIATION. This package models radiative heat transfer in complex three-dimensional geometries for grey and non-grey systems. Both Monte Carlo and discrete transfer methods are incorporated. CFX-RADIATION can be used as a stand alone package or interfaced with a flow and combustion modelling program such as CFX-F3D.

The following programs have been used for the calculations:

- grid generator: CFX-MESHBUILD;
- solution module: CFX-F3D version 4.1;
- radiation package: CFX-RADIATION;
- graphics module: CFX-VIEW;
- line graph module: CFX-LINEGRAPH;

These programs have been run on a Silicon Graphics Power Challenge workstation.

REFERENCE TO SECTION A.2.4.

[1] CFX-F3D user guide. Computational Fluid Dynamics Services, Oxfordshire, October 1995.

Participants and Contributors to Drafting and Review

Niessen, Hans	FZJ, Germany
Ball, Syd	ORNL, USA
Gao, Zuying	INET, China
Kugeler, Kurt	FZJ, Germany
Kuzavkov, Nikolay	OKBM, Russian Federation
Mejane, Albert	CEA, Saclay, France
Hishida, Makato	JAERI, Japan
Van Heek, Aliki	NERL, The Netherlands
Brey, Larry	IAEA
Cleveland, John	IAEA
Kendall, Jim	IAEA